6th International Conference

on

High-Performance Marine Vehicles

HIPER'08

Naples, Italy, 18-19 September 2008

Dr. Carlo Bertorello (Editor)

University of Naples "Federico II"
Department of Naval Architecture
and Marine Engineering

University of Naples "Parthenope"
Department of Applied Sciences

ISBN **88-901174-9-4**

Printed & Published at Comitato Organizzatore HIPER 08

Department of Naval Architecture and Marine Engineering

University of Naples Federico II,

Via Claudio 21, 80125 Naples, Italy

We acknowledge gratefully the support of our sponsors:

FOREWORD

The 6th HIPER conference is the second HIPER conference to be held in Italy. This reflects the internationally renowned tradition of shipping and naval architecture in this country. It also reflects the attraction of country, culture and the warm-hearted people of Italy who took the burden to organisation this year. My thanks go to Carlo and his team for making HIPER happen this year in Italy.

Volker Bertram

INTERNATIONAL SCIENTIFIC COMMITTEE

Prof. V. BERTRAM, ENSIETA, France

Prof. G. BOCCADAMO, University of Naples, Italy

Prof. D. BRUZZONE, University of Genoa, Italy

Dr. M. CAPONNETTO, Switzerland

Prof. P. CASSELLA, University of Naples, Italy

Prof. M.R.DAVIS, University of Tasmania, Australia

Dr. K. FACH, Germanischer Lloyd, Germany

Prof. A. FRANCESCUTTO, University of Trieste, Italy

Prof. F. FOSSATI, Politecnico di Milano, Italy

Prof. I. GRUBISIC, University of Zagreb, Croatia

Prof. J.A. KEUNING, University of Delft, The Netherlands

Prof. H. KIHARA, National Defence Academy, Japan

Dr. D. LAVIS, CDI Marine Company, USA

Dr. C. LUGNI, INSEAN, Italy

Prof. E. MESBAHI, University of Newcastle, UK

Dr. G. MIGEOTTE, ICARUS Design AS, Norway

Prof. A. PAPANIKOLAOU, NTUA, Greece

Mr. R. PATRICK, WEGEMT, UK

Prof. P. K. SAHOO, Australian Maritime College, Australia

Prof. R.A. SHENOI, University of Southampton, UK

Prof. A. SUBRAMANIAN, Department of Ocean Engineering, IIT Madras, INDIA

Table of Contents

APPROPRIATE TOOLS FOR FLOW ANALYSES FOR FAST SHIPS

Volker Bertram, Germanischer Lloyd, Hamburg/Germany, volker.bertram@GL-group.com

SUMMARY

An overview of computational tools for the hydrodynamic design of fast ships is given. The individual techniques are discussed, and suitable tools are recommended. Trends are discussed and illustrated by some advanced pioneering applications.

1. INTRODUCTION

In this paper we provide some background and examine some of the developments in fluid dynamics for examining flows in and around ships, where the focus is on fast ships. The work builds on earlier work for general ships, *Bertram and Couser (2007).* For the scope of this paper we interpret Computational Fluid Dynamics (CFD) to be a numerical, computer-based simulation of a fluid flow, modelled by solving a set of field equations describing the dynamics of the fluid flow. In this context, the field equations are (in increasing order of simplification), *Bertram (2000):*

1. Navier-Stokes equations. For practical problems, the Navier-Stokes equations can only be solved by making certain simplifications leading to the
2. Reynolds averaged Navier-Stokes equations (RANSE). These can be used to solve viscous fluid flows. Removal of the viscous components of the model yields the
3. Euler equations, which are often used in aerodynamic problems where compressibility is important. For ship-flow simulation they are less widely used. Removal of the compressibility terms gives the
4. Laplace and Bernoulli equations (potential flow). Because the effects of viscosity are often limited to a small boundary layer (for streamlined bodies with no separation), potential flow models are very useful, particularly for free surface flows.

Depending on the field equations being solved, different numerical representations of the fluid domain are may be employed. These can be summarised as follows:

1. Field methods – where the whole fluid domain is discretised, namely Finite Element Methods (FEM), Finite Difference Methods (FDM), Finite Volume Methods (FVM)
2. Boundary element methods (BEM)/panel methods – where only the fluid boundary needs to be discretised
3. Spectral methods

While in principle there could be many combinations of field equations and numerical techniques, in practice we see predominantly RANSE solvers based on FVM for solving viscous flows and Laplace/Bernoulli solvers using BEM or simpler analytic-numeric methods for inviscid, potential flow.

Before discussing the tools and trends in more detail, we will briefly discuss the question of whether and when to choose computational approaches and when model tests. Despite all the progress, and despite some marketing claims, computational methods are not able to consistently predict the power requirements of a ship with the same accuracy as model tests performed in professional model basins. CFD offers insight into flow details, overcoming also limitations of scale effects for viscous flows. CFD should thus be used for a preliminary selection of candidate designs and for aiding the design of hull and appendages. The final power prediction for the hull should be based on model tests in professional model basins.

There is a broad range of problems where CFD techniques are applicable; some of the key areas of interest to the naval architect are described below:

- Hull design, especially fore-body design;
- Design of appendages (alignment and form details of shafts, brackets, etc.);
- Propulsor design (efficiency, avoidance of excessive vibrations and cavitation);
- Unsteady ship motions, particularly seakeeping including slamming
- Aerodynamics, HVAC flows, fire simulation

Due to differences in scale, fluid, geometry etc., different CFD techniques are better suited to some problems than others. There is currently no single CFD technique that can be applied to all problems; for this reason, it is generally necessary to have a range of software tools to hand.

While CFD becomes increasingly important for ship design, simpler traditional analysis tools remain popular, since they frequently provide results with sufficient accuracy at low cost. Among these traditional methods are:

- Slender body theories for resistance (only applicable for slender hulls, e.g. catamaran demihulls)
- Strip theory for the prediction of ship motions.
- Coefficient methods for manoeuvring

2. REVIEW OF CURRENT TRENDS IN CFD METHODS

The majority of commercially available CFD codes are either RANSE / FVM for viscous flows and Laplace / BEM for inviscid potential flow. These will be discussed in greater depth in the following.

Potential flow methods are ideally suited to solve the steady 'wave resistance' problem (steady free-surface flow around ship neglecting viscous effects). Computations on a regular PC take typically 10-30 minutes, allowing rapid design exploration. Typically, panels are placed on the submerged part of the ship's hull and the free surface. If the vessel is operating in a confined waterway, the bottom and sides of the channel can also be modelled by including additional panels on these boundaries or by using mirror images of the panels. State-of-the-art fully non-linear wave resistance codes had become standard ship hull design tools by the mid-1990s whilst panel codes for propeller design had reached design maturity even earlier mainly pushed by developments for the aerospace industry.

First-generation wave resistance codes used only source elements to model displacement; propeller codes from the same era used only vortex or dipole elements to model lift. Later developments added lifting surfaces to wave resistance codes (to handle, for example, the keel of a sailing boat) and source elements to propeller codes (to handle thicker blades and the propeller hub). When lifting surfaces are included, it is also necessary to model the trailing vortex wake left downstream. Considerable effort has been made to accurately model the shape and tip roll-up of this wake as this has a significant impact on the accuracy of the induced drag calculation and interaction with downstream bodies.

For many design applications, RANSE solvers with an appropriate semi-empirical turbulence model are sufficient to model a wide variety of ship flows with sufficient accuracy and confidence to be practically useful. The past decade has seen a general trend towards more sophisticated turbulence models, with Reynolds stress models (RSM) and k-ϖ models now being widely favoured over the older k-ε models. Most RANSE solvers are also able to represent complex free surfaces including breaking waves and air entrapment using volume of fluid (VOF) or, perhaps more commonly, multi-phase flow solutions. RANSE solvers have gained in importance for the analysis of flows around the whole ship hull – an area which until relatively recently used to be the undisputed domain of potential flow solvers – because they can handle the complex geometries of the ship and free surface, including wave breaking.

3. COMMON APPLICATIONS

3.1. Resistance and propulsion (inviscid)

CFD generally gives correct ranking of sufficiently different designs, though absolute values of resistance are normally not accurate enough to exclude the need for towing tank tests. The strength of CFD analysis is that it allows a wider range of alternative hull designs to be tested than would be possible by tank testing alone and is ideally used for selection of promising candidate designs for further testing in the model basin. CFD also gives insight into where and how to modify a design, showing, for example, the detailed pressure distribution over the hull. It is often possible to calibrate a CFD code for a particular design with a "catch all" correlation factor with the experiment results; the correlation factor can be assumed constant for small changes in hull geometry and speed thus allowing further examination of design alternatives using CFD.

The industry workhorse for calculating steady free-surface flows is still the inviscid panel method. The first-generation codes followed Dawson's double-body approach and neither fulfilled the non-linear boundary condition on the free surface nor automatically adjusted the ship to a position of equilibrium. By the end of the 1980's, these drawbacks were overcome with second-generation codes, so-called fully non-linear codes. Amongst the best known of these codes are SHALLO (HSVA), RAPID (MARIN) and Shipflow-XPAN (Flowtech). These codes are regularly used to support design decisions, Fig.1 and Fig.2. They have been successfully applied to a large variety of ship types, including catamarans (with or without foils), frigates, etc.

However, they are not suitable for planing hulls. Over the past decade, these codes have become a standard design tool, increasingly deployed directly at the shipyard by designers rather than dedicated CFD specialists. These codes are particularly useful for the design of the bulbous bow and the forward shoulder of the ship when trying to minimise wave resistance. Although the pressure distribution over the majority of the ship (with the exception of the aft-body) is believed to be quite accurate and wave cuts computed by state-of-the-art codes usually agree well with experiments, the computed wave resistance for real ships may still differ considerably from measured residual resistance or even wave resistance estimated using form factor methods.

Ships with large transom sterns are particularly problematic. There are claims that so-called patch method codes, e.g. KELVIN (SVA Potsdam) and ν-SHALLO (HSVA), overcome these shortcomings by providing better resistance prognoses. These codes employ new techniques to improve accuracy, but very little has been published on these codes. However, there seems to be some general improvement in transom stern treatments that allows the typical rooster-tails, found behind fast ships, to be captured. For low to medium speeds, large transom sterns still pose a problem for these inviscid codes. In these situations, a free-surface RANSE simulation is recommended.

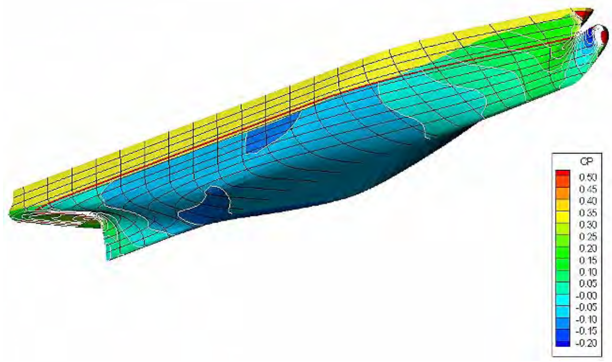

Fig.1: Typical wave resistance code application for fast ferry, HSVA (www.hsva.de)

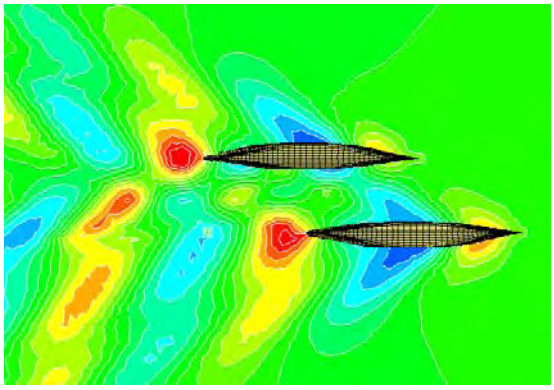

Fig.2: Wave pattern around asymmetric catamaran, HSVA (www.hsva.de)

Usually only the flow fields in the near-field or even in contact with the ship are of interest to the designer aiming to minimize power requirements. However, wave resistance codes have also been used in various projects to develop low-wash ships. This application of panel codes is still in development: design criteria are still to be determined by national and international authorities and the simulations shown so far are usually limited to steady flow conditions neglecting local river topologies and critical unsteady situations such as the deceleration of fast ferries approaching quays. Hybrid methods could be developed matching near-field simulations of the wave generation around the ship (using fully non-linear wave resistance codes or free surface RANSE) and matching the solution to codes used in coastal engineering that simulate the propagation of the wave field in arbitrary shallow-water topology. However, such simulations are rather specific to a particular river or estuary topology. For more general design purposes, a comparison of the near-field wave pattern using a wave resistance cod, usually suffices in practice: if, for a given speed, the waves generated in the vicinity of the ship are reduced, then the wash will also be reduced.

The handling of breaking waves remains a major problem for panel methods, be it for wave resistance or seakeeping. If wave breaking is important, a free-surface RANSE method is the tool of choice. However, maturity, short computational time, ease of grid generation and robustness of the codes explain why panel methods will continue to be the preferred tools for design engineers.

3.2. Resistance and propulsion (viscous)

Flow phenomena such as separation, vortex generation and non-uniformity of the wake field are dominated by viscous effects requiring more sophisticated CFD approaches. In practice, RANSE simulations are normally used where these viscous phenomena are significant. For most design applications, only steady flow is considered.

Most appendages (brackets, rudder, fins, etc.) are located in regions where viscosity cannot be neglected, but where the free surface can be ignored. In these situations CFD allows the simulation at full-scale Reynolds numbers, Fig.3, and thus offers a clear advantage over model tests. The CFD simulation can reveal, for example, how to align propeller shaft brackets so as to minimise resistance and adverse flow patterns in way of the propeller (which cause vibrations).

Similar applications appear for openings in the ship hull such as bow thruster tubes, waterjet inlets etc. Such computations, modelling the flow around appendages, account for a considerable share of viscous flow calculations carried out during design. Although these types of analyses are among the simplest ship applications of RANSE solvers, it is still industry practice to outsource the analysis to experts. This is because the quality of the results is very sensitive to meshing and other analysis parameters which require considerable user experience.

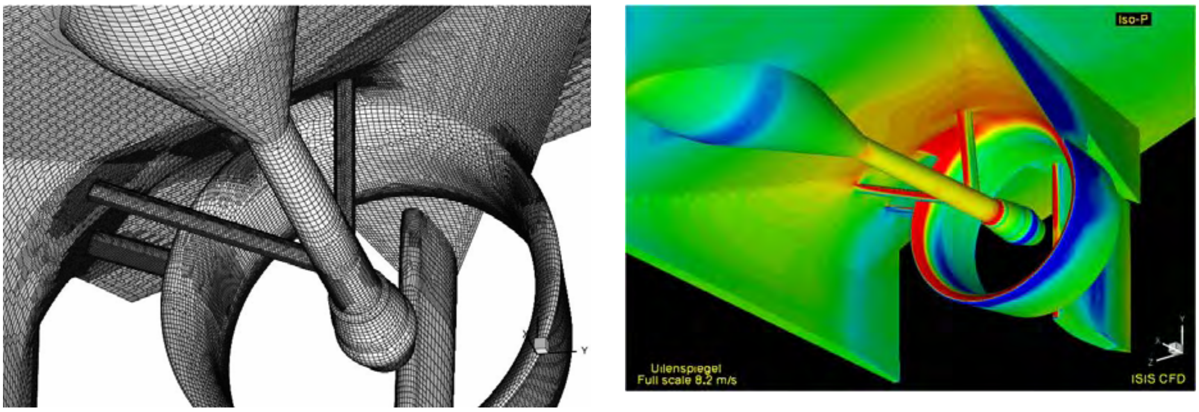

Fig.3: Grid (left) and CFD results for complex appendages, *Queutey et al. (2007)*

RANSE computations that include the effect of propellers (simulated propulsion test) usually model the propeller by applying body forces. Then the propeller geometry is not captured by the grid. Instead each cell in the propeller region is associated with a force representing a contribution to the lateral and rotational acceleration of the water imparted by the propeller. The body forces are often prescribed based on experience or experimental results. Alternatively, panel methods may be employed to predict the thrust and rotation distribution of the propeller. These simulations still appear to be limited to research applications and are not widely used in design. The body force model of the propeller is however frequently employed if the effect of the propeller on appendages in the aft-body is of interest, e.g. for rudders.

The simultaneous consideration of viscosity and wave making has progressed considerably over the past decade. A number of methods try to capture wave making with various degrees of success. The methods for computing flows with a free surface can be classified into two major groups:

- Interface-tracking methods define the free surface as a sharp interface whose motion is followed. They use moving grids fitted to the free surface and compute the flow of the liquid under the free surface only. Problems are encountered when the free surface starts folding or self-intersecting or when the grid has to be moved along walls with complicated shapes (for instance, the geometry of a real ship hull).
- Interface-capturing methods do not define a sharp boundary between liquid and gas and use grids which cover both liquid and gas filled region. The free surface is then determined by either Marker-and-Cell (MAC), Volume-of-Fluid (VOF), level-set or similar schemes.

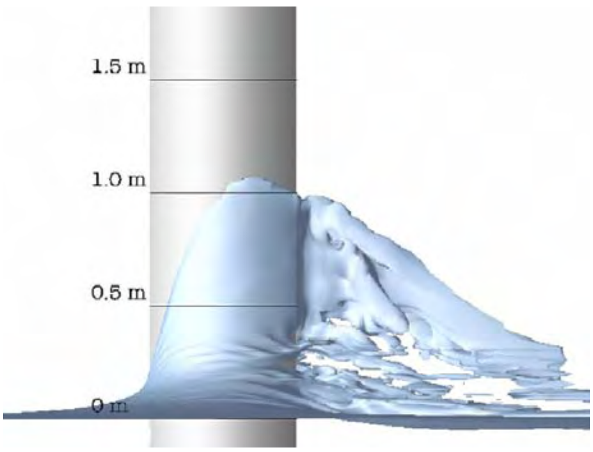

Fig.4: RANSE simulation for a surface-piercing strut, *El Moctar and Bertram (2001)*

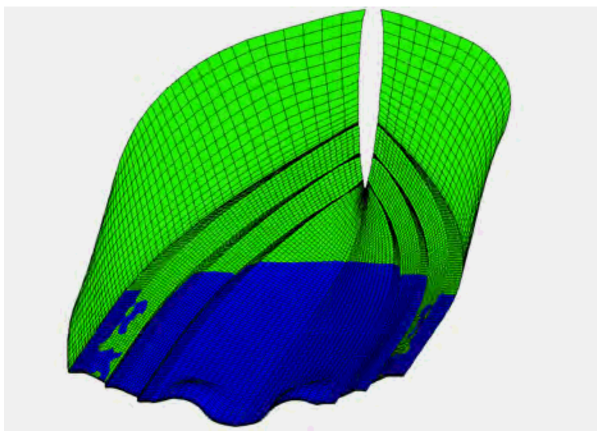

Fig.5: Planing hull simulation, *Caponnetto (2001)*

The trend is clearly towards interface-capturing methods as implemented, for example, in all major commercial RANSE codes. These are the preferred choice whenever wave breaking is of significant importance, e.g. for surface-piercing struts, Fig.4, blunt fore-bodies, etc. Most schemes reproduce the wave profile on the hull accurately, but some problems persist with numerical damping of the propagating ship wave. It is debatable if an accurate prediction of the wave pattern is necessary for practical applications, but certainly everyone would prefer to see this problem overcome. This may require considerably finer resolution and higher-order differencing, i.e. much higher computational times and storage capacities. For global wave system creation, the much cheaper wave resistance codes seem sufficiently accurate and are our recommended tool of choice.

For planing hulls, the classical Savitsky approach remains popular. However, real planing hull geometries violate the inherent assumptions of Savitsky's approach, e.g. concerning constant deadrise angle over the length of the hull. Free-surface RANSE computations yield good results, Fig.5, e.g. *Caponnetto (2000,2001)*. However, such computations require considerable skill (experience with the code), hardware (parallel clusters) and expensive software. The average designer is left with the choice between outsourcing these analyses to a few specialists worldwide or to live with significant errors in traditional simple methods.

3.3. Propeller

Inviscid flow methods (panel methods and vortex lattice methods) have long been used in propeller design as a standard tool yielding information comparable to experiments. Today, RANSE methods also yield good results for 'nice' propeller geometries. However, both panel methods and RANSE deteriorate for extreme propeller geometries due to grid problems. Also, certain types of cavitation still are not satisfactorily reproduced by the computations. Free-surface RANSE method are able to simulate also surface-piercing propellers, Fig.6, *Caponnetto (2003).* Special propulsors such as waterjets are best analysed using RANSE methods, Fig.7.

Most publications for propeller flows focus on open-water simulations. In practice, the propeller should be designed for the effective wake field of the full-scale ship, considering hull-propeller and propeller-rudder interactions. Complete RANSE simulations appear to be unnecessarily expensive and so far yield results no better than hybrid approaches that combine potential flow computations and RANSE.

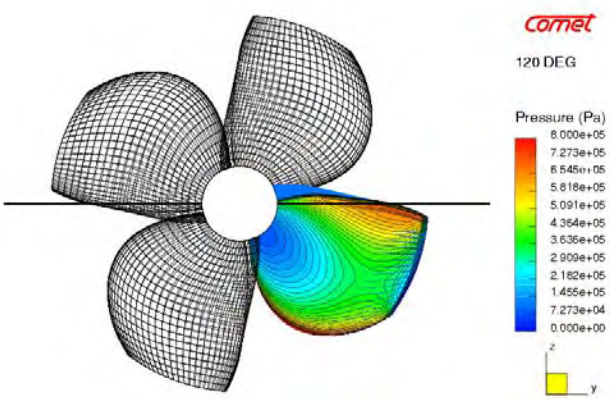

Fig.6: Surface-piercing propeller, *Caponnetto (2003)*

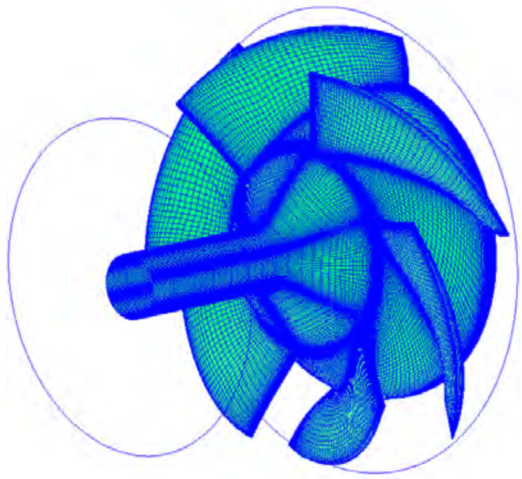

Fig.7: Grid for impeller in waterjet, *Seil (2003)*

3.4. Seakeeping

Although the underlying physical models are generally considered crude, strip methods are able to calculate most seakeeping properties of practical relevance accurately enough for displacement monohulls. Strip methods are generally applicable up to Froude numbers of 0.4. With some corrections, this range can be extended up to Froude numbers of 0.6. For displacement hulls at Froude numbers above 0.4, 2D+t methods (also called high-speed strip methods HSST) are fast and yield good results, *Bertram and Iwashita (1996). Söding (1988,1999)* developed a strip method for catamarans named SEDOS, Fig.8. However, the software is not available and the theory apparently too complex to reproduce.

For catamaran seakeeping, no simple recommendation can be given. 3-d potential flow codes for seakeeping are usually based on Green function methods (GFM). These work well for zero and low Froude numbers, but are computationally expensive for high Froude numbers, unless (unphysical) simplifications are introduced. These code frequently also neglect the real average floating position of the vessel at design speed and compute for the zero-speed floating position. For comparative evaluations, for heave and pitch motions, this approach is OK. Alternatively, 3-d Rankine Singularity Methods (RSM) may be used, but these have problems to enforce correct wave propagation for all speed-frequency combinations in frequency domain and are time-consuming in time-domain simulations.

Some pioneering applications of RANSE computations for ships in regular waves have appeared. Computing power is now the main limiting factor: even when powerful computer clusters are employed, simulations are limited to a few seconds. RANSE simulations make sense for strongly non-linear cases involving green water on deck and slamming, Fig.9, *Fach and Bertram (2006).*

Seakeeping of planing hulls is one area where RANSE simulations would be our recommended choice. Rolla Research in Switzerland and MTG in Germany have presented convincing applications for real planing hull geometries, *Caponnetto (2001), Caponnetto et al. (2003).* The RANSE code employed (COMET in both cases) was reported, in personal communication, to give "good results in 9 out of 10 cases", but such an analysis requires considerable experience with RANSE codes and significant hardware resources, forcing designers to outsource the services to select experts.

Slamming problems, even in two dimensions are very challenging. They involve rapidly changing local hull loads; hydro-elastic effects; interaction between trapped air pockets and the surrounding water; compressibility of water in localised regions, leading to the formation of shock waves; and complex water surface shapes due to the formation of jets. Traditional approaches work well for two-dimensional flows around wedges of suitable deadrise angle, but real ships are 3-d and do not have 'suitable' deadrise angles! CFD simulations have progressed immensely over the last decade, but are still limited to research applications. None of the methods developed so far incorporate all relevant phenomena and adaptive grid techniques appear mandatory to allow realistic computations in an acceptable time. Designers will continue to use the recommendations made by classification societies, which are in turn developed using a mix of full-scale experience, model tests and advanced simulations.

In practice, the ship designer will probably use strip methods for most problems. RANSE methods or non-linear strip methods may be employed by experts for a few specific, highly non-linear problems.

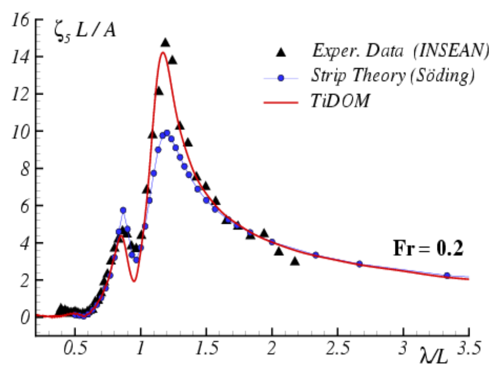

Fig.8: 3-d RSM and multihull strip method applied to a trimaran, *Landrini and Bertram (2002)*

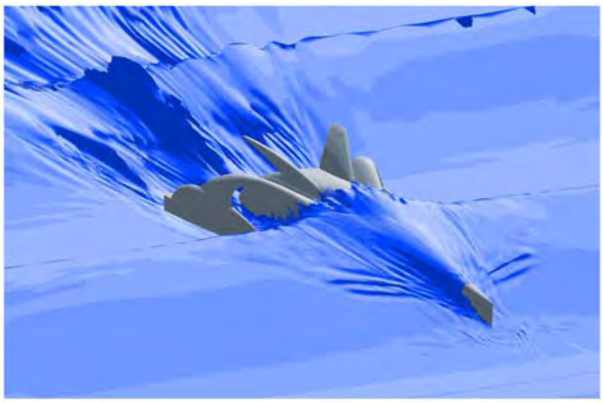

Fig.9: 'Earthrace' trimaran piercing through waves in RANSE simulation, *Ziegler et al. (2006)*

3.5. Manoeuvring

CFD simulations of ship manoeuvring remain limited to advanced research applications. For practical applications, the preferred choice is a force-coefficient method that employs various coefficients to approximate the forces acting on the ship (hull, rudder, propeller, thrusters, etc), *Bertram (2000).* Some of these coefficients can be predicted accurately by CFD, but usually empirical estimates or computations based on slender-body theory suffice.

However, CFD has gained rapid acceptance for rudder design. For many applications, potential flow models enhanced by empirical corrections are sufficient, but for large rudder angles (where the onset of separation is approached) and partially cavitating flows, RANSE simulation is the tool of choice, Fig.10. The designer strives to avoid rudder cavitation for rudder angles up to ±5°. This is the usual operating range for rudders during normal ship course keeping. Cavitation is almost unavoidable for highly loaded rudders at large rudder angles and in these situations it is normal practice to accept it. Modern RANSE codes with cavitation models predict location and extent of cavitation on rudders at full scale very well, Fig.11, *GL (2005), El Moctar (2007).*

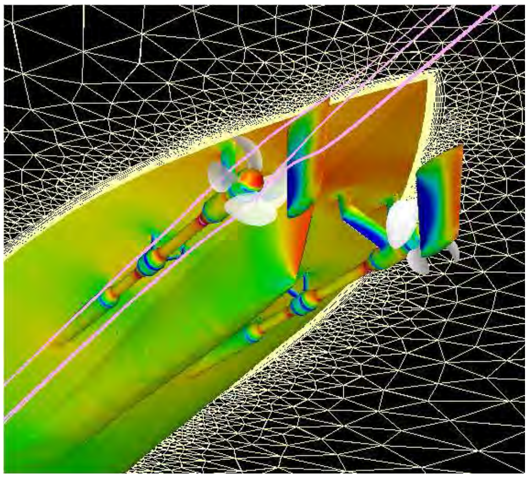

Fig.10: Hull-propeller-rudder simulation, *Hino (2007)*

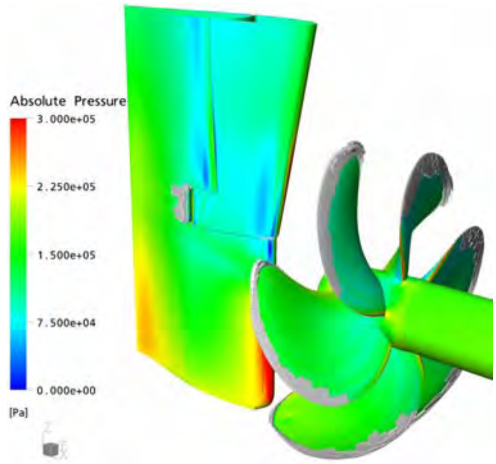

Fig.11: Cavitation on rudder, *El Moctar (2007)*

3.6. Aerodynamics, HVAC and Fire simulations

CFD may be applied to the airflow around the upper hull and superstructure of ships. Topics of interest are wind resistance, wind-over-the-deck conditions for helicopter landing, wind loads and tracing of funnel smoke. The differences between CFD and model-test results are not generally larger than between full-scale and model-scale results. However, due to the time involved in generating the computational mesh and in computing the flow patterns, CFD is usually not economically competitive when compared with routine wind tunnel model tests. For wind forces, empirical estimates usually work well enough for most ships. With decreasing time and cost of grid generation around complex ship super-structures, we may see more CFD applications for ship aerodynamics, but so far such simulations are only applied in research or in combination with other features, for example fire and ventilation flow simulations. Our tool of choice remains thus a wind tunnel in most design applications.

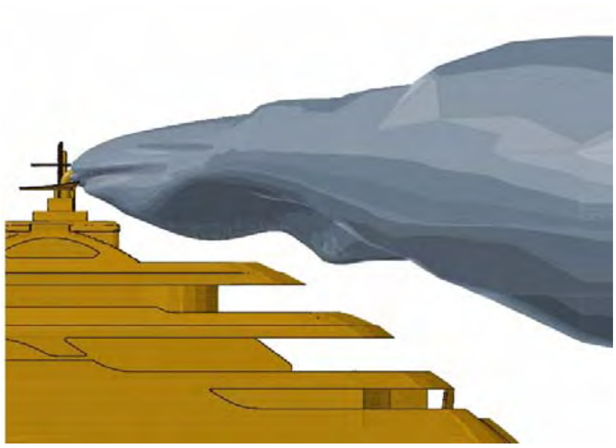

Fig.12: Smoke tracing on fast ferry, *Bertram and Couser (2007)*

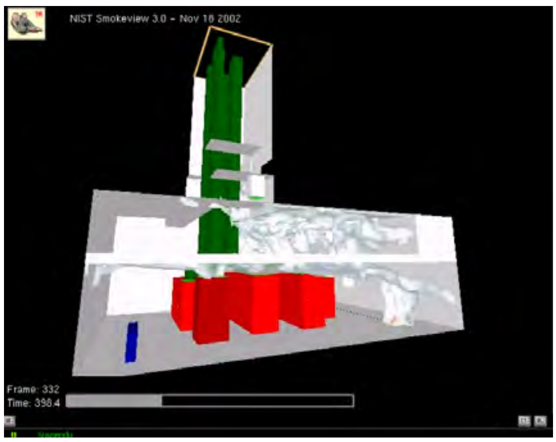

Fig.13: Fire simulation in engine room, *Bertram et al. (2004)*

For fire simulations in ships, different tools are employed, solving additional equations that describe the energy aspects and the combustion (chemical reaction). Applications have graduated from preliminary validation studies to more complex applications for typical ship rooms, e.g. *Bertram et al. (2004).*

The simulations are able to reproduce qualitatively all major fire characteristics, but presently available software and hardware do not yet yield reliable quantitative predictions, particularly not for larger and complex geometries. However, a lot more progress can be envisioned in the next decade and the fire simulations appear already suitable to give some general support both for fire containment strategies and for design alternatives.

The experience of hydrodynamic or aerodynamic flows is not directly transferable to fire simulations. Therefore, fire simulations should be left to experts, preferably those with experience in modelling such scenarios onboard ships.

4. IN-HOUSE OR OUTSOURCE?

Many of the software vendors provide consulting services, and there are specialist consultants and model basins which will perform CFD analyses. The quality of the results depends generally more on the skill of the operator than on the CFD tool used. Sufficient experience with the software, particularly the grid generation, is the decisive factor for the cost and quality of the analysis. As a simple rule of thumb: it becomes cost-effective to do the analyses in-house if you perform more than ten analyses per year and you are able to stay sufficiently up-to-date with the software and technology. If you only perform CFD analyses infrequently, it is advisable to outsource the analysis when the need arises.

To be able to use advanced CFD applications in-house requires:

- Specialist CFD staff, typically requiring several months training to become proficient in the use of an analysis package.
- Software licences for grid generators, flow solvers and post-processing tools (and possibly further codes);
- Significant computer resources, typically distributed PC clusters

This type of investment only pays off if CFD analyses are performed on a regular basis. Vendors frequently downplay the cost of initial training. For design offices and independent shipyards, there is little sense in using RANSE codes; it will normally be more cost-effective to outsource these analyses to specialists. However, inviscid, potential flow, wave resistance codes can be recommended for in-house use if there are ten or more projects per year. Similarly strip methods (or high-speed strip method for fast ships) for seakeeping analyses make sense because the codes can be run on standard PCs, generation of the input data is fast and relatively simple. In any case, generation of input data and interpretation of the result requires an understanding of the fundamental theory behind the code and its assumptions and limitations.

If you decide to buy software and use it in-house, we recommend using commercial software with large user groups in the shipbuilding industry. Commercial codes have the advantage of large user community pools of experience. This usually reduces the (re)occurrence of mistakes. This is not a general law, but a frequently observed fact. Also commercial codes are usually better validated and documented. The larger user community supports continuous development and enhancement of the software, in terms of both features and ease of use. From a business point of view, commercial codes often make more sense than one-off products fresh from universities or in-house researchers.

In evaluating different software products, pay attention to grid generation tools used. Grid generation is usually the most time-consuming (and thus expensive) part of each CFD analysis. Additional licences may be necessary for appropriate professional grid generators. Integrated CFD environments are the most user-friendly option. A noteworthy example is FRIENDSHIP-Framework, *Abt and Harries (2007).*

5. REFERENCES

ABT, C.; HARRIES, S. (2007), *A new approach to integration of CAD and CFD for naval architects*, 6th Conf. Computer and IT Applications in the Maritime Industries (COMPIT), Cortona, pp.467-479, http://www.compit07.insean.it/proceedings/Proceedings.pdf

AZCUETA, R. (2003), *Steady and unsteady RANSE simulations for planing crafts*, 7th Conf. Fast Sea Transportation (FAST), Ischia, http://azcueta.net/Publications/Azcueta_FAST03.pdf

BERTRAM, V. (2000), *Practical ship hydrodynamics*, Butterworth-Heinemann, Oxford, ISBN-13: 978-0750648516

BERTRAM, V.; COUSER, P. (2007), *CFD possibilities and practice*, The Naval Architect, September, pp.137-147

BERTRAM, V.; EL MOCTAR, O.M.; JUNALIK, B.; NUSSER, S. (2004), *Fire and ventilation simulations for ship compartments*, 4th Int. Conf. High-Performance Marine Vehicles (HIPER), Rome, pp.5-17

BERTRAM, V.; IWASHITA, H. (1996), *Comparative evaluation of various methods to predict seakeeping qualities of fast ships*, Schiff+Hafen 48/6, pp.54-58

CAPONNETTO, M. (2000), *Numerical simulation of planing hulls*, 3rd Num. Towing Tank Symp. (NuTTS), Tjärnö, http://www.rolla-propellers.ch/downloads/nutts_2000.pdf

CAPONNETTO, M. (2001), *Practical CFD simulations for planing hulls*, 2nd Conf. High-Perfor-mance Marine Vehicles (HIPER), Hamburg, pp.128-138, http://www.rolla-propellers.ch/downloads/hiper_2001.pdf

CAPONETTO, M. (2003), *RANSE simulations of surface piercing propellers*, 6th Numerical Towing Tank Symposium (NuTTS), Rome, http://www.rolla-propellers.ch/downloads/nutts_2003.pdf

CAPONNETTO, M.; SÖDING, H.; AZCUETA, R. (2003), *Motion simulations for planing boats in waves*, Ship Technology Research 50, pp.182-198

EL MOCTAR, O.M. (2007), *How to avoid or minimize rudder cavitation*, 10th Num. Towing Tank Symp. (NuTTS), Hamburg

EL MOCTAR, O.M..; BERTRAM, V. (2001), *RANSE simulations for high-Fn, high-Rn free-surface flows*, 4th Numerical Towing Tank Symposium (NuTTS), Hamburg

FACH, K.; BERTRAM, V. (2006), *High-performance simulations for high-performance ships*, 5th Int. Conf. High-Performance Marine Vehicles (HIPER), Launceston, 2006, pp.455-465

GL (2005), *Recommendations for preventive measures to avoid or minimize rudder cavitation*, Germanischer Lloyd, Hamburg,

HINO, T. (2007, *Marine CFD research at SRI/NMRI – Review and prospects*, 10th Numerical Towing Tank Symposium (NuTTS), Hamburg

LANDRINI, M.; BERTRAM, V. (2002), *Three-dimensional simulation of ship seakeeping in time domain*, Jahrbuch der Schiffbautechnischen Gesellschaft, Springer

QUEUTEY, P.; DENG, G.; VISONNEAU, M. (2007), *Study of scale effects around fully-appended ships with an unstructured RANSE solver*, 6th Conf. Computer and IT Applications in the Maritime Industries (COMPIT), Cortona, pp.260-274

SEIL, G.J. (2003), *RANS CFD for marine propulsors: A Rolls-Royce perspective*, 6th Numerical Towing Tank Symposium (NuTTS), Rome

SÖDING, H. (1988), *Berechnung der Bewegungen und Belastungen von SWATH-Schiffen und Katamaranen im Seegang*, IFS Report 483, Universitat Hamburg (in German)

SÖDING, H. (1999), *Seakeeping of multihulls*, 1. Int. Conf. High-Performance Marine Vehicles (HIPER), Zevenwacht

ZIEGLER, W.; FACH, K.; HOFFMEISTER, H., EL MOCTAR, O.M. (2006), *Advanced analyses for the EARTHRACE project*, 5th Conf. High-Performance Marine Vehicles (HIPER), Launceston, pp.101-108

INFLUENCE OF HEEL ON YACHT SAILPLAN PERFORMANCE

Fabio Fossati, Full Professor, Wind Tunnel - Politecnico di Milano, Italy, fabio.fossati@polimi.it
Sara Muggiasca, Researcher, Department of Mechanical Engineering, Politecnico di Milano, Italy

SUMMARY

This paper presents research activities carried out by the authors to investigate the influence of heel on yacht sailplan performance by means of wind tunnel test techniques and CFD numerical simulations. Main results concerning wind tunnel testing activities carried out in the Politecnico di Milano Twisted Flow Wind Tunnel investigating the upwind performance of sails both heeled and upright are presented. Finally the heeled plane approach which is largely used in the aerodynamic models available up to-date for VPP use is outlined and discussed

.

1. INTRODUCTION

Sailing yacht heeling effect on sails aerodynamics represents one of the tougher issue of upwind aerodynamics ([1] [3] [6] [7]) and some discussions have been recently found in literature] [8]. In fact this is a very complex topic with strong implications for methodologies to compute sailboat aerodynamics for Velocity Prediction Program design tool.

This paper deals with research activities carried out at Politecnico di Milano Twisted Flow Wind Tunnel in order to investigate the performance of upwind sails in heeled condition. This work is a part of an overall and comprehensive general research program started in 2005 with partial funding from the ORC with the aim to investigate a series of rig planform variations in mainsail roach and jib overlap in order to overcome some perceived inequities in the ratings of boats of various rig design racing under the International Measurement System (IMS).

The results of this investigation are used to assist the International Technical Committee (ITC) in changing the formulations in the ORC INTERNATIONAL VPP sail aerodynamic model.

This paper in the first part presents test arrangements, procedures and methodologies that have been carried out both for systematic gathering of wind tunnel data and subsequent analysis in order to describe aerodynamic behaviour of different sailplans both in upright and heeled condition. Some interesting experimental results and trends are presented and discussed.

Differences of sail performance at different heel configurations outlined by means of wind tunnel test results are clarified with the aid of numerical results obtained using RANS methods performed on the tested sailplan configurations. For this reason, during the tests authors gave special attention to measure also sails flying shapes in order to provide sails geometry useful for CFD purposes.

Paper presents also a detailed description of methods and techniques used by the authors in order to detect sails shapes.

Finally the so called “heeled plane approach” [3], [6], [7] which is largely used in the aerodynamic models available up to-date for VPP use is outlined and discussed.

2. TWISTED FLOW WIND TUNNEL

With the purpose of supporting, with a state of the art facility, the world-wide recognised excellence of Politecnico di Milano research in the field Wind Engineering as well as general Aerodynamics, Politecnico di Milano decided to design and build a new large wind tunnel having a very wide spectrum of applications and very high standards of flow quality and testing facilities. The Wind Tunnel has been fully operative since September 2001 and from the first year of operations has been booked for sailing yacht design applications.

Figure 1 shows an overview of the P.d.M. facility: it’s a closed circuit facility in a vertical arrangement having two test sections, a 4 x 4m high speed low turbulence and a 14 x 4m low speed boundary layer test section.

A peculiarity of the facility is the presence of two test sections of very different characteristics, offering a very wide spectrum of flow conditions, from very low turbulence and high speed in the contracted 4 x 4m section ($Iu<0.15\%$, $V_{max}=55$ m/s), to earth boundary layer simulation in the large wind engineering test section.

With reference to yacht sails aerodynamic studies, they are performed in the boundary layer test section which allows for testing large scale models (typically 1:10 -1:12 for IACC yacht model) with low blockage effects at maximum speed of 15 m/s.

A very important peculiarity concerning yacht aerodynamics is that since the wind speed increases with height due to the boundary layer phenomena and the boat speed is constant, this means that the apparent wind speed incident onto a yacht also increases with height and, in addition, its direction changes, rotating away from the yacht’s heading with increased height.

This is a very important topic in wind tunnel testing on sailing yacht scale models, that has to be carefully considered, because the forces developed by the sail plan are due to the apparent wind incident onto the sails and

the sail shape and trim is strongly related to the apparent wind profile.
Therefore, for proper similitude modelling, the apparent wind velocity shear and twist profile has to be reproduced in the wind tunnel for testing stationary models.

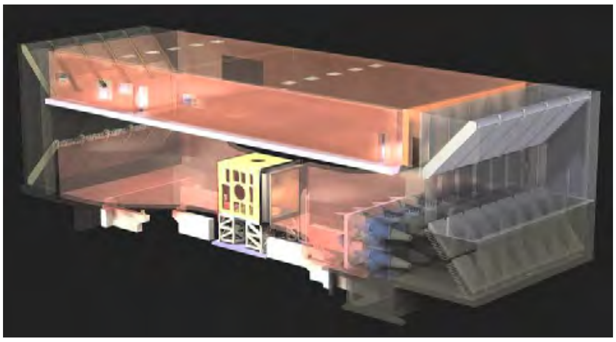

Figure 1. Politecnico di Milano Wind Tunnel

While the variation in wind speed with height can be modelled in the wind tunnel using similar procedures as for conventional wind engineering testing, the twisted flow is a more difficult task to deal with for a stationary wind tunnel yacht model, because the true and apparent wind speeds are coincident.
At this purpose the so called Twisted Vanes Device has been designed: the basic idea of the design process is to generate a large-scale vortex with its spin axis aligned with the wind tunnel steady state flow direction, resulting in a twisted flow area corresponding to the model location.
Moreover, basic design requests were the following:

- easy to adjust
- easy to install/remove
- economical solution both in terms of first installation and running costs

The originality of the Politecnico di Milano Twisted Flow Device compared to the other solutions [4] is the central positioning of the device, not occupying the entire tunnel section. In fact, the role of the Twisted Flow Device is just to turn left the lower part and to turn right the upper part of the flow. The side flow not passing though the vanes is allowed to move vertically balancing the flow rate.
Fig. 2 shows the Twisted Flow Device in the tunnel boundary test section.
A complete model, consisting of yacht hull body (above the waterline) with deck, mast, rigging and sails is mounted on a six component balance, which is fitted on the turntable of the wind tunnel (fig. 5). The turntable is automatically operated from the control room enabling a 360° range of headings.

3.1 Test arrangements and measurements setup

The large size of the low speed test section enables yacht models of quite large size to be used, so that the sails are large enough to be made using normal sail making techniques, the model can be rigged using standard model yacht fittings and small dinghy fittings without any additional work becoming too small to handle, commercially available model yacht sheet winches can be used and, most important, deck layout can be reproduced around the sheet winch, allowing all the sails to be trimmed as in real life.

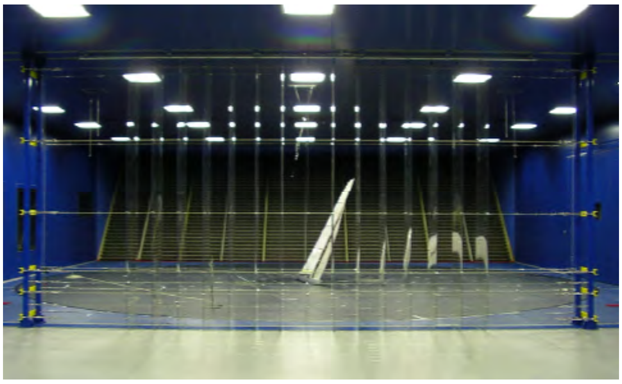

Figure 2. Twisted Flow Devices

Moreover the model yacht drum type sheets are operated through a 7 channel proportional radio control system, except that the aerial is replaced by a hard wire link and the usual joystick transmitter is replaced by a console with a 7 multi-turn control knobs that allow winch drum positions to be recorded and re-established if necessary. The sheet trims are controlled by the sail trimmer who operates from the wind tunnel control room.
Figs. 3 show a typical model mounted in the wind tunnel.

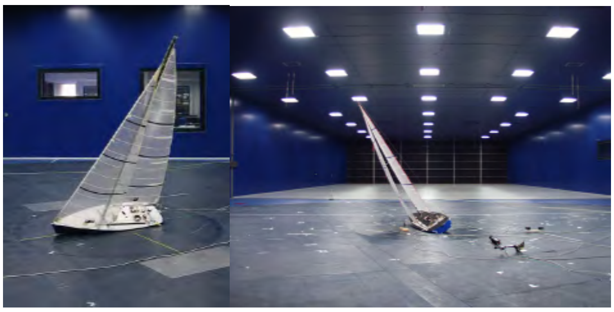

Figure 3. Yacht model in the boundary layer test section

A high performance strain gage dynamic conditioning system is used for balance signal conditioning purposes.
The balance is placed inside the yacht hull in such a way that X axis is always aligned with the yacht longitudinal axis while the model can be heeled with respect to the balance.
The wind tunnel is operated at a constant speed after the wind speed profile and wind twist have been properly tuned considering the desired targets, which are previously calculated considering the potential boat performance at different true wind speeds and yacht courses. As previously said the velocity profile can be simulated by means of independent control of the rotation speed of each fan joined to the traditional spires & roughness technique, while the twist can be simulated by twisting the flexible vanes by different amounts over

the height range. The wind tunnel speed is most usually limited by the strength of the model mast and rigging and the power of the sheet winches.
Data acquisition can be performed in several ways: the usual procedure provides direct digital data acquisition by means of National Instruments Data Acquisition Boards (from 12 to 16 bits, from 8 differential channels up to 64 single-ended) and suitably written programs according to Matlab standards.
The data acquisition software calculates the forces and moments using the dynamometer calibration matrix. The forces are shown in the virtual panel designed on the computer screen in real time so that the sail trim can be optimised because the effects of trimming the sails on the driving and heeling forces can be directly appreciated.
The model is set at an apparent wind angle and at a fixed heel. After a sail trim has been explored, actual measurements are obtained by sampling the data over a period specified by the test manager (generally 30 seconds) with a sample frequency specified too. An important feature of wind testing procedure is that the model should be easily visible during the tests so that the sail tell-tales can be seen by the sail trimmer. For this purposes some cameras placed in the wind tunnel as well as onboard allow a view similar to the real life situation (fig.4).

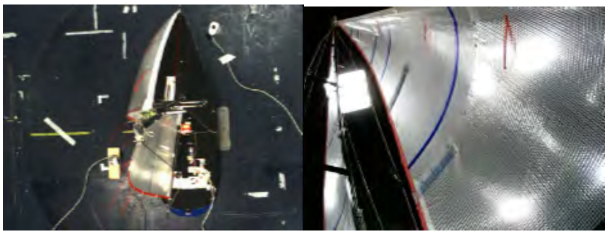

Figure 4. Wind tunnel top and deck camera view during testing

In order to correlate force measurement readings and the sail shape and in order to provide input data for CFD calculations, an in-house photogrammetric measuring system has been developed to recover flying shapes during tests (fig.5).

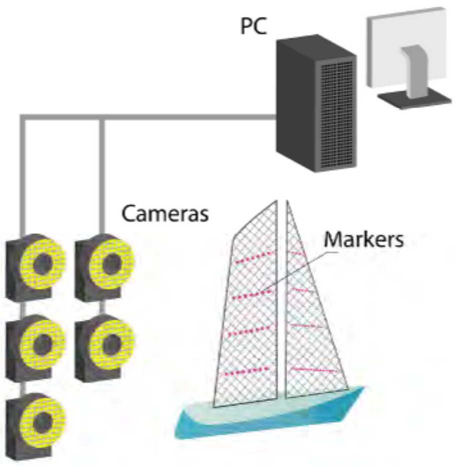

Figure 5. Flying shape measurement system layout

The photogrammetry based technique is relatively fast during the tunnel occupancy phase and in principle it requires only three digital images be recorded from useful points. In order to overcome difficulties arising from sails overlapping especially in downwind configurations and in order to be able to have at least three useful points in each part of the sails the system is equipped with eight cameras. For the present tests this system is composed of five cameras, filming reflective targets placed on sails in sync, and a PC equipped with acquiring and processing custom-made software. Cameras have resolution of 1392 x 1040 pixels, greyscale 1/2” CCD sensor, 17 fps (frames per second). Each of them mounts an optical zoom and a high intensity infrared (830 nm) LED illuminator, triggered to simultaneously flash with cameras frame rate. In order to reduce at the best cameras vibrations induced by the wind, it was decided to fix cameras on photographic heads constrained to the available stiffest points in the wind tunnel (fig.6).

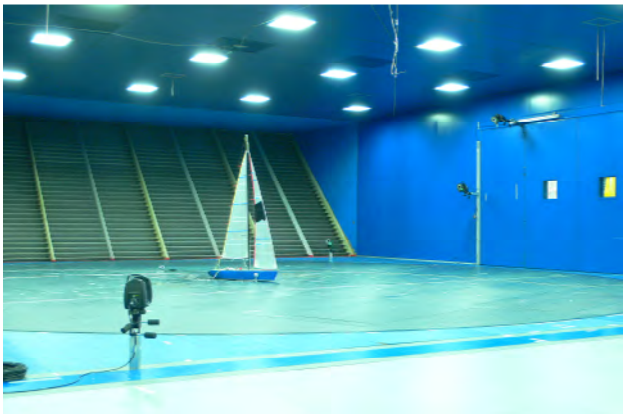

Figure 6. Yacht model and cameras in the wind tunnel

High reflective markers are glued on 8 horizontal sections of each sail plus one on the top, on both windward and leeward side (fig 7).

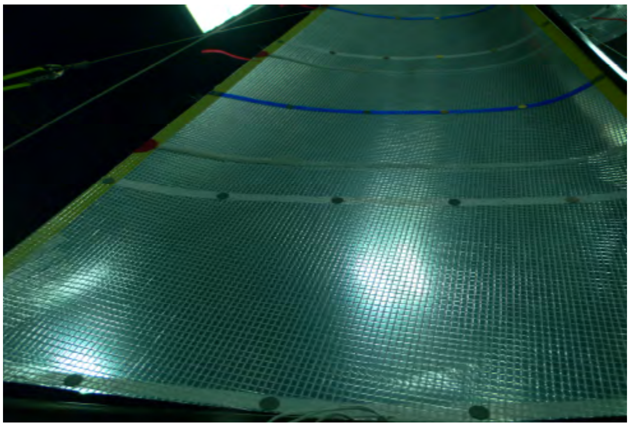

Figure 7. Reflective markers on the main

Then, a custom-made software performs real time blob detection and stores images sourced from cameras on a hard disk.

As a result of this routine a table with the 2D blob detected coordinates is available for post process.

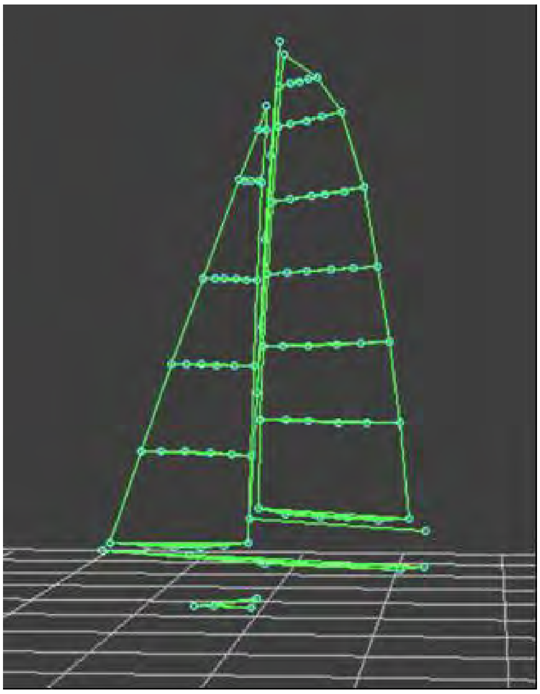

Figure 8. Sails flying shape detection process

Cameras have been previously calibrated using a custom built calibration frame.
The 3D marker points coordinate for each sail are then obtained by means of a DLT (Direct Linear Transformation) algorithm, reaching marker position with an uncertainty equal to 0,5 mm.
Marker coordinates are obtained as mean of their position over a 20[sec] acquisition period with 17 Hz acquisition rate.
Then this 3D points array are used for surface modelling as well as to extract the trim parameters as explained in [5].

3.2 Upwind sails testing procedure

For each apparent wind angle tested the first task was to reach the maximum driving force potentially achievable. At the same time it was observed the influence of the sails trimming changes using the data acquisition program that visualizes the forces acting on yacht model in real time.
Trimming the sails to obtain optimum sailing points proved to be the most challenging task of the testing process.
Attempts were made to carry out the job as systematically as possible. Firstly, the maximum drive point was found by trimming the sails to the best using the cameras views, the tufts on the sails and the force measurements output data.
From there, the heeling force would be reduced to simulate the trim of the sails for windier conditions. In fact in real life windy conditions, to keep the optimum heeling angle, heeling force has to be reduced by the crew. The sail trimming routine adopted was to choose the mainsail traveller position (initially quite high up to windward) and then to vary the incidence and the twist of the mainsail to power or de-power it, by over-trimming or easing the main traveller and main sheet.
The genoa was initially trimmed in order to have the maximum driving force condition and was fixed varying the mainsail shape.
Once a specific trimming condition is obtained using the real time force and moments values displayed by the data acquisition system, a 30 seconds acquisition sampling has been performed with 100Hz sample frequency, and both time histories and mean values of each measured quantity have been stored in a file.
The usual way of analysing data is to compare non dimensional coefficients, allowing to compare the efficiency of sails of different total area at different conditions of dynamic pressure. The first analysis performed is the variation of driving force coefficient Cx with heeling force coefficient Cy. They are given by the expressions:

$$Cx = \frac{Fx}{\frac{1}{2}\rho S v^2}$$

$$Cy = \frac{Fy}{\frac{1}{2}\rho S v^2} \qquad (1)$$

where

- Fx is the driving force
- Fy is the heeling force
- S is the actual sail area
- V is the wind speed
- ρ is air density

As an example fig. 9 shows a comparative plot of Cx versus Cy for the apparent wind angles tested. Each run (with its corresponding measured values) is shown for each AWA.

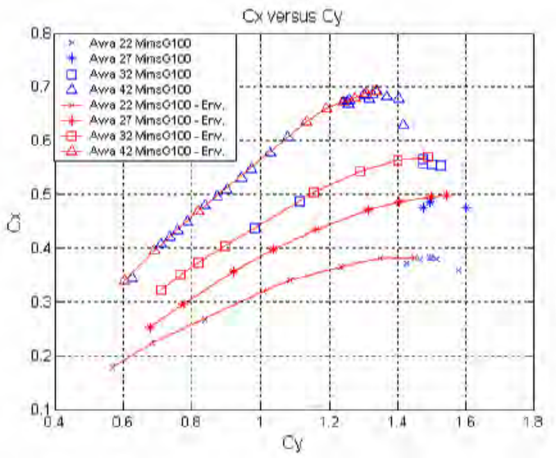

Figure 9: Driving force coefficient vs heeling force coefficient

It can be seen that there are some sails settings at the highest values of heeling force coefficients where the driving force is lower than the maximum value. These non optimum values were obtained by oversheeting the

sails such that the mainsail generally had a tight leech and the airflow separated in the head of the sail.
Therefore a selection was made to choose those points that formed the envelope curves (maximum Cx for a given Cy value) for each apparent wind angle (fig. 9).
Envelope curves have been drawn through the test points with the greatest driving force at a given heeling force. An example is reported in fig. 10.

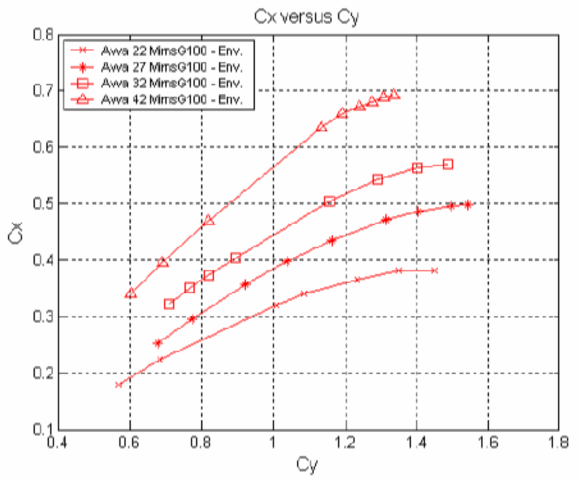

Figure 10. Driving force coefficient envelope vs heeling force coefficient

For the purpose of the analysis, in the following only these points will be used.
The centre of effort height, Ceh, is obtained by dividing the roll moment by the heeling force component in the yacht body reference system:

$$Ceh = \frac{Mx}{Fy}$$

As an example, a plot of its variation with heeling force for all angles can be seen in fig 11. Both all the measured values and the envelope of the points corresponding to maximum driving force at each heeling force are reported. The results are given in terms of ratio between centre of effort height from boat deck and mast height (P+BAS). The centre of effort longitudinal position, Cea, is obtained by dividing the yaw moment by the heeling force component in the yacht body reference system:

$$Cea = \frac{Mz}{Fy}$$

As an example, a plot of its variation with heeling force for all angles can be seen in fig 12. Both all the measured values and the envelope of the points corresponding to maximum driving force at each heeling force are reported. Cea is measured from the origin of the balance (positive to bow) which is placed behind the mast.
The results are given in terms of ratio between centre of effort longitudinal position from balance origin and yacht model waterline length.
It can be seen that Cea moves forward as Cy reduces. This is explained by the way the sails are de-powered.

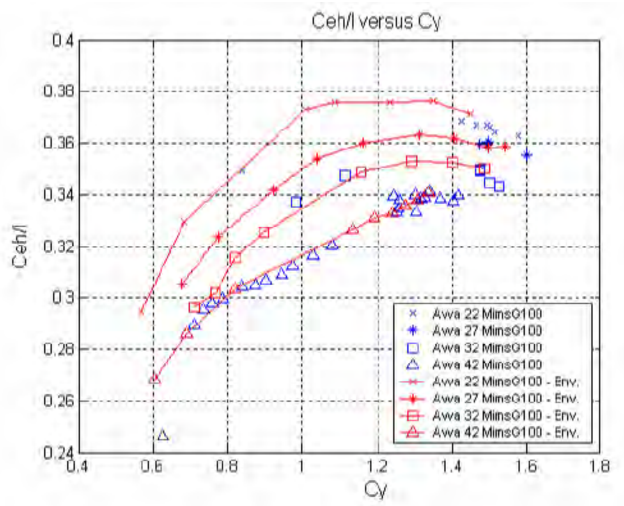

Figure 11. Centre of effort height vs heeling force coefficient

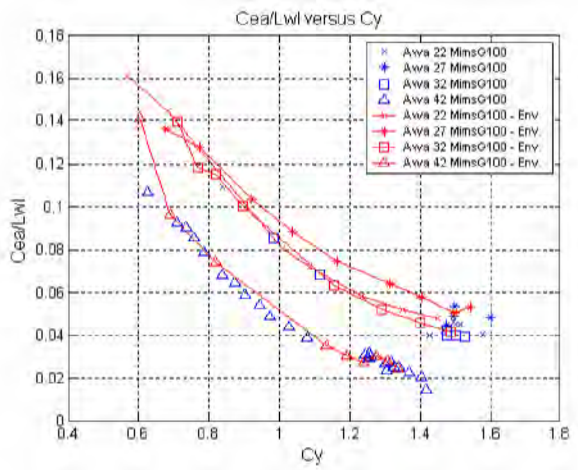

Figure 12. Centre of effort longitudinal position vs heeling force coefficient

3. SAILPLANS TESTED

According to the overall activities program 3 different main sails (with the same actual area but 3 different roaches) named Mims, Mhr, and Mtri and 3 different jibs with different overlap (named G100, G135 and G150) have been combined in a 92% fractionality configuration.. Note that the Mims mainsail has the IMS maximum allowed roach without any penalty applied according to the IMS rule.
Mainsail Roach level has been defined according to:

$$Roach = \frac{Area^{IMS}_{Main}}{P*E/2} - 1 \qquad (2)$$

Mainsails codes and dimensions are defined as follows:

	Roach	P	E
Mims	0.193	1.94	0.637
Mhr	0.335	1.94	0.571
Mtri	0.096	1.94	0.695

Tab. 1

Jib codes are defined as follows:

	Overlap
G100	100%
G135	135%
G150	150%

Tab. 2

All configurations were tested in upright condition and at 30° heeling too.
Only the IMS mainsail+135% jib have been tested at 15° heeled condition too.
Table 3 summarises the situation.

	Upright	Heel 15°	Heel 30°
Mims G100	X		X
Mims G135	X	X	X
Mims G150	X		X
Mhr G100	X		X
Mtri G100	X		X

Tab. 3

Figures 13-17 show the different sailplans during the tests.

Figure 13. MhrG100 sailplan

Figure 14. MtriG100 sailplan

Figure 15. MimsG100 sailplan

Apparent wind angles were chosen to be 22°, 27°, 32° and 42° which cover the upwind range.
For each apparent wind angle, sail trimming during the wind tunnel tests were performed according to the abovementioned procedure. All the sails trimming have been performed by Gigio Russo of North Sails Italia using the remote control console for model winches. At the same time it was observed the influence of the sails trimming changes using the data acquisition program that visualizes the forces acting on yacht model in real time.

Figure 16. MimsG150 salplan

Figure 17. MimsG135 sailplan

4. EXPERIMENTAL RESULTS

Using the aerodynamic driving force and aerodynamic heeling moment Fx and CMx component in the yacht body reference system the corresponding coefficients have been obtained as follows:

$$C_x = \frac{F_x}{\frac{1}{2}\rho S V_a^2} \qquad CM_x = \frac{M_x}{\frac{1}{2}\rho S H_{mast} V_a^2} \tag{3}$$

where

- Fx is the driving force
- Mx is the heeling moment
- S is the actual sail area
- Hmast is the mast height from the deck
- V_a is apparent wind speed
- ρ is air density

The apparent wind speed V_a and apparent wind angle are evaluated in the heeled plane perpendicular to the mast according to:

$$V_a = \sqrt{(-V_t\cos\gamma)^2 + (V_t\sin\gamma\cos\phi)^2} \qquad AWA = \text{arctg}\left(\frac{V_t\sin\gamma\cos\phi}{-V_t\cos\gamma}\right) \tag{4}$$

where γ represent the true wind angle (yaw angle), V_t is the wind tunnel flow velocity corresponding to the mean dynamic pressure at each run and ϕ is the heel angle.

Figures 18-21 show test results relevant to the mainsail medium roach and medium overlapping jib (MimsG135) sailplan in terms of envelope curves (maximum Cx for a given Cmx value) for each apparent wind angle.

In particular in each figure results are reported with reference to each apparent wind angle tested in upright and heeled condition too: in this case the resulting apparent wind angle according to eqn. 4 is shown in the legend.

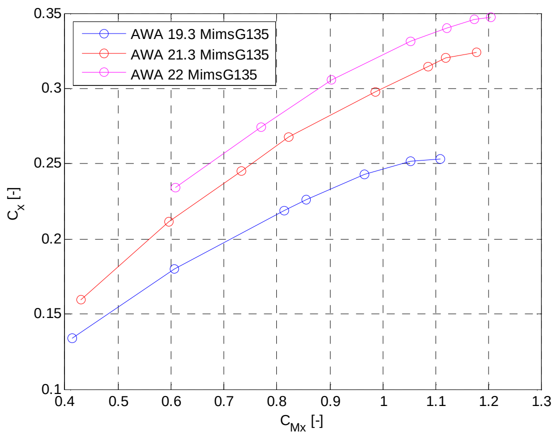

Figure 18. MimsG135 sailplan

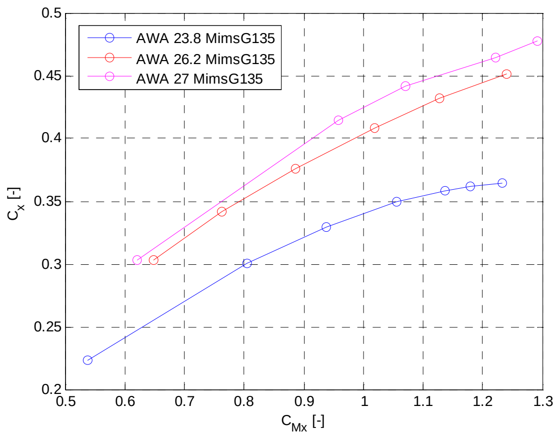

Figure 19. MimsG135 sailplan

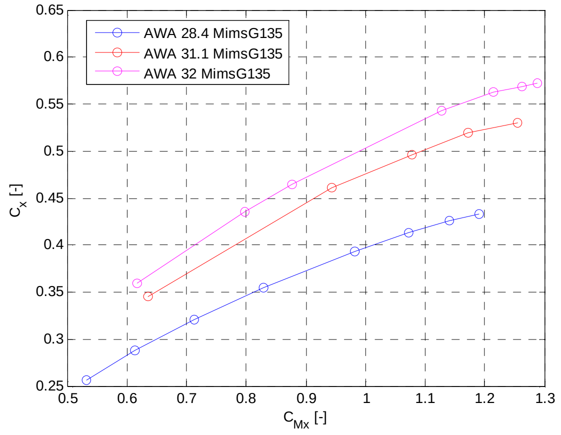

Figure 20. MimsG135 sailplan

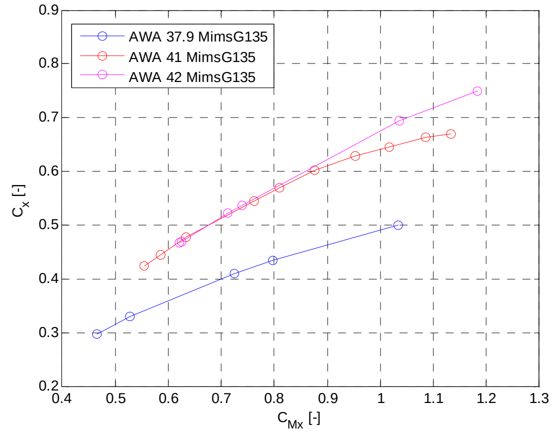

Figure 21. MimsG135 sailplan

As can be seen the effect of heel is to reduce the maximum driving force produced by sails at each apparent wind angle tested and this effect increases with the heeling angle increasing.
The same situation has been found for each sailplan tested: as an example figures 22-25 refer to max roach mainsail with non overlapping jib (MhrG100).

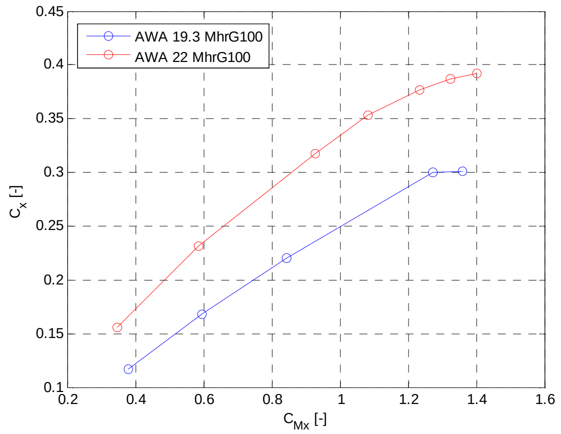

Figure 22. MhrG100 sailplan

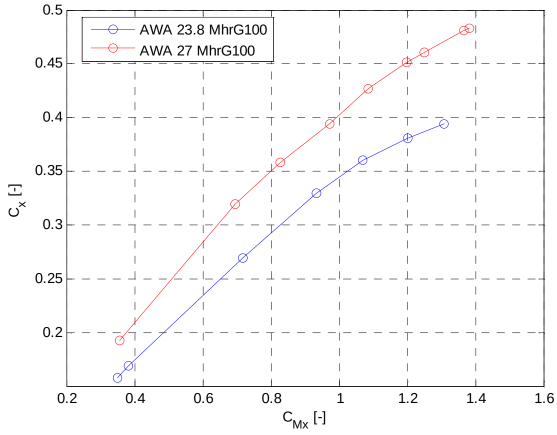

Figure 23. MhrG100 sailplan

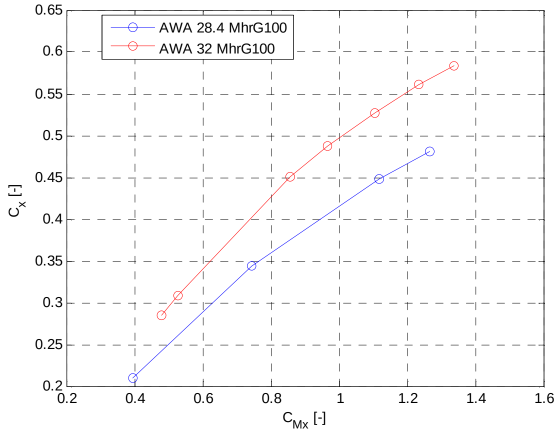

Figure 24. MhrG100 sailplan

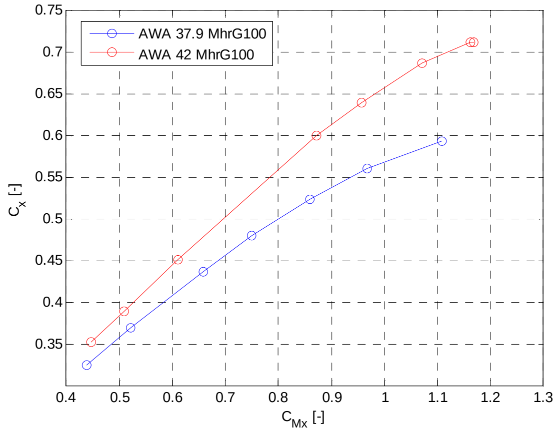

Figure 25. MhrG100 sailplan

Another interesting feature is that the reduction in driving force is more evident in fully powered condition than in the depowered ones and this is a general trend for each sailplan tested.
With reference to the mainsail medium roach and medium overlapping jib (MimsG135) sailplan figure 26 shows the ratio between the driving force coefficient at different heel angle and the same quantity in upright condition for each apparent wind angle relevant to the

sailplan trim allowing for the maximum driving force. These ratio can be interpreted as a sort of efficiency parameter of the sailplan heeled condition.

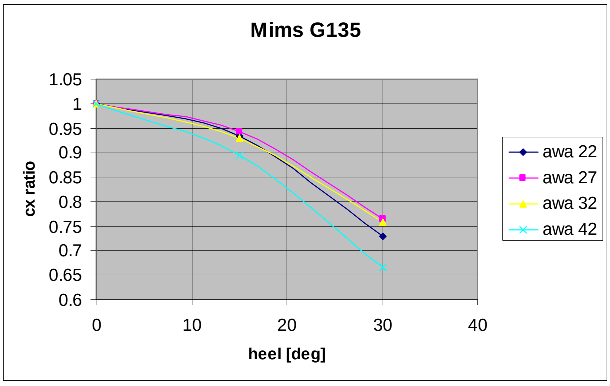

Figure 26. MimsG135 sailplan

Figure 27 is relevant to heeling force coefficient ratio of the same (MimsG135) sailplan.

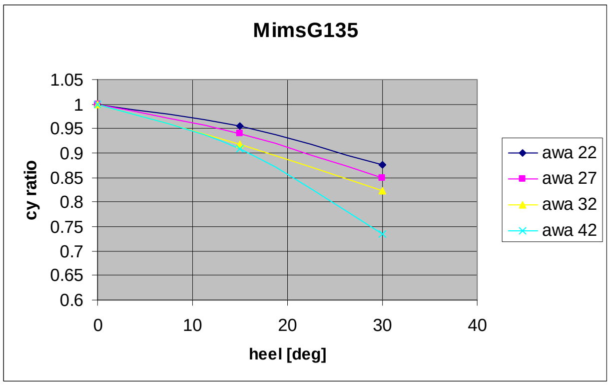

Figure 27. MimsG135 sailplan

All the performed tests revealed a decrease in sailplan driving force when the sailplan heels (figures 28-31).

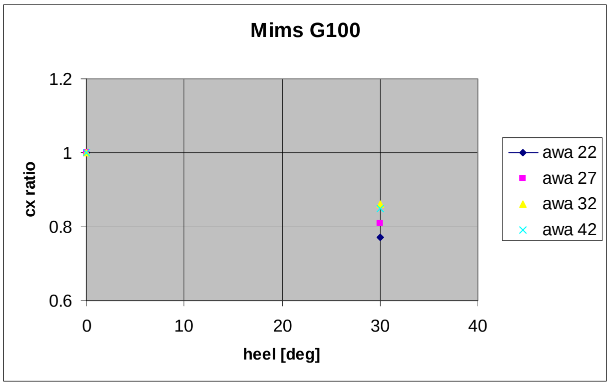

Figure 28. MimsG100 sailplan

In order to gain further understanding of the sailplans aerodynamic behaviour experimentally outlined numerical simulations have been carried out using RANS methods. In particular numerical simulations have been performed by means of FLUENT CFD code with the realizable k-ε turbulence model. A numerical model of each tested sailplan including hull and rigging has been carried out and put in the numerical model of the wind tunnel (figure 32). The boundary conditions were set to give a wind velocity profile similar to that in the wind tunnel.

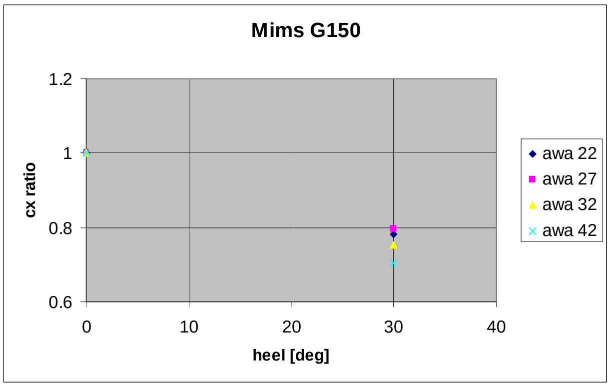

Figure 29. MimsG150 sailplan

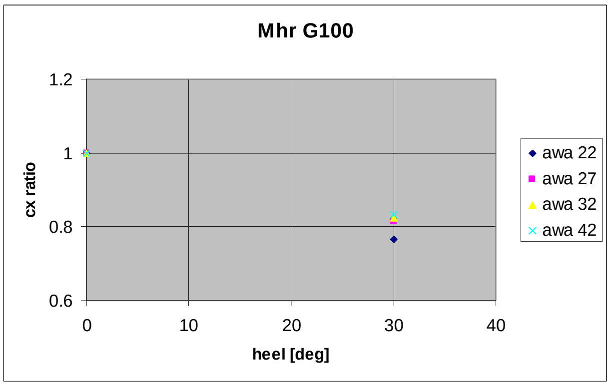

Figure 30. MhrG100 sailplan

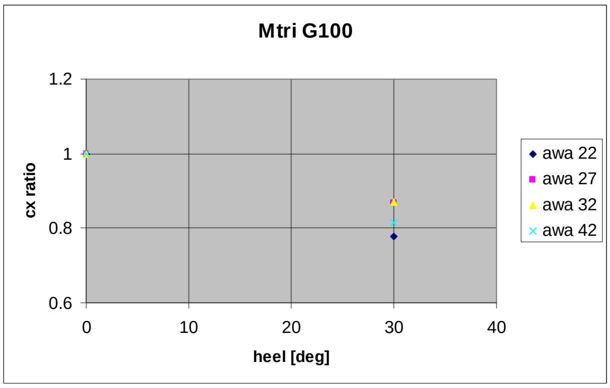

Figure 31. MtriG100 sailplan

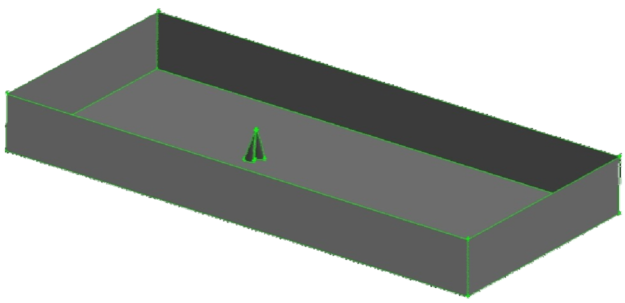

Figure 32. Wind tunnel and yacht numerical model

In the following, for lack of space, results concerning only the medium roach mainsail with non overlapping jib (MimsG100) will be reported.
Fig. 33 shows numerical model of sails including yacht hull, which has been used to simulate yacht upwind behaviour at different heel angles (sailing upright, 15°heeled and 30° heeled) .
Numerical simulation have been performed at 22° apparent wind angle and for each of the heel angle considered the flying shape corresponding to maximum drive condition trimming at different heel angle has been used in order to generate the numerical mesh.

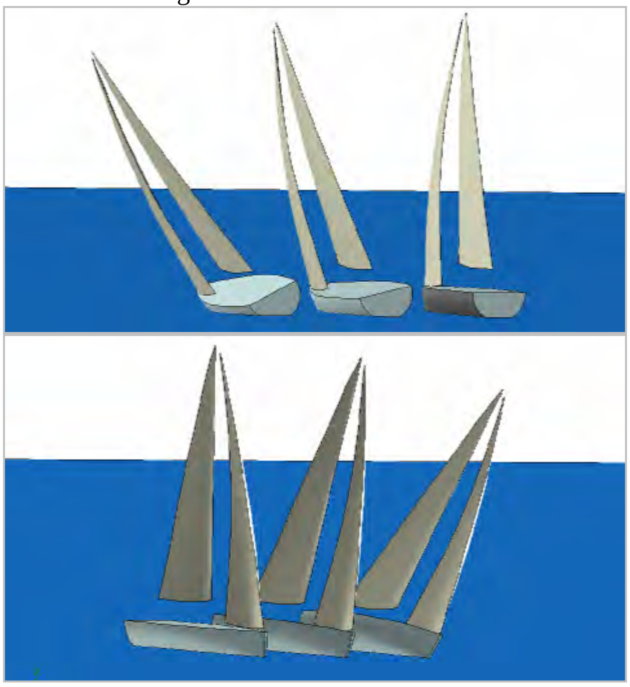

Figure 33. MimsG100 sailplan numerical model

Figures 34-35-36 show the MimsG100 sailplan leeward side pressure coefficient contour respectively for upright, 15°heeled and 30° heeled condition concerning 22° apparent wind angle close hauled sailing condition analysis.

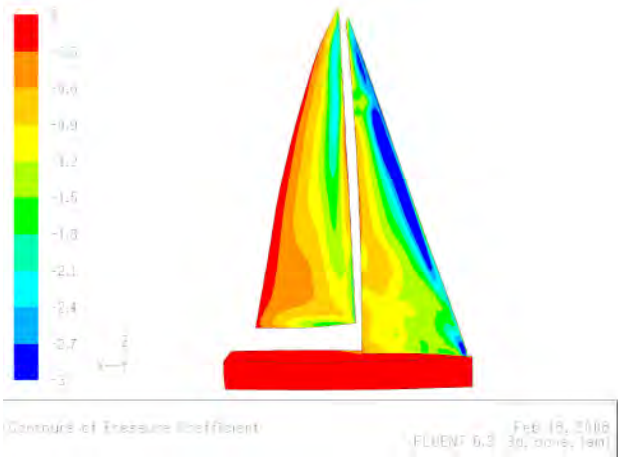

Figure 31. Leeward Cp contours in upright condition

As can be seen heel increasing result in a less of a pressure drop on both the sails, due to pressure decrease on the sailplan windward side; moreover in the lower part of the jib pressure increases with heel reducing the suction on the leeward side.
In order to understand this behaviour it's useful to refer to figures 41-42 which show the flow velocity vectors coloured by magnitude (normalised to the free stream incoming flow) in a plane perpendicular to the mast at 25% of mast height from the deck respectively for upright, 15°heeled and 30° heeled conditions.

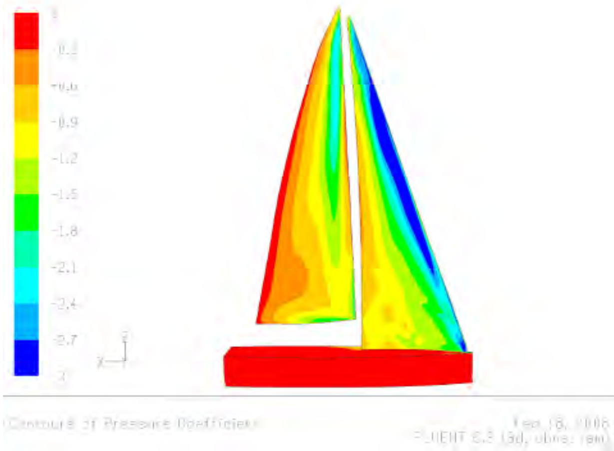

Figure 35. Leeward Cp contours at 15° heel

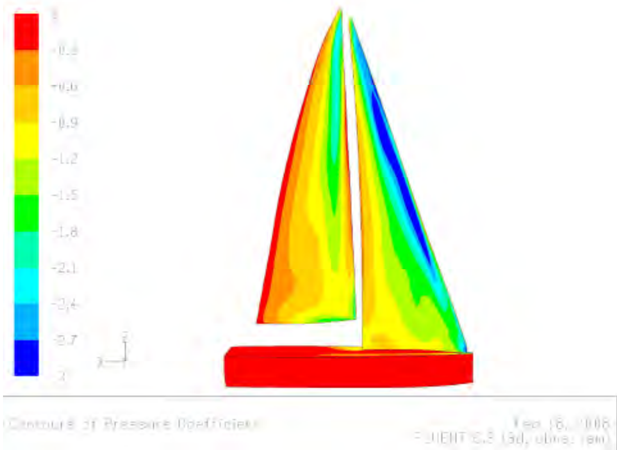

Figure 36. Leeward Cp contours at 30° heel

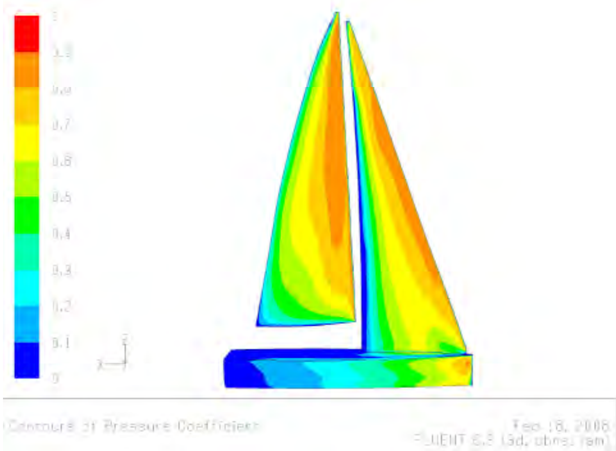

Figure 37. Windward Cp contours in upright condition

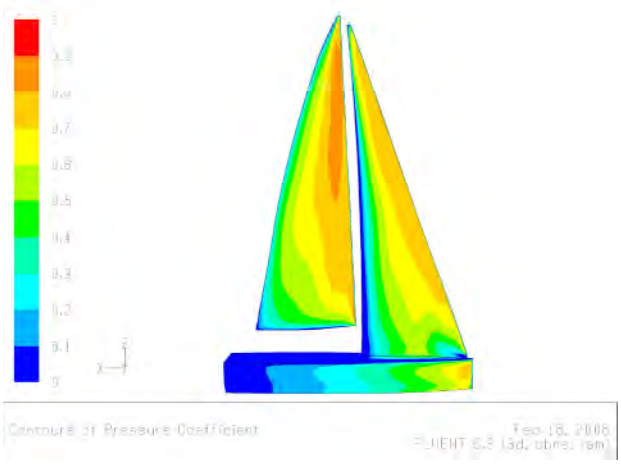

Figure 38. Windward Cp contours at 15° heel

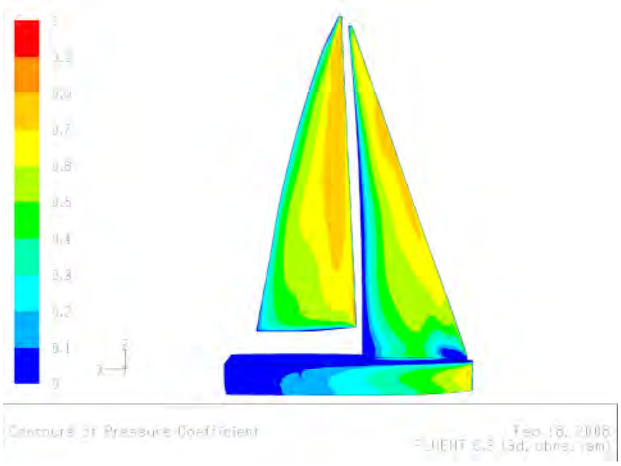

Figure 39. Windward Cp contours at 30° heel

When the yacht heels flow angle of attack reduces and the corresponding lift decreases, leading to a reduction of the driving force too. As can be seen upright condition is associated to some separation on the jib leeward side which disappears at higher heel angles, leading to a lift reduction too.

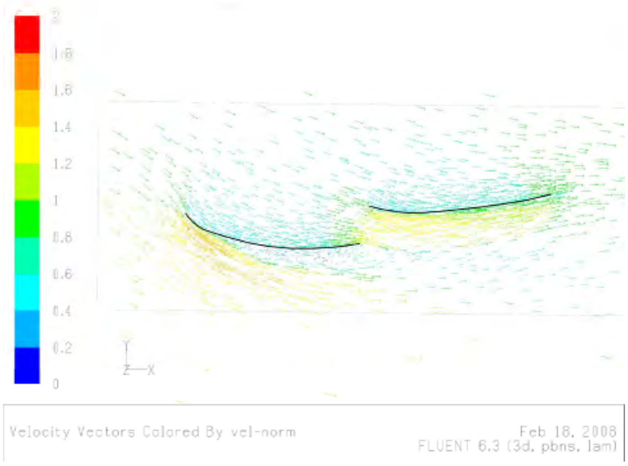

Figure 40. Velocity vectors in a plane perpendicular to the mast (25% mast height) in upright condition

This flow behaviour around the sails confirms also the apparent wind angle reduction associated to heeling as stated by the heeled plane model described in the next paragraph.

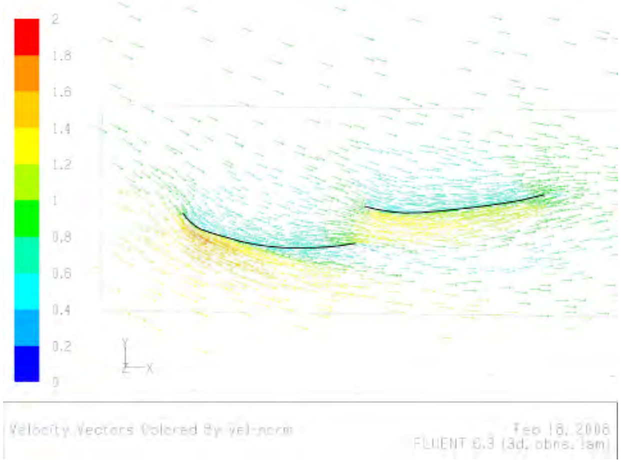

Figure 41. Velocity vectors in a plane perpendicular to the mast (25% mast height) at 15° heel

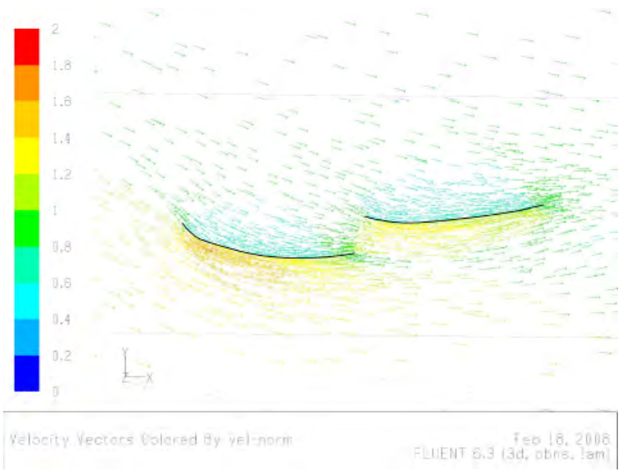

Figure 42. Velocity vectors in a plane perpendicular to the mast (25% mast height) at 30° heel

5. AERO MODELLING AND HEELED PLANE APPROACH: SOME CONSIDERATIONS

Since 1978 when the first velocity prediction programs for yachts was officially introduced for rating purposes the problem of modelling sail forces is a fundamental focus.

With reference to most of up to date available VPPs it can be said that aerodynamic model is mainly derived from the first aerodynamic model well known as Kerwin model [3].

Many principles of the aerodynamics of sails can be taken from the thin airfoil theory even if significant differences can be found: in a similar way to a wing yacht sails are lifting bodies where due to their shapes and the direction of the onset flow circulation appears increasing fluid velocity on the leeward side and decreasing velocity in the windward side with a

consequent high pressure region on the windward side and low-pressure region on the leeward side.
The lift and drag forces, resulting from the pressure regions around the sails can be expressed in terms of non-dimensional coefficients so that any forces and moments can be evaluated considering actual sail area and dynamic pressure of the free stream onset speed of the flow.
With reference to a wing the lift and drag coefficients are primarily a function of the angle of attack: on a sailing yacht this quantity is not easy to be defined due to continuous sails shape changing due to sails trimming. Hence in case of sails the angle of attack concept is replaced by the apparent wind angle which is the angle between the relative free-stream onset flow and the yacht centreline.
Moreover the free-stream speed of the onset flow to be used in evaluate the dynamic pressure is usually considered to be the apparent wind speed.
Wind tunnel tests and full scale experiments are the most suitable way to evaluate the drag and lift coefficients of the sailplan for different apparent wind angles considering the sails geometry, the relative direction of the onset flow, the flow structure (gradient and twist) and the trim of the sails.
A typical representation of forces acting on the sailplan are based on lift and drag sailplan coefficients plotted against the apparent wind angle.
The effect of heel is generally taken into account using the so called effective angle theory [Jackson, Campbell] which is used to address the fact that the heel angle influences the flow around the sails since the onset flow can always been considered as being horizontal. As the yacht heels the onset flow is not longer perpendicular to the leading edge of the sails and due this the resulting lift and drag forces are different for each heel angle.
Each aero model must take into account for the fact that lift and drag coefficients are no only a function of the apparent wind angle but also of the yacht heel.
Kerwin [3] and the so called effective angle theory assume that the sails are insensitive to the flow component along their span (i.e. along the mast) and that only the flow component perpendicular to the mast produces the lift and drag forces.
This represents one of the tougher issue of upwind aerodynamics and some discussions have been found in literature also very recently [Jackson 2001], [Teeters Sea Horse].
Aim of this paragraph is to discuss the appropriateness of this assumption and to investigate in more details its consequences on results available from aero models based on this underlying hypothesis.
More in details the flow component along the chord of the sails can be seen as the flow component in the heeled plane, which is a plane perpendicular to the mast and this means that the sails are insensitive to the flow component along the mast.
As an example in fig. 44 all tests performed by the authors for MimsG100 sail plan are reported (136 runs).

In particular for each test performed (as indicated on the abscissa axis named “prove” in fig. 44) the 3 component of the aerodynamic measured force are reported.

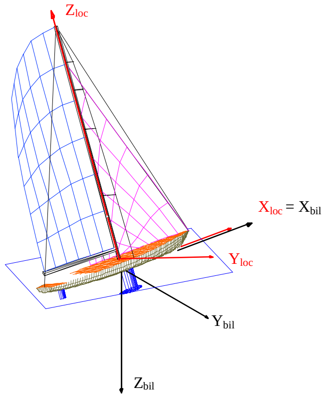

Figure 43. Balance and boat reference systems

With reference to fig. 44 blue symbols are relevant to balance axes aerodynamic force components (named “bil”) while red symbols are relevant to the boat reference system values (named “loc”) defined in fig. 43. More in details in figure 44:

- Runs 1-16 are 22° AWA and 30° heel tests
- Runs 17-28 are 27° AWA and 30° heel tests
- Runs 29-42 are 32° AWA and 30° heel tests
- Runs 43-62 are 22° AWA and 30° heel tests
- Runs 63-95 are 42° AWA and upright tests
- Runs 96-109 are 32° AWA and upright tests
- Runs 110-122 are 27° AWA and upright tests
- Runs 123-136 are 22° AWA and upright tests

As can be seen the aerodynamic force component along the mast (“zloc” component) is quite zero except for the 42°AWA runs: this was a systematic effects shown by tests with each sailplan tested.

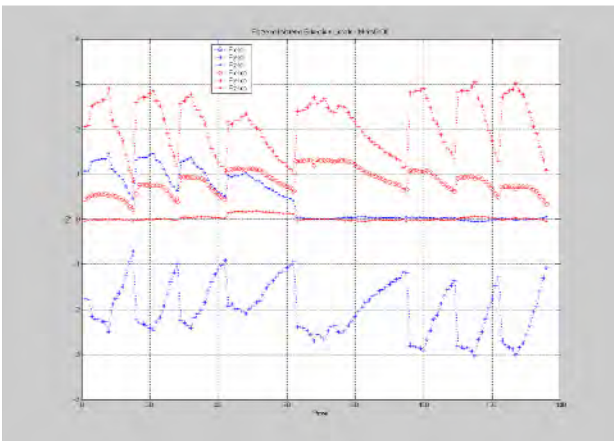

Figure 44. MimsG100 runs sequence

Experimental measures demonstrate that Kerwin assumption that the sails are insensitive to the flow component along the mast is substantially verified.

Coming back to the "heeled plane" model, the flow component in the heeled plane is called the effective flow and is defined by the effective angle and effective speed according to the following equations:

$$V_a = \sqrt{(-V_t \cos\gamma)^2 + (V_t \sin\gamma \cos\phi)^2}$$
$$AWA = \operatorname{arctg}\left(\frac{V_t \sin\gamma \cos\phi}{-V_t \cos\gamma}\right) \qquad (5)$$

where γ represent the true wind angle (yaw angle), V_t is the true wind speed and ϕ is the heel angle.
Using the driving and heeling aerodynamic force Fx and Fy component in the yacht body reference system the corresponding drag and lift forces components can be obtained as follows:

$$DRAG = -F_x \cos(AWA) + F_y \sin(AWA)$$
$$LIFT = F_x \sin(AWA) + F_y \cos(AWA) \qquad (6)$$

Then the corresponding drag and lift coefficients C_D and C_L can be evaluated:

$$DRAG = \frac{1}{2}\rho V_a^2 C_D(AWA) S$$
$$LIFT = \frac{1}{2}\rho V_a^2 C_L(AWA) S \qquad (7)$$

where S is the actual sailplan area.
So when the boat heels over the apparent wind angle decreases and the apparent wind speed reduces and this results in a loss of aerodynamic drive force.
This approach is very interesting because only one set of sails coefficients can be used to any heel angle.
As an example in figures 45-46 the C_D and C_L measured values at different AWA are reported for the medium roach mainsail+ non overlapping jib in upright condition. At each AWA, values corresponding to each run (i.e. each trim) performed are reported and red full dots correspond to the maximum driving force condition trimming point.

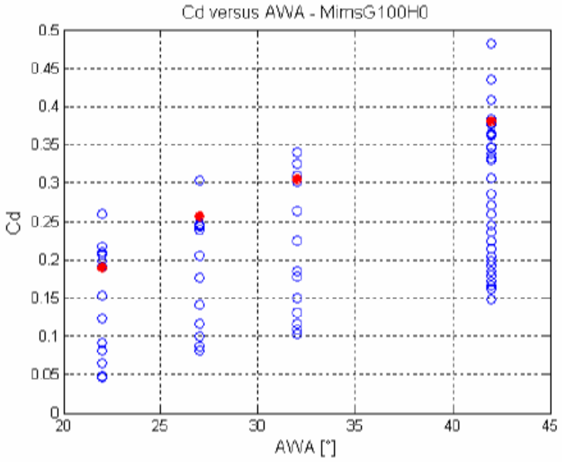

Figure 45. Drag coefficient vs apparent wind angle

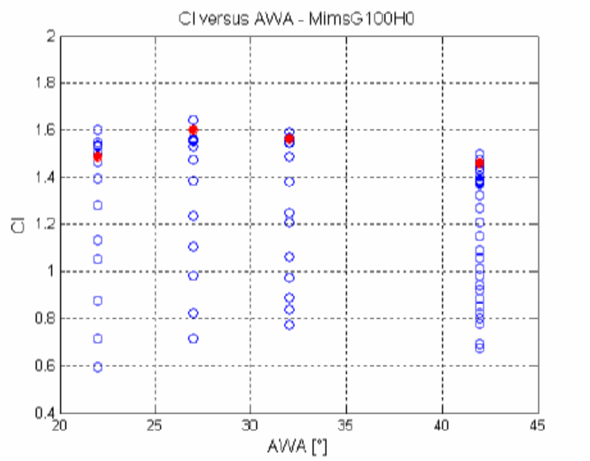

Figure 46. Lift coefficient vs apparent wind angle

Heel effect on sails aerodynamics is outlined in the following: in figures 43-44 the measured C_D and C_L values defined using the effective wind angle and effective wind speed according to eq.(5) are reported for the 30° heel condition too.

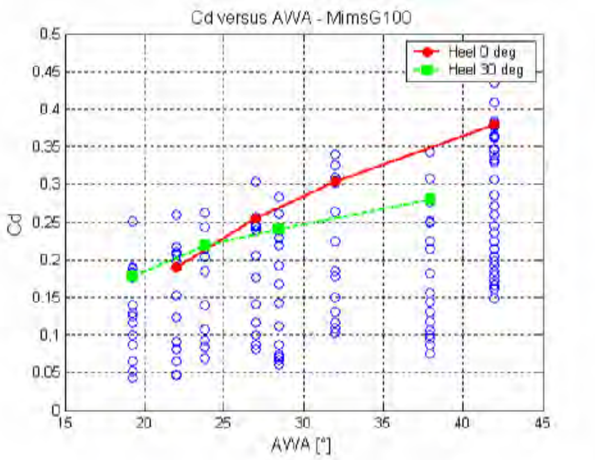

Figure 47. MimsG100 drag coefficient

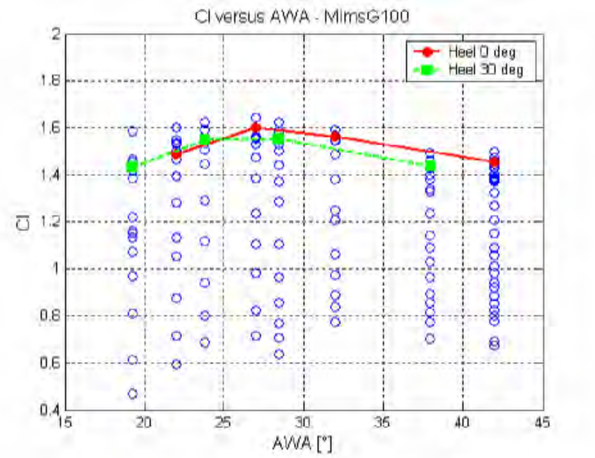

Figure 48. MimsG100 lift coefficient

Figures 49-50 refer to the medium roach + medium overlapping sailplan where upright, 15° heel and 30° heel configuration are reported.

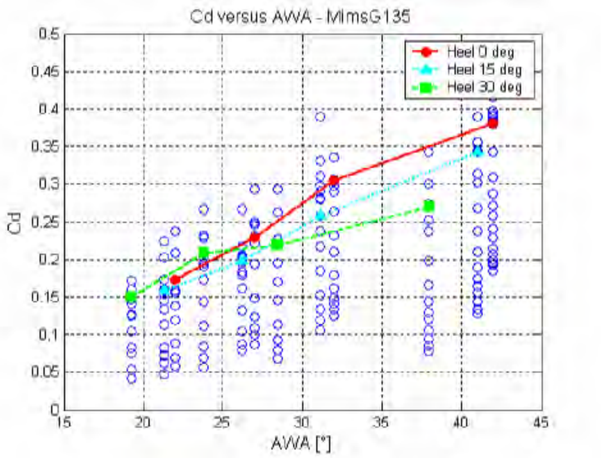

Figure 49. MimsG135 drag coefficient

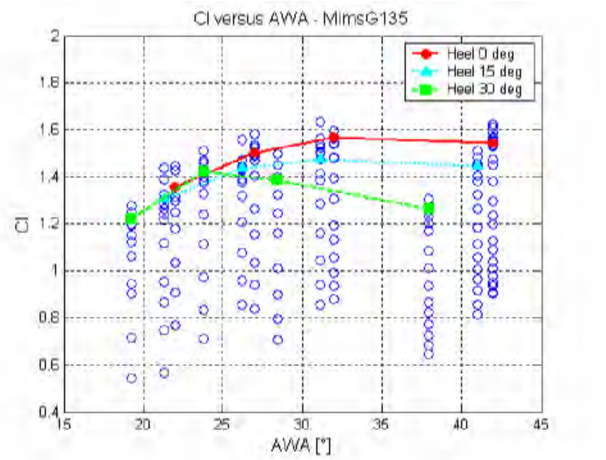

Figure 50. MimsG135 lift coefficient

As a general comment from the experimental obtained result it can be seen that C_D and C_L curves tend to be different with respect to AWA at different heels and differences are larger at wider apparent wind angles.
This trend is confirmed also for all the other sailplan tested (not reported here for lack of space reasons).
It should be also noticed that using the so called effective angle approach implies to move to any heel angle on the upright condition coefficients curves, depending on the effective wind angle, leading to a general lift and drag overestimation at wider angles while at the closer angles this error is going to reduce.
The corresponding situation for the abovementioned sailplan in terms of drive and heeling force is outlined in figures 51-52.
As can be seen at wider apparent wind angle using upright condition coefficients and effective wind angle both forces are overestimated.
This could also explain the reason why VPP solutions are generally obtained in association with large values of flat parameter: in fact depowering introduced by flat values sometime less than 0.5-0.6 are not realistic and probably due to overestimation of aerodynamic forces in heeled conditions.
An approach more consistent with experimental data could be to use C_D and C_L values, depending on actual yacht heel and on the actual apparent wind angle, obtained from an interpolation between the available experimental database.

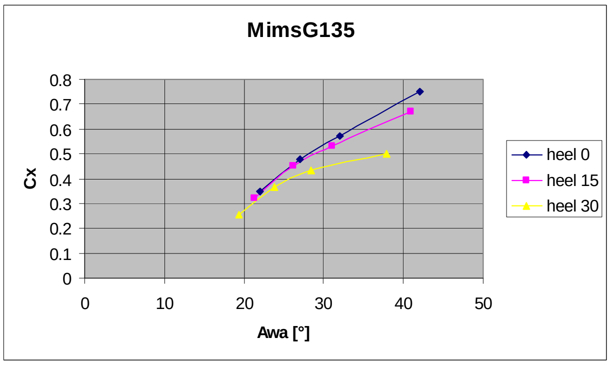

Figure 51. MimsG135 driving force coefficient

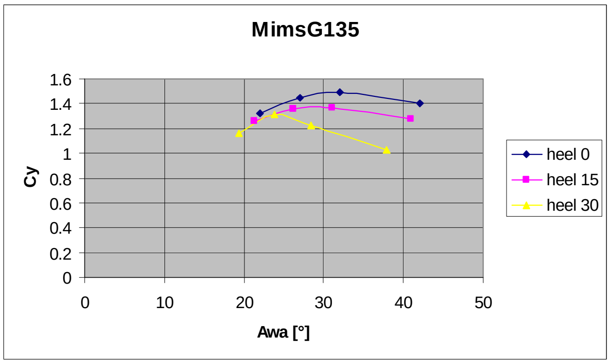

Figure 52. MimsG135 heeling force coefficient

Finally it's also interesting to mention that results and conclusion of the present paper go exactly in the opposite direction with respect of results presented in [8]. Despite that only qualitative results are reported in that paper without any details on the sailplan tested available, it's author's opinion that in principle results showing that there is no drop-off in driving force over the entire operational range of the sails until 30° heel are not particularly surprising and can be explained considering sails-hull interaction effects. Some wind tunnel tests recently performed by the authors on a IACC Version 5 yacht model on upwind sails at various heel angles (not reported here for confidentiality reasons) reveal that at 20° heel the effect of heel was to produce low base drag compared to other heel and associated higher driving force but that could be attributed to changes in the windage drag with heel: this moreover offers the prospect of investigating this feature together with hull shape to reduce windage at different heel angles
Another important point outlined from author's performed tests and affecting aerodynamic forces with heel was related to the boom height with respect to the deck: figure 53-54 show the wind velocity vectors coloured by normalisation to the free stream incoming flow in a vertical transverse plane that cuts the mainsail at 33% of boom length (from the mast) respectively for

upright, 15°heeled and 30° heeled conditions obtained from the abovementioned numerical simulations.

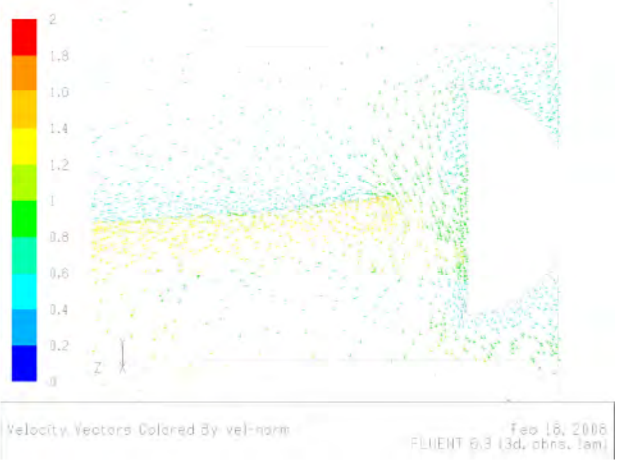

Figure 53. Velocity vectors in a vertical plane perpendicular to the boom in upright condition

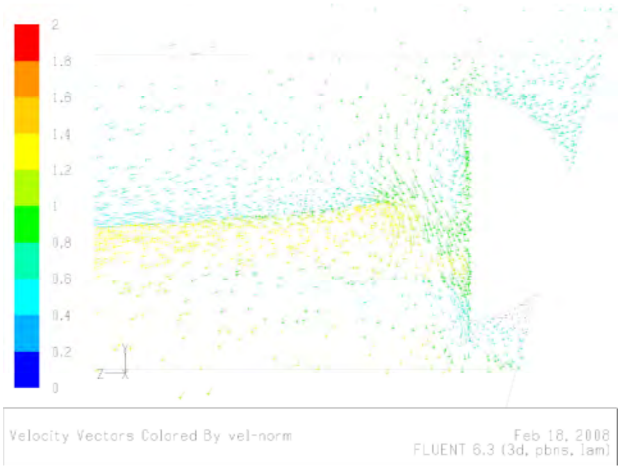

Figure 54. Velocity vectors in a vertical plane perpendicular to the boom at 15° heel

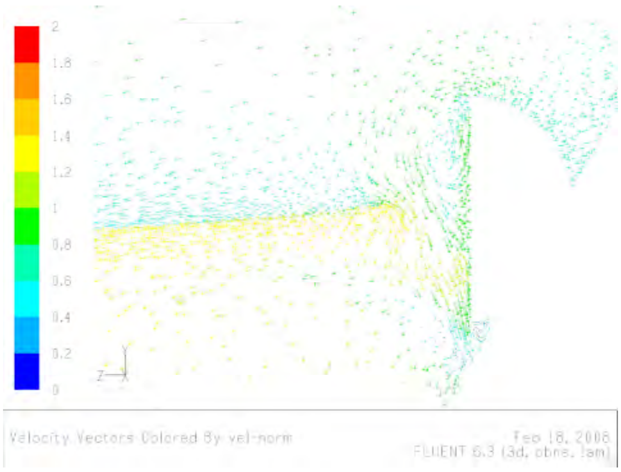

Figure 55. Velocity vectors in a vertical plane perpendicular to the boom at 30° heel

These figures show that a vortex generated by deck edge which increases with heel, but that doesn't affect substantially the flow under the boom: this leads to the angle of attack reduction associated to heel increasing the main reason in decreasing sailplan developed forces.

6. CONCLUSIONS

This paper gives an overview of the large amount of research activities carried out at Politecnico di Milano Twisted Flow Wind Tunnel in order to investigate the performance of upwind sails in heeled condition. Several rig planform variations in mainsail roach and jib overlap have been tested. Experimental results show that sailplan aerodynamic forces reduce with heeling, that drag and lift coefficients curves are different with respect to apparent wind angle at different heels and differences are larger at wider apparent wind angles.
This trend is confirmed for all the sailplan tested and has been clarified with the aid of numerical results obtained using RANS methods performed on the tested sailplan configurations.
Experimental results reveal that to the so called "heeled plane approach", largely used in the standard VPP aerodynamic models, leads to a general lift and drag overestimation at wider angles while at the closer angles this error is going to reduce. Main conclusion is that with reference to standard applications the so called heeled plane approach is quite adequate even if at upwind wider apparent wind angle both forces are overestimated.
Potential improvement of the generally used Kerwin's assumptions based aerodynamic model, in order to take into account heel effects, are finally outlined based on the available experimental database.

References

1. J. M. C. Campbell, & A. R. Claughton – Wind Tunnel Testing of Sailing Yacht Rigs – *13th HISVA symposium* – Amsterdam 1994

2. Fossati F. et al., 'Wind Tunnel Techniques for Investigation and Optimization of Sailing Yachts Aerodynamics', *High Performance Yacht Design Conference Auckland*, 14-16-Feb. 2006

3. Kerwin, JE "A velocity Prediction Program for Ocean racing yachts", Rep 78-11 MIT, July 1978

4. Fossati, F.& Zasso, A.& Viola I., "Twisted Flow Wind Tunnel Design for Yacht Aerodynamic Studies", Proc. of the 4th European and African Conference on Wind Engineering, J. Naprstek & C. Fisher, Prague, 11-15 July, 2005.

5. Fossati F. et al, "Experimental Database of Sails Performance and Flying Shapes in Upwind Conditions" Innov'sail 2008, RINA 29-30 May Lorient, 2008

6. P. S. Jackson, "Modelling the Aerodynamics of Upwind Sails" – Journal of Wind Eng. & Ind. Aerodyn., vol. 63 , 1996

7. P. S. Jackson, "An improved Upwind Sail Model for VPPs" – SNAME 15th CSYS, Annapolis, 2001

8. Teeters J., "The Story so Far", SeaHorse Magazine, July 2007

ON AN OCEANGOING FAST SWATH SHIP
WITHOUT PITCHING RESONACE

Hajime Kihara, National Defense Academy of Japan, hkihara@nda.ac.jp
Motoki Yoshida, Kyushu University, yoshidam@en.kyushu-u.ac.jp
Hidetsugu Iwashita, Hiroshima University, iwashita@naoe.hiroshima-u.ac.jp
Takeshi Kinoshita, Institute of Industrial Science, University of Tokyo, kinoshit@iis.u-tokyo.ac.jp

SUMMARY

Considering an oceangoing large fast ship, the punctuality of time schedule and delicate handling in navigation are required even in the rough sea. Thus the seaworthiness that there are no speed drop and absolutely no slamming gains in importance for the fast ships running in ocean waves. In the present work, a "Resonance-Motion-Free SWATH (RMFS)" ship is proposed as the ship satisfied with such requirements. As a first step of the study, experiments in towing tank and theoretical calculations based on the potential theory are carried out to figure out the performance of the RMFS in waves. Particularly the influence of vertical-plane stability due to small water plane area is examined with a soft-spring system. The results are compared with those of typical mono-hull and trimaran ships. The predominance of the RMFS regarding the seaworthiness is recognized.

1. INTRODUCTION

Recently the fast ships with the various hull forms such as a mono-hull, a catamaran and a trimaran attract lots of attention in the world. Above all, the research and development of the oceangoing large fast ship is an important subject. It is supposed that the accuracy of time schedule and delicate handling in navigation are required for the high-valued cargo for fast ship even in the rough sea. Accordingly, the speed drop and slamming, which are caused by large ship motions, must be suppressed at the lowest possible level. That is, the seaworthiness should be put ahead of the performance of resistance, power and fuel consumption especially for the ships running fast in ocean waves. From such a viewpoint, a SWATH ship is considered as a large fast one for the present study. So far there are a large amount of studies on the SWATH ship, e.g. [1][2][3]. Although some advantages for a SWATH ship are recognized in running in waves, it is well known that the control of vertical motions is important for such a ship because of the property with smaller water plane area than that of a mono-hull ship. Nevertheless, making the water plane area extremely small, we obtain the interesting feature with less restoring moment in pitch motion. This idea is already proposed by one of co-authors [4] and we call such a ship a 'Resonance -Motion-Free SWATH (RMFS)' in the present study.

The goal of our project is to establish the basic concept of the RMFS as an oceangoing large fast ship. For that purpose, besides for the hydrodynamic performance, the transport efficiency should be discussed from a viewpoint of the accuracy of time schedule and the transport quality after consideration like the damage of goods due to the slamming. However, as a first step, we examine the sea-keeping performance of the RMFS by means of the experimental and numerical approach. The present study has not got to the level to control the vertical plane stability yet, but the influence of the strut length and restoring moment in pitch motion is especially examined for the proposed RMFS. As a feasibility study, ship motions are compared among a mono-hull model, SWATH models including the RMFS and a trimaran model.

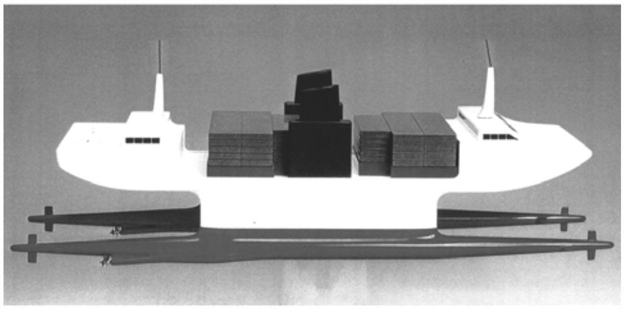

Fig.1 Rough design of Resonance-Motion-Free SWATH

Table 1 Principal Particulars of RMFS

Displacement tonnage : 24,000 t
Light weight :10,367 t
Power plants : 3,157 t
Dead weight : 13,633 t
Lighter : 1,000 t
Payload : 5,400 t, 540 containers (40 ft)
Fuel : 6,833 t
Upper hull : length:200 m, breadth:55 m
Lower hull : length:230 m, maximum diameter:8.85 m
Strut : length:90 m, maximum breadth:4.425 m
Draft : 12.85 m
Speed : 40 knots
Resistance : 655 t
Main engine : 8 Gas turbines (44,000 Ps), Total 352,000 Ps
Propulsion : 8 Contra-rotating propellers
Cruising distance : 4,800 nautical miles (Pacific ocean 5 days)
Controlling fin : 8 Fins, Total fin area 160 square meters

2. DESIGN CONCEPT OF THE SHIP

Our design policy of a oceangoing large fast ship is based on the requirements that the ship has 40 knots speed, and 5,000-10,000 tons payload, especially serve the good sea-keeping quality with no speed drop, absolutely no slamming in the waves of sea state 7 (with significant wave height of 6-9 meters) and so on. The outside view of the rough conceptual design [4] of the RMFS is shown in Fig.1. The RMFS has the capability of crossing 4,800 nautical miles of Pacific Ocean in 5 days at a high speed of 40 knots, with total engine power of 352,000 PS, as shown in Table 1. Four pairs of controlling fins are installed near the ends of lower hulls. Each fin should operate at one meter below the wave surface to maintain the stability and superior sea-keeping quality of the RMFS even in the rough sea.

3. MODEL TESTS

3.1 HULL FORMS

Experiments are implemented in two towing tanks. First, experiments of a mono-hull model are carried out at Ocean engineering tank in Kyushu University. The size of the model is 2.5(m) in length, L, 0.192(m) in breadth, B, and with a draft, d, of 0.064(m). The displacement of the model is equal to 14.71(kg).

Secondly, experiments of RMFS models are carried out at Ocean engineering basin in the University of Tokyo. The RMFS model consists of five parts: twin lower hulls, two struts and one upper deck, as shown in Fig.2 and Fig.3. In addition, four pairs of horizontal controlling fins and two pairs of vertical rudders are installed on the lower hulls. The length, L, of lower hull is 2.0(m) and it has circular cross section with the maximum diameter of 0.077(m). The cross sections of struts are elliptical with a length of 0.783(m) and the maximum breadth of 0.0385(m). The height of struts is approximately 0.215(m). Displacement of the model is 15.49(kg). Eight fins and four rudders are all fixed, whose attack angle for the longitudinal hull axes are set to zero degree.

3.2 EXPERIMENTAL CONDITIONS

Three kinds of tests are carried out using a mono-hull and RMFS models, i.e. forced oscillation tests in still water, restrained tests in waves and free motion tests in waves. Froude number, defined as $Fn = U/\sqrt{gL}$ with towing speed, U, and gravity acceleration, g, is 0.50 for mono-hull model and 0.433 for RMFS model. The adopted Froude number is common in all tests.

For the forced oscillation tests, oscillating frequencies are determined by dispersion relation $\omega = \sqrt{Kg}$ with the wave number K varying in a range of KL=2.0-40.0. For the restrained tests in waves to measure the wave exciting forces, regular waves are used as the incident waves and the range of non-dimensional wave length λ / L is 0.4-4.0. All tests are done in head sea condition. For the free motion tests in waves, experimental conditions are the same as those in the measuring wave exciting forces.

3.3 STRUT AND STABILITY

In addition to the experiments of the RMFS models, the ordinary SWATH models, whose strut length is equal to the length of the lower hull, is also tested to examine the influence of the strut length of the SWATH. The differences in both models for motion responses to waves are of interest. In the present study, the model supporting system using four pairs of soft springs is adopted as shown in Fig.2. This is because the restoring moment coefficient of the model has negative value and the model is unstable in measurement of ship motions. Supporting points are located at x=0.495(m), y=0.205(m) as shown in Fig.3. The springs are settled in a length of 0.100(m) with tensile stress and the model is supported by both upward and downward springs. Thus the free motion tests are carried out by using the models with four kinds of spring constants to examine the influence of the restoring moment in pitch motion. The restoring force and moment

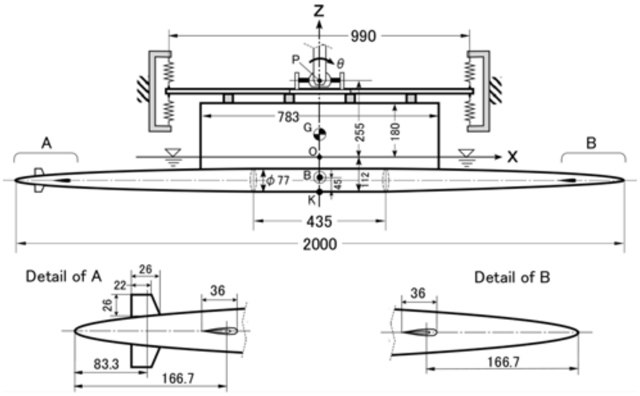

Fig. 2 Side view of the RMFS model

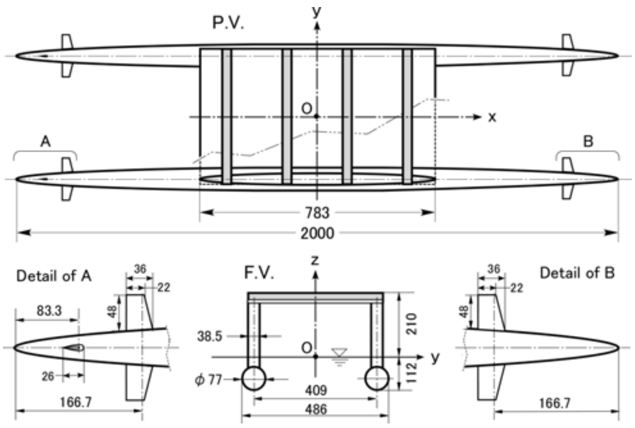

Fig. 3 Plan and front view of the RMFS model

Table 2 Restoring force of various ship models

Ship Models with L of 2(m)	Spring const. k (N/m)	Restoring force Net C_{33} (N/m)	Restoring moment Net C_{55} (N/m)
Mono-hull	-	2200.6	≈ 506.0
RMFS	-	464.0	-4.3
RMFS-A	35.0	744.0	64.4
RMFS-B	63.0	968.0	119.2
RMFS-C	84.0	1136.0	160.4
RMFS-F	120.0	1424.0	231.0
Ord. SWATH	-	1185.1	271.3
Ord. SWATH-F	120.0	2145.1	506.5
Trimaran	-	> 2200.0	> 506.0

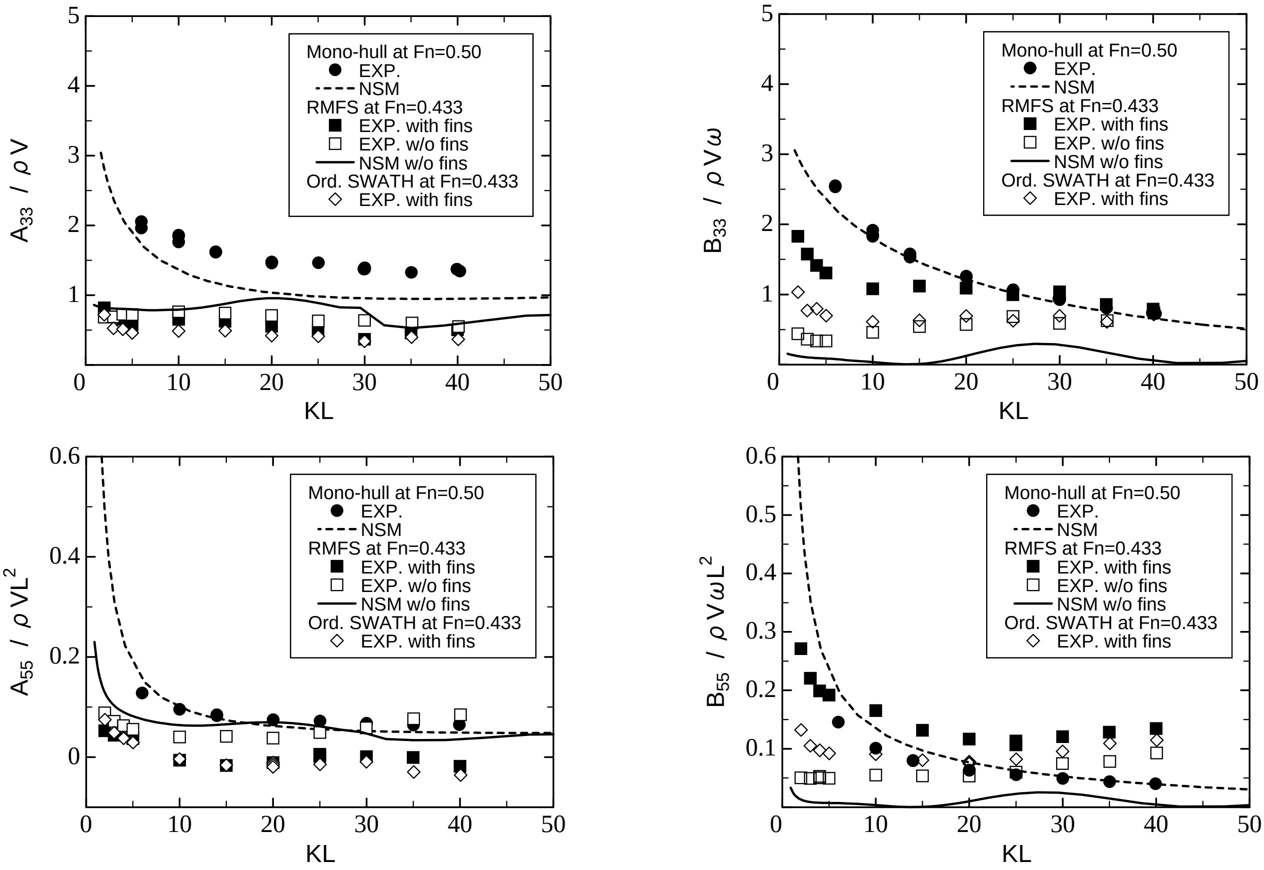

Fig.4 Added mass and damping coefficients for heave and pitch

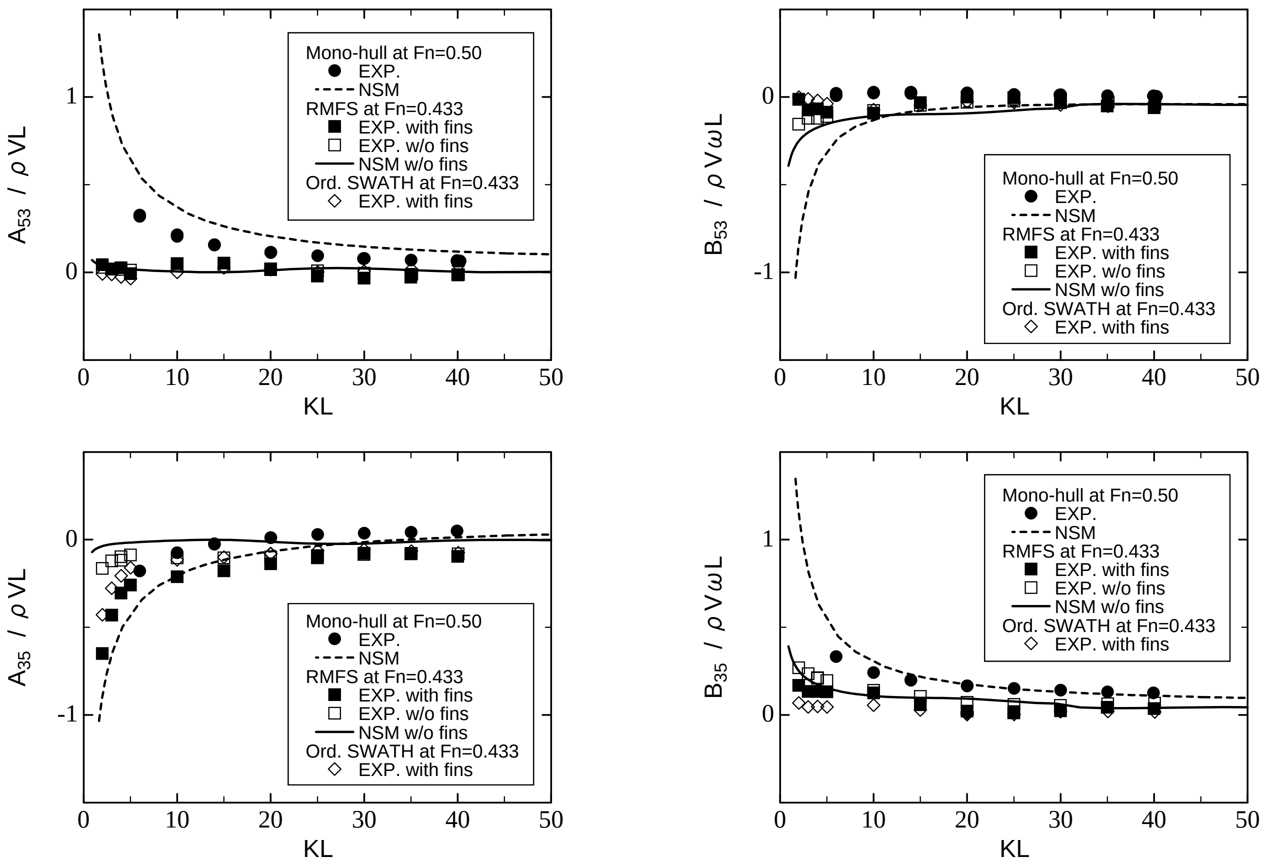

Fig.5 Coupled added mass and damping coefficients between heave and pitch

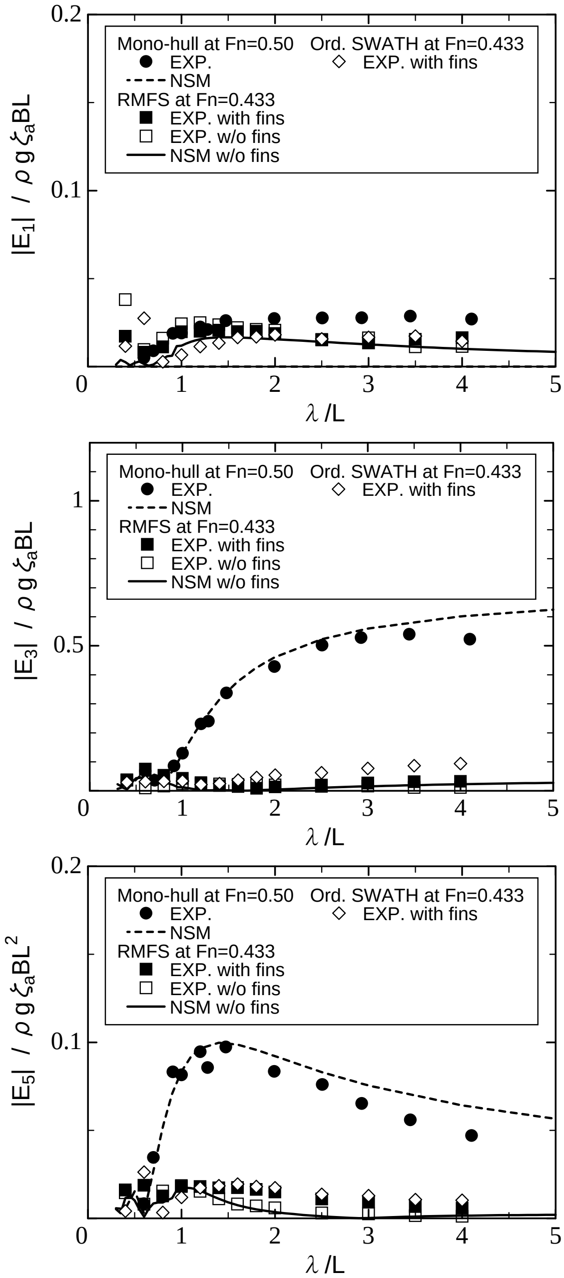

Fig.6 Wave exciting force and moment

of the models with a length of 2(m) are shown in Table 2, where values of the mono-hull and the trimaran are converted to the values of spring strength. Model tests with the each spring varied are introduced because the vertical-plane stability cannot be controlled in the present study using fixed fins. For the ordinary SWATH, the free motion tests with the spring support are also performed for comparison although this model has inherent stability.

4. RESULTS

4.1 ADDED MASS AND DAMPING COEFFICIENTS

Hydrodynamic forces and moments, measured in forced oscillation tests by pure heave or pure pitch motion, are shown in Fig.4 and Fig.5. Coefficients A_{ij} or B_{ij} denotes added mass and damping coefficient, respectively, in the *i*-mode direction induced by the oscillation motion of *j*-mode motion. They are normalized by the displacement or the product of displacement and the circular frequency, etc. Fig.4 shows the results in pure heave or pitch motion. On the other hand, Fig.5 shows the results in coupled terms between heave and pitch motion. Experimental results of the mono-hull in Froude number 0.50 and those of the RMFS in Froude number 0.433 with fins and without fins are plotted in the figures. Also calculated results by the new strip method (NSM) for these models are plotted. The viscous effects of lower-hulls and fins and the lift of fins are not considered yet in the calculation for the RMFS.

Experimental results of A_{33} and A_{55} shown in Fig.4 are small because the hull form of RMFS is considerably slender compared with that of mono-hull. Calculated results of both models nearly explain the tendency of experimental ones. Likewise, it can be observed from the experimental results of B_{33} that the order of decreasing magnitude for different hull forms is given as follows: the mono-hull, the RMFS with fins, the ordinary SWATH with fins and the RMFS without fins, while the magnitude of B_{55} decreases in order of the RMFS with fins, the mono-hull, the ordinary SWATH with fins and the RMFS without fins. For the model with fins, the effects on reducing pitch motion can be expected especially because of the large lever of pitching moment, in spite of the small fin area. In addition, it can be seen that calculated results of the RMFS are much smaller than experimental results. Calculated B_{33} and B_{55} are even smaller than experimental results of the RMFS without fins. The difference is due to both contribution of the fin lift and the viscous effect on lower-hulls and fins. In Fig.5, calculated results of both models coincide with experimental results and explain the tendency of those.

4.2 WAVE EXCITING FORCE AND MOMEMT

Measured results of wave exciting force and moment acting on the models are presented in Fig.6. In the figures, $|E_i|$ denotes the amplitude of force or moment in *i*-mode direction, and ζ_a is the incident wave amplitude. In the figures, calculated results by the NSM are also plotted. It is observed that experimental results of the amplitude of wave exciting force $|E_3|$ and moment $|E_5|$ in the case of RMFS are extremely small compared with that of the mono-hull. Consequently, the reason that the SWATH or the RMFS is called “wave excitationless ship” can be well understood. There is little difference in the wave exciting forces $|E_1|$ and $|E_3|$ between the models with and without fins, while there is apparent difference in the wave exciting moment $|E_5|$ between both models with and without fins. The cause is also the effect of fins with the large moment lever. In addition, it can be seen that the RMFS with shorter strut is slightly advantageous in both wave exciting force $|E_3|$ and moment $|E_5|$.

4.3 SHIP MOTION

The heave and pitch motion responses of some models are shown in Fig.7 and Fig.8. The RMFS-F is a model with the spring F as shown in Table 2 and it is represented as a model with largest restoring force and moment in the RMFS variants. In the computation of ship motions for the RMFS-F, the ship motions are assumed to be modeled

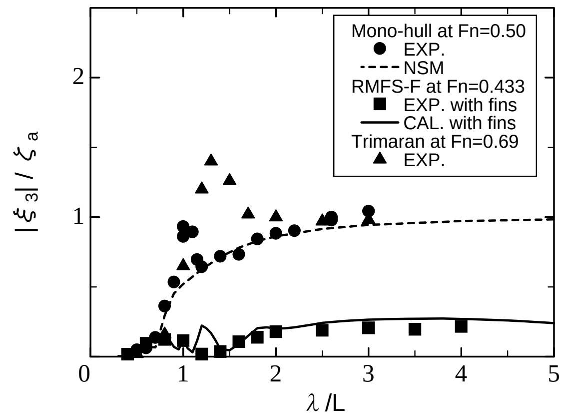

Fig.7　Comparison of hull forms for heave motion

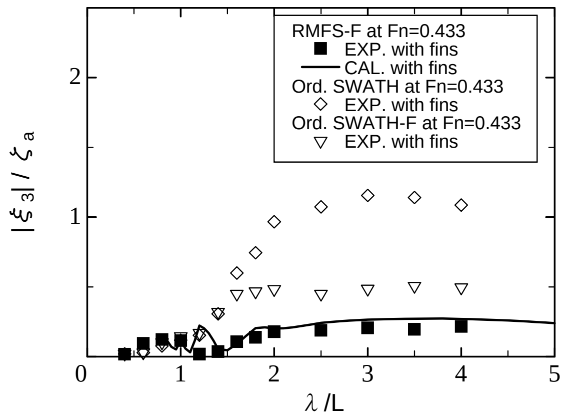

Fig.9　Influence of strut length on heave motion

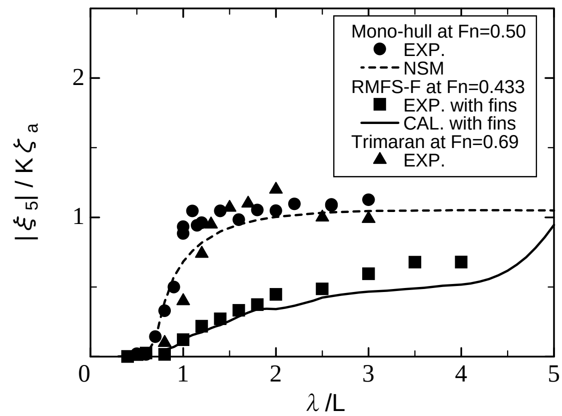

Fig.8　Comparison of hull forms for pitch motion

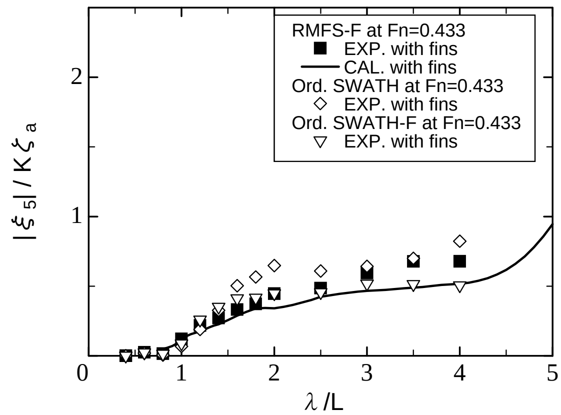

Fig.10　Influence of strut length on pitch motion

with linear differential equations. The measured values of radiation and diffraction forces in the experiments are used in the coefficients of such motion equations. These results are denoted by CAL. in both figures. Accordingly the computed results include the viscous effects and the lift of fins to some levels. Experimental results of the trimaran measured by Saito et al.[5] are also cited. In comparison with the difference among three hull forms, i.e. the mono-hull, the RMFS-F and the trimaran, it is observed that the motion responses of the mono-hull and the trimaran are larger than that of the RMFS-F in both cases of heave and pitch motion. Notably there exist resonant peaks particularly in heave motion. We can recognize that the RMFS model has the great advantage in seaworthiness.

Next we compare two SWATH typed models with different strut length, i.e. the RMFS-F and the ordinary SWATH. These results are shown in Fig.9 and Fig.10. In this comparison, the ordinary SWATH-F with the spring system is also examined besides the ordinary SWATH without the spring system. It is observed that the motion responses of the RMFS-F are small both in heave and pitch motion in comparison with the ordinary SWATH which has about the same restoring force and moment as the RMFS-F. The resonant point in the pitch motion for the ordinary SWATH is near 2.3 in wave length ratio. This causes the increments from the responses for the RMFS-F,

Table 3　Eigen period of ship models measured in zero-speed condition

Heave motion		
Ship Models	Eigen period T (s)	Corresponding wave length λ / L
RMFS-A	2.07	3.35
Ord. SWATH	1.63	2.08
Ord. SWATH-A	1.38	1.49

Pitch motion		
Ship Models	Eigen period T (s)	Corresponding wave length λ / L
RMFS-A	2.96	6.85
Ord. SWATH	1.72	2.30
Ord. SWATH-A	1.37	1.46

but it is not so large compare with that of heave motion. Therefore the influence of strut length on motion responses is more remarkable in heave motion than pitch motion.

Additionally the motion responses for the RMFS-A model are shown in Fig.11 and Fig.12. The computed results of ship motion denoted by CAL. include the viscous effects and the lift of fins, while such effects are not taken into account in the NSM computation. Eigen periods measured in zero speed condition are shown in Table 3. These values indicated in Fig.11 and Fig.12 are well coincident with each resonant point predicted by the

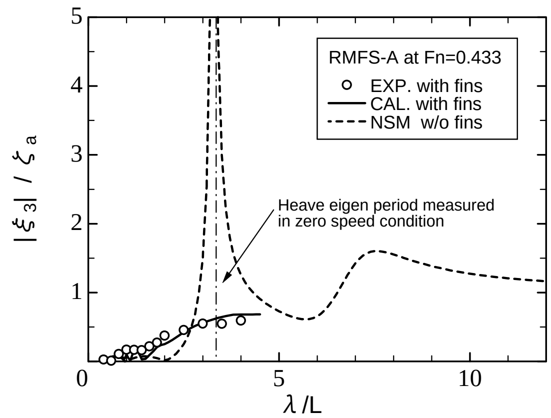

Fig.11 Heave motion of RMFS-A

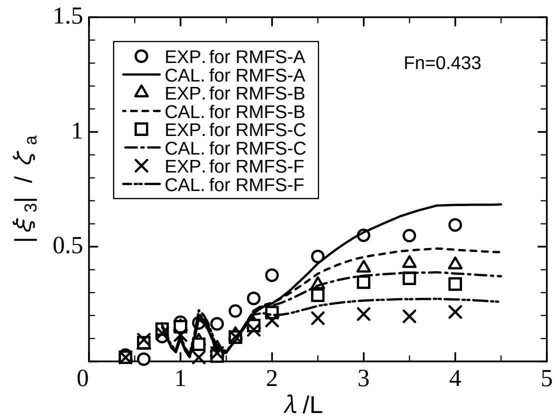

Fig.13 Influence of spring constants on heave motion

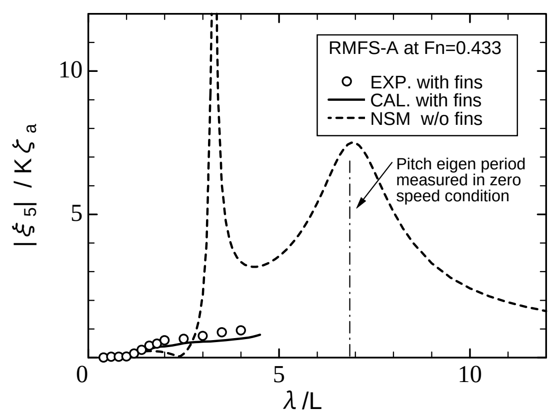

Fig.12 Pitch motion of RMFS-A

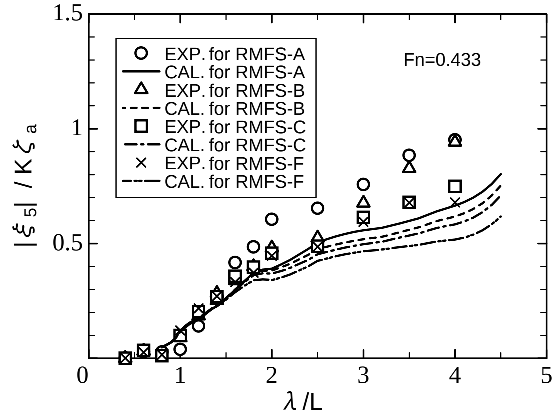

Fig.14 Influence of spring constants on pitch motion

NSM. In heave motion, effects by the fins make it possible to suppress an increase in motion very much even at the resonance. On the other hand, even in pitch motion, there are possibilities to suppress an increase below a certain level, although the encounter with such long waves rarely happens. However, we cannot discuss any more because we don't have any data about longer waves due to the limitation of our experimental facility. Finally in Fig.13 and Fig.14 we show the results on the influence of the soft spring system, which is equivalent to the proportional control action using the fin lift. To exert motion reduction in longer waves, a new control system of ship motion, instead of the present system, should be designed to make a good use of with the advantage of negative restoring moment.

5. CONCLUSIONS

The comparison of ship motion responses among three kinds of hull forms, using experimental results and some data cited from references, are discussed. As a result, it becomes clear that the heaving motion of the RMFS is very small in comparison with those of the mono-hull or the trimaran. On the other hand, the pitching motion of the RMFS is considerably small in comparison with the others as expected. On the strut length, its influence appears more remarkably in heave motion than pitch motion. The pitch motion for the RMFS is not as small as expected in comparison with that of the ordinary SWATH. These reasons are that the soft spring system used in experiments cannot take advantage of the characteristic of the RMFS model with negative restoring moment. Accordingly, a new control system of ship motion using the lift force by fins should be adopted. Additionally, experimental and simulation method need to be established to realize that control system.

ACKNOWLEDGMENTS

This study was performed by the assist of grant-in-aid for scientific research (No. 19206093), Japan Society for the Promotion of Science.

REFERENCES

[1] Lee, C. M. and Curphey, M. 'Prediction of motion, stability, and wave load of Small -Waterplane -Area Twin -Hull Ships', SNAME Transactions, vol. 85, pp.94-130, 1977.

[2] Ozawa, H. 'Basic characteristics of large-sized SWATH', Mitsui zosen technical review, vol.133, pp.1-8, 1988.

[3] Papanikolaou, A., Zaraphonitis, G., Androulakakis, M. 'Preliminary Design of a High-Speed SWATH Passenger Car/ Ferry', Journal Marine Technology, SNAME, Vol. 28, No.3, pp.129-141, 1991.

[4] Yoshida, T., Fujita, Y. and Fujino, M. 'A proposal of the CS-Swath as a Transocean High Speed Ship', Trans. RINA, Vol.142(B), pp.136-149, 2000.

[5] Saito, H., Ito, A. and Iwashita, H. 2007 Motion responses and wave loads of high-speed trimaran in waves, Conference proceedings, The Japan society of naval architects and ocean engineers, vol.4, 2007s-0s1-3.

A POTENTIAL PANEL METHOD FOR THE PREDICTION OF MIDCHORD FACE AND BACK CAVITATION

S. Gaggero & **S. Brizzolara**, University of Genoa (IT), Department of Naval Architecture and Marine Engineering

SUMMARY

Accurate predictions of the extent of thee sheet cavitation and the pressure distribution on the blade are crucial in the design and assessment of marine propulsor subjected to nonuniform unsteady flows. While, in normal operating conditions, cavitation occurs on the back side of the propeller and generally begins at the leading edge, when the propeller is subjected to a strong non axysymmetric flow cavitation can occur on the face side of the propeller. Moreover, at design advance coefficient, pressure distributions are often "flat" and this may lead to midchord or bubble cavitation.

In the present work a three dimensional boundary element method is developed and validated for the prediction of general cavity patterns and loading, with convergence and consistency studies. First the method is validated against 3D cavitating wings in order to check the ability to search for simultaneous face and back cavitation with arbitrary detachment point and, after, the most general case of a propeller is analyzed in order to investigate about the performances of the developed method.

1. INTRODUCTION

The design of modern marine propellers is more and more conditioned by the analysis of inception and developed cavitation. In recent years, the design of high speed marine vehicles has become increasing competitive together with a growing demand of heavily loaded propellers with request of very low noise and vibration levels onboard.

Cavitation, thus, is the more important inhibitor to the propulsion system and it is comprehensive the need of a simple and fast method to predict cavitation behaviour of the propeller in the design stage. As known, cavitation under all its different configurations can generate a number of problems *i.e.* additional noise, vibrations and erosions, as well as, variations in the developed thrust and torque. The study of cavitation is very much complicated by the presence of a fluid with two different phases and the effect of viscosity is, in many cases, significant.

Moreover, on modern propellers design, midchord cavitation and bubble cavitation may also appear and face cavitation is very common, specially if the propeller operates behind a strong nonuniform wake or in inclined shaft conditions.

The most advance computational tools for cavitation analysis on marine propellers are based on RANS equations solvers. However unsteady cavitating RANS analysis are quite computationally expensive, so potential flow theory can be adopted for the preliminary analysis and design of cavitating propellers.

At the University of Genova the development of a three dimensional boundary element method for the analysis of steady flow and steady cavitating flows was started by Caponnetto and Brizzolara [2]. Further developments have been made by Gaggero and Brizzolara [4], [5], with the inclusion of a wake alignment algorithm, an iterative Kutta condition and an unsteady solver for fully wetted flows.

In this work a panel method for the study of propellers subjected to cavitation is presented. The present method, first developed for the analysis of wings and after extended to treat the propeller problem, is limited to steady flow, adopts a sheet cavitation model and allows face and midchord cavitation. Since no universally accepted definition for midchord detachment exists, it can be defined as the detachment "well behind" the leading edge (Mueller and Kinnas [16]) and, although midchord cavitation often appears as cloud or bubble cavitation, in the framework of potential flow it can be treated again as sheet cavitation, because the attention is focused on global, mean and steady pressure distributions, for which the sheet cavitation model is enough.

At this stage of development also supercavitation is neglected. In some critical conditions, midchord cavitation but also leading edge cavitation could lead to supercavitation for certain sections (in the propeller case those close to the tip). The present numerical method neglects the effect of sheet cavitation thickness in the wake and solves supercavitating sections leaving them open at trailing edge. In fact the influence of the sheet cavitation bubble in the wake on the solution (pressure distribution on the body) can be considered small enough to be not taken into account: in an ongoing research it has been proved that allowing for supercavitation alters only the sheet bubble development near the trailing edge (where the influence of the wake bubble is more significant), determining only a small variation of the cavitating bubble volume, but the general behaviour of the solution obtained neglecting supercavitation remains valid. The pressure distribution, with the typical constant value equal to the vapour pressure in the cavitating zones, is still valid and the inclusion of supercavitation

does not alter the extension of the sheet cavitation on the solid boundaries.
The Laplace equation for the potential flow field is solved by using Green's second identity (Lamb [10], Lee J.T. [12]). To solve the problem numerically all the surfaces (the wing with its wake or the blade, the hub and the propeller wake) are discretized using quadrilateral *panair like* panels (Magnus [13], Gaggero & Brizzolara [4], [5]) with constant sources and dipoles distribution. Adequate boundary conditions are imposed on all the boundary surfaces and the cavity shape, unknown, is found iteratively. The predicted pressure distribution from the wetted non cavitating solution is adopted in order to formulate the initial leading edge or midchord cavity detachment line. This first choice is used and adjusted until the resulting cavity thickness is positive everywhere on the cavity and the pressure on the wetted part of the body is larger than the vapour pressure.

2. PROBLEM FORMULATION

2.1 INTEGRAL FORMULATION

Consider a right handed propeller rotating with constant angular velocity $\boldsymbol{\omega}$ in a axisymmetric incoming flow field $\boldsymbol{V}_\infty$ (same conclusion can be drawn for the simpler case of a wing subjected to an uniform inflow, neglecting the angular velocity term). In the (x_p, y_p, z_p) coordinate system that rotates with the propeller, the total velocity vector $\boldsymbol{V}$ can be written as the sum of the relative undisturbed inflow $\boldsymbol{V}_{rel}$ (known in the propeller reference system) and the perturbation potential velocity $\boldsymbol{q}_{ind}$, due to the velocity influence of the propeller itself on the velocity field:

$$\boldsymbol{V} = \boldsymbol{V}_{rel} + \boldsymbol{q}_{ind} \tag{1}$$

where the relative velocity $\boldsymbol{V}_{rel}$, in the propeller reference system, can be written as:

$$\boldsymbol{V}_{rel} = \boldsymbol{V}_\infty - \boldsymbol{\omega} \times \boldsymbol{r} \tag{2}$$

With the assumption of an inviscid, irrotational and incompressible fluid, the perturbation velocity can be written in terms of a scalar function, the perturbation potential, that satisfies the Laplace equation:

$$\begin{aligned} \boldsymbol{q}_{ind} &= \nabla\phi \\ \nabla^2\phi &= 0 \end{aligned} \tag{3}$$

By applying Green's second identity for the perturbation potential, the differential problem (3) can be written in integral form with respect to the potential ϕ_p at every point p laying onto the geometry boundaries. The perturbation potential ϕ_i represents the internal perturbation potential, that must be set equal to zero in order to simulate fluid at rest inside the boundaries of all the bodies subject to the external inflow (blades, hub, wing).

$$\begin{aligned} 2\pi\phi_p &= \int_{S_B+S_{CB}} \left[\phi_q - \phi_{qi}\right] \frac{\partial}{\partial \boldsymbol{n}_q} \frac{1}{r_{pq}} dS \\ &- \int_{S_B+S_{CB}} \left[\frac{\partial\phi_q}{\partial \boldsymbol{n}_q} - \frac{\partial\phi_{qi}}{\partial \boldsymbol{n}_q}\right] \frac{1}{r_{pq}} dS \\ &+ \int_{S_W} \Delta\phi_q \frac{\partial}{\partial \boldsymbol{n}_q} \frac{1}{r_{pq}} dS \end{aligned} \tag{4}$$

The subscript q corresponds to the variable point in the integration, $\boldsymbol{n}$ is the unit normal to the boundary surfaces and r_{pq} is the distance between points p and q.
Equation (4) expresses the potential on the propeller blade as a superposition of the potential induced by a continuous distribution of sources on the blade and hub surfaces and a continuous distribution of dipoles on the blade, hub and wake surfaces that can be calculated, directly, via boundary conditions, or, indirectly, inverting equation (4).

2.2 BOUNDARY CONDITIONS

For the solution of equation (4) a certain number of boundary conditions must be applied. Different approaches are possible: a fully linear approach, in which cavity velocities can be considered enough small to allow linearization of boundary conditions or a fully nonlinear one, in which singularities are located on the cavity surface that need to be found iteratively. On the other hand, an intermediate approach, the partial nonlinear approach, can be adopted, in order to take into account the weakly nonlinearity of the boundary conditions (the dynamic boundary condition on the cavitating part of the blade and the closure condition at its trailing edge) without the need to collocate the singularities on the effective cavity surface. If the cavity thickness can be considered enough small with respect to the chord, singularities can be placed on the body surface and problem nonlinearity can be solved with this assumption (see, for instance, figure 1).
On the wetted part of the body (the wing or the blades plus the hub) the kinematic boundary condition holds (the flow must be tangent to the body surface) and allows to define the source strengths in terms of the known inflow velocity relative to the propeller reference system:

$$\frac{\partial\phi_q}{\partial n_q} = -\boldsymbol{V} \cdot n_q \tag{5}$$

At the blade trailing edge the Kutta condition states that the flow must leave with a finite velocity or that the pressure jump at the blade trailing edge must be zero. In a steady problem, the Kutta condition allows to write the dipole intensities, constant along each streamlines (equivalent to each chordwise strip in the discretized formulation), on the wake, first, applying the "linear" Morino Kutta condition:

$$\Delta\phi_{T.E.} = \phi^U_{T.E.} - \phi^L_{T.E.} + \mathbf{V}_{rel} \cdot \boldsymbol{r}_{T.E.} \tag{6}$$

where the sup scripts U and L stand for the upper and the lower face of the trailing edge. After, the zero pressure jump can be achieved via an iterative scheme. In fact the pressure difference at trailing edge (or the pressure coefficient difference) at each m streamlines (or at each m blade strip for the discretized problem) is a non linear function of dipole intensities on the blade:

$$\Delta p_m(\phi) = p^U_m(\phi) - p^L_m(\phi) \tag{7}$$

So, an iterative scheme is required to force a zero pressure jump, working on dipoles strength on the blade (and, consequently, on potential jump on the wake). By applying a Newton – Raphson scheme with respect to the potential jump on the wake $\Delta\phi$, equal in the steady problem to the potential jump at blade trailing edge, the wake potential jump is given by:

$$\{\Delta\phi\}^{k+1} = \{\Delta\phi\}^k - \left[J^k\right]^{-1}\{\Delta p(\phi)\}^k \tag{8}$$

where the index k denotes the iteration, $[\Delta p(\phi)]^k$ is the pressure jump at trailing edge obtained solving the problem at iteration k (corresponding to the $\Delta\phi^k$ solution) and $\left[J^k\right]$ is the Jacobian matrix numerically determined (9):

$$J^k_{ij} = \frac{\partial \Delta p^k_i}{\partial \Delta\phi^k_j} \tag{9}$$

while, for the first iteration, the solution $\Delta\phi^k$ and the corresponding pressure jump is taken from the linear Morino solution (6).

Moreover the wake should be a streamsurface: the zero force condition is satisfied when the wake surface is aligned with the local velocity vector. In the present method this condition is only approximated and the wake surface is assumed frozen and laying on an helicoidal surface whose pitch is equal to the blade pitch. Assuming that the influence of the cavity bubble is small in the definition of the wake surface, an approach similar to that proposed by Gaggero & Brizzolara [4] can be adopted and the cavity solver could be improved using the aligned wake calculated for the steady non cavitating flow.

Analogous (kinematic and dynamic) boundary conditions have to be forced on the body cavitating surfaces, in order to solve for the singularities (sources and dipoles) distributed there (Caponnetto and Brizzolara [2], Fine [3], Mueller and Kinnas [16], Young and Kinnas [18], Vaz and Bosschers [17]).

On the cavity surface S_{CB} the pressure must be constant and equal to the vapour pressure or the modulus of the velocity, obtained via Bernoulli's equation, must be equal to the total velocity V_{Vap} on the cavity surface.

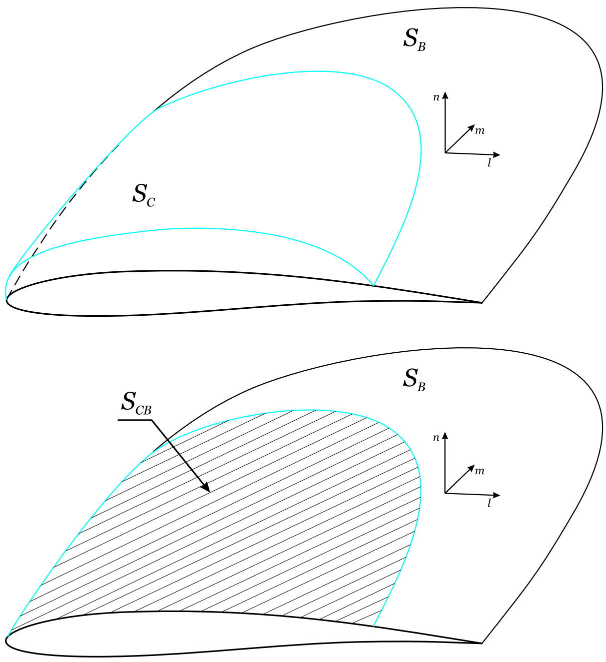

Figure 1: Exact (S_C) and approximate (S_{CB}) cavity surface definition.

If p_∞ is the pressure of the undisturbed flow field, p is the actual pressure and ρ is the flow density, in a propeller fixed reference system, Bernoulli's equation can be written in the following form:

$$p_\infty + \frac{1}{2}\rho\left|\mathbf{V}_\infty\right|^2 = p + \frac{1}{2}\rho\left[\left|\mathbf{V}\right|^2 - \left|\boldsymbol{\omega}\times\mathbf{r}\right|^2\right] + gy_{shaft} \tag{10}$$

If p_{Vap} indicates the vapour pressure of the flow, the modulus of the corresponding vapour pressure V_{Vap}, via equation (10) on the cavity surface, along each section of constant radius, , is equal to:

$$\left|\mathbf{V}_{Vap}\right| = \sqrt{\frac{2}{\rho}\left(p_\infty - p_{Vap}\right) + \left|\mathbf{V}_\infty\right|^2 + \left|\boldsymbol{\omega}\times\mathbf{r}\right|^2 - 2gy_{shaft}} \tag{11}$$

This dynamic boundary condition can be written as a Dirichlet boundary condition for the perturbation potential.

In order to obtain a Dirichlet boundary condition from the dynamic boundary condition it is necessary, first, (following Brizzolara and Caponnetto [2]) to define the controvariant components V^{α} and the covariant components V_{β} of the velocity vector $\boldsymbol{V}$:

$$\begin{aligned} &\boldsymbol{V} = V^{\alpha}\boldsymbol{e}_{\alpha} \\ &V_{\beta} = \boldsymbol{V}\cdot\boldsymbol{e}_{\beta} \rightarrow V_{\beta} = V^{\alpha}\boldsymbol{e}_{\alpha}\cdot\boldsymbol{e}_{\beta} \end{aligned} \qquad (12)$$

where $\boldsymbol{e}_{\alpha}$ are the unit vector of the reference system and α, β are equal to 1, 2 and 3. Defining the square matrix $g_{\alpha\beta} = \boldsymbol{e}_{\alpha}\cdot\boldsymbol{e}_{\beta}$ and its inverse $g^{\alpha\beta}$, the covariant component can be written as:

$$\begin{aligned} &V_{\alpha} = V^{\beta} g_{\alpha\beta} \\ &V_{\alpha} g^{\alpha\gamma} = V^{\beta} g_{\alpha\beta} g^{\alpha\gamma} = V^{\gamma} \end{aligned} \qquad (13)$$

Combining equations (12) with equations (13) the velocity vector $\boldsymbol{V}$ can be expressed in terms of the covariant components:

$$\boldsymbol{V} = g^{\alpha\beta} V_{\alpha}\boldsymbol{e}_{\beta} \qquad (14)$$

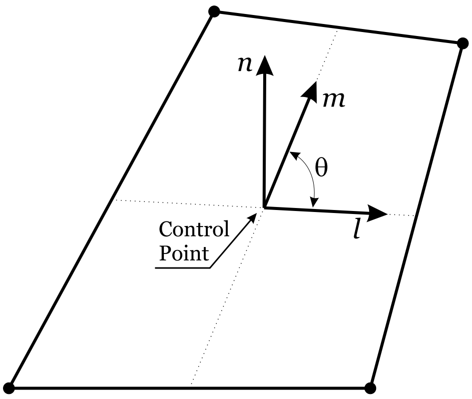

Figure 2: local non orthogonal panel coordinate system. Vectors $\boldsymbol{l}$ and $\boldsymbol{m}$ are formed by the lines connecting panel sides midpoints. Vector $\boldsymbol{n}$ is normal to $\boldsymbol{l}$ and $\boldsymbol{m}$.

In the present case (figure 2) the local coordinate system is defined by the vectors **l**, **m** and **n**, where $\boldsymbol{l}\cdot\boldsymbol{m} = \cos\theta$, $\boldsymbol{l}\cdot\boldsymbol{n} = 0$ and $\boldsymbol{m}\cdot\boldsymbol{n} = 0$. The $g_{\alpha\beta}$ and the $g^{\alpha\beta}$ matrix can, thus, be written in the following form:

$$\begin{aligned} g_{xy} &= \begin{bmatrix} 1 & \cos\theta & 0 \\ \cos\theta & 1 & 0 \\ 0 & 0 & 1 \end{bmatrix} \\ g^{xy} &= \frac{1}{\sin^2\theta}\begin{bmatrix} 1 & -\cos\theta & 0 \\ -\cos\theta & 1 & 0 \\ 0 & 0 & \sin^2\theta \end{bmatrix} \end{aligned} \qquad (15)$$

while the expression of the gradient can be obtained, from (14) and (15), as:

$$\nabla = \frac{1}{\sin^2\theta}\begin{bmatrix} 1 & -\cos\theta & 0 \\ -\cos\theta & 1 & 0 \\ 0 & 0 & \sin^2\theta \end{bmatrix}\begin{Bmatrix} \partial/\partial l \\ \partial/\partial m \\ \partial/\partial n \end{Bmatrix} \qquad (16)$$

The covariant component of the velocity on the non orthogonal reference system can be expressed as:

$$\begin{aligned} V_l &= \boldsymbol{V}_{rel}\cdot\boldsymbol{l} + \frac{\partial\phi}{\partial l} = U_l + \frac{\partial\phi}{\partial l} \\ V_m &= \boldsymbol{V}_{rel}\cdot\boldsymbol{m} + \frac{\partial\phi}{\partial m} = U_m + \frac{\partial\phi}{\partial m} \\ V_n &= \boldsymbol{V}_{rel}\cdot\boldsymbol{n} + \frac{\partial\phi}{\partial n} = U_n + \frac{\partial\phi}{\partial n} \end{aligned} \qquad (17)$$

And, from equation (14) the velocity vector is given by:

$$\begin{aligned} \boldsymbol{V} &= \left(\frac{1}{\sin^2\theta}\left(V_l - V_m\right)\cos\theta\right)\boldsymbol{l} \\ &+ \left(\frac{1}{\sin^2\theta}\left(V_m - V_l\right)\cos\theta\right)\boldsymbol{m} \\ &\qquad V_n\boldsymbol{n} \end{aligned} \qquad (18)$$

Assuming V_n vanishingly small, the normal component of the velocity can be neglected: in general it deteriorates the robustness of the solution and hardly influences the cavity extent as demonstrated by Fine [3].
Thus the modulus of the velocity becomes:

$$\left|\boldsymbol{V}\right|^2 = V_{\alpha}V_{\beta}g^{\beta\alpha} = \frac{1}{\sin^2\theta}\left(V_l^2 + V_m^2 - 2V_lV_m\cos\theta\right) \qquad (19)$$

Considering $\boldsymbol{l}$ approximately aligned with the local surface flow, it is possible to solve (19) with respect to $\partial\phi/\partial l$ (because, from equation (17) $V_l = U_l + \partial\phi/\partial l$) obtaining:

$$\begin{aligned} \frac{\partial\phi}{\partial l} &= -U_l + \left(\frac{\partial\phi}{\partial m} + U_m\right)\cos\theta \\ &+ \sin\theta\sqrt{\left|\boldsymbol{V}\right|^2 - \left(\frac{\partial\phi}{\partial m} + U_m\right)^2} \end{aligned} \qquad (20)$$

Equation (20) can be integrated to finally achieve a Dirichlet boundary condition for the perturbation potential, equivalent to the dynamic boundary condition. On the cavitating surface, where $\boldsymbol{V} = \boldsymbol{V}_{Vap}$, equation (20), after integration between bubble leading edge and bubble trailing edge, yields to:

$$\begin{aligned} \phi(m,l) = \phi_0(m) + \int_{L.E._{Bub}}^{T.E._{Bub}} \Bigg[&-U_l + \left(\frac{\partial\phi}{\partial m} + U_m\right)\cos\theta \\ &+ \sin\theta\sqrt{\left|\boldsymbol{V}_{Vap}\right|^2 - \left(\frac{\partial\phi}{\partial m} + U_m\right)^2}\,\Bigg] dl \end{aligned} \qquad (21)$$

where the only unknowns are the values of the perturbation potential at the bubble leading edge.
The kinematic boundary condition on the cavity surface, in steady flow, requires the flow to be tangent to the cavity surface itself.
With respect to the local (***l***,***m***,***n***) orthogonal coordinate reference system (figure 2), the cavity surface S_C (in terms of its thickness t) is defined as:

$$\boldsymbol{n} = t(\boldsymbol{l},\boldsymbol{m}) \rightarrow \boldsymbol{n} - t(\boldsymbol{l},\boldsymbol{m}) = 0 \tag{22}$$

and the tangency condition, by applying the covariant and the controvariant representation of velocity vectors and gradient defined above, can be written as:

$$\begin{aligned} \boldsymbol{V}\cdot\nabla\left(\boldsymbol{n}-t(\boldsymbol{l},\boldsymbol{m})\right) &= 0 \\ V_\alpha \nabla^\alpha\left(\boldsymbol{n}-t(\boldsymbol{l},\boldsymbol{m})\right) &= 0 \\ g^{\alpha\beta} V_\alpha \nabla_\beta\left(\boldsymbol{n}-t(\boldsymbol{l},\boldsymbol{m})\right) &= 0 \end{aligned} \tag{23}$$

Moreover:

$$\begin{aligned} \frac{\partial}{\partial l}\left(\boldsymbol{n}-t(\boldsymbol{l},\boldsymbol{m})\right) &= -\frac{\partial t}{\partial l} \\ \frac{\partial}{\partial m}\left(\boldsymbol{n}-t(\boldsymbol{l},\boldsymbol{m})\right) &= -\frac{\partial t}{\partial m} \\ \frac{\partial}{\partial n}\left(\boldsymbol{n}-t(\boldsymbol{l},\boldsymbol{m})\right) &= 1 \end{aligned} \tag{24}$$

And, from equation (16) and (23):

$$\frac{1}{\sin^2\theta}\{V_l, V_m, V_n\}\cdot \begin{bmatrix} 1 & -\cos\theta & 0 \\ -\cos\theta & 1 & 0 \\ 0 & 0 & \sin^2\theta \end{bmatrix} \cdot \begin{Bmatrix} -\partial t/\partial l \\ -\partial t/\partial m \\ 1 \end{Bmatrix} = 0 \tag{25}$$

Equation (25) yields to a differential equation for cavity thickness over the blade, with respect to the local reference system:

$$\begin{aligned} &\frac{\partial t}{\partial l}\left[\left(U_m+\frac{\partial\phi}{\partial m}\right)\cos\theta-\left(U_l+\frac{\partial\phi}{\partial l}\right)\right] + \\ &\frac{\partial t}{\partial m}\left[\left(U_l+\frac{\partial\phi}{\partial l}\right)\cos\theta-\left(U_m+\frac{\partial\phi}{\partial m}\right)\right] + \\ &\sin^2\theta\left(U_n+\frac{\partial\phi}{\partial n}\right) = 0 \end{aligned} \tag{26}$$

To solve for the cavity planform shape, another condition is required on the cavitating surface: the cavity height at its trailing edge must be zero (cavity closure condition).

This determines the necessity of an iterative solution to satisfy this, further, condition because the cavity height, computed via equation (26) is a non linear function of the solution (the perturbation potential ϕ) and of the extent of the cavity surface (via the dynamic boundary condition):

$$t(l_{T.E.}) = 0 \tag{27}$$

2.3 MIDCHORD FACE AND BACK CAVITATION

Midchord cavitation is becoming common in recent propeller designs: it is due to the attempt to increase efficiency, to the fact that, often, new design sections have flat pressure distributions on the suction side, or to the fact that a conventional propeller works in off design condition (Young and Kinnas [18], Mueller and Kinnas [16]).
The non axisymmetric flow a propeller may experience inside a wake is, often, characterized by smaller incoming velocities at certain angular positions: this traduces in small or negative angles of attack that may lead to face cavitation.
In order to capture simultaneously face and back cavitation and to allow midchord detachment, the theoretical formulation is exactly the same explained above with reference to the more common case of back cavitation only. The face cavitation problem can be treated exactly as the back cavitation problem, thus defining and adequate reference system (the face non orthogonal reference system needs to have the corresponding ***l*** unit vector pointing along the versus of the tangential velocity on the face of the profile) and imposing the same dynamic, kinematic and cavity closure conditions with respect to this, new, local reference system (figure 3).

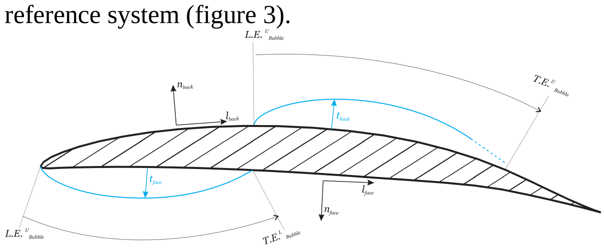

Figure 3: Back and Face reference coordinate system.

Arbitrary detachment line can be found, iteratively, applying criteria equivalent, in two dimensions, to the Villat-Brillouin cavity detachment condition (as in Young and Kinnas [18], Mueller and Kinnas [16]). Starting from a detachment line obtained from the initial wetted solution (and identified as the line that separates zones with pressures higher than the vapour tension from zones subjected to pressure equal or lower pressures) or an imposed one (typically the leading edge), the detachment line is iteratively moved according to:

- If the cavity at that position has negative thickness, the detachment location is moved toward the trailing edge of the blade.
- If the pressure at a position upstream the actual detachment line is below vapour pressure, then the detachment location is moved toward the leading edge of the blade.

3. NUMERICAL FORMULATION

Equation (4) is a second kind Fredholm's integral equation for the perturbation potential ϕ. Numerically it can be solved approximating boundary surfaces with quadrilateral panels, substituting integrals with discrete sums and imposing appropriate boundary conditions. The panel arrangement selected for this problem is the same adopted for the steady propeller panel method (Gaggero & Brizzolara [4], [5]), and, in discrete form, equation (4) takes the form:

$$\sum_{z=1}^{Z}\sum_{j=1}^{N} A_{ij}^{z}\mu_{j}^{z} + \sum_{z=1}^{Z}\sum_{m=1}^{M}\sum_{l=1}^{N_{W}} W_{iml}^{z}\Delta\phi_{ml}^{z} = \sum_{z=1}^{Z}\sum_{j=1}^{N} B_{ij}^{z}\sigma_{j}^{z} \qquad i=1,N\times Z \tag{28}$$

where N is the number of panels on the body (the key blade and its hub in the case of the propeller, as in Gaggero & Brizzolara [5], or the wing), Z is the number of blades (zero in the case of the wing) and A_{ij}, B_{ij}, W_{iml} are the influence coefficients of the dipoles (unknowns) and the sources (knows from the kinematic boundary condition) on the body and of the dipoles (knows from the Kutta condition) on the wake. Equation (28) represents a linear algebraic system valid for the wetted problem: in the cavitating case, the kinematic boundary condition (equation (5)) holds only on the wetted part of the surface, while from the dynamical boundary condition on the cavitating surface, the dipoles intensity (except for the dipoles intensity at bubble detachment) is known (equation (21)). Thus linear system (28) can be rewritten taking into account the boundary conditions on the cavitating surfaces. From the dynamic boundary condition (21), numerically solved via a quadrature technique, the dipoles intensity on each cavitating i panel of the j cavitating strip can be written as:

$$\phi_{ij} = \phi_{0j} + \sum_{i=L.E._{Bub.}}^{T.E._{Bub.}} F_{ij} \tag{29}$$

in which ϕ_{0j} is the perturbation potential, unknown, at the cavitation bubble leading edge for the j strip and F_{ij} is the numerical values of the integral in equation (21).

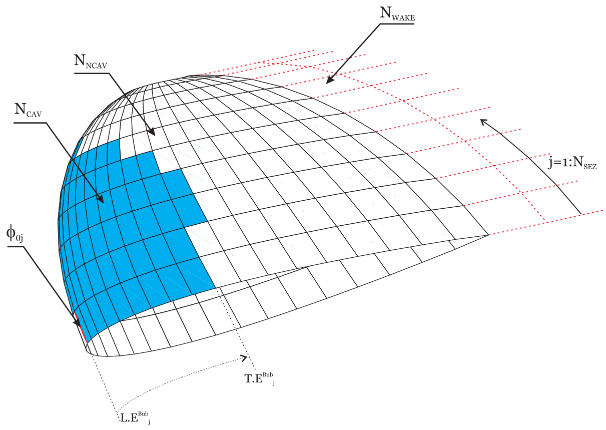

Figure 4: Blade numbering arrangement

With respect to figure 4, linear system (28) for the key blade (all the other blades, in the steady solution, are taken into account only via influence coefficients) becomes:

$$\sum_{j=1}^{N_{NCAV}} A_{ij}\mu_{j} + \sum_{j=1}^{N_{CAV}} B_{ij}\sigma_{j}^{cav.} + \sum_{j=1}^{N_{SEZ.}} \phi_{0j}\xi_{j}\left[\sum_{m=L.E._{j}^{Bub.}}^{T.E._{j}^{Bub.}} A_{ij}\right] = \sum_{j=1}^{N_{NCAV}} B_{ij}\sigma_{j} + \sum_{j=1}^{N_{SEZ.}} \xi_{j}\left[\sum_{m=L.E._{j}^{Bub.}}^{T.E._{j}^{Bub.}} F_{ij}A_{ij}\right] + \sum_{j=1}^{N_{WAKE}} W_{ij}\Delta\phi_{j} \tag{30}$$

where ξ_j is a cavitation index: if the j section is subjected to cavitation ξ_j is equal to 1, otherwise ξ_j is equal to 0.

Linear system (30) has N_{NCAV}+N_{CAV}+N_{SEZCAV} unknowns but only N_{NCAV}+N_{CAV} equations. Further N_{SEZCAV} equations can be written for the N_{SEZCAV} ϕ_0 unknowns. At the cavity leading edge the perturbation potential, for the back but also for the face cavitation problem, is calculated via extrapolation from previous values:

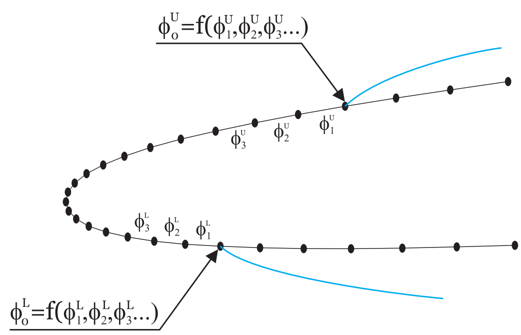

Figure 5: Extrapolation of perturbation potential at Cavity L.E.

$$\begin{aligned} \phi_0^U &= f\left(\phi_1^U, \phi_2^U, \phi_3^U, \dots\right) \\ \phi_0^L &= f\left(\phi_1^L, \phi_2^L, \phi_3^L, \dots\right) \end{aligned} \qquad (31)$$

Once the problem has been solved for a guessed cavity planform and the perturbation potential and the cavity source strengths are knowns, the cavity height on the blade can be computed by integrating equation (26).
Replacing the partial derivatives with finite difference formulae, it is possible to obtain a recursive expression for the cavity thickness at a point (*l,m*) as a function of cavity thickness on previous computed ones (*l-1, m-1*):

$$K_L\left(\frac{t_{l,m}-t_{l-1,m}}{\Delta l}\right)+K_M\left(\frac{t_{l,m}-t_{l,m-1}}{\Delta m}\right)+K_N=0 \qquad (32)$$

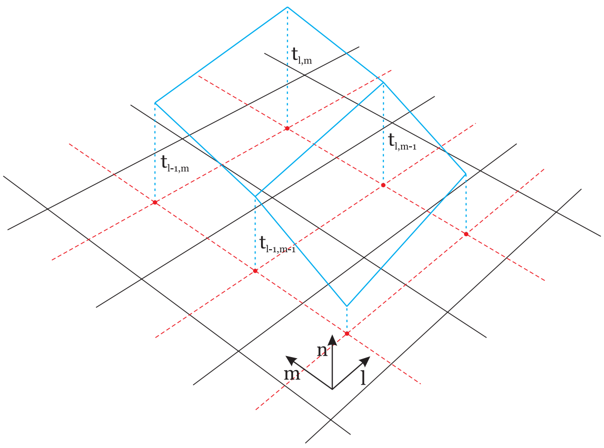

Figure 6: Finite difference arrangement for thickness calculation

To find the correct discrete cavity planform it is necessary to impose the cavity closure condition. The iterative approach adopted is shown in the flow chart of figure 7.
First, linear system (30) is solved with the first guessed cavity planform and all the unknowns (dipoles, sources and cavity thickness) are computed with the current configuration of cavitating and non cavitating panels. With this first guessed cavity shape the closure condition, normally, is not satisfied. Hence, the shape is iteratively changed, adding (if the cavity thickness is still positive) or subtracting (if the cavity thickness is already negative), at the trailing edge of each cavitating section, a panel and solving again the problem, with this new configuration of cavitating and non cavitating panels, until the cavity thickness at the bubble trailing edge is below a fixed threshold and, simultaneously, the derivative of cavity thickness at the same point with respect to the chordwise coordinate is negative (in order to select the stable solution).

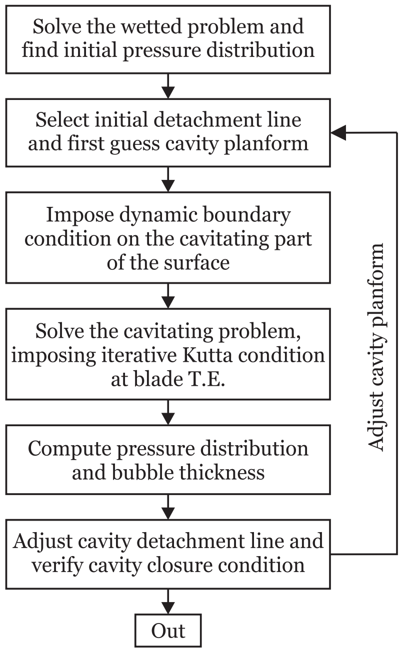

Figure 7: Cavitating flow solver flow chart

4. WEAKLY NONLINEAR SOLUTION

A major refinement in the solution could be achieved with a fully nonlinear solution, i.e. with all the singularities placed on the actual cavity surface. This would imply the application of a fully nonlinear boundary conditions and a further iterative approach that could render the solver extremely time expensive and less affordable for the preliminary design of a propeller.
An alternative efficient model in terms of robustness and accuracy is a partially nonlinear solver, with the singularities located on the foil surface, applied on a grid refined near the bubble leading and trailing edge (figure 8).

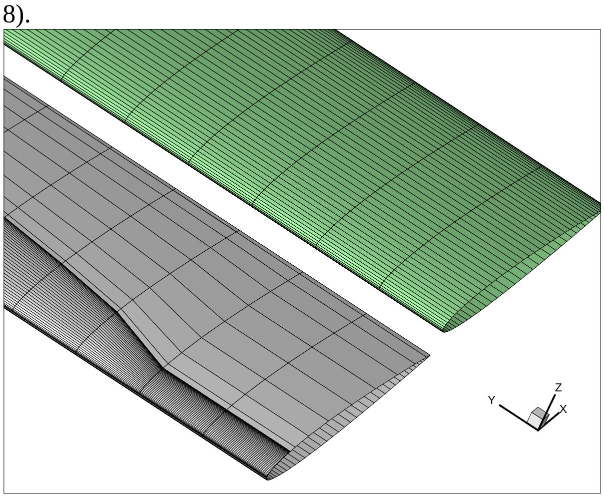

Figure 8: Comparison between initial grid and the regridded surface.

Also in this case, the best solution arises from an iterative approach, as presented in the flow chart of figure 9. After the first partial nonlinear cavity solution on the initial grid, surfaces are regridded in order to cluster panels near leading and trailing cavity bubble edge. Then the problem is solved until a converged solution is achieved.

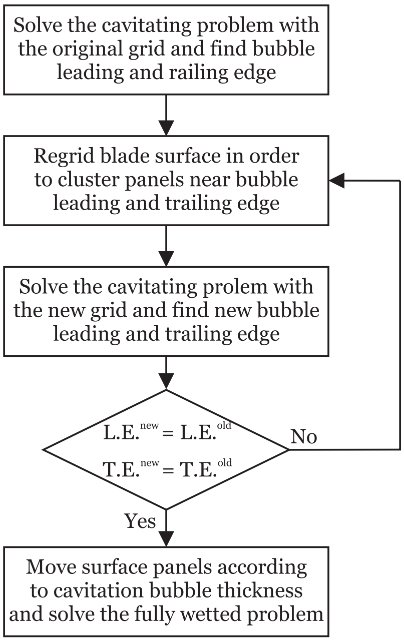

Figure 9: Partial nonlinear solver flow chart

However, regridding and recomputing influence coefficients at each iteration is quite time expensive. Thus, this partial nonlinear approach with regridding is useful to validate the implemented 3D solver: after convergence, the blade surface can be moved according to the computed cavity thickness and the so changed geometry adopted for a "fully wetted solution".

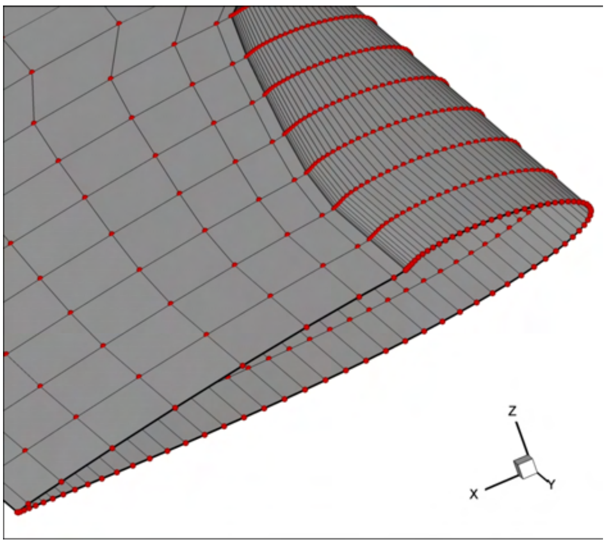

Figure 10: Deformed surface configuration

The fully wetted solution is a measure of the consistency of the cavitating solution. The sheet bubble cavitation has been computed, via the kinematic boundary condition, as a streamline for the flow, imposing that the total velocity on that streamline is equivalent to the vapour pressure. So, the wetted solution, computed on the deformed geometry, should shows a flat pressure distribution, equal to the vapour pressure, over all the computed cavitating area of the blade.

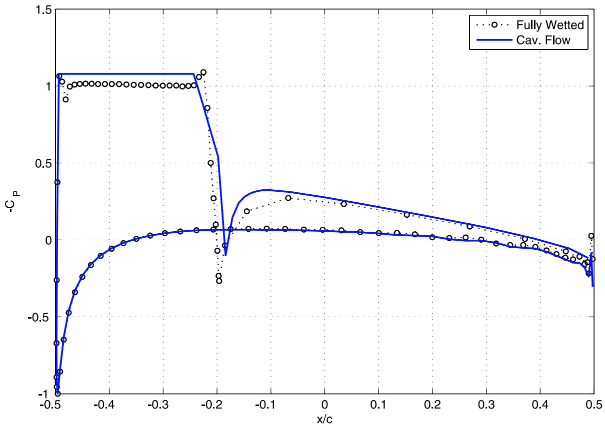

Figure 11: Consistency test, NACA0015 wing, α = 5°, y/s = 0

Figures 11 and 12 show the comparison between the fully wetted solution, computed on the deformed geometry obtained on the regridded surface, and the partial nonlinear solution without regridding. It is clear how the two solutions are in good mutual agreement: the fully wetted solution on the deformed geometry captures well the behaviour of pressure at the bubble leading and trailing edge and shows the typical flat vapour pressure zone.

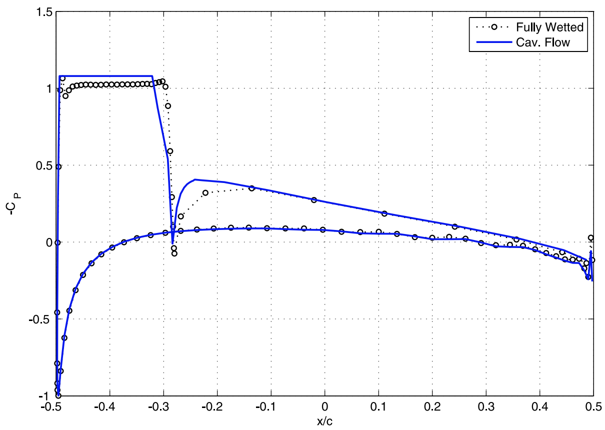

Figure 12: Consistency test, NACA0015 wing, α = 5°, y/s = 0.54

On the other hand, the partial nonlinear solution without regridding, with an adequate chordwise number of panels, ensures a sufficiently good solution, with a much greater computational efficiency.

5. NUMERICAL RESULTS

5.1 CONVERGENCE

To test the numerical cavitating flow solver, a convergence and consistency analysis based on three dimensional wings has been carried out, in order to check about the stability and the robustness of the code.
Unfortunately, it is quite difficult to find in literature a systematic study on cavitating wings: there are only few numerical results, while experimental data are, essentially, in terms of sketches or pictures of the cavity pattern recognized at the cavitation tunnel.
Thus, to validate the solver, a rectangular wing, NACA 0006 profile, with aspect ratio equal to 4, operating at a cavitation index $\sigma_V = (p - p_{Vap}) \big/ (0.5 \rho V^2)$ equal to 0.6 has been tested since, for this configuration, other numerical solutions are available (Bal & Kinnas [1]).
Figure 13 shows the behaviour of the solution, in term of developed cavity bubble, with the number of panels along the chord: this seems to be the most important parameter for the convergence, because of the assumption, in the dynamic boundary condition, that the velocity is almost aligned with the local ***l*** vector.
With respect to the fully wetted solver (Gaggero and Brizzolara [4]), the convergence is sensitively slower and an acceptable solution is achieved with a number of panel along the profile greater than seventy. In particular, the solution is affected by the number of panels at the trailing edge of the bubble, where the relative dimension of the panels is greater (due to the full cosine spacing that clusters point near the blade leading and trailing edge) and this influence the value of the dynamic boundary condition integral.

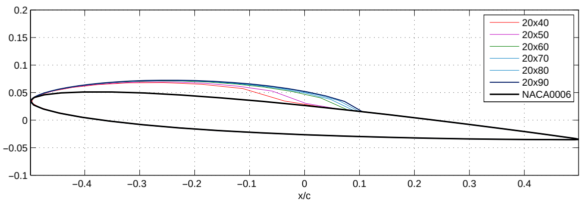

Figure 13: Convergence analysis, NACA 0006 profile, α=4°, σ_V=0.6 at midspan.

For this configuration other numerical results are available. Bal & Kinnas [1] performed a calculation with the code developed, for the first time, at M.I.T. by Fine [3], on the same rectangular wing. Their results, and a comparison with those from the present method, are reported in figure 14.

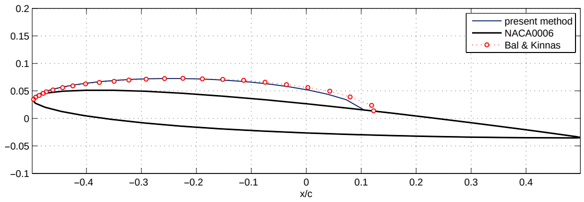

Figure 14: Comparison between preset method and results from Bal & Kinnas, NACA 0006 profile, α=4°, σ_V=0.6 at midspan.

The comparison between the present method and Bal & Kinnas shows an overall good agreement of the computed thickness on the midspan section. Only a little difference persists at cavity trailing edge: Bal & Kinnas predict a cavity planform slightly longer than that predicted by the present method.

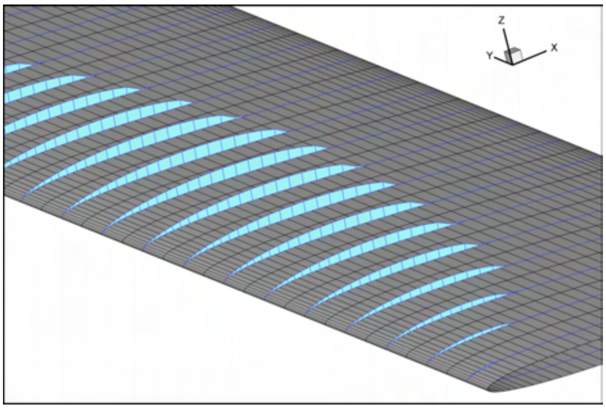

Figure 15: Cavity thickness distribution, NACA 0006 profile, α=4°, σ_V=0.6.

This difference can be attributed to a different cavity closure condition and to a different panel arrangement. Bal & Kinnas computation are performed using the so called "*panel split technique*" (Fine [3]) in order to reduce the influence of panels partially subjected to the cavity and partially subjected to the wetted flow on the stability of the solution. Their PROPCAV code find a continuous cavity planform iteratively using a cavity closure condition on the curvilinear coordinate along the profile, while present method works only in a discrete way, adding or subtracting an entire panel at the cavity trailing edge. Moreover they apply a grid refinement at the cavity trailing edge to reduce the error in the computation of the dynamic condition integral.

5.2 BACK AND FACE CAVITATION

Also for the case of face and back simultaneous cavitation, with arbitrary detachment line, no experimental data were available for validation. Only a numerical validation of the code (consistency and convergence) has been done therefore.

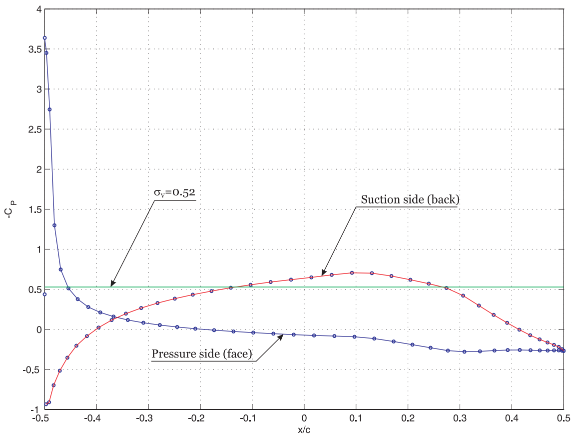

Figure 16: Pressure distribution based on the fully wetted solution.

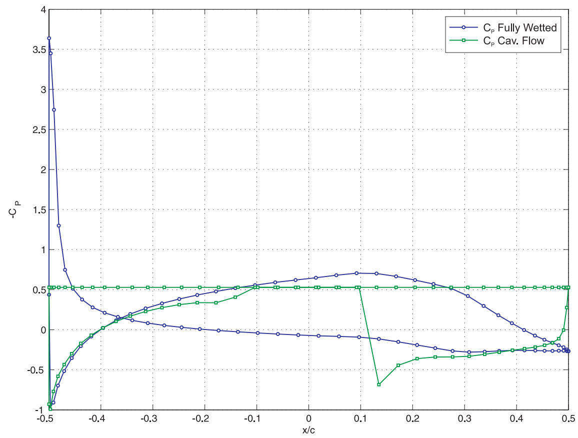

Figure 17: Pressure distribution based on the cavity solution.

Figure 16 shows the pressure distribution at midspan for a rectangular wing with NACA66 profile, *a08* camber line, thickness over chord ratio equal to 0.1, camber over chord ratio equal to 0.06, tested with a negative angle of attack (α = -3°), at a velocity of 20 m/s (σ_V = 0.52).
The pressure distribution is obtained in the fully wetted condition, *i.e.* without taking into account the risk of cavitation and its effects on the pressure distribution.
Working with a negative angle of attack determines an inversion in the pressure distribution at blade leading edge: the pressure side (face of the wing) is subjected to a pressure greatly lower than the vapour pressure, while the suction side (back of the wing) experiments such lower values of pressure only from midchord position.
So, it is clear the necessity of a code able to predict, simultaneously, face, back and midchord cavitation, in order to capture the effects of the cavity bubble on the pressure distribution (and, so, on the performance of the wing/propeller) also in off-design working conditions.
Figure 17 shows the pressure distribution obtained with the cavity solver and compares it with the fully wetted solution.
Three main aspects of the solution can be highlighted. First, face and back cavitation, with midchord detachment, is simultaneously well captured: it appears as a constant pressure distribution, equal to the vapour pressure, on all the areas subjected to the sheet cavity bubble. Secondly, from pressure diagram, the effect of the developed cavity can be outlined: the constant vapour pressure affects a length greater than that identified by the fully wetted solution, i.e. that area subjected to a pressure lower than the vapour tension. This is due to the fact that the cavity bubble detaches from the first point having pressure lower than vapour tension, but its length can overcome the chordwise extension of the lower pressure region found by the fully wetted solver.

The extension of the cavity bubble arises from the kinematic boundary condition and from the cavity closure condition, that impose the vapour pressure on all the length of the converged cavity bubble.
Finally, it can be noted that the iterative Kutta condition is able, also in the case of cavitating flows, to guarantee closed pressure diagrams at blade trailing edge, even if the profile is supercavitating and the cavity bubble has a finite thickness at its trailing edge.
Figure 18, instead, shows, for the same wing, the cavity shape at midspan. A smooth detachment, according to the Villat-Brillouin cavity detachment criteria is evident, either in the case of face leading edge detachment and in the case of midchord back detachment.
Figures 19 and 20 show a typical prediction of cavitation pattern obtained with the code using the previously detailed hydrofoil geometry. The blade is tested at positive and negative angles of attack (±9°), with a cavitation index σ_V equal to 1.47.

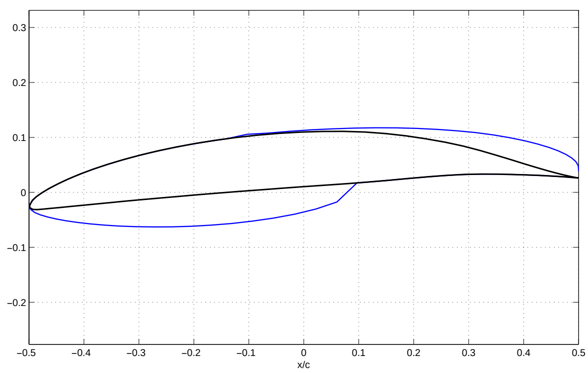

Figure 18: Cavity shape at midspan based on cavity solution.

Results show the ability of the code to detect back and face leading edge cavitation and to predict the correct pressure distribution on it (figure 21 and 22).

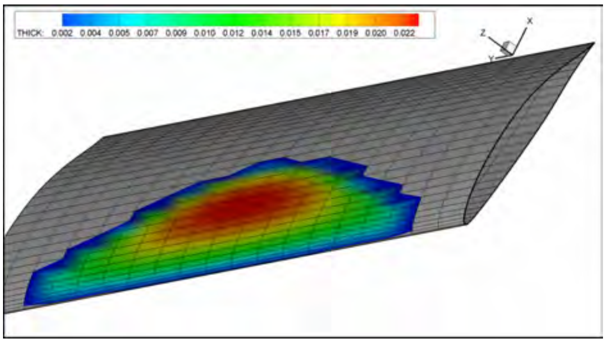

Figure 19: Cavity planform, NACA66 a08 hydrofoil, $\alpha = 9°$, $\sigma_V = 1.47$

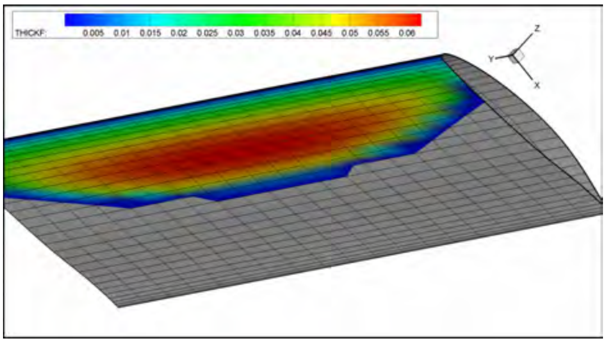

Figure 20: Cavity planform, NACA66 a08 hydrofoil, $\alpha = -9°$, σ_V=1.47

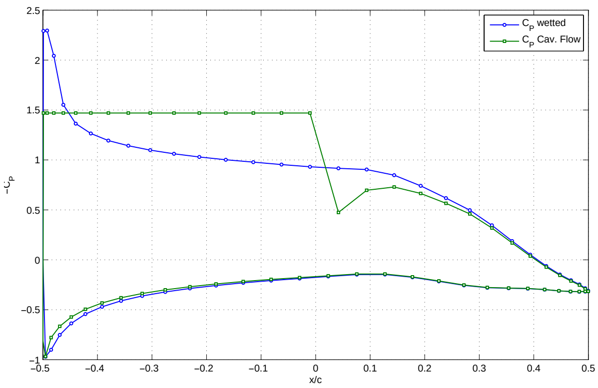

Figure 21: Pressure distribution at midspan, NACA66 a08 hydrofoil, $\alpha = 9°$, $\sigma_V = 1.47$ (wetted solution versus cavitating solution).

Finally figures 23 and 24 present a numerical validation of the code in case of simultaneous face and back cavitation. The test is performed by comparing the cavity shape of the same hydrofoil, once with positive camber and positive angle of attack, and the once with inverted (negative) camber and negative angle of attack.

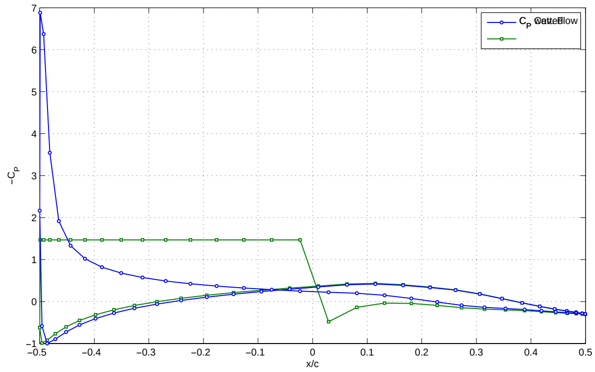

Figure 22: Pressure distribution at midspan, NACA66 a08 hydrofoil, $\alpha = -9°$, $\sigma_V = 1.47$ (wetted solution versus cavitating solution).

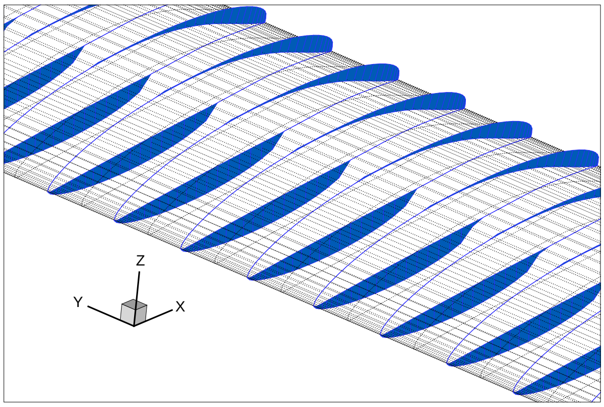

Figure 23: Validation of simultaneous face and back cavitation on an asymmetric rectangular hydrofoil, NACA 66 *a08*, $\alpha = +3°$.

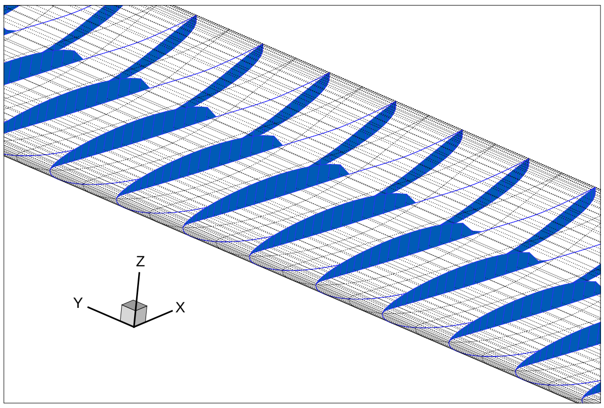

Figure 24: Validation of simultaneous face and back cavitation on an asymmetric rectangular hydrofoil, NACA 66 *a08*, $\alpha = -3°$.

As expected, the symmetry of the solution with respect to the *x-y* plane, is verified by the two calculation cases. Moreover a nice and smooth detachment for the back midchord bubble and for the leading edge face bubble is verified.

6. THE PROPELLER PROBLEM

The cavitating propeller problem represents the main scope of application for the devised potential panel method: predict the correct cavity extent on back and face sides is fundamental to calculate hydrodynamic forces, obtained via integration of pressure on the blade, for particular or off design operating conditions.
As in the case of hydrofoils (figure 21 and 22), integrating the wetted pressure distribution or the cavitating flow pressure distribution would lead to very different global values.

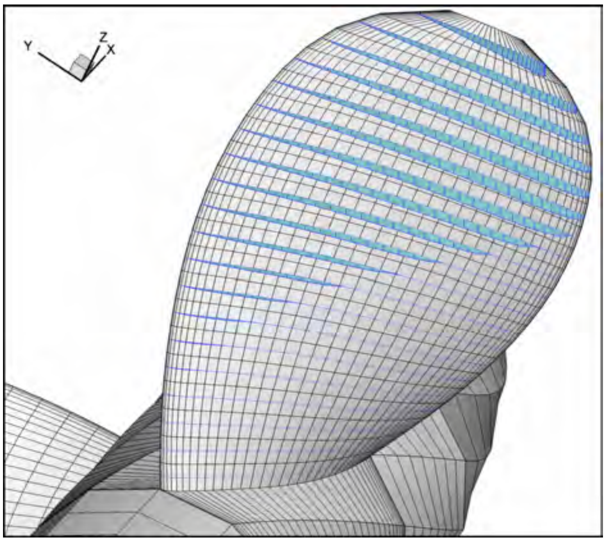

Figure 25: Propeller DTMB 4148, back cavitation, J = 0.6, σ_N = 1.5

As an example, the results obtained in the case of DTMB 4148 propeller are presented. The 4148 is a three blade propeller, adopted for a wide range of experimental measurements and numerical calculations, specially to test unsteady cavitation (Mueller and Kinnas [16], Young and Kinnas [18]).
Figure 25 shows the cavity shape for the propeller working at an off design advance coefficient *J = 0.6*, with cavitation index $\sigma_N = (p - p_{Vap})/(0.5\rho D^2 N^2)$ equal to 1.5.
The panelling arrangement is done with 20 sections along the radius and 70 panels along the chord, in order to obtain a satisfying solution, in terms of convergence and robustness, in a reasonable calculation time.
With this parameters choice, the cavity bubble develops only on the back side of the propeller and it detaches, mostly, at blade leading edge or just 2÷3 % aft the leading edge.
In extreme working conditions (different J or σ) the propeller goes into a face and midchord cavitation. As presented in figures 26 and 27, with a greater advance coefficient (that induces negative angles of attack) and a lower value of cavitation index (σ_N 0.9), the propeller is subjected to a face super-cavitation that starts from the leading edge (the cavity thickness is finite along almost all the blade trailing edge, as it is possible to see from figure 27).

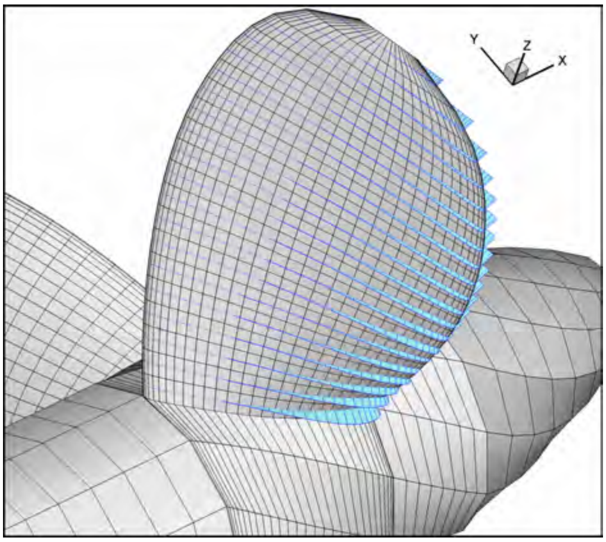

Figure 26: Propeller DTMB 4148, back cavitation, J = 1.1, σ_N = 0.9

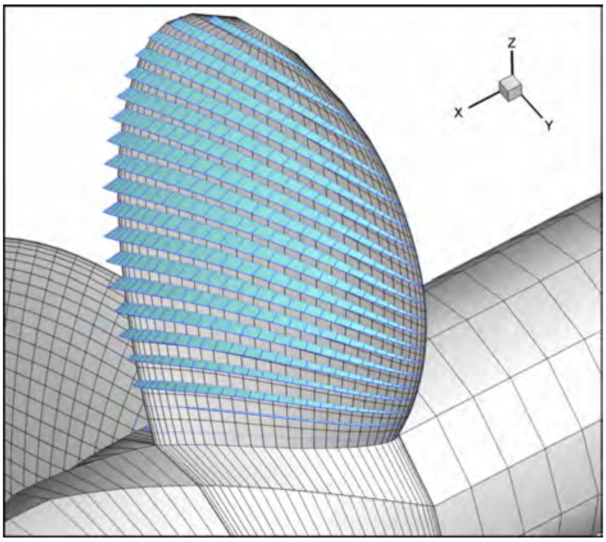

Figure 27: Propeller DTMB 4148, face cavitation, J = 1.1, σ_N = 0.9

On the back side, simultaneously, midchord cavitation occurs (figure 26) with a thinner bubble extended up to the blade trailing edge.
For validation of the cavitating propeller case a set of experimental tests carried out at the cavitation tunnel of the Department of Naval Architecture of the University of Genova, have been selected. The propeller model E033 is a four bladed propeller, having a diameter of

0.227m, with moderate rake and skew distribution and a base NACA16 profile.

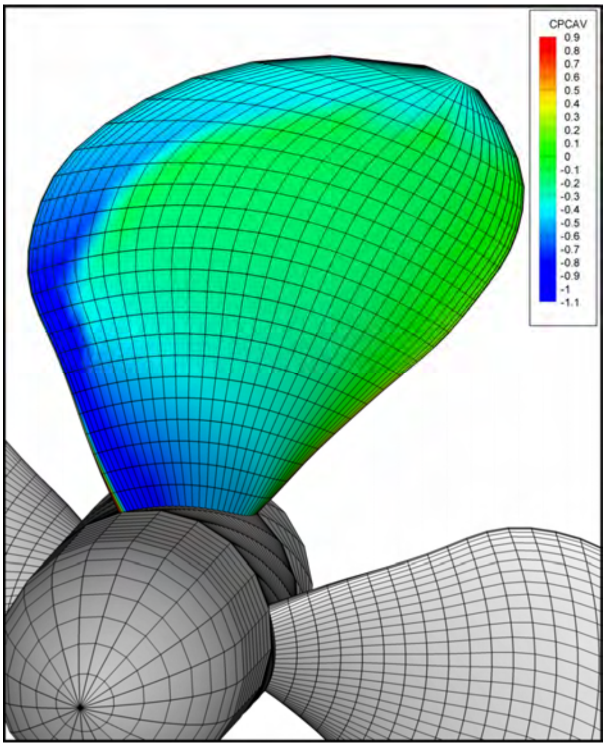

Figure 28: Propeller E033, J = 0.9, σ_N = 3.5, back pressure distribution

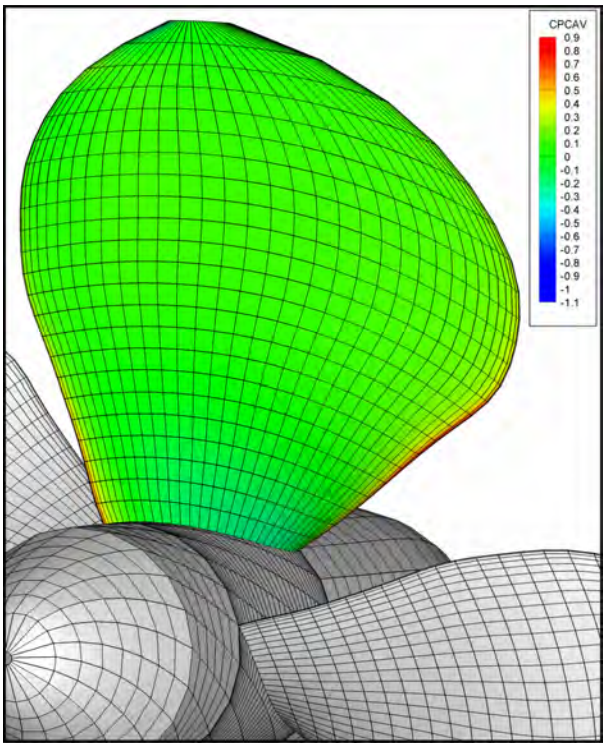

Figure 29: Propeller E033, J = 0.9, σ_N = 3.5, face pressure distribution

While it is quite difficult to directly measure pressure on the blade surface (so figures 28 and 29 report only computed pressure coefficient), a simple comparison between experiments and the numerical code can be carried out with respect to cavity extent.
Figures 30 and 31 show the predicted (left) and the real (right) cavity extent for the E033 propeller, tested at two different advance coefficients and at two different cavitation indexes.

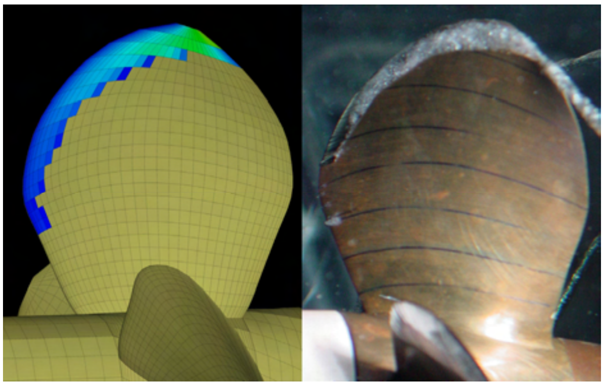

Figure 30: Propeller E033, J = 0.9, σ_N = 3.5

The propeller, in steady flow, is subjected only to back cavitation (observed during experiments and numerically computed), with a quite strong tip vortex cavitation, that the present method is still not able to predict. However, a satisfying prediction of the cavitation pattern on the blade is found.

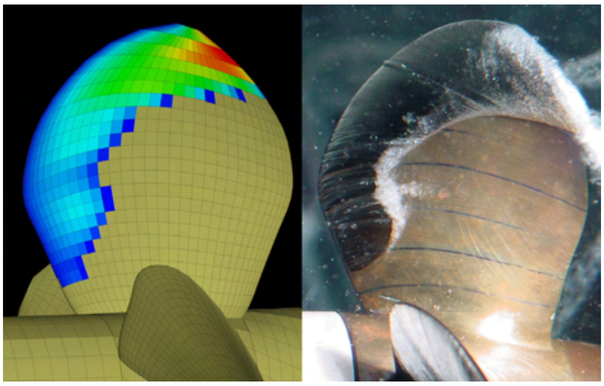

Figure 31: Propeller E033, J = 0.8, σ_N = 2.5

7. CONCLUSION

Theoretical and numerical details of a stationary potential flow panel method able to predict face and back cavitation on three dimensional lifting bodies, such as hydrofoils and propellers, have been presented in the paper. The method relies on a robust and generalized numerical scheme which allows the detachment of the bubble from multiple and sparse points on the modeled surfaces. Several application examples given in the paper demonstrate this ability of the code. The good

consistency of the partially non-linear model used to solve boundary conditions on the cavities, has been verified against a fully wetted model applied on the deformed hydrofoil surface with the previously computed cavity shape.
The accuracy and convergence of the method have been presented and discussed in the case of cavitating three dimensional hydrofoils, showing good correlation with similar numerical simulations.
The application of the method, in case of a propeller evidenced excellent correlation with experimental results in terms of predicted cavity planform shape.
Further developments of the presented method currently planned are the extension of the method to deal with non-stationary flows and the possibility to predict and solve super-cavitating bubbles.

8. REFERENCES

1. BAL S. and KINNAS S.A. 'A BEM for the Prediction of Free Surface Effects on Cavitating Hydrofoils'. *Computational Mechanics (28)*, 2002.

2. CAPONNETTO M. and BRIZZOLARA S. ' Theory and Experimental Validation of a Surface Panel Method for the Analysis of Cavitating Propellers in Steady Flow'. *PROPCAV '95 Conference, Newcastle Upon Tyne, U.K.*, 1995.

3. FINE N.E. 'Nonlinear Analysis of Cavitating Propellers in Nonuniform Flow'. *Ph.D Thesis, M.I.T. Department of Ocean Engineering*, 1992.

4. GAGGERO S. and BRIZZOLARA S. 'Exact Modelling of Trailing Vorticity in Panel Methods for Marine Propeller'. *2nd International Conference on Marine Research and Transportation, Ischia,* 2007.

5. GAGGERO S and BRIZZOLARA S. 'A Potential Panle Method for the Analysis of Propellers in Unsteady Flow'. *8th Symposium on High Speed Marine Vehicles*, *Naples*, 2008.

6. HOSHINO T. 'Hydrodynamic Analysis of Propeller in Unsteady Flow Using a Surface Panel Method', *Journal of the Society of Naval Architects of Japan, Vol. 174, pp 71-87*, 1993.

7. HOSHINO T. 'Numerical and Experimental Analysis of Propeller Wake by Using a Surface Panel Method and a 3-Component LDV', *18th Symposium on Naval Hydrodynamics*, 1991.

8. HSIN C.H. 'Development and Analysis of Panel Methods for Propeller in Unsteady Flow'. *Ph.D Thesis, M.I.T. Department of Ocean Engineering*, 1990.

9. JESSUP S. 'An Experimental Investigation of Viscous Effects of Propeller Blade Flow'. *Ph.D Thesis, The Catholic University of America,* 1989.

10. LAMB H. 'Hydrodynamics'. *Cambridge University Press*, 1932.

11. LEE H. 'Modelling of Unsteady Wake Alignment and Developed Tip Cavitation'. *Ph.D Thesis, The Environmental and Water Resource Engineering Department of Civil Engineering, The University of Texas at Austin*, 2002.

12. LEE J.T. 'A Potential Based Panel Method for the Analysis of Marine Propeller in Steady Flow'. *Ph.D Thesis, M.I.T. Department of Ocean Engineering*, 1987.

13. MAGNUS A.E. and EPTON M.A. 'PAN AIR-A Computer Program for Predicting Subsonic or Supersonic Linear Potential Flows About Arbitrary Configurations Using A Higher Order Panel Method', *Vol. 1. Theory Document (Version 1.0), NASA CR-3251*, 1980.

14. MASKEW B. 'VSAERO Theory Document'. *NASA Ames Research Center*, 1984.

15. MORINO L. and KUO C.C. 'Subsonic potential aerodynamic for complex configurations: a general theory'. *AIAA Journal, Vol. 12*, 1974.

16.MUELLER A.C. and KINNAS S.A. 'Propeller Sheet Cavitation Predictions Using a Panel Method'. *Journal of Fluids engineering, vol. 121*, 1999.

17. VAZ G. and BOSSCHERS J. 'Modelling Three Dimensional Sheet Cavitation on Marine Propellers Using a Boundary Element Method'. *6th International Symposium on Cavitation*, *The Netherlands*, 2006.

18. YOUNG Y.L. and KINNAS S.A. ' A BEM for the Prediction of Unsteady Midchord Face and/or Back Propeller Cavitation'. *Journal of Fluids Engineering, vol. 123*, 2001.

NONLINEAR SEAKEEPING ANALYSIS OF CATAMARANS WITH CENTRAL BULB

Dario Bruzzone[1], **Alessandro Grasso**[1] and **Igor Zotti**[2]

[1]University of Genoa - Department of Naval Architecture and Marine Technology, Italy
[2]University of Trieste - Department of Naval Architecture, Ocean and Environmental Engineering, Italy

SUMMARY

A nonlinear seakeeping analysis has been performed on a catamaran hull with a central body of revolution, advancing in head regular waves. Numerical simulations have been performed employing a weakly nonlinear methodology, which assumes linear radiation and diffraction forces and requires the computation of fully nonlinear Froude-Krylov and hydrostatic forces in the time domain. The procedure is divided into three steps: evaluation of dynamic sinkage and trim in steady water, evaluation of linear motions due to incident waves and prediction of nonlinear motions. A three-dimensional Rankine panel method has been used for the first two steps.
Results, for the catamaran with and without the appendage, have been compared with data obtained from experimental tests, both in terms of amplitude operators and time histories. Nonlinear effects, obtained varying the wave steepness, have been analyzed and the influence of the bulb on the nonlinear responses have been assessed.

1. INTRODUCTION

Multihull vessels represent a very important and widespread typology of high speed craft and catamarans result to be the most common, even if their seakeeping characteristics are generally worse than those of the other kind of vessels. Considering that behaviour in waves turns out to be a very important feature, particularly for vessels intended for passenger transportation, studies on new type of appendages, other than the classical hydrofoils, have been carried out in several researches; the installation of a central bulb between the hulls of a catamaran, has also been considered with the aim of improving resistance and seakeeping. Within the framework of previous research projects the authors of the present paper carried out investigations both numerically (linear analyses) [1] and by experimental tests [2].
In this paper a nonlinear seakeeping analysis is performed on a catamaran hard-chine hull and on a configuration of the same catamaran but with a central bulb (this catamaran concept was named BulbCat). The catamaran and the BulbCat were tested in regular waves at the towing tank of the University of Trieste.
Several researchers have focused their studies on methodologies capable of including nonlinear effects in the solution of the seakeeping problems, as the interest for motions and loads in heavy weather, when nonlinear effects become no more negligible, is remarkably increased in the years.
Different formulations have been proposed in literature in order to include nonlinear effects both with two and three dimensional approaches; they are generally solved in the time domain. Some of them combine linear with non linear terms, others apply fully nonlinear potential flow methods. Recently, studies have also been carried out in order to treat the viscous flow seakeeping problem, solving the Reynold averaged Navier-Stokes equations in the time domain. An extensive bibliography can be found in literature, but a comprehensive classification and review is given in [3].
Hybrid approaches (also called “blended methods”) allow to introduce some nonlinearities in the linear model, generally evaluating hydrostatic and Froude-Krylov forces, which are in fact easy to compute in time domain in their intrinsic nonlinear form, by pressure integration over the instantaneous wetted surface. Diffraction and radiation forces are instead obtained by transforming in the time domain their frequency domain counterparts. These methods, which can be employed in a wide range of applications, have been developed because of the problems associated with fully nonlinear computations (for instance, numerical stability and wave breaking) and in order to reduce computational time and resources required.
For the numerical simulations here proposed, a three-dimensional Rankine panel method has been employed for both the steady state and the linear seakeeping problems. Then, in order to take into account nonlinearities, a blended method of the family in the foregoing description has been used in a dual approach: Froude-Krylov and hydrostatic forces are evaluated in the time domain and the equation of motion are solved in the frequency domain (in their weakly nonlinear form) by an iterative procedure. All the codes employed have been developed at the University of Genoa.

2. MATHEMATICAL MODEL

As previously introduced, seakeeping analyses has been carried out employing a weakly nonlinear methodology, which allows to take into account nonlinear effects related to Froude-Krylov and hydrostatic forces; on the contrary, nonlinearities related to radiation and diffraction forces are supposed to be negligible.

This approach is really fast compared to fully nonlinear computations and provides results with engineering accuracy in a fairly wide range of sea states.
The methodology proceeds in three consecutive steps, i.e. the solution of the following problems:

- steady flow around a ship advancing at constant speed, for determining iteratively the dynamic sinkage and trim;
- linear seakeeping analysis, in order to evaluate radiation and diffraction forces solving the unsteady hydrodynamic problem for a proper number of meaningful arbitrary frequencies;
- weakly nonlinear seakeeping analysis.

2.1. DYNAMIC SINKAGE AND TRIM PREDICTION

In order to predict dynamic sinkage and trim, the problem of the steady state flow around a ship advancing at constant speed is solved. The present approach is based on the assumptions of inviscid fluid and irrotational flow, which allow the employment of a potential theory.
A right handed orthogonal coordinate system *(x,y,z)* advancing at the vessel speed *U* is defined. It maintains the *xy* plane coincident with the undisturbed free surface, *x* is the symmetry axis of the still water plane and is assumed positive astern, *z*-axis is positive upwards.
The total velocity potential Φ_S must satisfy the Laplace equation in the fluid domain Ω, a condition of no flow penetration on the hull surface S_H, as well as a kinematic and a dynamic condition on the free surface, which vertical position is given by $\eta(x,y)$.

$$\Delta\Phi_S = 0 \qquad \text{in } \Omega \tag{1}$$

$$\frac{\partial\Phi_S}{\partial\vec{n}} = 0 \qquad \text{on } S_H \tag{2}$$

$$\left.\begin{aligned} &\frac{\partial\Phi_S}{\partial x}\frac{\partial\eta}{\partial x}+\frac{\partial\Phi_S}{\partial y}\frac{\partial\eta}{\partial y}-\frac{\partial\Phi_S}{\partial z}=0 \\ &\frac{1}{2}\left(\nabla\Phi_S\cdot\nabla\Phi_S-U_\infty^2\right)+gz=0 \end{aligned}\right\} \qquad \text{on } z=\eta \tag{3}$$

Combining these equations with the radiation condition of no upstream waves, it is possible to set up a boundary value problem in terms of the unknown velocity potential.
The nonlinear free surface boundary conditions in (3), applied at $z = 0$, are linearised considering Φ_S as the sum of a double-model potential and an unknown perturbation potential of a lower order of magnitude. The double-model potential is evaluated solving the flow around a deeply immersed body composed by the model and its mirror with reference to the undisturbed free surface [4].
The wetted hull and a part of the free surface surrounding the body are approximated by flat quadrilateral panels, on which Rankine sources are applied. The influence coefficients for the velocity are find according to the Hess and Smith procedure [5], while the second order derivatives of the potential on the free surface are obtained by finite difference operators. Imposing the boundary conditions at the centre of each panel, a linear system of equations for the unknown source strengths is obtained and solved.
Hydrodynamic forces are then calculated integrating the pressures on the hull surface obtained by Bernoulli equation.
Sinkage and trim are then calculated using an iterative procedure to reach equilibrium among mass, hydrostatic and hydrodynamic forces and moments.
More details on the methodology can be found in [6].

2.2. LINEAR SEAKEEPING ANALYSIS

A three-dimensional Rankine panel method has been employed also for the evaluation of linear radiation and diffraction forces. The choice is related to the capability of this methodology to deal with the complex free surface flow pattern between the hulls of multi-hull vessels; moreover, it allows to better take into account the speed effects into the free surface boundary conditions.
A short description of the model is following presented; more details, however, can be found in [7].
Ship motions are defined by the instantaneous position of a body fixed reference system with respect to the previous system and may be described by a vector $\xi_k(t)$, with $k = 1,\ldots,6$.
Assuming a regular incident head wave of frequency ω

$$\eta(t)=\Re\left(\tilde{\eta}(\omega)\; e^{i\omega t}\right) \tag{4}$$

where $\tilde{\eta}(\omega)$ is the complex wave amplitude. If no transitory effects are present, the resultant motions will be described by

$$\xi_k(t)=\Re\left(\tilde{\xi}_k(\omega_e)\; e^{i\omega_e t}\right) \tag{5}$$

where $\tilde{\xi}_k(\omega_e)$ is the complex amplitude of the *k*-th motion component and ω_e the encounter frequency.
Under the hypothesis of small amplitude motions, $\tilde{\xi}_k$ can be determined solving the following system of equations:

$$\begin{aligned}&\sum_{k=1}^{6}\left[-\omega_e^2\left(M_{jk}+A_{jk}(\omega_e)\right)+i\omega_e B_{jk}(\omega_e)+C_{jk}\right]\tilde{\xi}_k = \\ &=\tilde{F}_j^D(\omega_e)+\tilde{F}_j^{FK}(\omega_e)\end{aligned} \tag{6}$$

where j = 1,2,3 refer respectively to the *x*, *y*, *z* force components and j = 4,5,6 to the corresponding three moment components. M and C represent the mass and hydrostatic restoring matrix, A_{jk} and B_{jk} are the added-mass and the damping coefficients, $\tilde{F}_j^D$ and $\tilde{F}_j^{FK}$ the complex amplitudes of diffraction and Froude-Krylov forces.
As the problem is linear, superposition of the motions due to each frequency component of the incident wave pattern can be used for determining ship motions with irregular seas.

Assuming incompressible and inviscid fluid and irrotational flow, the hydrodynamic problems related to the evaluation of the added mass and damping coefficients (i.e. radiation forces), as well as to the determination of diffraction forces may be solved applying the potential theory (Froude-Krylov forces are known analytically).
Let Φ be total velocity potential, which satisfies the Laplace equation in the fluid domain Ω:

$$\Delta\Phi = 0 \qquad \text{in } \Omega \tag{7}$$

The boundary conditions are imposed over the linearised boundaries $\partial\Omega$. Denoting with $\vec{V}_B$ the velocity of a point on the hull wetted surface and with $\vec{n}$ its outward normal vector, the boundary condition on the hull surface S_H is:

$$\frac{\partial\Phi}{\partial\vec{n}} = \vec{V}_B \cdot \vec{n} \qquad \text{on } S_H \tag{8}$$

Over the free surface a kinematic and a dynamic conditions are imposed, obtaining:

$$\frac{\partial^2\Phi}{\partial t^2} + 2\nabla\Phi\cdot\nabla\left(\frac{\partial\Phi}{\partial t}\right) + \frac{1}{2}\nabla\Phi\cdot\nabla(\nabla\Phi\cdot\nabla\Phi) + g\frac{\partial\Phi}{\partial z} = 0 \qquad \text{on } z = 0 \tag{9}$$

Finally, a radiation condition at infinity must be enforced to ensure the uniqueness of the solution.
The total potential Φ may be expressed as the sum of the potential of a steady base flow Φ_S and of a small unsteady perturbation potential Φ_{US}.

$$\Phi = \Phi_S + \Phi_{US} \tag{10}$$

The unsteady perturbation potential may be written as superposition of an incident wave potential ϕ_I , a diffraction potential ϕ_D and six radiation potentials:

$$\Phi_{US} = \phi_I + \phi_D + \sum_{k=1}^{6}\phi_k \tag{11}$$

Considering that the incident wave potential can be expressed in analytical form, the decomposition of the unsteady potential enables to study the total boundary value problem solving a set of a diffraction and six radiation problems.
Employing a Rankine source distribution $\sigma(Q)$, each potential in (11) may be expressed as:

$$\phi(P) = \int_{\partial\Omega}\frac{1}{r(P,Q)}\,\sigma(Q)\,dS \tag{12}$$

where $r(P,Q) = |P-Q|$.
The hull and a part of the free surface are approximated with quadrilateral panels, considering a uniform source strength on each. All the involved boundary value problems are hence solved in terms of these unknown source strengths.

A suitable radiation condition is finally posed at the forward border of the computational domain. In the present method radiated and diffracted waves are considered not to propagate ahead the ship and hence it can be applied only for $\omega_e U/g > 0.25$.
Since the free surface computational domain is limited, its extension must be carefully considered in order to avoid wave reflections; moreover, the dimensions of the free surface panels should be chosen taking into account incident, radiated and diffracted wave lengths.

2.2. WEAKLY NONLINEAR ANALYSIS

Considering a ship as an unconstrained rigid body subjected to gravity, radiation, diffraction, Froude-Krilov and hydrostatic forces. Applying the impulse theory [8], it is possible to write the equations of motion in theirs time domain form:

$$\sum_{k=1}^{6}\left(M_{jk} + A_{jk}^{\infty}\right)\ddot{\xi}_k(t) + B_{jk}^{\infty}\dot{\xi}_k(t) + \int_0^t h_{jk}(t-\tau)\,\dot{\xi}_k(\tau)d\tau = F_j^D(\eta,t) + F_j^H(\eta,t) + F_j^{FK}(\eta,t) \tag{13}$$

with $k = 1,...,6$ and being $\dot{\xi}$ and $\ddot{\xi}$ respectively the first and the second time derivatives of ξ. A_{jk}^{∞} and B_{jk}^{∞} mean the infinite-frequency added mass and damping coefficients, $F_j^D(t)$ represent the diffraction, $F_j^H(t)$ the hydrostatic (difference between buoyancy and mass forces) and $F_j^{FK}(t)$ the Froude-Krylov forces (and moments), while $h_{jk}(t)$ are the impulse response functions (or retardation functions).
The system of equations (13) is linear, as both coefficients and exciting forces do not depend on motions and theirs derivatives.
As shown by Ogilvie [9], systems (6) and (13) are related by Fourier transforms and the impulse responses can be derived from the frequency dependant added-mass and damping coefficients and vice versa.
Introducing fully nonlinear hydrostatic and Froude-Krylov forces in the system (13), it become:

$$\sum_{k=1}^{6}\left(M_{jk} + A_{jk}^{\infty}\right)\ddot{\xi}_k(t) + B_{jk}^{\infty}\dot{\xi}_k(t) + \int_0^t h_{jk}(t-\tau)\,\dot{\xi}_k(\tau)d\tau = F_j^D(\eta,t) + F_j^H(\eta,\xi,t) + F_j^{FK}(\eta,\xi,t) \tag{14}$$

Even if the nonlinear forces must be evaluated in the time domain, the system of equations (14) can be solved both in the time and in the frequency domain. The choice is related to the kind of analysis it is expected to be carried out. For this application the frequency domain has been preferred, as it allows to avoid the initial transient phase and it is faster, as the computational time is connected with the actual nonlinearities which are present and the time step is not constrained by time integration convergence requirements.

A time domain procedure can be found in [10], while following the frequency domain solution is briefly described.
Denoting with $\mathcal{F}$ the Fourier transform and with $\mathcal{F}^{-1}$ its inverse, $\xi_k(t)$ can be evaluated by:

$$\xi_k(t)=\mathcal{F}^{-1}\left[\tilde{\xi}_k(\omega_e)\right] \tag{15}$$

where ω_e is the encounter frequency and $\tilde{\xi}_k(\omega_e)$ is a frequency dependant complex amplitude obtained solving the system of equations in (16), which is the transform in the frequency domain of (14).

$$\begin{aligned}&\sum_{k=1}^{6}\left[-\omega_e^2\left(M_{jk}+A_{jk}(\omega_e)\right)+i\omega_e B_{jk}(\omega_e)\right]\,\tilde{\xi}_k(\omega_e)=\\&=\mathcal{F}\left[F_j^D(\eta,t)\right](\omega_e)+\mathcal{F}\left[F_j^H(\eta,\xi,t)+F_j^{FK}(\eta,\xi,t)\right](\omega_e)\end{aligned} \tag{16}$$

The system in (16) can not be solved as it is, because of the dependence of Froude-Krylov and hydrostatic forces on the ship motions. An iterative procedure is hence required, evaluating at each iteration the time domain nonlinear forces due to the motions obtained in the previous iteration. As first guess, the linear solution is used.
In order to make the procedure more robust, the following formulation has been adopted:

$$\begin{aligned}&\sum_{k=1}^{6}\left[-\omega_e^2\left(M_{jk}+A_{jk}(\omega_e)\right)+i\omega_e B_{jk}(\omega_e)+C_{jk}\right]\,\tilde{\xi}_k^p(\omega_e)=\\&=\mathcal{F}\left[F_j^D(\eta,t)\right](\omega_e)+\mathcal{F}\left[F_j^H\left(\eta,\xi^{p-1},t\right)+F_j^{FK}\left(\eta,\xi^{p-1},t\right)\right](\omega_e)+\\&+C_{jk}\tilde{\xi}_k^{p-1}(\omega_e)\end{aligned} \tag{17}$$

where p represent an iteration index and C is the linear hydrostatic restoring matrix.
For $\omega_e=0$, the following system has been employed instead of (17), supposing the incident wave pattern to have null mean:

$$\sum_{k=1}^{6}\hat{C}_{jk}^p\;\tilde{\xi}_k^p(0)=\mathcal{F}\left[F_j^H\left(\eta,\xi^{p-1},t\right)+F_j^{FK}\left(\eta,\xi^{p-1},t\right)\right](0) \tag{18}$$

where $\hat{C}$ is obtained as reported in (19).

$$\hat{C}_{jk}^p=-\frac{\partial F_j^H\left[\tilde{\xi}^{p-1}(0)\right]}{\partial\xi_k} \tag{19}$$

Froude-Krylov and hydrostatic forces are evaluated in the time domain, integrating hydrostatic and hydrodynamic pressure over the actual wetter surface under the incident wave profile. To that end, the hull is described employing bi-cubic surfaces, depending on two normalized parameters *u*, *v*. At each time step, the domain describing the wetted surface is evaluated, as well as the pressure distribution in it. Forces and moments are then calculated by analytical integrations of their distributions treated as bi-cubic function on the domain of the parameters *u*, *v*.
As the methodology employed is based on the potential flow approach, viscous effects are completely neglected. This approximation results generally satisfactory for estimating vertical motions of conventional slow ship, but in other cases, like the one analyzed in this paper, a viscous correction is required in order to avoid overestimation of the resonance peaks. The semi-empirical model employed is based on the cross flow approach and viscous forces are evaluated in the time domain as follow:

$$\begin{aligned}F_3^v(\xi,t)&=\frac{1}{2}\rho\int_L C_D(x)\;\;B(x)\;\;v_r(x,\xi,t)\left|v_r(x,\xi,t)\right|\;dx\\F_5^v(\xi,t)&=-\frac{1}{2}\rho\int_L x\;\,C_D(x)\;\;B(x)\;\;v_r(x,\xi,t)\left|v_r(x,\xi,t)\right|\;dx\end{aligned} \tag{20}$$

where ρ is the water density, C_D the sectional drag coefficient, B the maximum sectional breadth, v_r the vertical component of the relative velocity between water and ship and L the length of the wetted hull surface. The drag coefficients are estimated from experimental results on the base of the sectional shapes and are kept constant during the simulation.
Introducing the viscous correction, system (17) become

$$\begin{aligned}&\sum_{k=1}^{6}\left[-\omega_e^2\left(M_{jk}+A_{jk}(\omega_e)\right)+i\omega_e B_{jk}(\omega_e)+C_{jk}+\right.\\&\left.+V_{jk}^p(\omega_e)\right]\;\tilde{\xi}_k^p(\omega_e)=\mathcal{F}\left[F_j^D(\eta,t)\right](\omega_e)+\\&+\mathcal{F}\left[F_j^H\left(\eta,\xi^{p-1},t\right)+F_j^{FK}\left(\eta,\xi^{p-1},t\right)\right](\omega_e)+C_{jk}\tilde{\xi}_k^{p-1}(\omega_e)\end{aligned} \tag{21}$$

where

$$\begin{aligned}V_{jk}^p&=-\frac{\mathcal{F}\left[F_j^V\left(\eta,\xi^{p-1},t\right)\right]}{\tilde{\xi}_j^{p-1}} &&\text{if } j=k\\V_{jk}^p&=0 &&\text{if } j\neq k\end{aligned} \tag{22}$$

3. EXPERIMENTAL TESTS

The main characteristics of the investigated catamaran hull are shown in Table 1, while the body plan is shown in Figure 1. The model was built in 1:20 scale and tested at the University of Trieste towing tank (50 x 3.10 x 1.60 m).

Table 1
Main characteristics of the catamaran hull

Length at the waterline L_{WL} (m):	35.87
Breadth at the waterline B_{WL} (m):	11.33
Design Draught T (m):	1.58
Displacement Δ (t):	137.0
Wetted Surface (m^2):	272.2
Ratio S/L_{WL}:	0.225

Aim of the experiments was the evaluation of the effects on wave resistance and on seakeeping characteristics which can be obtained employing streamlined body of revolution placed between the demi-hulls [11].

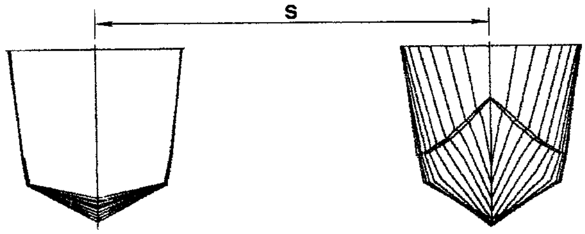

Figure 1
Catamaran body plan

Seakeeping tests have been carried out in head regular waves with a constant H_W/λ ratio equal to 1/80 (where H_W is the wave height and λ the wave length), whereas the λ/L_{WL} ratio has been varied between 0.5 and 2.0; a range of Froude Number between 0.4 and 0.8 has been considered.
The catamaran radius of gyration was approximately 0.22 L_{WL}, while the BulbCat model has been ballasted obtaining a radius of gyration close to 0.25 L_{WL}.
The appendages used for the experiments were derived from the Systematic Series 58 of the David Taylor Model Basin [12] (base forms 4155, 4156 and 4157). They are shown in Figure 2.

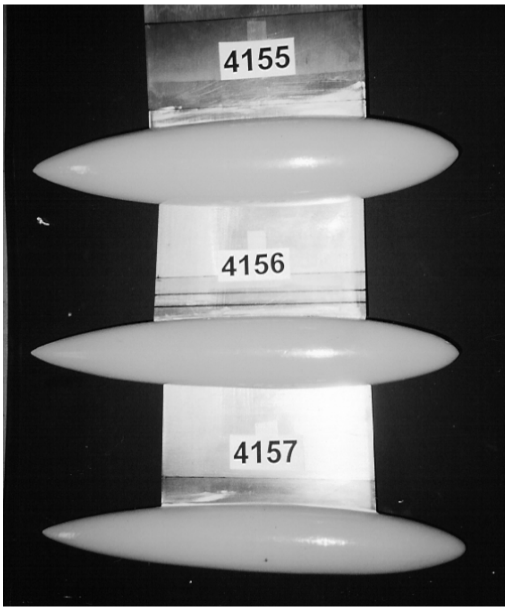

Figure 2
Appendages used in the experiences

The length of the base appendages was equal to $L_{WL}/5$.
Tests were performed at the same draft conditions and model displacement was consequently increased by the weight of the appendages and of the connecting plate. The bodies of revolution were placed between the demi-hulls in different longitudinal and vertical positions, in order to assess their influence on the variables analyzed. An example of configuration is given in Figure 3, while a picture of a test is shown in Figure 4.
The connection between the bodies of revolution and the hull can influence ship resistance and motions. The preliminary connection was made by two vertical arms with elliptic sections, but this solution provided scarcely effective, because it generated too high resistance and very large sprays, especially at high speeds. Later a vertical thin plate was used, with a breath half the length of the bulb and thickness 1.5 mm.
The plate vertical wedges were tapered, in order to reduce the resistance. The fore edge of the plate was placed at 0.20 L_{BULB} from the nose of the appendage.

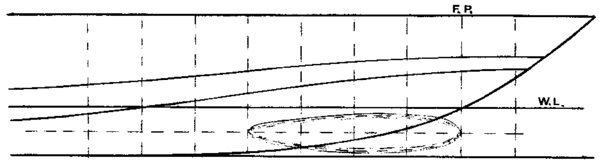

Figure 3
Profile of the appendages and their arrangement

Figure 4
Picture of a test

The presence of bulbs has generally shown a reduction of the pitch motion, which can amount up to 30% and is more remarkable when F_N is increased. Heave motion is more irregular and may present questionable results. At smaller speeds it is lightly reduced or increased, according to the selected λ/L_{WL} interval; at higher speeds its variations are inappreciable.

4. NUMERICAL CALCULATION AND RESULTS

Numerical simulations here reported regard the catamaran and on one of the configuration tested experimentally. Particularly, the test case examined concerned a BulbCat with the 4156 appendage; the nose of the bulb is placed at $L_{WL}/10$ forward the F.P., while the vertical position of its axis is at D/2 below the keel line, being D the diameter of the bulb. The Froude numbers considered are 0.4, 0.5 and 0.6.
A comparison between numerical and experimental results have been performed, both with linear and nonlinear models. From Figure 5 to Figure 16 comparisons of the transfer functions, for heave and pitch, are reported. In the nonlinear case, the "transfer function" reported is actually the response of the ship at the same frequency of the incident waves, which in the following will be referred as first harmonic.

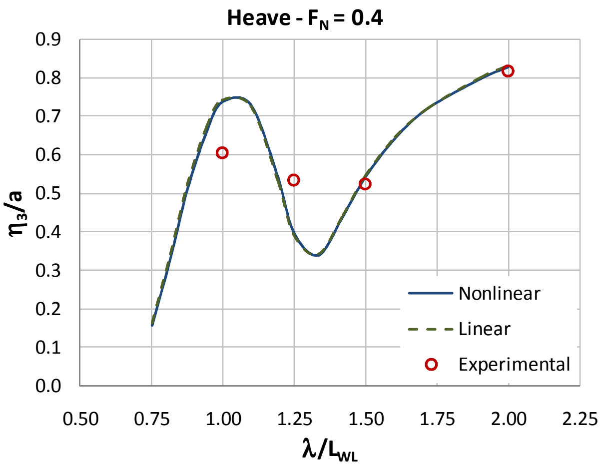

Figure 5
Heave transfer function of the catamaran (F_N = 0.4)

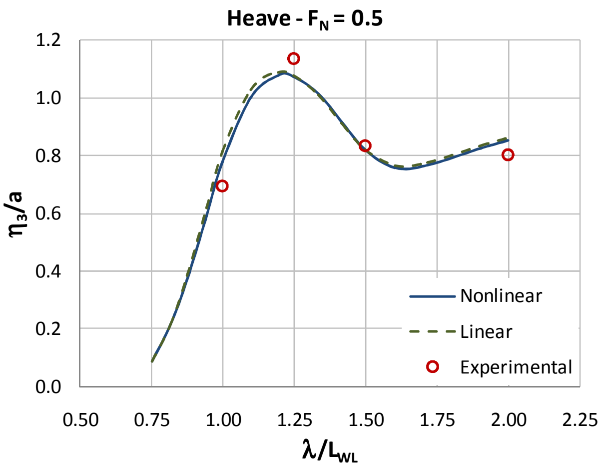

Figure 6
Heave transfer function of the catamaran (F_N = 0.5)

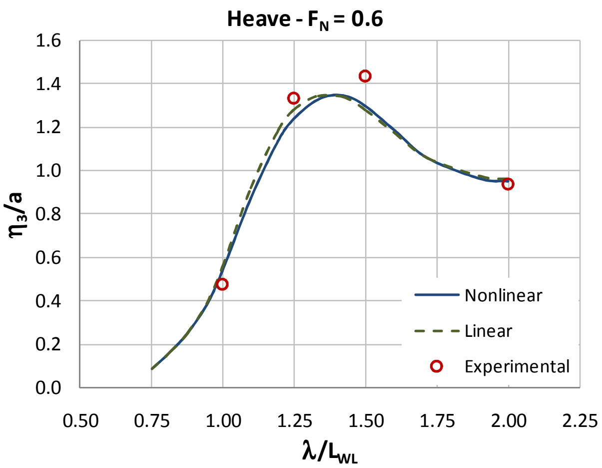

Figure 7
Heave transfer function of the catamaran (F_N = 0.6)

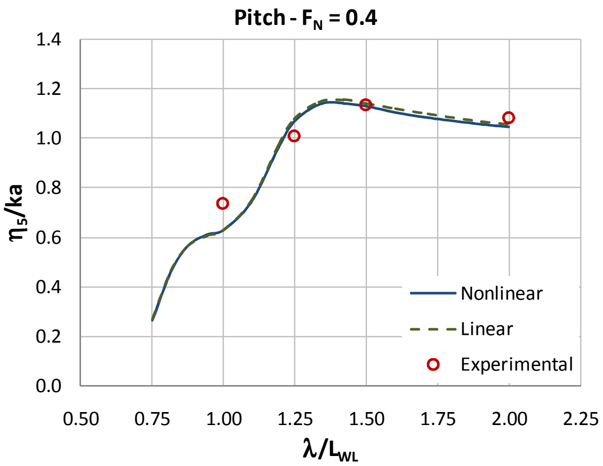

Figure 8
Pitch transfer function of the catamaran (F_N = 0.4)

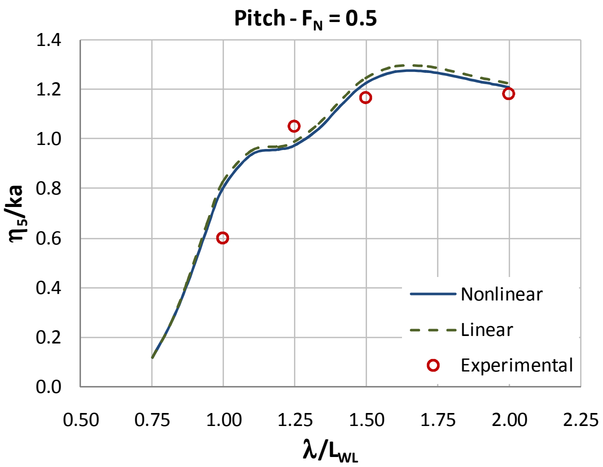

Figure 9
Pitch transfer function of the catamaran (F_N = 0.5)

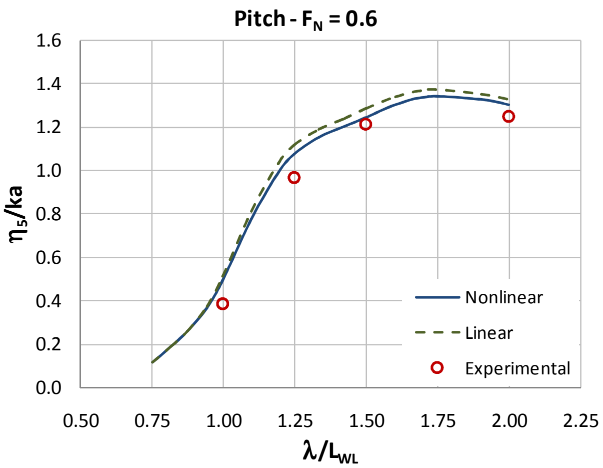

Figure 10
Pitch transfer function of the catamaran (F_N = 0.6)

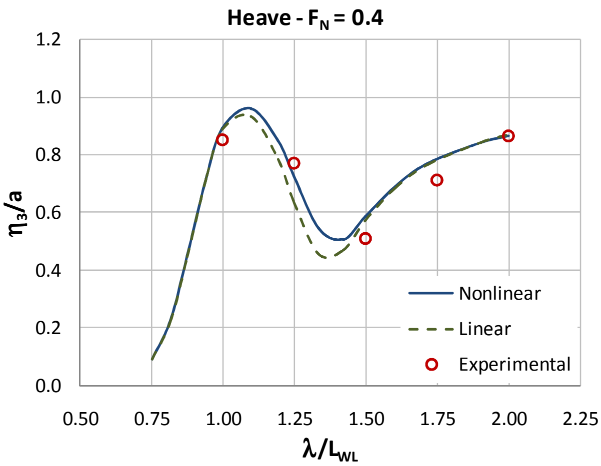

Figure 11
Heave transfer function of the Bulb Cat (F_N = 0.4)

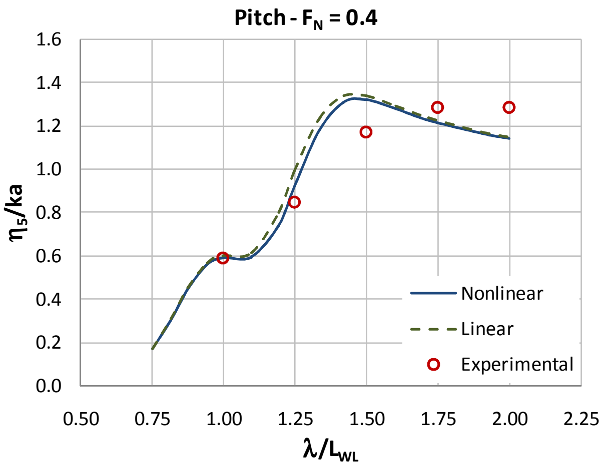

Figure 14
Pitch transfer function of the Bulb Cat (F_N = 0.4)

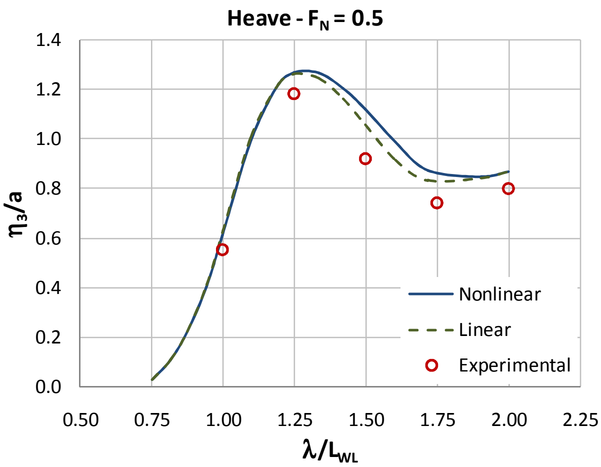

Figure 12
Heave transfer function of the Bulb Cat (F_N = 0.5)

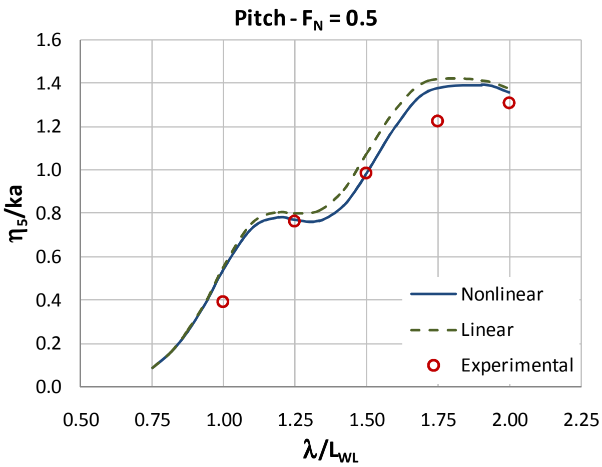

Figure 15
Pitch transfer function of the Bulb Cat (F_N = 0.5)

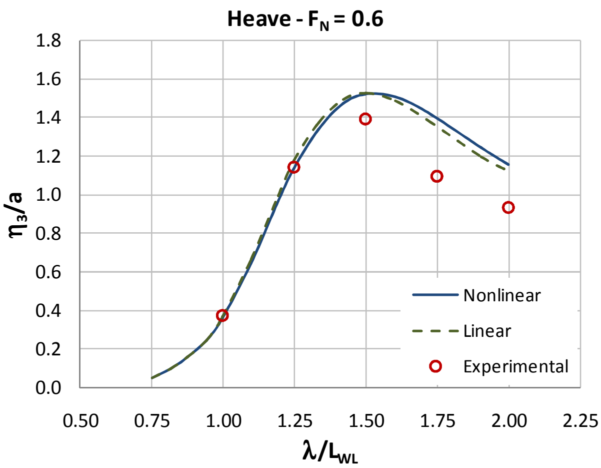

Figure 13
Heave transfer function of the Bulb Cat (F_N = 0.6)

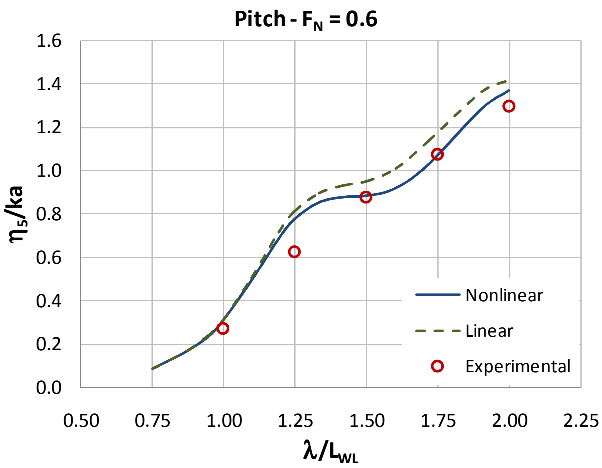

Figure 16
Pitch transfer function of the Bulb Cat (F_N = 0.6)

It should be noted that the wave steepness employed in experimental tests was small enough to involve small nonlinear effects. Notwithstanding, some cases show non negligible difference (for instance, see Figure 16) between linear and nonlinear results. This fact could be mainly related to variation of sinkage and trim due to nonlinear effects in the hydrostatic forces, rather than to higher harmonic components. Figure 16 and Figure 20, for instance, show as to an improvement of the prediction of dynamic sinkage and trim with the nonlinear methodology correspond an improved estimate of the motions. Even if dynamic sinkage and trim, evaluated by the nonlinear model, show a fairly good agreement in trend with experimental data in all the cases tested (examples in Figures from 17 to 20), sometime the plots result shifted (mainly for the BulbCat), probably due to inaccuracy of the steady state prediction. This can bring, in some cases, to a slightly worse evaluation of motions (see for instance Figures 13 and 19).

From Figure 21 to Figure 32 time histories (in ship scale) of heave and pitch for a regular incident wave with λ/L_{WL} = 1.5 are presented, comparing linear and nonlinear results with experimental records.

From Figure 33 to Figure 56 the dimensionless responses of heave and pitch for the first harmonic, as well as the dynamic sinkage and trim, are reported for wave steepness (*ka*, where *k* is the wave number and *a* the wave amplitude) of 0.01, 0.04, 0.05, 0.08.

Responses of the BulbCat seem to be more influenced by the wave amplitude than the ones of the catamaran, inducing a greater reduction of the response at the first harmonic. As the bulb generally remain completely immersed (and hence it does not cause local variation on hydrostatic forces) the different effect appears to be related to the modification of the motions due to radiation and diffraction forces, but also due to the differences of the mass and its distribution.

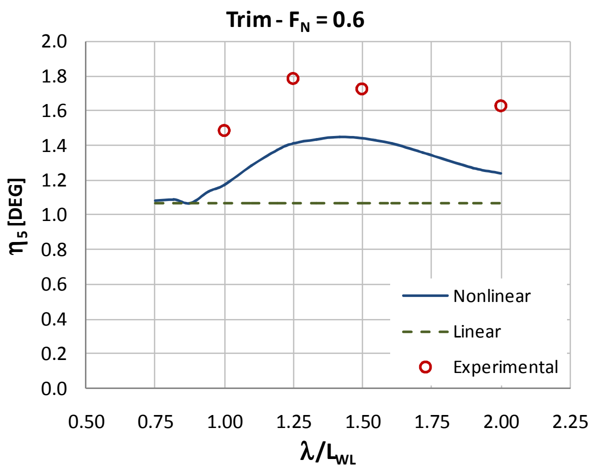

Figure 18
Trim comparison for the catamaran (F_N = 0.6)

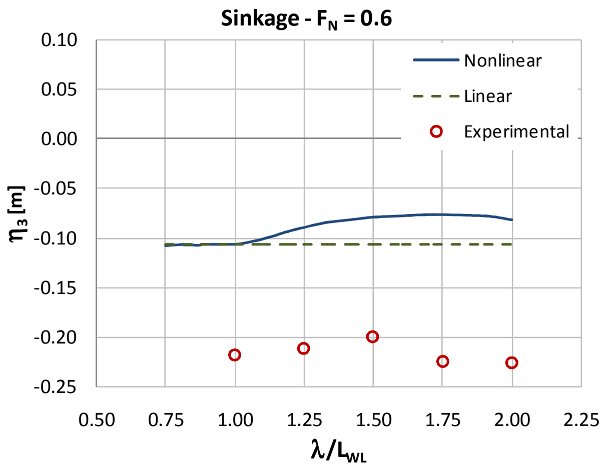

Figure 19
Sinkage comparison for the Bulb Cat (F_N = 0.6)

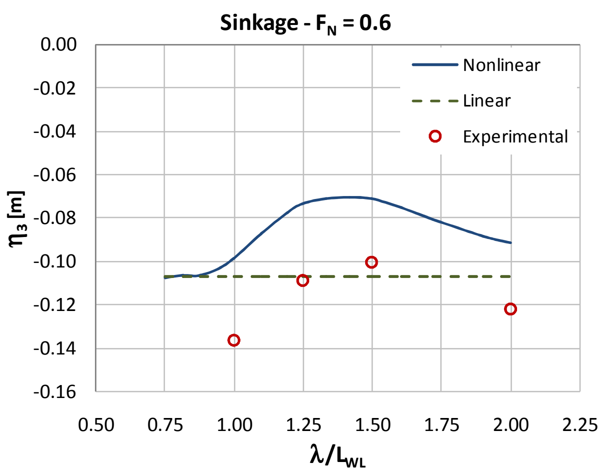

Figure 17
Sinkage comparison for the catamaran (F_N = 0.6)

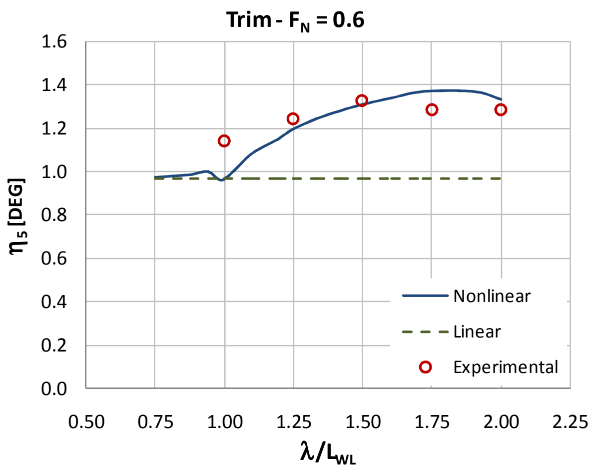

Figure 20
Trim comparison for the Bulb Cat (F_N = 0.6)

It should be noted that results are also influenced by nonlinear effects related to the viscous correction; particularly, the differences between 0.01 and 0.04 of the wave steepness seem to be mainly due to this factor.
Increasing the wave steepness, also the influence of higher harmonics become important and the responses due to the first harmonic only become less meaningful.

5. CONCLUSIONS

The paper presents a weakly nonlinear analysis for heave and pitch motions, in head seas with regular waves, performed on a catamaran and on a version of the same hull provided with a bulb appendage between the hulls (called BulbCat). An hybrid approach has been employed, combining linear radiation and diffraction forces, evaluated in the frequency domain, with non linear Froude-Krylov and hydrostatic forces, computed in the time domain. The influence of dynamic sinkage and trim has been also taken into account, evaluating them with a preliminary calculation which solves the steady state problem. Simulations have been performed for different velocities and wave steepnesses.
Comparisons between numerical results and experimental data shows a fairly good agreement, particularly for the catamaran. Considering the BulbCat, heave motions tend to be slightly overestimated for the lower frequencies at Froude numbers of 0.5 and 0.6, while the numerical peak in pitch at $F_N = 0.4$ is not clearly evidenced in experimental data although the numerical and experimental values are close. Dynamic sinkage and trim appear to be sometime worse predicted for the BulbCat and this can partially affects the seakeeping results. Nevertheless, the trends in variation of sinkage and trim, modifying the incident wave frequency, match experiments in a fairly good manner, indicating a good prediction of this nonlinear effect. Moreover, a good prediction of sinkage and trim seems to improve the evaluation of motions.
Nonlinear simulations show a reduction of both heave and pitch responses at the first harmonic increasing the wave steepness, particularly for the BulbCat. It should be noted that this reduction is also due to nonlinear effects associated to the viscous correction.
It should be finally remarked that, the more the wave steepness is increased, the less meaningful become the analysis of the first harmonic only, as the higher components effects become more important. This is true also for lower wave steepness if accelerations are considered.

6. REFERENCES

[1] BRUZZONE D., GUALENI P. – "The Prediction of Seakeeping Performance and Added Resistance in the Design of Multihull Vehicles", *Proc. of the 9th Symposium on Practical Design of Ships and Other Floating Structures, PRADS 2004, Lubecca, Sept. 2004., vol. I, pp.206-213*

[2] ZOTTI I. – "Hydrodynamic improvements of catamaran hulls when using streamlined bodies of revolution", *Proceedings of FAST 2003, Ischia, 2003, Session A1, pp. 9-18*

[3] BECK R., REED A. – "Modern Seakeeping Computations for Ships", *Twenty-Third Symposium on Naval Hydrodynamics, Val de Reuil, 2000*

[4] DAWSON C.W. – "A practical computer method for solving ship-wave problems", *Second International Conference on Numerical Ship Hydrodynamics, 1977*

[5] HESS J.L., SMITH A.M.O. – "Calculation of nonlifting potential flow about arbitrary three-dimensional bodies", *Journal of Ship Research (13-3), 1964*

[6] BRUZZONE D. – "Numerical evaluation of the steady free surface waves", *CFD Workshop Tokyo, Ship Res. Inst. Tokyo, 1994, Vol. I, pp.4.2.1-4.2.13*

[7] BRUZZONE D. – "Application of a Rankine source method to the evaluation of motions of high speed marine vehicles", *Proceeding of the 8th International Marine Design Conference, Athens, May 2003, Vol. II , pp.69-79*

[8] CUMMINS W.E. – "The Impulse Response Function and Ship Motions", *Schiffstechnik (47), 1962, pp. 101-109*

[9] OGILVIE T.F. – "Recent progress towards the understanding and prediction of ship motions", *6th Symposium on Naval Hydrodynamics, 1964, pp. 3-80*

[10] BRUZZONE D., GRASSO A. – "Nonlinear time domain analysis of vertical ship motions", *Archives of Civil and Mechanical Engineering, 2007, Vol. VII, N. 4, pp. 27-37*

[11] ZOTTI I. – "Hydrodynamic experiments on a catamaran hull with a central bulb, considering its resistance and seakeeping performances", *Maritime Transportation and Exploitation of Ocean and Coastal Resources Taylor & Francis Group, London, 2005*

[12] GERTLER M. – "Resistance Experiments on a systematic series of streamlined bodies of revolution for application to the design of high-speed submarines", *Report C-297, David Taylor Model Basin, April 1950*

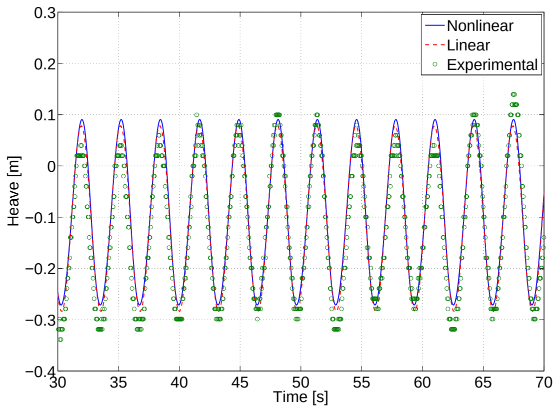

Figure 21
Heave time history of the catamaran
($F_N = 0.4 – \lambda/L_{WL} = 1.5$)

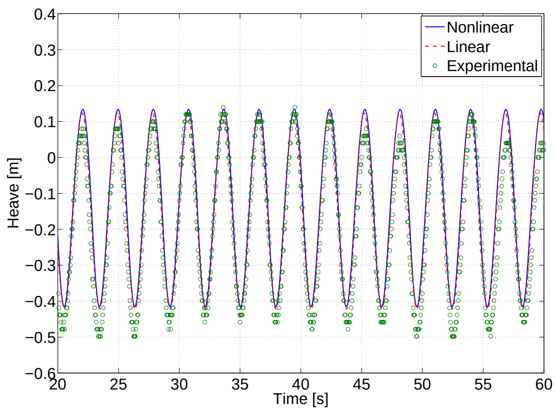

Figure 22
Heave time history of the catamaran
($F_N = 0.5 – \lambda/L_{WL} = 1.5$)

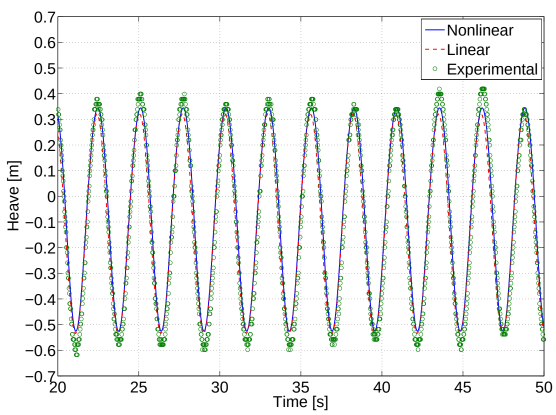

Figure 23
Heave time history of the catamaran
($F_N = 0.6 – \lambda/L_{WL} = 1.5$)

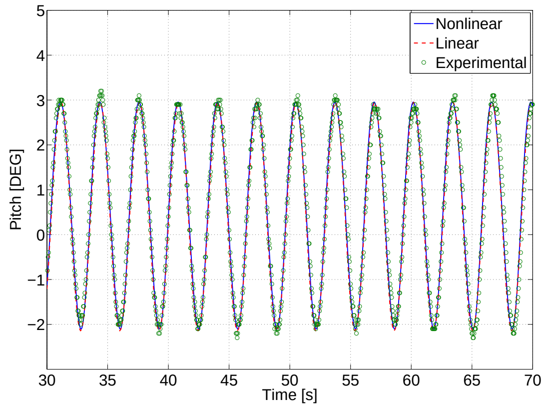

Figure 24
Pitch time history of the catamaran
($F_N = 0.4 – \lambda/L_{WL} = 1.5$)

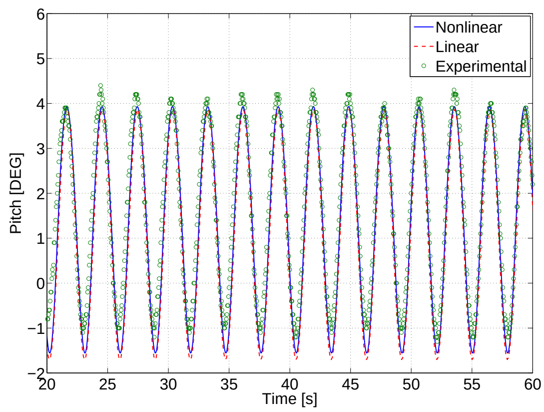

Figure 25
Pitch time history of the catamaran
($F_N = 0.5 – \lambda/L_{WL} = 1.5$)

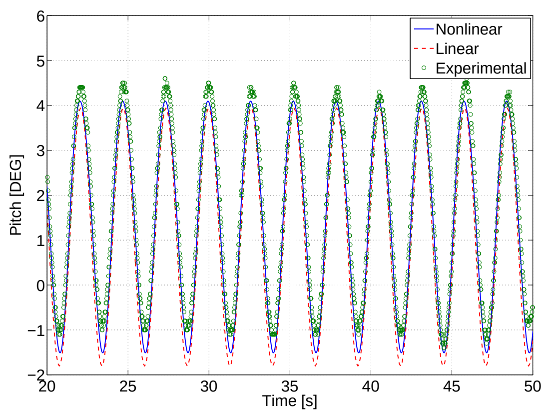

Figure 26
Pitch time history of the catamaran
($F_N = 0.6 – \lambda/L_{WL} = 1.5$)

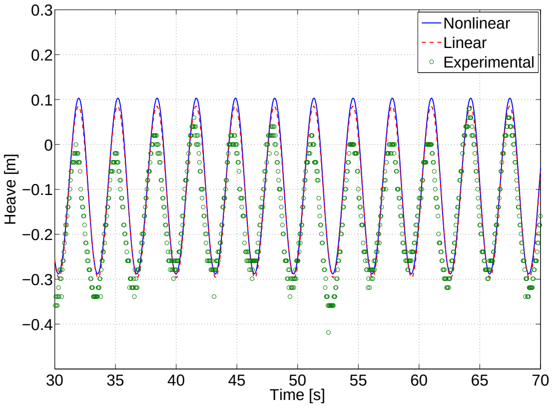

Figure 27
Heave time history of the Bulb Cat
($F_N = 0.4 – \lambda/L_{WL} = 1.5$)

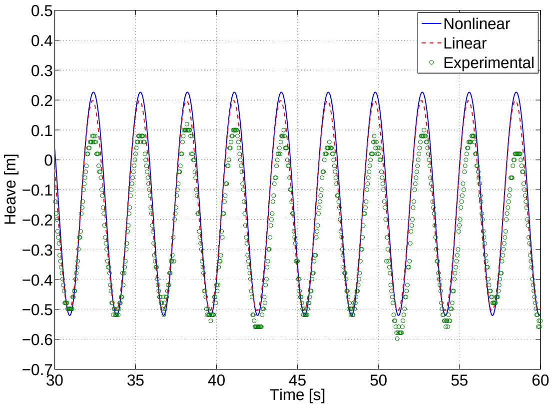

Figure 28
Heave time history of the Bulb Cat
($F_N = 0.5 – \lambda/L_{WL} = 1.5$)

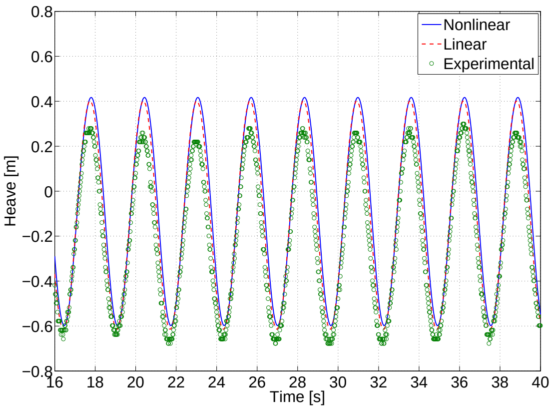

Figure 29
Heave time history of the Bulb Cat
($F_N = 0.6 – \lambda/L_{WL} = 1.5$)

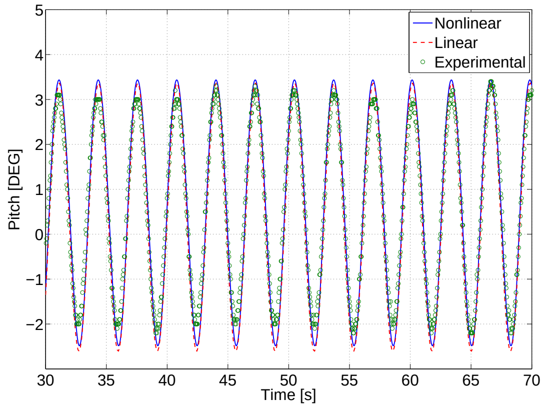

Figure 30
Pitch time history of the Bulb Cat
($F_N = 0.4 – \lambda/L_{WL} = 1.5$)

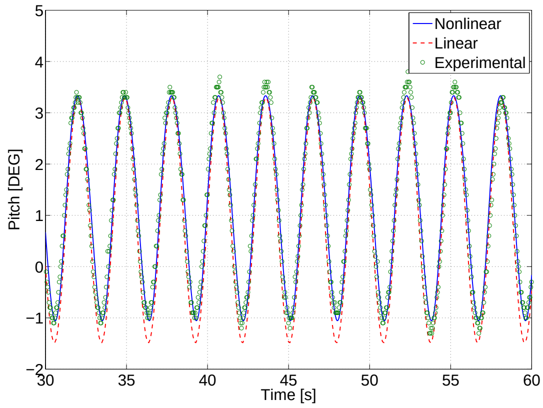

Figure 31
Pitch time history of the Bulb Cat
($F_N = 0.4 – \lambda/L_{WL} = 1.5$)

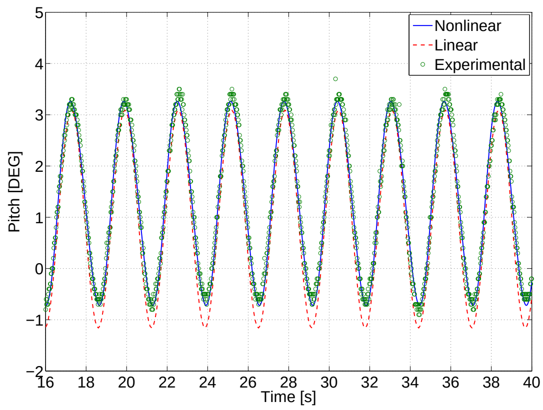

Figure 32
Pitch time history of the Bulb Cat
($F_N = 0.4 – \lambda/L_{WL} = 1.5$)

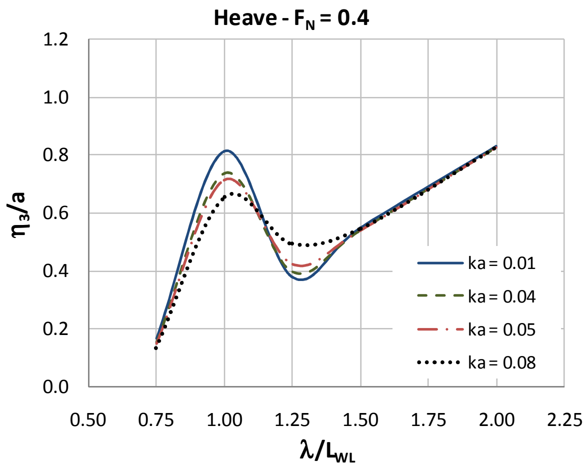

Figure 33
Heave first harmonic response
of the catamaran (F_N = 0.4)

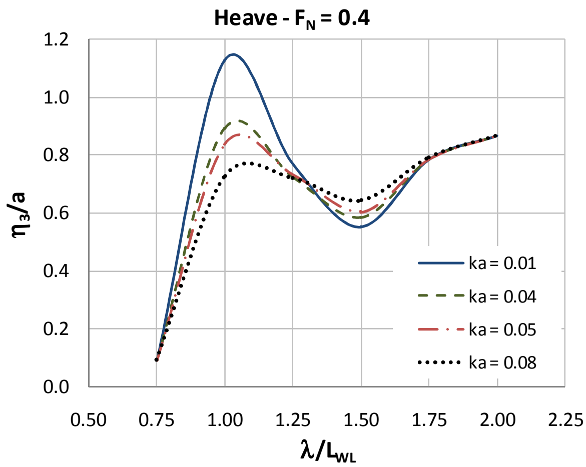

Figure 36
Heave first harmonic response
of the Bulb Cat (F_N = 0.4)

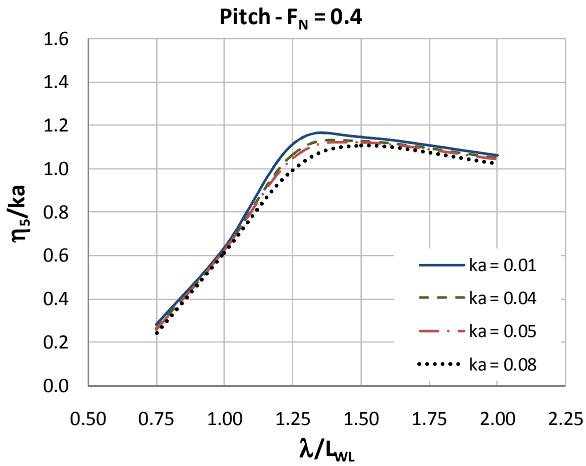

Figure 34
Pitch first harmonic response
of the catamaran (F_N = 0.4)

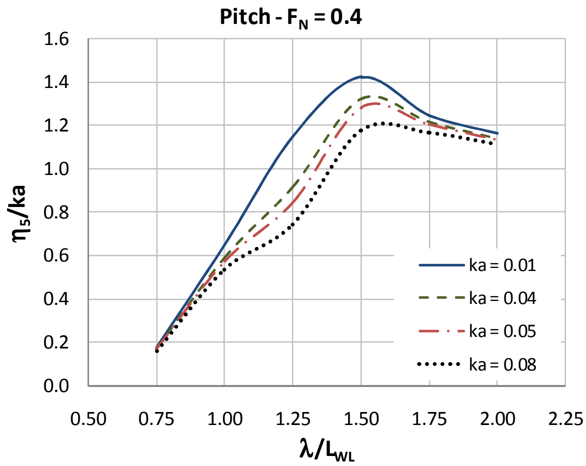

Figure 37
Pitch first harmonic response
of the Bulb Cat (F_N = 0.4)

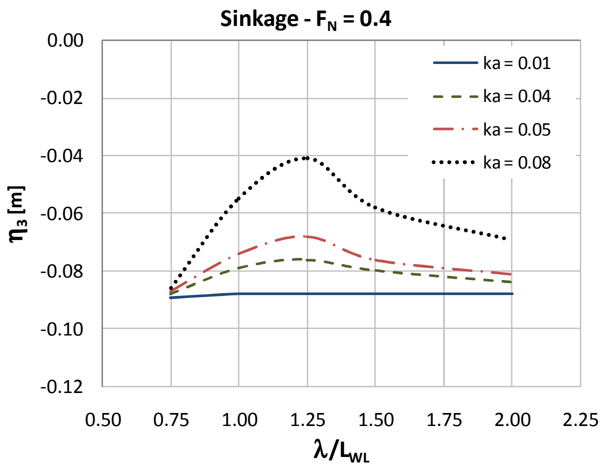

Figure 35
Sinkage of the catamaran (F_N = 0.4)

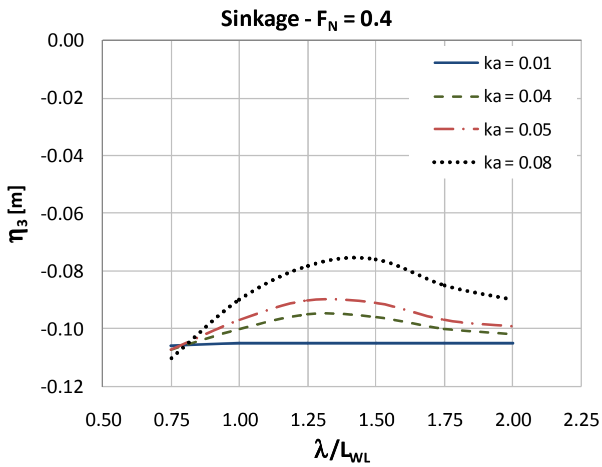

Figure 38
Sinkage of the Bulb Cat (F_N = 0.4)

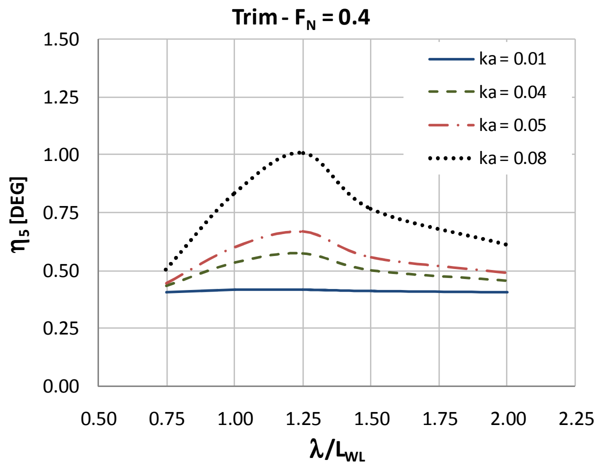

Figure 39
Trim of the catamaran (F_N = 0.4)

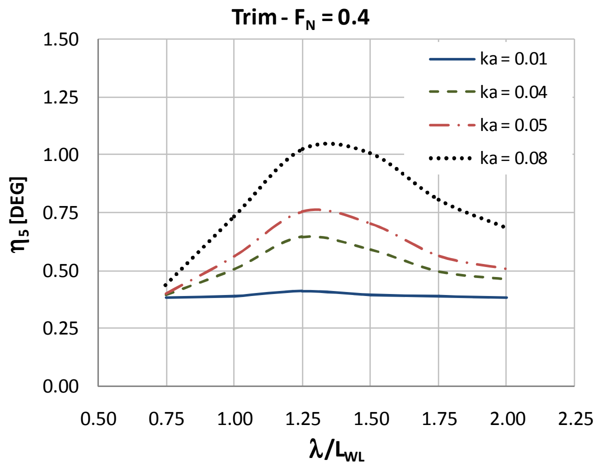

Figure 42
Trim of the Bulb Cat (F_N = 0.4)

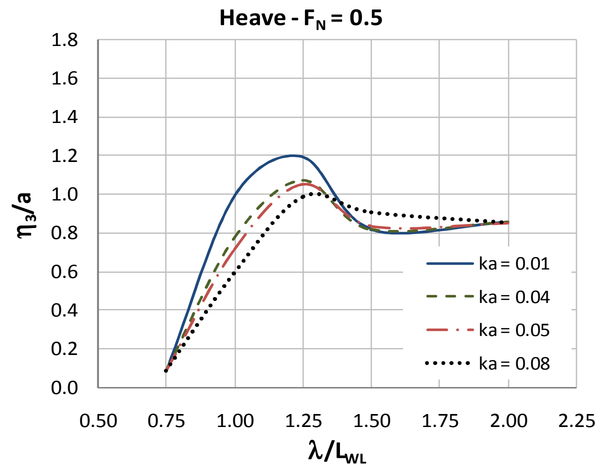

Figure 40
Heave first harmonic response
of the catamaran (F_N = 0.5)

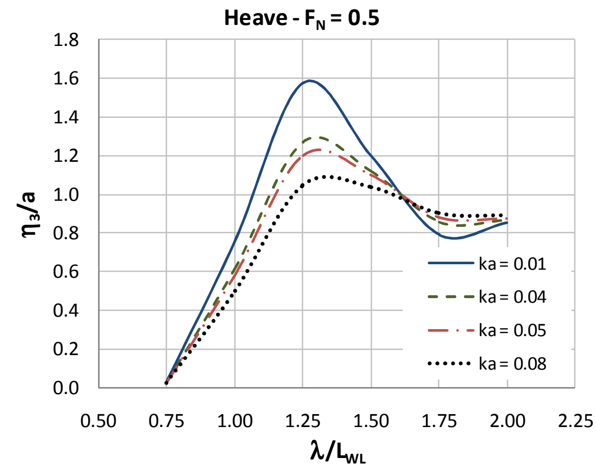

Figure 43
Heave first harmonic response
of the Bulb Cat (F_N = 0.5)

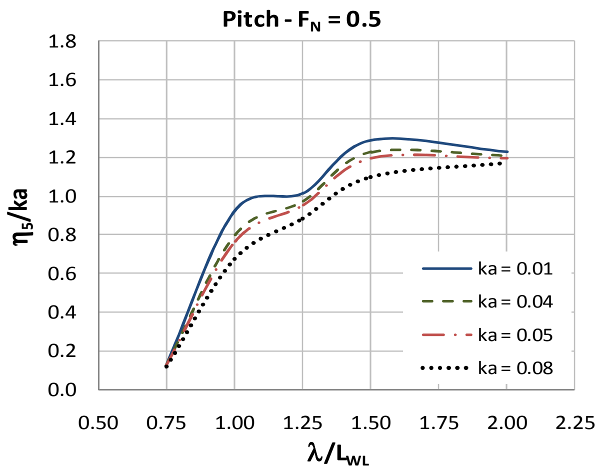

Figure 41
Pitch first harmonic response
of the catamaran (F_N = 0.5)

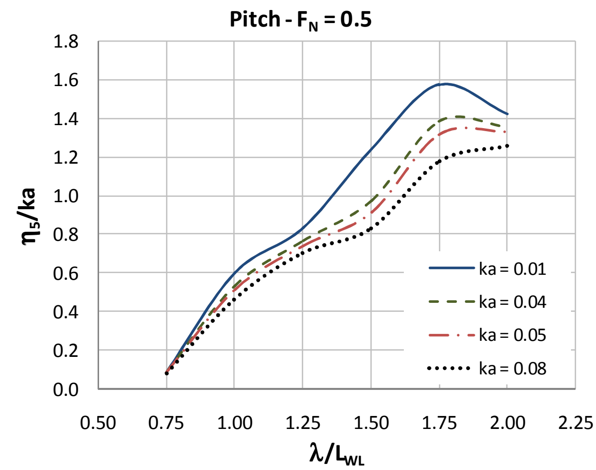

Figure 44
Pitch first harmonic response
of the Bulb Cat (F_N = 0.5)

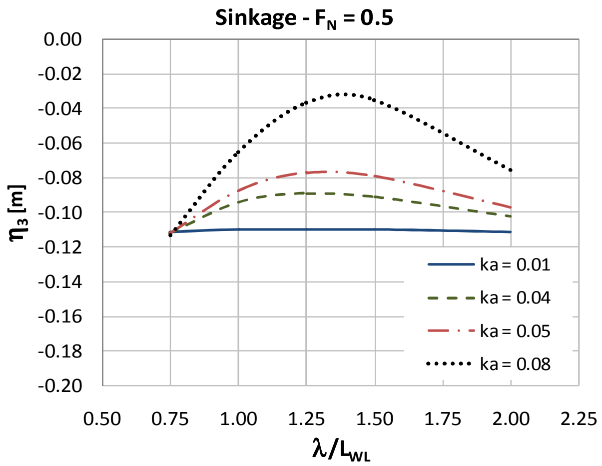

Figure 45
Sinkage of the catamaran (F_N = 0.5)

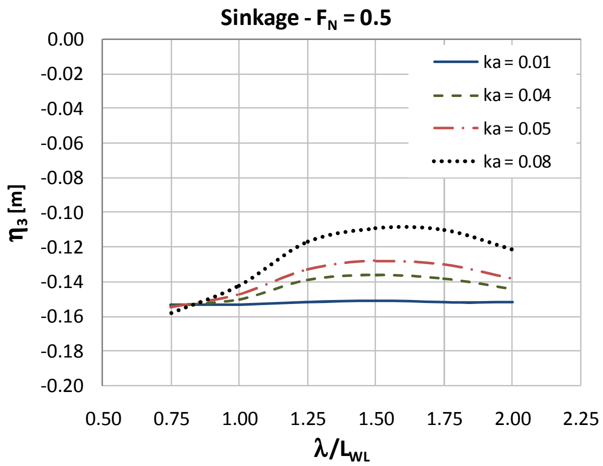

Figure 48
Sinkage of the Bulb Cat (F_N = 0.5)

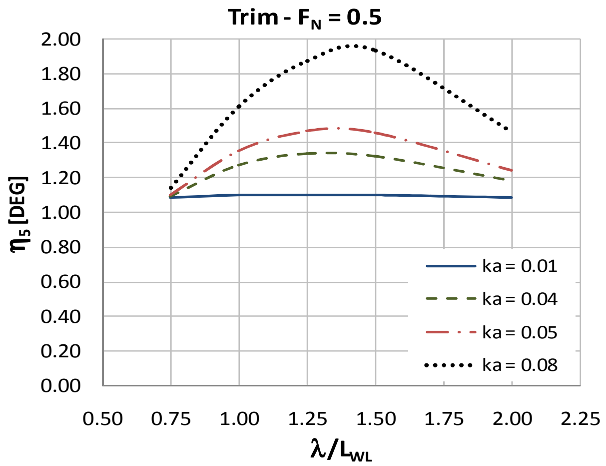

Figure 46
Trim of the catamaran (F_N = 0.5)

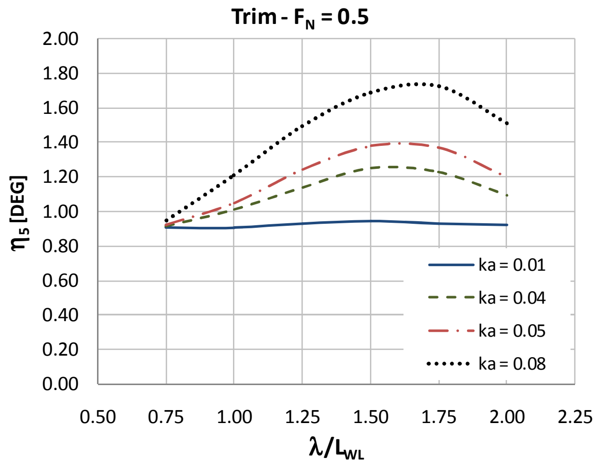

Figure 49
Trim of the Bulb Cat (F_N = 0.5)

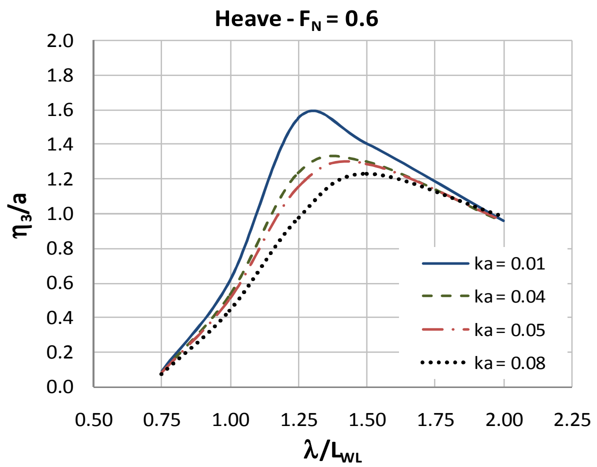

Figure 47
Heave first harmonic response
of the catamaran (F_N = 0.6)

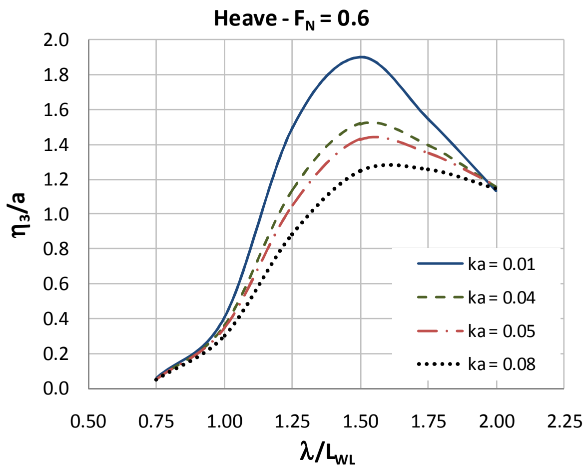

Figure 50
Heave first harmonic response
of the Bulb Cat (F_N = 0.6)

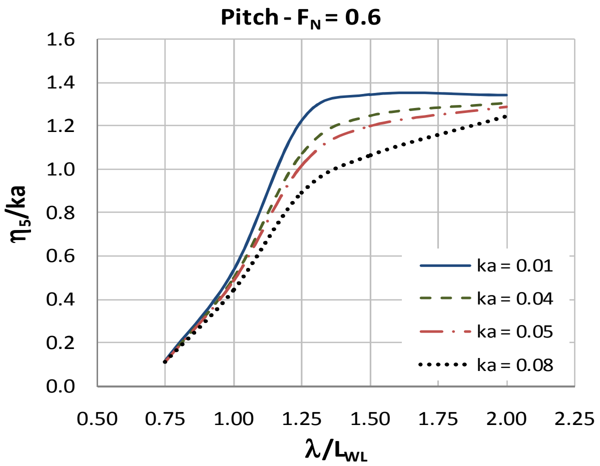

Figure 51
Pitch first harmonic response
of the catamaran (F_N = 0.6)

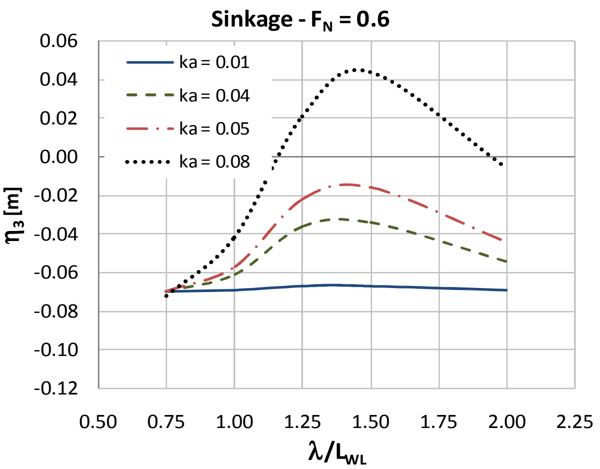

Figure 52
Sinkage of the catamaran (F_N = 0.6)

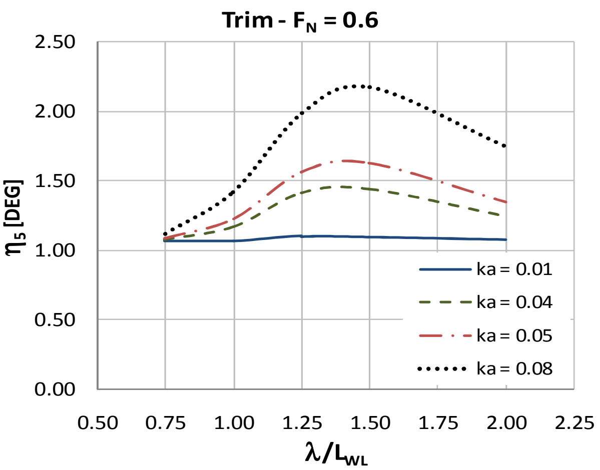

Figure 53
Trim of the catamaran (F_N = 0.6)

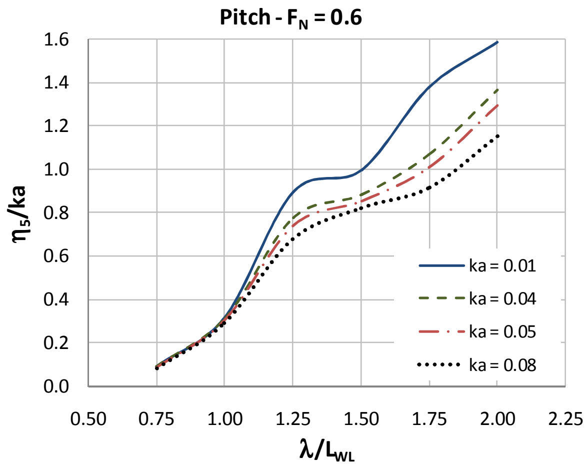

Figure 54
Pitch first harmonic response
of the Bulb Cat (F_N = 0.6)

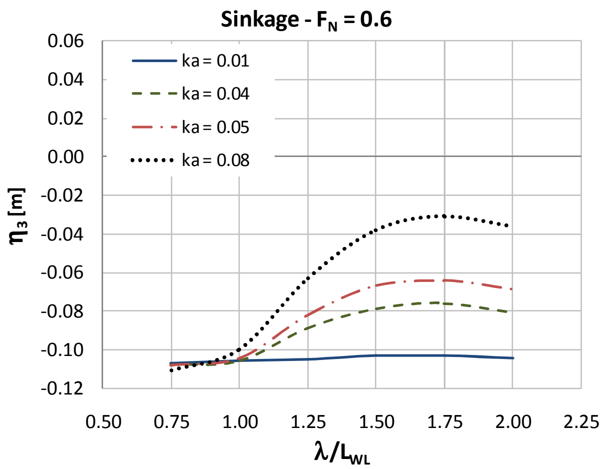

Figure 55
Sinkage of the Bulb Cat (F_N = 0.6)

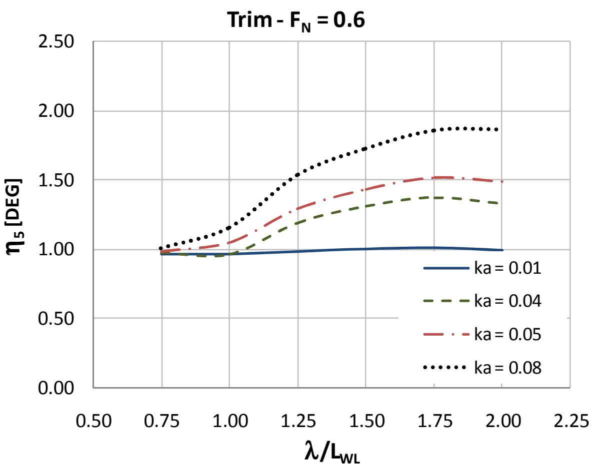

Figure 56
Trim of the Bulb Cat (F_N = 0.6)

HUMAN BODY VIBRATION RESPONSE MODELS IN THE CONTEXT OF HIGH SPEED PLANING CRAFT AND SEAT ISOLATION SYSTEMS

Thomas Coe, R.A. Shenoi and J.T. Xing, University of Southampton, United Kingdom

SUMMARY

Human exposure to vibration is increasingly the subject of health and safety legislation, legislation which can be applied to high speed craft. Within the European Union for example the Physical Agents Directive requires workplace exposure to vibration to conform to set limits or if not achievable, to be minimised. In order to address this issue at the design stage, human-seat interaction models can be used with seakeeping data to determine the effect of the isolation system on the vibration dose received.

In order to quantify the effect of an isolation system and optimise its performance for the behaviour of a specific hull form in realistic conditions during the design process, a human seat interaction model is used based on existing human response to vibration data and combined with a simplified model of the seat. To simulate the performance of a seat at sea, input loads taken from seakeeping predictions are used to develop a seat with ideal parameters for a particular hullform. A case study is presented illustrating a seat design specific to a particular hull form using the human body model to design for the most common conditions and also assessing the seat performance in the off-design condition. This case study is implemented using seakeeping input loads taken from towing tank tests.

1. INTRODUCTION

The effect of high speed craft (HSC) motions on the passengers and crew is becoming of increased interest to the designers and operators of these craft. The reasons for this are numerous and varied but include: the increased speed of high speed craft, the increased applications of high speed vessels in the commercial, leisure, rescue and military sectors and advances in structural design which mean that the strength of the HSC is no longer a limiting factor in how hard it can be driven. This effectively means that the physical limits of the crew become a key factor in limiting the performance of a high speed craft, particularly in waves.

The effect of vibration on passengers and crew is not trivial; studies have linked prolonged exposure to whole body vibration (WBV) with various health problems. Steyner[1] correlates a large number of studies on the subject and concludes that WBV is likely to be a factor in development of lower back pain. Neikerk and Barnard [2] report damage to lower back, kidneys and neck as well as brusies on the buttocks and inner thighs. Ensign et al [3] surveyed high speed boat operators within the United States Navy and reported a variety of injuries, including abdominal pain, torn ligaments, broken bones and damage to internal organs. Even in less extreme conditions mental and physical fatigue is reported [4].

As well as the physical dangers generated by WBV on fast craft, a second issue is that of incoming legislation. Within the European Union, the European Physical Agents Directive [5] stipulates that all employers must reduce vibration levels below certain limits or, if this is not possible, to minimize the vibration exposure.

To date the main method of mitigating the potential effects of whole body vibration is to retro-fit suspension seats of which there are a number commercially available. There are, however, several potential benefits to considering WBV during the design process, namely: the cost of these systems is considerable (of the order of thousands of US Dollars per seat) and for a small boat such as a RIB seating numerous people it may make financial sense to alter the hull form or reduce the planned operational speed rather than fit suspension seats.

Secondly, only a certain improvement in the vibration exposure can be achieved by using suspension seating, if this improvement is insufficient then hullform alterations may be considered at the design stage to improve the seakeeping of the vessel.

Finally, different vessels will have different seakeeping and hence vibration characteristics; by considering these it is possible to design or specify mitigation systems that are optimal for a particular vessel.

In order to achieve an understanding of the effects of HSC motions on the humans on board and give useful information to the designer, a design method is proposed consisting of a combination of a human body and seat model with the application of high speed craft motions based on CFD simulations, towing tank data or full scale trials.

Vibration is assessed using the Vibration Dose Value (VDV) outlined in the European Physical Agents Directive and relevant ISO standards. In order to illustrate this process, a case study is presented using towing tank data and the proposed model to assess two candidate seats as part of the design process.

2. PROPOSED DESIGN METHOD

There are benefits to considering human response to vibration at an earlier stage in the design process than it traditionally appears. In order to achieve this, a human-seat model can be used with numerical simulations or towing tank data to allow the severity of the vibration exposure to be quantified before the hull shape is fixed. A design method using a combination of ship motions data, seat models and a human body model to assess hullforms throughout the process is proposed. This allows designers to make informed decisions as to whether suspension mitigation systems are necessary or whether perhaps a slower but more sea-kindly hull is needed.

Of particular interest to European operators and designers is the European Physical Agents Directive [5]. This stipulates vibration limits in terms of the *VDV* (equation (1)). The Directive stipulates daily exposure action and limit values of 9.1 $m/s^{1.75}$ and 21 $m/s^{1.75}$ respectively. *VDV*, therefore, is used throughout to quantify the vibration experienced. A schematic of the design process, showing the key components needed to consider the human vibration exposure, is shown in Figure 1. Figure 2 illustrates the human, seat interaction model that is used to obtain the results required.

$$VDV = \sqrt[4]{\int_0^T a_w^4(t)\mathrm{d}t} \qquad (1)$$

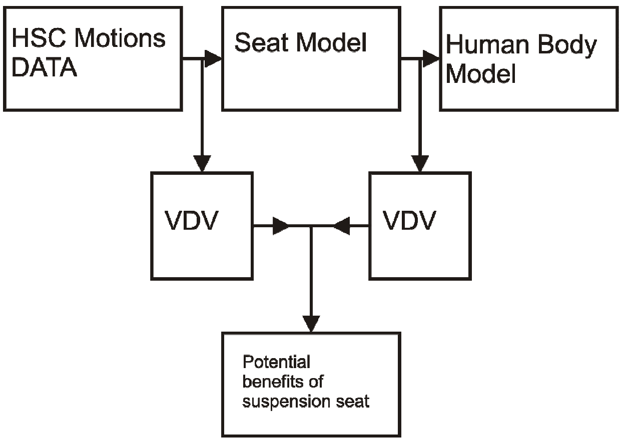

Figure 1. Schematic of design process

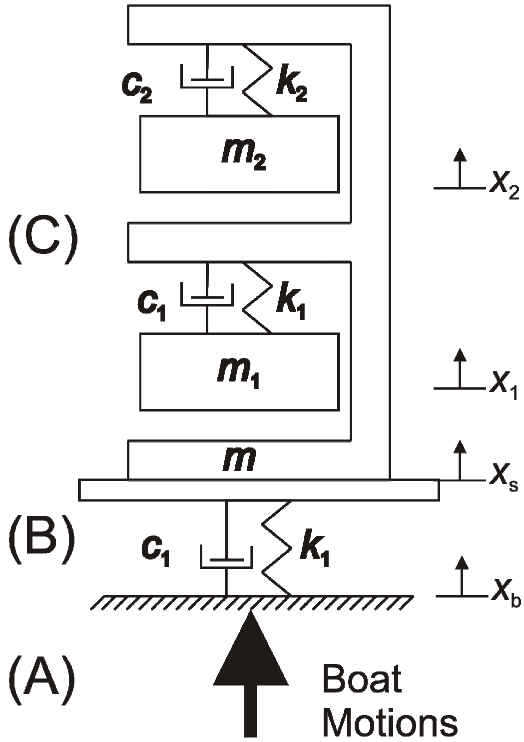

Figure 2. Human-seat model excited by boat motions

2.1 HSC MOTIONS DATA (A)

In order to assess the vibration environment on board a proposed HSC, knowledge of its motions is needed. These data can be obtained from a variety of sources depending on the stage of the design process and the facilities available to the designer, including: numerical predictions, towing tank data and full scale sea trials of a prototype. *VDV* requires acceleration, which should be measured and weighted in accordance with ISO standard 2631[6] to comply with the EU Directive.

2.2 SEAT MODEL (B)

In order to ascertain the effectiveness of the isolation seat, its response must be modelled. The model of the seat may be as simple or as complex as desired, ranging from modelling a typical bolster seat as a linear spring and damper to incorporating non-linear materials and friction between moving components. For initial design work, it is reasonable to consider the seat as a linear mass, spring and damper system such as the one shown in part A of Figure 2.

2.3 HUMAN MODEL (C)

The human body model is a key component of the design tool. A human being seated on a seat does not behave like a rigid mass when the seat is excited by base motions [7]. Hence it is necessary to utilise a more detailed model of the human when considering the human response to whole body vibration; a model that includes the stiffness and damping inherent in the human. The use of such models dates to the early study of the pilot ejection problem [8], where a single degree of freedom model was developed by Latham to model the response of the pilot. Since this first human body model was developed, other more sophisticated models have been created to represent the human response to vertical vibration. These models range in complexity from the single degree of freedom mass, spring, damper model through more complex models containing multiple degrees of freedom to models created using finite element methods which model the human in great detail. Wei and Griffin[9] consider several models for seat design for land based transport applications and conclude that a simple two degree of freedom model is sufficient to ensure that the seat behaves in the same way as it would when occupied by a human being. The model used by Wei and Griffin is shown as part (C) of Figure 2.

Human model theory

The equations of motion of the human model are given by

$$[\mathbf{M}]\{\ddot{\xi}\}+[\mathbf{C}]\{\dot{\xi}\}+[\mathbf{K}]\{\xi\}=\{\hat{\mathbf{F}}\}, \tag{2}$$

Where the mass [**M**], stiffness [**K**] and damping [**C**] matrices are

$$[\mathbf{M}]=\begin{bmatrix} m & 0 & 0 \\ 0 & m_1 & 0 \\ 0 & 0 & m_2 \end{bmatrix},$$

$$[\mathbf{K}]=\begin{bmatrix} k_1+k_2 & -k_1 & -k_2 \\ -k_1 & k_1 & 0 \\ -k_2 & 0 & k_2 \end{bmatrix},$$

$$[\mathbf{C}]=\begin{bmatrix} c_1+c_2 & -c_1 & -c_2 \\ -c_1 & c_1 & 0 \\ -c_2 & 0 & c_2 \end{bmatrix},$$

And the acceleration $\{\ddot{\xi}\}$, velocity $\{\dot{\xi}\}$ and displacement $\{\xi\}$ vectors are

$$\{\ddot{\xi}\}=\{\ddot{\mathrm{x}}_{\mathrm{b}} \quad \ddot{\mathrm{x}}_1 \quad \ddot{\mathrm{x}}_2\}^{\mathrm{T}}, \{\dot{\xi}\}=\{\dot{\mathrm{x}}_{\mathrm{b}} \quad \dot{\mathrm{x}}_1 \quad \dot{\mathrm{x}}_2\}^{\mathrm{T}},$$

$$\{\xi\}=\{x_{\mathrm{b}} \quad x_1 \quad x_2\}^{\mathrm{T}}.$$

The excitation force $\{\hat{\mathrm{F}}\}$ is

$$\{\hat{\mathbf{F}}\}=\{F_{\mathrm{b}} \quad F_1 \quad F_2\}^{\mathrm{T}}.$$

The method most commonly used to assess a human body model is the apparent mass, defined in equation (3) where $F(t)$ is the force measured at the seat and $\ddot{x}_{\mathrm{b}}$ is the acceleration measured at the seat

$$\frac{F(t)}{\ddot{x}_{\mathrm{b}}}=apparent\_mass\,. \tag{3}$$

By taking Laplace transforms, the apparent mass for the model can be found in the frequency domain and is given by

$$F(\mathrm{s})=ms^2x_{\mathrm{b}}+m_1s^2x_1+m_2s^2x_2$$

$$s=\omega\mathrm{i} \tag{4}$$

$$\frac{F(\omega\mathrm{i})}{\ddot{x}_{\mathrm{b}}(\omega\mathrm{i})}=\frac{\mathrm{D}+\mathrm{E}+(\mathrm{F}+\mathrm{G})\mathrm{i}}{\mathrm{A}+\mathrm{Bi}}$$

$$\begin{aligned}
&\mathrm{A}=k_1k_2-\omega^2(k_1m_2+k_2m_1)+m_1m_2\omega^4-c_1c_2\omega^2\\
&\mathrm{B}=(k_1c_2+k_2c_1)\omega-(m_1c_2+m_2c_1)\omega^3\\
&\mathrm{D}=(m+m_1+m_2)k_1k_2,\\
&-(mm_2k_1+mm_1k_2+m_1m_2k_1+m_1m_2k_2)\omega^2\\
&\mathrm{E}=mm_1m_2\omega^4-(mc_1c_2+m_1c_1c_2+m_2c_1c_2)\omega^2\\
&\mathrm{F}=(m+m_1+m_2)(k_1c_2+k_2c_1)\omega\\
&\mathrm{G}=-(mm_1c_2+mm_2c_1+m_1m_2c_2+m_1m_2c_1)\omega^3
\end{aligned}$$

The magnitude and phase angle are therefore

$$|m_a|=\sqrt{\frac{(\mathrm{D}+\mathrm{E})^2+(\mathrm{F}+\mathrm{G})^2}{(\mathrm{A}^2+\mathrm{B}^2)}} \tag{5}$$

$$\theta=\mathrm{a}\tan\left(\frac{(\mathrm{F}+\mathrm{G})}{(\mathrm{D}+\mathrm{E})}\right)-\mathrm{a}\tan\left(\frac{\mathrm{B}}{\mathrm{A}}\right) \tag{6}$$

Wei and Griffin publish the mass, stiffness and damping parameters of the model derived from experimental data

[9]. It is relatively straight forward, however, to determine the parameters using curve fitting techniques. Boileau et al [10] present a larger data set and the model is fitted to this. The parameters (Table 1) are identified using a least squares regression and a comparison between the experimental and model responses is shown in Figure 3.

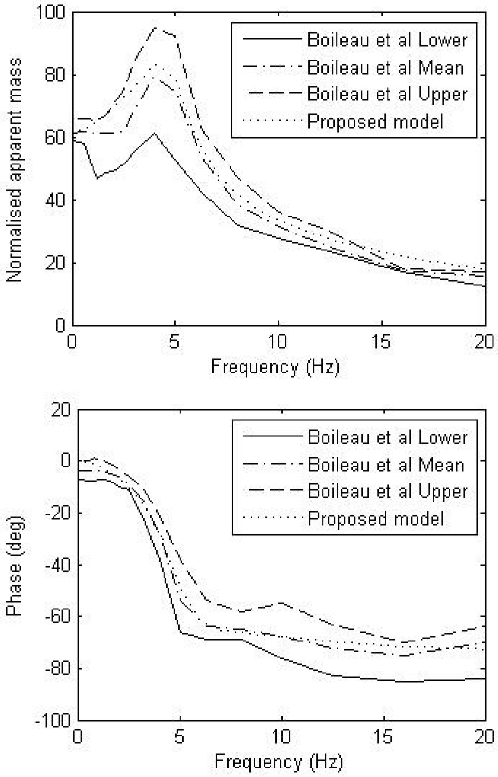

Figure 3. Human body model performance

Table 1. Model parameters based on Boileau et al. data

Parameter	Value
m (kg)	1.815914712
m_1 (kg)	37.9209655
m_2 (kg)	21.26311883
k_1 (N/m)	20033.27497
k_2 (N/m)	20142.65788
c_1 (Ns/m)	1895.558177
c_2 (Ns/m)	377.0241905

The human-seat model (Figure 2) has equations of motion as follows

$$[\mathbf{M}]\{\ddot{\xi}\}+[\mathbf{C}]\{\dot{\xi}\}+[\mathbf{K}]\{\xi\}=\{\hat{\mathbf{F}}\}, \tag{7}$$

where

$$[\mathbf{M}]=\begin{bmatrix} m & 0 & 0 \\ 0 & m_1 & 0 \\ 0 & 0 & m_2 \end{bmatrix},$$

$$[\mathbf{K}]=\begin{bmatrix} k_1+k_2+k_s & -k_1 & -k_2 \\ -k_1 & k_1 & 0 \\ -k_2 & 0 & k_2 \end{bmatrix},$$

$$[\mathbf{C}]=\begin{bmatrix} c_1+c_2+c_s & -c_1 & -c_2 \\ -c_1 & c_1 & 0 \\ -c_2 & 0 & c_2 \end{bmatrix},$$

and

$$\{\ddot{\xi}\}=\{\ddot{x}_s \quad \ddot{x}_1 \quad \ddot{x}_2\}^{\mathrm{T}}, \{\dot{\xi}\}=\{\dot{x}_s \quad \dot{x}_1 \quad \dot{x}_2\}^{\mathrm{T}},$$
$$\{\xi\}=\{x_s \quad x_1 \quad x_2\}^{\mathrm{T}}, \{\hat{\mathbf{F}}\}=\{F_s \quad F_1 \quad F_2\}^{\mathrm{T}}$$

when the seat is excited by base motions $\{\hat{\mathrm{F}}\}$ is given by

$$\{\hat{\mathbf{F}}\}=[\mathbf{C}]\{\dot{\xi}_{\mathbf{b}}\}+[\mathbf{K}]\{\xi_{\mathbf{b}}\} \tag{8}$$

For simple cases such as sinusoidal excitation the exact solution can be found however in reality $\{\xi_b\}$ is not a mathematical function and so the equations must be solved numerically.

2.4 QUANTIFYING RESPONSE

By combining the human-seat model with HSC motions data the designer can obtain the response of the occupied seat to the motions of the boat. Various methods of quantifying the vibration exposure exist [11], such as root mean square (RMS), root mean quad (RMQ) and the vibration dose value.

According to the European Union Directive *VDV* should be used and this is calculated for the seat and the deck using equation (1). In addition the performance of the seat can be quantified by the use of the *SEAT* value (equation (9)).

$$SEAT=\frac{VDV_{\mathrm{seat}}}{VDV_{\mathrm{deck}}}\times 100 \tag{9}$$

Other methods of quantifying vibration exposure can also be used instead of *VDV* (RMS etc)

3. CASE STUDY

3.1 INPUT DATA

The following case study demonstrates the application of the method outlined above for a high speed planing craft.

In this case the ship data is taken from model tests of a high speed planing hull forming part of a systematic series [12].

The models were fitted with heave and pitch potentiometers and vertical accelerometers at the LCG position and at the bow. Tests were carried out in irregular waves using a JONSWAP spectrum and at high speed. Further details can be found in Taunton et al. [12]. In order to highlight the potential problem, the example taken is the most extreme available, considering only the highest speed case, model speed of 12.051m/s and 0.6m significant wave height. The model was scaled using $\nabla^{\frac{1}{3}}$ to give the response for a 1.8 tonne planing craft at 45.5 knots and a significant wave height of 2.26 m.

The first stage of the design process is to determine whether or not the vibration is sufficiently severe to warrant action. The full scale acceleration data for two runs in the same sea state are weighted using the weighting factor stipulated in ISO standard 2631 [6] and the *VDV* is calculated. The acceleration data (Figure 4) illustrates severe impacts over 60 m/s^2. the *VDV* for the 27.26s exposure on the deck is 42.7682 m/s$^{1.75}$. This indicates an environment exceeding the daily exposure limit of 21 m/s$^{1.75}$ set by the European Physical Agents Directive.

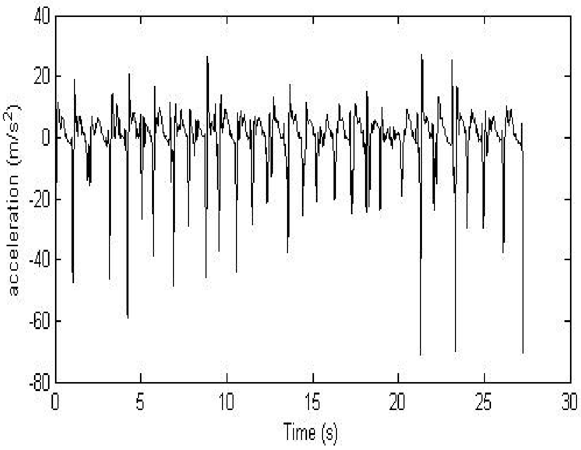

Figure 4. Acceleration time history at LCG at 45.5 knots

3.2 HUMAN SEAT INTERACTION

Having established the severity of the vibration environment, a seat can be incorporated into the model to determine its effectiveness. If a custom seat design is required it is necessary to determine suitable stiffness and damping to ensure that attenuation is provided at the natural frequency of the human (approx 4.5Hz, Figure 3) and also at the most common excitation frequency. Mansfield [11] states that in order to achieve this a suspension seat should have a first natural frequency at approximately 2 Hz. Due to the large amount of energy typically found at low frequencies, however, a lower natural frequency is desirable. By considering the power spectral density of the boat motions the frequency at which most excitation takes place is found (Figure 5). This shows that the majority of the energy is at approximately 1 Hz. Choosing a seat with a spring stiffness of 2050 N/m gives a natural frequency of 0.8 Hz for a 20 kg, seat giving attenuation at the most common excitation frequency and at the natural frequency of the human.

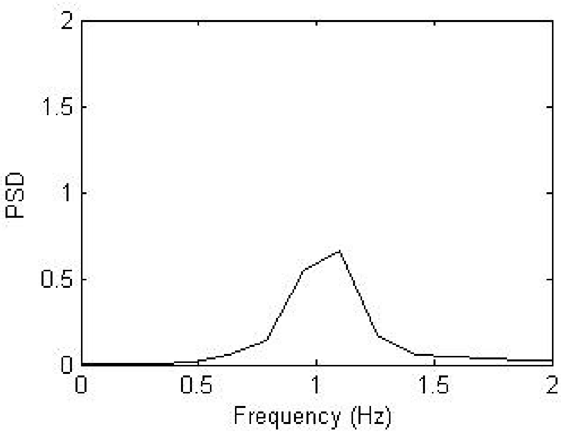

Figure 5. Full scale power spectral density from towing tank model

In order to demonstrate the human-seat model, two cases are considered: the first being a suspension seat and the second being a typical foam bolster seat of the type found on many high speed craft. Examples of the type of seats modelled are shown in Figure 6 however it should stressed that these are not the actual seats which are modelled. The properties of the two seats are shown in Table 2.

Table 2. Suspension seat details

Seat	Stiffness (N/m)	Damping (N/m/s)
Foam	130900	1000
Suspension	2050	1400

Figure 6. Example of seat types modelled (a) typical foam seat (courtesy of Ribcraft[13]) and (b) Stidd suspension seat (courtesy or Stidd[14])

The acceleration time history is applied to the base of both seats using a transient finite element analysis, allowing the acceleration to be calculated on the seat and consequently the *VDV* and *SEAT* values.

3.3 RESULTS

The acceleration time histories for one high speed run with two seats are shown in Figure 7, along with the input acceleration at the deck. The figure shows the foam seat actually amplifying accelerations and when compared with a suspension seat is clearly inferior. This is quantified by the *VDV* and *SEAT* values shown in Table 3. The *SEAT* values show that the suspension seat provides double the isolation provided by the foam seat.

Table 3. *VDV* and *SEAT* values for the two example seats

Seat	*VDV*	*SEAT* Value
Foam	35.2606	108.5223
Suspension	17.2867	53.2037

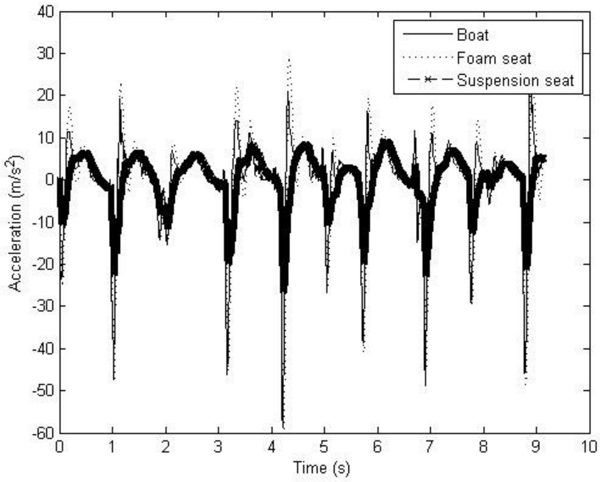

Figure 7. Comparison of seat responses

4. DISCUSSION

Implementation of the human-seat model with model test data successfully illustrates the potential benefits of including a suspension seat and allows the designer to make a better informed decision as to whether a seat is beneficial. The conditions used for the case study are deliberately extreme; being beyond the bounds of normal operation for most HSCs, however, the options available to the designer are illustrated. Alternative hullforms can be tested to establish their *VDV* reduction potential and compared with the cost of installing a particular suspension seat.

There are, however, several potential areas to improve the model. Firstly, the model test data is not representative of the actual conditions experienced. The model is driven at a constant speed through the waves, whereas during operation the helmsman can vary the speed in an active manner to reduce excessive impacts. This means that the actual *VDV* values recorded are likely to be higher than the corresponding values in the same conditions at sea. Secondly, more complex seat models would also improve the model predictions, for example the seats are of infinite travel; end-stop impacts are not modelled and these can cause significant peak accelerations if the seat reaches its limit of travel [11, 15]. Thirdly, no attempt is made to simulate any use of the legs to absorb vibration, something which occurs when using the straddle seats often found on board high speed craft.

CONCLUSIONS

The vibration environment experienced on a HSC is severe and there is evidence of adverse effects on passengers or crew. At present the effects of vibration on humans are not considered at the design stage. Seakeeping tests are a key part of the design process for a high speed craft. By using a human-seat model, additional information can be gained during the design process on the vibration experienced by the vessel's crew and steps can be taken to mitigate against this before the final design is fixed. Results obtained from the model are qualitatively as expected however due to the ethical issues surrounding human experimentation it is difficult to validate the model quantitatively at the high accelerations experienced on board a HSC.

AKNOWLEDGEMENTS

The authors would like to acknowledge the support of the Engineering and Physical Sciences Research Council (EPSRC) and MARSTRUCT in this research.

REFERENCES

[1]. R.M. STEYNER, *Whole Body Vibration and Shock; A Literature Review*. 2001, London: Health and Safety Executive.

[2]. J. NIEKERK and C.M. BARNARD, *Suspension Seat for High Speed, Off-Shore RIB*, in *41st UK Conference on Human Response to Vibration*. 2006, Qinetiq: Qinetiq, Farnbrough, UK.

[3]. W. ENSIGN, J.A. HODGDON, W.K. PRUSACZYK, S. AHLERS, D. SHAPIRO, and M. LIPTON, *A survey of self reported injuries among special boat operators*. 2000, Naval Health Research Centre: San Diego.

[4]. T. DOBBINS. *new EU Directive limits allowable shock exposure. The employer is now liable. What must we do -as employer - as operator - as boat builder?*
. in *Seawork 2006*. 2006. Souhampton, UK.

[5]. EUROPEAN UNION DIRECTIVE, *Directive 2002/44/EC of the European Parliament and of the council of 25th June 2002 on the minimum health and safety requirments regarding the exposure of workers to the risks arising from physical agents (vibration) (Sixteenth individual Directive within the meaning of Article 16(1) of Directive 89/391/EEC*. 2002, European Union.

[6]. ISO2631, *ISO 2631;2003 Mechanical vibration and shock -- Evaluation of human exposure to whole-body vibration*. 2003, International Standards Organisation.

[7]. M.J. GRIFFIN, *Handbook of human vibration*. 1990, London: Academic Press.

[8]. F. LATHAM, *A Study in Body Ballistics: Seat Ejection* Proceedings of the Royal Society of London, Series B, 1957. **147**(926): p. 121-139.

[9]. L. WEI and M.J. GRIFFIN, *Mathematical models for the apparent mass of the seated human body.* Journal of Sound and Vibration, 1998. **212**(5): p. 855-874.

[10]. P.E. BOILEAU, X. WU, and S. RAKHEJA, *Definition Of A Range Of A Range Of Idealized Values To Characterize Seated Body Biodynamic Response Under Vertical Vibration.* Journal of Sound and Vibration, 1998. **215**(4): p. 841-862.

[11]. N.J. MANSFIELD, *Human response to vibration*. 2005, Boca Raton, Fl.: CRC Press. 227.

[12]. D.J. TAUNTON, D.A. HUDSON, R.A. SHENOI, and D.A. ALLEN, *Experimental Investigation into the Characteristics of a Series of High Speed, Hard Chine, Planing Hulls in Waves*. 2008: Submitted for Publication.

[13]. WWW.RIBCRAFT.CO.UK. 2008.

[14]. WW.STIDD.COM/PRODUCTS/SHOCK.HTM. 2008.

[15]. R. CRIPPS, S. REES, H. PHILLIPS, C. CAIN, D. RICHARDS, and J. CROSS, *Development of a Crew Seat System for High Speed Rescue Craft*, in *FAST 2003*. 2003: Naples, Italy.

CURE OPTIMIZATION OF HIGH PERFORMANCE RESINS FOR MARINE VEHICLES

Njaramalala Rabearison, LBMS EA 4325, Naval and Offshore Structures Laboratory, ENSIETA, Brest, France.
Christian Jochum, LBMS EA 4325, Naval and Offshore Structures Laboratory, ENSIETA, Brest, France.
Jean-Claude Grandidier, LMPM Laboratory, ENSMA, Futuroscope, France.

SUMMARY

This paper focuses on the problem of thermosetting resins commonly used for structural design in marine applications. The main difference between marine and previous well known aerospace applications lies in the thickness observed for marine structural parts that is much more important. If it is obvious that low densities of thermosetting composites associated with their high strengthening are very attractive for the designers to improve payload and reduce energy costs, the curing of such technical materials becomes delicate as the thickness increases (more than 3-4 mm). Thus a 3D curing model, based on the couplings between the thermal and the chemistry, is presented. The FEM solving technique was used and results obtained enables local and central information for cure optimization strategy such as temperature gradients and degree of cure gradients. A validation of the model was provided by comparisons with experimental data and thickness effects on curing quality are highlighted.

1. INTRODUCTION

It is well known today that the use of composites for structural applications has become increasingly important. In particular, thermosetting laminates are more and more used for transportation applications to improve payload and reduce energy costs. Their low densities in association with their high strengthening are quite attractive for the designers. These trends have recently emerged in naval and offshore construction since the optimization of the structures became inevitable. Simultaneously to the economical interest of this kind of high performance composites, numeric tools were developed for design efficiency. Of course, low cost access to computational mechanics computers made it easier for the designers, but at the same time several works were done by the scientific community to improve composite material description and modeling.
Hence, the question of the manufactured laminate's quality is becoming a new strategic question. In behalf of design improvement and costs optimization for thermosetting laminates applications, a highly accurate knowledge of material properties and of the internal state obtained at the end of the manufacturing process is required. This is especially crucial for thick laminates that are more and more developed, namely for naval and offshore applications. Thermal gradients are generated because of the thermo activated and exothermic behavior of thermosetting resins leading to several imperfections (bubbles, cracks, etc …) therefore decreasing the quality of the composite. The main factor is the thermal history applied during the curing within the matter. As the thickness increases (actually more than 3-4 mm), the coupling effect between the thermo activated and exothermic behavior of thermosetting systems cannot be neglected. The quality of the laminate obtained is therefore quite different from the theoretical considerations that designers used to apply. An example of cure defects is shown in Fig. 1 for a thick carbon epoxy raiser tube.

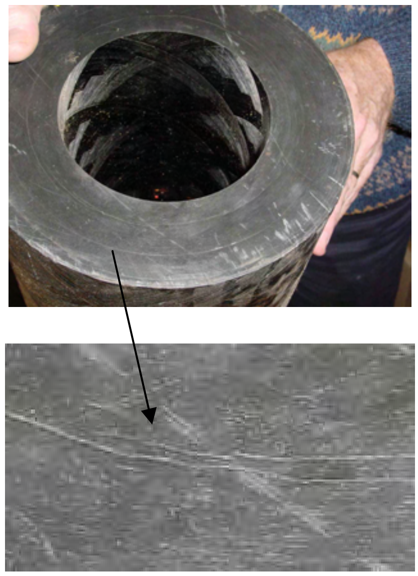

Fig. 1. Defects across thickness in an 80 mm thick carbon epoxy raiser tube (by courtesy of IFREMER: French Research Institute for Sea Exploitation).

To face the question of laminate quality of curing, foundations of a thermal, chemical, species diffusion and mechanical coupling model for cure simulation were presented by the authors in a previous work [1] within a thermodynamic framework based on finite simulation. If this was satisfactory from a theoretical point of view, it appears obvious that all the couplings could not be taken into account for industrial simulation according to the heaviness of coupling parameters definition. Nevertheless, in order to provide an industrial tool being able to provide as easily as possible appropriate information for the description of the curing, knowledge resulting from the previous, more theoretical, work presented by the authors was improved and is presented in this paper. Thus, the strategy of a three-dimensional finite element modeling (FEM) approach of the curing, devoted to industrial FEM software like Abaqus©, is exposed in this paper. In order to provide rapidly strategic information about curing quality, only the thermal and chemical coupling problem is analyzed here.

Indeed, ability to predict internal thermal history, and hence local degree of curing information, can be considered as a powerful and strategic way for further studies of the question of internal stress development, residual stress and gradients of properties. Therefore, thermal history prediction was considered as the main information for cure optimization because of the thermo activated and exothermic behavior of high performance resins.

To face this challenge, description of a thermal and chemical coupling model for cure simulation is presented by the authors in the second part of the paper, devoted to finite element simulation. The finite element simulation was considered as a possible and helpful way to understand cure quality gradients as explained in the third part of the paper. Results are compared with experimental data of internal temperature and are presented in the fourth part of the paper. They demonstrate the applicability of a finite element modeling approach to provide local information during the curing.

Consequently, in the fifth part of the paper, an application towards cure schedule optimization is presented and discussed.

2. THE 3D CURE KINETICS COUPLING MODEL

Curing thermosetting materials generally involves the transformation of low molecular weight liquids to amorphous networks with infinite molecular weight by means of exothermic chemical reactions. One of the most widely used methods for cure kinetics determination of thermosetting resin system is the differential scanning calorimetric (DSC) method. Therefore dynamic and isothermal measurements were done in a conventional DSC in order to quantify the released heat during curing and to determine the degree of chemical conversion or degree of cure. The degree of cure is defined as the ratio of the released heat up to the current time by the total or the ultimate heat of reaction. It ranges from 0 for uncured resin to 1 for completely cured resin and denotes the thermo hardening process of an epoxy resin that belongs to a phase change from a liquid state to a solid state. However, the curing is also an exothermal reaction and the heat produced by the reaction helps to its activation. A coupling between the thermal and the chemistry exits and can be illustrated by the heat transfer equation whose simplified expression, without species diffusion, can be written as:

$$\rho\, Cp\frac{dT}{dt} = -\,\mathrm{div}\{\lambda_T\,[-\overrightarrow{\mathrm{grad}}\,T\,]\} + f_v + \rho\,\Delta H^r\,\frac{d\alpha}{dt} \qquad (1)$$

The reactive blend evolution is described by the degree of conversion of the chemical reaction also called degree of cure and usually denoted by α. The parameter α is governed by a time derivative equation with temperature dependent parameters as detailed in the cure kinetics section. Cp stands for specific heat and λ_T stands for thermal conductivity. f_v denotes the heat flow imposed by the oven, $\rho\Delta H^r d\alpha/dt$ is the heat flow produced by the chemical reaction and $d\alpha/dt$ is the rate of degree of conversion.

2.1. EPOXY CURE KINETICS

The resin system used in this study is a three-component anhydride-epoxy system from Ciba. The blend consists of a bifunctional DGEBA-type epoxy (Araldite LY556, EEW=183-192 g/eq, n=0.3), a tetra-functionnal anhydride hardener (methyl-tetrahydrophthalic anhydride HY 917, anhydride equivalent weight = 166g/eq), and an accelerator (l-methyl imidazole DY 070). The components were mixed in LY 556/HY 917/DY 070 weight ratio of 100/90/1, resulting in a stoichiometric epoxy-anhydride mixture.

A lot of empirical models, [2-5], have been suggested for degree for cure kinetics. It appears that the most widely used model in the literature for epoxy systems seems to be the phenomenological Kamal and Sourour model [6] of cure kinetics. This model was chosen for the LY556 epoxy system studied in this paper and is expressed by equation (2). This model accounts for an autocatalytic reaction in which the initial reaction rate is not zero.

$$\frac{d\alpha}{dt} = (K_1 + K_2\,\alpha^m)(1-\alpha)^n$$
$$\text{with } K_1 = A_1\exp\left(\frac{-E_1}{RT}\right) \text{ and } K_2 = A_2\exp\left(\frac{-E_2}{RT}\right) \qquad (2)$$

Where α is the degree of cure corresponding to $d\alpha/dt$, T is the temperature, R is the universal gas constant and m, n, A_1, A_2, E_1, E_2 are constants which are calculated from the curve fit using the degree of cure rate measured by isothermal DSC scans. K_1 and K_2 are specific rate constants following an Arrhenius form and are temperature dependent. The constant K_1 was graphically deduced since it denotes the initial reaction rate at the beginning of the reaction start, and is given by the intercept of plots of degree of conversion rate versus degree of cure.

Nevertheless, as the curing evolves, the chemical degree of conversion rate is less and less important and the thermosetting reaction becomes diffusion controlled [7, 8-12].

Thus, a semi-empirical relationship (3) proposed by Fournier et al. [8], and based on free volume consideration, was chosen for the description of diffusion effects. Fournier et al. [8] extended the Kamal and Sourour model by a diffusion factor $f_d(\alpha)$ such as:

$$\frac{d\alpha}{dt} = (K_1 + K_2\,\alpha^m)(1-\alpha)^n f_d(\alpha)$$

$$\text{with } f_d(\alpha) = \left[\frac{2}{(1+\exp[(\alpha-\alpha_f)/b])} - 1\right] \qquad (3)$$

α_f is the degree of conversion measured at the end of a given isothermal curing and b is an empiric diffusion constant of the material.

Equation (3) fits the best experimental data for the cure kinetics of the LY556 epoxy resin as highlighted in Fig. (2). Impact of diffusion factor must therefore be taken into account.

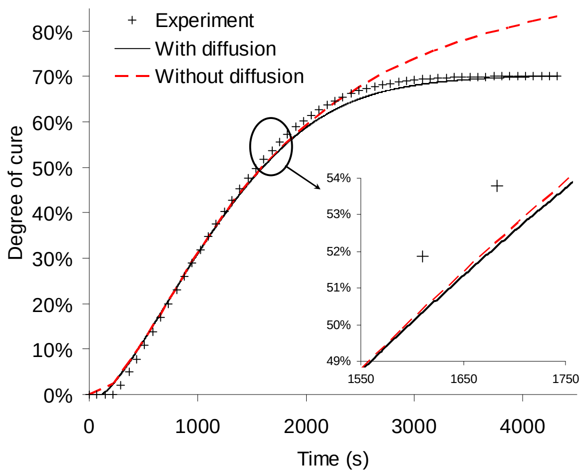

Fig. 2: Diffusion factor impact on the Kamal and Souror autocatalytic model (100°C isothermal curing).

Hence cure kinetics parameters identified for the LY556 epoxy resin are presented in Table 1.

m	b	A_1 (s^{-1})	A_2 (s^{-1})	E_1 (KJ/mol)	E_2 (KJ/mol)
0.74	0.0452	$1.779e^{+5}$	$1.226e^{+9}$	63.647	85.979

Table1: Cure kinetics coefficients of Kamal and Sourour model associated with Fourier et al. diffusion factor for the LY556 epoxy resin.

The other parameters, such as n and $\alpha_{f,}$ were found to vary linearly with the temperature and are displayed in Fig. 4 and Fig. 5.

Nevertheless, the solving of the equation of heat transfer (1) requires material parameters evolution laws during the curing. This question is detailed in next subsection for thermal properties such as specific heat and conductivity.

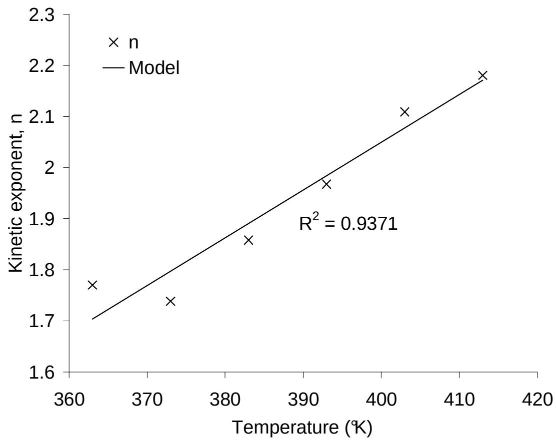

Fig. 3: Plots of the estimated value of the kinetic parameter n.

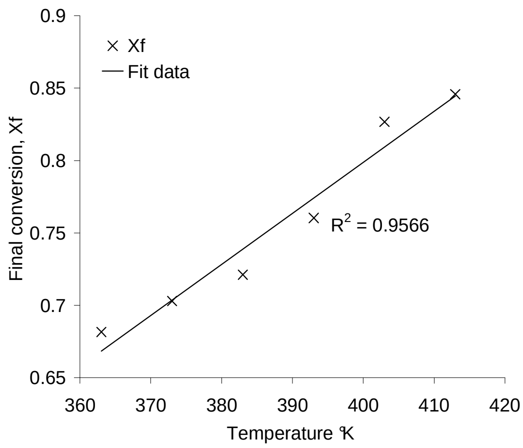

Fig. 4: Evolution of α_f versus isothermal curing temperature.

2.2. EPOXY THERMAL PROPERTIES MODELLING

With increasing thickness, mass effect of the epoxy has to be taken into account because of the exothermal aspect of the thermosetting reaction. This statement is clearly demonstrated by equation of heat transfer (1) where the coupling between the thermal and the chemistry appears. Descriptions of specific heat and thermal conductivity evolution during the curing are therefore required for the solving of the heat transfer equation.

2.2.1. SPECIFIC HEAT C_P (J/G°C)

It was assumed, as a first approach, that specific heat evolution during the curing can be described by a linear mixture rule relation, weighted by the degree of cure, between the liquid state (resin) and the solid state (matrix), as follows:

$$Cp\,(\alpha,T) = (1-\alpha)\,Cp\,(0,T) + \alpha\,Cp\,(1,T) \qquad (4)$$

Cp (0,T) is the liquid resin specific heat dependency on temperature before the start of the thermosetting reaction. Cp (1,T) is the fully cured matrix specific heat dependency on temperature. Identification of Cp (0,T) and Cp (1,T) lead to almost linear evolution versus temperature as provided by Van Mele et al. [12] works on the same epoxy blend and were defined as follows:

$$Cp\,(0,T) = 1.8500+0.002625T \quad (J/g°C)$$

$$Cp\,(1,T) = 1.3125+0.004437T \; J/g°C \text{ for } T<Tg_{infinity} \qquad (5)$$

$$Cp\,(1,T) = 1.8500+0.002625T \; J/g°C \text{ for } T\geq Tg_{infinity}$$

with $Tg_{infinity}$ = 136°C, for the LY556 epoxy.

$Tg_{infinity}$ denotes the glass transition temperature of the fully cured matrix.

2.2.2. THERMAL CONDUCTIVITY λ (W/M°C)

In the same way as for specific heat, it was also chosen to express the thermal conductivity by a linear mixture rule relation weighted by the degree of cure as follows:

$$\lambda(\alpha,T) = (1-\alpha)\,\lambda(0,T) + \alpha\,\lambda(1,T)$$
$$\lambda(1,T) = -2.727\;10^{-4}\,T+3555.529\;10^{-4}\;(W/m°C) \qquad (6)$$
$$\text{and } \lambda(0,T) = 0.188 \; W/m°C$$

$\lambda(0,T)$ and $\lambda(1,T)$ stand for liquid resin and fully cured matrix, temperature dependant, thermal conductivity evolutions.

2.2.3. HEAT FLOW OF THE THERMOSETTING REACTION (W/M^3)

DSC analysis enables the determination of the heat flow of the thermosetting reaction at a given temperature. The heat flow $\phi(t)$ produced by the chemical reaction associated to the curing of a thermosetting resin is a linear function of the rate of degree of cure with a slope corresponding to the mass enthalpy variation ΔH^r of the reaction such as:

$$\phi(t) = \rho\,\Delta H^r(T)\,d\alpha/dt \qquad (7)$$

ρ denotes the density. Density variation during the curing was not taken into account here since its variation is very small [9] and hence was fixed at ρ=1170.6Kg/m^3. ΔH^r temperature dependency during the cure corresponds to enthalpy temperature dependency that was indentified by several isothermal DSC scans. Therefore, ΔH^r was considered as following a linear evolution that ends at the ultimate value H_U of 354 ± 25 J/g, in agreement with the literature for the same epoxy resin system [12] or similar epoxy-anhydride system [13].

3. THE FEM MODELLING

3.1. SOLVING STRATEGY

Equations of the thermo chemical coupling problem to solve are related to the transient thermal analysis (equation of heat transfer (1)) and the cure kinetics evolution law (equation (3)). The solving was developed with the Abaqus® V. 6.5.4 finite element software. Three user subroutines were developed in Fortran 90 to take into account the couplings and were connected together. Precise details of the numerical strategy were presented by the author in a previous work [14]. The user subroutine facility enables the time, temperature and degree of cure updating for every integration point in the local element coordinate system.

3.2. FINITE ELEMENTS MODEL

The modeled structure is a cylindrical block of resin (diameter 32 mm, height 30 mm) poured in a steel tube with a thickness of 6mm and is displayed in Fig. 5.

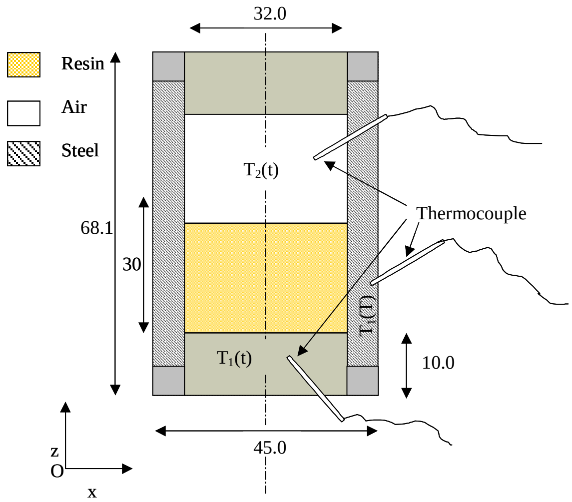

Fig. 5: Experimental device for the curing of thick epoxy samples.

Due to the axial symmetry of the structure the mesh was performed with 8-node thermally coupled axisymmetric solid, biquadratic displacement, bilinear temperature CAX8T elements of the Abaqus® element library.
The heating of the steel tube containing the liquid resin was reproduced by the FEM analysis. A special attention was given to the determination of the convexion interaction determination between the steel test tube and the air of the oven in order to reproduce as realistic as possible real conditions of heating.
The full model requires 240 elements and 787 nodes for results convergence. The computation time takes around 25 min on a Pentium IV HT desktop at 3.20 GHz with 2Go of Ram.

4. CURE SIMULATION RESULTS

4.1. LOCAL TEMPERATURE PREDICTION

4.1.1. APPLICATION TO THE LY556 EPOXY RESIN

Actually, three thermocouple probes were put inside of the resin to record internal temperature evolutions. Points 1, 2 and 3 stand respectively for the centre of the block, the lateral edge of the block at the middle of its height, and at the bottom of the block as displayed in Fig. 6.

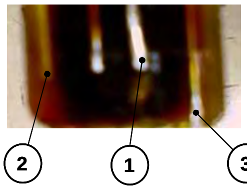

Fig. 6 Thermocouple probes position inside of the epoxy matrix.

Comparisons between internal temperature prediction given by the model and measurements are displayed in Fig. 7. Internal temperature predicted (full lines) almost fit experimental data recorded during the curing (dashed lines).

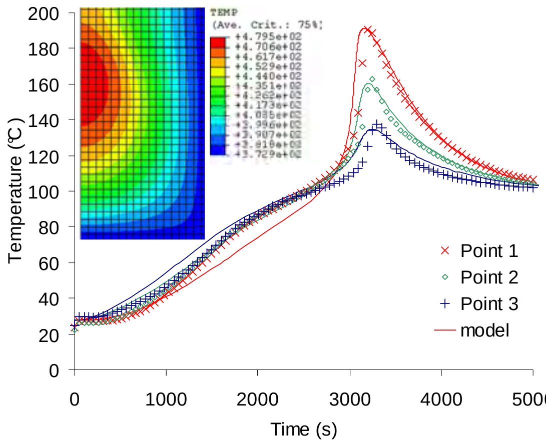

Fig. 7 Comparison between local temperatures predicted by the model and from measurements (LY556 epoxy resin, ramp 3°C/min and 100°C plateau).

Amplitude and appearance of the exothermic behavior of the curing were predicted in a very satisfactory way by the model for the curing of a thick block of epoxy resin. Nevertheless, the feasibility of the FEM 3D coupling technique was also checked for a different thermosetting system, and namely a glass fibre polyester resin composite as presented in following subsection.

4.1.2. APPLICATION TO A GLASS FIBRE POLYESTER RESIN COMPOSITE

The same methodology of the 3D cure kinetics modeling was tested on data provided by Bailleul [15] about a glass polyester composite. Corresponding cure kinetics and thermal properties of the polyester composite were updated in the model by the data provided by Bailleul. The composite sample simulated concerns an axisymmetric shape with a height of 60 mm and a width of 12 mm. This shape stands for a representative elementary volume of the composite laminated panel that was heated between two electric heating plates.
Results obtained by the model for internal temperature prediction at the middle of the thickness are shown in Fig. 8.

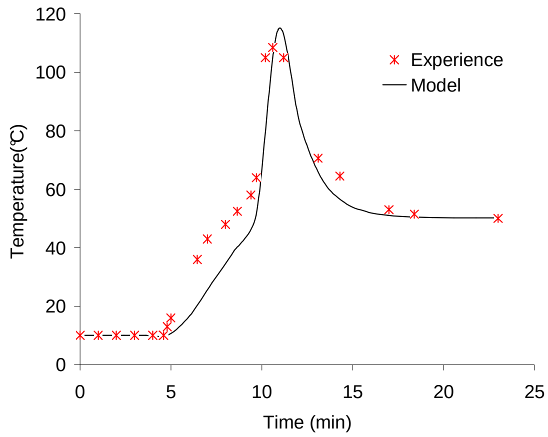

Fig. 8 Internal temperature predicted by the coupling model within a glass polyester laminated panel and comparison with the local measured temperature given by Bailleul [15].

Internal temperature predicted by the coupling model for the glass polyester laminate fits almost well with the measured temperature, except during the heating ramp. Simulation results during this step are depending on initial heating conditions propagated by the electric heating plates that were previously stabilized at 50°C. A strong transient thermal step is thus applied and was estimated, according to Bailleul data, to be around 15°C/min.

4.2. THICKNESS EFFECT

4.2.1. THERMAL GRADIENTS

This section presents results for thickness effect on the curing of the LY556 epoxy resin block presented in the third chapter of the paper. Three different thicknesses were studied: 7.5mm, 15 mm and 30 mm. The cure schedule was the same for each thickness and consisted of a 3°C/min ramp followed by a 100°C plateau.
Temperature results were carried out for four characteristic points as illustrated in Fig. 9.

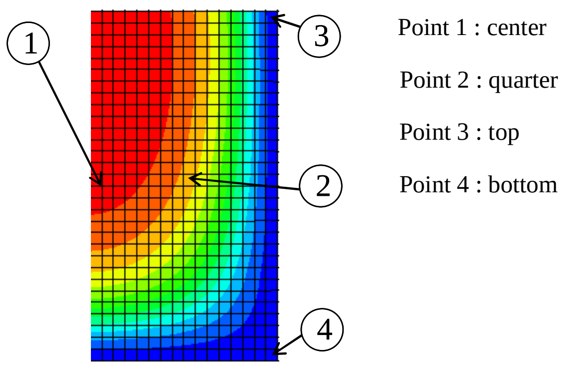

Fig. 9 Characteristic points for thickness effect study.

As seen before in Fig. 7, the centre of the block corresponds to the hottest point during the curing. Resin thickness effect on the temperature reached at this point must clearly be taken into account as highlighted in Fig 10.

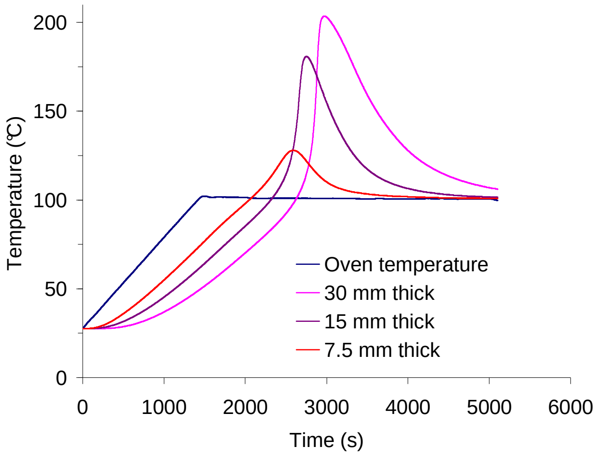

Fig. 10 Centre temperature evolution versus thickness for the curing of the LY556 epoxy resin.

In this figure, peak level increases with thickness and reached more than 203°C. Thus, for the 30 mm thickness, internal temperature level reached two times the oven temperature. If one can consider that thickness consideration could be neglected below 7.5 mm (the peak reached with this thickness did not exceed 128°C that seems to be acceptable), it must strongly be considered for higher level of thickness as demonstrated in Fig. 10. More precisely, strong thermal gradients are developed within the matrix block with increasing thickness as shown in Fig. 11 to 13. Consequently, gradients of degree of curing will be developed within the matrix, and hence increase the heterogeneity of the material as presented in next subsection.

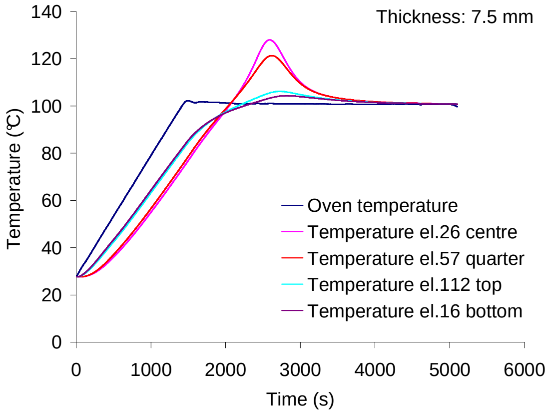

Fig. 11 Thermal gradients predicted within a 7.5mm thick epoxy matrix during the 3°C/min ramp and 100°C plateau.

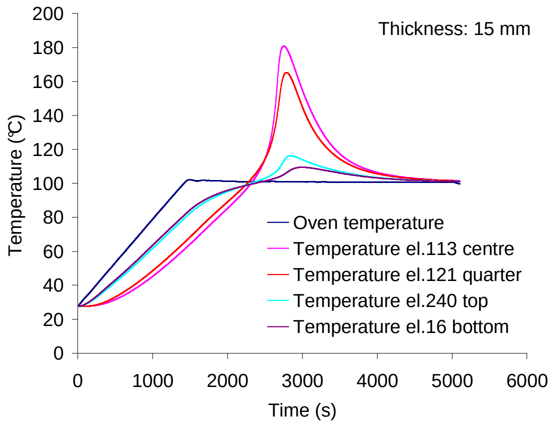

Fig. 12 Thermal gradients predicted within a 15mm thick epoxy matrix during the 3°C/min ramp and 100°C plateau.

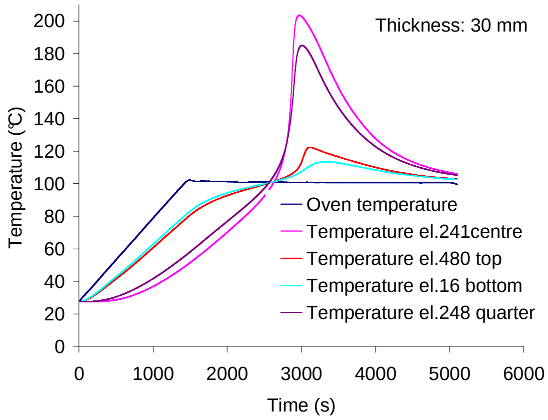

Fig. 13 Thermal gradients predicted within a 30mm thick epoxy matrix during the 3°C/min ramp and 100°C plateau.

4.2.2. DEGREE OF CURE GRADIENTS

The solving of the thermal and chemical coupling model presented in this paper enables, simultaneously to local temperature prediction for each point of the matrix block, prediction for corresponding local degree of cure. Degree of cure description within the volume of the matrix block is strategic information for future mechanical and internal stress estimations as already explained by the authors [1]. Indeed, as degree of cure accounts for matrix formation, gradients of curing will necessarily lead to gradients of matrix state and hence properties gradients within the epoxy block. This is one of the basic mechanisms for internal stress developments. Thermal and curing gradients must therefore be considered for cure optimization strategy.

Thus, thickness effects on degree of cure predictions are presented in Fig. 14 to 16.

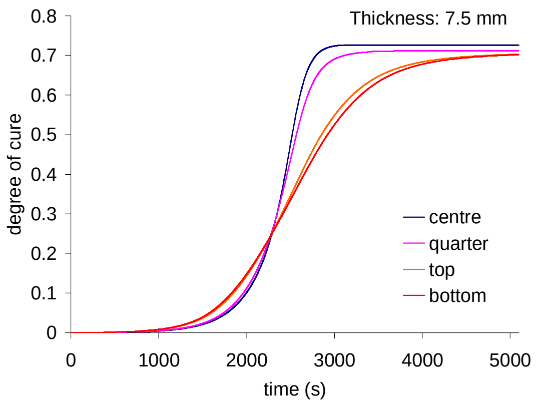

Fig. 14 Degree of cure gradients predicted within a 7.5mm thick epoxy matrix during the 3°C/min ramp and 100°C plateau.

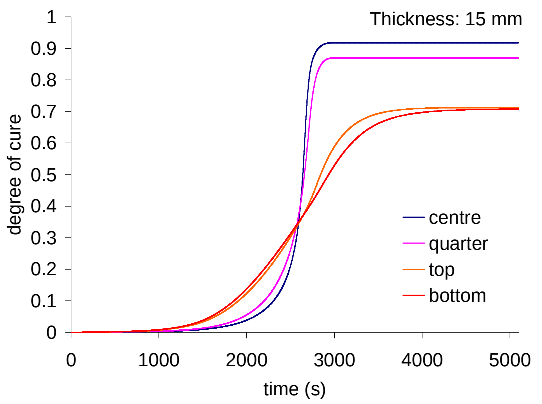

Fig. 15 Degree of cure gradients predicted within a 15mm thick epoxy matrix during the 3°C/min ramp and 100°C plateau.

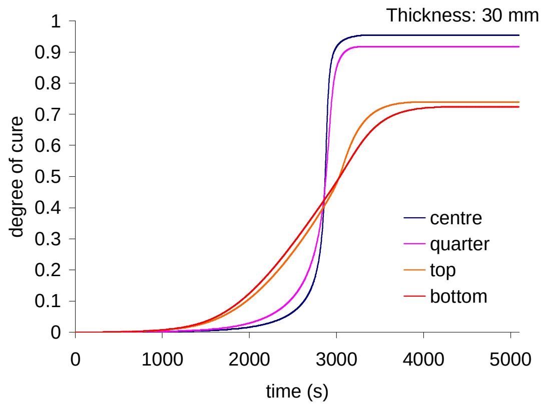

Fig. 16 Degree of cure gradients predicted within a 30mm thick epoxy matrix during the 3°C/min ramp and 100°C plateau.

4.2.3. DISCUSSION

As expected, strong degree of cure gradients are developed during the curing within the matrix with increasing thickness. If the curing could be considered homogeneous for the 7.5 mm thick epoxy matrix, in regard to the final degree of cure reached at the end of the plateau (Fig. 14), strong degree of cure gaps are rapidly developed as the thickness increases. The matrix obtained at the end of the curing cannot be considered as a homogeneous material. The quality of the curing is not satisfactory and this has to be considered for structural applications. On the other hand, even if the degree of cure reached at the end of the plateau tends to be same within the block as shown if Fig. 14, its history during the curing differs significantly. This might lead to possible effects on internal stress development during the curing and this question is worth to be studied by future coupling models including the mechanics of the matrix in formation. Furthermore, comparison between exothermal peaks and degree of cure gradients obtained at the end of the curing plateau highlights the coupling between the thermal and the chemistry. Matrix curing heterogeneity is developed with exothermal peak growth.
Moreover, it appears that for each thickness studied, exothermal peaks are related to the same degree of conversion area around 55%. This is central information since it coincides with the gel point of the LY556 epoxy system.

5. APPLICATION TO CURE OPTIMIZATION STRATEGY

From manufacturers and users point of view about thick composites structures, it is obvious to understand that the question of cure homogeneity improvement appears as a strategic and relevant question. The FEM modeling approach exposed in this paper has demonstrated its applicability for local information prediction such as temperature and degree of conversion for real 3D structural parts. Therefore, with regard to manufacturers and designers, one of the direct applications of the model is to provide information about cure schedule effects on curing quality.
This aspect is presented in this section for the curing of the 30 mm thick epoxy block. In order to highlight exothermal effects on local temperature at the centre of the block, a curing with a 3°C/min ramp followed by a 140°C plateau was first studied. Temperature evolution predicted is shown in Fig. 17 and lead to an exothermal peak of 243°C. For the LY556 epoxy matrix, such a level of internal temperature causes thermal degradation since thermo gravimetric analysis showed that the thermal degradation started around 200°C.
The question to face is therefore how should the cure schedule be modified to avoid thermal degradation on one hand and on the other hand to perform a degree of conversion as high as possible with at the same time gradients of curing as low as possible.

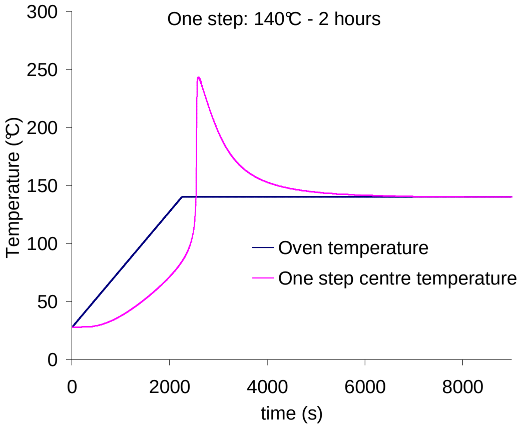

Fig. 17 Centre temperature prediction for the 30 mm thick epoxy block with a direct one step curing (3°C/min ramp and 2 hours 140°C plateau).

The degree of cure gradients analysis has highlighted the relation between the gel point and the exothermal peak. A logical way therefore to minimize exothermal effects is to split the curing into two steps. The first step is especially scheduled to perform the gelation reaction at a low plateau level in order to minimize corresponding exothermal effects. A second step can then be scheduled at a higher plateau level to allow the curing to reach degree of cure as high as possible during the remaining time.
This strategy was applied to the 30 mm thick epoxy block and a two steps cure schedule was chosen: ramps at 3°C/min with a first step at a 80°C plateau for 1 hour followed by a second step at a 140°C plateau for 1 hour.
Convincing results are displayed in Fig. 18 since no exothermal peak was obtained for the two steps curing in comparison with the direct one step curing.
However, the central question is curing quality. This request was examined by the comparison between degrees of cure obtained at the end of the curing as shown in Fig. 19.

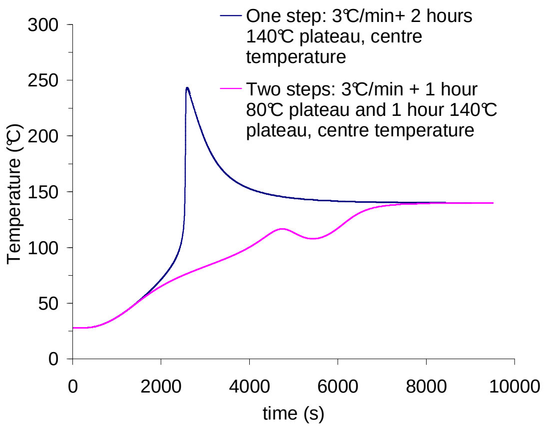

Fig. 18 Cure schedule effect on exothermal peak.

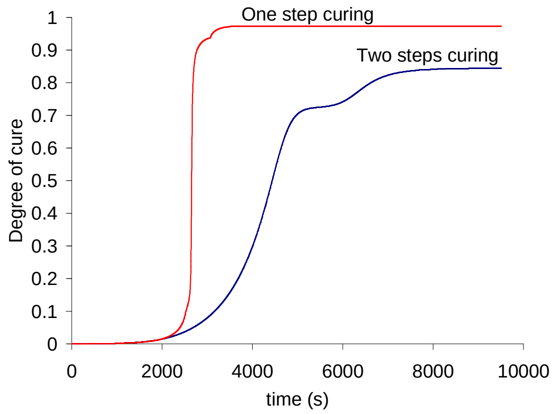

Fig. 19 Cure schedule effect on degree of cure predicted at the centre point of the matrix block.

5.1. DISCUSSION

As expected, degree of cure histories presented in Fig. 19 are completely different between the two curing schedules. The one step curing induces strong degree of cure evolution whereas the two steps curing schedule produces a more soft evolution of the curing. Nevertheless, the final level of curing obtained at the end of the plateau differs only of about 13 % between the two cure schedules. Moreover, the 84 % of degree of cure reached by the two steps curing is quite satisfactory from a mechanical point of view in regard to matrix properties and usual curing levels for epoxies.
On the other hand, the two steps curing appears to be much more homogeneous within the matrix block, in comparison within the direct one step curing as displayed in Fig. 20 and 21. As highlighted in Fig. 21, the curing level of the matrix is quite homogeneous within the block at the end of the plateau. This is a very encouraging result for cure optimization application of the model presented in this paper. However a significant difference in degree of cure history is observed within the matrix and is then vanished during the second curing plateau. As told before degree of cure history effects on internal stress developments is worth to be studied by future coupling models including the mechanics of the matrix in formation.

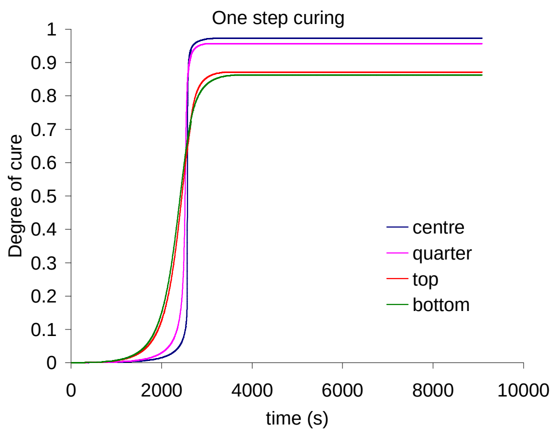

Fig. 20 One step curing degree of cure gradients within the epoxy matrix.

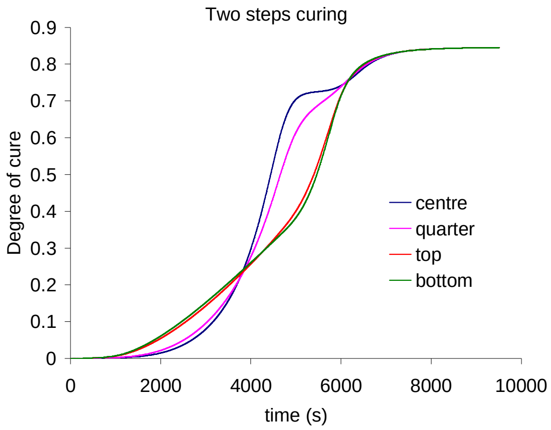

Fig. 21 Two steps curing degree of cure gradients within the epoxy matrix.

6. CONCLUSION

A 3D curing model was presented in this paper by taking into account the couplings between the thermal and the chemistry. FEM tools were used for the solving of the coupling problem. Results obtained demonstrate the applicability and relevancy of this kind of approach for local information about curing quality for real structural parts. Furthermore, the cure simulation model presented enables easily and in a convenient way cure optimization simulations. Of course, it is well known by the manufacturers that the slower the curing is, the better the quality will be. But the know-how becomes more and more difficult for thick structural composite parts. From this point of view, the FEM 3D model presented is surely a powerful way to face possible quality problems of the curing as it provides central information for cure optimization.
The 3D model is currently continued to take into account the coupling with the mechanics of the matrix during its curing. This should lead in a short time to strategic information about internal stress developments.

7. ACKNOWLEDGEMENTS

This work was funded by the Brest Metropole Oceanne council of the city of Brest. The material support of the ENSIETA graduate school of engineering and of the IFREMER Institute in Brittany are gratefully acknowledged.

8. REFERENCES

1 JOCHUM, Ch., GRANDIDIER, J.-C., ”Thick laminates quality for ship design”, Australian Journal of Mechanical Engineering, ISSN: 1448-4846, Volume 4, No 2, pp 151-164., 2007.

2 HSIAO, K.-T., LITTLE, R., RESTREPO, O., MINAIE, B., “A study of direct cure kinetics characterization during liquid composite molding”, Journal of Composites Part A: applied science and manufacturing, Departement of Mechanical Engineering, University of South Alabama, USA, p1-925 , 2005.

3 SUNIL, C. J., LIU, X.L., LAM, Y.C., “A numerical approach to the modelling of polymer curing in fibre-reinforced composites”, Journal of Composites Science and Technology, Department of Mechanical Engineering, Monash University, Clayton Campus, Melbourne, Victoria 3168, 59 : 1003-1013, 1998.

4 JIANHUA, L., SUNIL, C. J., LAM, Y.C., “Curing optimization for pultruded composite sections”, Journal of Composites Science and Technology, School of Mechanical and producting Engineering, Nanyang Technological University Singapour, 62 : 457-467, 2001.

5 BOGGETI, T.A., GILLESPIE, Jr J.W., “Two-dimensional cure simulation of thick thermosetting composites”, J Comp Mater, 25 : 239-73, 1991.

6 KAMAL, M.R., SOUROUR, S., "Differential scanning calorimetry of epoxy cure: isothermal cure kinetics". *Thermochim acta*, Vol. 14, no.1-2, pp.41-59, 1976.

7 HARSCH, M., KARGER-KOCSIS, J., HOLST, M., "Influence of fillers and additives on the cure kinetics of an epoxy/anhydride resin", *European Polymer Journal*, Vol. 43, 1168-1178, 2007.

8 FOURNIER, J., WILLIAMS, G., DUTCH, C., ALDRIDGE, G. A., “Changes in molecular dynamics during bulk polymerization of an epoxide amine system as studied by dielectric relaxation spectroscopy, *Macromolecules*, 29(22): 7097 – 7107, 1996.

9 LOPEZ, J., LOPEZ-BUENO, I., NOGUEIRA, P., RAMIREZ, C., ABAD, M.J., BARRAL, L. CANO, J.,"Effect of poly (styrene-co-acrylonitrile) on an epoxy amine resin", *Polymer Journal*, Vol. 42 1669-1677, 2001.

10 PERRIN, F.X., NGUYEN, H. T. M., VERNET J.L. "Chimico-diffusion kinetics and TTT cure diagrams of DGEBA-DGEBF/amine resins cured with phenol catalyst", *European Polymer Journal*, 2007.

11 VAN MELE, B., VAN ASSCHE, G., VAN HEMELRIJCK, A., "Modulated Differential Scanning Calorimetry to study reacting polymer system", Journal of reinforced plastic and composites, Vol.18, N°10, 1999.

12 VAN MELE, B., VAN ASSCHE, G., VAN HEMELRIJCK ,A., "Modulated Differential Scanning Calorimetry to study reacting polymer system", Journal of reinforced plastic and composites, Vol.18, N°10, 1999.

13 Moon-Kwang Um et al, "A study of cure kinetics by use of dynamic differential scanning calorimetry", Composite science and technology 62: 29-40, 2002.

14 RABEARISON, N., JOCHUM, Ch. , GRANDIDIER, J.C., "A FEM coupling model for properties predictions during the curing of an epoxy matrix", Submitted to *Computational Materials Sciences*, COMMAT-D-07-00602, 2007.

15 BAILLEUL, J.L., GUYONVARCH, G., GARNIER, B., JARNY, Y., DELAUNAY, D., Identifications des propriétés thermiques de composites fibres de verre/résine thermodurcissables: Application à l'optimisation de procédés de moulage. *Rev Gen Therm*. 35, 65-77, 1996.

MARINE PROPULSION SYSTEM DYNAMICS DURING SHIP MANOEUVRES

Michele Viviani, Department of Naval Architecture and Marine Engineering (DINAV), Genoa University, Italy
Marco Altosole, Department of Naval Architecture and Marine Engineering (DINAV), Genoa University, Italy
Marco Cerruti, Fincantieri C.N.I. Spa – Naval Vessel Business Unit - Genoa, Italy
Arcangelo Menna, Italian Navy
Giulio Dubbioso, Italian Navy, PhD Student at DINAV

SUMMARY
Marine propulsion plants can experience large power fluctuations during tight manoeuvres. During these critical situations, dramatic increases of shaft torque are possible, up to and over 100% of the steady values in straight course. In the case of a twin-screw ship turning circle, the two shaft lines dynamics can be completely different in terms of required power and torque. This phenomenon, if not correctly considered, is potentially dangerous, especially for propulsion plants with two shaft lines powered via a unique reduction gear, which can be subject to significant unbalances.
The paper presents a simulation approach able to represent the dynamics of a twin-screw ship propulsion plant in these critical working conditions. The numerical model includes the ship manoeuvrability and the dynamic behaviour of prime movers, shaft lines, propellers and propulsion control system. Numerical results obtained have been compared to full-scale measurements in order to validate the proposed simulation approach.

1. INTRODUCTION
As it is well known, ships during maneuvers can experience large fluctuations of required shaft power from the propulsion plant. This is especially true in case of very tight maneuvers, like turning circle at, or in proximity to, maximum rudder angles, and can result in considerable increase of shaft power, or shaft torque if propeller revolutions are kept constant, up to and over 100% of steady values in a straight course recorded during the approach phase to the maneuver.
Despite the fact that this behavior is qualitatively well known, there is not a wide amount of quantitative data available in literature; however, these effects could be potentially dangerous, if not correctly predicted and cared for, for some particular kinds of propulsion plant, in which for instance two shaft axes are powered by the same prime mover via a unique reduction gear, like in some of the latest naval ships (see example in following Figure 1).

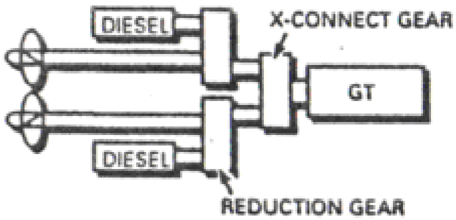

Fig. 1: Propulsion layout with two shaftlines and common reduction gear

In this case, the possibility of significant unbalances of forces on the reduction gear itself and of strongly different power increase for the shaft axes exists; unfortunately, a very low amount of data is available for this kind of propulsion plant, considering also its rather recent introduction and application.
In order to bridge this gap, in a recent work [1] an analysis of data available for the more common propulsion configuration with two completely separated shaftlines and related prime movers (see example in next Figure 2) has been carried out. In particular, standard turning circle maneuvers at different speeds and rudder angles for a series of twin screw naval ships have been analyzed, and a common trend for shaft power increase has been found, as it will be briefly summarized in following paragraph 2.

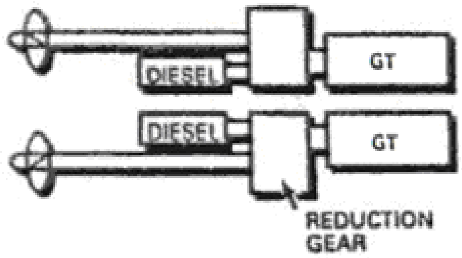

Fig. 2:Typical propulsion layout with separated shaftlines

As a result, a simplified (but very effective from the point of view of propulsion plant simulation) approach has been proposed, in which the asymmetric behaviour of the two shaftlines, which is likely to be due to oblique flow, asymmetrical wake fraction variation and tangential speed variation, is attributed only to an asymmetrical wake fraction variation, which implicitly includes all other effects.
Values of this asymmetric wake fraction variation obtained from the analysis of full scale and model scale tests are summarised in following paragraph 2.
On the basis of the mentioned results, in this work a simulation approach, developed by University of Genoa, is presented. This approach is able to represent the dynamics of a marine propulsion plant of a twin-screw ship in these critical working conditions during manoeuvres. The numerical model includes the ship manoeuvrability and the dynamic behaviour of prime movers, shaft lines, propellers and propulsion control system. In particular, the study deals with the simulation of the two different shaft lines dynamics during Turning

Circle and ZigZag manoeuvres and how the propulsion controller influences the performance of the entire propulsion system.
Numerical results obtained have been compared to full-scale measurements in order to validate the proposed simulation approach.

2. SUMMARY OF PREVIOUS RESULTS

As anticipated in previous paragraph 1, in a recent work [1] an analysis of manoeuvring data for 5 different naval ships, whose non-dimensional data is presented in following Table 1, has been carried out. Most of data was taken from full scale sea trials, while for Ship 5 free runing model tests were available too.

	C_B	L/B	B/T	A_R/LT	F_R Range
Ship 1/1	0.64	6.61	2.92	2.1%	0.08-0.28
Ship 1/2	0.64	6.61	2.92	4.3%	0.08-0.29
Ship 2	0.48	5.29	3.21	1.9%	0.11-0.27
Ship 3	0.50	8.61	3.32	4.1%	0.21-0.42
Ship 4	0.48	6.91	3.46	3.4%	0.22-0.44
Ship 5	0.51	7.89	3.63	4.0%	0.14-0.40

Table 1: Main non-dimensional data of ships analyzed

In particular, following data are represented:
- block coefficient C_B
- length to beam ratio L/B
- beam to draft ratio B/T
- rudder area percentage with respect to lateral area represented by LT
- range of ship speed (in terms of Froude number)
-

Different ship types are included, ranging from rather slow Auxiliary ship and Replenishment and Logistic support ship to fast Frigates and Corvettes. All ships present a twin screw propulsion configuration, with completely separated propulsion plants, however prime movers are various, including Diesel Engines, Electrical Motors and Gas Turbines, or combinations of them; both CPP and FPP configurations are present in the analysis. Finally, two different stern configurations on the same hull for Ship 1 are analyzed, and namely single and twin rudder configuration for Ship 1/1 and Ship 1/2 respectively.
For all ships turning circle maneuvers at different speeds and, when available, different rudder angles, have been considered (for a total of 52 trials), with particular attention to ship speed, propeller RPM and shaft power.
Power increase during maneuvers at different speeds and rudder angles with respect to power required for straight course in the approach phase have been evaluated, considering both peak values in the initial transient phase and stabilized values (which in general result about 10-15% lower than peak ones). Since RPM are kept constant during all maneuvers when no automation intervention is present, torque increase is equal to power increase.
Despite ships analyzed have significant differences from many points of view, a common trend for all trials (in which automation is not acting) was found, with an external shaft power increase of about 85-105% and an internal shaft power increase of about 30-50% in correspondence of the maximum rudder angles; influence of Froude number seems negligible.
For the highest ship speeds considered, automation plays a key role, limiting power increase by means of RPM or propeller pitch reduction for both internal and external shafts to similar values (different from ship to ship depending on different power margins), since at this speed propulsion plant is already utilized near to its full capabilities.
Stabilized power increases obtained for all ships are summarized in following Figures 3 and 4 for internal and external shafts respectively as a function of rudder angle (tests with automation influence have been omitted). In both figures the mean line is drawn, together with two additional lines shifted up and down by 10%; as it can be seen, despite presenting a certain scatter, a clear tendency results in all cases.

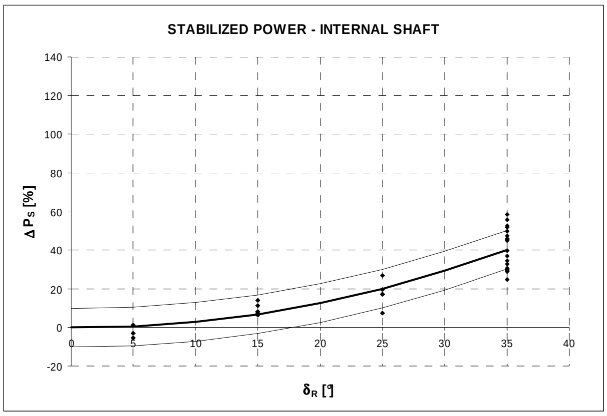

Fig. 3: Stabilized power - Summary – Internal shaft

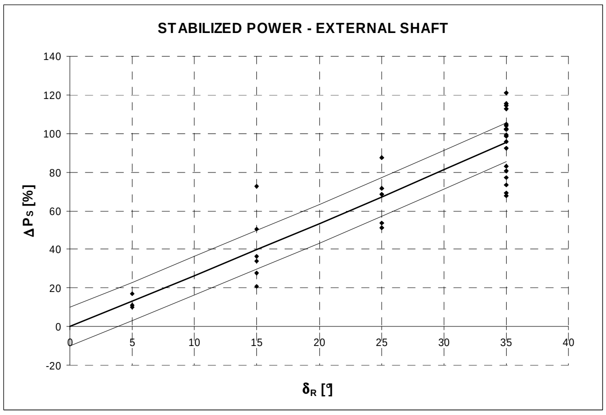

Fig. 4: Stabilized power - Summary – External shaft

Possible reasons investigated in [1] for the shaft power increase, apart from the obvious speed reduction during the maneuver, are oblique flow and asymmetrical variations of longitudinal and tangential speed at the propeller plane; the effect of the first phenomenon is widely covered in literature (see for example [2][3]), while from the analysis of extensive experimental tests at PMM on different hull shapes reported in [4] and [5] both longitudinal and tangential speed variations during manoeuvres were found.

In view of the development of a simulator including ship maneuvering and automation plant, asymmetrical wake fraction variation has been considered the most straightforward and easy to be evaluated from usual data recorded during sea trials.

A procedure similar to the analysis of a self-propulsion test has been adopted, evaluating new values of the propeller advance coefficient J during manoeuvre in correspondence of recorded values of torque (and consequently K_Q), and then calculating the “asymmetrical wake fraction variation”.

In particular, variation of J is partially due to reduction of ship speed during manoeuvre, which results in higher torque coefficient K_Q (point J1 in figure 5), then the following effective functioning points J_{ext} and J_{int} are reached by means of the asymmetrical variation of wake fraction.

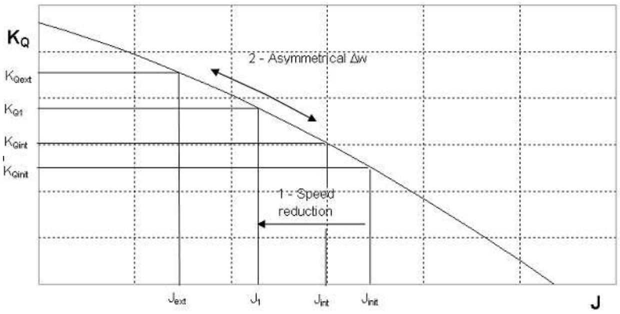

Fig. 5: Asymmetrical variation of advance coefficient J

The following steps are adopted for the analysis of manoeuvring data:

1. Evaluation of equivalent open water torque on internal and external shafts on the basis of recorded power and propeller revolutions, in accordance to (1)

$$Q_O = \frac{P\eta_r}{2\pi N} \quad (1)$$

$$\eta_r = \frac{Q_O}{Q} \quad (2)$$

where Q_O is the open water torque, Q and P are the delivered torque and power and N are propeller revolutions and η_R is the relative rotative efficiency, defined in (2) (adopting value from self-propulsion test),

2. Evaluation of correspondent torque coefficient K_Q for both shafts on the basis of (3)

$$K_Q = \frac{Q_O}{\rho N^2 D^5} \quad (3)$$

3. Evaluation of advance coefficient J value needed in order to obtain K_Q, interpolating from propeller characteristic curves

$$J = V_a / ND \quad (4)$$

$$V_a = (1-w)V_s \quad (5)$$

where Va is the propeller advance velocity, D is propeller diameter, w is the wake fraction and V_s is the ship speed.

4. Evaluation of correspondent advance velocity:

$$V_a = JND \quad (5)$$

5. Finally, “effective value” of wake fraction can be computed:

$$(1-w) = V_a / V_{s(evol)} \quad (6)$$

where $V_{S(evol)}$ is stabilized ship speed during turning circle maneuver

In the following Table 2 values of wake fraction variation Δw, defined in (7) are reported in correspondence to maximum rudder angle and for different ranges of Froude Number (where low stands for a value lower than 0.15 and high for a value higher than 0.3).

$$\Delta w = w_{evol} - w \quad (7)$$

	F_r	Δw_{int}	Δw_{est}
Ship 1/2	Mean	-0.56	-0.02
Ship 2	Mean	-0.38	0.24
	Low	-0.34	0.14
Ship 3	Mean	-0.10	0.29
Ship 4	High	-0.15	0.16
Ship 5	Mean	-0.17	0.25

Table 2: Values of wake fraction variation

In most of cases, a similar trend has been found on the basis of this analysis, i.e. flow on the internal shaft appears accelerated (with a reduction of wake fraction value), while flow on the external shaft appears to be decelerated (with an increase of wake fraction value).

However, these data present a significant scatter (see for instance negative value for Ship 1 external shaft), due to the fact that they “incorporate” also other effects whose entity varies from ship to ship; in particular, it is likely that influence of variation of tangential speed has a strong influence on this scatter.

A complete insight of the problem could be obtained only by means of numerical simulations (still very difficult and computationally demanding for such a complex phenomenon with interactions between hull, rudders and propellers) or by means of an extensive experimental campaign with the aim of analysing flow in correspondence to propeller location during manoeuvres.

Both these approaches would be very expensive since, in order to have a clear understanding of the problem, analysis of different ships and hullforms should be carried out, thus further multiplying the effort needed.

From this point of view, it is believed that the values of wake fraction variations for different ships which have been computed, despite being affected by errors arising from experimental nature of data analysed and by implicit inclusion of different effects (such as tangential speed), can be already readily applied to similar ships during design phases if required.

In case significantly different ships are considered, free running model tests appear to be probably the least expensive alternative to complicated numerical calculation or experimental campaigns with PMM, providing scale effects are properly considered.

With this aim, a dedicated series of free running model tests has been performed by INSEAN at its facility at Lake Nemi on Ship model n°5 (model scale 1:25) [1], and the results of the comparison with full scale data are reported in following Figures 6 and 7; it has to be noted that, in order to be able to compare results at high speed (in which propeller revolutions are reduced in full scale during maneuvers), P/N^3 variations are reported in figures instead of power variations.

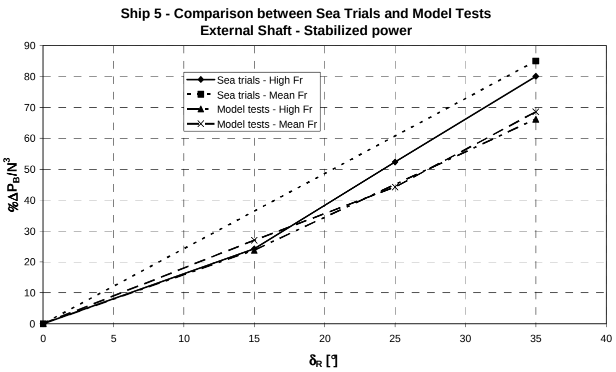

Fig. 6: Ship 5 – Comparison between Sea Trials and Model Tests results – External Shaft

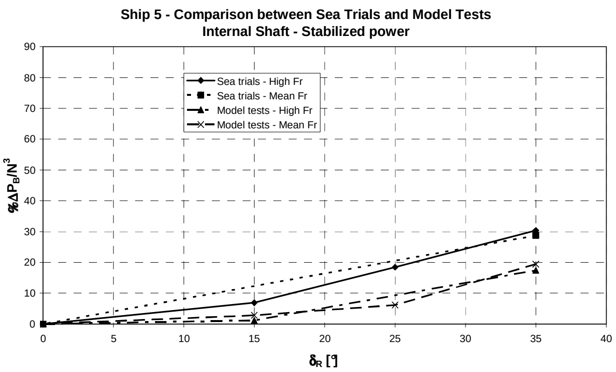

Fig. 7: Ship 5 – Comparison between Sea Trials and Model Tests results – Internal Shaft

From the analysis of Figures 6 and 7, it is clear that, as a general trend, free running model tests tend to underestimate power increases, with values lower of about 10-15% in correspondence to maximum rudder angle for both external and internal shafts.

These results do not allow to draw a general conclusion, since a higher number of data would be needed to verify the tendencies and investigate possible physical reasons. Nevertheless, it is believed that this tendencies can be already applied in case simulations are needed in order to test different automation system strategies; it has to be noted moreover that, if asymmetrical wake fraction variation calculation is performed and the scale factor for torque increase is considered, mean values of -0.17 and 0.26 for internal and external shaft respectively are obtained, thus remarkably in line with data obtained from sea trials.

As a general result of the previous study, it was therefore remarked that asymmetrical power variations during manoeuvres can be very significant and, for unconventional propulsion plant arrangements which differ from the usual ones, they represent a potential risk, with the need for a dedicated strategy of the automation plant. It is believed, in particular, that these effects can be considered by means of series of simulations, testing during design phases different automation strategies and allowing to reduce considerably risks connected to asymmetrical power increase and time needed for calibration of the automation plant itself during sea trials.

In the present study, the modification of the maneuvering and propulsion plant simulation software already available at DINAV (see for example [6][7][8][9]) in order to consider asymmetrical behaviour during manoeuvres is described (see paragraph 2); in order to test the modified simulator, a ship different from those already analysed in previous studies for which experimental results were available (see paragraph 3) has been schematised, and results obtained have been compared with experimental data (see paragraph 4).

2. SIMULATOR DESCRIPTION

The ship behaviour is simulated by means of a mathematical model that is able to predict the interactions between the propulsion system dynamics and the ship manoeuvrability.

This mathematical model consists of a set of differential equations, algebraic equations and tables that represent the various elements of the propulsion system: the automation, the engines, the propellers, the shaft lines and the ship motions (surge, sway and yaw).

In particular, the modelled propulsion plant consists of a twin shaft arrangement with controllable pitch propellers, where each shaft is driven, through a gearbox, by two prime movers.

The schematic of the modelled ship dynamics is shown in Figure 8, where it is possible to see the several main components involved in the simulation process.

The implementation of the numerical code has been made in MATLAB-SIMULINK® software environment, a wide used platform for the dynamic systems simulation.

For each element illustrated in Figure 8, numerical models with different level of accuracy have been developed, taking into account the general objective of a good balance between the reliability of the simulation results and the code performance.

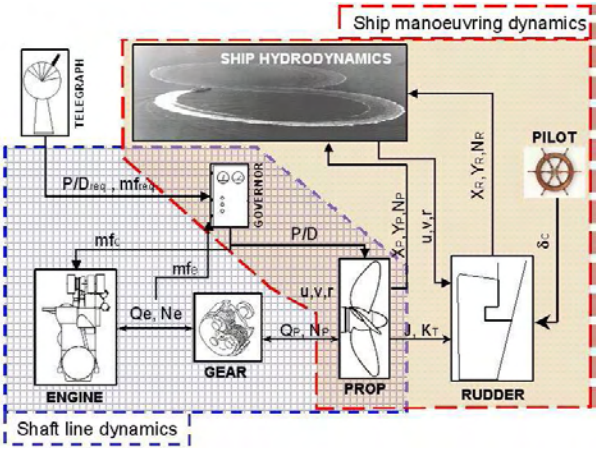

Fig. 8: Simulator functional scheme

Propulsion plant and ship dynamics are mainly represented by differential shaft line equation:

$$2\pi J_p \frac{dn(t)}{dt} = Q_e(t) - Q_p(t) \tag{8}$$

J_p= polar moment of inertia;

Q_e= engine torque;

Q_p= propeller torque;

n =shaft speed;

and by traditional maneuverability equations:

$$\text{Surge: } \sum F_x = m_x(\dot{u} - vr) \tag{9}$$
$$\text{Sway: } \sum F_y = m_y(\dot{v} + ur)$$
$$\text{Yaw: } \sum M_z = I_{zz}\dot{r}$$

u = ship speed in surge direction;

v = ship mass in sway direction;

r =ship rotation speed ;

m_x= ship mass in surge direction ;

m_y= ship mass in sway direction ;

I_{zz} = ship inertia moment about z-axis;

F_x =forces acting on the ship in x-axis direction;

F_y = forces acting on the ship in y-axis direction;

M_z = moments acting on the ship about z-axis;

Other main differential equations are included in the automation model, in order to represent the fuel flow regulation of the engines.
Detailed information about the entire structure of the ship simulation model can be found in [6], [7], [8], [9]. In the present paper, the modification of the model in order to consider separated shaftlines is described.

Shaftline dynamics, as anticipated, are governed by equation (8). From this equation, in particular, it is possible to calculate the propeller speed n, where the engine torque Q_e is evaluated by means of a mathematical model based on the thermodynamic process of the engine, while the propeller torque Q_p is evaluated by means of the open water propeller tests for several blade positions.
Once calculated *n(t)* from shaft line dynamics equation and *V(t)* from maneuverability equations, it is possible to obtain the propeller advance coefficient *J(t)* using the matrix values of the wake fraction *w(t)*.

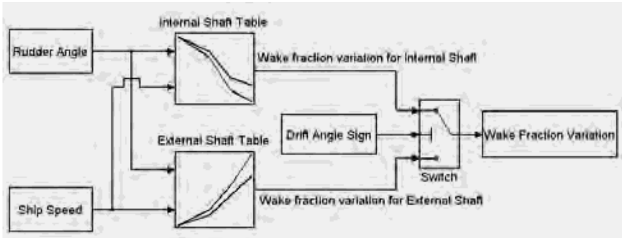

Fig. 9 – Calculation of wake fraction variation

In Figure 9 the calculation process of the wake fraction variation, adopted in the simulation model of each propeller, is shown. The two tables, representing the values of Δw for each shaft, perform 2-D linear interpolation of the two inputs, the ship speed and the rudder angle. At each time instant it is then possible to calculate the proper wake factor variation on the base of the drift angle sign. In fact the “switch” block passes the first input or the third input on the base of the second input, meaning a starboard or port side turning circle of the ship.
As presented in previous paragraph, Δw values are computed from stabilized parts of the manoeuvre. If the scheme indicated in Figure 9 were directly adopted without additional considerations, sudden variations of Δw would occur once a certain rudder angle is given, thus generating erroneous power peaks during transients; this would be particularly significant for manoeuvres in which large parts are in transient mode (e.g. ZigZag). In order to overcome this problem, the effective Δw value adopted instantaneously is evaluated in accordance to following equation:

$$\Delta w(t) = \Delta w_i(t)\,\frac{\beta(t)}{\beta_{evol}} \tag{10}$$

where Δw_i is the value obtained by interpolation, β is the current value of drift angle and β_{evol} is the drift angle value during the stabilized turning circle at the considered speed and rudder angle.
By using this calculation routine, the simulator is able to realize which is the external or the internal shaft during the ship turning circle and then to calculate the proper wake fraction in order to evaluate the propeller advance

coefficient J(t). Once J(t) is known, it is possible to evaluate $K_Q(t)$ and $K_T(t)$, respectively for propeller torque and thrust calculation.

3. TEST CASE

3.1 SHIP CHARACTERISTICS

As already anticipated, in order to test the modified simulator described in the previous paragraph 2, a sixth ship, different from those already analysed in [1] and listed in table 1, has been considered.
Main characteristics of this ship are summarised in the following:

C_B	0.585
L/B	7.32
B/T	4.35
A_R/LT	3.7%
F_R	0.17÷0.31

This ship is equipped with a propulsion plant with completely separated shaftlines and two prime movers per shaft (similar to the one schematized in Figure 2).

3.2 SEA TRIAL DATA ANALYSIS

Turning circle and ZigZag manoeuvres with different rudder angle and different ship speed performed during sea trials have been made available for the present analysis, as reported in next Table 3:
.

TURNING CIRCLE		
δ	SPEED	
±35	Fn=0.17	Fn=0.31
±25		
±15		
ZIG ZAG		
20-20	Fn=0.17	Fn=0.31

Table 3 – Experimental tests

As a first step, as already performed in [1], Turning circle manoeuvres (for which maximum power fluctuations are experienced) have been considered, in order to obtain values for the simulator. Main physical parameters investigated are ship speed, shaft rpm and shaft power.
ZigZag manoeuvres are not considered initially, since they are utilized in order to validate the simulator behaviour in correspondence to manoeuvres different to those used for the simulator itself calibration.

In the following Table 4, results in terms of shaft power increment during turning circle tests are summarized in percentage notation in relation to the values before the rudder execute point.
For a better understanding, these results are visualized in the following figures 10 and 11.

δ	0.17		0.31	
	ΔP% EXT	ΔP% INT	ΔP% EST	ΔP% INT
35	80	15	54	40
-35	72	38	53	51
av	**76**	**26**	**53**	**46**
25	64	13	46	24
-25	69	24	52	29
av	**66**	**18**	**49**	**26**
15	35	9	42	13
-15	29	10	48	23
av	**32**	**9**	**45**	**18**

Table 4 – Experimental Power Increments

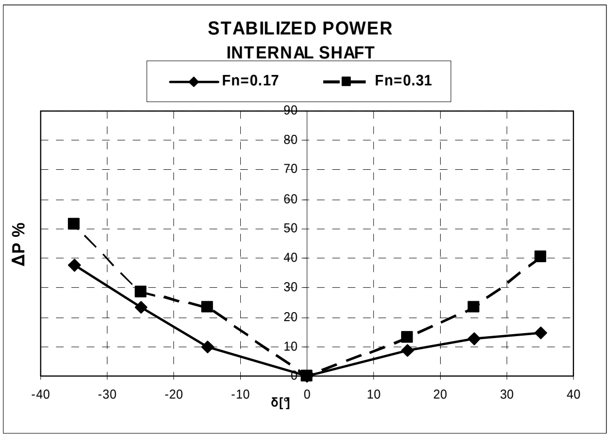

Fig. 10: Ship 6 – Stabilized Power – Internal shaft

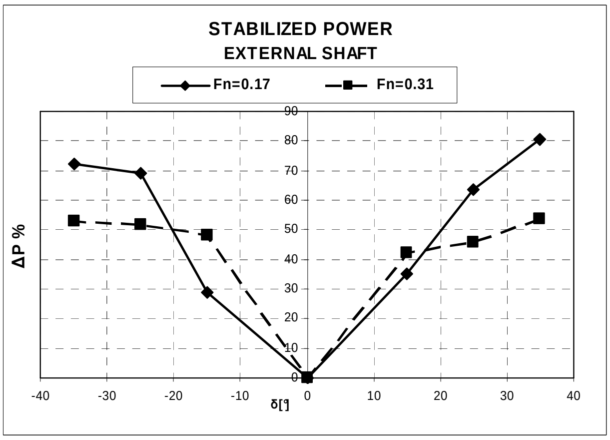

Fig. 11: Ship 6 – Stabilized Power – External shaft

Also in this case, as already found in previous work, an almost symmetrical behaviour for port and starboard maneuvers has been experienced (considering unavoidable external disturbances during sea trials).
In particular, external shaft power increase is higher (with maximum values of about 80% in correspondence to F_R=0.17) than internal shaft power increase (which is about 35-45% for all cases, except a spurious lower increase for one of the two manoeuvres in correspondence to the lower speed analysed). In the case

of external shaft at higher speed, power increase is lower because of limitations introduced by automation, since maximum allowed power of the plant is reached; in particular, automation acts by means of a reduction of the propeller blade pitch.
Power increase values computed for the present ship (for manoeuvres where automation is not acting) are compared with previous ones and reported in following Figures 12 and 13, which are the same of previous Figures 1 and 2 with the addition of these new data.

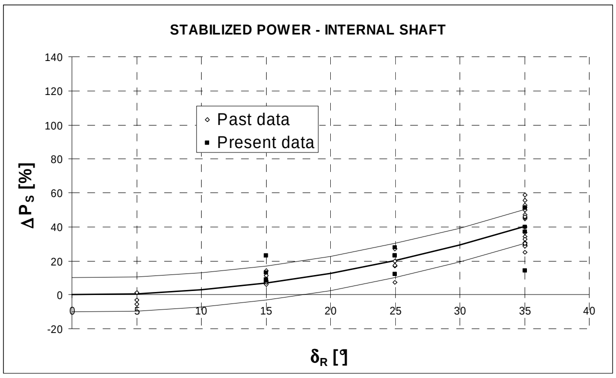

Fig. 12: Stabilized power – Internal shaft
Comparison between present ship and previous results

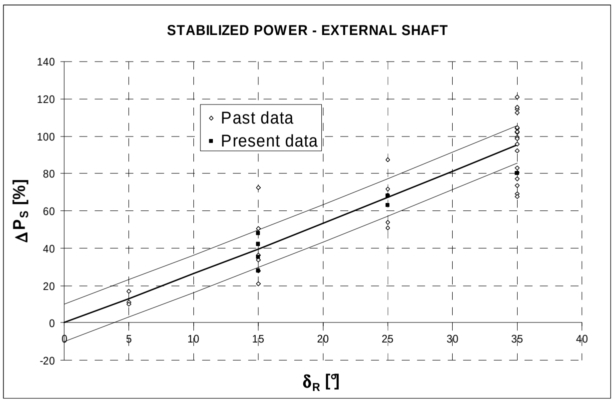

Fig. 13: Stabilized power – External shaft
Comparison between present ship and previous results

As it can be seen, present ship results are generally within the mean ranges already found in [1], especially for the intermediate rudder angles considered, while for the highest rudder angle (35°), power increases experienced in this case are lower.
As a second step, experimental test results have been utilized to calculate the values of Δw for internal and external shaft, using the procedure described in the previous paragraphs.
In particular, in order to consider that power recorded for the two shaftlines is not perfectly symmetrical (both in the approach phase with a rectilinear path and during the manouever), Δw values have been calculated considering mean power, speed and RPM in the rectilinear phase and during port and starboard manoeuvres.
In following Table 5 and Figures 14 and 15, different values of Δw in correspondence to different values of rudder angle and ship speed, evaluated adopting this strategy, are reported:

δ[°]	F_R=0.17		F_R=0.31	
	Δw_{int}	Δw_{est}	Δw_{int}	Δw_{est}
35	-0.254	0.189	-0.34	0.13
25	-0.213	0.105	-0.28	0.08
15	-0.076	0.042	-0.107	0.027
0	0	0	0	0

Tab. 5: Values of wake fraction variation – Ship 6

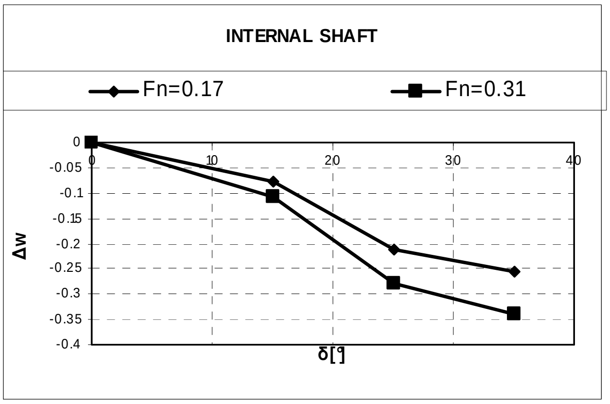

Fig. 14: Values of wake fraction variation – Ship 6
Internal shaft

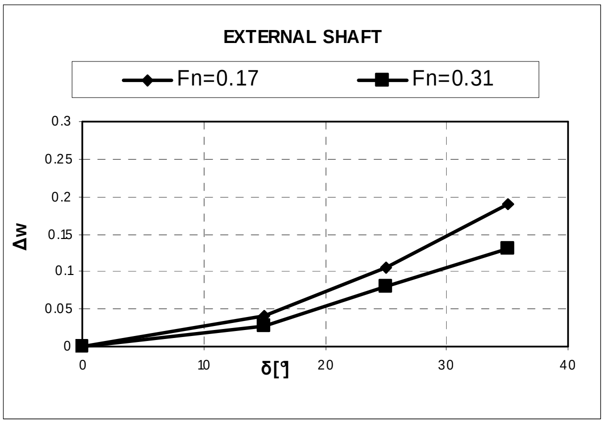

Fig. 15: Values of wake fraction variation – Ship 6
External shaft

Also in this case, values computed for sixth ship fall in the range already found in [1]. Unfortunately, as already pointed out, it has not been possible up to now to find a common law for all ships, and values of wake fraction variation present a significant scatter from ship to ship, thus obliging to analyse experimental data in order to construct a simulator which behaves correctly.
This fact points out the difficulty to predict this particular behaviour of twin screw propellers ship during manouever, and the need to better understand the complex and variable flow pattern near the two propellers and its relation to stern shape. In particular, main reasons for this scatter are the different drift angles each ship reaches during the manouever and the possible effect of

different tangential speed variation. Both these phenomena are implicitly included in the Δw values, thus generating a certain scatter.
It has to be pointed out, however, that main purpose of this work is to test if the modified simulator is able to reproduce the behaviour recorded during experimental manoeuvres for a determined ship; as already considered [1], in fact, if a ship considerably different has to be simulated, data from free running model tests can be utilised, if proper scale factors are adopted.

4. SIMULATION RESULTS

In following paragraph 4.1, results obtained inserting values reported previously in the modified simulator and reproducing turning circle and zigzag manoeuvres are reported. These results are compared with experimental ones for validation of the model.
In paragraph 4.2, the simulator itself is used in order to analyse a wider range of manoeuvres to investigate the possible propulsion plant behaviour.

4.1 COMPARISON OF SIMULATION RESULTS AND EXPERIMENTAL DATA

In following Figures 16-19, the internal and external shaft stabilized power increments recorded during simulated turning circle manouevers at Fn=0.17 and at Fn=0.31 are compared with sea trial results. In particular, for experimental data port and starboard manoeuvres results are reported together with the mean values, while for the simulator a single curve is reported due to its implicit symmetry.
It can be seen that the simulator allows to reproduce fairly well the qualitative behaviour recorded during sea trials.
Considering in particular the manoeuvres at the higher speed, regarding the internal shaft a slight overestimation in correspondence to the lower angles and a slight underestimation in correspondence to the higher angles are recorded, while external shaft power is underestimated in the whole range.

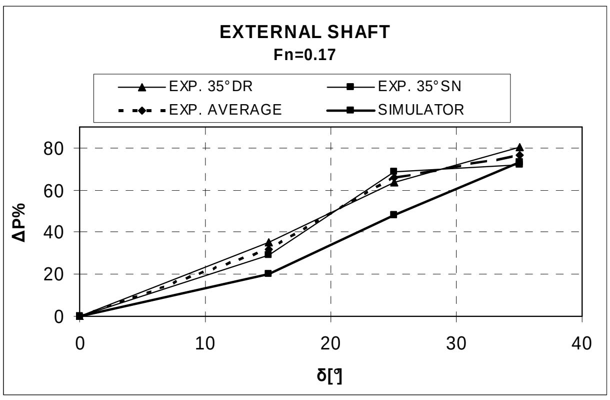

Fig. 16: Simulation results vs experimental data Turning circle – Stab. power – External shaft – F_R=0.17

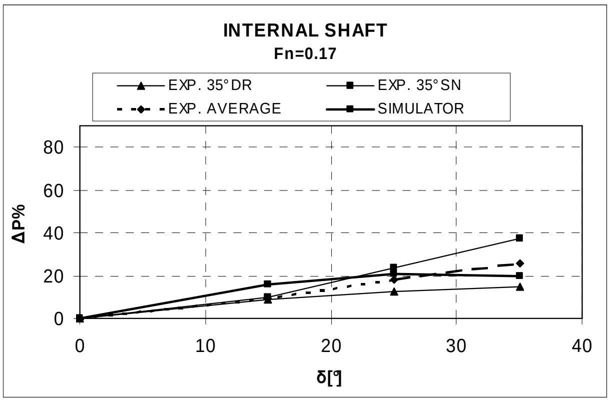

Fig. 17: Simulation results vs experimental data Turning circle – Stab. power – Internal shaft – F_R=0.17

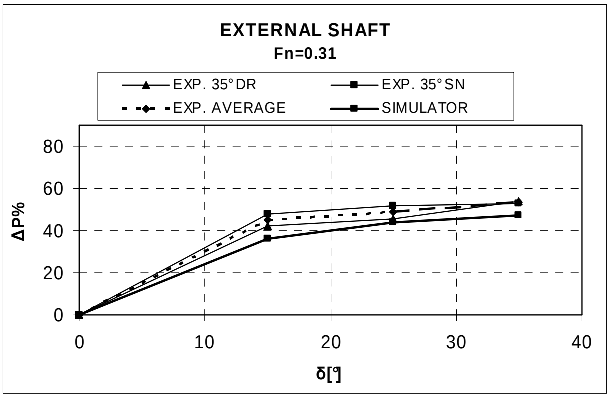

Fig. 18: Simulation results vs experimental data Turning circle – Stab. power – External shaft – F_R=0.31

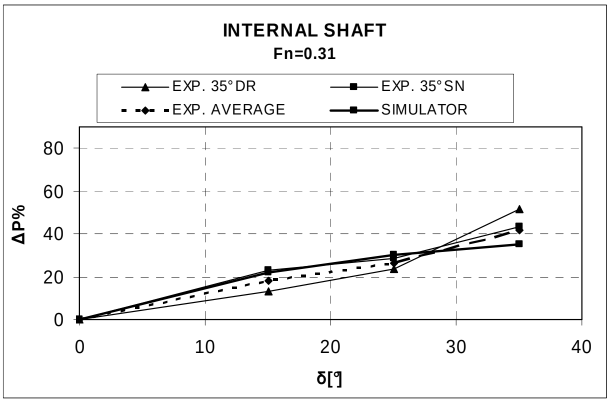

Fig. 19: Simulation results vs experimental data Turning circle – Stab. power – Internal shaft – FR=0.31

It has to be noticed, however, that differences are very low (being less than 10%) and the most important phenomena are captured, with an almost linear power increase for the internal shaft and the automation effect clearly visible for the external shaft.
Considering the manoeuvres at lower speed, the qualitative behaviour is again reproduced, even if for the

external shaft power in correspondence to lower angles a higher error (about 15%) is experienced.

In order to have a better insight in the simulator behaviour, the complete time histories of the most important parameters have been analysed; as an example, in following Figures 20-22 external and internal power and ship speed are reported for the turning circle manoeuvre in correspondence to the lower ship speed and the higher rudder angle.

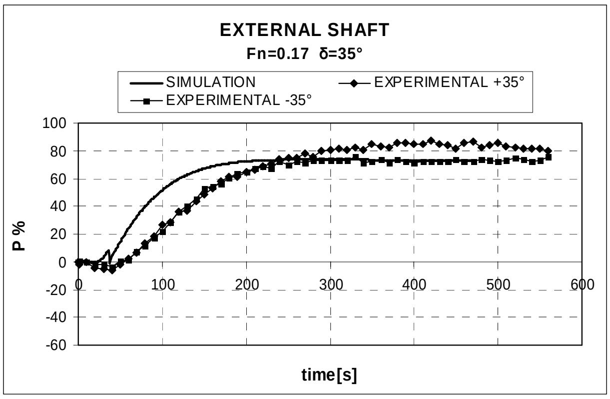

Fig. 20: Simulation results vs experimental data Turning circle – Power – External shaft – F_R=0.17 - δ=35°

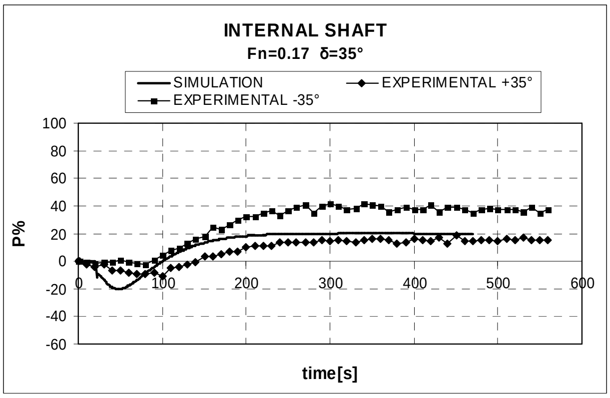

Fig. 21: Simulation results vs experimental data Turning circle – Power – Internal shaft – F_R=0.17 - δ=35°

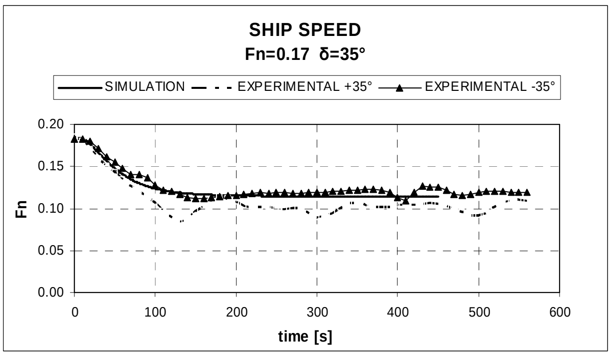

Fig. 22: Simulation results vs experimental data Turning circle – Ship speed – F_R=0.17 - δ=35°

It can be seen that time histories are again well reproduced, both for power increments and ship speed.

In following Figures 23 and 24, increments of P/N^3 values instead of absolute power values are reported, in order to consider the possible different behaviour in terms of propeller revolution during different manoeuvres and simulations.

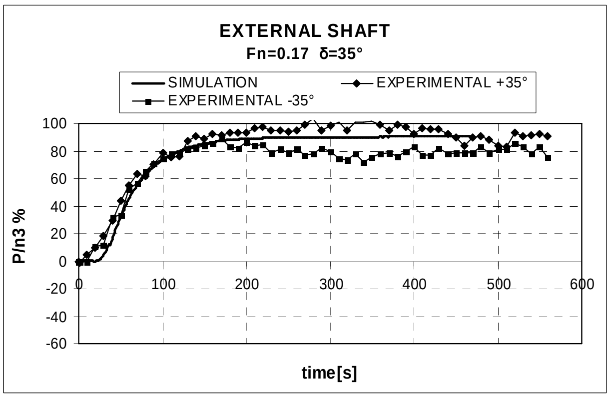

Fig. 23: Simulation results vs experimental data Turning circle – P/N^3 – External shaft – F_R=0.17 - δ=35°

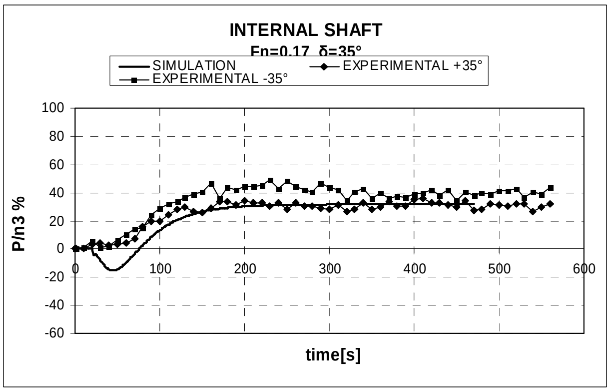

Fig. 24: Simulation results vs experimental data Turning circle – P/N^3 – Internal shaft – F_R=0.17 - δ=35°

It can be seen that the adoption of this alternative representation allows to collapse data for the internal shaft, showing again a very good agreement between simulated and experimental results. Moreover, this representation allows also to improve the results in terms of timing of the power increase for the external shaft.

The unique problem remaining is linked to the initial power reduction for the internal shaft (limited anyway to about 15%), which is probably linked to a too fast introduction of the Δw value. From this point of view, therefore, the assumption of linearity between Δw and β should be further considered, while it seems correct for the external shaft.

Similar results have been obtained for other turning circle manoeuvres, even if they are not represented in the present paper for the sake of simplicity.

A final comparison has been made considering also the overall trajectories obtained using the simulator; in particular, in the following Figure 25 simulated and experimental turning circle trajectories in correspondence of the higher rudder angle and the lower ship speed are reported.

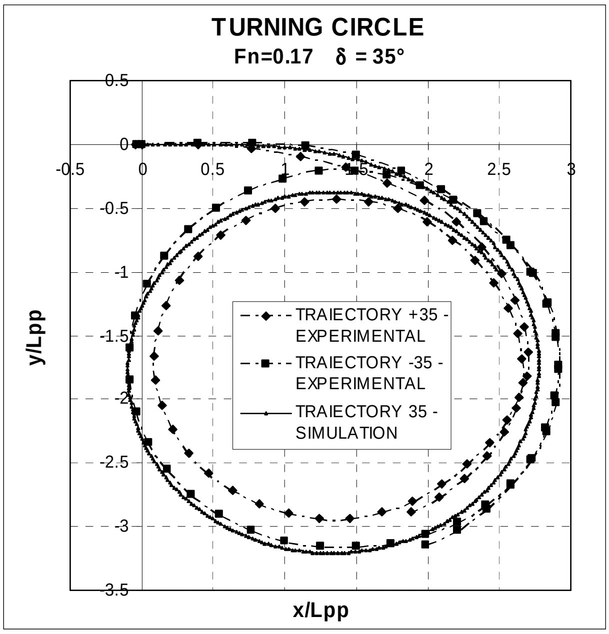

Fig. 25: Simulation results vs experimental data
Trajectory – F_R=0.17 - δ=35°

Also from this point of view, a good correspondence between simulations and experiments has been obtained.
In order to analyse the simulator behaviour in correspondence to manoeuvres different from the ones utilised for calibration, two ZigZag manoeuvres have been considered. In particular, 20°/20° ZigZag manoeuvres have been simulated in correspondence to the two speeds analysed.
In following Figures 26-27 and 28-29, P/N^3 and ship speed time histories are reported for the higher and lower ship speed respectively. As an example, moreover, typical ship heading versus rudder angle time history is also reported in following Figure 30 for the lower ship speed. It can be seen that also in correspondence to the zigzag manoeuvre a rather good correspondence has been found, stressing the simulator capability of capturing also manoeuvres different from the ones used for the calibration.

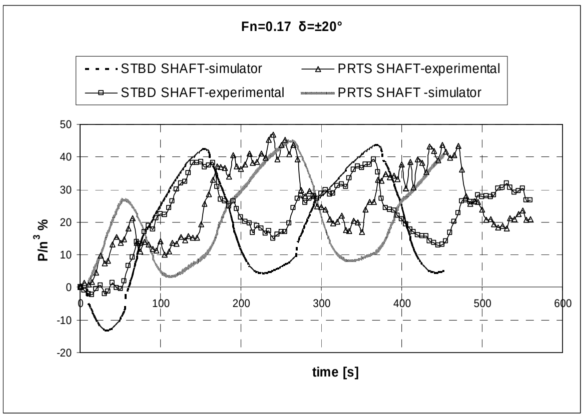

Fig. 26: Simulation results vs experimental data
P/N^3 - ZigZag 20°/20° - F_R=0.17

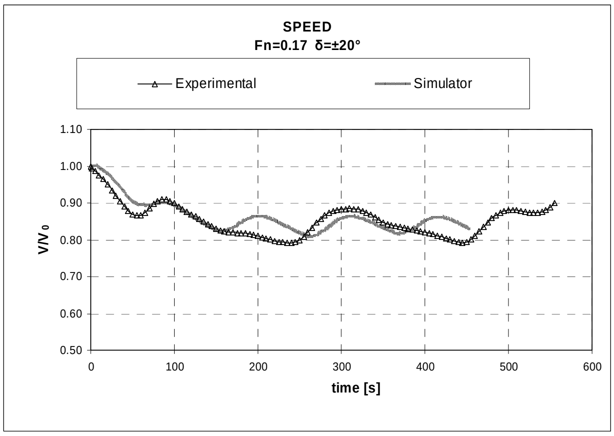

Fig. 27: Simulation results vs experimental data
Ship speed - ZigZag 20°/20° - F_R=0.17

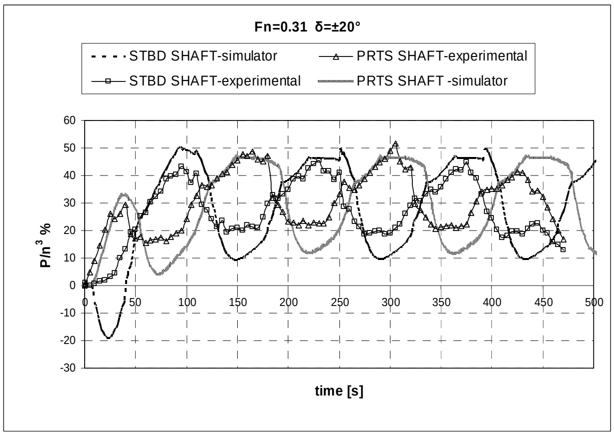

Fig. 28: Simulation results vs experimental data
P/N^3 - ZigZag 20°/20° - F_R=0.31

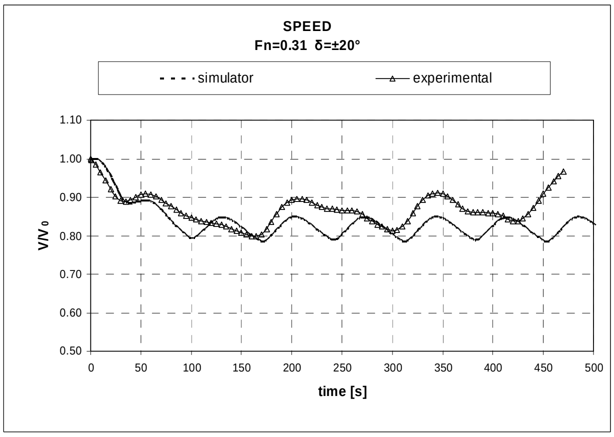

Fig. 29: Simulation results vs experimental data
Ship speed - ZigZag 20°/20° - F_R=0.31

Once again, the problem of initial internal shaft power reduction is experienced, while the $\Delta w - \beta$ linearity assumption seems to allow a good capturing of shaft power time history in the remaining part of the manoeuvre, stressing the capability of the simulator of reproducing manoeuvres with large transients like the ZigZag manoeuvres. In particular, peak increment values are very well captured for both manoeuvres, while slightly larger hollows are predicted.

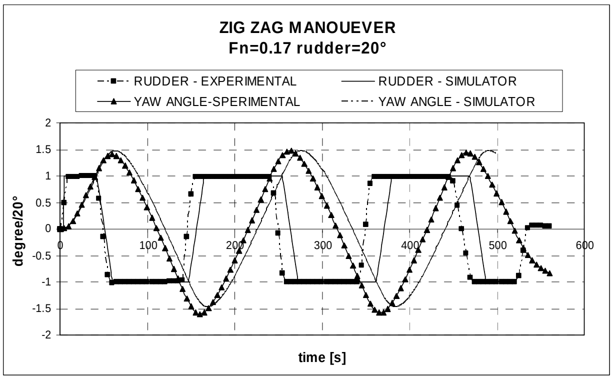

Fig. 30: Simulation results vs experimental data
Ship heading and rudder angle - ZigZag 20°/20° - F_R=0.17

Regarding manoeuvring parameters, ship speed reduction is well captured as an average, even if a certain difference seems to exist, with correct speed oscillations at twice the rudder frequency for the simulator and lower speed oscillations for the experiments; this difference is probably due to the full scale automation plant behaviour. Overshoot angles are also well captured, and a slight period overestimation (about 5%) is experienced.

4.2 PROPULSION PLANT BEHAVIOUR ANALYSIS

After validating the mathematical model adopted in the simulator, a series of different manoeuvres have been performed in order to analyse the propulsion plant behaviour in correspondence to different conditions. In particular, turning circle manoeuvres in correspondence to maximum rudder angle at different speeds have been simulated, since this is the condition for which the maximum shaft power increases are experienced.
In following Figures 31 and 32, results in terms of power and torque increases at different speeds are reported.
In particular, two different curves are represented; the one with continuous line is referred to a possible functioning with one prime mover per shaft up to F_R=0.25 and two prime movers for higher speeds (indicated as Mode 1), while the dotted line is referred to a functioning with both prime movers at all speeds (indicated as Mode 2).

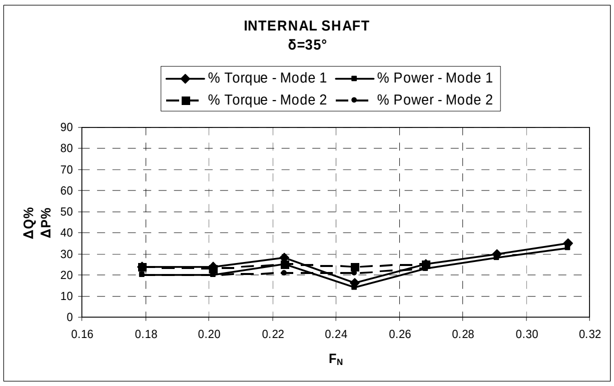

Fig. 31: Stab. Power/Torque increases at different speeds
Turning circle at maximum rudder angle – Internal shaft

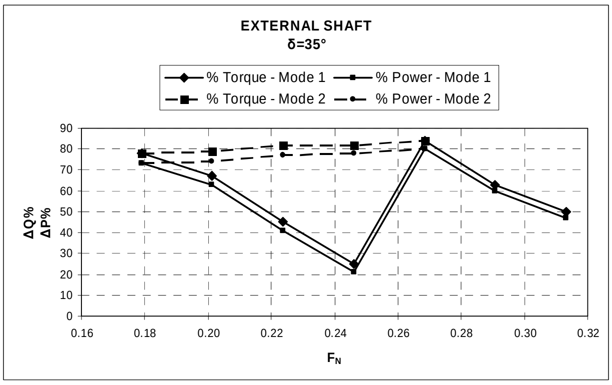

Fig. 32: Stab. Power/Torque increases at different speeds
Turning circle at maximum rudder angle – External shaft

In the first case, automation acts in correspondence to two speed ranges, i.e. the intermediate ones for which one prime mover allowed power is saturated and the maximum ones for which two prime movers allowed power is saturated; in the second case, obviously, automation acts only in correspondence to highest speeds. In both cases, therefore, the two separated shaftlines are controlled by automation, which limits power increase when prime movers allowed power is saturated, while when prime movers are not saturated the power increases at different speeds are almost constant (about 75-80% for the external one and 20-35% for the internal one).
In the following paragraph, some considerations about possible different behaviour in correspondence to different propulsion plant configurations are reported.

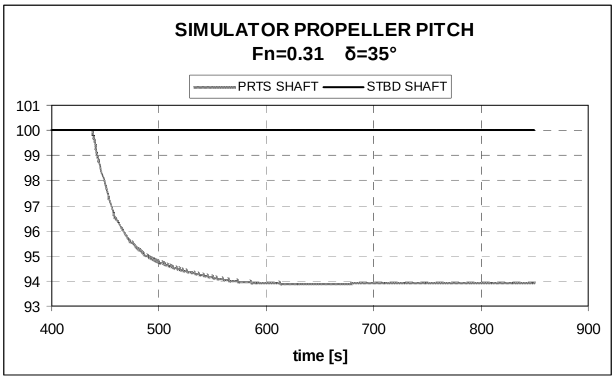

Fig. 33: Example of propeller blade angle reduction
Turning circle – F_R=0.31 - δ_R=35°

It has to be mentioned that automation acts by means of a reduction of propeller blade angle (see example in following Figure 33), which is the same behaviour recorded during sea trials.

4.3 FURTHER CONSIDERATIONS

As presented in previous paragraph 4.1, a mathematical model which allows to consider with a satisfactory approximation the real behaviour of a ship propulsion plant including automation system has been developed and tested successfully against different experimental data.

Moreover, different possible manoeuvres have been simulated for the same ship in order to analyse her behaviour, and the results confirm that the automation plant is able to limit power increases in different propulsive configurations (i.e. one prime mover per shaft or two prime movers per shaft) in correspondence to a propulsion system with completely separated shaftlines.
It is believed that such a model could be of great help in order to simulate the behaviour of the proulsion system in correspondence to a different configuration with shaftlines coupled to their prime movers by means of a unique reduction gear (as in Fig.1).
In such a case, high power (and torque) increases could be experienced by shaft axes if not properly controlled, and the reduction gear itself could experience significant unbalances on the two axes, with possible vibrations and fluctuating loads.
As an example, assuming that the automation controls only parameters of the prime movers and considering a power increase of 80% for the external shaft and 20% for the internal shaft, values of power increase for the two shafts can be estimated.
In particular, in correspondence to a ship speed for which the maximum power of the prime mover(s) is reached during manoeuvres, the external and internal shaftlines would experience a total power 20% higher and 20 % lower respectively than their maximum during rectilinear path at 100% power, thus resulting in a considerable overload of a shaftline, and in a difference of about 50% between the unbalanced torques.
As a consequence, the need for a direct control of torque on the two shaftlines is evident, together with a tuning of the automation in order to avoid problems on the shaftlines themselves, not controllable only at the prime mover(s) level.
Regarding maximum power (or torque) on the shaftlines, this could be reduced during manoeuvres by means of a reduction of propeller blade angle (if CPP are equipped) or propeller revolutions (both for CPP or FPP). It has to be underlined that probably a reduction of propeller revolutions is less fast than a pitch reduction, and this has to be carefully taken into account.
Moreover, for what regards the unbalance of torques on the two output shafts of the reduction gear, it has also to be pointed out that in case of CPP automation could decouple the two shaftlines by means of different propeller blade angles, while in case of FPP the possible reduction of propeller revolutions cannot reduce the unbalances, but only the absolute values of the two torques.
From these points of view, it is believed that a complete simulator of the propulsion system, including also a detailed mathematical model of the reduction gear and of the automation control, is necessary in order to simulate the different scenarios that the ship can encounter during her operation and evaluate the correct countermeasures to avoid possible problems and failures.

5. CONCLUSIONS

In this paper a simulation approach able to represent the dynamics of a twin-screw ship propulsion plant taking into account the significant unbalances which can be generated in correspondence to manoeuvring conditions has been presented. The developed numerical model includes ship manoeuvrability, taking into account the effects of maneuvers on shaftlines load and the dynamic behaviour of prime movers, shaft lines, propellers and propulsion control system.
Numerical results obtained have been compared to full-scale measurements in order to validate the proposed simulation approach, with satisfactory results.
It is believed that this method, despite presenting some simplifications, can be a useful tool for the control system designer for twin screw ships with coupled shaftlines (see figure 1), which can experience shaft overloads or forces unbalances on the reduction gear if the described phenomenon is not properly taken into account.
Next steps needed to gain a further insight into the problem consist in a complete modeling of a ship propulsion plant with coupled shaftlines, with particular attention to the cross connected reduction gear and to the optimization of the automation system strategy, with all necessary controls needed to prevent possible problems.
Moreover, a further analysis and comparison of model tests and full scale trials would allow to have a better understanding of the existing scale effects, allowing to have more reliable predictions of shaft unbalances if ships significantly different from the ones already analysed have to be considered.

6. ACKNOWLEDGEMENT

The authors gratefully acknowledge contributions from Fincantieri C.N.I., Cetena, INSEAN and Italian Navy, which made available sea trials and model tests data for the present study.

REFERENCES

1. VIVIANI, M., PODENZANA BONVINO, C., MAURO, S., CERRUTI, M., GUADALUPI, D., MENNA, A., “Analysis of Asymmetrical Shaft Power Increase During Tight Manoeuvres”, 9th International Conference on Fast Sea Transportation (FAST2007), Shanghai, China, 2007
2. CASSELLA, P., ‘Performance of a Screw Propeller in Non Axial Flow’, Tecnica Italiana, 1971
3. CASSELLA, P., ‘On the Propeller in Yaw: a Comparison between some Results obtained from the Equivalent Section theory and the Experimental Ones’, Tecnica Italiana, 1971
4. LONGO, J. & STERN, F., ‘Effects of drift angle on model ship flow’, Experiments in Fluids 32, 2002
5. LONGO, J., YOON, H. S., TODA, Y. & STERN, F., ‘Phase–Averaged 3D PIV/Wave Elevations and Force / Moment Measurements for Surface Combatant in PMM Maneuvers’, Proceedings 26th Symposium on Naval Hydrodynamics, 2006

6. ALTOSOLE, M., FIGARI, M., D'ARCO, S., 'Design and Optimisation of Propulsion Systems by Dynamic Numerical Simulation', Proceedings NAV 2003, Palermo, Italy, 2003
7. BENVENUTO, G., BRIZZOLARA, S., FIGARI, M., 'Simulation Of The Propulsion System Behaviour During Ship Standard Manoeuvres', Proceedings PRADS, 2001
8. BENVENUTO, G., BRIZZOLARA, S., CARRERA, G., 'Ship Propulsion Numerical Simulator: Validation of the Manoeuvrability Module', Proceedings NAV 2003, Palermo, Italy, 2003
9. ALTOSOLE, M., BAGNASCO, A., BENVENUTO, G., CAMPORA, U., FIGARI, M., D'ARCO, S., GIULIANO, M., GIUFFRA, V., SPADONI, A., MICHETTI, S., RATTO, A., ZANICHELLI, A., 'Real Time Simulation of the Propulsion Plant Dynamic Behaviour of the Aircraft Carrier Cavour', Proceedings INEC 2008, Hamburg, Germany, 2008

HYDRODYNAMIC LIFT IN A TIME-DOMAIN PANEL METHOD FOR THE SEAKEEPING OF FAST SHIPS

Pepijn de Jong, Delft University of Technology, The Netherlands
Frans van Walree, Maritime Research Institute, The Netherlands

SUMMARY

A method is presented for the seakeeping of high speed craft with transom stern flow. The method consists of a time domain boundary element method utilizing a free surface Green function. For the solution a combined source-doublet formulation is applied, while satisfying two boundary conditions explicitly. Firstly, a zero normal flow on the body condition and secondly a condition at the transom stern based on the unsteady Bernoulli equation to model transom stern flow. The solution is done in two steps. First a source system is solved in absence of the transom condition and subsequently the doublet strength is solved incorporating the previously solved source strengths and the transom condition. Although the formulations enable a non-linear treatment of the submerged hull form, partial linearization is employed for computational efficiency.

The fundamentals are elaborated and subsequently the method is applied to wedge shapes with constant forward speed in calm water. The results are compared with the outcome of Savitsky's empirical model for planing wedges and with a number of alternative formulations with encouraging results. Although the method is capable of dealing with unsteady seakeeping problems in the present paper it will only be applied to steady cases, as development is ongoing.

NOMENCLATURE

$1+k$	Form factor
β	Deadrise angle
η	Free surface vertical location
λ	Wetted length/beam ratio
μ	Doublet strength
ω	Wave frequency
Φ	Velocity potential
Φ^d	Disturbance velocity potential
Φ^w	Wave velocity potential
ψ	Wave direction
ρ	Density of water
σ	Source strength
τ	Past time or trim angle
$\underline{V}$	Rigid body velocity
ξ,η,ζ	Location source point
ζ_a	Wave amplitude
B	Beam
C_D	Cross-flow drag coefficient
C_f	ITTC friction coefficient
C_{L_0}	Lift coefficient flat plate
C_{L_β}	Lift coefficient deadrise planing surface
C_v	Beam Froude number
F_{zv}	Cross-flow drag force
Fn	Froude number
G	Green function
g	Gravity constant
G^0	Rankine part of Green function
G^f	Free surface (memory) part of Green function
J_0	Bessel function of order zero
k	Wave number
L_c	Wetted length chine
L_k	Wetted length keel
n	Normal to surface
p,q	Field en source point
p_a	Atmospheric pressure
R_v	Viscous resistance
Rn	Reynolds number
S	Wetted surface
t	Time
U_{vel}	Constant forward speed
V_N	Projection normal velocity on free surface
V_n	Normal velocity
x_0,y_0,z_0	Earth fixed coordinates
z_T	Vertical location transom

1 INTRODUCTION

The continuous demand for high speed operation while fulfilling existing and extended operational and mission requirements has become a constant challenge for the naval architect. There is a perpetual competition in the industry to develop innovative methods of reducing resistance and expanding maximum speeds in a seaway.

Evaluation of advanced and/or high speed concepts requires advanced numerical tools that can deal with the hydrodynamic issues involved on a first principles basis. Investigations should not be limited to issues like motion induced accelerations in the vertical plane, but need to address course keeping and dynamic stability as well.

The research presented in this paper is aimed at developing a practical numerical model for the evaluation of the seakeeping behavior of high speed vessels in terms of motions, acceleration levels, loads and dynamic behavior.

The formulation of the numerical model is based on the work of Lin and Yue [6] and further developed by Van Walree [10, 11] and Pinkster [7]. The formulation originally adopted by Van Walree employs unsteady impulsive sources on the hull with combined source-doublet-elements to represent submerged lifting control surfaces. The free surface boundary conditions are linearized to the undisturbed free surface, while it is possible to retain the body boundary condition on the actual submerged geometry. Practically, it is necessary to linearize the body boundary condition as well, to reduce the computational burden of the method, enabling the seakeeping analysis to run on a normal desktop computer.

The numerical model is capable of dealing with significant forward speeds and arbitrary three-dimensional (large amplitude) motions due to the transient Green function, as shown by for example King et al. [5]. The free surface linearization in the numerical model is a disadvantage, especially for high speed cases, where significant nonlinear free surface effects can occur. The recent implementation of pressure stretching based on the calculation of the free surface deformation as presented by De Jong et al. [2] provide a means to partly overcome this disadvantage.

In the current paper this method is further extended for application to high speed vessels. For these vessels, mostly fitted with a transom stern, the flow is characterized by high pressure values in the stagnation regions along the waterline in the fore part and smooth separation from the stern at moderate and high speeds. The flow around the body develops significant hydrodynamic lift, while the transom typically is left dry.

In the existing code the high pressure regions near the bow are well predicited, however the flow leaving at the stern is not modeled very well. The flow leaving the stern can be modeled in two ways in the existing code:

- By applying a dummy segment elongating the ship at the stern. This ensures that the streamlines remain attached at the stern location instead of developing very large velocities around the transom edge, although at the same time the total pressure at the transom edge does not equal atmospheric pressure, violating the Bernoulli equation.

- By empirically post-process the pressure distribution near the transom with a function that decreases the total pressure over a certain length to the atmospheric pressure at the transom edge, as proposed by Garme [1]. Although the pressure distribution now is more in agreement with experimental experience this does not have any influence on the solution itself.

Both approaches largely ignore dynamic effects that are important when considering for instance the forward speed motion damping in waves. The latter is especially important for the damping of pitching motions at high forward speed. Emperical evidence suggests that flow leaving the transom plays an important role in this.

Another solution is the applicition of a combined source-doublet distribution on the hull coupled with a trailing edge condition and wake sheet equivalent to the one used for foils. This condition can be formulated in such way that both the flow separates tangentially at the transom and that the dynamic pressure and the hydrostatic pressure at the transom edge are equal to the atmospheric pressure. Reed et al. [8] proposed such condition making use of the steady linearized Bernoulli equation applied just fore and aft of the transom stern. By employing this condition the flow at the transom will smoothly separate at the stern while satisfying the atmospheric pressure expected with a dry transom, while at the same time the doublet elements introduce the possibility of circulation lift, possibly enhancing the prediction of trim and rise. To allow for dynamic effects the unsteady Bernoulli equation is used in present model.

Besides the implementation of a transom condition, the solution process is modified as well. As pointed out by Reed et al. [8] presetting of the source strength and subsequent solution for the doublet strength often yields instable results. For this reason a solution in two steps has been implemented, where first the source strength is solved without the transom condition and secondly the doublet strength is solved using the known source strengths and the transom condition.

The new method is applied to wedge shapes traveling in a fixed reference position with constant forward speed in calm water and the resulting vertical force is compared with the results of the semi-empirical model by Savitsky [9]. Different versions of the code are compared. Although development is still ongoing, the comparison shows that the new method with a two step solution process and with a trailing edge condition based on the work of Reed et al. [8] shows the best agreement.

The second section will describe the numerical background of the model and will detail the transom condition and solution process. The next section will present the comparison of the different versions of the code with the Savitsky empirical model. The final section will summarize the conclusions and recommendations that follow from the research presented in this paper.

2 NUMERICAL BACKGROUND

The numerical method presented in this paper is an extension of the work presented by Lin and Yue [6], Pinkster [7] and Van Walree [11]. The code containing the numerical method is termed PANSHIP.

2.1 TIME DOMAIN GREEN FUNCTION METHOD

Potential flow is assumed based on the following simplifications of the fluid:

- The fluid is homogeneous
- The fluid is incompressible

- The fluid is without surface tension
- The fluid is inviscid and irrotational

The medium of interest is water, while there is an interface with air. The ambient pressure is assumed to equal zero. The water depth is infinite and waves from arbitrary directions are present. Under all these assumptions it can be shown that the Laplace equation, resulting from conservation of mass, is valid in the interior of the fluid:

The following definitions are used to describe the domain:

- $V(t)$ is the fluid volume, bounded by:
- $S_F(t)$ the free surface of the fluid,
- $S_H(t)$ the submerged part of the hull of the ship,
- $S_W(t)$ wake sheets and
- $S_\infty(t)$ the surface bounding the fluid infinitely far from the body.

Assuming linearity, the total potential can be split into two parts, the wave potential and the disturbance potential

$$\Phi = \Phi^w + \Phi^d \tag{1}$$

The wave potential is given by:

$$\Phi^w = \frac{\zeta_a g}{\omega} e^{kz_0} \sin\left(k\left(x_0 \cos\psi + y_0 \sin\psi\right) - \omega t\right) \tag{2}$$

The subscript 0 refers to earth fixed coordinates. At the free surface two conditions are imposed. First, a kinematic condition assuring that the velocity of a particle at the free surface is equal to the velocity of the free surface itself.

$$\frac{\partial\eta}{\partial t} + \nabla\Phi \cdot \nabla\eta - \frac{\partial z_0}{\partial t} = 0 \quad \forall\, \underline{x_0} \in S_F \tag{3}$$

Second, a dynamic condition assuring that the pressure at the free surface is equal to the ambient pressure. For this condition use is made of the unsteady Bernoulli equation in a translating coordinate system.

$$\frac{\partial\Phi}{\partial t} + g\eta + \frac{1}{2}\left(\nabla\Phi\right)^2 = 0 \quad \forall\, \underline{x_0} \in S_F \tag{4}$$

Both can be combined and linearized around the still water free surface, yielding:

$$\frac{\partial^2\Phi}{\partial t^2} + g\frac{\partial z_0}{\partial t} = 0 \quad \text{at } z_0 = 0 \tag{5}$$

On the instantaneous body surface a zero normal flow condition is imposed be setting the instantaneous normal velocity of the body equal to:

$$V_n = \frac{\partial\Phi^d}{\partial n} + \frac{\partial\Phi^w}{\partial n} \quad \forall\, \underline{x_0} \in S_H \tag{6}$$

At a large distance from the body (at S_∞) the influence of the disturbance is required to vanish.

$$\Phi^d \to 0 \quad \frac{\partial\Phi^d}{\partial t} \to 0 \tag{7}$$

At the start of the process, apart from the incoming waves, the fluid is at rest, as is reflected in the initial condition.

$$\Phi^d\Big|_{t=0} = \frac{\partial\Phi^d}{\partial t}\Big|_{t=0} = 0 \tag{8}$$

In this time-domain potential code the Green function given in will be used. This Green function specifies the influence of a singularity with impulsive strength (submerged source or doublet) located at singularity point $q(\xi,\eta,\zeta)$ on the potential at field point $p(x_0,y_0,z_0)$.

$$\begin{aligned} G(p,t,q,\tau) = G^0 + G^f = \frac{1}{R} - \frac{1}{R_0} + \\ 2\int_0^\infty \left[1 - \cos\left(\sqrt{gk}\,(t-\tau)\right)\right] e^{k(z_0+\zeta)} J_0(kr)\, dk \\ \text{for } p \neq q\,,\ t \geq \tau \end{aligned} \tag{9}$$

It has been shown, by for example Pinkster [7], that the Green function satisfies both the Laplace equation and the boundary conditions, making it a valid solution for the boundary value problem stated above. Using the above, it is possible to derive a boundary integral formulation. The first step is to apply Greens second identity to:

$$\Phi^d\left(\underline{\xi},t\right) \text{ and } \frac{\partial G}{\partial\tau}\left(\underline{x}_0,\underline{\xi},t,\tau\right) \tag{10}$$

Subsequently the resulting volume integral is equal to zero by using the Laplace equation. Integrating in time yields for the surface integral:

$$\int_0^t \int_{S_{FHW}(\tau)} \left(\Phi^d G_{\tau n} - G_\tau \Phi^d_n\right) dS d\tau = 0 \tag{11}$$

Next, the free surface integral is eliminated by virtue of the Green function. Finally, a general formulation of the nonlinear integral equation is obtained for any field point:

$$\begin{aligned} 4\pi T\Phi^d(p,t) = -\int_{S_{HW}(t)} \left(\Phi^d G^0_n - G^0\Phi^d_n\right) dS + \\ \int_0^t \int_{S_{HW}(\tau)} \left(\Phi^d G_{\tau n} - G_\tau\Phi^d_n\right) dS d\tau + \\ \frac{1}{g}\int_0^t \int_{L_w(\tau)} \left(\Phi^d G_{\tau\tau} - G_\tau\Phi^d_\tau\right) V_N dL d\tau \end{aligned} \tag{12}$$

V_N is the projection of the normal velocity at the curve in the plane of the free surface, for example $G^0_n = \frac{\partial G^0}{\partial n}$, and T is defined as:

$$T(p) = \begin{cases} 1 & p \in V(t) \\ 1/2 & p \in S_H(t) \\ 0 & \text{otherwise} \end{cases} \tag{13}$$

Now the choice of surface singularity elements can be made. The current version of the code is able to deal with source-only distributions and combined source-doublet distributions or any mix of the both. For the purposes of this paper a combined source-doublet distribution distributed on the body surface will be elaborated. The source strength is set equal to the jump in the normal derivative of the potential between the inner (-) and outer (+) sides of the surface, while the doublet strength is set equal to the jump of the potential across the inner and outer surfaces. This results in:

$$\left.\begin{aligned} \Phi^{d+} - \Phi^{d-} &= -\mu \\ \frac{\partial \Phi^{d+}}{\partial n} - \frac{\partial \Phi^{d-}}{\partial n} &= \sigma \end{aligned}\right\} \forall \quad q \in S_H \tag{14}$$

For the infinite thin wake sheets there is no jump in the normal derivative of the potential:

$$\left.\begin{aligned} \Phi^{d+} - \Phi^{d-} &= -\mu \\ \frac{\partial \Phi^{d+}}{\partial n} &= \frac{\partial \Phi^{d-}}{\partial n} \end{aligned}\right\} \forall \quad q \in S_W \tag{15}$$

Substituting equations 13, 14 and 15 in eq. 12, taking the normal derivative for a field point lying on the outer face of the hull and applying the body boundary condition eq. 6 results in an expression for the normal velocity at field point $p(\underline{x}_0, t)$ in terms of integrals over time and source points $q(\underline{x}_0, t)$

$$\begin{aligned} 4\pi\left(V_{n_p} - \frac{\partial \Phi^w}{\partial n_p}\right) &= 2\pi\sigma(p,t) + \\ &\int_{S_H(t)} \sigma(q,t) \frac{\partial G^0}{\partial n_p} dS + \int_{S_{HW}(t)} \mu(q,t) \frac{\partial^2 G^0}{\partial n_p \partial n_q} dS - \\ &\int_0^t \int_{S_H(\tau)} \sigma(q,\tau) \frac{\partial^2 G^f}{\partial n_p \partial \tau} dS d\tau - \\ &\int_0^t \int_{S_{HW}(\tau)} \mu(q,\tau) \frac{\partial^3 G^f}{\partial n_p \partial n_q \partial \tau} dS d\tau - \\ &\frac{1}{g} \int_0^t \int_{L_w(\tau)} \sigma(q,\tau) \frac{\partial^2 G^f}{\partial n_p \partial \tau} V_N V_n dL d\tau - \\ &\frac{1}{g} \int_0^t \int_{L_w(\tau)} \mu(q,\tau) \frac{\partial^3 G^f}{\partial n_p \partial \tau^2} V_N dL d\tau \end{aligned} \tag{16}$$

Equation 16 is the principal equation to be solved to obtain the unknown singularity strengths. Two steps have yet to be taken:

1. The definition of a Kutta or trailing edge condition to formulate the problem as such that an unique solution can be obtained.
2. To chose an appriopiate solution scheme to obtain an equal amount of equations and unknowns, as for now there are roughly double the number of unknowns (one source strength and one doublet strength per panel) per equation (one normal velocity condition per panel);

The first step will be elaborated in section 2.3 and the latter in section 2.4.

2.2 LINEARIZATION

Especially the evaluation of the free surface memory term of the Greens function requires a large amount of computational time. These terms need to be evaluated for each control point for the entire time history at each time step. To decrease this computational burden, the evaluation of the memory term has been simplified. For near time history use is made of interpolation of predetermined tabular values for the memory term derivatives, while for larger values further away in history polynomials and asymptotic expansion are used to approximate the Green function derivatives.

Moreover, the position of the hull relative to the past time panels is not constant due to the unsteady motions, making recalculation of the influence of past time panels necessary for the entire time history. This recalculation results in a computational burden requiring the use of a supercomputer. To avoid this burden, the unsteady position of hull is linearized to the average position (moving with the constant forward speed). Now the memory integral can be calculated a priori for use at each time step during the simulation.

The prescription of the wake sheets in this linear approach leads to a flat wake sheet behind the hull. Again a constant distance exist to the past time wake panels. Only the influence coefficients of the first row of wake elements need to be calculated at each time step, until the maximum wake sheet length is reached. For all other rows the induced velocity can be obtained by multiplying the influence by their actual circulation.

2.3 WAKE MODEL

The wake model is necessary for an unique solution of the potential problem set up in terms of a mixed source soublet formulation. The wake model relates the dipole strength at the trailing edge of lifting surfaces to the location and shape of a wake sheet, by using the unsteady linearized Bernoulli equation in the body fixed axis system, as proposed by Reed et al. [8] for steady cases.

$$gz_T = U_{vel}\left(\frac{\partial \Phi^d}{\partial x} + \frac{\partial \Phi^w}{\partial x}\right) - \left(\frac{\partial \Phi^d}{\partial t} + \frac{\partial \Phi^w}{\partial t}\right) \tag{17}$$

This condition will be appoximately satisfied at the transom edge. In fact, it will not be satisfied exactly at the transom edge due to numerical problems arising when evaluating influence functions on panel edges. Instead, the condition will be satisfied at the collocation points of the last hull panel row in front of the transom edge.

The wave influence can be calculated by taking the appropiate derivatives of eq. 2. The tangential induced velocities of all singularities at source points $q\left(\underline{\xi}, t\right)$ at the transom edge panels $w(\underline{x}_0,t)$ are given by:

$$4\pi\frac{\partial\Phi^d}{\partial x}(w,t) = -2\pi\frac{\partial\mu(w,t)}{\partial x}+ \int_{S_H(t)}\sigma(q,t)\frac{\partial G^0}{\partial x}dS+\int_{S_{HW}(t)}\mu(q,t)\frac{\partial^2 G^0}{\partial x\partial n_q}dS- \int_0^t\int_{S_H(\tau)}\sigma(q,\tau)\frac{\partial^2 G^f}{\partial x\partial\tau}dSd\tau- \int_0^t\int_{S_{HW}(\tau)}\mu(q,\tau)\frac{\partial^3 G^f}{\partial x\partial n_q\partial\tau}dSd\tau- \frac{1}{g}\int_0^t\int_{L_w(\tau)}\sigma(q,\tau)\frac{\partial^2 G^f}{\partial x\partial\tau}V_N V_n dLd\tau- \frac{1}{g}\int_0^t\int_{L_w(\tau)}\mu(q,\tau)\frac{\partial^3 G^f}{\partial x\partial\tau^2}V_N dLd\tau \quad (18)$$

Because constant strength singularities are used, it is not possible to directly obtain the x-derivative of μ. The solution is to estimate this derivative at the transom edge panel by using the value of μ at the panel just in front of this panel and at the panel just behind the transom edge panel, the first wake sheet panel and dividing over the length. $i+1$ refers to the panel directly upstream and $i-1$ refers to first wake panel downstream of the transom panel as indicated in figure 1.

$$\frac{\partial\mu(w,t)}{\partial x}\approx\frac{\mu_{i+1}-\mu_{i-1}}{2L_{pan}} \quad (19)$$

The disturbance part of the second term of eq. 17 can be evaluated as follows:

$$4\pi\frac{\partial\Phi^d}{\partial t}(w,t) = -2\pi\frac{\partial\mu}{\partial t}(p,t)+ \int_{S_H(t)}\frac{\partial\sigma}{\partial t}(q,t)G^0 dS+\int_{S_{HLW}(t)}\frac{\partial\mu}{\partial t}(q,t)\frac{\partial G^0}{\partial n_q}dS- \int_0^t\int_{S_H(\tau)}\sigma(q,\tau)\frac{\partial^2 G^f}{\partial t\partial\tau}dSd\tau- \int_0^t\int_{S_{HW}(\tau)}\mu(q,\tau)\frac{\partial^3 G^f}{\partial t\partial\tau\partial n_q}dSd\tau- \frac{1}{g}\int_0^t\int_{L_w(\tau)}\sigma(q,\tau)\frac{\partial^2 G^f}{\partial t\partial\tau}V_N V_n dLd\tau- \frac{1}{g}\int_0^t\int_{L_w(\tau)}\mu(q,\tau)\frac{\partial^3 G^f}{\partial t\partial\tau^2}V_N dLd\tau+ \int_{L_w(t)}\mu(q,t)\frac{\partial G^0}{\partial n_q}V_N dL \quad (20)$$

The final term appears due to time derivation of the doublet waterline integral and the fact that the time integration border of this integral is dependent on time. This term is simplified using the free surface boundary condition and the definition of the Green's function.

The implementation of eq. 20 is slightly more complicated, as the doublet G^0-terms and the wake terms are estimated by a simple first order backward scheme. The other terms are calculated analytically as the approximation method is unsuitable for these terms.

The wake sheet position and shape is prescribed to reduce the computational effort. This prescription is that a wake element remains stationary once shed. This eliminates the effort needed to calculate the exact position of each wake element at each time step. This violates the requirement of a force free wake sheet. However, for practical purposes this does not have significant influence as shown by Van Walree [11] and Katz and Plotkin [3].

Per time step only the first wake row, consisting of the elements attached to the transom edge, is treated as unknown. Once shed these wake elements keep their strength. The number of extra equations by the above condition is equal to the number of wake panels in the first wake row.

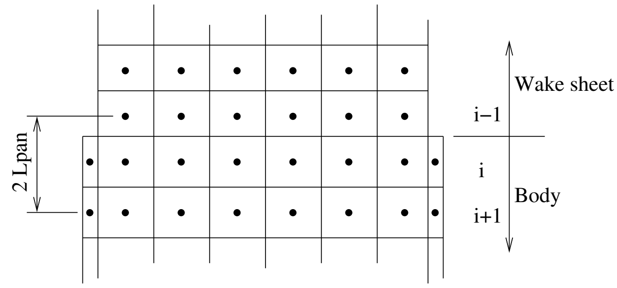

Figure 1: Panel identification for local $d\mu/dx$

2.4 SOLUTION

Equation 16 and equations 17-20 are discretized in terms of a combined source-doublet element distribution on the hull and an equivalent vortex ring elements on the wake surface. In the current method constant strength quadrilateral source and doublet panels are used. This results in a system that is over-determined as both a source strength and a doublet strength are defined for each hull panel. On top of this there are unknown doublet strengths in the first wake row. To resolve this a number of possibilities exist. Two of these are:

1. To set the source strength equal to the undisturbed normal velocity at each body panel. In this, the memory integrals of the past time influences of the sources and doublets could be included.
2. To solve the system in two steps. Step one is to solve for the source strength without wake influences and without the G^0-influences of the doublet panels. The second step consists of a solution for the doublet strengths and first wake row strengths including the wake influences and with the G^0 influences of the source strengths determined in the first step in the right hand side.

The second method is chosen as it gives the best results, as shown in the next section.

Figure 2 illustrates the system that is solved for the combined sourcedoublet system, with known source strengths.

The latter can be obtained by any of the two methods. First the different parts of the influence matrix A:

$A1$ The normal G^0-influence terms of the doublet singularities of the body on the other panels and themselves.

$A2$ The normal G^0-influence terms of the first wake row singularities on the body panels.

$A3$ The tangential G^0-influences of the body singularities on the u-velocity on the pressure condition (applied on the last hull panel row at the transom edge) as well as the term used to construct the local doublet x-derivative in equation 19. Additionally the estimated terms for the time derivative at the transom condition that are dependent on the current doublet strength.

$A4$ The tangential G^0-influences of the first wake row singularities on the other first wake row and themselves as well as their contribution to the local doublet x-derivative in equation 19 and their contribution to the time derivative in the transom pressure condition.

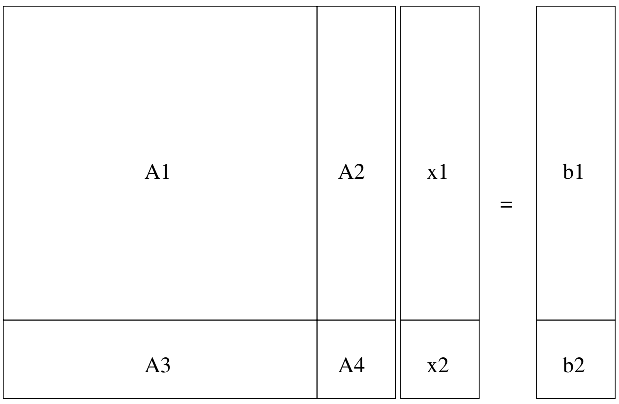

Figure 2: Setup of solution of combined source-doublet system

The solution vector $\underline{b}$ contains in the $b1$-part the unknown doublet strength on the body and in part $b2$ the unknown doublet strengths of the first wake row. The RHS vector part $x1$ houses the normal velocity contributions of all memory integrals and known G^0-integrals on each body panel along with the local wave and rigid body normal velocities. The $x2$-part of the RHS vector $\underline{x}$ holds all memory and known G^0-term contributions to the u-velocity and $d\Phi/dt$ at the transom panels along with the wave velocity in x-direction.

At the start of the simulation the body is impulsively set into motion. At each subsequent time step the body is advanced to a new position with an instantaneous velocity. Both position and velocity are known from the solution of the equation of motion. The singularity strengths are obtained by solving the systems following from either of the both methods.

2.5 FORCE EVALUATION

Forces can be obtained from integration of the pressure at each collocation point over the body. The pressures can be obtained by using the unsteady Bernoulli equation (in a body fixed axis system):

$$\frac{p_a - p}{\rho} = \frac{1}{2}\left\{\left(\frac{\partial\Phi}{\partial x}\right)^2 + \left(\frac{\partial\Phi}{\partial y}\right)^2 + \left(\frac{\partial\Phi}{\partial z}\right)^2\right\} + \frac{\partial\Phi}{\partial t} - \underline{V}\cdot\nabla\Phi \quad (21)$$

In eq. 21 $\underline{V}$ is the total velocity vector at the collocation point of the rigid body, including rotations.

The spatial derivatives of the potential in eq. 21 follow straight from the solution. The only difficulty remaining is to obtain the time derivative. For the contribution of the wake and the Rankine part of the doublet panels this can be done by utilizing a straightforward backward difference scheme. However, this gives unstable results when used for the contribution of the source panels and the memory part of the doublet panels to the time derivative. This can be resolved by calculating the time derivative of these contributions analytically from the Green function derivatives.

This means that additional Green function derivatives need to be obtained, besides the derivatives needed for the solution itself. Furthermore, the time derivative of the source strength is needed. One solution is to derive this derivative directly from the solution itself:

$$\begin{aligned} &\underline{\sigma} = A_\sigma^{-1}\underline{x} \\ &\frac{d}{dt}\underline{\sigma} = A_\sigma^{-1}\frac{d}{dt}\underline{x} \end{aligned} \quad (22)$$

In this equation A_σ is the matrix relating the source strengths via the Rankine influences to the RHS. The vector $\underline{x}$ is the RHS vector of the solution, containing all influences due to incident wave, free surface memory effects and rigid body motions in terms of normal velocity in the collocation points. To obtain the time derivative of the free surface memory part of this vector, again extra Green function derivatives need to be obtained. The time derivative of the wave contributions can be obtained analytically. The time derivative of the rigid body velocity is the rigid body acceleration. This acceleration is multiplied by the inverse of the Rankine influence matrix that equals the added mass. This contribution can be transferred to the mass times acceleration part of the equation of motion.

2.6 VISCOUS RESISTANCE

With respect to the viscous resistance R_v, empirical formulations are applied to each part separately (hull, outriggers, lifting surfaces). The formulations used can be generalised as follows:

$$\begin{aligned} &R_v = \frac{1}{2}\rho U_{vel}^2 S(1+k)C_f \\ &C_f = \frac{0.075}{(log_{10}(Rn) - 2)^2} \end{aligned} \quad (23)$$

where U is the ship speed, S is the wetted surface area, k is a suitable form factor, and Rn is the Reynolds number of the body part considered.

2.7 VISCOUS DAMPING

Especially for high speed vessels, having only slight potential damping, viscous damping can play an important role. This is especially true around the peak of vertical motions. Then forces that arise due to separation in the bilge region due to vertical motions can be of significance. The magnitude of these forces depends on oscillation frequency, Froude number and section shape. In the current model a cross flow analogy is used to account for these forces. The viscous damping coefficient only depends on section shape, other influences are neglected. The following formulation is used in a strip wise manner:

$$F_{zv} = \frac{1}{2}\rho V_r |V_r| S C_D \tag{24}$$

V_r is the vertical velocity of the section relative to the local flow velocity, while S is the horizontal projection of the section area. The cross-flow drag coefficient C_D has values in-between 0.25 and 0.80.

3 RESULTS

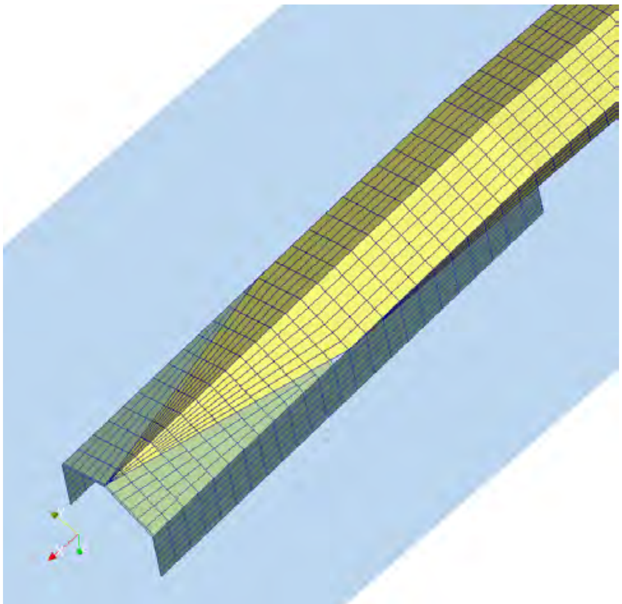

Figure 3: Typical geometry seen from below, including wake sheet

In this section results of a number of calculations are shown with wedges traveling with constant foward speed through calm water fixed in a reference position. The length over beam ratio is 4.3, the deadrise is 15 degrees and trim either 3 or 6 dgrees. Figure 3 shows a typical wedge paneling, including wake sheet. The results are meant as a preliminary investigation of the applicability of the method and the improvement of adjusted method over previous versions. Currently the results are limited to steady cases, in a later stage the method will be applied to unstaedy cases.

3.1 GRID STUDY

To investigate the influence of the number of elements on the predicted vertical force calculations have been performed with a wedge shape with 15 degrees deadrise, 6 degrees trim for three different Froude numbers for a grid with respectively 248, 444 and 828 elements. Figure 4 shows the ratio of the total vertical force with the displacement for these calculations.

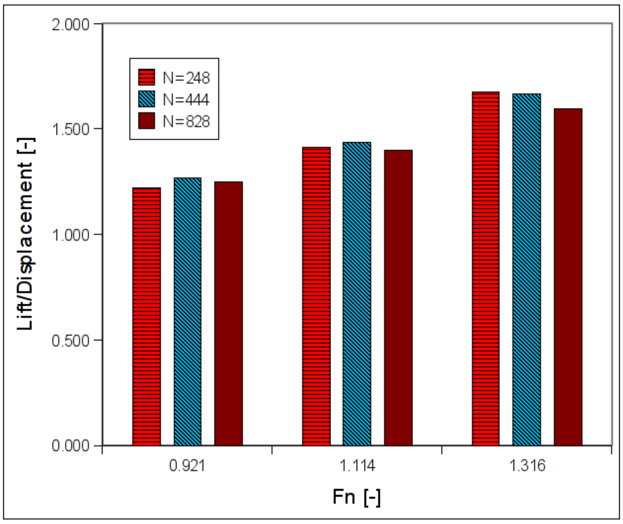

Figure 4: Grid study

It shows that the results are quite independent of the number of elements, although for the highest Froude number the calculation with 828 elements shows a slight deviation from the calculations with less elements. Especially the high pressure regions along the waterline in the fore part could be responsible for this deviation. The pressure varries rapidly over this region while the currently used discretization is possibly not fine enough at that location to resolve that gradient properly. Although the influence on the total force is only slight, the sufficient resolution of the high pressure gradients in the fore part requires ongoing attention.

3.2 COMPARISON OF METHODS

Figures 5, 6 and 7 show three-dimensional representations of the total pressure calculated with 3 different version of the code, respectively:

1. A source-only formulation with an empirical transom pressure modification based on the work of Garme [1].

2. A combined source-doublet formulation with a Kutta condition based on that for two-dimensional foils. The source strength is fixed by the incoming flow plus memory effects, the doublet strength is solved for.

3. A combined source-doublet formulation with the transom condition based on the Bernoulli equation presented in this paper. Both the source strength and the doublet strength are solved for in two steps as presented in this paper.

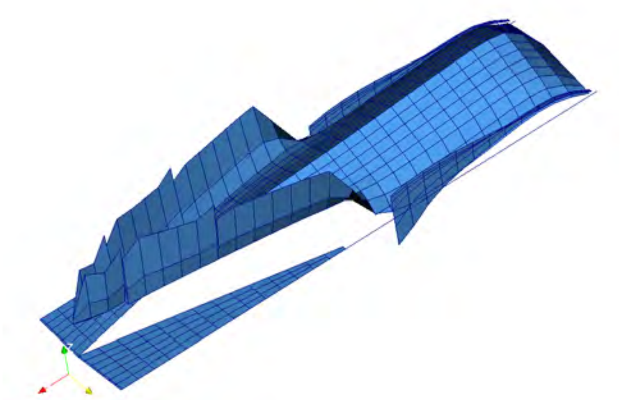

Figure 5: Total pressure plotted on the xy-grid for a source-only formulation with an empirical transom pressure correction

The empirical transom pressure correction according Garme [1]:

$$\frac{a}{BC_v} = 0.35$$
$$f_{red} = tanh\left(\frac{2.5}{a}x_1\right) \tag{25}$$

Where the correction length a is determined in the first equation (Garme uses a factor of 0.34 for his model), with B the width of the transom and C_v the beam Froude number. The second equation determines the pressure reduction factor f_{red}, with x_1 the distance in front of the transom. The reduction factor becomes unity at a distance a in front of the transom and is zero at the transom. The resulting total pressure for a source-only formulation using this correction is shown in figure 5.

The Kutta condition for a finite angle trailing edge for a two-dimensional foil as presented by Katz and Plotkin [3] is that the wake doublet strength becomes equal to the difference in doublet strength of the upper and lower foil sides at the trailing edge. For a ship hull with transom stern the upper foil side is absent and one could do by transferring the doublet strength of the last hull panels before the transom edge to the first wake row, ensuring velocity continuity. The resulting total pressure is shown in figure 6.

Figure 6: Total pressure plotted on the xy-grid for a source-doublet formulation with a Kutta condition derived from foils

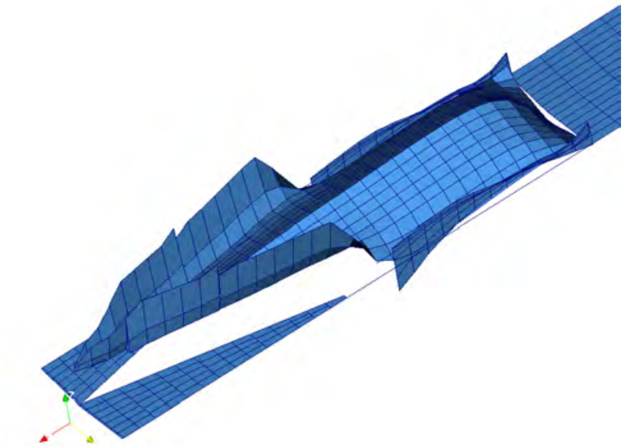

Figure 7: Total pressure plotted on the xy-grid for a source-doublet formulation with Bernoulli transom condition

Figure 7 shows the resulting total pressure for the method presented in this paper with the Bernoulli transom condition and two step solution. When comparing the three figures it shows that the pressure distribution in the fore part is not affected very much by the choice of element distribution or transom condition/correction. For the source-only formulation the pressure in the fore part is marginally larger. The differences show mostly at the transom.

The empirical formulation does result in zero pressure at the transom (figure 5), but its region of influence is confined to a region close to the transom. The Kutta condition based on two-dimensional foils with a combined source-doublet system (figure 6) does reduce the pressure near the transom somewhat. However, the pressure is not reduced to zero at the transom edge, voilating the Bernoulli equation there. The formulation with the Bernoulli transom condition (figure 7) does reduce the pressure to zero at the transom edge. Not exactly though, most probably due to the fact that the transom condition is satisfied at the collocation point of the last panel row before the transom instead of at the transom itself, as pointed out in the previous section. The influence of the transom flow condition is on larger region around the transom, when compared with the other two methods and the predicted vertical force will be less.

All three methods calculate somewhat unbelievable pressures on the submerged part of the body above the chines, especialy at the point where the chines cross the water surface. In real life these parts of the body would be at least partly dry, something that is ignored by the free surface linearization. Remarkable are the near transom pressures in this part in the last figure. Due to the Bernoulli condition one expects the total pressure to approach zero here. Closer inspection is necessary here.

Figures 8 and 9 show a comparison of the ratio of the total vertical force (lift) with the displacement for different code versions with the outcome with Savitsky's empirical model for the vertical lift, Savitsky [9]. In Savitsky's model first the lift for a flat plate at trim angle τ is predicted by:

$$C_{L_0} = \tau^1.1 \left[0.0120\lambda^{1/2} + \frac{0.0055\lambda^{5/2}}{C_v^2} \right] \tag{26}$$

With λ:

$$\lambda = \frac{L_k + L_c}{2B} \qquad L_k - L_c = \frac{B\,tan\beta}{\pi\,tan\tau} \tag{27}$$

β is deadrise angle, τ the trim angle, L_k the wetted length of the keel and L_c the wetted length of the chine taking into account the actual wetted width (due to wave rise). The lift of a deadrise planing surface is then calculated by:

$$C_{L_\beta} = C_{L_0} - 0.0065\beta C_{L_0}^0.60 \tag{28}$$

The code versions that are compared in figures 8 and 9 are:

- Source-only formulation with near transom empirical pressure correction (source pc)
- Source-doublet formulation with Bernoulli transom condition and two step solution (dbl transom)
- Source-doublet formulation with Kutta condition and fixed source strength (dbl kutta/no pc)
- Source-doublet formulation with Kutta condition and fixed source strength and near transom empirical pressure correction (dbl kutta pc)
- Source-doublet formulation with Bernoulli transom condition and fixed source strength (dbl transom src fixed)

Figure 8 shows results for a wedge with 15 degrees deadrise and 3 degrees trim and figure 8 shows results for a wedge with 15 degrees deadrise and 6 degrees trim.

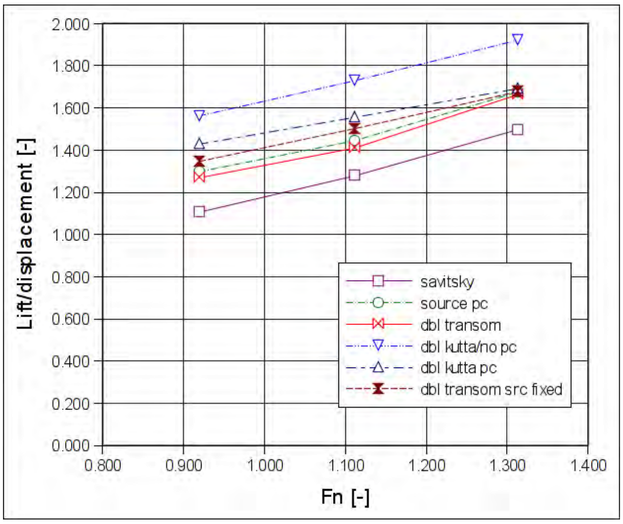

Figure 8: Comparison of the lift/displacement ratio for 3 degrees trim

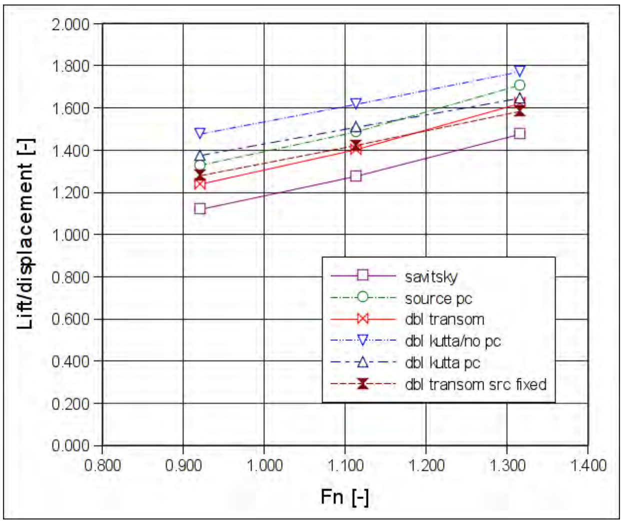

Figure 9: Comparison of the lift/displacement ratio for 6 degrees trim

The method outlined in the paper with the Bernoulli transom condition and two step solution (first source system and subsequently the doublet system) clearly produces results closest to Savitsky's empirical model. Using the same method, but setting the source strength a priori equal to the incoming flow and just solving for the doublet system performs only slightly worse.

The combined source-doublet system with the Kutta condition derived from foils with a finite trailing edge angle clearly produces too much lift relative to the other methods. Introducing the empirical near transom pressure correction obviously reduces the total vertical force and drastically improves this method. However, a source-only formulation with the same empirical pressure correction performs much better. Of course it is possible to enhance this method further by fitting the empirical pressure correction better for the case under consideration, this, however, is only possible for cases where one has this opportunity.

The comparison for the two trim angles is very similar, the computational methods performing slightly better at 6 degrees trim. However, the emperical model predicts a lower lift in all cases. There could be a number of reasons for this. Among these:

- Panship is not aimed for the high speeds Savitsk's model is aimed for. The predictions here are in the lower speed regime for the empirical model with C_v ranging from 1.9 tot 2.7, while the speeds are quite large for the numerical model with the Froude numer over the length ranging from 0.9 tot 1.3.

- Both methods include buoyancy in the vertical force. Panship includes the hydrostatics based on the calm water wetted geometry. The the empirical model includes in the lift the buoyancy of a flat plate at least partly, but when corrected for deadrise the buoyancy is also implicitly corrected with measured data. Two-dimensional empirical models based on wedges impacting the water surface often include a buoyancy correction factor reducing the hydrostatic force at high forward speeds. This is related to the fact that part of the geometry is dry when saling at high speeds, refer to for instance Keuning [4].

- Panship is a potential method without viscosity. Absence of viscosity generally leads to overprediction of the lift. The model inlcudes empirical formulations for viscous effects (refer to sections 2.6 and 2.7). The influence of the tweaking of the coefficients in these formulations on the lift needs to be studied.

- Panship does not include wave rise and dry chines, free surface effects that are ignored by the linearization of the free surface.

Also a larger number of panels and a better resolution of the large pressure gradients in the bow area could reduce the predicted lift somewhat as indicated by the grid study.

4 CONCLUSION AND FUTURE WORK

A transom flow condition has been incorporated into a time-domain potential flow panel method for the seakeeping of high speed ships using a combined source-doublet formulation on the hull with a wake sheet extending from the transom. The method makes use of the unsteady linearized Bernoulli equation to ensure that the pressure at the transom becomes zero. The potential method makes use of a transient Green function with a linearized free surface condition. Although it is possible to solve on the actual submerged body surface below the calm waterline, also the body boundary condition is linearized to reduce the computational effort. The source and doublet strengths are obtained by solving per time step two systems:

- A source system without the presence of the wake sheet and the influence of the current time step doublet elements

- A doublet system extended with the transom condition and wake sheet. The source strength determined in the previous step are treated as knowns in this system.

As a preliminary validation study the method has been applied to the lift generated on wedges moving with constant forward speed through calm water. The predicted total vertical force has been compared with the outcome of an empirical model by Savitsky for planing deadrise surfaces and to the outcome of alternative formulations using only source elements or combined source-doublet elements with an alternative Kutta condition with a wake sheet.

Although development is still ongoing, it has been showed that the new method using the transom condition performs best, and offers the advantage over an empirical pressure correction that the physical properties of the flow are better incorporated into the solution. Of course the empirical pressure correction could be modified to improve its predictions, but still the flow properties at the transom would not be properly solved for. Especially for seakeeping cases where one is interested in for instance pitch damping due to the accelerated flow leaving the transom this is important.

Still, it is evident that the current numerical model overpredicts the lift in comparison with the empirical model. This could have a number of reasons, one being the absence of viscosity in the numerical model, another the use of the full calm water hydrostatics in the numerical model. The latter is in contrast with for instance semi-empirical models based on the two-dimensional wedge impact for high speed planing often use buoyancy correction factors. The first can only be addressed by tweaking the viscous coefficients of the model, the latter needs to be investigated. It should be noted that the comparison here has been carried out at the minimum speed range of the empirical model and at the maximum speed range of the numerical model.

Future work includes the further implementation and validation of the unsteady transom condition and to study the influence of this condition on ship motions in seaways. Also some details of the current implementation need attention, specifically the pressure on the above chine wetted regions near the transom, the number of elements used to predict the pressure peak along the waterline in the fore part and the influence of satifying the transom pressure condition on the centers of the last hull panels instead of exactly at the transom.

ACKNOWLEDGEMENTS

The authors gratefully acknowledge the permission of the participants of the FAST project: Royal Netherlands Navy, Damen Shipyards at Gorinchem (NL), Royal Schelde Group at Vlissingen (NL), Marin at Wageningen (NL), and the TUDelft (NL) to use the results of the FAST project.

References

[1] K. Garme. Improved time domain simulation of planing hulls in waves by correction of the near-transom lift. *International Shipbuilding Progress*, 52(3):201–230, 2005.

[2] P. de Jong, F. van Walree, J.A. Keuning, and R.H.M. Huijsmans. Evaluation of the free surface elevation in a time-domain panel method for the seakeeping of high speed ships. In *Proceedings of the Seventeenth Int. Offshore and Polar Engineering Conference*, Lisboa, 2007.

[3] J. Katz and A. Plotkin. *Low-speed aerodynamics*. Cambridge University Press, second edition, 2001.

[4] J. A. Keuning. *The nonlinear behaviour of fast monohulls in head waves*. PhD dissertation, Delft University of Technology, Shiphydromechanic Laboratory, 1994.

[5] B. K. King, R. F. Beck, and A. R. Magee. Seakeeping calculations with forward speed using time-domain analysis. In *Proceedings 17th Symposium on Naval Hydrodynamics*, pages 577–596, 1988.

[6] W. M. Lin and D. Yue. Numerical solutions for large-amplitude ship motions in the time domain. In *Proceedings of the 18th symposium on naval hydromechanics*, pages 41–65, Ann Arbor, 1990.

[7] H. J. M. Pinkster. *Three dimensional time-domain analysis of fin stabilised ships in waves*. Master's Thesis, Delft University of Technology, 1998.

[8] A. Reed, J. Telste, and C. Scragg. Analysis of transom stern flows. In *Eighteenth Symposium on Naval Hydrodynamics*, pages 207–219, 1991.

[9] D. Savitsky. Hydrodynamic design of planing hulls. *Marine Technology19*, 1(1):71–95, 1964.

[10] F. van Walree. *Computational methods for hydrofoil craft in steady and unsteady flow*. PhD thesis, Delft University of Technology, 1999.

[11] F. van Walree. Development, validation and application of a time domain seakeeping method for high speed craft with a ride control system. In *Proceedings of the 24th Symposium on Naval Hydrodynamics*, July 2002.

THE USE OF A VERTICAL BOW FIN FOR THE COMBINED ROLL AND YAW STABILIZATION OF A FAST PATROL BOAT

J Alexander Keuning, Shiphydromechanics Department, Delft University of Technology, Netherlands
Guido L Visch, Shiphydromechanics Department, Delft University of Technology, Netherlands

SUMMARY

From many research projects it is known that for fast patrol boats the motion behavior in large stern quartering and following seas is often a limiting situation for its operability. The broaching tendency that may occur with most of the relatively small (shorter then 50 meters) and fast (more then 25 knots) patrol boats often implied that a significant change in forward speed or heading had to be made to prevent serious problems. The rudder action of the aft rudders in particular in stern quartering seas, required to keep the boat more or less "on track", significantly aggravates the rolling motion of the ship and so the tendency towards a broach. A vertical fin at the bow however would have an opposite and thus positive effect on the roll motions in those conditions. By using this forward vertical fin (or bow rudder) to control the yaw motion of the ship in large waves, in addition to the rudders aft, due to the direction of the lift force and its phase the rolling motion is reduced instead of increased, contributing significantly to the resistance against broaching. The introduction of such a vertical fin on a conventional bow is difficult due to all kinds of practical reasons.
The very shape of the hull according to the AXE Bow Concept, introduced by the author in earlier publications since 2001, however makes it quite feasible to place such a vertical controllable fin at the foremost end of the ship.
In the paper the mechanism and the physics involved of such a vertical bow fin in stabilizing the yaw and roll motions in waves will be described. In addition the results of an extensive series of experiments with an AXE Bow model fitted with various realizations of such bow fins will be presented. Finally a series of tests with a free running model fitted with such a bow fin has been carried out in the sea keeping tank of MARIN in stern quartering seas to check the principle behind the idea.
A limited number of these results will be presented in the paper.

NOMENCLATURE

Lwl	Length waterline
Bwl	Breadth waterline
T	Draft amidship
V	Displacement
Vmax	Maximum Speed
GMt	Transverse Metacentric Height
k	k-factor
Fy	Side Force
Mz	Yaw Moment
Mx	Roll Moment

1. INTRODUCTION

The use of fast craft in a seaway has always posed many challenges to the comfort of those on board and the safety of the ship. Partly this is due to the fact that most applications of fast ships are restricted to the relatively smaller vessels. If we consider ships with speeds in excess of 25 knots as "fast", their typical length is generally restricted to 50 meters over all. This implies that the waves they encounter tend to be relatively large compared to the ship size. Improvement of the sea keeping behavior of the ship may typically be found in increasing the pure size of the ship, but this comes at a cost.
In the past decades considerable attention has been paid to improving the operability of fast ships in head waves because in those conditions severe damage to people on board as well as to the ship itself could be experienced. The emphasis was on the limitation of the vertical accelerations and in particular the big peaks, i.e. the slams. Typical improved hull forms have been developed and build, such as the Enlarged Ship Concept, Ref [1], [2] and the AXE Bow Concept, Ref [3] and [4]. Much has been achieved in this respect and the operability has been increased significantly. In the present study emphasis is placed on other restricting phenomena when sailing with fast ships in a seaway.
One of these limiting phenomena is the tendency to broach when sailing at speed in following or stern quartering seas.

1.1 THE BROACHING PHENOMENON

Broaching is a well known phenomenon and may be best described as a coupled roll-yaw and pitch motion of the ship. From full scale experience and systematic research it is known that this broaching behavior is often introduced through a combination of a lack of transverse stability of the ship (at speed) and insufficient directional stability.
What generally happens can, in physical terms, best be described as follows: the ship is sailing at high speed in stern quartering seas. Through the high speed the encounter frequency of the ship with the waves is low. Let us now assume the waves come in from the port quarter. When a high wave reaches the stern of the ship the stern is lifted. Because more often then not the sterns

of these ships are broad and flat the ship is simultaneously heeled to starboard. Through this combined pitch and roll motion the bow is now more deeply submerged in the wave crest just in front of the boat. This deep submergence in combination with the roll angle introduces an asymmetry and so a considerable yawing moment on the ship to port. In addition the whole sequence of events leads to a considerable loss of directional stability. This is further aggravated by the fact that these ships in most cases have two rudders each at one of the ship of which the port (windward) rudder will now most likely be partly lifted out of the water.
In order to keep the ship as much as possible on a straight track considerable rudder action is e required. The rudders are pulled over to starboard to correct for the course change and the yawing moment. The rudders, placed aft and underneath the hull, generate a lift force to port and so a counter balancing yawing moment to starboard. Simultaneously however they also generate a considerable rolling moment and in the particular situation under consideration to starboard, which leads to an increase in the undesirable roll motion. If all goes well control is maintained and the boat brought back to its original course with the roll- and the pitch angle at reasonable and manageable values. In the worst case the yaw motion gets out of control and the ship ends up in beam seas at excessive heel, sometimes even leading to a capsize. The photos in Figure 1 show the two phases of a moderate broach.

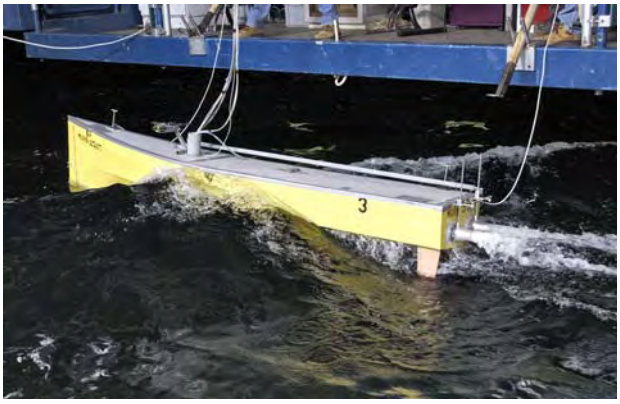

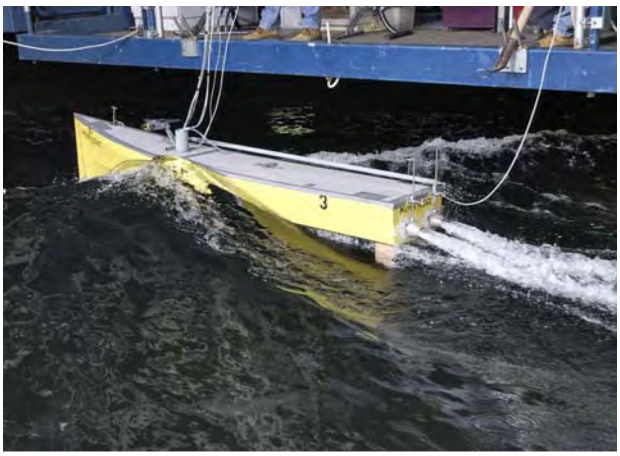

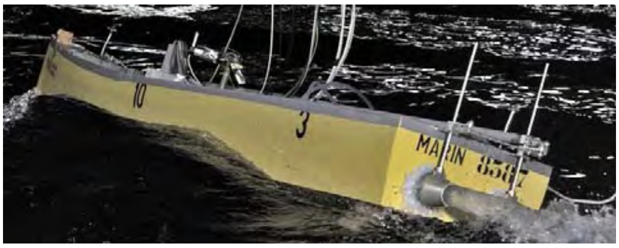

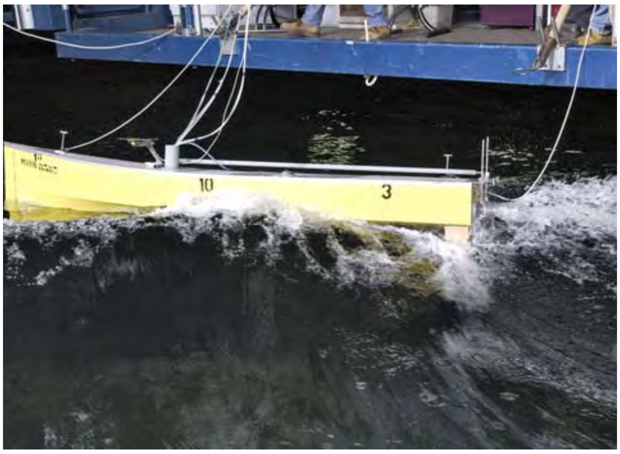

Figure 1. Phases of an AXE hull model without bow fin broaching.

It is known that the phenomenon is most eminent in waves in between 1.3 and 1.5 times the ship length and so for a 40 meter vessel this implies that the encounter frequency becomes almost zero with such waves (i.e. wavelength of 60-70 meters) at or around 20 knots.
Solutions for preventing or reducing the broaching tendency of a ship in typical environmental conditions, such as the North Sea, can be found in:

- Increasing the length of the ship (design issue)
- Increasing or decreasing the speed of the ship considerably (operational issue)
- Changing the heading of the ship with respect to the waves (operational issue)

- Increasing the transverse stability of the ship and so reduce the roll angle (Design and operational)
- Increasing the directional stability by the addition of skegs aft (design issue)
- Appling an additional vertical bow fin (bow rudder) fore.

1.2 POSSIBLE DESIGN SOLUTION

The possible solution which will be evaluated further in this report, is the last one: i.e. an additional vertical fin at the bow. It is designed to reduce the tendency to broach. The very shape of the AXE Bow hull and fore body makes it possible to introduce such a vertical bow fin without much difficulty.

The philosophy behind this is that the vertical bow fin forwards effectively generates the desired yawing moment to keep the ship on track because it is more immersed than emerged as is the case with the rudders aft while at the same time it produces a roll moment that reduces the prevailing roll angle.

A typical vertical bow fin or bow rudder fitted on an AXE Bow could look like depicted in Figure 2.

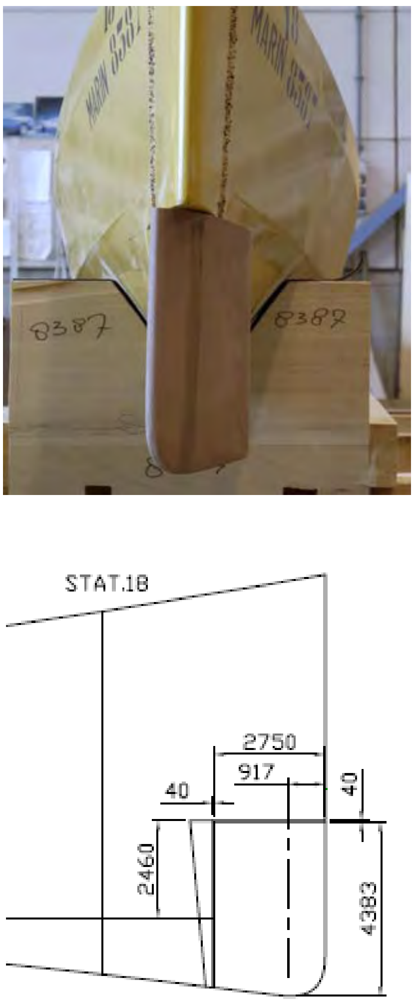

Figure 2. Bow Fin fitted at an AXE hull model

The presumed advantages of a vertical bow fin for yaw and roll motion control in stern quartering and following waves are:

- The rudder remains immersed on the most important moment, i.e. when the bow is pushed down and the stern is pushed up.
- It generates a large additional yaw moment
- It generates a considerable roll moment,
- In the coupled roll, yaw and pitch motion of a ship in following and stern quartering waves it has a positive contribution to the roll stabilization

Possible disadvantages could be:

- Increased calm water resistance due to the transition between rudder and hull
- Increased construction weight at the bow

2. VALIDATION OF THE PRINCIPLE IDEA

To check whether the principal idea works it was decided to carry out a dedicated model experiment with a model of an AXE Bow in the new seakeeping basin of MARIN at Wageningen.
This test was carried out in conjunction with the FAST Project described in previous publications, Ref [4] and Ref [5]. The model used was the AXE Bow model of the FAST project, a 55 meter long patrol boat capable of speeds up to 50 knots.
Main Particulars of the ship are:

Length	=	55.0	meter
Beam WL	=	8.46	meter
Draft midship	=	2.26	meter
Displacement	=	517	tons
Speed max	=	50	knots
GMt	=	2.50	meter

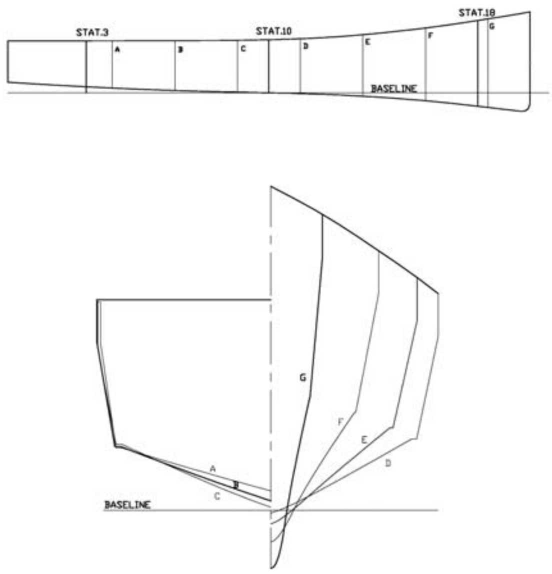

Figure 3. Linesplan of the used Aexebow model

The model was equipped with two water jets with steerable nozzles. The maximum deflection angle of the nozzles was restricted to 23 degrees either side. At the aft end also two fixed skegs were fitted to the hull.
The tests were carried out with the free running model, solely propelled by the two waterjets. The unique SMB facility of MARIN allows the model to run completely free of the towing carriage in irregular waves from any direction. The course of the model is controlled by an autopilot. In the tests with the bow fin there was a direct 1:1 mechanical link between the steering adjustment of the waterjets and the bow rudder. Only the direction of the deflection of the bow fin was reversed with respect to the aft “rudders” to yield a similar yaw moment resulting from the bow fin as was established with the steering nozzles aft.
The tests were carried out in one typical North Sea spectrum, which, according to the available wave scatter diagrams of that area, is only exceeded 5% of the time all year round. The main particulars of this spectrum are
:

- a significant wave height Hs equal to 2.50 meter,
- a peak period Tp equal to 6.75 sec and
- a energy distribution over the frequency range according to the normalized Jonswap spectrum.

Considering the wavelengths in the spectrum a forward speed of around 20 knots was chosen because this posed the largest likelihood of broaching in the situation chosen, i.e. a wave incidence angle of 315 degrees (i.e. port stern quartering). In the spectrum realization a considerable number of tests was carried out to obtain a test run duration of circa 2 hours at full scale.
The tests were carried out both with the AXE Bow model **without** vertical bow fin and with the model fitted **with** the vertical bow fin. The main particulars of the bow fin used are those depicted in Figure 2.

The results are presented in the following figures: in Figure 5 the results for the conventional AXE Bow and in Figure 6 the results for the AXE Bow fitted with the vertical bow fin.
The results are presented as plots of the probability of exceedance (in percentage of the total number in the entire time trace) of the peaks and the through of the time signal under consideration. The horizontal scale is sized to fit the Rayleigh distribution, which comes out as a straight line. The extremes of the peaks and troughs are found at the far right side of the plots, i.e. with the low probability of exceedance.

As may be seen from these results the effect of the application of the vertical bow fin in these conditions is quite significant:
The significant roll amplitudes are reduced by some 30% and the maximum roll amplitude encountered during the 2 hours even by some 40%. For the ship without bow fin the maximum roll angle to starboard is slightly larger than the maximum roll to port. The average roll angle over the entire track is some 0.5 degrees to starboard, which is understandable with the waves coming from the port stern quarter.

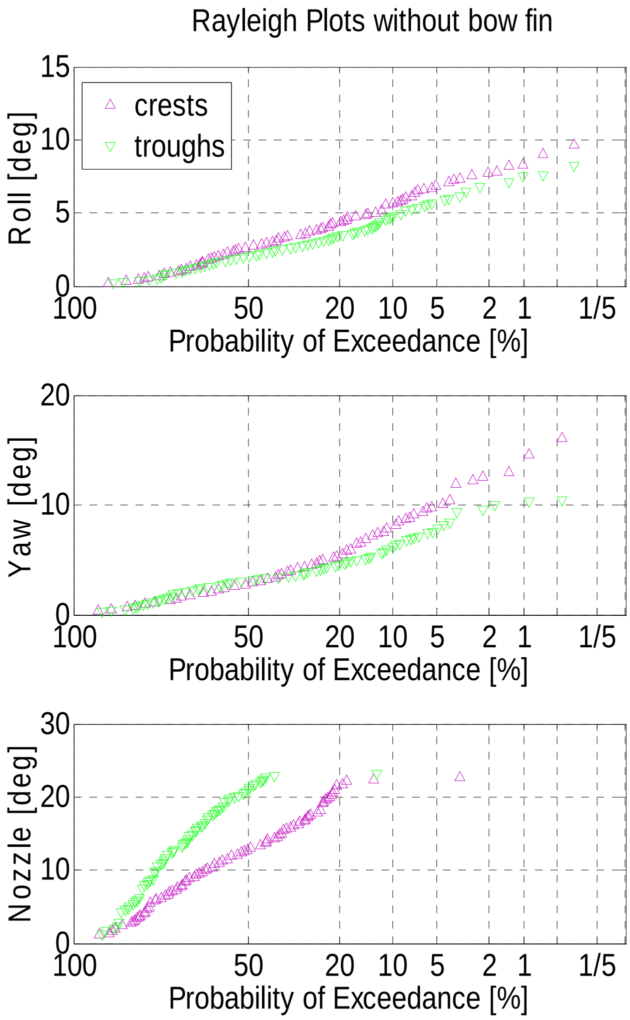

Signal	unit	Mean	stdev	Min	Max
Roll	deg	0,38	2,21	-8,41	9,88
Yaw	deg	0,00	2,97	-10,66	16,40
Aft-Rudder	deg	-4,06	11,88	-23,57	23,10

Figure 4. Rayleigh Plots and Statistics without bow fin

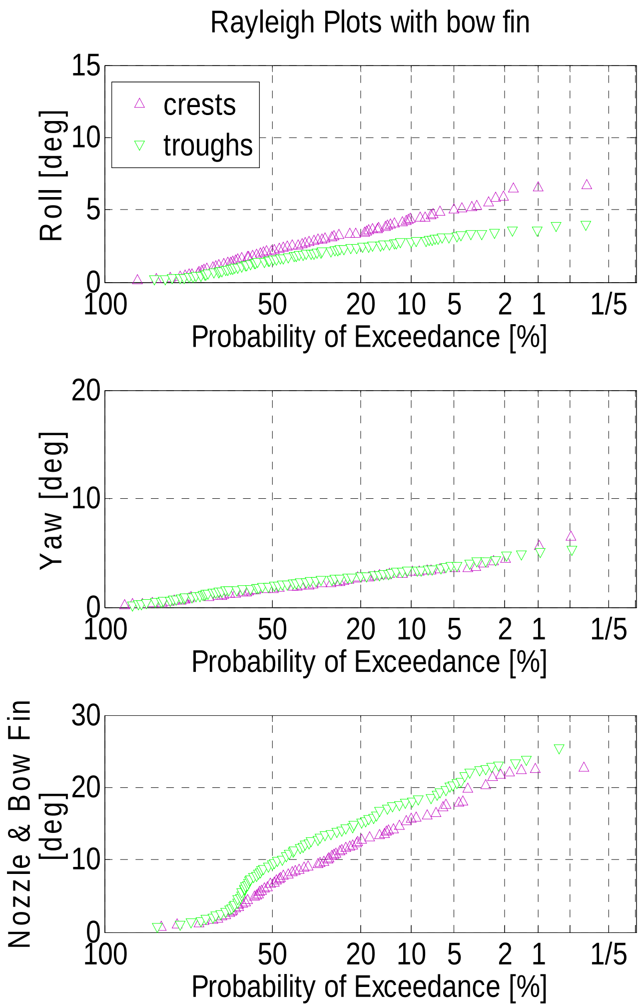

Signal	unit	Mean	stdev	Min	Max
Roll	deg	0,55	1,56	-4,08	6,82
Yaw	deg	0,00	1,49	-5,39	6,55
Nozzle & Bow Fin	deg	-2,79	8,00	-25,86	23,23

Figure 6. Rayleigh Plots and Statistics with bow fin

It is also of interest to note that with the application of the bow fin the reduction of the roll amplitudes to port is considerable larger than the reduction to starboard. This may be partly explained by the fact that the autopilot used to keep the ship "on track" is controlling the nozzles for the ship without bow fin and both the nozzles and the fin for the model with bow fin. This autopilot has as only input signal the yaw angle (course of the ship) and not the roll motion. The average offset in the course due to the wave action from port quarters shows up as an average nozzle angle of circa 2.5 degrees. This yields the differences in the distribution of peaks and troughs in roll for the model with vertical bow fin. Because the bow fin introduces a significant roll moment and this is not the case with the waterjet nozzles which are placed much closer to the vertical center of gravity of the ship.
An autopilot which controls the combination of both, i.e. controlling yaw and roll simultaneously, in a way similar to the already existing "rudder-roll" stabilizers, may possibly overcome this phenomenon. For the time being the "average" between the distributions of the peaks and the troughs could be considered for the sake of comparison. The roll angle reduction in that situation with the bow fin added increases then even further and well to over 50%!
A similar trend may be seen with the yaw motion:with the bow fin added the yaw motion is significantly smaller than without. Here the reduction in both the significant and the maximum amplitudes is also in the order of 50%. In particular the reduction in the extreme values of yaw and roll are of interest because these may be the introduction of a broach.
From the registration of the rudder angles during the tests it may be seen that much less rudder action (i.e. smaller angles) is necessary to keep the ship on track for the model with bow fin. This is understandable because the amount of control (surfaces) has been increased significantly. In the situation without bow fin the maximum nozzle angle is reached more often than not. In the situation with bow fin this is hardly the case, which leaves much more room to control the ship in those conditions.

The general conclusion that may be drawn from this experiment is that the application of the vertical bow fin in stern quartering seas is very effective indeed in reducing both the roll and the yaw motion.

3. THE VARIOUS CONCEPTS OF THE BOW FIN

Now the validity of the concept has been demonstrated, the actual design of the fin and the design of a controller had to be assessed.
The first step in this process was to establish the effectiveness of various bow fin designs in generating side force, yaw moment and rolling moment with respect to the one used during the tests at MARIN.
The aim of the series of experiments was to determine the minimum size rudder that is adequate for the job. The reason behind this aim is found in some structural and interior layout limitations and the possible negative effect of the bow fin on the calm water resistance because the fin will not be used for a certain amount of time and should therefore generate as little disturbance as possible in those conditions.
This aim was to be achieved by measuring a number of the hydrodynamic derivatives necessary for inclusion in the mathematical model available at the Ship hydrodynamic Department (FASTSHIP) for all configurations considered feasible as vertical bow fin on the AXE Bow.
The following six different configurations have been examined:

The first three are all vertical bow fins incorporated in the bow profile of the AXE Bow model as presented above. In principle it is a change the rudder area established by keeping the height of the rudder as in the original design used in the MARIN tests and reducing the chord length in two steps yielding the original or large rudder, the medium rudder and the small rudder. The principal dimensions of these rudders are depicted in the Figure 7a, 7b and 7c below.

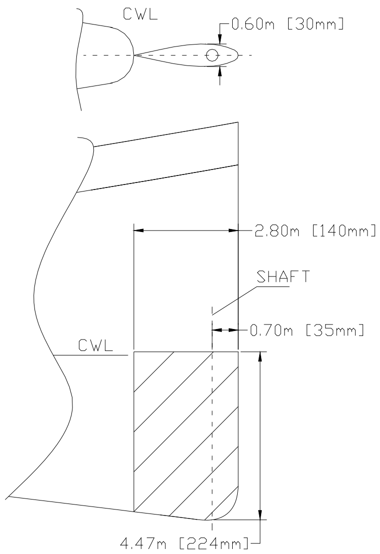

Figure 7a. Large bow fin

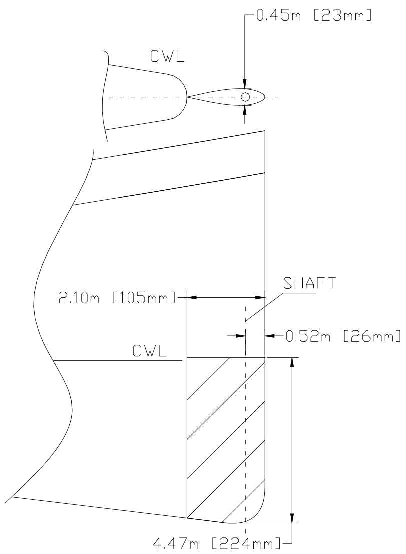

Figure 7b. Medium bow fin

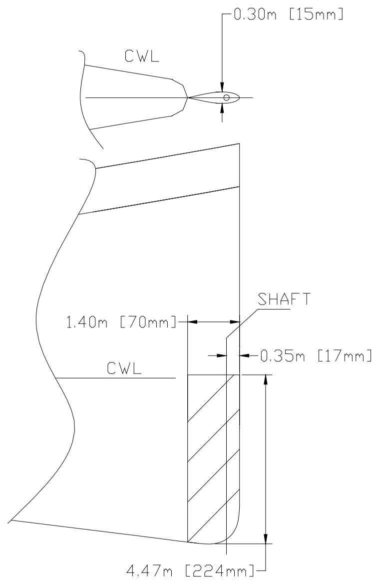

Figure 7 Small bow fin

The reduction of the bow fin area by reducing the chord length of the fins implies an effective increase in the aspect ratio of the fins. This had the additional beneficial effect that the beam of the cross section just after the aperture in which the fin was fitted became smaller also. This makes the transition or “blending” of the vertical bow fin shape, with its typical foil type cross section, into the hull more streamlined.
Another possible realization of the bow fin is found in the use of a so called Magnus Rotor in the most forward part of the bow section. The other three configurations investigated were all based on the use of a Magnus rotor.
The Magnus rotor works to the effect that a rotating cylinder placed in a flow generates a lift force perpendicular to the incoming flow. The lift force generated is proportional to the velocity of the incoming flow, which is the speed of the ship Vs in m/sec, the rotation angular velocity or ω in rad/sec of the cylinder and the radius of the cylinder in m squared. From earlier tests it is known that the Magnus rotor is a very efficient lift generating device.
The very shape of the AXE Bow with its rounded sections lends itself very well for the application of such a rotor. Without extruding from the hull shape as is a rotor with a diameter of 0.35 meter can be placed at the bow. The rotor is extended in length till the design water line of the ship.
The biggest challenge lies in the incorporation of the rotor in the hull shape and the design of the hull shape just abaft and in the vicinity of the rotor. No results in the literature were known about the effect of this on the lift generating capabilities of the Magnus rotor. Three different configurations have been tested:

- Configuration 1 with the hull of the ship “faired” around the aft half of the rotor. This configuration yields almost no deviation from the original bow design

- Configuration 2 with a gap just behind the rotor in length equal to the diameter of the rotor, which is then rotating in a sort of “gap”. This gap will have some influence on the calm water resistance when the rotor is not in use.
- Configuration 3 with a Magnus rotor extending below the bow. In real life this would be a retractable rotor. The shape of the AXE Bow lends itself very well to such a set up. It yields an unobstructed hull when not in use and a most likely very effective rotor when used. In addition the shape of the AXE Bow places this rotor at a considerable distance below the center of gravity generating large roll moment.

The principal dimensions of the three configurations are depicted in the Figure 8a, 8b and 8c.

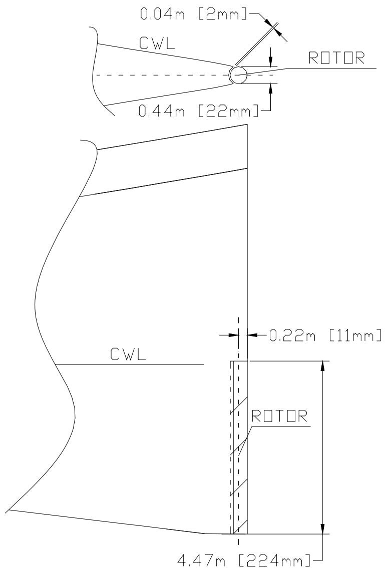

Figure 8a. Faired in Rotor

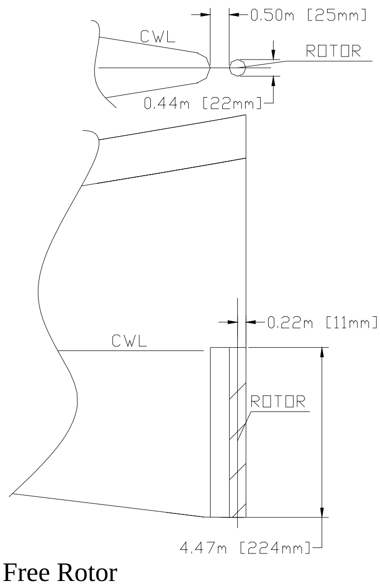

Figure 8c. Free Rotor

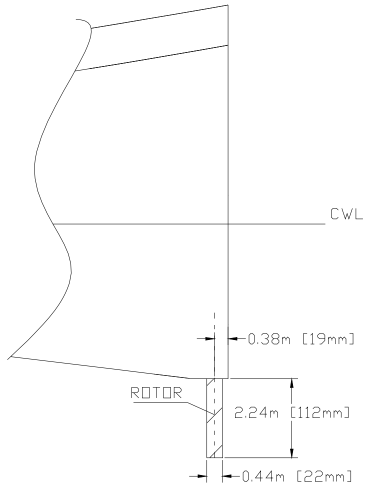

Figure 8c. Retractable Rotor

An extensive series of experiments have been carried out using the same model of the AXE Bow as used in the previous MARIN free sailing experiments described above. In the present tests however the model was not fitted with the waterjets but with two rudders aft. This was done because for the sake of comparison the rudders produced much more repeatable results than the waterjets, with their flow dependent steering properties. The dimensions of these conventional aft rudders are presented in Figure 9.

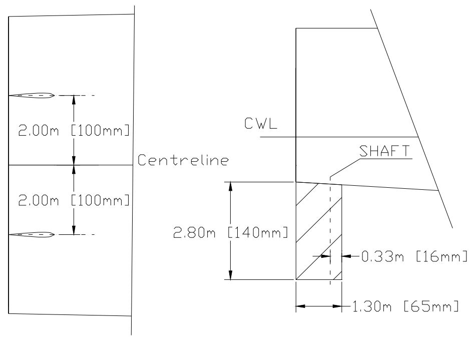

Figure 9. Conventional rudders

All configurations of a vertical bow fin as mentioned above have been fitted to the model and consequently been tested in the tank.

The new series of tests have been carried out in the towing tanks of the Delft University of Technology. The tank is 142 meters long, 4.25 meters wide and has a maximum water depth of 2.5 meters. The towing carriage is capable of achieving speeds up to 8.0 meters per second.
During the tests the model was rigidly connected to the towing carriage by means of a six component dynamometer and the six degrees of freedom oscillator called “Hexamove” which was used in this measurement setup as a model position and attitude manipulator. Forces and moments have only been measured on the

model as a whole, no forces on the rudders or rotors have been measured separately. The test layout is depicted in Figure 10.

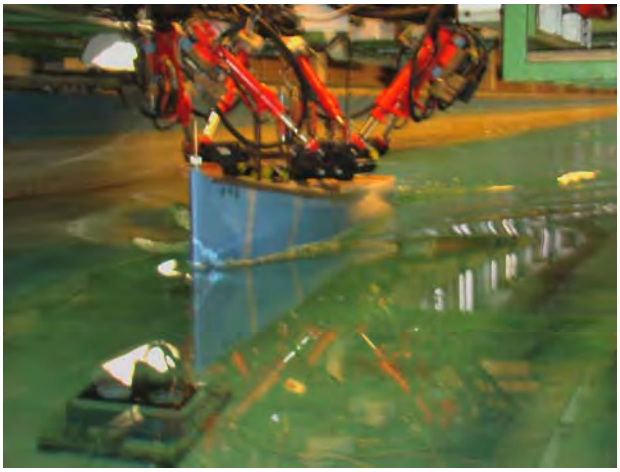

Figure 10. Hexamove setup

The tests have been carried out with the model in the calm water trim and sinkage corresponding to the forward speed under consideration. The following parameters and all their possible combinations have been varied during the tests:

- Forward speed of the model at 15, 25 and 35 knots full scale for the bow rudders and at 15 and 20 knots for the rotors, due to limitations imposed by the available facilities at that time.
- The fin angle between minus 20 and plus 20 degrees
- Three different yaw angles, i.e. 0 and plus and minus 5 degrees.
- In the case of the Magnus rotors different relations between forward and rotational velocity of the rotor expressed in the "k" factor, i.e. k = .

The tests generated a large amount of results for use in the mathematical model. In the context of the present paper only a limited amount of the results can be presented. These results are primarily aimed at facilitating the comparison between the various configurations.

In Figure 12a and 12d the side force on the ship is presented at 15 knots. This speed has been chosen because it makes a comparison between the configurations possible since it is used with all configurations. In Figure 12a the results for the bow fins are presented and in Figure 12d the results for the rotors. For the sake of comparison the same results for the conventional rudders aft are presented in the rudders figure.

In Figure 12b and 12e the yaw moments of the various configurations is presented, once again in Figure 12b for the bow fins and in Figure 12e for the rotors. Here too, the results for the aft rudders are presented in the rudders figure.
Finally in Figure 12c the roll moment is presented for the bow fins and in Figure 12f the results for the rotors.

Direction	Positive
Aft Rudder Angle	Trailing Edge Starboard
Bow Fin Angle	Trailing Edge Starboard
Bow Rotor	Anticlockwise From above

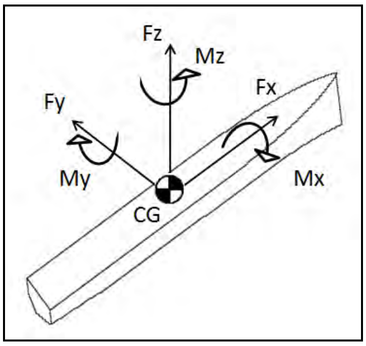

Figure 11. Defenitions

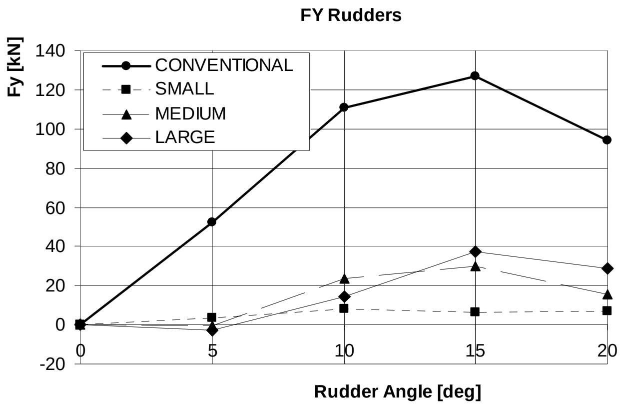

Figure 12a. Side Forces Rudders

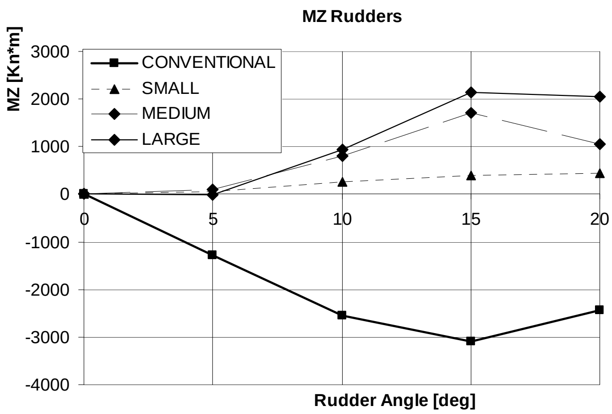

Figure 12b. Yaw Moments Rudders

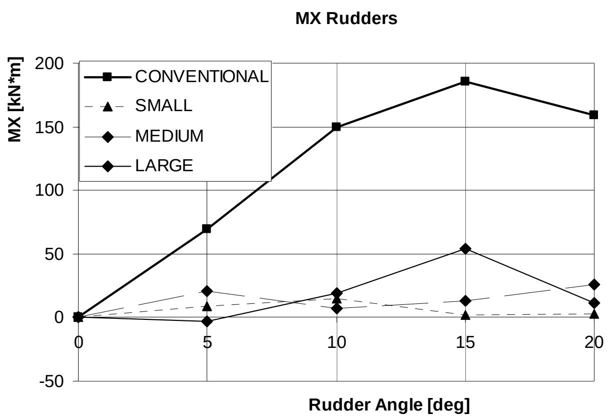

Figure 12c. Roll Moments Rudders

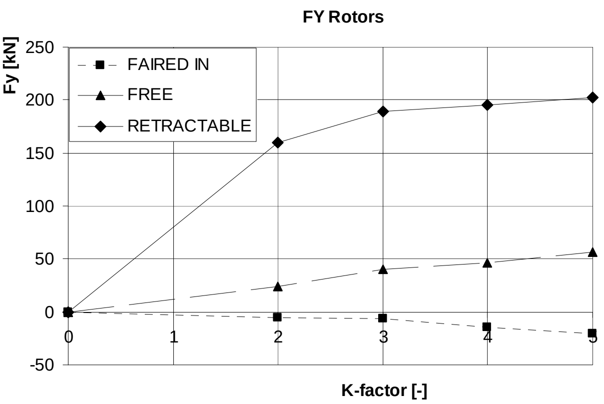

Figure 12d. Side Forces Rotors

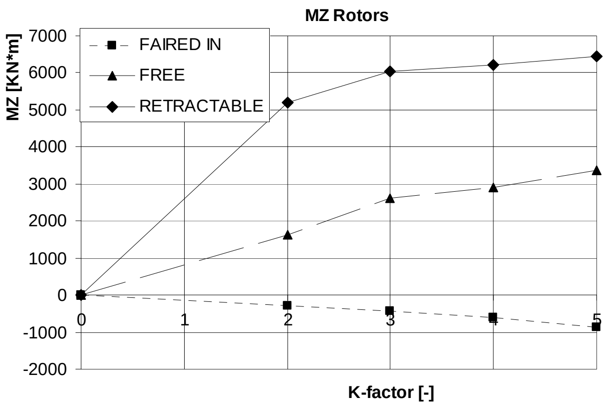

Figure 12e. Yaw Moments Rotors

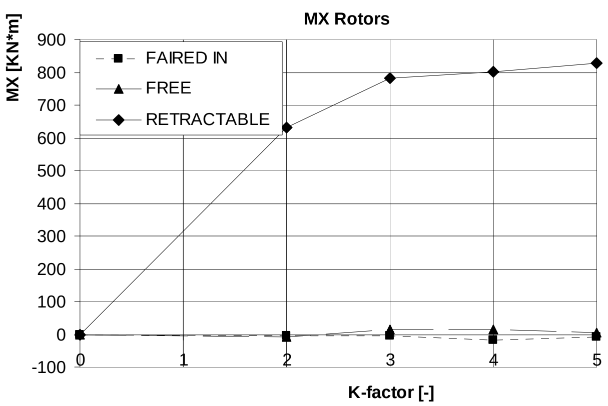

Figure 12f. Roll Moments Rotors

What may be concluded from these results is that the small fin at the bow generates a maximum side force of circa 10 kN, the medium fin a maximum of 30 kN and the large fin a maximum of 40 kN. So the larger size bow fin is certainly the largest lift generator, although it is not proportional to size. However they all compare relatively low in efficiency with the conventional rudders, which generates a maximum lift force of around 120 kN. It should be noted however that this is generated by two conventional rudders aft. The total area of the conventional rudders aft added together is still almost half the area of the large vertical bow fin fore. Because they operate underneath the hull there efficiency is greatly enhanced by the end plate effect of the hull. This reduced efficiency of the bow fins may, amongst others be attributed to the rather complicated flow around the interception of the trailing edge of the fin with the hull geometry and also to ventilation effects. It was noted during the tests that serious ventilation could occur in the more heavily loaded conditions of the foils. This could be remedied by placing the top chord of the fins lower in the water guaranteeing a larger distance to the free surface or by the use of fences at the top. None of these have in the present study been investigated.

In the “near to broaching” condition however this difference in efficiency could be quite different because at least one of the aft rudders may certainly be lifted partly out of the water as can be seen on the photographs in Figure 1. This will yield a serious reduction in efficiency due to loss of submerged rudder area and also ventilation effects.

When the yaw moments of the three bow fins are compared the similar trend may be observed: the large fin produces roughly 2100 kNm, the medium fin 1800 kNm and the small fin 500 kNm. As may be observed in the generated side force as well the maximum moment is reached at 15 degrees fin angle and not at 20, except with the small fin.. The maximum yaw moment with the conventional rudders is 3100 kNm and also reached at a 15 degrees rudder angle. The difference in side force production is larger between rudder and fins as the differences in yaw moment.

The generated roll moments of the three bow fins are also significantly smaller than those generated with the conventional rudders, i.e maximum 14 kNm, 28 kNm and 60 kNm compared to some 186 kNm for the aft rudders.

Although not shown here all forces and moments are strongly dependent on the forward speed. In most cases the increment with speed is rather more then quadratic.

The results for the rotor show in general that the “faired in” rotor design is hardly more effective then the smallest fin in all modes, ie. for side force, yaw moment and roll moment. The rotor with “the gap” behind it, i.e. (configuration 2) is far more effective and approaches the large bow fin in characteristics.

By far the most effective is the (retractable) bow rotor in configura-tion 3. Although the rotor used in the tests is only half the span of the other two rotors it out performs

all the others. This can of course be explained by the fact that it is completely undisturbed by any other part of the structure. In addition combined with the AXE Bow hull it is so deeply submerged that it is entirely free from ventilation effects in any of the conditions tested.
The biggest advantage may be however found in the relatively enormous roll moment it generates when compared with all the others, fins and rotors and in particular also with the conventional rudders aft. The retractable rotor outperforms the aft rudders in this respect with a factor of around 4.
For the rotor in configuration 3 it is also obvious that the maximum lift is achieved at lower values of k, implying lower number of revolutions.
The relative differences in calm water resistance of all the configurations is compared in Figure 13. From these results it is obvious that the "faired in" rotor has the least resistance increase

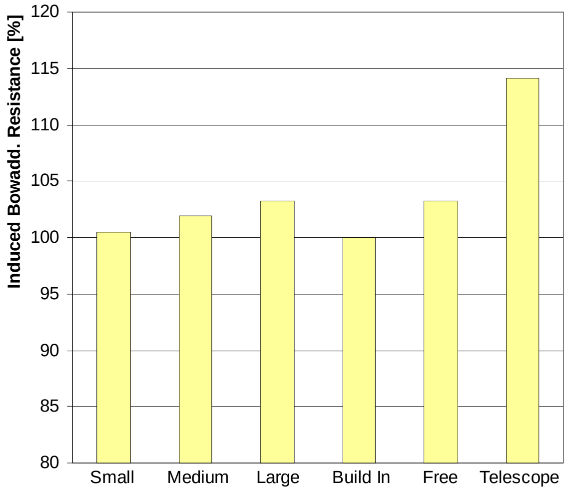

Figure 13. Comparison Rudders and Rotors

The retractable rotor has the largest resistance increase when deployed, which will obviously be the case in beam seas to following seas, in which conditions the resistance increase is less of an issue.

4. CONCLUSIONS

From the results of these experiments it may be concluded that a vertical bow fin will have a beneficial effect on the controllability of a fast ship in following and stern quartering seas.
The configuration most suited, when combined with an AXE Bow hull shape is the retractable rotor underneath the bow. Second best is the medium to large bow fin.
There is a great opportunity for a combined yaw-roll autopilot under these circumstances.

References

[1] J A Keuning and J Pinkster
"Optimization of the seakeeping behavior of a fast monohull"
FAST Conference Proceedings, Southampton UK 1995
[2] J A Keuning and J Pinkster
"Further design and seakeeping investigations into the Enlarged Ship Concept"
FAST Conference Proceedings, Sydney Australia 1997
[3] J A Keuning, J Pinkster and F van Walree
"Further inverstigations in the hydrodynamic performance of the AXE Bow Concept"
WEGEMT Conference on High Performance Vehicles September 2002, Ischia Italy
[4] J A Keuning, S Toxopeus and J Pinkster
"The effect of the bow shape on the seakeeping Performance of a fast monohull"
FAST Conference Proceedings Southampton September 2001
[5] FAST Project
Seakeeping Model tests for two patrol vessels
MARIN 19112-1-SMB

NUMERICAL AND EXPERIMENTAL STUDY OF WAVE RESISTANCE FOR TRIMARAN HULL FORMS

Thomas Maynard, Research student at Australian Maritime College, PO Box 986, Launceston, TAS 7250, Australia
Prasanta K Sahoo, Senior Lecturer (Hydrodynamics), National Centre for Maritime Engineering and Hydrodynamics, AMC/UTAS, Launceston, TAS 7250, Australia
Jon Mikkelsen, Senior Instructor (Naval Architecture), Faculty of Applied Science and Engineering, University of British Columbia, Vancouver, BC, Canada.
Dan McGreer, Principal Engineer, Aker Yards Marine Inc., Vancouver, British Columbia, Canada.

SUMMARY

This paper investigates a systematic series of high-speed trimaran hull forms. Trimaran vessels are currently of interest for many new high speed ship projects due to the high levels of hydrodynamic efficiency that can be achieved compared to mono-hull and catamaran hull forms. The core of the study involves determining the wave resistance for each model in the series in conjunction with varying longitudinal side hull locations. The methods employed to determine the wave resistance of each trimaran model comprise of computational fluid dynamics (CFD) suite SHIPFLOW, theoretical slender body theory and experimental investigations.

The trimaran hull forms are transom stern high-speed displacement hull form vessels possessing moderately high L/B ratios. A wide variety of data was acquired due to the parametric space and various side hull locations. As a result, these data shows clear trend from which accurate assessments could be made. Results presented in this paper offer considerable promise and it is envisaged that further work need to be completed before further understanding can be gained.

1. INTRODUCTION

The development of the trimaran hull form originates from the general increase in slenderness ratio of a mono-hull vessel, to increase the speed of a vessel with corresponding reduction in required power. Investigations into the resistance of trimarans have proven that such hull forms have lower resistance at high speeds when compared with catamarans and mono-hulls of similar displacement. Other advantages of a trimaran over more conventional hulls are an increase in deck space, an increase in stability and passenger comfort. An example of a low resistance high speed trimaran is the *Ilian Voyager*. A 21 m trimaran built to demonstrate the efficiency of the powered trimaran hull form. The *Ilian Voyager* holds the record for the fastest circumnavigation of the British Isles without refueling.

Having three separate hulls on a trimaran creates a higher total wetted surface area compared to a similar mono-hull or catamaran. This higher wetted surface area increases the frictional resistance therefore creating comparatively higher resistance at low speeds. At high speeds the wave making resistance is relatively low due to the use of slender hulls. This is based on the widely accepted assumption that as the vessel becomes finer the wave making resistance decreases. Wave making resistance is also affected by the interference between the separate hull wakes. Optimum placement of the side hulls will result in a wake interference that reduces this resistance. The combination of a slender hull form and optimum placement of side hulls can result in a much lower resistance at high speeds when compared to both catamaran and mono-hull designs.

This paper constitutes an analysis of a systematic series of trimaran hull forms with the effects of various side hull locations on wave resistance. Comparisons are drawn between the methods, which include application of computational fluid dynamics, the slender body theory and experimental work to predict the wave resistance.

The systematic series of trimaran hull forms under analysis was based on the AMECRC systematic series of high-speed transom stern displacement hull-forms, where the outriggers are scaled versions of the main hull. The trimaran series were simulated using CFD suite SHIPFLOW and using the Slender Body Method (SBM). The data generated was then compared against experimental data. The experimental data obtained by Kiso (2001) was further complimented with additional tests to validate the original data for one trimaran model.

2. BACKGROUND

Pattison and Zhang (1995) have presented resistance characteristics of trimarans when compared against similar vessels of mono-hull or catamaran configurations.

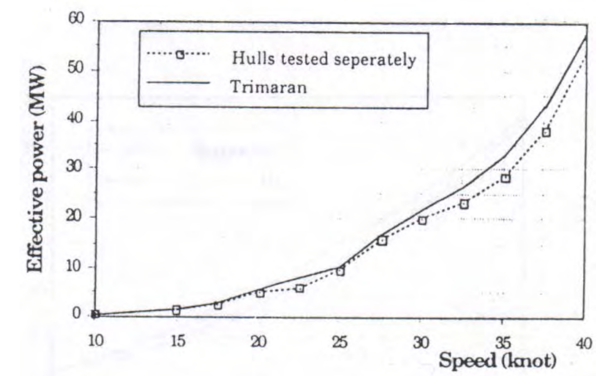

Figure 1: Influence of viscous interference on effective power, Pattison and Zhang(1995)

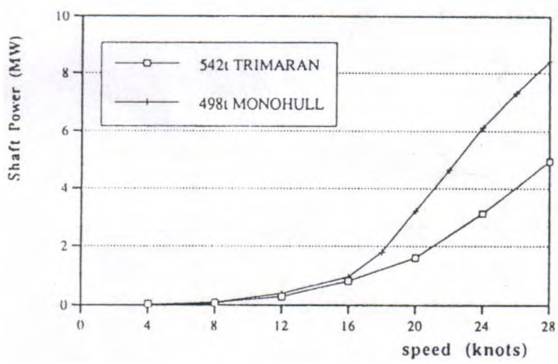

Figure 3: Shaft Power for mono-hull and trimaran offshore patrol vessels, Pattison and Zhang(1995)

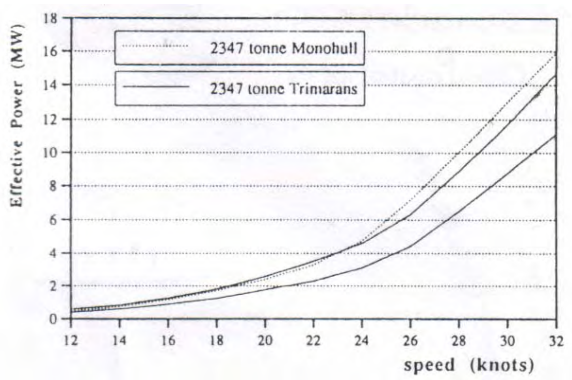

Figure 2: The effective power of a trimaran and mono-hull of the same displacement, Pattison and Zhang(1995)

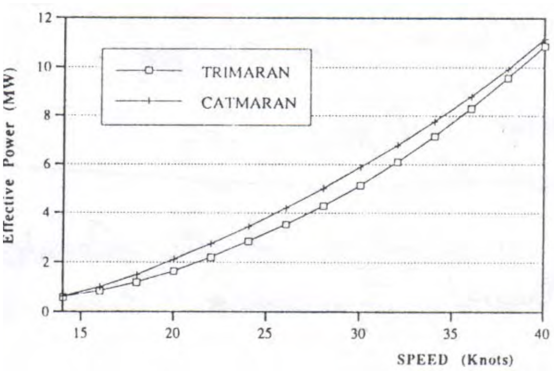

Figure 4: Effective power for a 700 tonne trimaran and catamaran, Pattison and Zhang (1995)

Figure 1 depicts the resistance of a trimaran when towed separately and as a whole, which clearly shows that interference plays as advantageous role in reducing resistance and hence effective power. Figure 2 is a comparison between a slender mono-hull frigate against a trimaran of the same displacement. The upper curve of the trimaran is at 5 % side hull displacement whereas the lower curve is the prediction for a slender monohull and suggests the lower limit for trimaran resistance. Figure 3 compares the significant difference in power between trimaran and mono-hull offshore patrol vessels of similar displacement. This comparison shows the trimaran to have lower resistance at all speeds. Figure 4 is the comparison of a geometrically similar catamaran and trimaran where the resistance is determined by use of Taylor series.

The paper by Ackers et al (1997) investigates the resistance characteristics of trimaran hull form configurations. Primarily the key areas of focus involve the interference effects between main and side hull(s). The variables for the experiments include side hull configuration, as illustrated in Figure 5, side hull locations, side hull angle of attack, ranging from -2º to 4º, and side hull displacement, corresponding to 5.8%, 8.4%, 10.9% and 13.6% total displacement of the trimaran.

In order to calculate the interference effects of each configuration both the non-interference residuary resistance and the actual residuary resistance were found. The non-interference residuary resistance was obtained by testing each hull separately over a range of speeds. Equation 1 was used to find the non-interference residuary resistance of the whole trimaran, where ratio of the wetted surfaces is employed.

$$C_{RNI} = C_{RMH}\left(\frac{S_{MH}}{S_T}\right) + C_{RSH}\left(\frac{2\times S_{SH}}{S_T}\right) \quad (1)$$

As the side hull are smaller than the main hull the corresponding Reynolds number is much smaller and as a result, the frictional resistance must be calculated for both sides and the main hulls as shown in Equation 2.

$$C_{FT} = C_{FMH}\left(\frac{S_{MH}}{S_T}\right) + C_{FSH}\left(\frac{2 \times S_{SH}}{S_T}\right) \qquad (2)$$

From this the residuary resistance, C_R, can be obtained by subtracting C_{FT} from C_F. The relative interference effects of each side hull configuration can be obtained by subtracting C_{RNI} from C_R, this value is represented as a percentage, see Equation 3. Thus, to determine the increase in residuary resistance of trimaran configurations, multiply the non-interference residuary resistance by the percent interference.

$$\Delta C_R = C_R - C_{RNI} \qquad (3)$$

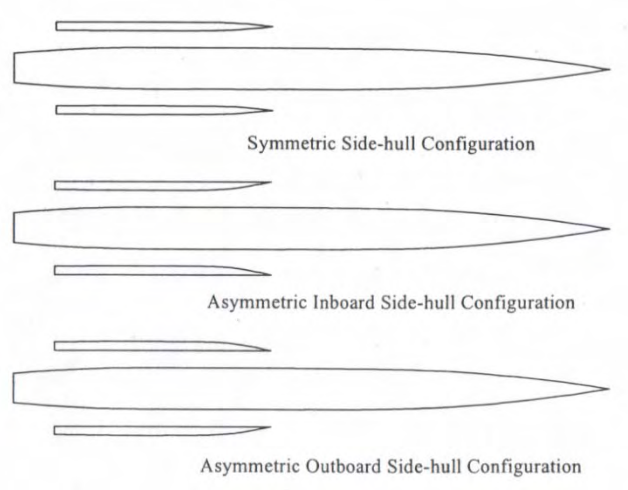

Figure 5: Model side hull configurations (Ackers et al (1997))

According to Ackers et al (1997), as a result of the investigation into the resistance characteristics of trimaran hull forms, the following conclusions can be drawn:

- A well designed trimaran could out perform a mono-hull of the same displacement at high speeds, as a 15% or greater powering advantage can be expected.

- Contour plot prove to be a useful design tool as they clearly show interference effects of both transverse and longitudinal side hull locations.

- From the data obtained within the test matrix range, it was generally found that displacement had little impact on interference.

- In relation to side hull symmetry, the interference significantly depends on the inboard face of the side hull. Generally it was found a side hull with symmetry minimizes baseline resistance.

The paper by Suzuki and Ikehata (1993) focuses on determining the optimum position of trimaran outriggers in order to minimise wave resistance. The study of the trimaran configuration involves representing the hull form mathematically, with cosine waterlines and parabolic frame lines, which then enable the resistance to be calculated mathematically. Furthermore, the study has been validated by obtaining data through model testing. For this study the configuration shown in Figures 6 and 7 were adopted by the authors.For symmetrical hull forms at the fore and aft, the main hull is mathematically represented by Equation 4 and the side hull by Equation 5.

$$y = \pm b \cos\frac{\pi}{2}x\left\{1 - \left(\frac{z}{t}\right)^4\right\} \qquad (4)$$

$$y \pm y_0 = \pm b_0 \cos\frac{\pi}{2\lambda_0}(x - x_0)\left\{1 - \left(\frac{z}{t_0}\right)^4\right\} \qquad (5)$$

Suzuki and Ikehata (1993) state that in the present examples, the side hull are scaled down versions of the main hull, with a scale factor of 1/3. As a result of this the displacement of the side hulls becomes 1/27 of the main hull. This displacement is much lower than the optimum value found by Seo et al (1973), which states that by satisfying the conditions below in Equation 6, maximum wave cancellation can be expected. As a result of this the side hulls required are unpractical as they are too large.

$$\begin{aligned} &\nabla_0 / \nabla = 0.6 \sim 0.7 \\ &x_0 = 2\pi F_n^2 \\ &y_0 = 0.4 \end{aligned} \qquad (6)$$

Model experiments were carried in order to validate the hydrodynamic effects of the side hulls. The models were developed to allow numerous side hull configurations, providing a large database of information regarding wave, trim and sinkage analysis. The model names and side hull locations are shown in Table 1.

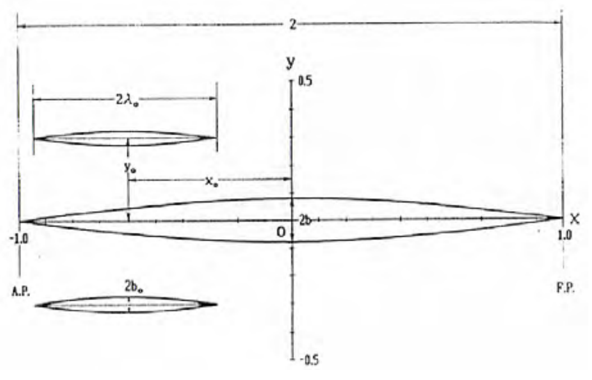

Figure 6: Trimaran Coordinate System, Suzuki & Ikehata (1993)

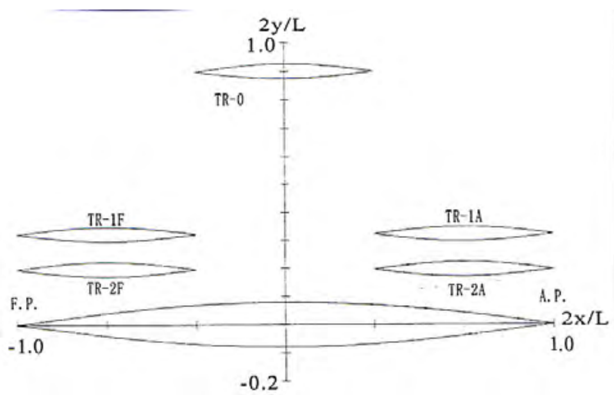

Figure 7: Model Testing Configuration, Suzuki & Ikehata (1993)

As a result of the investigation by Suzuki & Ikehata (1993) the following conclusions were established:

- Through linear superposition of amplitude functions for the main hull and side hulls the wave resistance can be minimized by optimizing the locations of the side hulls.
- Generally the residuary resistance coefficients of a trimaran are larger then the coefficients of each hull, treated as a mono-hull. However, through optimization of side hull positions at set Froude numbers, the trimaran hull form possesses lower residuary resistance coefficients.
- Changes of trim and sinkage caused by side hull locations can change the residuary resistance, as the side hull located at the stern of the main hull possesses low residuary resistance then when located at the bow.
- In order to lower the wave resistance caused by wave making interaction between the main and side hulls, optimization of side hull locations need to be analyzed.

Table 1: Model Names and Position of Side Hulls, Suzuki & Ikehata (1993)

Model Name	Design Fn	x_0	y_0
MH-0	-	without side hulls	
TR-0	-	0.0000	+-0.9000
TR-1 A	0.4	-0.6667	+-0.3220
TR-1 F		0.6667	
TR-2 A	0.5	-0.6667	+-0.1950
TR-2 F		0.6667	

The paper by Suzuki et al (1997) focuses on using the Rankine source panel method in order to numerically dictate the wave making characteristics of the trimaran hull form. This method is adopted in order to account for the hydrodynamic lifting forces on the side hull due to interference. The study is based around previous work conducted by Suzuki and Ikehata (1993), where the numerically predicted resistance coefficients are compared to results obtained through physical experiments. The numerical analysis for the study involved taking the ordinary Rankine source method and modifying it to allow for the lifting force, by applying the vortex lattice method. This method allows for a further optimized side hull configuration in relation to wave resistance. Suzuki et al (1997) concluded by stating that using the Rankine source panel method, the effects from hydrodynamic lift are accounted for. The studies undertaken prove to be quite similar to the physical experimental data, in relation to wave resistance coefficients. The importance of analyzing wave patterns caused by hull interaction for a trimaran is vital in order to dictate an accurate tool for predicting and investigating the optimum positions for the hulls.

The paper by Yeung et al (2004) emphasizes the importance and consideration of wave drag for high-speed vessels operating at Fn 0.5 and above. The study involves analyzing and expanding on the formulation for Michell's resistance for single hull forms, where the hull is considered thin, i.e., low L/B ratio. Not only is frictional resistance analyzed but the resistance caused by the interference between the hulls. From the thin-ship theory, the expression for total wave resistance is shown in Equation 7, where the second sum considers wave interference given the number of hulls.

$$R_{wT} = \sum_{i=1}^{n} R_{wi} \div \sum_{i=1}^{n-1} \sum_{j=i+1}^{n} R_{wi \Leftrightarrow j} \qquad (7)$$

Specialized quadrature techniques are used to provide internet based 'resistance evaluator' that dictates effects of stagger and separation, in order to optimize the volumetric distribution of a trimaran. The predictions are validated through experimental data for various multi-hull configurations. Yeung et al (2004) examine and optimize the trimaran hull form using the computer based program, TRIRES. As a result, given a specific design, the optimal volumetric distribution and stagger can be determined.

The paper by Brizzolara et al. (2005) investigates the hydrodynamic behavior and inference effects for different trimaran hull form configurations, particularly fast trimaran ferries. The primary objective is to obtain the optimum hull form configuration; this is undertaken with the help of CFD tools together with modulus for automatic geometry generation and algorithms. An in depth analysis was conducted involving systematically varied configurations to the trimaran as well as numerical calculations regarding wave making resistance.

The trimaran hull design was based on a general hull form for current fast transportation vessel, possessing a round bilge main and side hulls. The models were developed with a scale of 1/50.The parameters for both the actual hull and model are given in Table 2. The test matrix for the trimaran configurations are illustrated in Table 3, where stagger (ST) values dictate the longitudinal positions of the side hulls in regards to transom location. The clearance (CL) values represent the transverse locations of the side hulls in regards to hull symmetry. The models were tested for Fn 0.35 to 0.60.

Table 2: Vessel Principal Characteristics, Brizzolara et al (2005)

	Full Scale		Model	
	Main	**Side**	**Main**	**Side**
Scale Factor	1.00	0.33	50.00	50.00
L_{WL} (m)	105.6	35.19	2.11	0.70
T (m)	4.42	0.69	0.09	0.01
B (m)	8.83	1.65	0.18	0.03
Δ (t, kg)	2318.	14.37	18.12	0.11
V_{MAX} (kn)	36.00	36.00		
C_B	0.55	0.35	0.55	0.35
L/B	11.96	21.50	11.96	21.50
B/T	2.00	2.39	2.00	2.39

Table 3: Towing Test Matrix, Brizzolara et al (2005)

	ST / L_{WL}			
CL /	0%	10%	20%	30%
9.90%	P11	P12	P13	P14
11.10%	P21	P22	P23	P24
13.40%	P31	P32	P33	P34
15.00%	P41	P42	P34	P44

The CFD method incorporated used a linear Rankine sources panel method to find the solution of the free surface potential flow. Brizzolara et al. (2005) states that to correctly predict wave resistance of high speed hulls, the dynamic attitude of the hull must be modeled; the numerical method presented in the paper satisfactorily achieves this. The automatic optimizer method is based on an algorithm coupled with a CFD solver and an intermediary program that generates the panel mesh for each hull configuration. Results of the optimizer are shown in Figure 8.

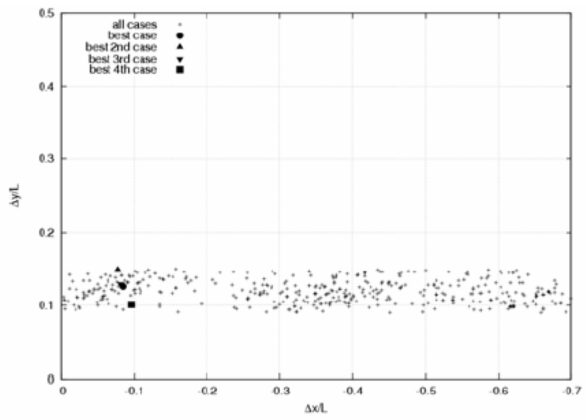

Figure 8: Plot of the evaluated individuals by optimisation algorithm, Brizzolara et al. (2005)

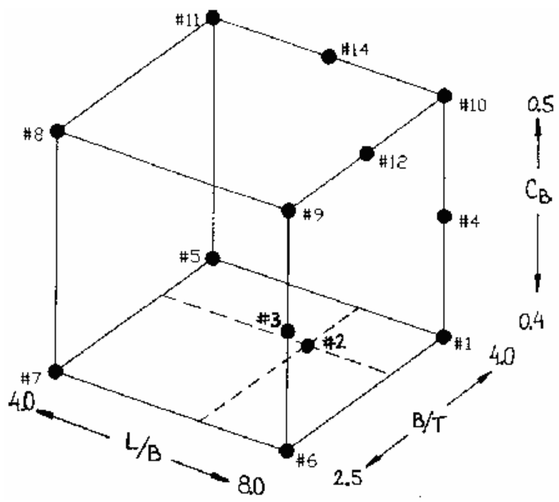

Figure 9: AMECRC Systematic Series ‘Parameter Space, Bojovic (1995)

As a result of the paper an automatic optimization method has been developed in relation to side hull locations for given Fn. Effects of trim and sinkages have been discussed due to their critical effects to the wave resistance. Further investigations involve considering volumetric distribution and relative volume and dimension of side hulls.

3. HULL FORM

The trimaran hull forms under investigation have been developed from the systematic series developed by the Australian Maritime Engineering Cooperative Research Centre (AMECRC) as illustrated in Figure 9. Seven of the fourteen models were selected for computation as trimaran models, since some of the models were too wide to be considered as trimaran models. The scale factor of the side hulls are based on a previously constructed trimaran configuration involving Model 9 of the AMECRC series. The parameter space of the series is shown in Table 4.

Table 4: AMECRC Systematic Series parameters [Bojovic (1995)]

Parameters	L/B	B/T	C_B	LCB aft of midship	C_P	C_{WL}	A_T/A_X	B_T/B_X
Minimum	4	2.5	0.4	5.40%	0.626	0.796	0.296	0.964
Maximum	8	4	0.5					

Table 5: Constant Particulars

	Symbol	Value		Symbol	Value
L_{WL} (main)	L_1	1.6	B_{WL} (side)	B_2	0.092
L_{WL} (side)	L_2	0.7344	Block Coefficient	C_B	0.50
Scale (side)	λ	0.459	Prismatic Coefficient	C_P	0.626
B_{WL} (main)	B_1	0.2	Waterplane Coefficient	C_{WL}	0.796

The configuration of Model 9 as a trimaran model is shown in Table 5 Figure 10 and Figure 11.

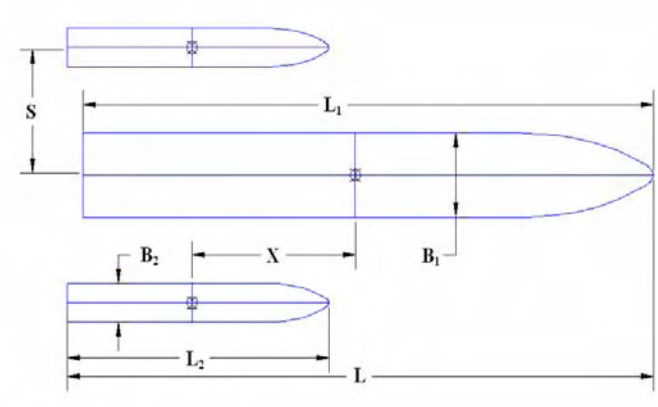

Figure 10: Typical Configuration of Trimaran model

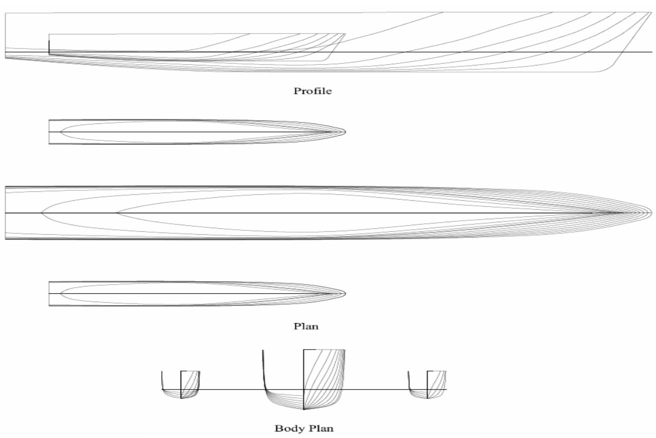

Figure 11: Configuration of Model 9 as a Trimaran

4. TEST MATRIX

The trimaran model particulars and test matrix are a major factor in the project; the development involved setting a constant transverse side hull location with different longitudinal locations, as shown in Tables 6 and 7. The speed increments employed for each method vary depending on complexity and computational time.

The variables were selected to represent practical trimaran configurations in order to produce a clear trend in the data obtained. As stated by Suzuki and Ikehata (1993) and Benjamin et al (1997), in high-speed applications the side hulls of the trimaran should be placed towards the aft end with regards to the main hull in order to reduce resistance.
Furthermore the stagger ratio (X/L_1) refers to the distance between the mid-ship of each individual hull, as resembling the longitudinal stagger employed by Suzuki and Ikehata (1993). From previous studies, such as Suzuki (1993), the maximum wave resistance coefficient is generally found to be around Fn 0.5 to 0.6, thus the corresponding speed range was selected to cover this range of Froude numbers.

Table 6: Variable Particulars

		Symbol	Values						
Trimaran Model		**TRI**	**1**	**3**	**4**	**6**	**9**	**10**	**12**
Displacement	[kg]	Δ_1	6.33	11.372	7.148	10.103	12.781	7.989	9.829
Displacement	[kg]	Δ_2	0.612	1.1	0.691	0.977	1.236	0.773	0.951
Displacement	[kg]	Δ	7.554	13.571	8.531	12.057	15.253	9.534	11.73
Draft (main)	[m]	D_1	0.05	0.08	0.05	0.08	0.08	0.05	0.062
Draft (side)	[m]	D_2	0.023	0.037	0.023	0.037	0.037	0.023	0.028
Block Coefficient		C_B	0.396	0.447	0.477	0.395	0.5	0.5	0.497
Beam-Draft Ratio		B/T	4	2.5	4	2.5	2.5	4	3.25

Table 7: Test Conditions for TRI-9

Condition	**Fn**	**Long. Location**		**Trans. Location**	
		X/L_1	(m)	S/L_1	(m)
1	0.3 to 1	-0.2	-0.32	0.2	0.32
2	0.3 to 1	-0.3	-0.48	0.2	0.32
3	0.3 to 1	-0.4	-0.64	0.2	0.32

5. COMPUTATIONAL FLUID DYNAMICS

Computational Fluid Dynamics (CFD) software, SHIPFLOW, has been employed here to determine the wave resistance of trimaran hull forms. The wave resistance coefficients are calculated by using the potential flow, boundary layer and Navier-Stokes methods implemented in SHIPFLOW. By splitting the flow into three regions an efficient approximation of the flow equations may be made and complete flow calculation may be accomplished in a few hours. The zoning configuration adopted by SHIPFLOW is represented in Figure 11.

- ZONE 1 – This is the potential flow region, where the flow is calculated using a higher order panel method, also known as the Rankin source method. The fluid flow is represented as continuous streamlines beginning forward of the bow and finishing at the stern, where the flow is assumed to be steady, incompressible and irrotational.

- ZONE 2 – This is the boundary layer region, where the flow is obtained using a 3D momentum integral method. The method begins at the stagnation point(s) at the bow and continues along the surface of the hull, incorporating flow in the corresponding laminar, laminar to turbulent transition and turbulent regions.

- ZONE 3 – The Reynolds-Average Navier-Stokes method is incorporated in this zone to calculate the energy and adverse resistance at the stern region of the hull. The majority of the wave resistance is obtained using this method, as the interference between the viscous boundary layers for the region is calculated. Due to the complexity of this method, a significant amount of computational time is consumed.

The SHIPFLOW modules executed for the analysis included XMESH and XPAN. The XMESH program is initially run to verify the panelization of the body and free-surface; it is then executed in conjunction with the XPAN module. XPAN is based on a boundary element surface singularity panel process, using Rankine sources, in order to solve the potential flow around three dimensional bodies, and consequently the wave resistance coefficients.

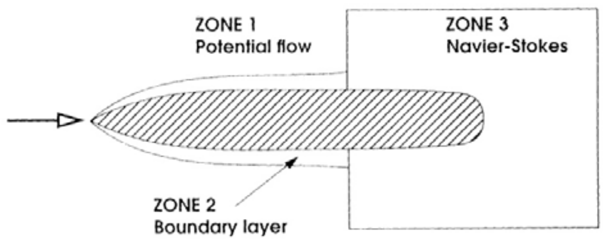

Figure 11: Schematic Diagram of SHIPFLOW Calculation Zone

6. SLENDER BODY METHOD (SBM)

The wave resistance coefficients were also calculated for the series of trimaran hulls using an analytical process known as the Slender Body Method (SBM). The process entails calculating the energy in the free surface wave pattern produced by a slender vessel and thus the vessel's wave resistance. Wave patterns can be visually represented for both mono and multi hull forms. The SBM is based on Michell's Integral where a linear first order approach is employed to predict the wave resistance. The fundamentals behind the theory involve obtaining the source strength as a function of the longitudinal deviation of the hull, where a line of sources is distributed along the centre plane. The wave resistance is acquired by integrating the forward and aft components of the pressure normal to the body over the surface of the hull; where the apparent pressure around the body that causes disturbance in the free surface is dictated from the flow around the body.

The original integral developed by Michell (1898) to predict the wave resistance of vessels is shown below:

$$R = \frac{4\rho v^4}{\pi g}\int_1^\infty \left(I^2 + J^2\right)\frac{\lambda^2 d\lambda}{\sqrt{\lambda^2 - 1}}, \tag{8}$$

where

$$\lambda = mv^2 / g\ ,$$

$$I = \int_0^\infty \int_{-}^{\infty} f(x,z) e^{-\lambda^2 gz/v^2} \cos \lambda gx / v^2 dxdz \tag{9}$$

$$J = \int_0^\infty \int_{-}^{\infty} f(x,z) e^{-\lambda^2 gz/v^2} \sin \lambda gx / v^2 dxdz \tag{10}$$

The SBM employed is predominantly based on the studies undertaken by Tuck, Scullen, and Lazauskas (2002). The study emphasized on efficiently and accurately computing flow fields and wave patterns both near and far of moving high-speed vessels, including conventional hulls, multi-hulls and submarines. As stated by Tuck, Scullen and Lazauskas (2002), precise wave resistance results as well as visual wave patterns with fine detail can be obtained rapidly on inexpensive computers. The calculations incorporated use distributions of Havelock sources to inherently generate flow by assuming an inviscid incompressible fluid flowing irrotationally. The Havelock sources represent point sources within the free surface. As stated by Couser, Wellicome and Molland (1998), with regards to the SBM, each individual hull must have a relatively high slenderness ratio (i.e. length: beam) in order to obtain accurate results.

7. EXPERIMENTAL TESTING

The tank testing was conducted at the Australian Maritime College Ship Hydrodynamics Centre (AMCSHC). The tank has a manned carriage containing a two post dynamometer for measuring resistance together with various instrumental and computer amenities for automatic data acquisition. The tank testing data used in this study was originally conducted by Kiso (2001) on the TRI-9 model. To ensure accuracy in the original data by Kiso (2001), one of the trimaran configurations was replicated and tested over the range of Froude numbers. Analogous results were attained in comparison to the original data, as shown in Figure 12. Thus the original data was used throughout this study.

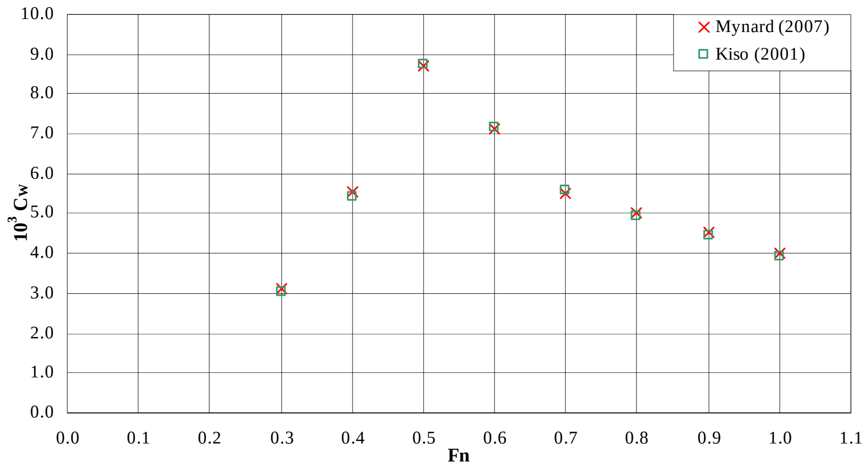

Figure 12: Comparison between Tank Testing Results, TRI-9, X/L_1 -0.2

As discussed and illustrated by Kiso (2001) and Hebblewhite (2006), due to the very low freeboard and cross members of the model, mono-film sheets are required to keep green water to a bare minimum, as shown in Figure 13. The additional forces of the mono-film sheets are not considered to significantly contribute to the overall results, as a clear trend in the data was evident.

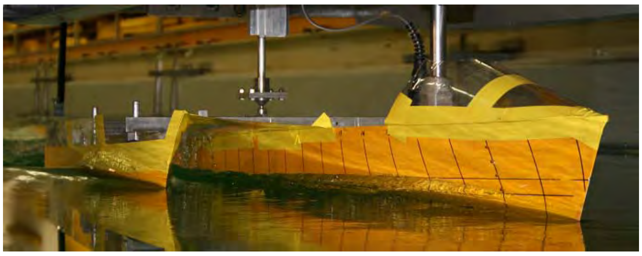

Figure 13: TRI-9, Fn 0.7, X/L_1 -0.2

8. RESULTS AND ANALYSIS

The results obtained through SHIPFLOW v3.3 were compared against side hull location for each individual trimaran and also compared against the series at each individual side hull location, over the range of Froude numbers. The following Figures 14, 15 and 16 represents the comparison between the wave resistance coefficients, for each trimaran model with longitudinal conditions X/L_1 -0.2, -0.3 and -0.4.

In each instance the maximum C_W for each trimaran is found to occur at around Fn 0.5. This is also evident for both X/L_1 -0.3 and -0.4. Furthermore there is a clear trend in the data obtained for each model over the range of Froude numbers. TRI-9 clearly has a greater C_W over the range of side hull locations; this was to be expected due to TRI-9 possessing the largest C_B and lowest B/T and $L/\nabla^{1/3}$ values. Alternatively the lowest C_W values were obtained by TRI-1 comprising of the lowest C_B and highest B/T and $L/\nabla^{1/3}$ values. The SHIPFLOW C_W results for the trimaran model TRI-9 are shown in Figure 17. As discussed by Kiso (2001), at approximately Fn = 0.3 to 0.6 the lowest C_W can be obtained with the side hulls longitudinally located at X/L_1 -0.4. Furthermore at Fn > 0.6 the minimum is found at X/L_1 -0.2.

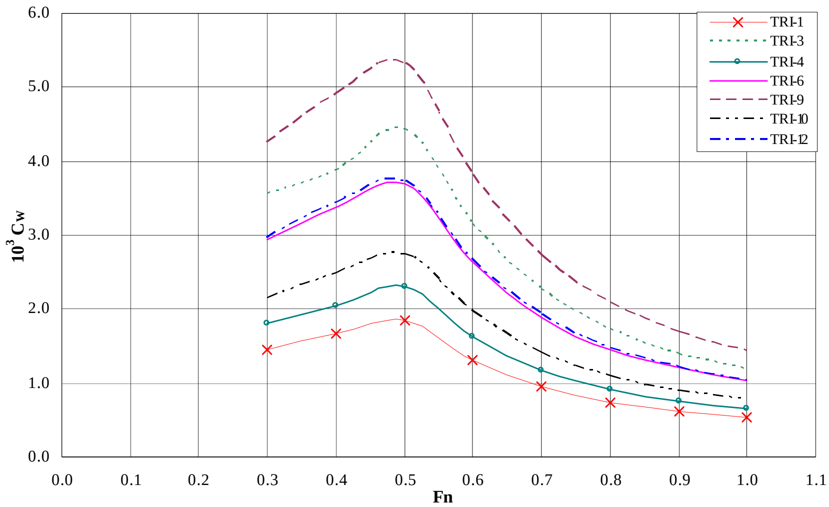

Figure 14: Wave Resistance Coefficients, SHIPFLOW, X/L_1 -0.2

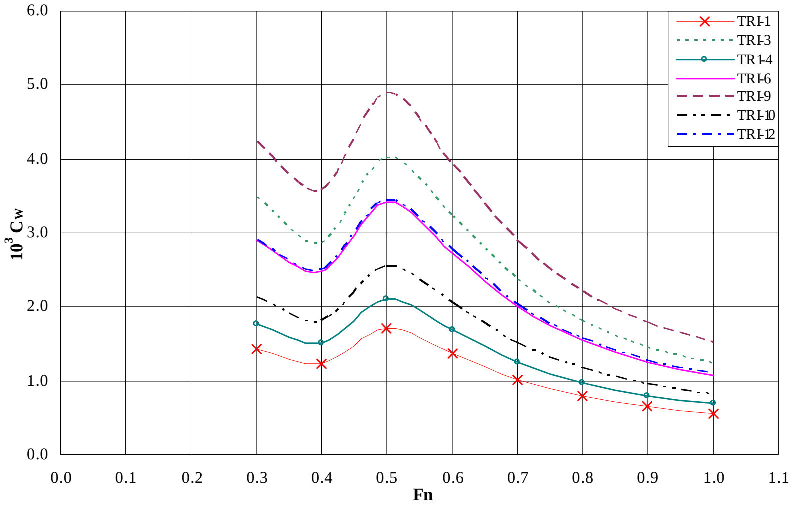

Figure 15: Wave Resistance Coefficients, SHIPFLOW, X/L_1 -0.3

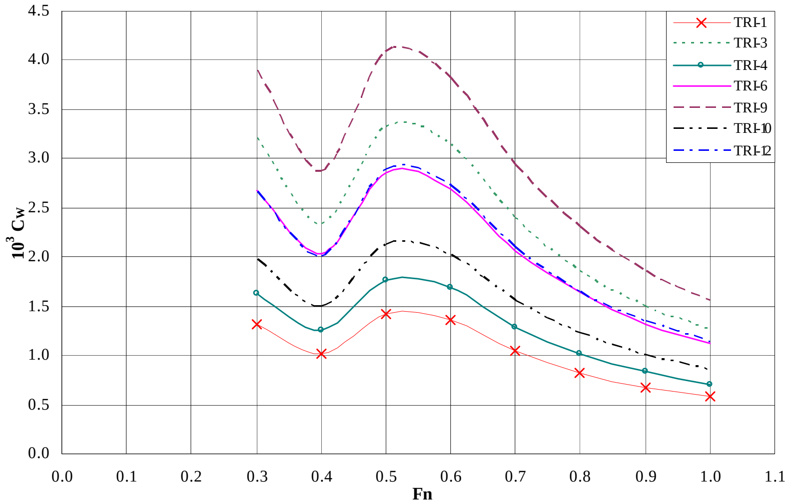

Figure 16: Wave Resistance Coefficients, SHIPFLOW, X/L_1 -0.4

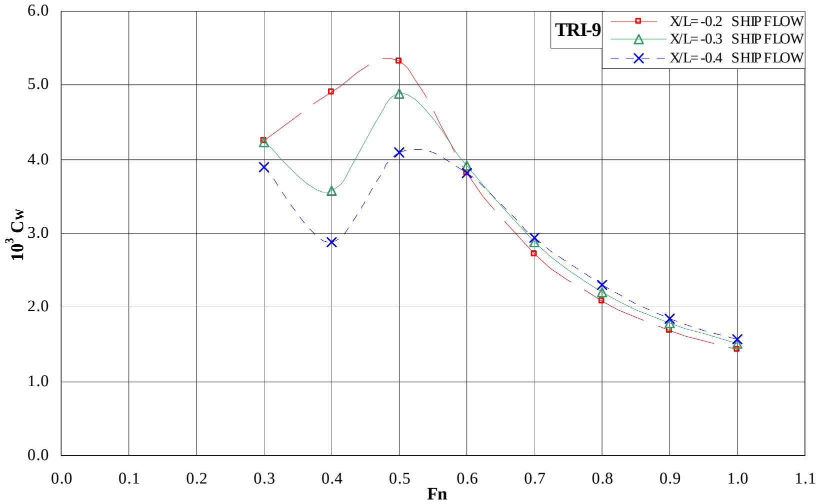

Figure 17: Wave Resistance Coefficient, SHIPFLOW, TRI-9, X/L_1 -0.2, -0.3, -0.4

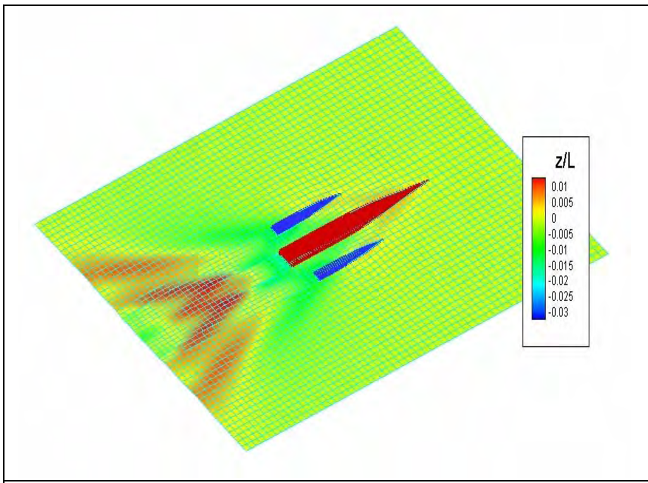

TRI-1

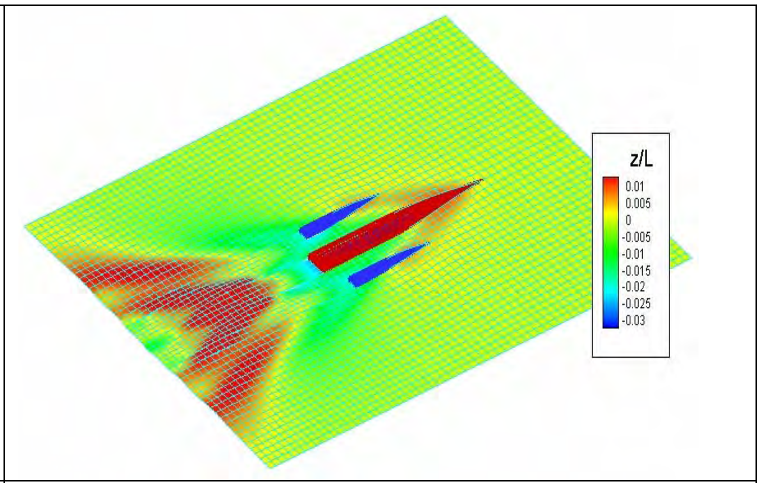

TRI-3

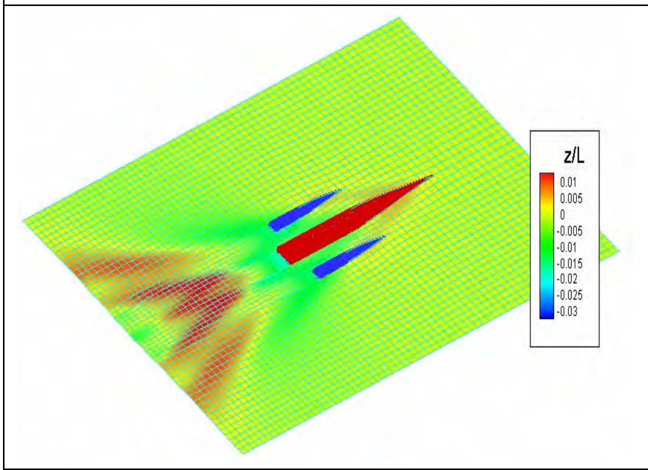

TRI-4

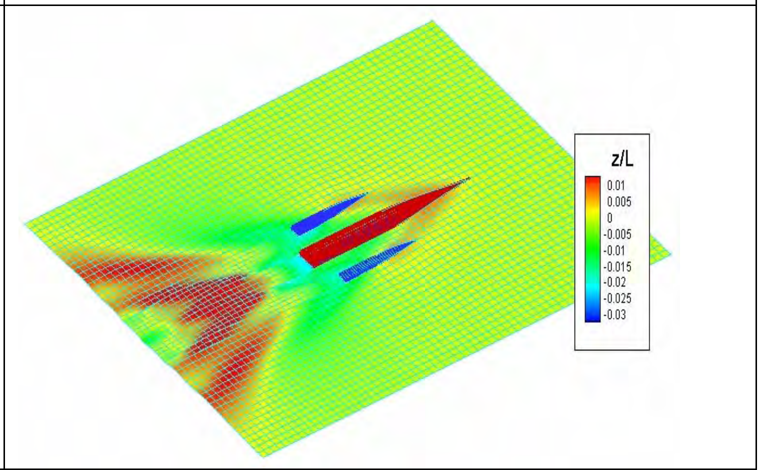

TRI-6

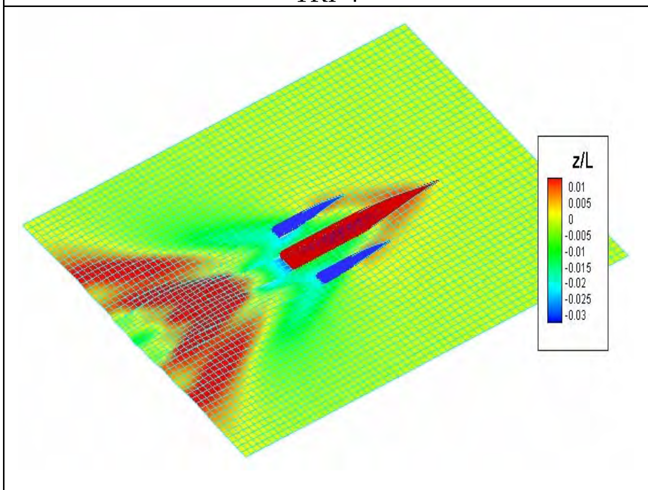

TRI-9

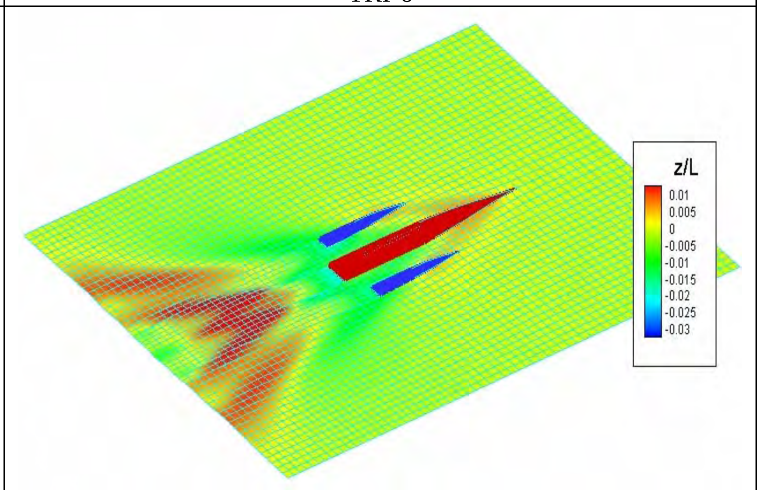

TRI-10

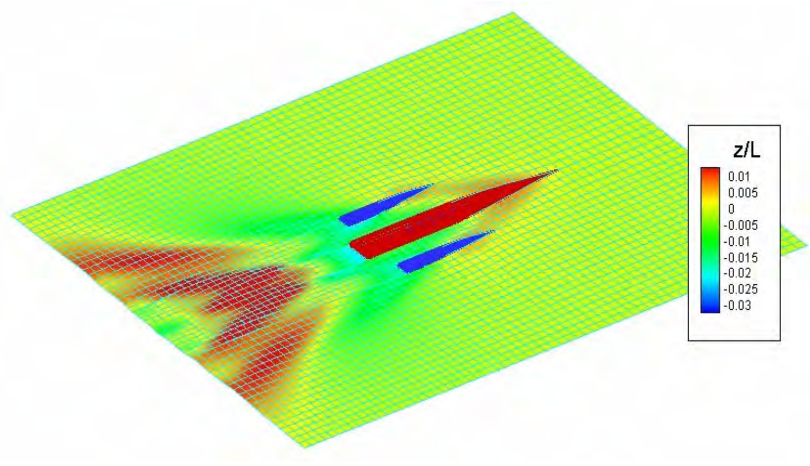

TRI-12

Figure 18: Wave Pattern, SHIPFLOW at Fn 0.5 and X/L_1 -0.2

The Figure 18 illustrates the wave patterns for each trimaran model at Fn 0.5 with longitudinal side hull location of X/L_1 -0.2. Clear trends in the wave elevations are evident. The images reflect the results discussed above.

In SBM each model was run over the range of Fn values corresponding to the test matrix. The wave pattern can be visualized as a solid render or by isometric elevation lines, as shown in Figure 19.

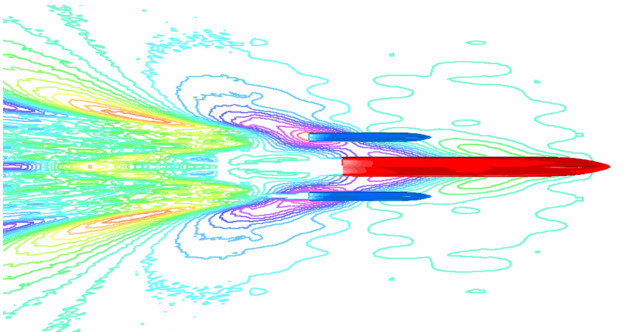

Figure 19: Sample Wave Pattern – Isometric Elevation Lines

The results obtained using the SBM are shown in Figures 20, 21 and 22 at longitudinal side hull locations of X/L_1 -0.2, -0.3 and -0.4. Due to the small increments employed over the range of speeds, clear maximum points in the data are evident. The maximum C_W values for X/L_1 -0.2 are found at Fn 0.487. The maximum C_W values for X/L_1 -0.3 are found at Fn 0.513 and at X/L_1 -0.4, the maximum is found at Fn 0.55.

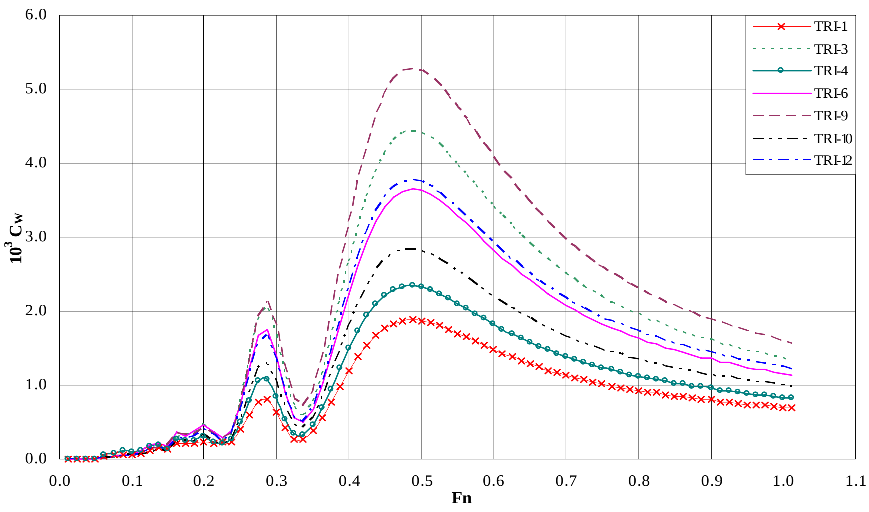

Figure 20: Wave Resistance Coefficients, SBM, X/L_1 -0.2

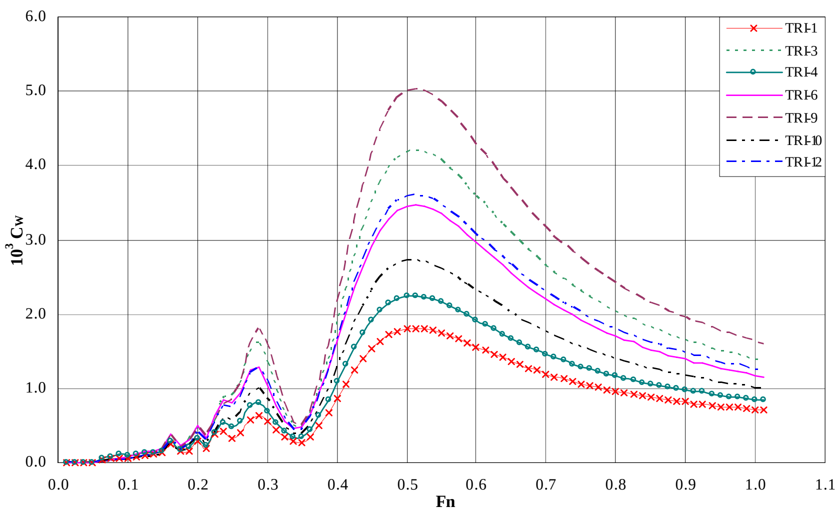

Figure 21: Wave Resistance Coefficients, SBM, X/L_1 -0.3

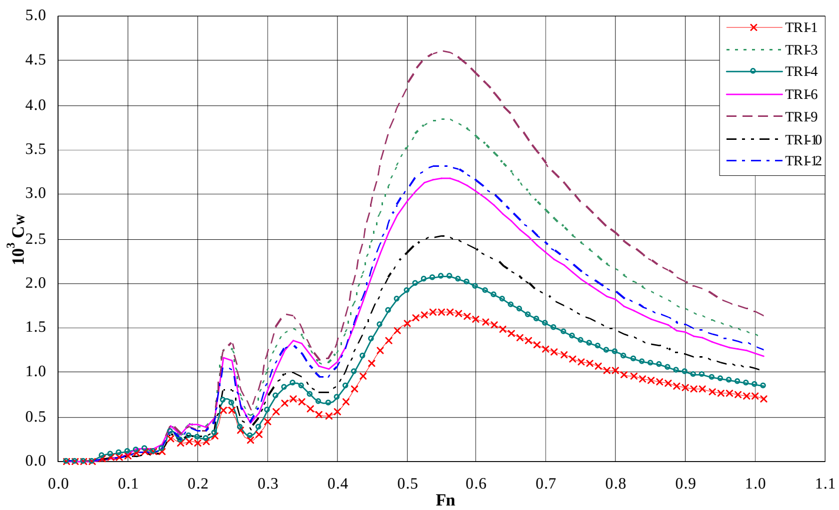

Figure 22: Wave Resistance Coefficients, SBM, X/L_1 -0.4

The effects on longitudinal side hull locations for TRI-9 are represented in Figure 23, as determined using the SBM. The optimum location to achieve minimum C_W values for Fn from 0.4 to 0.55 is X/L_1 -0.4 and for Fn > 0.55, the lowest C_W values are found with X/L_1 -0.2. The data obtained for Fn < 0.4 appears to be inconsistent, thus no conclusions have been made in relation to optimum side hull locations.

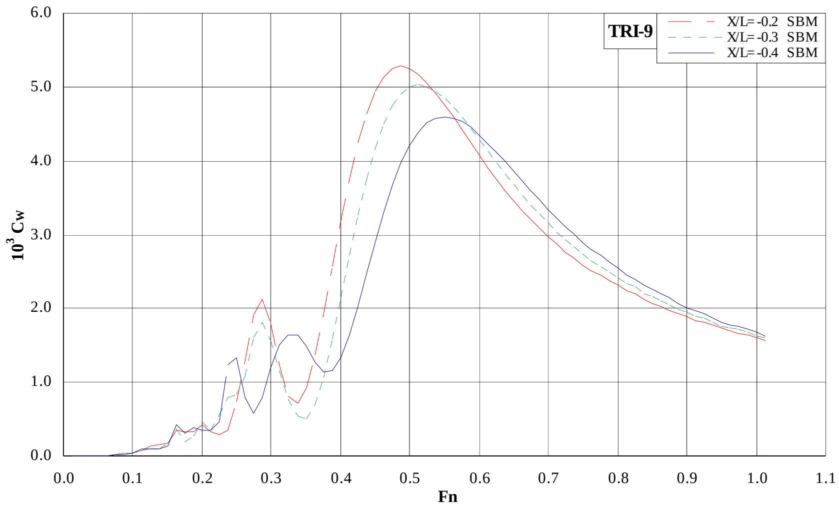

Figure 23: Wave Resistance Coefficient, Slender Body Method, TRI-9, X/L_1 -0.2, -0.3, -0.4

This section shows the comparisons between the data obtained through tank test and applying the ITTC'78 method, the SHIPFLOW data and the SBM. As shown in Figure 24, 25 and 26, the data obtained using SHIPFLOW and the slender body method are quite comparable for Fn > 0.5. Although it is quite evident that the experimental results are significantly larger, the trends in the data are quite similar for Fn > 0.5. As shown in Figure 24 for X/L=-0.2, the difference between the data is quite uniform. For X/L=-0.3 and -0.4 the difference is minimal at Fn equal to 0.5 then increase at the Fn increases.

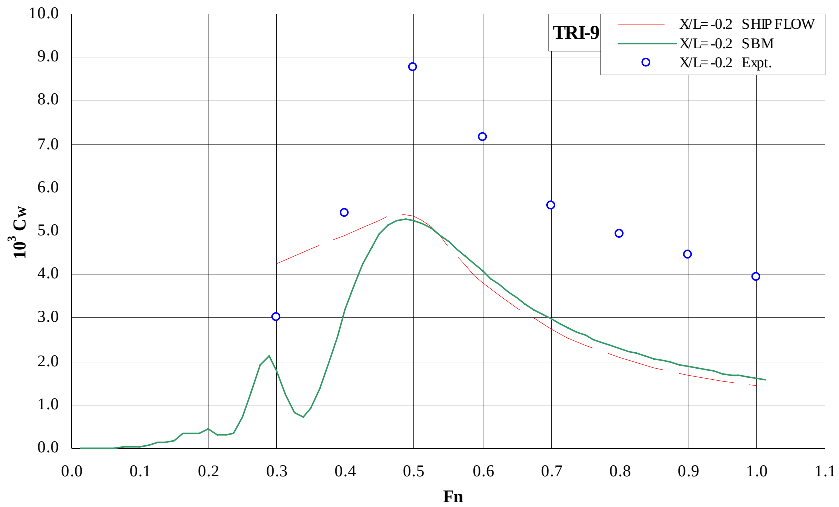

Figure 24: Wave Resistance Coefficients, Expt., SHIPFLOW and SBM, TRI-9, X/L=-0.2

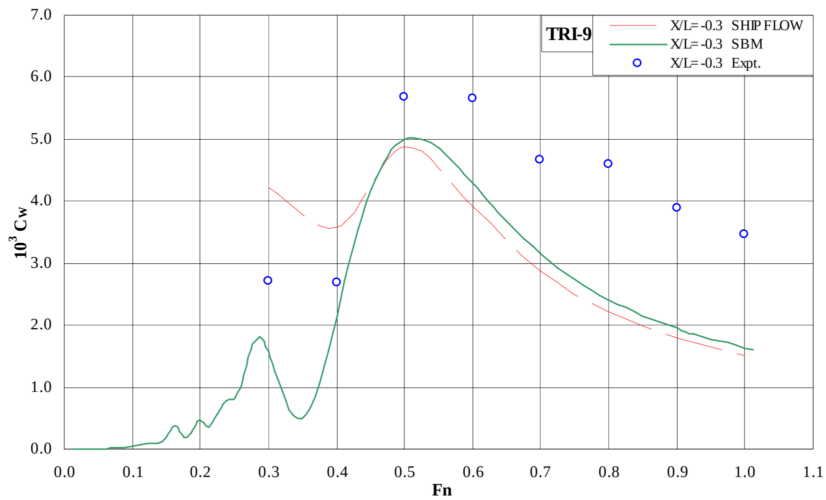

Figure 25: Wave Resistance Coefficients, Expt., SHIPFLOW and SBM, TRI-9, X/L=-0.3

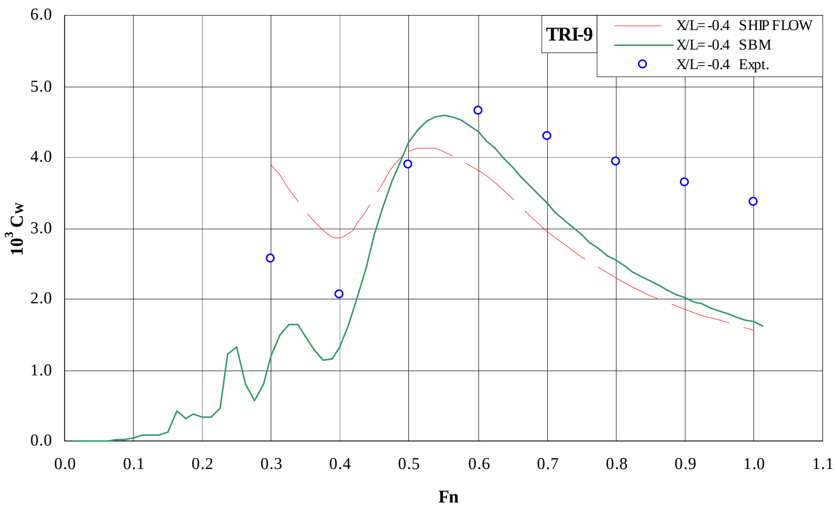

Figure 26: Wave Resistance Coefficients, Expt, SHIPFLOW and SBM, TRI-9, X/L=-04

9. CONCLUSIONS

This paper investigates through numerical and experimental work, the wave resistance characteristics of a systematic series of round bilge displacement trimaran hull forms based on the AMECRC systematic series. Although limited experimental work was carried out, mainly on TRI-9, sufficient knowledge has been gathered to conclude an appropriate location for side hulls based on operational speed requirements. It is envisaged that further experimental work need to be undertaken to validate the numerical simulations and propose a regression model for rapid resistance estimation for trimaran hull forms.

ACKNOWLEDGEMENTS

The authors would like to express their sincere gratitude to The Australian Maritime College, Australia, the University of British Columbia and Aker Yards in Vancouver, Canada for their support, encouragement throughout the course of this research work. The authors also extend their sincere thanks to numerous people without whose valuable contributions this paper would not have seen the light of the day.

10. REFERENCES

Lindström, J, Sirviö, J, Rantala, A, (1995): “Superslender Monohull with Outriggers”, Proc. Of Third International Conference on Fast Sea Transportation, *(FAST’95)*,pp

Mizine, I. and Amromin, E. (1999): "*Large High Speed Trimaran – Concept Optimisation*", Proc. Of Fifth International Conference on Fast Sea Transportation, (*FAST'99)*, pp 643-647

Pattison, D.R. and Zhang, J.W. (1995): "*Trimaran Ships*," Transaction of Royal Institution of Naval Architects, Vol
137, pp 143-161

Ackers, B.B. et al. (1997): *"An Investigation of the Resistance Characteristics of Powered Trimaran Side-hull Configurations"*, Trans. Of Society of Naval Architects and Marine Engineers, Vol. 105, pp 349-373

Suzuki, K., Nakata, Y., Ikehata, M. and Kai, H. (1997): "*Numerical Predictions on Wave Making Resistance of High-Speed Trimaran"*, Proc. Of Fourth International Conference on Fast Sea Transportation, (*FAST'97)*, pp 611-617

Yang, C. (2001): "*Practical Hydrodynamic Optimisation of a Trimaran"*, Trans. Of Society of Naval Architects and Marine Engineers, Vol. 109, pp. 185-196

Migali, A., Miranda, S. and Pensa, C. (2001): "*Experimental Study on the Efficiency of Trimaran Configuration for High-Speed Very Large Ships"*, Proc. Of Sixth International Conference on Fast Sea Transportation, *(FAST 2001)*, pp 109-113

Suzuki, K. and Ikehata, M. (1993): "*Fundamental Study on Optimum Position of Outriggers of Trimaran from View Point of Wave Making Resistance*", Proc. Second International Conference on Fast Sea Transportation *(FAST '93)*, Vol. 1, pp 1219-1230

Yeung, R. W., Poupard, G. and Toilliez, J. O. (2004): *"Interference – Resistance Prediction and Its Application to Optimal Multi-Hull Configuration Design*", Trans. Society of Naval Architects and Marine Engineers, Vol 112, pp 142-169

Brizzolara, S., Bruzzone, D. and Tincani, E. (2005): "*Automatic Optimisation of a Trimaran Hull Form Configuration*", Proc. Eighth International Conference on Fast Sea Transportation *(FAST '05)*, Vol 1, pp. 1-10

Tuck, E.O., Scullen, D.C., and Lazauskas, L. (2002): "Sea Wave Pattern Evaluation. Part 6 Report: Viscosity Factors", University of Adelaide, Department of Applied Mathematics, 14 pp

OPTIMISATION OF COMPOSITE BOAT HULL STRUCTURES AS PART OF A CONCURRENT ENGINEERING ENVIRONMENT

Adam Sobey, James Blake and Ajit Shenoi
University of Southampton, Southampton/England[1]

SUMMARY

The boat building industry is one which often has low profit margins and in a worldwide market each yard must be highly competitive. Further to this the global interest in environmental issues will increasingly put pressure on companies to go "green" both in the areas of production and performance. Concurrent engineering is a design technique, used in many industries, which lays claim to great benefits for its users. This paper looks to outline the development of a concurrent engineering environment as an aid for the leisure boat building industry. The work focuses on a concurrent design tool which optimises mass and cost comparing the relative benefits between first principles design methods and classification society rules.

NOMENCLATURE

a_{mn} = Coefficient for grillage analysis
b,g = Number of transverse beams and longitudinal girders
B,L = Breadth and length of panels
c_s, d_s = Stiffener web thickness and height
$D_{g,b}$ = Structural rigidity of girders and beams
E_s = Young's modulus of stiffener
$I_{web,crown}$ = Second Moment of Area of web or crown
$L_{web,crown}$ = Length of web or crown
m,n = Wave numbers
p = Pressure
P_{cr} = Critical Pressure
q(x,y) = Pressure at a given point on plate
Q_{mn}, $\bar{Q}_{ij}$ = Reduced Stiffness terms
$U_{mn}, V_{mn}, W_{mn}, X_{mn}, Y_{mn}$ = Coefficients for initial conditions of TSDT
w = Deflection in z direction
x,y,z = Dimensions of panel
$\gamma^{0,1}$ = Stiffness functions
$\epsilon^{0,1,2}$ = Stiffness functions
σ_{cri} = Critical buckling stress
υ_{12} = Poission's ratio
$\phi_{x,y}$ = Initial conditions of TSDT

1 INTRODUCTION

Boat design involves interdependencies between different subsystems of a vessel. It is the relationship between these subsystems that determines the difference between a design that meets customer requirements and makes a profit or one that fails to meet these criteria. "Concurrent engineering" uses parallel design processes with interdependent project teams to ensure that all the expertise of the design engineers are utilised during the entire span of the design. Typical linear design can allow subsystems to concentrate overly on the individual task and lose sight of the overall objectives as seen in fig. 1.

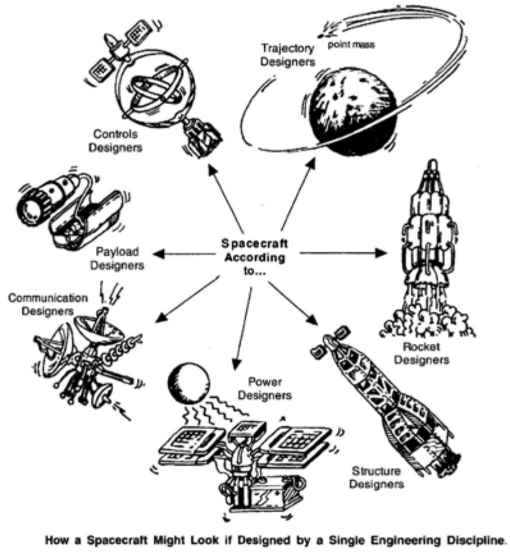

Fig.1: Individual task orientated design [1]

As a result, the relationships between the different subsystems of the boat are identified, impacts of change are readily assessed and ultimately a boat targeting customer requirements is produced. As part of concurrent engineering, subsystems are developed by separate members of the design team and it is the way that these design engineers work together that determines the success of the project. This process allows designers the ability to best comprehend the aims and difficulties faced by other subsystems. An example of subsystem concurrency is "design for production" which creates links between designing a boat for function while also producing at reduced cost, this leads to a cost effective and efficient final product. The ability to amalgamate different subsystems of design, through concurrent tools, allows designers to focus on the general design aims rather than those of the subsystem with more ease.

Finding the optimum solution between effective design and low cost makes design complex due to numerous inputs and the interactions between each variable. It has been said that 5-7% of a product's cost comes from the design and this can have an effect of 70-80% on the final cost [2]. This therefore means that the production costs can be greatly reduced at the design stage. It is therefore important that this design stage is done quickly while fulfilling customer requirements to reduce cost and increase sales. Being first to market or releasing at a defined market peak are also factors governing overall sales, this combined with fast design, allows for either increased quality or reduced cost and adds emphasis to a fast design process while increasing sales. Computational methods are increasingly being used to decrease the time taken to optimise these designs while still accurately finding the optimum result. The ability to work in parallel also means the time to complete a design will also be shorter from start to finish.

An important part of marine structural engineering are classification society rules as conforming to these rules has a certain implicit recognition in port legislation. It is therefore important to make sure that either classification society rules are used, relevant to the country sold in, or that first principle methods are determined safe by those same societies. Classification society rules are based on general rules for the design of boats which include safety factors. It has been considered recently that the use of classification society rules, while ensuring a safe boat and fast design cycle, may lead to over-engineering due to these safety factors. This will lead to heavier hulls increasing the cost to build, decreasing the performance and increasing emissions during use. ISO 12215-5 for scantling determination has recognised this fact and has tried to reduce these safety factors [3]. Other structural engineering societies outside of the marine sector have also changed the manner in which there rules are made such as in civil engineering where classification rules have switched to partial probabilistic approaches for design [4]. It might still be possible to produce boats with lighter hulls through the use of first principles approaches. First principle methods can be passed through classification societies but the process can be expensive as all calculations must be carefully checked and this process incurs added cost and increased design time. It is therefore important that first principles methods are modeled accurately, while giving large increases in either cost effectiveness or boat operating efficiency, so that they can be used as a comparison with classification society rules to determine if safety factors should be reduced. Tools that can quickly predict optimum first principle hull topologies will also allow designers to compare these solutions with classification society designs allowing decisions to be made into whether further investigation is required.

This paper shows the development of a method for concurrent engineering for the leisure boat industry. This method is extended through the use of a structural optimisation for stiffened FRP boat panels allowing optimisation between cost and mass of stiffened panels. The paper shows the ability of concurrent engineering techniques to help the leisure boatbuilding industry and goes on to show a method of design that will allow concurrent team work throughout the design. The paper develops a structural design tool using genetic algorithms for optimisation combined with elastic stress modified grillage theory for stiffener structural analysis and third order shear deformation theory (TSDT) for the plate structural analysis. The method also develops an optimisation algorithm using classification society rules, the example of which is Lloyd's Register Rules and Regulations for the Classification of Special Service Craft. This comparison allows a cost analysis between a first principle method and classification society rules to determine the benefits between the two methods and investigate potential cost savings. The aim of this method would be to give a fast determination of performance efficiencies that could be developed using hull scantlings generated from first principles while developing a better understanding of the production issues for the hull designer. This will allow development of boat hulls that produce fewer emissions, are more efficient and cheaper.

2 CONCURRENT ENGINEERING

Concurrent engineering is a powerful tool used in many industries. During the late 1990's shipbuilding companies started to switch to concurrent engineering systems and found success [5]. Many companies within the aerospace industry also made the transition and found success from Airbus through Airbus Concurrent Engineering (ACE) [6] and Boeing military aircraft company in 1999 [7]. Astronautics is another industry where concurrent engineering has been used with NASA and ESA developing the Project Design Centre (PDC) at the Jet Propulsion Laboratory in 1994 [8] and Concurrent Design Facility (CDF) at ESTEC in 1998 [9] respectively. These companies have continued to use and improve these design environments. Concurrent engineering has been defined in many ways and a set of common key points is:

- Parallel design
- Multidisciplinary team
- Facility
- Software infrastructure
- Support and understanding for the environment

Further to these techniques other tools often fall under the umbrella of concurrent engineering [11]:

- Integrated Project Teams (IPT)
- Digital Product Definition (DPD)
- Digital Pre-assembly/Mock-up (DPA)
- Computer Integrated Manufacturing (CIM)
- Lean Manufacturing (LM)
- Design for X-ability (DFX)
- Total Quality Management (TQM)
- Quality Function Deployment (QFD)
- Supplier Involvement on Product Team (SI)
- Customer Involvement on Product Team (CI)

Table I: Comparison of Industry Characteristics [10]

Characteristic	Shipbuilding	Aerospace	Automotive	Boatbuilding
Production Facilities	Few simultaneous	Few simultaneous	1000's simultaneous	Few simultaneous
Development Process	Concurrent design Production	Design Prototype Custom manufacture	Design prototype Bulk manufacture	Straight to production Custom Manufacture
Design Collaboration	Real time	Pre-production	Pre-production	Pre-production

These tools all combine to produce an effective design environment, focusing on communication of data and information, and have produced positive impact upon the design process and the results found. Concurrent engineering uses parallel design processes where all members of a design team with relevant experience are used. This form of design also takes into account design between members that may not share the same physical location as the rest of the team.

Each industry has its own, different, characteristics that determine the way in which design and production are carried out as can be seen from Table I.

It is important to study each individual industry as each different sector will have characteristics specific to the methods of production, design processes and resources available. The ways in which different design processes must be done and the nature of the products calls for different styles to the design process. Boat building is similar to shipbuilding in that it must be done quickly without the ability to have prototypes for testing before being sent to sea. This is makes it more difficult to create designs that are very safe and where failure must not occur. Aerospace is also similar to boatbuilding due to the level of customisation of each design and the ability to finish the design before production starts. The different characteristics of each industry must therefore be compared between these other industries and boatbuilding to determine how concurrent engineering should be done within the British boatbuilding community covered in section 2.1.

2.1 CONCURRENT ENGINEERING IN BRITISH BOATBUILDING

Concurrent engineering has been shown to be useful in other industries similar to that of boatbuilding, examples of which are shown for shipbuilding in Table II, and aerospace shown in Table III.

The use of consultants or companies in partnership are used throughout boatbuilding with one company being in control of the design and production but having others either aid these processes or being completed under their supervision. This means that communications, which are difficult within a company, develop further issues as the process becomes split, not only geographically, but between communications networks. From a questionnaire of companies in Britain[2], none of the respondants carried out all

Table II: Concurrent Engineering in Shipbuilding [5]

Characteristic	Change
Development time	30-70%reduction
Engineering changes	65-90%reduction
Time to market	20-90%reduction
Overall quality	200-600%improvement
Productivity	20-110%improvement
Dollar sales	5-50%improvement
Return on assets	20-120%improvement

Table III: Concurrent Engineering in Aerospace [11]

Characteristic	Change
Development time	50% reduction
Engineering changes	50% reduction
Cost Savings	$68M reduction

of their design and production in house. This can lead to less involvement from production engineers into the design process resulting in expensive and difficult to build designs. Without this feedback to design from production complicated vessels will be continually reproduced due to the evolutionary nature of the design process.

Boatbuilding in Britain is viewed as evolutionary rather than revolutionary as shown by 100% of the respondents of the questionnaire. Evolutionary design relies heavily on previous products meaning that a large part of previous designs can be reused and improved. Leisure boatbuilding has tight profit margins, leading to problems in using expensive software or developing in house software and also means that the level of IT support can be lower. Further to this, due to the evolutionary nature of the design process concept design may not involve all of the members of the team that should be involved.

The boatbuilding industry has wide variation within Britain due to the differences in size, management techniques and the products that are produced. Some companies already use concurrent engineering within their design facilities while others have not heard of the process. This means that the concurrent engineering environment used must be very flexible to suit the needs of the different sorts of business resources and management.

The respondants of the questionnaire placed a very high value on impressing the customer and this shows that the

[2] Initial survey is composed of 7 of the 20 companies having responded so far

quality of the design is viewed as a key part in the successful sale of boats in the leisure boat industry. Less attention was paid to the cost of the product due to the nature of the business where extra costs can be passed on to the customer. An area that scored very poorly was that of innovation which had the lowest score from all of the participants of the questionnaire indicating the dependence on previous designs and company styles. The concurrent engineering environment therefore had to be cheap, easy to use and learn, while being easy to update but to allow all of the advantages that concurrent engineering has brought to other industries.

2.2 CONCURRENT ENGINEERING ENVIRONMENT

A concurrent engineering environment is being developed by the authors. The idea of this system is to easily connect with the current resources at the different boat building yards. The main concurrent system has been developed to allow effective communication of data and information between the different subsystems, e.g. structures, propulsion, etc.. The environment will also allow a quick and easy method, for anyone who could be of benefit to the process, of checking the progress of the design and adding comments and changes where applicable. This system also had to take into account the possibility of using consultants who may be asked to work on part(s) of the design but from whom it may be important to keep hidden from certain discussions and other subsystems of the design.

The transfer of data could have been acheived in two main ways. One of these was to transfer all of the information between all of the subsystems in the environment, fig. 2. The problem with this method is that once a large number of subsystems have been added it would be a long process trying to attach new subsystems or software creating a more complicated and expensive task for companies. This method would allow direct transfer of data from one subsystem to another allowing a fast and memory inexpensive system.

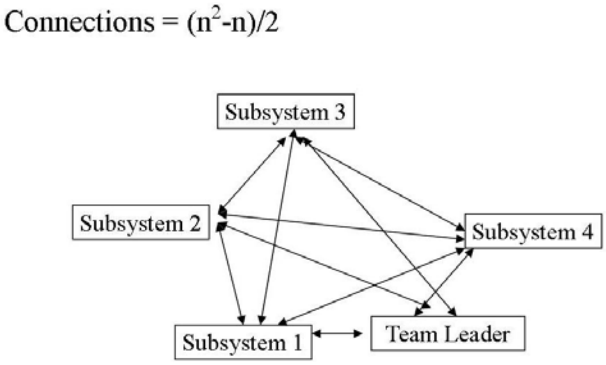

Fig.2: Direct data transfer

The second method, fig. 3, uses a central hub to store the data and this requires less time and cost to update. A further benefit is that the hub can be used to keep track of all of the data for the design in one centralised database.

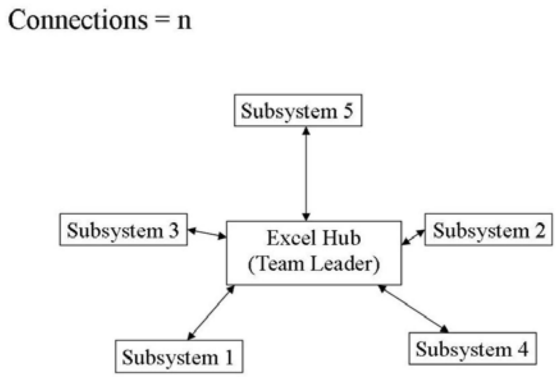

Fig.3: Hub data transfer

The transfer of the data was done using Microsoft Excel which was chosen as it is easy to use with large recognition worldwide. Further to this it is also cheap and has been used, until recently, in many of the top concurrent facilities around the world e.g. ESTEC. The spreadsheets allow data to be passed around the system quickly and easily allowing changes in one subsystem to permeate through the design as can be seen from fig. 4. This allows easy inference of how changes made in one system will affect the design and production of the entire vessel. The aim of the concurrent engineering system is to make sure that all of the designers are working together towards one final goal. This means that designers must be able to easily disseminate information from other areas of the design and be able to quickly determine how changes they make in their own subsystems affect all the other parts of the vessel. This ability to easily visualise the direction of the design will also allow the team leader to keep track of the design and determine, more easily, how close to the customer requirements the boat is and in which direction changes need to be made to make sure they are fulfilled.

Further to this development the use of grid computing has also been looked at. The ability for companies to work together in a conglomerate, by sharing resources, would allow the companies access to faster computing and also the possibility of sharing floating licenses. Companies would then have more expensive or more diverse software than may be currently available and to use more computationally expensive design methods. This computational sharing could also be added to through the use of shared databases reducing the strain on individual companies to gather their own data without compromising their competitive edge against each other. These databases could range from joint efforts on materials testing to gathering information on potential suppliers on parts or materials allowing the lowest prices and best quality of service.

The concurrent engineering environment that is being developed for the British boatbuilding industry has been based upon the characteristics of the mentor companies involved. This means that the environment has been developed with readily available software to remain low cost

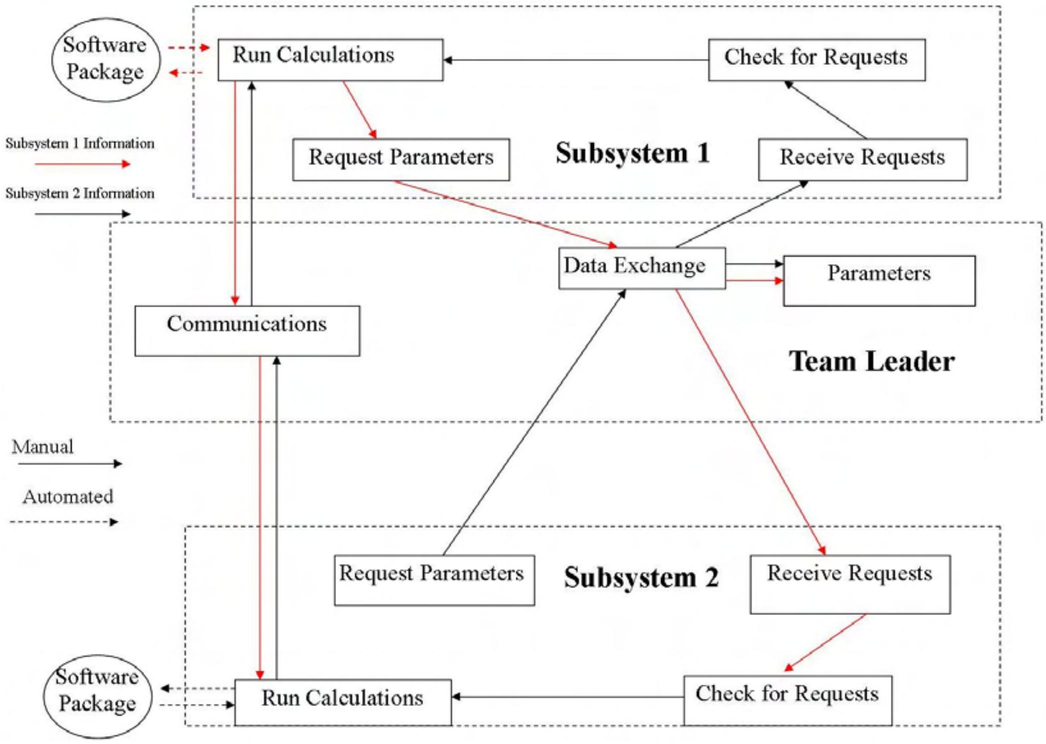

Fig.4: Data exchange process

which also allows an ease of use from the members of the boat building industry. The ability to change software packages without wholesale changes will allow longer life for the project and include evolution with time to better suit the needs of the companies involved.

The environment is therefore based upon a number of spreadsheets to hold the data of the design. These spreadsheets can be set up so that changes in one subsystem will automatically trickle through the rest of the design. This allows an easy comparison into how one area of the design will affect the rest of the design. Due to the nature of concurrent engineering being communication based, the system has been set up so that updates will occur at predetermined design breaks which allow the designers time to discuss the next design session while the system updates. These updates will automatically save a design history, keeping track of the changes of the design and the reasons behind why these choices were made. The information from the design will be transferred predominantly through direct contact in design sessions as subsystem designers have discussions throughout the design stages. Boat building companies work closely in partnership with other companies and consultants meaning that these groups cannot be in the design studio for the entire design and little direct contact may be made. It is also important to keep a record of why design decisions were made and keeping track of these reasons as the manner in which the design evolved will be important for future designs. The information can be kept track of using a standard web-based collaboration and document management platform e.g.Microsoft SharePoint. This system will allow each designer an area to develop on the internet so that changes to the subsystem can be seen in graphical form, pictures from the design can be posted and queries can be made by other members of the design team.

3 DESIGN TOOLS

For each subsystem in the boat the designer in charge of that area will use different tools to aid the process of design. Concurrency within the design team can be aided if these tools themselves are built around the concurrent approach. It is with this in mind that a structural optimiser has been developed as a concurrent design tool to encompass multiple areas of the design process and to allow an insight into other areas of the design and production to the design engineers. The methodology of the design is shown in fig. 5 with the different sections being expanded upon in sections 3.1 to 3.3.

The design process starts with concept design of the boat. It is at this stage that the design goals will be set and possible solutions to these goals are created.

3.1 CONCEPT DESIGN TOOLS

At the start of the design process it is important to fully define the concept that the design engineers will be working to and is the first step of fig. 5. This is an important stage as parallel design processes, like concurrent engineering, involve more engineers working on a problem. This means that if at any stage the project needs to be redesigned more man hours have been invested leading to higher expense as

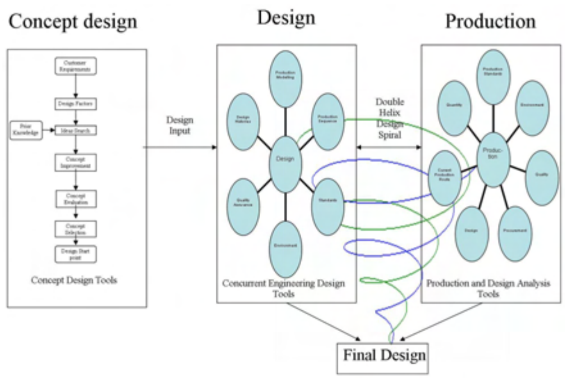

Fig.5: Stages of project design

shown in Aitshalia et al. [12]. Further to this the ability to influence the product cost is at its highest in the concept design as is the ability to make changes to the design, fig. 6. This means that mistakes made in the concept design will have the furthest reaching consequences allowing production of a boat that does not reach the correct market or one that is expensive to produce. It is therefore important for concurrent engineering that concept design is done well. Due to the nature of the process all the members of the company who could be beneficial at this stage will be involved and this means that the process should be more focused. The concept design stage is therefore laid out in fig. 7.

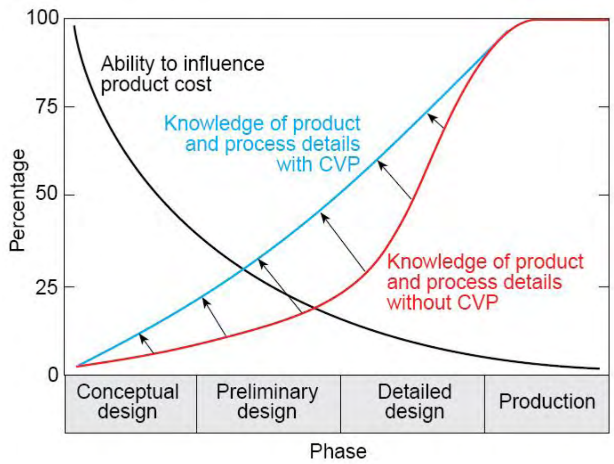

Fig.6: Importance of Concept Design [13]

The concept design stage can be acheived in different ways but the method chosen uses Quality Function Deployment (QFD) and Concept Design Analysis (CODA). These methods take the customer requirements and, with the input of previous boats and the knowledge of the design engineers, produces initial values for the design process as well as the overview of the boat that should be produced during the design phase. The concept design follows a number of steps as follows:

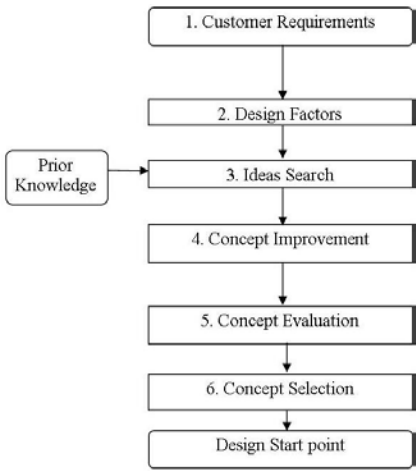

Fig.7: Concept Design Processes

1. The design must start with the goals of the project. These will come from discussion with customers about what they would like to purchase and knowledge of products of rival and the designers own company.
2. Once the goals of the design have been decided upon the next stage is to determine the measurable quantities that are most important to the concept and to judge how much these different quantities will effect the customer requirements that have been chosen.
3. The third step is a combination between looking at old designs, due to the evolutionary nature of boat designs, and trying to include new concepts within these to develop ideas about how the customer goals can be solved.
4. The next stage is to develop some conceptual ideas for how to solve the problem generating a list of potential solutions.
5. Once the concepts have been generated it is then important to try and develop the ideas further to see if the concepts can be improved to better suit the designs goals.
6. Finally the concepts must be judged against each other and a final design must be chosen that will then be taken on for further development.

From here the design can be started in greater detail taking the ideas from the concept design and some initial quantities and iterating these through to give a completed detailed design.

3.2 DETAILED DESIGN TOOLS

The stage after concept involves a more detailed look at the design. Detailed design involves an iterative process to produce the full design for the vessel. For the current tool being developed the focus for the design tools has been that of the boat structure and therefore fig. 8 covers the areas affecting the design of the hull of the boat. This process is the longest section in the design and the development of concept design and initial design tools can take the design further down the design spiral, shown in fig. 5, reducing the number of iterations required and hence the overall time for the design.

3.2.1 DESIGN TOOLS

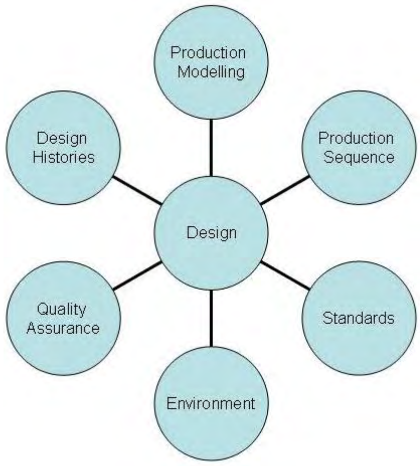

Fig.8: Design Inputs

- Production modelling - The ability to determine the potential cost benefits that could be gained from the yard if the designer changed the geometry of the boat. This will need to be a compromise between cost efficiency, performance and aesthetics.
- Production sequence - The cost to change the manner in which the production yard actually produces the boats will affect the types of new designs that can be produced. The production sequence will also play a factor in determining the maximum quality, production rate and the materials available for a given production technique.
- Standards - The standards will determine the structural geometry for the boat though it is possible to use first principles methods.
- Environment - This will be the effect of the vessel, when in use, upon the environment. Being 'green' is becoming more and more important in legislation and therefore emphasis on more environmentally friendly vessels will become important.
- Quality assurance - The quality of the design must be determined so that it is assured that the structures will fulfill the customer requirements.
- Design histories - The previous designs developed by the company will affect the way in which new designs are created and therefore experience of advantages and disadvantages from previous designs will be very important.

Different subsystems must work together to form a design that fits the requirements for the vessel. Each subsystem will need to work with a different set of other parts of the boat. It is determining which subsystems will have the most impact on a designer and which other areas of the vessel the designer will have the most impact upon that will allow an optimum design. For each of the subsystems of the boat all of these important relationships will need to be determined. Once these relationships have been determined for a subsystem it is then possible to produce concurrent tools that focus on one section of the design but which also takes into account other key sections. This approach could be followed for other subsystems but the current tool focuses on structures for boat hulls, the development of which is given in more detail in section 4.

3.2.2 DESIGN HISTORIES

As has been shown the process of design in boat building is an evolutionary rather than a revolutionary process. This means that each of the products has a strong resemblance to previously created products. Designers can learn important lessons from models that have been previously developed at a company. The use of comparative design histories will allow new engineers to easily determine which old designs are closest to the current design and any relevance a model might have to the new design. This comparison will stop designers redoing work that has been previously done and to spend time looking at solutions that have not been considered or to further develop ideas that may not have been looked at in detail.

The design history tool will therefore be based upon computer recognition of the current design and making a comparison between the current and past designs. Neural networks can be used to make an automated comparison between the current design and the histories of previous vessels. Neural networks work on a basis of learning adapting the weighting system throughout the network through feedback which can be either user controlled or predetermined. Since the learning environment can be created through feedback from designers it would be possible to create design history tools that were specific to each design, class, type, designer, company and the industry as a whole or to take different elements from each. This ability to learn also means that the judgement of which design histories are similar to the current design can also be affected by the production engineers so that components that were expensive or difficult to build will be less likely to be brought up than those that were cost effective.

The neural networks will work by taking the dimensions of a component, an example diagram for an engine is shown in fig. 9, and comparing these to the pre-created neural network for both old and new engine types. The first stage will be to recognise that the dimensions are referring to that of an engine. Once this is done the different dimensions can be used to determine similar engine types in the example one neuron is created for power and one for volume. Weightings are applied to encourage or discourage certain

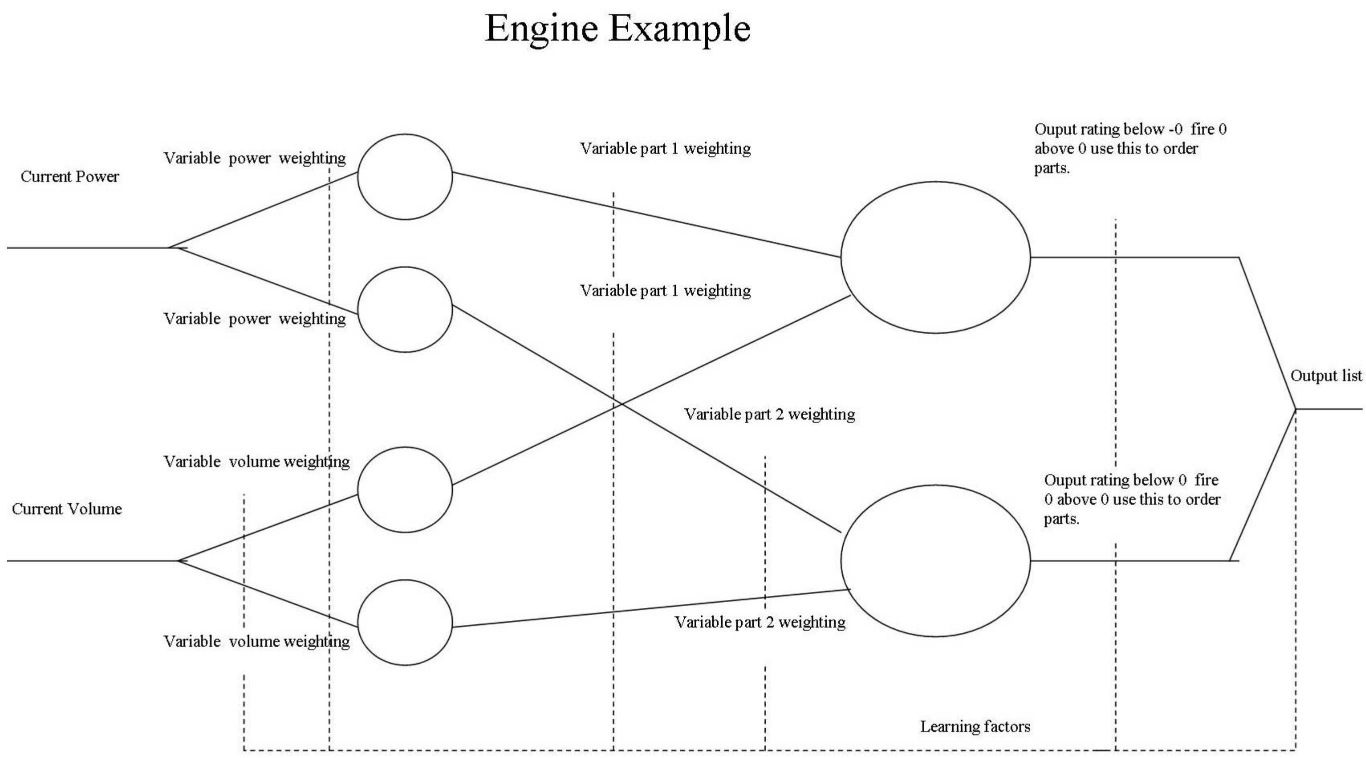

Fig.9: Neural Networks to compare designs: Engine example

engines from being chosen and the equations in eq.1 are used to determine how similar the engines are. If the engines have similar volumes or power then the neuron fires a signal to the second layer to determine if the volume and power combined are similar. If this second layer determines that the engines are similar the neuron fires and these engines can then be ranked giving the designer a list of candidate engines for the current state of design. If none of the engines fire off neurons in the second layer then engines can be rated, based on weightings of importance of dimension, from the results of the first layer to give an idea of the engines used previously. This list can then be altered and rated by the designer changing the weightings in the network so that future searches are more productive.

$$\begin{array}{l} \sum w_j f[j] \geq [i] \to 1 \\ \sum w_j f[j] < [i] \to 0 \end{array} \tag{1}$$

As part of the design history tool it will also be possible to create a database of components. This database could then be used to indicate potential new suppliers and rate the quality of service from old suppliers. This ability would allow designers to use the feedback gained from production staff and to avoid the use of companies that will add expense or time to the production process. Complaints about fast breakdowns of parts could also be kept to avoid the use of these components in the future. If done as a British boatbuilding collaboration, companies that are slow or poor quality will be rated badly and members of different companies will be able to know not to use certain suppliers. The tool runs during design breaks allowing the spreadsheets of the system to update and run comparisons with other databases without using up computer resources. Once started the tool will search the centralised hub of data in the data exchange, shown in fig. 4, and compare the current design to these numbers. Through the weighting system other factors will be taken into account like the similarity between the current design and previous one and whether the design worked well when it was built. The system will also look through a database of currently available parts and determine if any are similar to the current requirements so that designers can start thinking about exact dimensions at an earlier stage in the design.

The use of the design histories can also be used to speed up the process of optimisation by allowing the focus of the search to be in areas that have previously been used. It would also be possible to run the optimisation and then pick out the closest previous hull shape to this design to save on production costs. This ability could be used to make sure that the optimisation tools become part of the evolutionary process and help the company stick to its style of design but would have the disadvantage of not giving possible new ideas to designers into how the design could be made better, reducing the possibility for future innovation.

3.3 PRODUCTION TOOLS

As has been shown earlier it is important to make sure that the production team has an input into the design stage. This is due to most of the cost coming from the production stage which becomes impossible to change once the design stage is completed. Designers often do not know how the design stage will affect the costs at the production stage and due to this relationship between the two teams, tools that predict the reaction of the production process and production engineers are key to low cost designs.

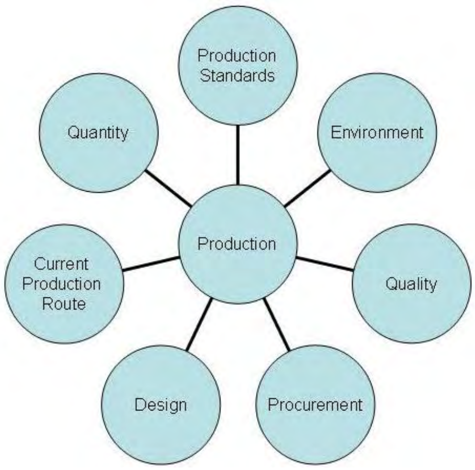

Fig.10: Production Inputs

Each of the bubbles in the diagram therefore represents an input into the decision process for production and affects the choices made about which is the best route to take to produce a certain vessel or how expensive this route will prove to be.

- Production standards - Standards do not just apply to design. Production yards must conform to health and safety standards as well as other legislation.
- Environment - Being "environmentally friendly" during the production process is an increasingly important factor. The need to reduce emissions for better worker health and safety is another issue to be considered.
- Quality - The quality of the boat will be a key part of the production process and a compromise will need to be found between producing a large volume of cheap boats and the quality of the finish on the hulls.
- Procurement - The expense of the materials used and new materials that become available will determine the final cost of the vessel.
- Design - The design process will play a large part in the production process as the geometry, layup etc. of the boat will affect the difficulty constructing the boat. A well thought out design will reduce the cost of production.
- Current production route - The production route can be changed depending on the volume of boats being produced and the expense of moving equipment around the shop floor. This will also take into account previous production routes that have been used at the yard.
- Quantity - The amount of boats that will be built effects the likelihood of using a certain production process as the equipment and the expertise may be expensive to hire but a large volume of product may make this change worth while. This value may include other boats the company is considering on producing.

4 STRUCTURAL DESIGN TOOL

As part of the concurrent engineering environment a tool has been developed to optimise boat hull structures for both mass and cost. As stated earlier this has be done to allow the design engineers an insight into the production methods to be used and to allow material selections and scantling determination to be shown with production in mind. The tool would be an early detailed design tool to allow structural engineers an idea of where the optimum scantlings would be placed before layout and other factors came into place. The optimisation has been carried out through the use of genetic algorithms which allow wide ranging fast searches to be carried out. The optimisation is finished using a hill-climb method to ensure that the optimum value has been found. The algorithm for this process is shown in fig. 11. The structural modeling of this tool has been covered in more depth in Sobey et al. [14].

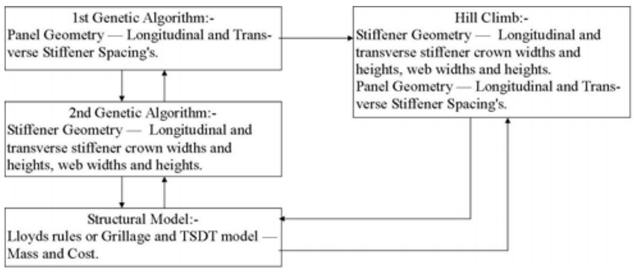

Fig.11: Structural optimisation tool processes

4.1 FIRST PRINCIPLES DESIGN

The first principles method of design has been built using Navier's Grillage method combined with elastic stress analysis for stiffeners and TSDT for the plates. The stiffeners are made up of 4 elements the geometry of which is shown in fig. 12. The panels are made out of lateral beams and transverse girders with an orthogonal force on the plate as shown in fig. 13.

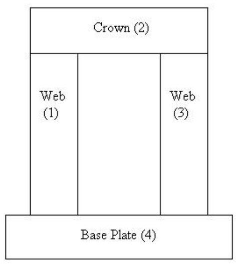

Fig.12: Stiffener Geometry

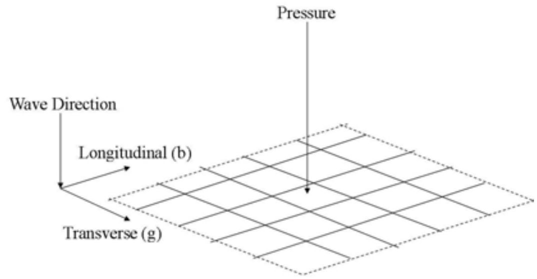

Fig.13: Grillage layout

4.1.1 NAVIER GRILLAGE

Navier grillage method has been used as the results given from this method very closely approximate those of computationally more expensive methods [15]. The use of genetic algorithms to optimise the results required that each generation of the code had a short run time. It is possible to find the deflection of the stiffeners from the Navier grillage theory found from [16] and seen in eq. 2. The deflection of the grillage allowed the stress and shear stress in the stiffeners to be determined to check to see if failure would occur:

$$w(x,y) = \sum_{m=1}^{\infty}\sum_{n=1}^{\infty} a_{mn} \sin\frac{m\pi x}{L} \sin\frac{n\pi y}{B} \tag{2}$$

the coefficient from eq. 2 can be found from eq. 3:

$$a_{mn} = \frac{16PLB}{\pi^6 mn\left\{m^4(g+1)\dfrac{D_g}{L^3} + n^4(b+1)\dfrac{D_b}{B^3}\right\}} \tag{3}$$

For use in a genetic algorithm it is important that the models are fast and therefore a wave number of 17 was used as beyond this point no significant increase in accuracy was found.

4.1.2 THIRD ORDER DEFORMATION THEORY

The deflection in the girders and beams could therefore be found but due to the manner in which grillage theory assumes that all of the stresses pass to the stiffeners it is also important to make sure that the panel does not fail. The modelling for the panels has been done using third order shear deformation theory as this allows laminates to be taken into account but is more computationally efficient than using deformation theories of higher orders. The equation to give the forces at each point on the panel can be found from:

$$q(x,y) = \sum_{n=1}^{\infty}\sum_{m=1}^{\infty} Q_{mn} \sin\alpha x \sin\beta y \tag{4}$$

where $\alpha = \frac{m\pi}{L}, \beta = \frac{n\pi}{B}$ and Q_{mn} is the lateral loading on the plate which is given by:

$$Q_{mn}(z) = \frac{4}{LB}\int_0^L\int_0^B q(x,y)\sin\frac{m\pi x}{L}\sin\frac{n\pi y}{B} \tag{5}$$

It is then possible to find the coefficients of the boundary conditions using the stiffness matrix [C] by substituting into the equations of motion where $Q_{mn} = \frac{-16q_0}{\pi^2 mn}$:

$$[C][\Delta] = \begin{vmatrix} 0 \\ 0 \\ Q_{mn} \\ 0 \\ 0 \end{vmatrix} \qquad [\Delta] = \begin{vmatrix} U_{mn} \\ V_{mn} \\ W_{mn} \\ X_{mn} \\ Y_{mn} \end{vmatrix} \tag{6}$$

The stiffness matrix [C], found from eq. 6, can be used to show the relation between the stress resultants and the strains:

$$\begin{vmatrix} \{N\} \\ \{M\} \\ \{P\} \end{vmatrix} = \begin{vmatrix} [A] & [B] & [E] \\ [B] & [D] & [F] \\ [E] & [F] & [H] \end{vmatrix} \begin{vmatrix} \{\epsilon^{(0)}\} \\ \{\epsilon^{(1)}\} \\ \{\epsilon^{(2)}\} \end{vmatrix} \tag{7}$$

$$\begin{vmatrix} \{Q\} \\ \{R\} \end{vmatrix} = \begin{vmatrix} [A] & [D] \\ [D] & [F] \end{vmatrix} \begin{vmatrix} \{\gamma^{(0)}\} \\ \{\gamma^{(2)}\} \end{vmatrix} \tag{8}$$

The values relating to this matrix [C] can be found from the use of Eq.9

$$(A_{mn}, B_{ij}, D_{mn}, E_{ij}, F_{mn}, H_{ij}) =$$
$$(\bar{Q}_{ij}, \bar{Q}_{mn})(1, z, z^2, z^3, z^4, z^6)dz$$
$$(i,j = 1,2,6), \quad (m,n = 1,2,4,6) \tag{9}$$

It is then possible to determine the values of the strains from the displacement relations.

$$\begin{vmatrix} \{\epsilon_{xx}\} \\ \{\epsilon_{yy}\} \\ \{\epsilon_{xy}\} \end{vmatrix} = \begin{vmatrix} \frac{\partial u_0}{\partial x} + \frac{1}{2}\left(\dfrac{\partial w_0}{\partial x}\right)^2 \\ \frac{\partial v_0}{\partial y} + \frac{1}{2}\left(\dfrac{\partial w_0}{\partial y}\right)^2 \\ \frac{\partial u_0}{\partial y} + \frac{\partial v_0}{\partial x} + \frac{\partial w_0}{\partial x}\frac{\partial w_0}{\partial y} \end{vmatrix} + z \begin{vmatrix} \dfrac{\partial \phi_x}{\partial x} \\ \dfrac{\partial \phi_y}{\partial y} \\ \dfrac{\partial \phi_x}{\partial y} + \dfrac{\partial \phi_y}{\partial x} \end{vmatrix}$$
$$+z^3 \begin{vmatrix} -c_1\left(\dfrac{\partial \phi_x}{\partial x} + \dfrac{\partial^2 w_0}{\partial x^2}\right) \\ -c_1\left(\dfrac{\partial \phi_y}{\partial y} + \dfrac{\partial^2 w_0}{\partial y^2}\right) \\ -c_1\left(\dfrac{\partial \phi_x}{\partial y} + \dfrac{\partial y}{\partial x} + 2\dfrac{\partial^2 w_0}{\partial x \partial y}\right) \end{vmatrix} \tag{10}$$

$$\begin{vmatrix} \{\epsilon_{yz}\} \\ \{\epsilon_{xz}\} \end{vmatrix} = \begin{vmatrix} \phi_y + \frac{\partial w_0}{\partial y} \\ \phi_x + \frac{\partial w_0}{\partial x} \end{vmatrix} + z^2 \begin{vmatrix} -c_2\left(\phi_y + \dfrac{\partial w_0}{\partial y}\right) \\ -c_2\left(\phi_x + \dfrac{\partial w_0}{\partial x}\right) \end{vmatrix} \tag{11}$$

From this equation it is then possible to determine the stresses that will be created in the plates from [17].

4.2 CLASSIFICATION SOCIETY RULES

A classification society rules model for structures has also been built using Lloyd's Register Rules for Special Service Craft. The models that have been produced use Part 8 Chapter 3. The model uses minimum values to generate the geometries where available and uses genetic algorithms to generate dimensions where these values do not exist. The results produced have been created using a panel 12m by 0.5m and a pressure on the panel of 0.024kPa the calculations for which were found in Part 8 Chapter 3. To make a fair comparison the same cost models, pressure and panel size have been used for both the first principles design and the classification society rules.

4.3 FAILURE CRITERIA

Further to previous work [14] failure criteria have been added to the model to better constrain the tool itself. The failure criteria used came from the 'World Wide Failure Exercise' (WWFE) [18], [19] and [20]. The choice made for each failure type can be seen from Table IV.

Table IV: Failure Criteria [21]

Failure Type	Criteria
Predicting the response of lamina	Puck [22], [23] and Tsai [24], [25]
Predicting final strength of multidirectional laminates	Puck
Predicting the deformation of laminates	Zinoviev [26], [27] and Puck

The report concluded that buckling 'did not address the prediction of buckling modes of failure' [21]. Buckling is a key part of failure in hull stiffeners and therefore an Euler based rule, seen in equation 12, has been used to constrain the model. This will be further developed to determine the characteristics of the model using post-buckling analysis.

$$\sigma_{cri} = \frac{6.97\pi^2 E_s}{12(1 - \upsilon_{12}^2 (d_s/c_s)^2)} \tag{12}$$

5 RESULTS

From the results shown it is possible to compare the first principles approach to that of the classification society rules. The results have also been compared with the dimensions, costs and masses gathered before the failure criteria were added to the optimisation.

Table V: Cost and Mass comparison

Rules	Mass(kg)	Cost(£)
Lloyd's Rules		
Pre-Failure	99.24	352.21
Post-Failure	151.42	371.92
First Principles		
Pre-Failure	88.11	338.56
Post-Failure	104.12	315.60

Table VI: Longitudinal Stiffener Geometry

Rule base	Web Height	Web Thickness	Crown Width	Crown Thickness
Lloyd's Rules				
Pre-Failure	55mm	4.1mm	55mm	1mm
Post-Failure	13.3mm	5.35mm	75mm	5.35mm
First Principles				
Pre-Failure	70mm	0.5mm	126mm	0.5mm
Post-Failure	58mm	6mm	2mm	2mm

Table VII: Transverse Stiffener Geometry

Rule base	Web Height	Web Thickness	Crown Width	Crown Thickness
Lloyd's Rules				
Pre-Failure	70mm	4.7mm	85mm	1mm
Post-Failure	56.8mm	4.13mm	178.6mm	4.13mm
First Principles				
Pre-Failure	69mm	0.5mm	55mm	0.5mm
Post-Failure	58mm	4mm	2mm	1mm

Table VIII: Panel Geometry

Rule Base	Longitudinal Stiffener Spacing	Transverse Stiffener Spacing	Panel Thickness
Lloyd's Rules			
Pre-Failure	425mm	500mm	6.1mm
Post-Failure	893mm	500mm	12.6mm
First Principles			
Pre-Failure	962mm	500mm	2mm
Post-Failure	9950mm	499mm	8mm

As was expected the introduction of more constraints increased the size of the stiffeners and therefore increased the cost and the mass of the designs. These new designs are much more similar to each other compared to the lesser constrained models. The first principles method still has a lower mass and cost than that of the classification society rules. The size of the crown is still very short and thin compared to a typical top-hat stiffener and therefore more constraints will need to be added to sort out this topology. The generally small size of the stiffeners is caused by the positioning of the panels themselves as these are situated above the waterline on the side of the hull and therefore are subjected to a low predicted pressure. This requires smaller stiffeners to withstand this pressure.

6 CONCLUSION

This paper outlines the requirements for a concurrent engineering environment for use in the leisure boatbuilding industry. Comparisons are drawn with other industries that have been using concurrent engineering for many years and characteristics for this environment have been assessed. Further to this the paper looks at an optimisation tool between structures and production and reports the progress made due to the addition of failure criteria.

For further development of the engineering environment and the optimisation tool it is hoped that in the future:

- it will be possible to test the flexibility and usefulness of the concurrent engineering environment the system using 3rd year students at the University of Southampton as part of one of their modules. This test will be to determine the level of increased performance gathered from concurrent engineering and will also be used to test the robustness of the system.

- More replies will be gathered from the questionnaire to create a sector survey of British boatbuilding industry allowing a look at the way in which design is done within the boat building industry.

- A direct method will also be used in a comparison with the classification society rules to see if improvements in speed and accuracy can be gained over stochastic methods due to the smaller amount of inputs that are required for classification society rules. The system will also be expanded to include ISO 12215 standards for structural design.

- Further development of the first principles method will be required requiring a comparison with FEA modelling for validation of results.

- Failure to produce successful first principles results will require response surface methods to be investigated allowing the use of FEA modelling for the structures as part of the optimisation approach.

References

[1] T.P. SARAFIN. *Spacecraft structures and mechanisms : from concept to launch*. Dordrecht : Kluwer Academic, 1995.

[2] K.G. SWIFT and N.J. BROWN. Implementation strategies for design for manufacture methodologies. *Proc. Instn Mech. Engrs Part B: J. Engineering Manufacture*, vol. 217, 2003.

[3] R. CURRY. An assessment of iso 12215 small craft hull construction with classification society rules. *Transactions of The Royal Institution of Naval Architects Part B: International Journal of Small Craft Technology*, vol. 147, 2004.

[4] J.M.C. CADAI, T.J. STRATFORD, L.C. HOLLAWAY, and W.G. DUCKETT. *Strengthening metallic structures using externally bonded fibre-reinforced polymers*. Classic House, 2004.

[5] G. BENNET and T. LAMB. Concurrent engineering: Application and implementation for shipbuilding. *Journal of Ship Production*, vol. 12(2):pp.107–125, 1996.

[6] R. HAAS and M. SINHA. Concurrent engineering at airbus: A case study. *International Journal of Manufacturing Technology and Management*, vol. 6(3/4):pp.241 – 253, 2004.

[7] R. SHISHKO. The proliferation of pdc-type environments in industry and universities. Proceedings of the 2nd EUSEC, Munich, 2000.

[8] S. FINKEL, M. WILKE, H. METZGER, and M. WAHNFRIED. Design centers - transferring experience from astronautics to aeronautics. Proceedings of the 12th Annual Symposium of INCOSE International Council on Systems Engineerins, Las Vegas, 2002.

[9] M. BANDECCHI, B. MELTON, B. GARDINI, and F. ONGARO. The esa/estec concurrent design facility. Proceeding of EuSec, 2000.

[10] M. GWYTHER. It worked for fridges! - why shipbuilding needs an industry-specific plm solution, 2007.

[11] M.A. EAGLESHAM. *A Decision Support System for Advanced Composites Manufacturing Cost Estimation*. PhD thesis, Virginia Polytechnic Institute and State University, 1998.

[12] F. AITSAHLIA, JOHNSON E., and WILL P. Is concurrent engineering always a sensible proposition? *IEEE Transactions on Engineering Management*, vol. 42(2), 1995.

[13] J.S. LOMBARDO, E. MIHALAK, and S.R. OSBORNE. Collaborative virtual prototyping. *Johns Hopkins APL Technical Digest*, vol. 17(3):pp.295 – 304, 1996.

[14] A.J. SOBEY, J.I.R. BLAKE, and R.A. SHENOI. Optimization of composite boat hull structures. In *Computer and Information Management Applications for Shipbuilding (COMPIT),Liege*, pages pp.502–515, 2008.

[15] J. CLARKSON. *The elastic analysis of flat grillages*. Cambridge University Press, 1965.

[16] G. VEDELER. *Grillage Beams*. Grondahl and son, 1945.

[17] R.N. REDDY. *Mechanics of Laminated Composite Plates and Shells*. Second Edition, CRC Press, 2004.

[18] A.S. KADDOUR, M.J. HINTON, and P.D. SODEN. A comparison of the predictive capabilities of current failure theories for composite laminates: additional contributions. *Composites Science and Technology*, vol. 64:pp.449–476, 2004.

[19] M.J. HINTON, A.S. KADDOUR, and P.D. SODEN. Evaluation of failure prediction in composite laminates: background to 'part b' of the exercise. *Composites Science and Technology*, vol. 62:pp.1481–1488, 2002.

[20] M.J. HINTON, A.S. KADDOUR, and P.D. SODEN. Evaluation of failure prediction in composite laminates: background to 'part c' of the exercise. *Composites Science and Technology*, vol. 64:pp.321–327, 2004.

[21] P.D. SODEN, A.S. KADDOUR, and M.J. HINTON. Recomendations for designers and researchers resulting from the world-wide failure exercise. *Composites Science and Technology*, vol. 64:pp.589–604, 2004.

[22] A. PUCK and H. SCHURMANN. Failure analysis of frp laminates by means of physically based phenomenological models. *Composites Science and Technology*, vol. 58:pp.1045–1067, 1998.

[23] A. PUCK and H. SCHURMANN. Failure analysis of frp laminates by means of physically based phenomenological models. *Composites Science and Technology*, vol. 62:pp.1633–1662, 2002.

[24] K. LIU and S.W. TSAI. A progressive quadratic failure criterion for a laminate. *Composites Science and Technology*, vol. 58:pp.1023–1032, 1998.

[25] A. KURAISHI, S.W. TSAI, and K.K.S. LIU. A progressive quadratic failure criterion, part b. *Composites Science and Technology*, vol. 62:pp.1683–1695, 2002.

[26] P.A. ZINOVIEV, S.V. GRIGORVIEV, O.V. LEBEDEVAB, and L.P. TAIROVA. The strength of multilayered composites under a plane-stress state. *Composites Science and Technology*, vol. 58, 1998.

[27] P.A. ZINOVIEV, O.V. LEBEDEVA, and L.P. TAIROVA. A coupled analysis of experimental and theoretical results on the deformation and failure of composite laminates under a state of plane stress. *Composites Science and Technology*, vol. 62:pp.1711–1723, 2002.

APPLICATION OF THE ORTHOTROPIC PLATE THEORY TO GARAGE DECK DIMENSIONING

Antonio Campanile, Masino Mandarino, Vincenzo Piscopo
Department of Naval Architecture and Marine Engineering, The University “Federico II”, Naples

SUMMARY

This paper focuses on the application of orthotropic plate bending theory to stiffened plating. Schade’s design charts for rectangular plates are extended to the case where the boundary contour is clamped, which is almost totally incomplete in the afore mentioned charts.
A numerical solution for the clamped orthotropic plate equation is obtained. The Rayleigh-Ritz method is adopted, expressing the vertical displacement field by a double cosine trigonometric series, whose coefficients are determined by solving a linear equation system. Numerical results are proposed as design charts similar to those ones by Schade. In particular, each chart is relative to one of the non-dimensional coefficients identifying the plate response; each curve of any chart is relative to a given value of the torsional parameter η_t, in a range comprised between 0 and 1, and is function of the virtual aspect ratio ρ, comprised between 1 and 8, so that the asymptotic behaviour of the orthotropic plate for $\rho \to \infty$ is clearly shown.
Finally, some numerical applications relative to ro-ro decks are presented, in order to evaluate the accuracy and the capability of the proposed technique for stiffened deck analysis. Obtained results are examined in order to draw a usable procedure for dimensioning deck primary supporting members, taking into account the interaction of the two orthogonal beam sets.

1. INTRODUCTION

Schade, 1942, proposed some practical general design curves, based on the “orthotropic plate” theory, in order to obtain a rapid, but accurate, dimensioning of plating stiffeners. Schade considered four types of boundary conditions for the orthotropic partial differential equation: all edges rigidly supported but not fixed; both short edges clamped, both long edges supported; both long edges clamped, both short edges supported; all edges clamped. The last case with all edges clamped was left almost totally incomplete. The few data useful for this boundary condition were taken from Timoshenko et al., 1959, and Young, 1940, as given for the isotropic plate only for the torsional coefficient value $\eta_t = 1$ and for a range of the virtual aspect ratio ρ comprised between 1 and 2.
In this work a numerical solution of the clamped orthotropic plate equation is obtained. Numerical results are presented in a series of charts similar to those ones given by Schade.
Obtained results are applied to the analysis of ro-ro garage decks, taking into due consideration the characteristic distribution of wheeled loads. In particular, two typical structural configurations have been examined and results are discussed aiming at obtaining a simple procedure for primary supporting member dimensioning.

2. A NUMERICAL SOLUTION OF THE CLAMPED RECTANGULAR ORTHOTROPIC PLATE EQUATION

Orthotropic plate theory refers to materials which have different elastic properties along two orthogonal directions. In order to apply this theory to panels having a finite number of stiffeners, it is necessary to idealize the structure, assuming that the structural properties of the stiffeners may be approximated by their average values, which are assumed to be distributed uniformly over the width and the length of the plate.

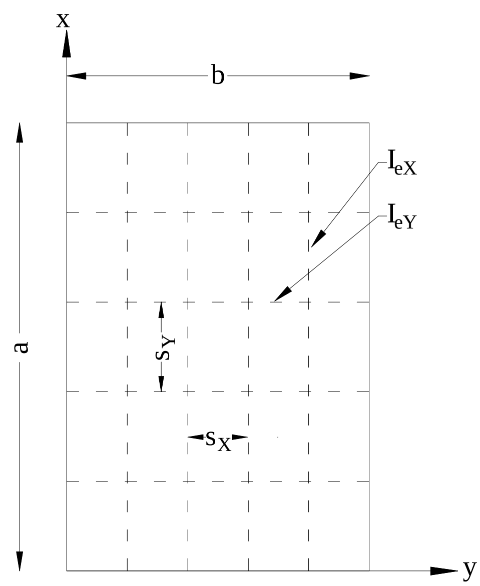

fig. 1

Referring to the coordinate system of fig.1, the deflection field in bending is governed by the so called Huber’s differential equation:

$$D_X \frac{\partial^4 w}{\partial x^4} + 2H \frac{\partial^4 w}{\partial x^2 \partial y^2} + D_Y \frac{\partial^4 w}{\partial y^4} = p(x, y) \qquad (1)$$

where:

- D_X is the unit flexural rigidity around the y axis;

- D_Y is the unit flexural rigidity around the *x* axis;
- $H = \eta_t \sqrt{D_X D_Y}$ according to the definition by Schade;
- *p* is the pressure load over the surface.

It is noticed that the behaviour of the isotropic plate with the same flexural rigidities in all directions is a special case of the orthotropic plate problem.
Indicating with *n* the normal external to the plate contour, a numerical solution of the orthotropic plate equation with the boundary conditions:

$$w=0 \text{ and } \frac{\partial w}{\partial n} = 0 \tag{2}$$

along all edges is presented. Now, as the plate domain is rectangular, the boundary conditions (2) become:

$$w=0 \text{ and } \frac{\partial w}{\partial x} = \frac{\partial w}{\partial y} = 0 \tag{3}$$

So any displacement function, satisfying the boundary conditions (3), must belong, with the first order derivatives, to the function space with compact support in Ω, i.e. $w \in C_0^1(\Omega)$, having denoted by Ω the function domain.
Now, two solution methods are available: the double cosine series and the Hencky's method. The second one is well known to converge quickly but does pose some difficulties with regard to programming due to over/underflow problems in the evaluation of hyperbolic trigonometric functions with large arguments. The double cosine series method, instead, is devoid of the over/underflow issue but is known to converge very slowly.
If *a* and *b* are the plate lengths in the *x* and *y* directions respectively, the vertical displacement field may be expressed by means of the following double cosine series:

$$w(x,y) = \sum_{m=1}^{M}\sum_{n=1}^{N}\left(1-\cos 2\pi m\frac{x}{a}\right)\cdot\left(1-\cos 2\pi n\frac{y}{b}\right)w_{m,n} \tag{4}$$

whose terms satisfy the boundary conditions (2). The unknown coefficients $w_{m,n}$ may be determined using the Rayleigh-Ritz method, searching for the minimum of a variational functional. Now, denoting by *u* and *f* two classes of functions belonging to a Hilbert Space, for linear differential operators as:

$$\ell u = f \tag{5}$$

that are auto-added and defined positive, it is possible to find a numerical solution of the equation (5) searching for the stationary point of the functional:

$$F(u) = \frac{1}{2}\int_{\Omega} \ell u \cdot u d\Omega - \int_{\Omega} f \cdot u d\Omega \tag{6}$$

The linear operator ℓ of the equation (5) is auto-added if, $\forall u(x,y) \in L^2(\Omega)$ and $\forall v(x,y) \in L^2(\Omega)$ satisfying the boundary conditions (3), it is verified that:

$$\int_{\Omega} \ell u \cdot v d\Omega = \int_{\Omega} \ell v \cdot u d\Omega \tag{7}$$

where Ω is an open set of $\Re^k$.
Now, let us consider the generalized integration by parts formula:

$$\int_{\Omega}(uD_i v)dt = \int_{\partial\Omega} uv(\underline{e}_i \circ \underline{n})d\sigma - \int_{\Omega}(vD_i u)dt \tag{8}$$

where $\underline{n}$ is the versor of the normal external to ∂A and $\underline{e}_i$ is the versor of t_i axis. First of all, in order to apply the equation (8), it is necessary to suppose that $\Omega \subset \Re^2$ is a regular domain, i.e. that it is a limited domain with one or more contours that have to be generally regular curves. In the case under examination, as Ω is a rectangular domain, these conditions are certainly verified. Furthermore, as $w \in C_0^1(\Omega)$, it derives that:

$$\int_{\Omega}(uD_1 v)dt = -\int_{\Omega}(vD_1 u)dt \tag{9}$$

but, thanks to the boundary conditions (3), it is also possible to verify that:

$$\int_{\Omega}(uD^{\alpha} v)dt = (-1)^{|\alpha|}\int_{\Omega}(vD^{\alpha} u)dt \tag{10}$$

whatever is the multi-index $\alpha = (\alpha_1, \alpha_2)$ with $|\alpha| \le 4$, having denoted by $|\alpha| = \alpha_1 + \alpha_2$ the sum of the derivation number respect to the first variable and the second one, respectively. From equation (10) it is immediately verified the condition (7), as the partial differential operators are of even order.
Furthermore the linear operator ℓ is defined positive if it is verified that:

$$\int_{\Omega} \ell u \cdot u d\Omega > 0 \tag{11}$$

Applying the generalized integration by parts formula, the integral (11) becomes:

$$\int_{\Omega}\left[D_X\left(\frac{\partial^2 w}{\partial x^2}\right)^2 + 2H\left(\frac{\partial^2 w}{\partial x \partial y}\right)^2 + D_Y\left(\frac{\partial^2 w}{\partial y^2}\right)^2\right]dA > 0 \; \forall w \neq 0 \tag{12}$$

If it was w=0, thanks to the continuity of the displacement function, it would result:

$$\frac{\partial^2 w}{\partial x^2} = \frac{\partial^2 w}{\partial x \partial y} = \frac{\partial^2 w}{\partial y^2} = 0 \quad \forall (x,y) \in \overset{\circ}{\Omega} \tag{13}$$

so obtaining:

$$\begin{cases} \dfrac{\partial w}{\partial x} = \text{const.} \\ \dfrac{\partial w}{\partial y} = \text{const.} \end{cases} \quad \forall(x,y) \in \overset{o}{\Omega} \tag{14}$$

and then, thanks to the continuity on the boundary:

$$\frac{\partial w}{\partial x} = \frac{\partial w}{\partial y} = 0 \quad \forall(x,y) \in \overset{0}{\Omega} \tag{15}$$

From eq. (15) it would result:

$$u = \text{const.} \quad \forall(x,y) \in \overset{o}{\Omega} \tag{16}$$

and then, thanks to the continuity on the boundary:

$$u = 0 \quad \forall(x,y) \in \overset{o}{\Omega} \tag{17}$$

So the condition (11) must be necessarily verified.
In order to find the coefficients of eq. (3), it is imposed that the functional (5) is stationary:

$$\frac{\partial F}{\partial w_{m,n}} = 0 \tag{18}$$

In this case the functional (6) is written as follows:

$$\Pi(w) = \frac{1}{2}\int_{\Omega}\left[D_X w\frac{\partial^4 w}{\partial x^4} + 2Hw\frac{\partial^4 w}{\partial x^2 \partial y^2} + D_Y w\frac{\partial^4 w}{\partial y^4}\right]dA + \\ -\int_{\Omega} wpdA \tag{19}$$

Applying the generalized integration by parts formula the functional (19) becomes:

$$\Pi(w) = \frac{1}{2}\int_{\Omega}\left[D_X\left(\frac{\partial^2 w}{\partial x^2}\right)^2 + 2H\frac{\partial^2 w}{\partial x^2}\frac{\partial^2 w}{\partial y^2} + D_Y\left(\frac{\partial^2 w}{\partial y^2}\right)^2\right]dA + \\ -\int_{\Omega} wpdA \tag{20}$$

To carry out the computations, it is convenient to use the following coordinate transformations:

$$x = a\xi \quad ; \quad 0 \le \xi \le 1 \tag{21.1}$$

$$y = b\eta \quad ; \quad 0 \le \eta \le 1 \tag{21.2}$$

so that the series is given in nondimensional coordinates:

$$w(\xi,\eta) = \sum_{m=1}^{M}\sum_{n=1}^{N}(1-\cos 2\pi m\xi)\cdot(1-\cos 2\pi n\eta)w_{m,n} \tag{22}$$

Then the functional is written in the form:

$$\hat{\Pi}(w) = \frac{\Pi(w)}{ab} = \\ = \frac{1}{2}\int_0^1\int_0^1\left[\frac{D_X}{a^4}\left(\frac{\partial^2 w}{\partial \xi^2}\right)^2 + \frac{2H}{a^2b^2}\frac{\partial^2 w}{\partial \xi^2}\frac{\partial^2 w}{\partial \eta^2} + \frac{D_Y}{b^4}\left(\frac{\partial^2 w}{\partial \eta^2}\right)^2\right]d\xi d\eta + \\ -\int_0^1\int_0^1 wpd\xi d\eta \tag{23}$$

and the stationary point is obtained imposing the *MxN* equations system:

$$\frac{\partial}{\partial w_{m,n}}\hat{\Pi}(w) = 0 \qquad \text{for } m=1\ldots M\ ;\ n=1\ldots N \tag{24}$$

So, considering p as uniformly distributed, the generic equation, for $m = \overline{m}$ and $n = \overline{n}$, assumes the form:

$$\frac{\partial}{\partial w_{\overline{m},\overline{n}}}\int_0^1\int_0^1\left[D_X\left(\frac{\partial^2 w}{\partial \xi^2}\right)^2 + 2\left(\frac{a}{b}\right)^2 H\frac{\partial^2 w}{\partial \xi^2}\frac{\partial^2 w}{\partial \eta^2} + D_Y\left(\frac{a}{b}\right)^4\left(\frac{\partial^2 w}{\partial \eta^2}\right)^2\right]d\xi d\eta = \\ = 2pa^4\frac{\partial}{\partial w_{\overline{m},\overline{n}}}\int_0^1\int_0^1 wd\xi d\eta \tag{25}$$

As regards the second member of equation (25), it is certainly possible to write the partial differential operator under the integral sign, so obtaining:

$$\int_0^1\int_0^1\frac{\partial}{\partial w_{\overline{m},\overline{n}}}wd\xi d\eta = \int_0^1\int_0^1(1-\cos 2\pi\overline{m}\xi)\cdot(1-\cos 2\pi\overline{n}\eta)d\xi d\eta = 1 \tag{26}$$

The first integral at the left hand side of the equation (25) becomes:

$$\int_0^1\int_0^1\frac{\partial}{\partial w_{\overline{m},\overline{n}}}\left(\frac{\partial^2 w}{\partial \xi^2}\right)^2 d\xi d\eta = \int_0^1\int_0^1 2\frac{\partial^2 w}{\partial \xi^2}\frac{\partial}{\partial w_{\overline{m},\overline{n}}}\frac{\partial^2 w}{\partial \xi^2}d\xi d\eta = \\ = 32\pi^4\overline{m}^2\sum_{m=1}^{M}\sum_{n=1}^{N}m^2 w_{m,n}\int_0^1\cos 2\pi\overline{m}\xi\cos 2\pi m\xi d\xi\int_0^1(1-\cos 2\pi\overline{n}\eta)\cdot \\ \cdot(1-\cos 2\pi n\eta)d\eta = 8\pi^4\overline{m}^4\left(w_{\overline{m},\overline{n}} + 2\sum_{n=1}^{N}w_{\overline{m},n}\right) \tag{27}$$

In a similar way, the third term becomes:

$$\int_0^1\int_0^1\frac{\partial}{\partial w_{\overline{m},\overline{n}}}\left(\frac{\partial^2 w}{\partial \eta^2}\right)^2 d\xi d\eta = 8\pi^4\overline{n}^4\left(w_{\overline{m},\overline{n}} + 2\sum_{m=1}^{M}w_{m,\overline{n}}\right) \tag{28}$$

Manipulating similarly the second term, it is obtained:

$$\int_0^1\int_0^1\frac{\partial}{\partial w_{\overline{m},\overline{n}}}\left(\frac{\partial^2 w}{\partial \xi^2}\cdot\frac{\partial^2 w}{\partial \eta^2}\right)d\xi d\eta = 16\pi^4\overline{m}^2\sum_{m=1}^{M}\sum_{n=1}^{N}n^2 w_{m,n}\int_0^1\cos 2\pi m\xi\cdot \\ \cdot(1-\cos 2\pi\overline{m}\xi)d\xi\cdot\int_0^1\cos 2\pi n\eta(1-\cos 2\pi\overline{n}\eta)d\eta +$$

$$+16\pi^4\bar{n}^{-2}\sum_{m=1}^{M}\sum_{n=1}^{N}m^2 w_{m,n}\int_0^1\left(1-\cos 2\pi\bar{m}\xi\right)\cos 2\pi m\xi d\xi\int_0^1\cos 2\pi\bar{n}\eta\cdot$$

$$\cdot\left(1-\cos 2\pi n\eta\right)d\eta = 8\pi^4\bar{m}^{-2}\bar{n}^{-2}w_{\bar{m},\bar{n}} \qquad (29)$$

Introducing the expressions (27), (28), (29), the left hand side of equation (25) can be so expressed:

$$\left\{D_X\left[\bar{m}^4 w_{\bar{m},\bar{n}}+\sum_{n=1}^{N}2\bar{m}^4 w_{\bar{m},n}\right]+D_Y\left(\frac{a}{b}\right)^4\left[\bar{n}^4 w_{\bar{m},\bar{n}}+\sum_{m=1}^{M}2\bar{n}^4 w_{m,\bar{n}}\right]+\right.$$

$$\left.+2\left(\frac{a}{b}\right)^2 H\bar{m}^{-2}\bar{n}^{-2}w_{\bar{m},\bar{n}}\right\}8\pi^4 \qquad (30)$$

Introducing the torsional coefficient η_t and the virtual side ratio defined as:

$$\rho=\frac{a}{b}\sqrt[4]{\frac{D_Y}{D_X}} \qquad (31)$$

the equation (25) can be so written:

$$4\pi^4\left\{\frac{1}{\rho^4}\left[\bar{m}^4 w_{\bar{m},\bar{n}}+\sum_{n=1}^{N}2\bar{m}^4 w_{\bar{m},n}\right]+\bar{n}^4 w_{\bar{m},\bar{n}}+\sum_{m=1}^{M}2\bar{n}^4 w_{m,\bar{n}}+\right.$$

$$\left.+\frac{2\eta_t}{\rho^2}\bar{m}^{-2}\bar{n}^{-2}w_{\bar{m},\bar{n}}\right\}=\frac{pb^4}{D_Y} \qquad (32)$$

Defining the non dimensional vertical displacements:

$$\delta=\frac{w}{\frac{pb^4}{D_Y}} \quad ; \quad \delta_{m,n}=\frac{w_{m,n}}{\frac{pb^4}{D_Y}} \qquad (33)$$

the system finally becomes:

$$4\pi^4\left\{\frac{1}{\rho^4}\left[\bar{m}^4\delta_{\bar{m},\bar{n}}+\sum_{n=1}^{N}2\bar{m}^4\delta_{\bar{m},n}\right]+\bar{n}^4\delta_{\bar{m},\bar{n}}+\sum_{m=1}^{M}2\bar{n}^4\delta_{m,\bar{n}}+\right.$$

$$\left.+\frac{2\eta_t}{\rho^2}\bar{m}^{-2}\bar{n}^{-2}\delta_{\bar{m},\bar{n}}\right\}=1 \;;\bar{m}=1...M \text{ and } \bar{n}=1...N \qquad (34)$$

Even if the double cosine trigonometric series converges very slowly, adopting sufficiently high values for M and N, it is possible to obtain a very accurate solution of the equation (1) with the boundary conditions (2).

3. CHARACTERIZATION OF THE BEHAVIOUR OF CLAMPED STIFFENED PLATES

The orthotropic plate bending theory can be applied to the plate of fig. 1, reinforced by two systems of parallel beams spaced equal distances apart in the x and y directions. The rigidities D_X and D_Y of equation (1) can be specialized as follows:

$$D_X=\frac{EI_{eX}}{s_X}=Ei_X \qquad (35.1)$$

$$D_Y=\frac{EI_{eY}}{s_Y}=Ei_Y \qquad (35.2)$$

where E is the Young's modulus and s_X (s_Y) is the distance between girders (transverses). It is noticed that I_{eX} (I_{eY}) is the moment of inertia, including effective width b_{eX} (b_{eY}) of plating and the attached ordinary stiffeners of long (short) repeating primary supporting members, respect to the axis whose eccentricity from the reference plane (z = 0) is to be determined as follows:

$$\frac{b_{eX}}{1-\nu^2}\int_{P_x}(z-e_X)dz+\int_{A_x}(z-e_X)dA+\left(\frac{b_{eX}}{s_{eX}}-1\right)\int_{a_x}(z-e_X)dA=0 \qquad (36.1)$$

$$\frac{b_{eY}}{1-\nu^2}\int_{P_y}(z-e_Y)dz+\int_{A_y}(z-e_Y)dA+\left(\frac{b_{eY}}{s_{eY}}-1\right)\int_{a_y}(z-e_Y)dA=0 \qquad (36.2)$$

where s_{eX} and s_{eY} are the spacings between ordinary stiffeners and P_i, A_i and a_i are the plating, the supporting member and the ordinary stiffener section areas, respectively. The moments of inertia have to be determined applying the following equations:

$$I_{eX}=\frac{b_{eX}}{1-\nu^2}\int_{P_x}(z-e_X)^2dz+\int_{A_x}(z-e_X)^2dA+\left(\frac{b_{eX}}{s_{eX}}-1\right)\int_{a_x}(z-e_X)^2dA \qquad (37.1)$$

$$I_{eY}=\frac{b_{eY}}{1-\nu^2}\int_{P_y}(z-e_Y)^2dz+\int_{A_y}(z-e_Y)^2dA+\left(\frac{b_{eY}}{s_{eY}}-1\right)\int_{a_y}(z-e_Y)^2dA \qquad (37.2)$$

The torsional coefficient η_t and the virtual side ratio ρ can be specialized according to Schade's works:

$$\eta_t=\sqrt{\frac{i_{pX}i_{pY}}{i_Xi_Y}} \qquad (38.1)$$

$$\rho=\frac{a}{b}\sqrt[4]{\frac{i_Y}{i_X}} \qquad (38.2)$$

where i_{pX} (i_{pY}) is the moment of inertia of effective breadth of plating working with long (short) supporting stiffeners per unit length. In the following r_{Xp} (r_{Yp}) is the vertical distance of the associated plating working with long (short) supporting stiffeners from the section neutral axis, while r_{Xf} (r_{Yf}) is the distance of the free flange from the section neutral axis.

The meaning of the two parameters is quite clear. In particular, the torsional coefficient η_t, which lies between 0 and 1, exists because only the plating is subject to horizontal shear, while both the plating and stiffeners are subject to bending stress. Obviously η_t=1, and $i_{pX}=i_{pY}=i_X=i_Y$, represents the isotropic plate case. The virtual side ratio ρ is the plate side ratio modified in accordance with the unit stiffnesses in the two directions; as usual, it has been admitted that ρ is always equal to or greater than unity.

In the next the quantities represented in the diagrams are presented.

Deflection at center, fig. 2: the vertical displacement at the plate center ($\eta=\xi=0.5$) is the maximum and is so expressed:

$$w_{\max} = k_W \frac{pb^4}{Ei_Y} \tag{39.1}$$

where:

$$k_W(\rho,\eta) = \sum_{m=1}^{M}\sum_{n=1}^{N}\delta_{m,n}(1-\cos\pi m)(1-\cos\pi n) \tag{39.2}$$

Edge bending stress in plating, fig. 3: these curves give the bending stress in the plating at the centers of edges where fixity exists. The stress at the center of such an edge may be treated as the maximum along that edge. The maximum stresses in the plating in the long and short directions respectively are:

$$\sigma_{XpSUP} = \frac{E}{1-\nu^2}\frac{1}{a^2}\left.\frac{\partial^2\delta}{\partial\xi^2}\right|_{\substack{\xi=0\\ \eta=\frac{1}{2}}} r_{Xp}\frac{pb^4}{Ei_Y} \tag{40.1}$$

$$\sigma_{YpSUP} = \frac{E}{1-\nu^2}\frac{1}{b^2}\left.\frac{\partial^2\delta}{\partial\eta^2}\right|_{\substack{\eta=0\\ \xi=\frac{1}{2}}} r_{Yp}\frac{pb^4}{Ei_Y} \tag{40.2}$$

as along the edges it results:

$$\left.\frac{\partial^2\delta}{\partial\eta^2}\right|_{\substack{\xi=0\\ \eta=\frac{1}{2}}} = 0 \quad and \quad \left.\frac{\partial^2\delta}{\partial\xi^2}\right|_{\substack{\eta=0\\ \xi=\frac{1}{2}}} = 0 \tag{41}$$

The equations (40.1) and (40.2) become:

$$\sigma_{XpSUP} = k_{XpSUP}(\rho,\eta)\frac{pb^2 r_{Xp}}{\sqrt{i_X i_Y}} \tag{42.1}$$

$$\sigma_{YpSUP} = k_{YpSUP}(\rho,\eta)\frac{pb^2 r_{Yp}}{i_Y} \tag{42.2}$$

where:

$$k_{XpSUP}(\rho,\eta) = \frac{1}{\rho^2}\frac{4\pi^2}{1-\nu^2}\sum_{m=1}^{M}\sum_{n=1}^{N}\delta_{m,n}m^2(1-\cos\pi n) \tag{43.1}$$

$$k_{YpSUP}(\rho,\eta) = \frac{4\pi^2}{1-\nu^2}\sum_{m=1}^{M}\sum_{n=1}^{N}\delta_{m,n}n^2(1-\cos\pi m) \tag{43.2}$$

Edge bending stress in free flanges, fig. 4: these curves give the bending stress in the free flanges at the centers of edges where fixity exists. The stress at the center of such an edge may be treated as the maximum along that edge. The maximum stresses in the free flanges for girders and transverses are respectively:

$$\sigma_{XfSUP} = -E\frac{1}{a^2}\left.\frac{\partial^2\delta}{\partial\xi^2}\right|_{\substack{\xi=0\\ \eta=\frac{1}{2}}} r_{Xf}\frac{pb^4}{Ei_Y} \tag{44.1}$$

$$\sigma_{YfSUP} = -E\frac{1}{b^2}\left.\frac{\partial^2\delta}{\partial\eta^2}\right|_{\substack{\eta=0\\ \xi=\frac{1}{2}}} r_{Yf}\frac{pb^4}{Ei_Y} \tag{44.2}$$

The equations (44.1) and (44.2) can be re-written as follows:

$$\sigma_{XfSUP} = -k_{XfSUP}(\rho,\eta)\frac{pb^2 r_{Xf}}{\sqrt{i_X i_Y}} \tag{45.1}$$

$$\sigma_{YfSUP} = -k_{YfSUP}(\rho,\eta)\frac{pb^2 r_{Yf}}{i_Y} \tag{45.2}$$

where:

$$k_{XfSUP}(\rho,\eta) = \frac{4\pi^2}{\rho^2}\sum_{m=1}^{M}\sum_{n=1}^{N}\delta_{m,n}m^2(1-\cos\pi n) \tag{46.1}$$

$$k_{YfSUP}(\rho,\eta) = 4\pi^2\sum_{m=1}^{M}\sum_{n=1}^{N}\delta_{m,n}n^2(1-\cos\pi m) \tag{46.2}$$

It is important to note that when $\rho \to \infty$ k_{YfSUP} is substantially independent on η_t and is equal to $\frac{1}{12}$ that is the beam theory value. Furthermore the curves show that for low values of η_t the maximum deflections and stresses parallel to the short direction occur at values of ρ between 1.5 and 2.0: this indicates that the long beams add to the load taken by the short beams, instead of helping to support it.

Bending stress in free flanges at center, fig. 5: these curves give the bending stress in the free flanges at the center of the panel in long and short directions respectively. The stresses:

$$\sigma_{XfCEN} = -E\frac{1}{a^2}\left.\frac{\partial^2\delta}{\partial\xi^2}\right|_{\substack{\xi=\frac{1}{2}\\ \eta=\frac{1}{2}}} r_{Xf}\frac{pb^4}{Ei_Y} \tag{47.1}$$

$$\sigma_{YfCEN} = -E\frac{1}{b^2}\left.\frac{\partial^2\delta}{\partial\eta^2}\right|_{\substack{\eta=\frac{1}{2}\\ \xi=\frac{1}{2}}} r_{Yf}\frac{pb^4}{Ei_Y} \tag{47.2}$$

can be so expressed:

$$\sigma_{XfCEN} = k_{XfCEN}(\rho,\eta)\frac{pb^2 r_{Xf}}{\sqrt{i_X i_Y}} \tag{48.1}$$

$$\sigma_{YfCEN} = k_{YfCEN}(\rho,\eta)\frac{pb^2 r_{Yf}}{i_Y} \tag{48.2}$$

where:

$$k_{XfCEN}(\rho,\eta) = -\frac{4\pi^2}{\rho^2}\sum_{m=1}^{M}\sum_{n=1}^{N}\delta_{m,n}m^2\cos\pi m(1-\cos\pi n) \tag{49.1}$$

$$k_{YfCEN}(\rho,\eta) = -4\pi^2 \sum_{m=1}^{M}\sum_{n=1}^{N} \delta_{m,n} n^2 \cos \pi n (1-\cos \pi m) \qquad (49.2)$$

It is important to note that when $\rho \to \infty$ k_{YfCEN} is substantially independent on η_t and is equal to $\frac{1}{24}$ that is the beam theory value.

In order to verify the goodness of the method, the following tables shows a comparison between the values obtained applying the Rayleigh-Ritz method and the ones taken from Timoshenko et al., 1959, for the isotropic plate (η_t=1.00).

Deflection at center		
ρ	**Timoshenko**	**k_W (η_t = 1.00)**
1.00	0.00126	0.00126
1.20	0.00172	0.00172
1.40	0.00207	0.00207
1.60	0.00230	0.00230
1.80	0.00245	0.00245
2.00	0.00254	0.00253
∞	0.00260	0.00260

tab. 1

Edge bending moment in short direction		
ρ	**Timoshenko**	**$(1-\nu^2)K_{YpSUP}$ (η_t =1.00)**
1.00	0.0513	0.0510
1.20	0.0639	0.0636
1.40	0.0726	0.0724
1.60	0.0780	0.0779
1.80	0.0812	0.0811
2.00	0.0829	0.0828
∞	0.0833	0.0833

tab. 2

Edge bending moment in long direction		
ρ	**Timoshenko**	**$(1-\nu^2)K_{XpSUP}$ (η_t =1.00)**
1.00	0.0513	0.0510
1.20	0.0554	0.0558
1.40	0.0568	0.0570
1.60	0.0571	0.0571
1.80	0.0571	0.0571
2.00	0.0571	0.0571
∞	0.0571	0.0571

tab. 3

fig. 2 - Deflection at center

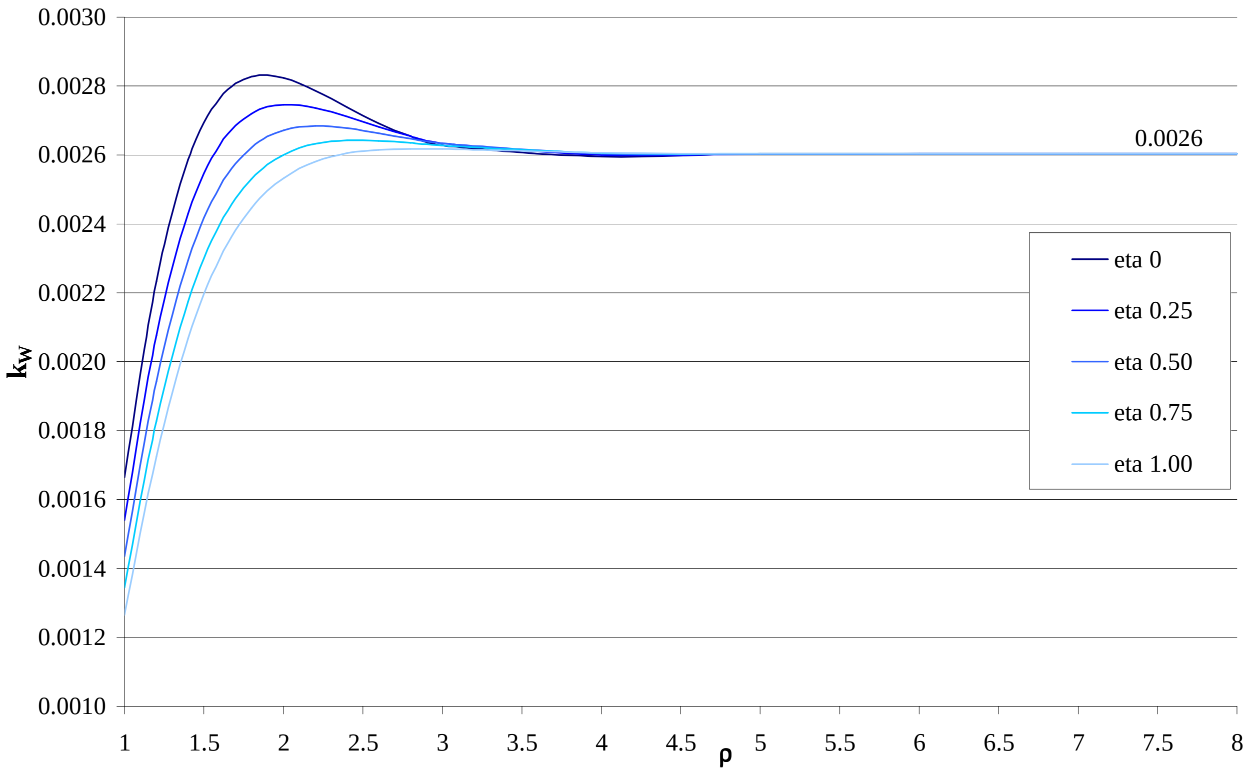

fig. 3 - Edge bending stress in plating

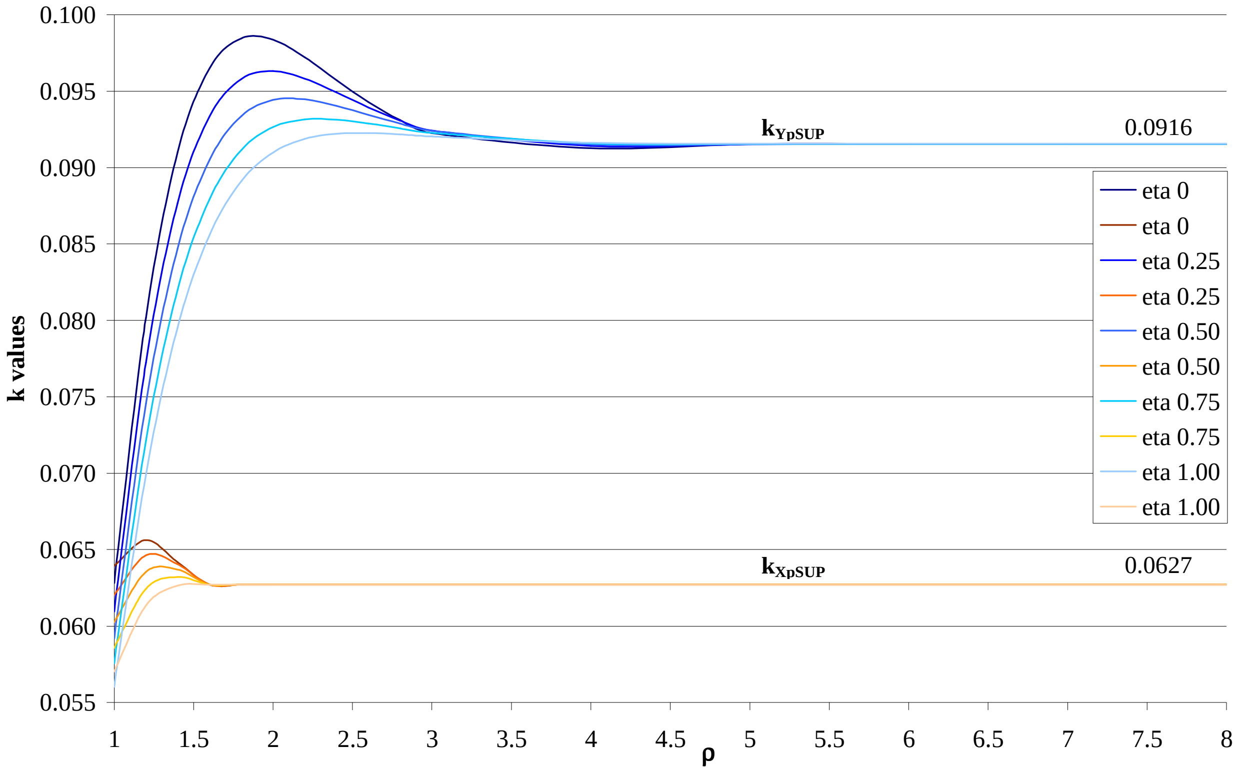

fig. 4 - Edge bending stress in free flanges

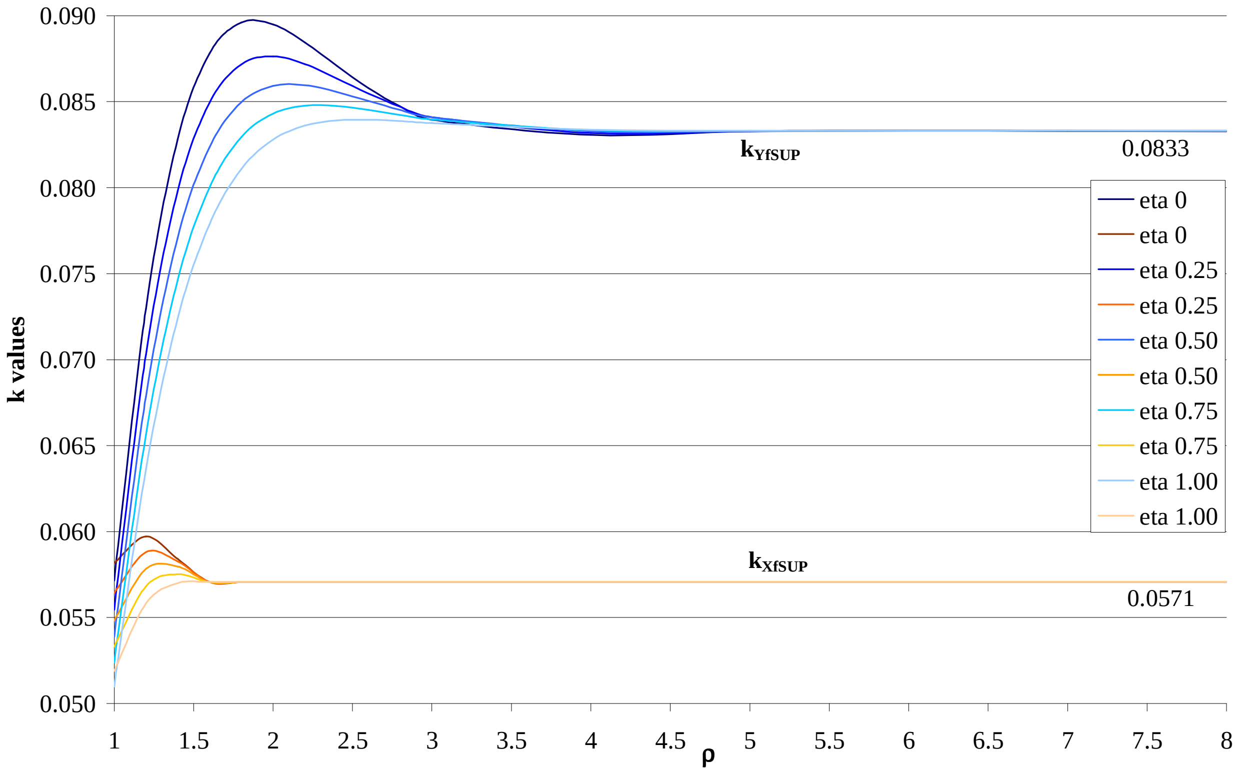

fig. 5 - Bending stress in free flanges at center

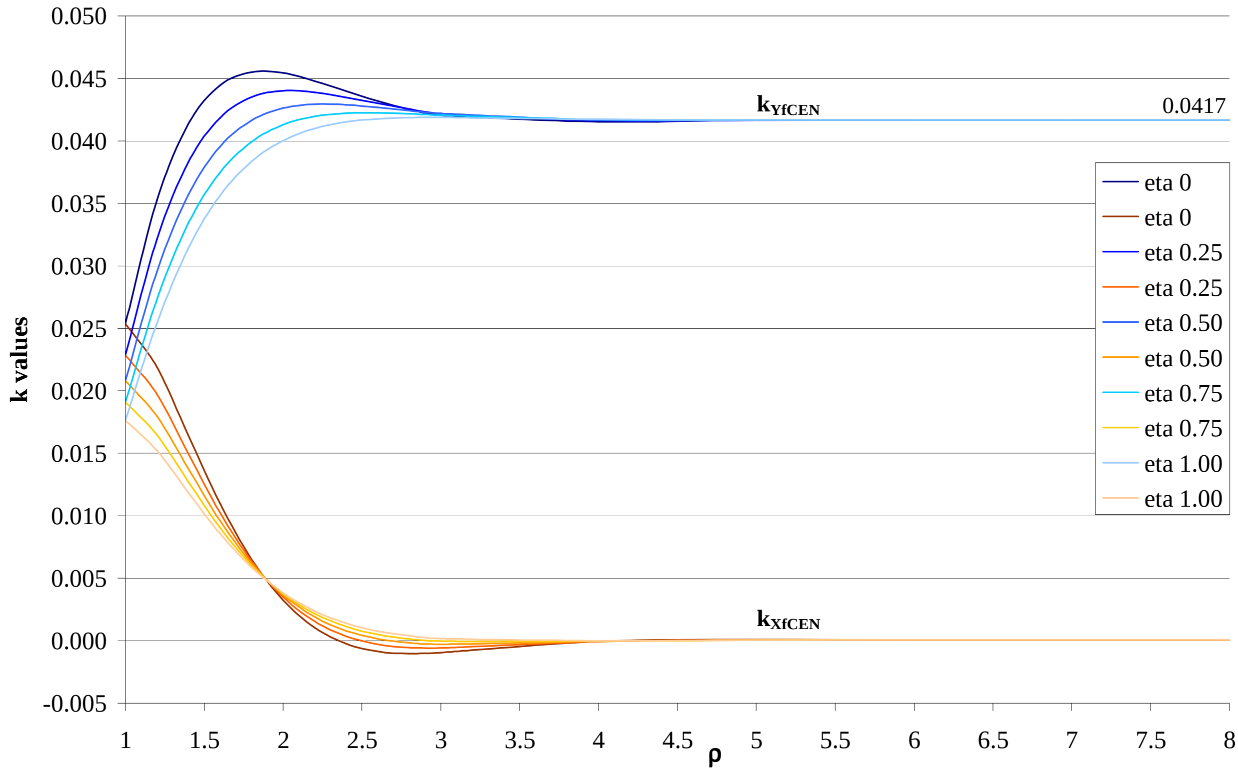

4. CONVERGENCE OF THE METHOD

In the following, the influence of the number of harmonics on k values is shown. Particularly, assuming ρ=5 and η=0.50, $M=N$ has been varied from 5 up to 100, in order to obtain a number of harmonics comprised between 25 and 10000.
If the number of harmonics is > 4900, i.e. M=N > 70, a good convergence in the assessment of k values, and then of the proposed curves, is obtained for practical purposes, as it can be appreciated from fig. 6, 7, 8.

fig. 7 - $k_{Y\rho SUP}$ convergence

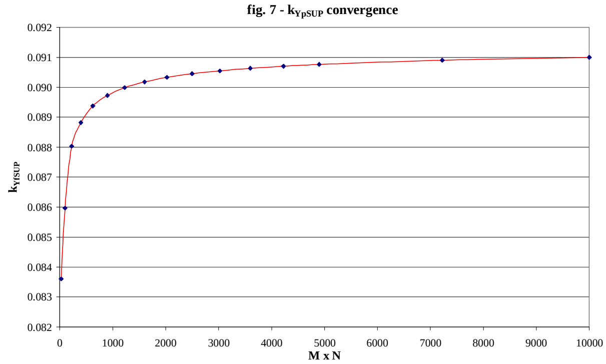

fig . 6 - k_W convergence

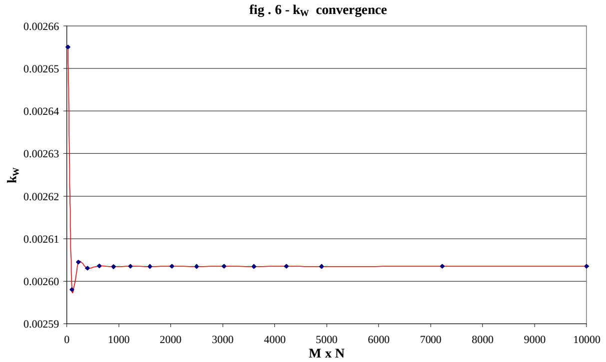

fig. 8 - $k_{X\rho SUP}$ convergence

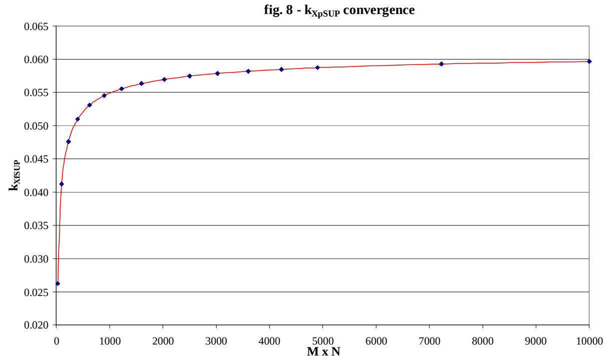

5. THE CASE OF DISCONTINUOUS LOADS

The partial differential equation (1) has been written with reference to a distributed normal pressure load which is a continuous function in the plate $\aleph$.

Let's now suppose that $p \in L^2(\Omega)$, so that the set of discontinuity points has zero measure according to Lebesgue.

Let's define with $\aleph_0 \subseteq \aleph$ the point set where p is continuous and with $\aleph_1 \subset \aleph : m(\aleph_1) = 0$ the point set where p is discontinuous.

The two subsets $\aleph_0$ and $\aleph_1$ define a partition of $\aleph$:

$$\begin{cases} \aleph_0 \cup \aleph_1 = \aleph \\ \aleph_0 \cap \aleph_1 = \varnothing \end{cases} \tag{50}$$

Rigorously, as (1) is valid point by point only where p is continuous, the functional (19) has to be extended only to the $\aleph_0$ domain. But, as p is continuous almost everywhere in $\aleph$, the functional $\Pi(w)$ can be extended to the entire $\aleph$ domain. It is noticed that, as $w \in L^2(\Omega)$, according to the Schwartz-Holder inequality, $pw \in L^1(\Omega)$, e.g. [4].

Moreover, as an integral extended to a set of zero measure is equal to zero according to Lebesgue, the following equalities hold:

$$\Pi(w)\big|_{\aleph_0} = \Pi(w)\big|_{\aleph_0 \cup \aleph_1} = \Pi(w)\big|_{\aleph} \tag{51}$$

Then, it is possible to apply the equation (1) not only when the load function is continuous in $\aleph$, but also when it is continuous almost everywhere in $\aleph$, in both cases extending the functional (19) to the entire domain according to the identity (51).

The extension to load functions continuous almost everywhere according to Lebesgue is particularly useful when it is necessary to schematize the wheeled loads. In this case, in fact, the effective load distribution can be modelled as an equivalent pressure, transversally constant but longitudinally discontinuous:

$$p_{eq.}(\xi,\eta) = p_i \qquad \forall \xi \in [\alpha_i, \beta_i]; \quad \forall \eta \in [0,1] \tag{52}$$

6. THE EQUIVALENT PRESSURE FOR WHELED LOAS

For primary supporting members subjected to wheeled loads, yielding checks have to be carried out considering a maximum pressure load, equivalent to the maximum vertical, static and dynamic, applied forces; the static part can be evaluated with the following relation, suggested by R.I.NA., 2005:

$$p_{eq.stat.} = \frac{n_V Q_A}{ls}\left(3 - \frac{X_1 + X_2}{s}\right) g \tag{53}$$

in which it is assumed:

- n_V = maximum number of vehicles located on the primary supporting member;
- Q_A = maximum axle load in t;
- X_1 = minimum distance, in m, between two consecutive axles;
- X_2 = minimum distance, in m, between the axles of two consecutive vehicles;
- l = span, in m, of the primary supporting members;
- s = spacing, in m, of primary supporting members.

The maximum total equivalent pressure is the sum of the static term and the dynamic one and can be expressed in kN/m^2 as follows:

$$p_{eq.\max} = (1 + a_Z) p_{eq.stat.} \tag{54}$$

where a_Z is the ship vertical acceleration.

The following figure shows the origin of the formula (53).

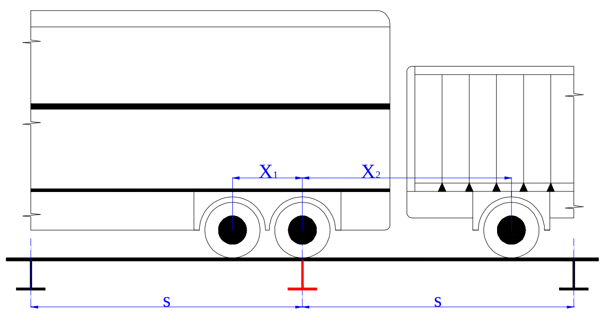

fig. 9

The three wheels give the following contributions to eq. (53):

- $p_{eq.stat.0} = \dfrac{n_V Q_A}{ls} g$
- $p_{eq.stat.1} = \dfrac{n_V Q_A}{ls}\left(\dfrac{s - X_1}{s}\right) g$
- $p_{eq.stat.2} = \dfrac{n_V Q_A}{ls}\left(\dfrac{s - X_2}{s}\right) g$

The equation (53) is valid only if an axle is located directly on a supporting member, but if this condition is not verified the previous relation can't be directly applied. So, it is convenient to generalize the eq. (53) as follows:

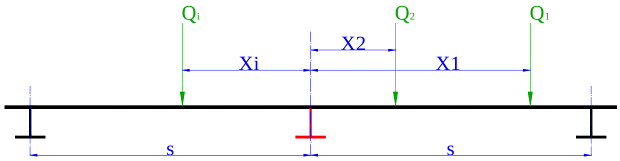

fig. 10

$$p_{eq.stat.} = \frac{n_V}{ls} \sum_{i=1}^{n_A} Q_{Ai} \left(1 - \frac{X_i}{s}\right) g \tag{55}$$

where n_A is the number of axles between $-s$ and s and X_i is the distance of the *i-th* axle load from the considered supporting member. From eq. (55), the actual equivalent pressure p_i, including inertial force, is obtained similarly to eq. (54).
In such a way it is possible to model the load distribution on the deck on the basis of axle loads and geometric characteristics of vehicles.
As in this case the deck isn't loaded by a uniform pressure load, but by a load function discontinuous at intervals, the integral at the second term of (25) has to be replaced as follows:

$$
\begin{aligned}
&2a^4 \frac{\partial}{\partial w_{\bar{m},\bar{n}}} \int_0^1 \int_0^1 pw\, d\xi\, d\eta = \\
&= 2\, p_{eq.\max}\, a^4 \sum_{i=1}^{n_T} \kappa_i \int_{\alpha_i}^{\beta_i} \left(1-\cos 2\pi\bar{m}\xi\right) d\xi \int_0^1 \left(1-\cos 2\pi\bar{n}\eta\right) d\eta = \\
&= 2\, p_{eq.\max}\, a^4 \sum_{i=1}^{n_T} \kappa_i \left(\beta_i - \alpha_i - \frac{sen 2\pi\bar{m}\beta_i - sen 2\pi\bar{m}\alpha_i}{2\pi\bar{m}} \right)
\end{aligned}
\quad (56)
$$

where n_T is the number of intervals where p is continuous, coinciding with the number of transverses, $p_{eq.max}$ is the maximum equivalent pressure given by (54) and κ_i is defined as follows:

$$\kappa_i = \frac{p_i}{p_{eq.\max}} = \frac{p[\alpha_i, \beta_i]}{p_{eq.\max}} \quad (57)$$

7. ANALYSIS OF SOME TYPICAL RO-RO DECK STRUCTURES

In the following it has been investigated the influence of the longitudinal distribution of wheeled loads on girder and transverse stresses, in order to highlight the "plate effect" which re-distributes the load peaks on transverses, unlike the isolated beam scheme.
Two decks are analyzed: the first one is relative to a fast ferry, the second one to a Ro-ro Panamax ship (see Campanile et al., 2007).

7.1 ANALYSIS OF A RO-RO FAST FERRY DECK

It has been carried out the evaluation of the stresses acting on the primary supporting members of a fast ferry used to carry vehicles; the ship main dimensions are: L_{bp} = 97.61 m; B = 17.10 m ; D = 10.40 m; Δ = 1420t. All transverses and girders have a 320x10+150x15 T section, while longitudinals are 60x6 offset bulb plates, in high-strength steel with σ_{yield}=355 N/mm^2.
The data assumed in the analysis are:

- L_X=80 m;
- $l=L_Y$=16 m;
- s_X = 2 m;
- s_Y = 2 m;
- s_{eX} = 0.5 m;
- t = 8 mm;
- X_1 = 3000 mm;
- X_2 = 2200 mm;
- Q_A = 1.2 t;
- n_V = 7;
- a_Z= 0.909g;
- I_{eX} = 29146 cm^4;
- I_{eY} = 29067 cm^4;
- I_{pX} = 5190 cm^4;
- I_{pY} = 5359 cm^4;
- r_{Xf} = 28.47 cm;
- r_{Yf} = 28.38 cm;
- ρ = 5;
- η_t = 0.18.

In fig. 11 the deck scheme is shown.

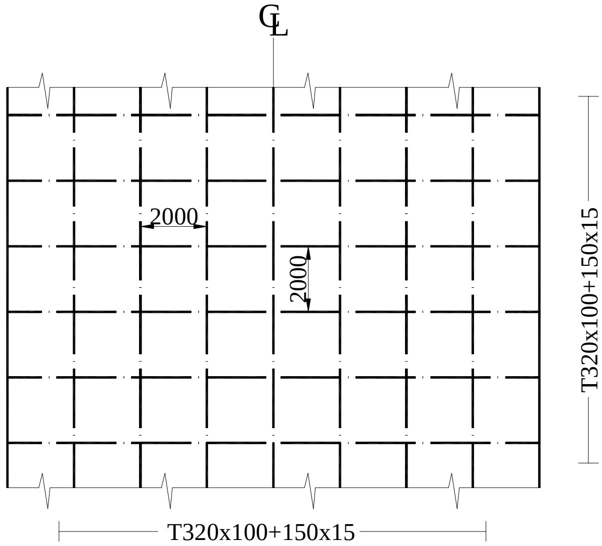

fig. 11

From (53) the maximum static equivalent pressure is $p_{eq.stat.}$ = 2575 N/m^2 so that, considering the vertical acceleration, the maximum total pressure is $p_{eq.max}$ = 4914 N/m^2. The longitudinal distribution of the equivalent pressure p_i and σ_{YfSUP} stresses are listed in tab. 4 where:

- Transv. indicates the current transverse;
- X' is the distance in mm of the first axle respect to the current transverse in the interval [α_i , β_i];
- X'' is the distance in mm of the second axle (if present) respect to the current transverse in the interval [α_i , β_i];
- κ_i is the ratio between the pressure on the *i-th* transverse and the maximum one;
- α_i indicates the aft limit, respect to the origin, of the *i-th* interval where $p=p_i$ is continuous;
- β_i indicates the fore limit, respect to the origin, of the *i-th* interval;
- n_A indicates the number of axles in the interval [α_i , β_i];
- $k_{Yf-Orth.}$ is the factor, determined by the orthotropic plate theory, to be inserted in (45.2) to determine the stress in the free flange of the *i-th* transverse with reference to $p=p_{eq.}$;
- k_{Yf-FEM} is the factor obtained by the FEM analysis of the corresponding structure.

Trans.	X' mm	X'' mm	κ_i	α_i m	β_i m	n_A	k_{Yf} Orth.	k_{Yf} FEM
1	1400	1600	0.50	1	3	2	0.0089	0.0109
2	400	1800	0.90	3	5	2	0.0269	0.0308
3	200	---	0.90	5	7	1	0.0421	0.0476
4	800	---	0.60	7	9	1	0.0525	0.0584
5	1200	1000	0.90	9	11	2	0.0592	0.0660
6	1000	---	0.50	11	13	1	0.0636	0.0699
7	0	---	1.00	13	15	1	0.0663	0.0730
8	200	---	0.90	15	17	1	0.0655	0.0733
9	1800	1200	0.50	17	19	2	0.0645	0.0716
10	800	1400	0.90	19	21	2	0.0643	0.0717
11	600	---	0.70	21	23	1	0.0644	0.0711
12	400	---	0.80	23	25	1	0.0642	0.0710
13	1600	600	0.90	25	27	2	0.0632	0.0707
14	1400	1600	0.50	27	29	2	0.0631	0.0698
15	400	1800	0.90	29	31	2	0.0638	0.0707
16	200	---	0.90	31	33	1	0.0637	0.0709
17	800	---	0.60	33	35	1	0.0632	0.0699
18	1200	1000	0.90	35	37	2	0.0629	0.0702
19	1000	---	0.50	37	39	1	0.0636	0.0698
20	0	---	1.00	39	41	1	0.0648	0.0757
21	200	---	0.90	41	43	1	0.0636	0.0711
22	1800	1200	0.50	43	45	2	0.0629	0.0696
23	800	1400	0.90	45	47	2	0.0632	0.0703
24	600	---	0.70	47	49	1	0.0637	0.0691
25	400	---	0.80	49	51	1	0.0638	0.0703
26	1600	600	0.90	51	53	2	0.0631	0.0706
27	1400	1600	0.50	53	55	2	0.0632	0.0699
28	400	1800	0.90	55	57	2	0.0642	0.0713
29	200	---	0.90	57	59	1	0.0644	0.0708
30	800	---	0.60	59	61	1	0.0643	0.0708
31	1200	1000	0.90	61	63	2	0.0645	0.0719
32	1000	---	0.50	63	65	1	0.0655	0.0714
33	0	---	1.00	65	67	1	0.0663	0.0725
34	200	---	0.90	67	69	1	0.0636	0.0702
35	1800	1200	0.50	69	71	2	0.0592	0.0642
36	800	1400	0.90	71	73	2	0.0525	0.0570
37	600	---	0.70	73	75	1	0.0421	0.0449
38	400	---	0.80	75	77	1	0.0269	0.0282
39	1600	---	0.20	77	79	1	0.0089	0.0094

tab. 4

The following diagrams show the equivalent pressure and the σ_{Yf} stress longitudinal distribution.

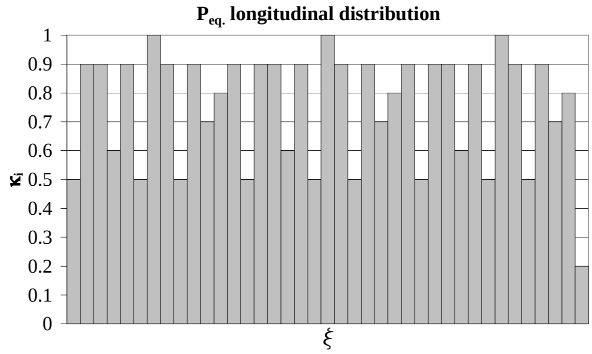

fig. 12

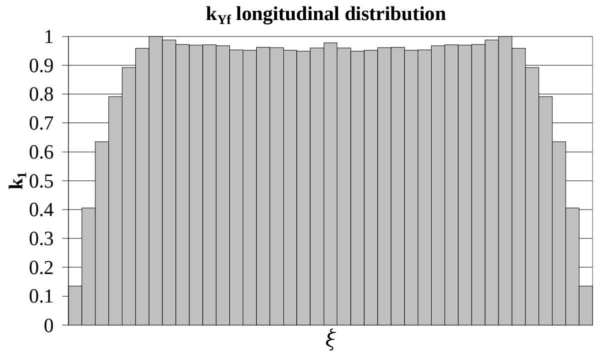

fig. 13

where:

$$k_1 = \frac{k_{Yf}}{k_{Yf-\max.}} \tag{58}$$

This analysis shows that there is a significant re-distribution of σ_{Yf} stresses that can't be evaluated by the isolated beam model. This effect unload the most loaded transverses and load the least loaded ones.
The maximum stresses on girders and transverses are:

- σ_{Xf} = 100 N/mm^2
- σ_{Yf} = 163 N/mm^2

It is noticed that by a coarse mesh FEM analysis the following maximum stresses have been obtained:

- $\sigma_{Xf\text{-}FEM}$= 115 N/mm^2
- $\sigma_{Yf\text{-}FEM}$= 175 N/mm^2

If the deck were loaded by the uniform pressure p = 4914 N/m^2, equal to the maximum equivalent pressure, from fig. 4 it is obtained that the maximum stresses on girders and transverses would be:

- $k_{Xf\text{-}unif.}$= 0.0571→ $\sigma_{Xf\text{-}unif.}$= 141 N/mm^2
- $k_{Yf\text{-}unif.}$= 0.0833→ $\sigma_{Yf\text{-}unif.}$= 205 N/mm^2

Correspondingly by a coarse mesh FEM analysis, the following stresses have been obtained:

- $\sigma_{Xf\text{-unif.FEM}}$= 146 N/mm^2
- $\sigma_{Yf\text{-unif.FEM}}$= 214 N/mm^2

Now, let us define the mean load parameter χ:

$$\chi = \frac{\sum_{i=1}^{n_T} \kappa_i}{n_T} \tag{59}$$

which in the case under examination is 0.75.
As it occurs that:

$$\psi_X = \frac{\sigma_{Xf}}{\sigma_{Xf-unif.}} = \frac{k_{Xf}}{k_{Xf-unif.}} = 0.71 \tag{60.1}$$

$$\psi_Y = \frac{\sigma_{Yf}}{\sigma_{Yf-unif.}} = \frac{k_{Yf}}{k_{Yf-unif.}} = 0.80 \tag{60.2}$$

approximately the following positions can be done:

$$k_{Xf} \cong \chi \cdot k_{Xf\text{-unif}} \tag{61.1}$$

$$k_{Yf} \cong \chi \cdot k_{Yf\text{-unif}} \tag{61.2}$$

Furthermore, in order to appreciate the roles of girders and transverses, the total external force work has been decomposed in three components, two of which have been associated to transverses and girders on the basis of the strain energy expression.
If the deck is loaded with a uniform equivalent pressure *p*, the total external work is:

$$L_e = \frac{1}{2}\frac{p^2 b^5 a}{Ei_Y}\sum_{n=1}^{N}\sum_{m=1}^{M}\delta_{m,n} \tag{62}$$

On the other hand, if the deck is loaded by a load function discontinuous at intervals and *p* is the maximum equivalent pressure, the total external work is:

$$L_e = \frac{1}{2}\frac{p^2 b^5 a}{Ei_Y}\sum_{i=1}^{n_T}\kappa_i\sum_{n=1}^{N}\sum_{m=1}^{M}\delta_{m,n}\left(\beta_i - \alpha_i - \frac{sen2\pi m\beta_i - sen2\pi m\alpha_i}{2\pi m}\right) \tag{63}$$

For the plate configuration under examination the strain energy can be evaluated as follows:

$$L_i = \frac{1}{2}\int_A\left[D_X\left(\frac{\partial^2 w}{\partial x^2}\right)^2 + 2H\frac{\partial^2 w}{\partial x^2}\frac{\partial^2 w}{\partial y^2} + D_Y\left(\frac{\partial^2 w}{\partial y^2}\right)^2\right]dA \tag{64}$$

The components corresponding to the three terms within square brackets are separately evaluated: the first and third ones can be attributed to girder longitudinal bending and beam transverse bending, respectively; the second term can be attributed to coupled flexural and torsional effects in plating.
Namely, the first term is:

$$L_{girder} = \frac{1}{2}\int_A D_X\left(\frac{\partial^2 w}{\partial x^2}\right)dA = \frac{8\pi^4}{\rho^4}\frac{p^2 b^5 a}{Ei_y}k_{girder}$$

where:

$$k_{girder} = \sum_{\bar{m}=1}^{M}\sum_{\bar{n}=1}^{N}\sum_{m=1}^{M}\sum_{n=1}^{N}\delta_{\bar{m},\bar{n}}\delta_{m,n}\bar{m}^2 m^2\int_0^1\cos 2\pi m\xi\cos 2\pi\bar{m}\xi d\xi \cdot$$
$$\int_0^1(1-\cos 2\pi n\eta)(1-\cos 2\pi\bar{n}\eta)d\eta = \frac{1}{4}\sum_{\bar{m}=1}^{M}\sum_{\bar{n}=1}^{N}\bar{m}^4\delta_{\bar{m},\bar{n}}\left(\delta_{\bar{m},\bar{n}} + 2\sum_{n=1}^{N}\delta_{\bar{m},n}\right) \tag{65}$$

The third term, similarly, is:

$$L_{transv} = \frac{1}{2}\int_A D_Y\left(\frac{\partial^2 w}{\partial y^2}\right)^2 dA = 8\pi^4\frac{p^2 b^5 a}{Ei_y}k_{transv.}$$

where:

$$k_{transv.} = \sum_{\bar{m}=1}^{M}\sum_{\bar{n}=1}^{N}\sum_{m=1}^{M}\sum_{n=1}^{N}\delta_{\bar{m},\bar{n}}\delta_{m,n}\bar{n}^2 n^2\int_0^1\cos 2\pi n\eta\cos 2\pi\bar{n}\eta d\eta \cdot$$
$$\int_0^1(1-\cos 2\pi m\xi)(1-\cos 2\pi\bar{m}\xi)d\xi = \frac{1}{4}\sum_{\bar{m}=1}^{M}\sum_{\bar{n}=1}^{N}\bar{n}^4\delta_{\bar{m},\bar{n}}\left(\delta_{\bar{m},\bar{n}} + 2\sum_{m=1}^{M}\delta_{m,\bar{n}}\right) \tag{66}$$

The second term is developed as follows:

$$L_{distors.} = \frac{1}{2}\int_A 2H\frac{\partial^2 w}{\partial x^2}\frac{\partial^2 w}{\partial y^2}dA = 16\pi^4\frac{\eta_t}{\rho^2}\frac{p^2 b^5 a}{Ei_y}k_{distors.}$$

where:

$$k_{distors.} = \sum_{\bar{m}=1}^{M}\sum_{\bar{n}=1}^{N}\sum_{m=1}^{M}\sum_{n=1}^{N}\delta_{\bar{m},\bar{n}}\delta_{m,n}\bar{n}^2 m^2\int_0^1\cos 2\pi m\xi(1-\cos 2\pi\bar{m}\xi)d\xi \cdot$$

$$\int_0^1\cos 2\pi\bar{n}\eta(1-\cos 2\pi n\eta)d\eta = \frac{1}{4}\sum_{m=1}^{M}\sum_{n=1}^{N}m^2 n^2\delta_{m,n} \tag{67}$$

Applying these equations to the examined structure, it is obtained:

$L_e = 24610\,Nm$

$L_{girder} = 1131\,Nm$

$L_{transv.} = 22857\,Nm$

$L_{distors.} = 622\,Nm$

Corresponding percent ratios are:

$$L_{girder} = 4.6\% \;\text{-}\; L_{transv.} = 92.9\% \;\text{-}\; L_{distors.} = 2.5\%$$

It is apparent that transverses absorb the most part of the total external work; also the mean strain energy per unit length absorbed by each transversal supporting member is much greater than that one absorbed by girders:

$$l_{girder} = \frac{1131}{7\cdot 80} = 2\frac{Nm}{m}$$

$$l_{transv.} = \frac{22857}{39\cdot 16} = 37\frac{Nm}{m}$$

7.2 ANALYSIS OF A RO-RO PANAMAX DECK

It has been carried out the evaluation of the highest stresses acting on the primary supporting members of a Ro-ro PANAMAX ship used to carry heavy vehicles; the ship main dimensions are: L_{bp} = 195.00 m; B =32.25 m; D = 25.92 m; Δ = 44200 t.
Transverses and girders, have, respectively, 970x11+320x30 and 970x12+280x30 T sections, while longitudinals are 240x10 offset bulb plates, in high-strength steel with σ_{yield} = 355 N/mm^2. The data assumed in the analysis are:

- L_X=160 m;
- $l=L_Y$=24 m;
- s_X = 4 m;
- s_Y = 2.463 m;
- s_{eX} = 0.667 m;
- t = 14 mm;
- a_Z= 0.411g;
- n_V = 8 ;
- I_{eX} = 967698 cm^4;
- I_{eY} = 911559 cm^4;
- I_{pX}= 178784 cm^4;
- I_{pY}= 244515 cm^4;
- r_{Xf} = 83.66 cm;
- r_{Yf} = 75.30 cm;
- ρ = 7.41;
- η_t = 0.22.

The deck scheme is shown in fig. 14.

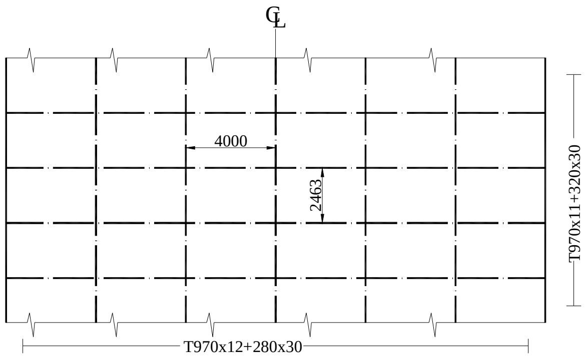

fig. 14

The reference vehicle has the main dimensions and the static axles loads shown in fig. 15.

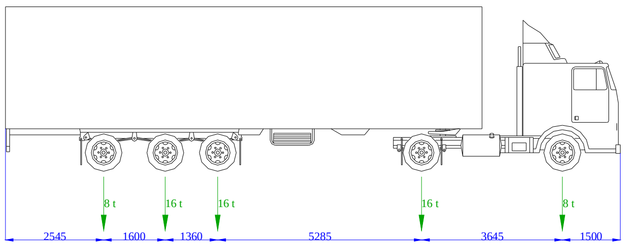

fig. 15

The maximum total pressure is $p_{eq.max}$ = 48647 N/m^2. The longitudinal distribution of the equivalent pressure is shown in tab.5.

Trans.	Q_{A1} t	Q_{A2} (t)	Q_{A3} (t)	X_1 (mm)	X_2 (mm)	X_3 (mm)	κ_i
1	11.29	0	0	1997	0	0	0.06
2	11.29	22.58	0	466	1133	0	0.58
3	22.58	22.58	0	1329	30	0	0.89
4	22.58	0	0	2432	0	0	0.01
5	22.58	0	0	389	0	0	0.52
6	22.58	11.29	0	2073	1571	0	0.21
7	11.29	0	0	891	0	0	0.20
8	0	0	0	0	0	0	0.00
9	11.29	22.58	0	25	1625	0	0.51
10	22.58	22.58	0	837	522	0	0.89
11	22.58	0	0	1940	0	0	0.13
12	22.58	0	0	881	0	0	0.40
13	22.58	11.29	0	1581	2063	0	0.27
14	11.29	0	0	400	0	0	0.26
15	0	0	0	0	0	0	0.00
16	11.29	22.58	0	516	2116	0	0.33
17	11.29	22.58	22.58	1946	346	1013	0.96
18	22.58	0	0	1449	0	0	0.25
19	22.58	0	0	1372	0	0	0.27
20	22.58	0	0	1090	0	0	0.34
21	11.29	0	0	91	0	0	0.30
22	11.29	0	0	2371	0	0	0.01
23	11.29	0	0	1008	0	0	0.18
24	11.29	22.58	22.58	1454	145	1505	0.95
25	22.58	22.58	0	2317	957	0	0.41
26	22.58	0	0	1864	0	0	0.15
27	22.58	0	0	599	0	0	0.47
28	11.29	0	0	583	0	0	0.24
29	11.29	0	0	1880	0	0	0.07
30	11.29	0	0	1500	0	0	0.12
31	11.29	22.58	22.58	963	636	1997	0.76
32	22.58	22.58	0	1826	466	0	0.66
33	22.58	0	0	2356	0	0	0.03
34	22.58	0	0	107	0	0	0.59
35	11.29	0	0	1074	0	0	0.17
36	11.29	0	0	1388	0	0	0.13
37	11.29	0	0	1991	0	0	0.06
38	11.29	22.58	0	472	1128	0	0.58

39	22.58	22.58	0	1335	25	0	0.89
40	22.58	0	0	2438	0	0	0.01
41	22.58	0	0	384	0	0	0.52
42	22.58	11.29	0	2078	1566	0	0.21
43	11.29	0	0	897	0	0	0.20
44	0	0	0	0	0	0	0.00
45	11.29	22.58	0	20	1620	0	0.52
46	11.29	22.58	22.58	2443	843	517	0.89
47	22.58	0	0	1946	0	0	0.13
48	22.58	0	0	876	0	0	0.40
49	22.58	11.29	0	1587	2058	0	0.27
50	11.29	0	0	405	0	0	0.26
51	0	0	0	0	0	0	0.00
52	11.29	22.58	0	511	2111	0	0.33
53	11.29	22.58	22.58	1952	352	1008	0.96
54	22.58	0	0	1455	0	0	0.25
55	22.58	0	0	1367	0	0	0.27
56	22.58	0	0	1096	0	0	0.34
57	11.29	0	0	86	0	0	0.30
58	11.29	0	0	2377	0	0	0.01
59	11.29	0	0	1003	0	0	0.18
60	11.29	22.58	22.58	1460	140	1500	0.95
61	22.58	22.58	0	2323	963	0	0.41
62	22.58	0	0	1859	0	0	0.15
63	22.58	0	0	604	0	0	0.46
64	11.29	0	0	578	0	0	0.24

tab. 5

The following diagrams show the equivalent pressure and k_{Yf} longitudinal distribution.

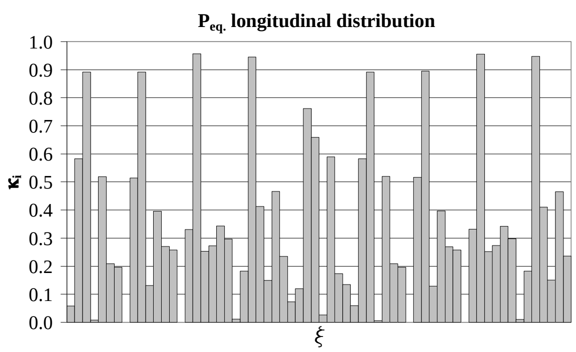

fig. 16

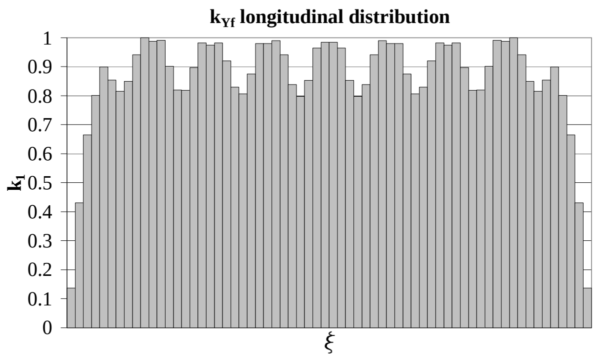

fig. 17

The maximum stresses on girders and transverses are:

- $\sigma_{Xf} = 154$ N/mm^2
- $\sigma_{Yf} = 176$ N/mm^2

If the deck were loaded by the uniform pressure $p = p_{eq.max} = 48647$ N/m^2, the maximum stresses on girders and transverses would be:

- $k_{Xf\text{-SUP-unif.}} = 0.0571 \rightarrow \sigma_{Xf\text{-unif.}} = 446$ N/mm^2
- $k_{Yf\text{-SUP-unif.}} = 0.0833 \rightarrow \sigma_{Yf\text{-unif.}} = 475$ N/mm^2

so obtaining:

$$\psi_X = \frac{\sigma_{Xf}}{\sigma_{Xf-unif.}} = \frac{k_{Xf}}{k_{Xf-unif.}} = 0.35 \qquad (68.1)$$

$$\psi_Y = \frac{\sigma_{Yf}}{\sigma_{Yf-unif.}} = \frac{k_{Yf}}{k_{Yf-unif.}} = 0.37 \qquad (68.2)$$

As in this case $\chi = 0.35$ -see equation (59)-, approximately the positions (61.1) and (61.2) can be done, too. Concerning the strain energy components it is obtained:

$$L_e = 306225\,Nm$$
$$L_{girder} = 18624\,Nm$$
$$L_{transv.} = 280462\,Nm$$
$$L_{distors.} = 7139\,Nm$$

Corresponding percent values are:

$$L_{girder} = 6.0\% \;-\; L_{transv.} = 91.6\% \;-\; L_{distors.} = 2.4\%$$

The mean strain energies per unit length absorbed by each transverse and each girder are:

$$l_{girder} = \frac{18624}{5 \cdot 160} = 23\frac{Nm}{m}$$
$$l_{transv.} = \frac{280462}{64 \cdot 24} = 183\frac{Nm}{m}$$

8. PRELIMINARY DIMENSIONING OF RO-RO DECK PRIMARY SUPPORTING MEMBERS

Previous analyses have shown that the effective wheeled load distribution, expressed by means of the mean load parameter χ, has great influence on the loading of girders and transverses.

Particularly, it has been observed that transverses absorb the great part of the load, while girders contribute to a re-distribution of stresses, unloading the most loaded transverses and loading the least loaded ones.

In a previous work, see [6], a procedure for dimensioning of girders and transverses on the basis of the orthotropic plate theory has been proposed, considering a uniform pressure on deck and so neglecting the effective load longitudinal distribution.

From the numerical results of sections 7.1 and 7.2 it seems appropriate to assume for the pressure the mean equivalent pressure load $\chi p_{eq.max}$. Moreover, as for garage decks the aspect ratio ρ is much greater than 1, it is possible to assume $k_{Yf\text{-}SUP} = 0.0833$ and $k_{X\ f\text{-}SUP} = 0.0571$.

Indicating with $\sigma_{all\ tr.}$ and $\sigma_{all\ long}$. the allowable stresses for transverses and girders respectively, and with $p_{eq.max}$ the maximum pressure transmitted by wheels according to equation (54) it's possible to calculate the section modulus for transverses by the following relation:

$$W_{eYMIN.} \geq \chi \frac{0.0833 \cdot p_{eq.\max} \cdot L_Y^2 \cdot s_Y}{\sigma_{all.tr.}} \qquad (69)$$

where $p_{eq.max}$ is in N/m^2, L_Y and s_Y in m, $\sigma_{all.tr.}$ in N/mm^2 and $W_{eYMIN.}$ in cm^3.The modulus is inclusive of plating effective breadth b_{eY}.

The condition valid for girders is:

$$W_{eXf} \geq \chi^2 \frac{0.0033 \cdot p_{eq.\max}^2 \cdot L_Y^4 \cdot s_X \cdot s_Y}{I_{eY} \cdot \sigma_{all.long.}^2} r_{Xf} \qquad (70)$$

where $p_{eq.max}$ is in N/m^2, L_Y, s_Y and s_X in m, I_{eY} in cm^4, r_{Xf} in cm, $\sigma_{all.long.}$ in N/mm^2 and W_{eXf} in cm^3.

9. CONCLUSIONS

In this work the orthotropic rectangular plate bending equation with all edges clamped has been solved adopting the Rayleigh-Ritz method. Numerical calculations have been systematically performed in case of uniform pressure, varying two non-dimensional parameters, namely the virtual side ratio and the torsional coefficient. Response non-dimensional parameters, in terms of maximum deflection and maximum stresses, are given in a series of charts for their easy application. Some comparisons with well known published data and FEM analyses give a validation to the method.

The method has been applied to ro-ro garage decks, taking into account in this case a load variable along the deck length, according to the geometrical and mass characteristics of the reference vehicle.

Two typical ro-ro ships have been examined. It has been highlighted that transverse beams absorb the most part of the external work done by the pressure load, as it could be expected. Besides, it has been found that there is an appreciable re-distribution of the load, so that almost the same maximum stresses are obtained considering simply the mean pressure acting uniformly on the deck; then those stresses can be evaluated directly by the orthotropic plate charts.

From that, the suggestion for a simple procedure for the preliminary dimensioning of ro-ro deck primary supporting members is given.

10. REFERENCES

1. SCHADE H.A., 'Design Curves for Cross-Stiffened Plating under Uniform Bending Load', *Trans. SNAME*, 49, 1941.
2. TIMOSHENKO S., WOINOWSKY-KRIEGER S., 'Theory of Plates and Shells', Mc-Graw-Hill Book Company, 1959.
3. YOUNG D., 'Analysis of Clamped Rectangular Plates', *Journal of Applied Mechanics*, Volume 7, No.4, December 1940.
4. FIORENZA R., 'Appunti delle lezioni di Analisi Funzionale', Gli Strumenti di Coinor, 2005.
5. RINA, 'Rules for the Classification of Ships', 2005.
6. CAMPANILE A., MANDARINO M., PISCOPO V., "Considerations on dimensioning of garage decks", ICMRT 2007.

ADHESIVE BONDING IN MARINE STRUCTURES

Dirk Brügge, Karsten Fach, Wolfgang Franzelius,
Germanischer Lloyd, Hamburg/Germany, karsten.fach@GL-group.com

SUMMARY

For High Speed Craft adhesives are used for the panes, seat rails, the rudder bearings in the housing, and propulsion shafts. This paper describes specialities of the design of adhesive bonds, rules and guidelines as well as approval aspects for adhesives and manufacturing requirements. Exemplarily for panes of a cruise vessel a calculation method is compared with full-scale measurements and Finite Element analyses. Adhesive bonding is a suitable way of joining elements if all relevant conditions are fulfilled

1. INTRODUCTION

Structural components are already adhesively bonded in many areas of technology. In aeronautics, highly stressed and safety relevant aluminium parts have been bonded since the 1930s. In the automotive industry, bonding techniques have already completely displaced other joining methods in some areas, e.g. for the bonding of brake pads with the substrate material. In civil engineering, sometimes subsequent strengthening must be appled to structures made of reinforced concrete, e.g. in houses, bridges and hydraulic steel engineering. Adhesive bonding has been applied in civil engineering since the 1970s for technical, commercial or aesthetic reasons, *Hugenschmidt (1980).* In shipbuilding, adhesive bonding is predominantly found in high-performance marine vehicles. Adhesives are used for bonding window panes, seat rails, rudder bearings in the housing and also propulsion shafts, Fig.1, as well stiffening members for small craft. We will here assess the practical aspects of adhesive bonding in marine structures and how they relate to the underlying theoretical concepts.

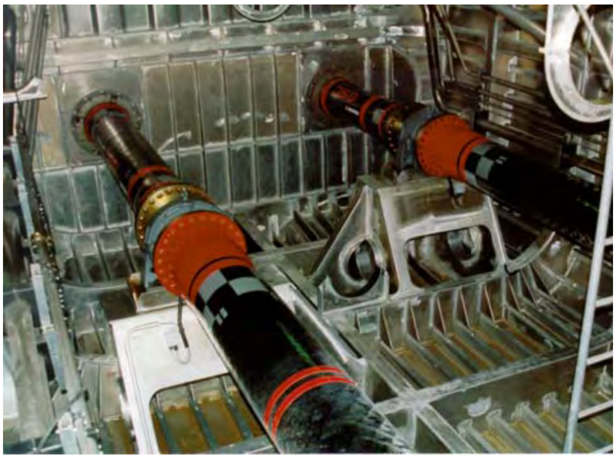

Fig.1: Carbon propulsion shaft on a high-speed craft (bonded FRP to metal flange)

2. DESIGN OF ADHESIVE JOINTS

2.1. Specification

At the beginning of the design process stands a proper specification. Only when the requirements, loads and environmental conditions are known with the greatest possible precision can an adhesive bond be designed with success. Although this requirement appears to be evident, frequently the necessary care is not taken in practice.

A specification should include at least the following points:

- Required service life of the adhesive joint – the required service life can be identical to the lifetime of the component, but may also be selected to be shorter. In the latter case, a good repair possibility must be provided.
- Extreme load – it must be defined how often this occurs, how long it has an effect and what the prevailing temperature is.
- Fatigue loads – if possible, the fatigue load should be specified in Markov matrices, Table I. Normally these matrices consist of *j* rows and three columns (containing amplitude, associated mean value and the number of cycles). In many cases, it suffices to define an average temperature and humidity for the design life. However, if very high or very low temperatures are likely to occur, an extended consideration may be necessary.

Table I: Example of a Markow matrix

Amplitude [kN]	Mean value [kN]	Number of load cycles [ ]
10.0	-5	12508
10.0	0	12359
10.0	5	56248
…		
12.5	-10	95625
12.5	-5	41588
12.5	0	51236
…		
15.0	-5	58753
…		

- Media effects – media effects in the form of (sea) water, UV radiation, acids and lyes (also detergents) etc. must be taken into account.
- Impact – here it is particularly important to know the ambient temperature (or even better the temperature inside the adhesive layer) during the impact loading. The duromeric adhesives can become brittle, whereas with the elastomeric adhesives the increase in the modulus of elasticity can lead to additional stresses which can no longer be neglected.
- In addition, there are also the load cases such as transport, commissioning and maintenance, each with due consideration of the load duration and the climate.
- Fire protection – the relevant points here are fire load, toxicity, fume development and the functional capability must be observed. For most structural connections, the maintenance of structural integrity is also required in the event of fire for a certain period of time. With adhesive joints, this requirement results in great effort with regard to cooling and insulation and is thus often not realizable.

In the case of joints or components that are subject to approval, the specification must usually be submitted for examination. For some components, completed specifications, guidelines or regulations are already available at the approval bodies. On the basis of this (examined) specification, the design of the adhesive joint can now commence.

2.2 Design Methods

Depending on what consequences follow the failure of an adhesive joint, a damage-tolerant or even a redundant bond will be required. If redundancy is demanded, this presents a clear task description and need not be discussed any further here. Proper fulfilment of a requirement for a damage-tolerant design is difficult to assess in many cases. The assessment can be based on a fracture-mechanics approach in conjunction with a material exhibiting a high resistance to tear propagation, or by dividing the joint into a large number of separate bonds. This will be explained with the aid of the following example taken from wind turbine technology.

The rotor blades of wind turbines are made of glass-fibre reinforced plastic (GRP) or, in some cases, also of wood. The blades are bolted onto the hub or a blade bearing. One of the possible design variants is that each bolt is screwed into a thread insert, Fig.2, which is bonded to the GRP. For the rotor blade of a 600 kW wind energy conversion system, for example, 48 bolts of the type M24 10.9 are needed. If the bond of one threaded insert were to fail, this would not lead to immediate failure of the component. It will be possible to operate the system safely until the next inspection (periodical survey) is due. Another design variant is to bond a metal ring into the blade root, Fig.3. In this case, it must be assumed that a crack, after initiating at a certain point, will spread over the entire circumference. Such a crack can lead to failure of the entire adhesive joint within a short space of time if the tear-growth resistance is not high enough.

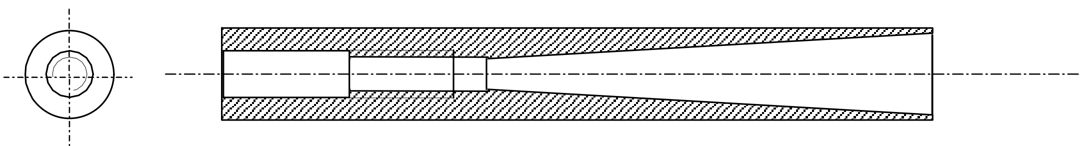

Fig.3: Schematic representation of a threaded insert

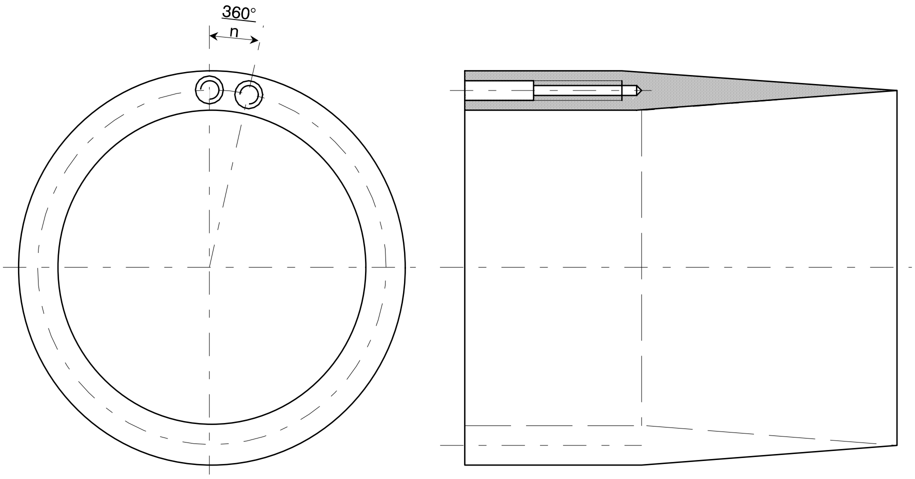

Fig.3: Metal ring with N threaded holes

Design methods also include the differentiation between a duromeric (high-strength) and an elastomeric (highly elastic) adhesive joint. Elastomeric joints comprise exclusively of self-supporting bonds in which the focus is on flexibility (permanent displacements in the range from 10% to 20%), where the forces transferred are low. An example here would be the bonding of window panes on ships. For the duromeric adhesive joints (a permanent transfer of several MPa is possible), the focus is on the transfer of force and where an appreciable displacement of the parts to be joined is not desired.

2.3 Determination of properties

For a safe dimensioning of adhesive joints, test samples with similar design compared to the final design should be used for determining the properties. This is because the properties to be determined must be assigned to the adhesive joint and should not represent characteristics of the adhesive itself. For instance, if components with different material properties are bonded together, complex stress states can arise relatively quickly, as a result of differing rigidities and Poisson ratios. The example of force application by a metal flange for a fibre reinfoced plasic (FRP) pipe will be used to clarify this, Fig.4. If the FRP pipe is bonded on the outside, then owing to the greater transversal contraction of the FRP pipe during tensile loading of the pipes, a shear stress will arise in the adhesive joint that is superimposed with compressive stress. If now the pipe is subjected to compression loading or if the FRP pipe is inside bonded, the shear stress is superposed with a tensile stress. The difference in strength can be quite considerable, *Sutherland (1999).*

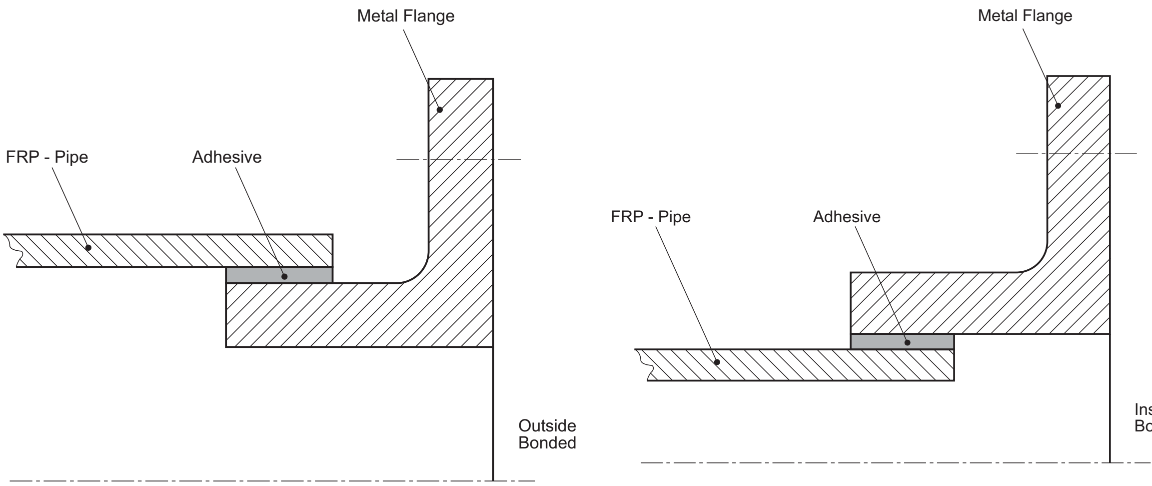

Fig.4: FRP – Pipe to metal flange connection

The tensile lap-shear strength according to DIN EN 1465 quoted in almost every data sheet must be regarded as not being representative of most adhesive joints. For example, to determine the tensile lap-shear strength of highly elastic adhesives for window-pane bonding, a test sample for this type of thick-film bonding in shipbuilding was developed in cooperation with the Frauenhofer IFAM, Center of Adhesive Bonding Technology (IFAM), Bremen. By using aluminium strips 10 mm thick, an adhesive film thickness of 3 mm and an overlapping length of 20 mm, the later component is represented to a much better degree than is the case in DIN EN 1465, *Wacker (2000).*

In the testing of adhesive joints, not only the strength properties, but also the appearance of the fracture, are decisive. For each sample, the relationship between adhesive failure and cohesive failure must be specified, because only then can the influence of media on the bond be assessed. During water conditioning of samples, frequently an increase in strength and fracture strain is noted initially, followed – after long-term conditioning – by a decrease in the properties. In this case, the water first functions as a softener and stress peaks can be better reduced. However, when the water molecules diffuse to the interface between adhesive and base material, then these results in either a reduction of the adhesion, or on bondline corrosion. This is not detected in a result solely strength-oriented evaluation.

The determination of properties is usually only allowed to be performed by an accredited testing laboratory or under the supervision of a representative from the approval body.

2.4 Approval of adhesives

The adhesives used for adhesive joints require an approval in almost all industry sectors (shipbuilding, wind energy etc.). Such an approval is normally only valid for a defined sector. For the approval, either minimum properties must be met or the test results from the static short-term, long-term or cyclic-dynamic investigations, with and without conditioning (frequently also for various thickness of adhesive) are listed in material data sheets. The dimensional stability under heat or the glass transition temperature must also be dtermined as part of the approval process.

In the regulations, guidelines and manufacturers' specifications, statements are also often made on conditioning. This conditioning is intended to simulate the climatic stresses existing during the lifetime of the components in an accelerated manner. With a service life of up to 20 years and products that sometimes have only been on the market for a few months, or with proven products in new application areas, the limited
The pane dimensions ($l_s \times b_s \times t_s$) are 1830 × 870 × 8 mm³. The Young's modulus of the window panes is E_s =70 GPa. The Young's modulus of the adhesive at room temperature is E = 1 MPa while the shear modulus is G = 0.8 Ma. The adhesive thickness is t_{adh} = 6 mm. The bonding temperature is T_o=15°C, where the working temperature range for this adhesive is -25°C to +60°C. The proposed life is 30 years. The design pressure is P_{max} = 11 kPa.

The deflection *f* of a simple supported plate may be calculated as follows

information value of such artificial ageing must be apparent to everyone. Nevertheless, without such an artificial ageing the long-term properties of adhesive joints are always overestimated.

The regulations of Germanischer Lloyd for the material approval of adhesives are subdivided into the following sections.

- Adhesives for duromeric bonding: Rules for Classification and Construction, II – Materials and Welding, Part 2 – Non-metallic Materials, Chapter 1 – Fibre Reinforced Plastic and Bonding.
- Adhesives for elastomeric bonding: Rules for Classification and Construction, II – Materials and Welding, Part 2 – Non-metallic Materials, Chapter 3 – Guidelines for Elastomeric Adhesives and Adhesive Joints.

2.5 Stress and deformation assessment

For adhesive joints, stresses and deformations should always be assessed. As part of the assessments, the visco-elastic material properties should be considered through reduction factors. Conservative approaches must be chosen for the modelling. According to the calculation method used in *Wacker (2000)* the bonding for toughened safety glass should be calculated roughly. The window panes are to be used for a cruise vessel in the deckhouse area, Fig.5.

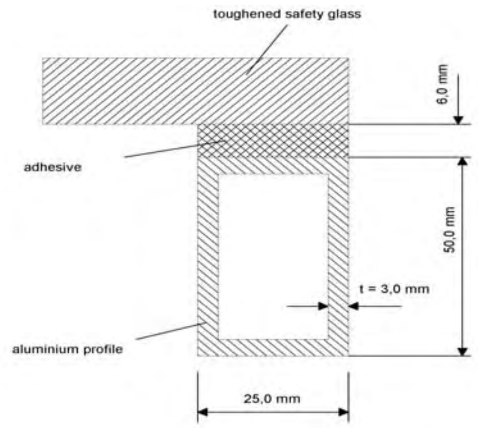

Fig.5: Adhesive pane joint

$f = 11 \cdot \xi \cdot p \cdot b_s^4/(E_s \cdot t_s^3) = 11 \cdot 0.007 \cdot 11 \cdot 870^4/(70000 \cdot 8^3) = 13.54$ mm

ξ is the coefficient of diaphragm efficiency b/l (aspect ratio)

The arc length will be approximated as follows, considering the smaller side, where stresses will usually be higher:

$B_s = (b_s^2 + 16 \cdot f^2/3)^{0.5} = (870^2+16 \cdot 13.54^2/3)^{0.5} = 870.56$ mm

Considering a simply supported beam with a uniform load, the deflection angle may be derived as:

$\sin \alpha = 3.2 \cdot f/B_s = 3.2 \cdot f/B_s = 0.04977 = 2.853°$

The permissible stress can be determined as follows:

$\sigma_{perm} = \sigma_{ch} \cdot f_T \cdot f_M \cdot f_L \cdot f_D \cdot f_G / S$

σ_{perm} is the permissible stress, σ_{ch} the characteristic stress = 4.0 MPa (determined with similar specimens), f_T the material reduction coefficient for temperature unlike test temperature =0.9 (manufacturer specifications), f_M the material reduction coefficient for medium impact = 0.8 (design particulars), f_L the material reduction coefficient for long time load = 0.5 (constant pressure load for 1 hour), f_D the material reduction coefficient for dynamic impact = 0.75, f_G the material reduction coefficient for different geometrical properties of specimen and structure = 1 (specimen similar to structure), and S the safety factor = 3. This yields σ_{perm} = 0.36 Mpa.

The actual stresses may be determined by using, *Wacker (2000):*

$$\sigma_v = \frac{R-1}{2R} \cdot \left[\frac{b \cdot \tan\alpha}{2d} \cdot E + \frac{p \cdot l_s \cdot b_s}{2b \cdot (l_s + b_s)}\right] + \frac{1}{2R}\sqrt{(R+1)^2 \cdot \left[\frac{b \cdot \tan\alpha}{2d} \cdot E + \frac{p \cdot l_s \cdot b_s}{2b \cdot (l_s + b_s)}\right]^2 + 12 \cdot R \cdot \left[\frac{\Delta_{st} + \Delta_{sp}}{d} \cdot G\right]^2}$$

We have α=2.853°, width of bonding b = 25 mm, thickness of bonding d = 6 mm, coefficient of thermal expansion of aluminium $\alpha_{al} = 24 \cdot 10^{-6}$ K^{-1}, coefficient of thermal expansion of glass $\alpha_{gl} = 7 \cdot 10^{-6}$ K^{-1} elongation of the elastic curve's neutral axis Δ_{sp}= (870.56-870)/2= 0.28 mm, temperature difference $\Delta T = T_{max} - T_{production}$ = 60-15 = 45 K, elongation due to temperature difference $\Delta_{st} = 0.5 \cdot l \cdot (\alpha_{al} - \alpha_{gl}) \cdot \Delta T = 0.5 \cdot 870 \cdot (24-7) \cdot 10^{-6} \cdot 45 = 0.333$ mm. The aspect ratio of compression and tension stresses is R=1.3 (evaluated by IFAM, based on several PU-resins). Thus:

$$\sigma_v = \frac{1.3-1}{2 \cdot 1.3} \cdot \left[\frac{25 \cdot \tan 2.853}{2 \cdot 6} \cdot 1 + \frac{0.011 \cdot 1830 \cdot 870}{2 \cdot 25 \cdot (1830 + 870)}\right] + \frac{1}{2 \cdot 1.3} \cdot \sqrt{(1.3+1)^2 \cdot \left[\frac{25 \cdot \tan 2.853}{2 \cdot 6} \cdot 1 + \frac{0.011 \cdot 1830 \cdot 870}{2 \cdot 25 \cdot (1830 + 870)}\right]^2 + 12 \cdot 1.3 \cdot \left[\frac{0.333 + 0.28}{6} \cdot 0.8\right]^2}$$

$\sigma_v = 0.277$ MPa $< \sigma_{perm} = 0.36$ MPa.

This illustrates the procedure to confirm the chosen width and thickness of the bonding line.

2.6 Experiments and numerical validation

In addition to the computation in section 2.5, a hydrostatic pressure test was carried out. Different panes with thickness values of 8.0 mm, 10.0 mm and 12.0 mm were tested to verify the optimal ratio between pane thickness and bonding specimen, in relation to the deflection. As an example, the test results for a 8.0 mm pane are discussed below. These diagrams also contain results from a finite element (FE) analysis performed by the window designer.

The toughened safety glasses were bonded on an aluminium frame/plate construction and were loaded with water pressure to gain a result of the load and deformability behaviour, Fig.6. The surface tension σ_x and σ_y were recorded via strain gauges, bonded in the centre of the panes. The deflection was measured with inductive position encoder and recorded together with the surface tension results. The surface tension of the panes can be derived with the following equation, using the Young's Modulus (E = 70.000 MPa) and the Poisson ratio (μ = 0, 23):

$$\sigma_x = (\varepsilon_x + \mu \cdot \varepsilon_y) \cdot E$$

$$\sigma_y = (\varepsilon_y + \mu \cdot \varepsilon_x) \cdot E$$

The pressure was increased in steps up to a maximum of 22.6 kN/m²; the data was noted after 3 minutes. At the pressure of 22.6 kN/m² the system failed, Fig.7.

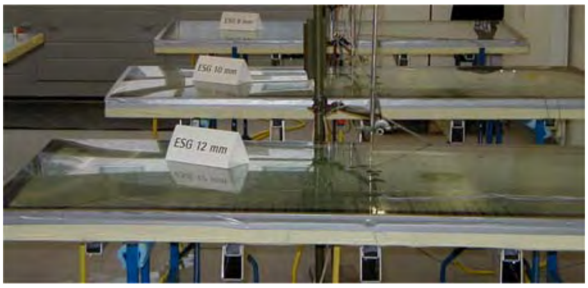

Fig.6: Test stand for the pane approval

Fig.7: Failure of pane approval (p =22.6 kN/m²)

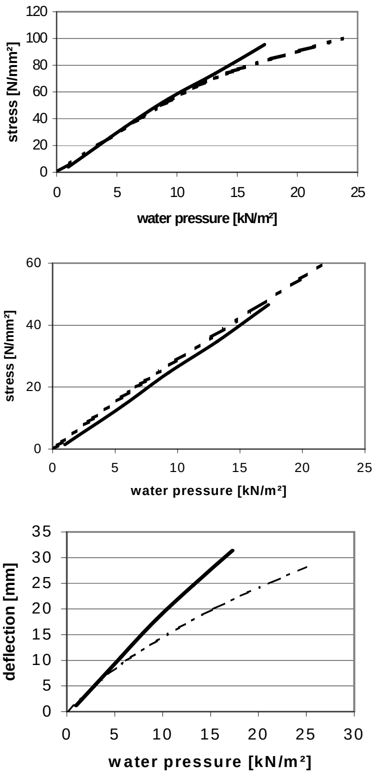

Fig.8: Stress in the pane in X-direction (top), Y-direction (centre) and deflection *f* (bottom) of pane as functions of the water pressure; –· – FE prediction, —— measurements

FE analysis and the deflection pre-calculated in section 2.5 (13.54 mm at a pressure of 11 kN/m²) agree well. The slightly higher FE result may based on the additional elongation within the bonding. To compare the test result with the pre-calculated deflection, the deflection of the aluminium construction has to be considered (substituted) because the measured values were influenced by the "lifting" effect. The deflection of the Aluminium supporting structure profile was approximately 5 mm which leads to an acceptable "corrected" deflection value.

It seems inevitable to conduct further testing and FE analysis to obtain reliable results for bonding, the more so as the theoretical approach available so far obviously reflects reality insufficiently. A close co-operation of classification societies with the bonding industry is to be aimed at, especially to develop reliable material data.

For luxury yachts and passenger ships, large window surfaces are a characteristic feature. At the same time, smooth surfaces form a good advertisement for the shipyards producing such vessels. To prevent welding deformation at a late stage of window assembly these panes are bonded to an increasing degree wherever possible. Through the large dimensions to be found in shipbuilding and the resulting large tolerances and deformations, bonds of several millimetres in thickness are the rule. For the superstructure of a 138 m motor yacht with large glass surfaces on the upper decks, the FE method was used to perform an investigation concerning the influence of bonding on the deformation behaviour with various adhesive thicknesses, *Gujer (2001).* Here the rigidity of the various elements was determined with local FE models, and this was then transformed into the global model. Investigations were performed with three different adhesive-layer thicknesses and without windows.

Structural deformation e.g. due to hogging and sagging should be defined via global FE model. These results must be considered while determining the adhesive joints. This examination can just be performed with a local FE model and in no case within a stress and deformation assessment like in section 2.5. Anyhow, any structural deformation has an essential influence on the adhesive and must be considered.

3. WORKSHOP REQUIREMENTS

3.1 Workforce qualification

Since non-destructive testing of the final product with a conclusive statement is not possible, bonding must be regarded as a special process. In practice, errors must be avoided from the start or at least detected as soon as they originate. For this reason, workforce qualification is particularly important. In fact, it is the most important factor for achieving the desired objectives. A profound knowledge of bonding technology sharpens the practitioner's consciousness in all phases of production and increases acceptance for this new technology.

The necessary level of qualification for the workforce is usually underestimated for several reasons:

1. Bonding only requires a low level of craftsman's skill and so it seems to be child's play.
2. Minor errors in bonding lead to failure of the adhesive joint only after a long interval. Therefore, failure of the joint after weeks or months is often blamed on the adhesive. However, this judgement only applies in very few cases, because the design of the adhesive joint, under consideration of the reduction factors, leads to the initial coverage of procedural errors.
3. Because bonding is not as widely used as traditional joining techniques (like welding), it is only mentioned in passing in the vocational training or study courses.

For these reasons, all approval bodies demand the appropriate qualification of the workforce employed in the execution of adhesive joints subject to approval. Moreover, the workforce must have sufficient knowledge in the field of surface treatment and the handling of the adhesive. This can be provided through suitable training by the adhesive manufacturer, in conjunction with a test conducted by a recognized testing institute or under the supervision of the approval body.

The three-level personnel qualification of the European Welding Federation (EWF) is supported and in part already required by Germanischer Lloyd. This qualification programme is structured in a similar way to that of welding. The person doing the work must be able to provide evidence of having completed training as an “European Adhesive Bonder” (according to EWF 3305).

3.2 Production Facilities

The production facilities (adhesive processing shops) must be designed such that the requirements of the approval body regarding climate, cleanliness and working hygiene can be fulfilled. These conditions, which are necessary to ensure uniform quality of the adhesive joints, are checked during a workshop inspection. Furthermore, one work instruction and the associated “documentation accompanying each stage of production” are examined as a spot check during the workshop inspection.

The requirements for the production facility can be found in the corresponding regulations, guidelines or manufacturer’s specification. Requirements commonly encountered are listed below.

The necessary climate primarily depends on the adhesive to be used. At temperatures below 10 °C, the curing process of almost all adhesives is so slow that this temperature can be regarded as the lower limit. The upper temperature limit is mainly determined by the available pot time of the adhesive.

When applying the adhesive and joining the parts a relative humidity of more than 70% shall be avoided, because the danger that the dewpoint is reached as a result of temperature fluctuations, evaporation of solvents etc. is still sufficiently low at this humidity value. For the adhesive systems that require moisture for cross-linkage, a relative humidity of at least 30% must be ensured. For the purposes of quality assurance, it is absolutely necessary to measure and record the climate prevailing during the bonding process and during the curing period by means of calibrated thermo-hydrographs. Nevertheless if these enviromental conditions cannot be provided, the processing conditions shall be co-ordinated with the adhesive manufacturer and Germanischer Lloyd.

Special attention must be paid to maintaining cleanliness. Dust-producing processes cannot be tolerated in the vicinity during or after surface treatment. Adequate provision of consumables, such as cleaning agents and the cloths at the workplace, also contributes towards a uniformly high level of quality.

3.3 Production planning

The bonding technology must be considered at an early stage during the production planning. In the planning, it must be ensured that dust-producing or hot work (such as welding) is not performed at the same time as the bonding activities. Furthermore, processes generating a large amount of heat, such as cutting and welding, must not be performed near the adhesive joints, otherwise there may be irreversible damage to the bond. Of course, spot welding in combination with bonding may be used (e.g. within the automotive industry) and could also be useful within similar production processes. Special consideration has to be taken to high stress areas, where spot welding will cause unintentional stress concentration and tension peaks.
The curing times must also be taken into account for the production planning. Depending on the climate, adhesive and joint, these can range from only a few minutes to several weeks. The last point to be mentioned is the reference sample for the adhesive process. If, for example, bonding is to take place on painted surfaces, the reference sample must pass through the same production steps in parallel with the component, namely “surface preparation of the base material for painting”, “painting” and “surface preparation for bonding”. Only in this way will it be possible to ensure that e.g. an adhesion failure of paint to base material can be detected.

3.4 Production instruction and production record

The production record (i.e. documentation accompanying each stage of production) and the production instruction are vital. They must be coordinated and matched to the particular case at hand. Within the production instruction, all quality-relevant working steps and materials must be described allowing a reproducible production of the adhesive joint. The most important points are:

- Description of the base material and its initial surface condition (alloy, strength, rolled, plated, anodized, corrosion protection coating for metals, resin system used in the case of composite materials, dot-print coating for glass, scratch-proof coating for PC/PMMA etc.)
- Specification of all working steps for the surface treatment with climatic limits and designation of tools, fixtures and other aids; type of application procedure for the primer with film thickness and venting evoporation time
- Specification of the permissible time interval between the end of surface preparation and the time of bonding, if necessary in relation to the climate
- Description of the adhesive
- Pot time and setting conditions for the adhesive

In addition to the production instruction, there must be a suitable production record, i.e. documentation accompanying each stage of production. This documentation should be in the form of a checklist, so that the person responsible in each case can make the relevant entries, e.g. location, data, batch number of the materials used, and climate. The more details are included in this production record, the simpler the clarification of damage and possibly also fault localization will be. And example for documentation accompanying each stage of production is given in *GL (2002).* Both the production instruction and the production documentation are examined by the approval body.

4. REQUIREMENTS FOR FIRE PROTECTION

Like all plastics, adhesives are generally flammable making fire protection an issue. The requirements made of fire protection depend chiefly on the ship type and operational profile. In the rules and codes, the adhesives are not treated explicitly. Rather the materials are classified into various fire classes, such as fire-retardant (as tested following IMO (1998) and non-combustible. Pertinent requirements include:

- Seagoing ships according to SOLAS 74 (International Convention for the Safety of Life at Sea, 1974): The structure of these ships must be made of steel, or from an equivalent material from the viewpoint of fire safety. Therefore no structural (load-bearing) adhesive joints may be applied here. Other adhesive joints may only be used in the areas in which there are no special requirements for fire protection. For example, this applies to windows and doors in the outside area (provided that these are not located in the area relevant to freeboard).
- Fast ships according to the HSC Code: According to the HSC Code, the bonding of structural connections is not excluded. In order that structural adhesive joints may be used, they must first be subjected to a fire test in which it is verified that the structural integrity is maintained in the event of fire for a certain period of time. This is usually associated with a great amount of effort regarding the insulation and cooling of the adhesive joint.
- Recreational craft: The requirements for fire protection are prescribed in the GL Construction Rules and in EN ISO 9094-1. In these rules and in the standard, only very limited requirements are posed for the materials and therefore for adhesives. For instance, flame resistance is required for the adhesive if it is to be used for the separating surfaces near the petrol engines and petrol tanks.
- Lifeboats: The International Life-Saving Appliance Code (LSA Code, Resolution MSC.48(66) 1997) regulates the requirements regarding fire protection for lifeboats and free-fall boats. The LSA code allows to use fire-retardant materials for the hull and fixed superstructures. Therefore bonding techniques may be used if the adhesives are flame-resistant. An exception is presented by the fire-protected lifeboats for tankers, which are subject to extended requirements.

With regard to the toxicity and fume development, requirements are only prescribed for adhesives if these are used in inner spaces and present a free (visible) surface. If this is the case, the adhesives must meet the same requirements as other combustible materials according to the FTP Code.

5. FINAL REMARKS

Designers have to considers many factors when using adhesive bonding for joining. Due to the complexity and the lack of non destructive tests for adhesive bonding, classification societies have to be involved in the structural design and also in the manufacturing process. Theoretical determinations during the design phase are common but still verification by tests is required. The workforce must prove its technical knowledge by training and education, workshop approvals are requested and the adhesive has to be approved. However, numerous cases show that adhesive bonding can be applied successfully also in shipbuilding.

6. REFERENCES

HUGENSCHMIDT, F. (1980), *Verstärken bestehender Betonkonstruktionen mittels geklebter Armierungen* [Strenghtening of Existing Concrete Structures Using Bonded Reinforcements], VDI-Report 384, Kunststoffe im Betonbau, ISBN 3-18-090384-3

GL (2002), *Rules for Classification and Construction II. Materials and Welding, 2 – Non-metallic Materials, 3 – Guidelines for Elastomeric Adhesives and Adhesive Joints*, Germanischer Lloyd, Hamburg

SUTHERLAND, H.J. (1999), *On the fatigue analysis of wind turbines*, SAND99-0089, Sandia National Laboratories, New Mexico

WACKER, G. (2000), *Kleben – Ein neues Fügeverfahren im Schiffbau* [Bonding - a New Joining Process in Shipbuilding], Handbuch der Werften XXV, Schiffahrts-Verlag Hansa, Hamburg, ISBN 3-87700-106-8

GUJER, P. (2001), *Berücksichtigung von Klebeverbindungen bei globalen FE-Analysen am Beispiel eines Glasaufbaus* [Consideration of Adhesive Joints for Global FE Analyses, with the Example of a Glass Superstructure], TUHH and Germanischer Lloyd

IMO (1998), *International Code for Application of Fire Test Procedures, (FTP – Code),* Resolution MSC.61(67), International Maritime Organisation

ON THE SAINT-VENANT BENDING-SHEAR STRESS IN THIN-WALLED BEAMS

Vincenzo Piscopo, Department of Naval Architecture and Marine Engineering, The University “Federico II”, Naples

SUMMARY

Thin-walled elastic beams represent a significant simplified model to analyze longitudinally developed structures made up of thin shell elements. This simplified model is particularly useful in the global analysis of complex structures, assimilable to beams, with multi-connected cross-sections, such as the hull girders. The main advantage of this theory, as regards the finite element analysis, is the great easiness in the structure schematization and the possibility to obtain a simple physical model, that permits to clearly understand the behaviour of the structure and to properly design it.
Particularly, this paper focuses on the application of Saint-Venant bending-shear theory to thin-walled beams, generally analyzed assuming the fundamental Vlasov hypothesis of maintenance of the cross-section contour. New relations have been obtained for the tangential stresses and the normal ones; a numerical method, based on a Ritz variational procedure, has been developed and a procedure to determine the vertical position of the shear center is presented. Finally, in order to verify the suitability of the proposed theory, two numerical applications, the first one based on a simplified structure considered by Hughes, the second one based on a bulk-carrier, have been carried out.

1. INTRODUCTION

The theory of thin-walled elastic beams takes its name from the work of V.Z. Vlasov who, in 1940, published a quite comprehensive book collecting the results of an entire lifetime of scientific activity devoted to the theory of thin-walled structures, particularly with open cross sections, subjected to non-uniform torsion.
The fundamental assumption of Vlasov theory is the observation that thin-walled beams, subjected to beam-end loads only, deform without developing substantial shear deformation in the shell middle surface and any distorsion of the cross-sections in their plane.
Thanks to these fundamental hypotheses, Vlasov developed a new beam model whose main features are:

- further to Navier rigid body motion, cross-section may develop warping out of its plane;
- these warping displacements may be obtained by the product of a warping function, variable along the contour of the section, but independent from the position along the beam axis, by a twist function which depends on the position along the beam only.

In this way the separation of cross-sectional and along-the-axis variables is assumed, so that the axial displacement may be expressed as a sum of products of coupled functions, one independent from the position along the axis and the other independent from the position on the section.
The two fundamental assumptions of Vlasov theory are generally adopted for thin-walled beams subjected to bending and shear, too, regarding as totally restrained the lateral contraction of the beam cross-section. In the following, this fundamental hypothesis is removed, and a new theory, substantially based on the Saint-Venant displacement field for bending and shear, is developed, considering as totally free the section lateral contraction.
Particularly, the warping function will be determined, as usual, by means of a numerical procedure applied to the Euler-Lagrange functional associated to the indefinite equilibrium equation projected along the beam axis.
The fundamental differences between Vlasov and Saint-Venant theories will be pointed out, particularly for the tangential stress field evaluation, verifying that the Vlasov tangential stress field can be regarded as the limit of the Saint-Venant one, when the material Poisson modulus $\nu \rightarrow 0$. Finally, two numerical applications are developed; the first one is based on the Hughes section, already analyzed by means of Vlasov theory in a previous work, in order to point out the principal differences between the two theories, particularly for the tangential stress field evaluation, and the agreement with the results obtained by a FEM analysis carried out by the program ANSYS; the second one, instead, is based on a bulk-carrier.

2. THE SAINT-VENANT BENDING-SHEAR DISPLACEMENT FIELD

Let us regard the hull girder cylindrical body as a Saint-Venant solid, composed of homogeneous and isotropic material, and loaded only on the two beam-ends, hypothesis certainly true if the external loads have modulus negligible, if compared to the one of the internal stress characteristics. Let us define the global Cartesian frames, sketched in *Fig. 1*, with origin *G* in correspondence of the midship structural section centre, and *y*, *z* axes defined in the section plane and coinciding with the section principal axes of inertia.

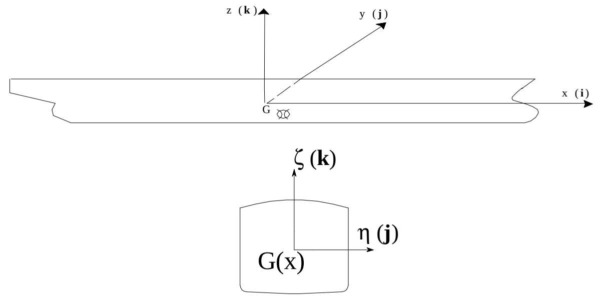

Fig. 1 – Global and local coordinate systems

Let us also define the local Cartesian frames, with origin *G(x)* in correspondence of the cross-structural section at the *x*-abscissa, *x*-axis coinciding with the global one and η, ζ axes defined in the section plane and coinciding with the principal axes of inertia of the section at *x*-abscissa.
Denoting by *u*, *v*, *w* the three displacement components in the *x*, η, ζ directions respectively, with a mixed $P(x,\eta,\zeta)$ representation, and assuming the Saint-Venant hypotheses i.e.: body forces' negligibility, lateral surface unloaded, $\sigma_y = \sigma_z = \tau_{yz} = 0$ everywhere in the body, it is well known that a displacement field is a *Saint-Venant field* only if it satisfies the following conditions:

1) Navier equations

$$\begin{cases} \varepsilon_y = \varepsilon_z = -\nu\varepsilon_x \\ \gamma_{yz} = 0 \end{cases} \tag{1}$$

2) Indefinite equilibrium equations

$$\begin{cases} \dfrac{\partial \tau_{xy}}{\partial x} = 0 \\ \dfrac{\partial \tau_{xz}}{\partial x} = 0 \\ \dfrac{\partial \tau_{xy}}{\partial \eta} + \dfrac{\partial \tau_{xz}}{\partial \varsigma} = -\dfrac{\partial \sigma_x}{\partial x} \end{cases} \tag{2}$$

3) Boundary condition on the lateral surface

$$\boldsymbol{\tau}\cdot\mathbf{n} = 0 \tag{3}$$

where ν is the material Poisson modulus and **n** is the unit vector normal to the solid lateral surface.
Now, the Saint-Venant bending-shear displacement field can be so introduced:

$$\begin{cases} u = \vartheta(x)\varsigma + \dfrac{Q}{GI}\varphi(\eta,\varsigma) \\ v = -\nu\dfrac{d\vartheta}{dx}\eta\varsigma \\ w = w_0(x) + \dfrac{\nu}{2}\dfrac{d\vartheta}{dx}\left(\eta^2 - \varsigma^2\right) \end{cases} \tag{4}$$

where *Q* is the vertical shear, constant with *x*; *I* is the section inertia moment about its η-axis; *G* is the tangential modulus (first Lamé constant); $\varphi(\eta,\varsigma)$ is the warping function, constant with *x*; $\vartheta(x)$ is the rotation of the section about its η-axis, positive if counter-clockwise; $w_0(x)$ is its ζ translation, connected with the rotation $\vartheta(x)$ by the geometrical condition of orthogonality between the section and the elastic surface z=0 [1]:

$$\vartheta(x) = -\frac{dw_0}{dx} \tag{5}$$

As the condition *Q* = const. permits to assume:

$$\frac{d^3\vartheta}{dx^3} = 0 \tag{6}$$

it is possible to verify that the equations (4) define a Saint-Venant displacement field.

3. THE SAINT-VENANT BENDING-SHEAR STRAIN AND STRESS FIELDS

With the previous assumptions and notations, the strain components (for small deformation) are then given by:

$$\begin{cases} \varepsilon_x = \dfrac{d\vartheta}{dx}\varsigma \\ \varepsilon_y = -\nu\varepsilon_x \\ \varepsilon_z = -\nu\varepsilon_x \end{cases} \tag{7.1}$$

$$\begin{cases} \gamma_{xy} = \dfrac{Q}{GI}\dfrac{\partial\varphi}{\partial\eta} - \nu\dfrac{d^2\vartheta}{dx^2}\eta\varsigma \\ \gamma_{xz} = \dfrac{Q}{GI}\dfrac{\partial\varphi}{\partial\varsigma} + \dfrac{\nu}{2}\dfrac{d^2\vartheta}{dx^2}\left(\eta^2 - \varsigma^2\right) \\ \gamma_{yz} = 0 \end{cases} \tag{7.2}$$

Now, starting from the basic expressions:

$$\sigma_x = \frac{E}{1+\nu}\left[\varepsilon_x + \frac{\nu}{1-2\nu}\left(\varepsilon_x + \varepsilon_y + \varepsilon_z\right)\right] \tag{8.1}$$

$$\tau_{ij} = G\gamma_{ij} \tag{8.2}$$

the only non-null stress components are:

$$\begin{cases} \sigma_x = E\dfrac{d\vartheta}{dx}\varsigma \\ \tau_{xy} = \dfrac{Q}{I}\dfrac{\partial\varphi}{\partial\eta} - \nu G\dfrac{d^2\vartheta}{dx^2}\eta\varsigma \\ \tau_{xz} = \dfrac{Q}{I}\dfrac{\partial\varphi}{\partial\varsigma} + \dfrac{\nu}{2}G\dfrac{d^2\vartheta}{dx^2}\left(\eta^2 - \varsigma^2\right) \end{cases} \tag{9}$$

As regards the indefinite equilibrium equations, which naturally involve all the stress components, they can be rewritten neglecting the body forces and the pressure loads. The system of the indefinite and boundary equilibrium equations is written as follows:

$$\begin{cases} \operatorname{div}\boldsymbol{\Sigma} = 0 \\ \boldsymbol{\Sigma}\,\mathbf{n} = \mathbf{0} \end{cases} \tag{10}$$

where $\boldsymbol{\Sigma}$ is the stress tensor and **n** is the unit vector normal to the section boundary (positive outside).
The only relevant scalar equations, in a study of the hull girder strength, are the *x*-projections of the vectorial (10), because the other ones are implicitly verified by the Saint-Venant displacement field (4).
In the further hypothesis of cylindrical body, assuming $\mathbf{n}\cdot\mathbf{i}=0$ and making the position $\boldsymbol{\tau} = \tau_{xy}\mathbf{j} + \tau_{xz}\mathbf{k}$, the equilibrium conditions inside the body and on the boundary can be so rewritten:

$$\begin{cases} \dfrac{\partial \tau_{xy}}{\partial \eta} + \dfrac{\partial \tau_{xz}}{\partial \varsigma} = -\dfrac{\partial \sigma_x}{\partial x} \\ \boldsymbol{\tau}\cdot\mathbf{n} = 0 \end{cases} \tag{11}$$

Now, as in thin-walled beams the cross- section can be imagined as made up of branches of constant thickness *t*, it is useful to refer each branch to an appropriate local system of orthogonal curvilinear coordinates.
Concerning this, let ℓ_1, ℓ_2 and ℓ be three parallel curves (*Fig .2*) of a given branch, the first two lying on the structure boundary and the third one coinciding with the centre line; then the orthogonal curvilinear coordinates (ξ, *s*, *n*) can be so introduced:

- *s* is the curvilinear abscissa on the centre line, with the O origin in either extremity (node) of the line;
- *n* is the linear abscissa on the thickness line through the considered point P, with origin on ℓ;
- $\xi = \mathrm{x} - \bar{\mathrm{x}}$ (with: $\bar{\mathrm{x}}$=global coordinate of the considered cross section) is the linear abscissa with origin in O, on the parallel through O, to the *x*-axis of the global frame.

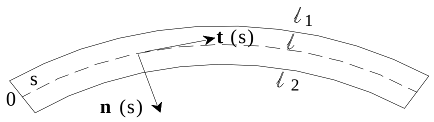

Fig . 2 – Local curvilinear coordinate system

Now, applying the relations $\gamma_{\mathrm{pq}} = 2(\mathbf{E}\mathbf{e}_{\mathrm{p}})\cdot\mathbf{e}_{\mathrm{q}}$ for p≠q and $\varepsilon_{\mathrm{p}} = (\mathbf{E}\mathbf{e}_{\mathrm{p}})\cdot\mathbf{e}_{\mathrm{p}}$, it is possible to rewrite the strain components as regards the local curvilinear coordinate system, having denoted by **E** the strain tensor written with regard to the orthonormal basis {**i**,**j**,**k**} and by $\mathbf{e_p}$ the unit vector of the local coordinate system as regards the orthonormal basis.
Denoting by $\varphi(\mathrm{s},\mathrm{n})$ the function composed of the three ones: $\varphi(\eta,\varsigma)$, $\eta(\mathrm{s},\mathrm{n})$ and $\varsigma(\mathrm{s},\mathrm{n})$, by α_{ij} the director cosine of the unit vector ***i*** of the local coordinate system as regards the unit vector **j** of the orthonormal basis and applying the condition of orthogonality of the unit vectors *s* and *n*, the strain field, written with regard to the local curvilinear coordinate system, becomes:

$$\begin{cases} \varepsilon_x = \dfrac{d\vartheta}{dx}\varsigma \\ \varepsilon_s = \varepsilon_y\alpha_{sy}^2 + \varepsilon_z\alpha_{sz}^2 = -\nu\varepsilon_x \\ \varepsilon_n = \varepsilon_y\alpha_{ny}^2 + \varepsilon_z\alpha_{nz}^2 = -\nu\varepsilon_x \end{cases} \tag{12.1}$$

$$\begin{cases} \gamma_{\mathrm{xs}} = \dfrac{\mathrm{Q}}{\mathrm{GI}}\dfrac{\partial\varphi}{\partial\mathrm{s}} - \nu\dfrac{\mathrm{d}^2\vartheta}{\mathrm{dx}^2}\eta\varsigma\alpha_{\mathrm{sy}} + \dfrac{\nu}{2}\dfrac{\mathrm{d}^2\vartheta}{\mathrm{dx}^2}\left(\eta^2-\varsigma^2\right)\alpha_{\mathrm{sz}} \\ \gamma_{\mathrm{xn}} = \dfrac{\mathrm{Q}}{\mathrm{GI}}\dfrac{\partial\varphi}{\partial\mathrm{n}} - \nu\dfrac{\mathrm{d}^2\vartheta}{\mathrm{dx}^2}\eta\varsigma\alpha_{\mathrm{ny}} + \dfrac{\nu}{2}\dfrac{\mathrm{d}^2\vartheta}{\mathrm{dx}^2}\left(\eta^2-\varsigma^2\right)\alpha_{\mathrm{nz}} \\ \gamma_{\mathrm{ns}} = -\nu\varepsilon_{\mathrm{x}}\left(\alpha_{\mathrm{ny}}\alpha_{\mathrm{sy}} + \alpha_{\mathrm{nz}}\alpha_{\mathrm{sz}}\right) = 0 \end{cases} \tag{12.2}$$

From the eq. (12.1) and (12.2), it seems clear that there is a substantial difference between the Vlasov theory and the Saint-Venant one. In fact, while in the first it is substantially admitted an “anisotropic” behaviour of the branch, rigid through the thickness, in the second it is obtained an elastic behaviour along the thickness, too, according to the assumption of cross-section’s free contraction. It is important to remark that also in this case the distortion term γ_{ns} is equal to zero, according to the Vlasov theory.
Now, before writing the stress components, it is convenient to determine the function $\dfrac{\mathrm{d}^2\vartheta}{\mathrm{dx}^2}$. Starting from the expression of the bending moment:

$$M(x) = \int_A \sigma_x\varsigma dA = EI\frac{d\vartheta}{dx} \tag{13}$$

it is obtained:

$$\frac{d\vartheta}{dx} = \frac{M(x)}{EI} \tag{14.1}$$

and then:

$$\frac{\mathrm{d}^2\vartheta}{\mathrm{dx}^2} = \frac{\mathrm{Q}}{\mathrm{EI}} \tag{14.2}$$

Now, concerning the stress components, starting from eq. (12.1) and (12.2), they can be so rewritten:

$$\begin{cases} \sigma_{\mathrm{x}} = \dfrac{\mathrm{M(x)}}{\mathrm{I}}\varsigma \\ \sigma_{\mathrm{s}} = \sigma_{\mathrm{n}} = 0 \end{cases} \tag{15.1}$$

$$\begin{cases} \tau_{\mathrm{xs}} = \dfrac{\mathrm{Q}}{\mathrm{I}}\dfrac{\partial\varphi}{\partial\mathrm{s}} - \nu\mathrm{G}\dfrac{\mathrm{Q}}{\mathrm{EI}}\left[\eta\varsigma\alpha_{\mathrm{sy}} - \dfrac{\alpha_{\mathrm{sz}}}{2}\left(\eta^2-\varsigma^2\right)\right] \\ \tau_{\mathrm{xn}} = \dfrac{\mathrm{Q}}{\mathrm{I}}\dfrac{\partial\varphi}{\partial\mathrm{n}} - \nu\mathrm{G}\dfrac{\mathrm{Q}}{\mathrm{EI}}\left[\eta\varsigma\alpha_{\mathrm{ny}} - \dfrac{\alpha_{\mathrm{nz}}}{2}\left(\eta^2-\varsigma^2\right)\right] \end{cases} \tag{15.2}$$

Then the differential problem (11) becomes:

$$\begin{cases} \dfrac{\partial \tau_{xs}}{\partial s}+\dfrac{\partial \tau_{xn}}{\partial n}=-\dfrac{\partial \sigma_x}{\partial x} \quad \forall P\in \overset{\circ}{A} \\ \tau_{xn}=0 \quad \forall P\in Fr(A) \end{cases} \tag{16}$$

if A is the cross-section domain. The differential problem (16), by (15.1) and (15.2), can be rewritten as follows:

$$\begin{cases} \nabla^2\varphi=-\dfrac{1}{1+\nu}\varsigma \quad \forall P\in \overset{\circ}{A} \\ \dfrac{\partial\varphi}{\partial n}=\dfrac{\nu}{2(1+\nu)}\left[\eta\varsigma\alpha_{ny}-\dfrac{\alpha_{nz}}{2}\left(\eta^2-\varsigma^2\right)\right]\forall P\in Fr(A) \end{cases} \tag{17}$$

First of all, the differential problem (17) points out that φ depends, by means of the Poisson modulus, on the material, supposed homogeneous and isotropic, and on the cross-section's geometry.
Now, it is well known that the necessary solvability condition for the Poisson equation with Neumann boundary conditions is the following:

$$\int_{Fr(A)}\frac{\partial\varphi}{\partial n}ds=\int_A\nabla^2\varphi dA \tag{18}$$

The first term of equation (18) becomes:

$$\int_{Fr(A)}\frac{\partial\varphi}{\partial n}ds=\int_{Fr(A)}\left[\eta\varsigma\alpha_{ny}-\frac{\alpha_{nz}}{2}\left(\eta^2-\varsigma^2\right)\right]ds=0 \tag{19.1}$$

and, thanks to the Gauss theorem:

$$\int_A\frac{\partial}{\partial\eta}(\eta\varsigma)dA-\frac{1}{2}\int_A\frac{\partial}{\partial\varsigma}\left(\eta^2-\varsigma^2\right)dA=0 \tag{19.2}$$

so obtaining:

$$\int_A\varsigma dA+\int_A\varsigma dA=0 \tag{19.3}$$

as ζ is a principal axes of inertia. Now the eq. (18) becomes:

$$\int_A\nabla^2\varphi dA=0 \tag{20.1}$$

and, considering the first of (17), it can be so rewritten:

$$\int_A\varsigma dA=0 \tag{20.2}$$

so that the solvability condition is satisfied.

Now, denoting by the suffix i the restriction of this differential system to the *i-th* branch, by t_i the thickness branch, constant with the curvilinear abscissa s, and by l_i its length, it is possible to rewrite the differential problem in a local form as follows:

$$\begin{cases} \dfrac{\partial \tau_{xs,i}}{\partial s}+\dfrac{\partial \tau_{xn,i}}{\partial n}=-\dfrac{\partial \sigma_{x,i}}{\partial x} \quad \forall(s,n)\in[0,l_i]\times\left]-\dfrac{t_i}{2},\dfrac{t_i}{2}\right[\\ \tau_{xn,i}=0 \quad n=\pm\dfrac{t_i}{2};\forall s\in[0,l_i] \end{cases} \tag{21}$$

First of all, the negligibility of the thickness branch as regards its length permits, without great errors, to neglect the dependence of the functions $\eta(\mathrm{s},\mathrm{n})$ and $\varsigma(\mathrm{s},\mathrm{n})$ on the variable n, regarding them as functions of the only curvilinear abscissa s, evaluated on the branch centre line:

$$\eta_{\mathrm{i}}(\mathrm{s})=\eta_{\mathrm{m,i}}+\frac{\eta_{\mathrm{n,i}}-\eta_{\mathrm{m,i}}}{\mathrm{l_i}}\mathrm{s} \tag{22.1}$$

$$\varsigma_{\mathrm{i}}(\mathrm{s})=\varsigma_{\mathrm{m,i}}+\frac{\varsigma_{\mathrm{n,i}}-\varsigma_{\mathrm{m,i}}}{\mathrm{l_i}}\mathrm{s} \tag{22.2}$$

having denoted by the suffixes m and n the initial and the final nodes of each branch, respectively.
With this simplification, the local form of the differential problem becomes:

$$\begin{cases} \nabla^2\varphi_i=-\left(1-\dfrac{\nu}{2(1+\nu)}\right)\varsigma_i(s) \\ \dfrac{\partial\varphi_i}{\partial n}=\dfrac{\nu}{2(1+\nu)}\left[\eta_i\varsigma_i\alpha_{ny,i}-\dfrac{\alpha_{nz,i}}{2}\left(\eta_i^2-\varsigma_i^2\right)\right] \end{cases} \tag{23}$$

The problem (23) can be so rewritten, too:

$$\begin{cases} \nabla^2\varphi_{\mathrm{i}}=-\mathrm{k}_\nu\varsigma_{\mathrm{i}}(\mathrm{s}) \\ \dfrac{\partial\varphi_{\mathrm{i}}}{\partial \mathrm{n}}=\beta_\nu\left[\eta_{\mathrm{i}}\varsigma_{\mathrm{i}}\alpha_{\mathrm{nyi}}-\dfrac{\alpha_{\mathrm{nz,i}}}{2}\left(\eta_{\mathrm{i}}^2-\varsigma_{\mathrm{i}}^2\right)\right] \end{cases} \tag{24}$$

having formally done the following positions:

$$\begin{cases} \mathrm{k}_\nu=\dfrac{2+\nu}{2+2\nu} \\ \beta_\nu=1-\mathrm{k}_\nu=\dfrac{\nu}{2(1+\nu)} \end{cases} \tag{25}$$

The first of (24) permits to point out a remarkable property of the warping function $\varphi(\eta,\varsigma)$: the symmetry of the structural section A respect to the ζ axis, allows to introduce the parity notion, respect to η, for functions defined on A. As the function ζ is certainly even on A, the other one $\nabla^2\varphi$ will be consequently even; what is verified , if φ is, in turn, even, as it will be from now on admitted.

4. GLOBAL AND LOCAL DEVELOPMENT OF THE WARPING FUNCTION

The next assumption that, from now on, will be done, is the negligibility of the stress component directed along the thickness. In particular, the component τ_{xn}, already null in correspondence of the branch boundary, will be assumed null along the thickness too, imposing for the *i-th* branch the following condition:

$$\tau_{xn,i} = 0 \quad \forall(s,n) \in [0, l_i] \times \left[-\frac{t_i}{2}, \frac{t_i}{2}\right] \qquad (26)$$

Thanks to this assumption, the tangential stress field can be rewritten as follows:

$$\begin{cases} \tau_{xs} = \dfrac{Q}{I}\dfrac{\partial\varphi}{\partial s} - \beta_\nu \dfrac{Q}{I}\left[\eta\varsigma\alpha_{sy} - \dfrac{\alpha_{sz}}{2}\left(\eta^2 - \varsigma^2\right)\right] \\ \tau_{xn} = 0 \end{cases} \qquad (27)$$

Now, let us introduce the generalized shear sectional force:

$$Q = \int_A \tau_{xs}\alpha_{sz} dA + \int_A \tau_{xn}\alpha_{nz} dA \qquad (28)$$

having always denoted by α_{ij} the director cosine of the unit vector ***i*** of the local coordinate system as regards the unit vector **j** of the orthonormal basis. As the assumption (26) implies the following relation:

$$Q = \int_A \tau_{xs}\alpha_{sz} dA \qquad (29)$$

it follows that the tangential stress field τ_{xs} doesn't necessarily balance the vertical shear. So, in order to remove the problem, it is necessary to introduce, in the indefinite equilibrium equation (24), a corrective factor *k*:

$$\begin{cases} \nabla^2\varphi_i = -\dfrac{k_\nu}{k}\varsigma_i(s) \\ \dfrac{\partial\varphi_i}{\partial n} = \beta_\nu\left[\eta_i\varsigma_i\alpha_{ny,i} - \dfrac{\alpha_{nz,i}}{2}\left(\eta_i^2 - \varsigma_i^2\right)\right] \end{cases} \qquad (30)$$

Furthermore, taking into account that $\dfrac{\partial^2\varphi}{\partial n^2}$ is punctually null on *A*, by the integration on *A* of the Poisson equation, it is immediately verified that:

$$\int_A \frac{\partial^2\varphi}{\partial s^2}\varsigma dA = -\frac{k_\nu}{k} I \qquad (31)$$

Applying the generalized integration by parts formula, it is possible to obtain the following relation:

$$\int_A \frac{\partial^2\varphi}{\partial s^2}\varsigma dA = \int_{Fr(A)} \frac{\partial\varphi}{\partial s}\varsigma(\hat{s}\circ\hat{n})dS - \int_A \frac{\partial\varphi}{\partial s}\frac{d\varsigma}{ds} dA \qquad (32)$$

and, as it results $\hat{s}\circ\hat{n} = 0$, the equation (32) becomes:

$$\int_A \frac{\partial\varphi}{\partial s}\frac{d\varsigma}{ds} dA = \frac{k_\nu}{k} I \qquad (33)$$

Remembering this result, let us consider again the equation (29) that becomes:

$$Q = \frac{Q}{I}\int_A \frac{\partial\varphi}{\partial s}\frac{d\varsigma}{ds} dA - \beta_\nu \frac{Q}{I}\int_A \eta\varsigma\frac{d\eta}{ds}\frac{d\varsigma}{ds} - \frac{1}{2}\left(\frac{d\varsigma}{ds}\right)^2\left(\eta^2 - \varsigma^2\right) dA \qquad (34)$$

and, by (33), can be so expressed:

$$Q = Q\frac{k_\nu}{k} - \beta_\nu \frac{Q}{I}\int_A \eta\varsigma\frac{d\eta}{ds}\frac{d\varsigma}{ds} - \frac{1}{2}\left(\frac{d\varsigma}{ds}\right)^2\left(\eta^2 - \varsigma^2\right) dA \qquad (35)$$

So the constant *k* can be immediately obtained:

$$k = \frac{k_\nu}{1 + \beta_\nu \dfrac{\int_A \left[\eta\varsigma\dfrac{d\eta}{ds}\dfrac{d\varsigma}{ds} - \dfrac{1}{2}\left(\dfrac{d\varsigma}{ds}\right)^2\left(\eta^2 - \varsigma^2\right)\right] dA}{I}} \qquad (36)$$

Furthermore, the warping function must be the solution of a Neumann problem, defined except an arbitrary constant. To make the solution determined, it is necessary to impose the condition $\varphi_i = 0$ in correspondence of any *i-th* node of the section, so that the differential problem now becomes:

$$\begin{cases} \nabla^2\varphi = -\dfrac{k_\nu}{k}\varsigma \quad \forall P \in \overset{\circ}{A_i} \\ \dfrac{\partial\varphi}{\partial n} = \beta_\nu\left[\eta\varsigma\alpha_{ny} - \dfrac{\alpha_{nz}}{2}\left(\eta^2 - \varsigma^2\right)\right] \\ \varphi_i = 0 \end{cases} \qquad (37)$$

and finally, with reference to the *i-th* branch, the local form of the differential problem can be so rewritten:

$$\begin{cases} \dfrac{\partial^2\varphi_i}{\partial s^2} + \dfrac{\partial^2\varphi_i}{\partial n^2} = -\dfrac{k_\nu}{k}\varsigma_i(s,n) \quad \forall(s,n) \in [0, l_i] \times \left]-\dfrac{t_i}{2}, \dfrac{t_i}{2}\right[\\ \dfrac{\partial\varphi_i}{\partial n} = \beta_\nu\left[\alpha_{ny,i}\eta_i\varsigma_i - \dfrac{\alpha_{nz,i}}{2}\left(\eta_i^2 - \varsigma_i^2\right)\right] \\ \varphi_i(0,0) = \varphi_{m,i} \quad ; \quad \varphi_i(l_i,0) = \varphi_{n,i} \end{cases} \qquad (38)$$

5. THE RITZ METHOD FOR THE NUMERICAL EVALUATION OF THE WARPING FUNCTION

To solve the problem (38) it is necessary to assume that all branches are straight, then approximating a curvilinear one by a sufficient number of straight branches with nodes on its centre line.

To apply the method to the hull girder, it is also necessary to substitute the bulb sections with the equivalent angle profiles (with the net thickness of the web equal to that one of the bulb section, and the other three dimensions obtained imposing equal values of the net areas and inertia moments, and equal centre positions).

The previous Poisson equation is the Euler-Lagrange equation of the following functional, having denoted by *M* the number of branches on the half section:

$$U = 2\sum_{i=1}^{M}\int_0^{l_i}\int_{-\frac{t_i}{2}}^{\frac{t_i}{2}}\left[\frac{1}{2}\left|\nabla\varphi_i(s,n)\right|^2 - \frac{k_\nu}{k}\varsigma_i(s)\varphi_i(s,n)\right]dsdn \qquad (39)$$

where the integral extended to the *i-th* branch coincides with the local form of the Poisson equation.

Therefore, to solve the Poisson equation with some boundary condition is equivalent to finding the function that satisfies the same boundary conditions and minimizes the corresponding functional *U*.

So, the warping function can be seen as the sum of two functions: the first one $\varphi_i^*(s)$ defined on the branch centre line and variable with the curvilinear abscissa *s*, the second one $\delta_i(s,n)$ variable along the thickness and the branch and null in correspondence of the centre line:

$$\varphi_i(s,n) = \varphi_i^*(s) + \delta_i(s,n) \quad \text{with } \delta_i(s,0) = 0 \qquad (40)$$

The two functions solution of the Neumann problem are:

$$\varphi_i^*(s) = \varphi_{m,i}^* + \left(\frac{\varphi_{n,i}^* - \varphi_{m,i}^*}{l_i} + \frac{k_\nu}{k}\frac{l_i(\varsigma_{n,i} + 2\varsigma_{m,i})}{6}\right)s - \frac{k_\nu}{k}\left(\varsigma_{m,i} + \frac{\varsigma_{n,i} - \varsigma_{m,i}}{3l_i}s\right)\frac{s^2}{2} \qquad (41.1)$$

$$\delta_i(s,n) = \beta_\nu\left[\alpha_{ny,i}\eta_i(s)\varsigma_i(s) - \frac{\alpha_{nz,i}}{2}\left(\eta_i^2(s) - \varsigma_i^2(s)\right)\right]n \qquad (41.2)$$

The expression (41.1) can be obtained integrating twice the equation $\frac{d^2\varphi_i^*(s)}{ds^2} = -\frac{k_\nu}{k}\varsigma_i(s)$ with the boundary conditions $\varphi_i^*(0) = \varphi_{m,i}^*$ and $\varphi_i^*(l_i) = \varphi_{n,i}^*$. The second one, instead, is obtained integrating respect to the variable *n*, the equation $\delta_i(s,n) = \int\beta_\nu\left[\alpha_{ny,i}\eta_i(s)\varsigma_i(s) - \frac{\alpha_{nz,i}}{2}\left(\eta_i^2(s) - \varsigma_i^2(s)\right)\right]dn$ with the boundary condition $\delta_i(s,0) = 0$.

To determine the warping function's nodal values, it is necessary to search for the extremals of the functional *U*. The stationarity condition permits to write *P* linear equations, if *P* is the nodes number on the half section:

$$\frac{\partial}{\partial\varphi_k}\sum_{i=1}^{M}\int_0^{l_i}\int_{-\frac{t_i}{2}}^{\frac{t_i}{2}}\left[\frac{1}{2}\left|\nabla\varphi_i(s,n)\right|^2 - \frac{k_\nu}{k}\varsigma_i(s)\varphi_i(s,n)\right]dsdn = 0 \qquad (42)$$

The uniform continuity of the integrand function allows the derivation under integral sign, so obtaining:

$$\sum_{i=1}^{n(k)}\int_0^{l_i}\int_{-\frac{t_i}{2}}^{\frac{t_i}{2}}\frac{\partial}{\partial\phi_k}\left[\frac{1}{2}\left|\nabla\varphi_i(s,n)\right|^2 - \frac{k_\nu}{k}\varsigma_i(s)\varphi_i(s,n)\right]dsdn = 0 \qquad (43)$$

for k=1,…P

having denoted by *n(k)* the number of branches concurrent in the *k-th* node.

Now, as $\delta_i(s,n)$ doesn't depend on the warping function nodal values, this term is uninfluential in the variational calculus and so the equation (43) can be so rewritten:

$$\sum_{i=1}^{n(k)}\int_0^{l_i}\int_{-\frac{t_i}{2}}^{\frac{t_i}{2}}\frac{\partial}{\partial\phi_k}\left[\frac{1}{2}\left(\frac{d\varphi_i^*}{ds}\right)^2 - \frac{k_\nu}{k}\varsigma_i(s)\varphi_i^*(s)\right]dsdn = 0 \qquad (44)$$

for k=1,…P

and as no term depends on the variable *n*:

$$\sum_{i=1}^{n(k)}t_i\int_0^{l_i}\frac{\partial}{\partial\varphi_k}\left[\frac{1}{2}\left(\frac{d\varphi_i^*}{ds}\right)^2 - \frac{k_\nu}{k}\varsigma_i(s)\varphi_i^*(s)\right]ds = 0 \qquad (45)$$

for k=1,…P

Denoting – on each branch concurrent in the *k-th* node – by *r* the node different from the *k-th* one, the following system is obtained:

$$\sum_{i=1}^{n(k)}\frac{t_i}{l_i}\left(\varphi_k^* - \varphi_{r,i}^*\right) = \frac{k_\nu}{k}\frac{1}{6}\sum_{i=1}^{n(k)}t_il_i\left(2\varsigma_k + \varsigma_{r,i}\right) \qquad (46)$$

for k=1,…P

6. ANALYSIS OF THE BENDING-SHEAR STRESS

The restriction to the *i-th* branch of the stress components becomes:

$$\begin{cases}\sigma_{x,i}(x,s) = \sigma_{xB,i}(x,s)\\ \tau_{xs,i}(s,n) = \tau_{M,i}(s) + \tau_{G,i}(s) + \tau_{T,i}(s,n)\end{cases} \qquad (47)$$

The normal stress can be so expressed:

$$\sigma_{xB,i}(x,s) = \frac{M(x)}{I}\varsigma_i(s) = \frac{M(x)}{I}\left(\varsigma_{m,i} + \frac{\varsigma_{n,i} - \varsigma_{m,i}}{l_i}s\right) \qquad (48)$$

while the tangential ones are the sum of three terms:

$$\begin{cases} \tau_{M,i}(s) = \dfrac{Q}{I}\dfrac{d\varphi_i^*}{ds} \\ \tau_{G,i}(s) = -\beta_\nu \dfrac{Q}{I}\left[\eta_i(s)\varsigma_i(s)\alpha_{sy,i} - \dfrac{\alpha_{sz,i}}{2}\left(\eta_i(s)^2 - \varsigma_i(s)^2\right)\right] \\ \tau_{T,i}(s,n) = \dfrac{Q}{I}\dfrac{\partial}{\partial s}\delta_i(s,n) \end{cases} \quad (49)$$

with:

$$\frac{d\varphi_i^*}{ds} = \frac{\varphi_{n,i}^* - \varphi_{m,i}^*}{l_i} + \frac{k_\nu}{k}\frac{l_i(\varsigma_{n,i} + 2\varsigma_{m,i})}{6} - \frac{k_\nu}{k}\left(\varsigma_{m,i} + \frac{\varsigma_{n,i} - \varsigma_{m,i}}{2 l_i}s\right)s \quad (50.1)$$

$$\frac{\partial}{\partial s}\delta_i(s,n) = \beta_\nu\left(\eta_{m,i} + \frac{\eta_{n,i} - \eta_{m,i}}{l_i}s\right)n \quad (50.2)$$

The constant k can be evaluated as follows:

$$k = \frac{k_\nu}{1 + \dfrac{\beta_\nu}{I}(S_1 - S_2 + S_3)} \quad (51)$$

with:

$$S_1 = \frac{1}{3}\sum_{i=1}^{M}\frac{t_i}{l_i}(\eta_{n,i} - \eta_{m,i})(\varsigma_{n,i} - \varsigma_{m,i})(2\eta_{m,i}\varsigma_{m,i} + 2\eta_{n,i}\varsigma_{n,i} + \eta_{m,i}\varsigma_{n,i} + \eta_{n,i}\varsigma_{m,i})$$

$$S_2 = \frac{1}{3}\sum_{i=1}^{M}\frac{t_i}{l_i}(\varsigma_{n,i} - \varsigma_{m,i})^2(\eta_{m,i}^2 + \eta_{n,i}^2 + \eta_{m,i}\eta_{n,i})$$

$$S_3 = \frac{1}{3}\sum_{i=1}^{M}\frac{t_i}{l_i}(\varsigma_{n,i} - \varsigma_{m,i})^2(\varsigma_{m,i}^2 + \varsigma_{n,i}^2 + \varsigma_{m,i}\varsigma_{n,i}) \quad (52)$$

7. THE HORIZONTAL SHEAR: DETERMINATION OF THE SHEAR CENTER VERTICAL POSITION

As any ship section is generally symmetric as regards the vertical ζ-axis, it is not necessary to determine the transverse position of the shear center, as it will lie on the symmetry plane. Instead, as it is fundamental to determine the vertical position of the shear center, in the following a theory, based on the Saint-Venant displacement field for the horizontal shear, is developed. Assuming the global and local Cartesian frames sketched in *Fig. 1*, it is possible to verify that the following displacement field is a Saint-Venant field:

$$\begin{cases} u = -\vartheta_H(x)\eta + \dfrac{Q_H}{GI_\varsigma}\varphi_H(\eta,\varsigma) \\ v = v_0(x) + \dfrac{\nu}{2}\dfrac{d\vartheta_H}{dx}(\eta^2 - \varsigma^2) \\ w = \nu\dfrac{d\vartheta_H}{dx}\eta\varsigma \end{cases} \quad (53)$$

where Q_H is the horizontal shear, constant with x; I_ζ is the section inertia moment about its ζ-axis; G is the tangential modulus (first Lamé constant); $\varphi_H(\eta,\varsigma)$ is the warping function, constant with x; $\vartheta_H(x)$ is the rotation of the section about its ζ-axis, positive if counter-clockwise; $v_0(x)$ is its η translation, connected with the rotation $\vartheta_H(x)$ by the geometrical condition of orthogonality between the section and the elastic surface y=0:

$$\vartheta_H(x) = \frac{dv_0}{dx} \quad (54)$$

With the previous assumptions and notations, the strain components (for small deformation) are then given by:

$$\begin{cases} \varepsilon_{x,H} = -\dfrac{d\vartheta_H}{dx}\eta \\ \varepsilon_{y,H} = -\nu\varepsilon_{x,H} \\ \varepsilon_{z,H} = -\nu\varepsilon_{x,H} \end{cases} \quad (55.1)$$

$$\begin{cases} \gamma_{xy,H} = \dfrac{Q_H}{GI_\varsigma}\dfrac{\partial\varphi_H}{\partial\eta} + \dfrac{\nu}{2}\dfrac{d^2\vartheta_H}{dx^2}(\eta^2 - \varsigma^2) \\ \gamma_{xz,H} = \dfrac{Q_H}{GI_\varsigma}\dfrac{\partial\varphi_H}{\partial\varsigma} + \nu\dfrac{d^2\vartheta_H}{dx^2}\eta\varsigma \\ \gamma_{yz,H} = 0 \end{cases} \quad (55.2)$$

Now, starting from the basic expressions (8.1) and (8.2), the only non-null stress components are:

$$\begin{cases} \sigma_{x,H} = -E\dfrac{d\vartheta_H}{dx}\eta \\ \tau_{xy,H} = \dfrac{Q_H}{I_\varsigma}\dfrac{\partial\varphi_H}{\partial\eta} + \dfrac{\nu}{2}G\dfrac{d^2\vartheta_H}{dx^2}(\eta^2 - \varsigma^2) \\ \tau_{xz,H} = \dfrac{Q_H}{I_\varsigma}\dfrac{\partial\varphi_H}{\partial\varsigma} + \nu G\dfrac{d^2\vartheta_H}{dx^2}\eta\varsigma \end{cases} \quad (56)$$

Introducing, now, the local curvilinear coordinates system of *Fig. 2*, the stress field can be rewritten as follows:

$$\begin{cases} \sigma_{x,H} = -E\dfrac{d\vartheta_H}{dx}\eta \\ \tau_{xs,H} = \dfrac{Q_H}{I_\varsigma}\dfrac{\partial\varphi_H}{\partial s} + \nu G\dfrac{d^2\vartheta_H}{dx^2}\left[\eta\varsigma\alpha_{sz} + \dfrac{\alpha_{sy}}{2}(\eta^2 - \varsigma^2)\right] \\ \tau_{xn,H} = \dfrac{Q_H}{I_\varsigma}\dfrac{\partial\varphi_H}{\partial n} + \nu G\dfrac{d^2\vartheta_H}{dx^2}\left[\eta\varsigma\alpha_{nz} + \dfrac{\alpha_{ny}}{2}(\eta^2 - \varsigma^2)\right] \end{cases} \quad (57)$$

It is convenient, now, to determine the function $\frac{d^2\vartheta_H}{dx^2}$. Starting from the expression of the bending moment:

$$M_\varsigma(x) = -\int_A \sigma_x \eta dA = EI_\varsigma \frac{d\vartheta_H}{dx} \quad (58)$$

it is possible to obtain:

$$\frac{d\vartheta_H}{dx} = \frac{M_\varsigma(x)}{EI_\varsigma} \quad (59.1)$$

and then:

$$\frac{d^2\vartheta_H}{dx^2} = -\frac{Q_H}{EI_\varsigma} \quad (59.2)$$

Now, starting from eq. (59.1) and (59.2), the stress components can be so rewritten:

$$\begin{cases} \sigma_{x,H} = -\dfrac{M_\varsigma(x)}{I_\varsigma}\eta \\ \tau_{xs,H} = \dfrac{Q_H}{I_\varsigma}\dfrac{\partial\varphi_H}{\partial s} - \nu G \dfrac{Q_H}{EI_\varsigma}\left[\eta\varsigma\alpha_{sz} + \dfrac{\alpha_{sy}}{2}\left(\eta^2 - \varsigma^2\right)\right] \\ \tau_{xn,H} = \dfrac{Q_H}{I_\varsigma}\dfrac{\partial\varphi_H}{\partial n} - \nu G \dfrac{Q_H}{EI_\varsigma}\left[\eta\varsigma\alpha_{nz} + \dfrac{\alpha_{ny}}{2}\left(\eta^2 - \varsigma^2\right)\right] \end{cases} \quad (60)$$

Concerning the third of the indefinite equilibrium equations (2) and the boundary condition on the lateral surface (3), and taking into account the assumptions (22.1) and (22.2), the local form of the differential system becomes:

$$\begin{cases} \nabla^2\varphi_{H,i} = -k_\nu \eta_i(s) \\ \dfrac{\partial\varphi_{H,i}}{\partial n} = \beta_\nu\left[\eta_i\varsigma_i\alpha_{nz,i} + \dfrac{\alpha_{ny,i}}{2}\left(\eta_i^2 - \varsigma_i^2\right)\right] \end{cases} \quad (61)$$

having formally done the positions (25). It is noticed that the boundary condition is valid for $n = \pm\frac{t_i}{2};\ \forall s \in [0, l_i]$

Now, thanks to the assumption (26), and taking into account that the tangential stress field τ_{xs} doesn't necessarily balance the horizontal shear, it is necessary to introduce a corrective factor k_H, so that the system (61) becomes:

$$\begin{cases} \nabla^2\varphi_{H,i} = -\dfrac{k_\nu}{k_H}\eta_i(s) \\ \dfrac{\partial\varphi_{H,i}}{\partial n} = \beta_\nu\left[\eta_i\varsigma_i\alpha_{nz,i} + \dfrac{\alpha_{ny,i}}{2}\left(\eta_i^2 - \varsigma_i^2\right)\right] \end{cases} \quad (62)$$

where the boundary condition is now valid through the thickness, too.

Furthermore, taking into account that $\frac{\partial^2\varphi_H}{\partial n^2}$ is punctually null on A, by the integration on A of the Poisson equation, it is immediately verified that:

$$\int_A \frac{\partial^2\varphi_H}{\partial s^2}\eta dA = -\frac{k_\nu}{k_H} I_\varsigma \quad (63)$$

Applying the generalized integration by parts formula, it is possible to obtain the following relation:

$$\int_A \frac{\partial^2\varphi_H}{\partial s^2}\eta dA = \int_{Fr(A)} \frac{\partial\varphi_H}{\partial s}\eta(\hat{s}\circ\hat{n})dS - \int_A \frac{\partial\varphi_H}{\partial s}\frac{d\eta}{ds}dA \quad (64)$$

and, as it results $\hat{s}\circ\hat{n} = 0$, the equation (63) can be so rewritten:

$$\int_A \frac{\partial\varphi_H}{\partial s}\frac{d\eta}{ds}dA = \frac{k_\nu}{k_H} I_\varsigma \quad (65)$$

Remembering this result and considering the generalized horizontal shear sectional force, it is possible to obtain the constant k_H:

$$k_H = \frac{k_\nu}{1 + \beta_\nu \dfrac{\int_A \left[\eta\varsigma\dfrac{d\eta}{ds}\dfrac{d\varsigma}{ds} + \dfrac{1}{2}\left(\dfrac{d\eta}{ds}\right)^2\left(\eta^2 - \varsigma^2\right)\right]dA}{I_\varsigma}} \quad (66)$$

Now, as the warping function must be the solution of a Neumann problem, defined except an arbitrary constant, it is possible to remove this indeterminacy assigning the condition $\varphi_{H,i} = 0$ in correspondence of any *i-th* node of the section. Similarly to the vertical shear, with reference to the *i-th* branch, the local form of the differential problem can be so rewritten:

$$\begin{cases} \dfrac{\partial^2\varphi_{H,i}}{\partial s^2} + \dfrac{\partial^2\varphi_{H,i}}{\partial n^2} = -\dfrac{k_\nu}{k_H}\eta_i(s,n) \quad \forall(s,n)\in[0,l_i]\times\left]-\dfrac{t_i}{2},\dfrac{t_i}{2}\right[\\ \dfrac{\partial\varphi_{H,i}}{\partial n} = \beta_\nu\left[\eta_i\varsigma_i\alpha_{nz,i} + \dfrac{\alpha_{ny,i}}{2}\left(\eta_i^2 - \varsigma_i^2\right)\right] \\ \varphi_{H,i}(0,0) = \varphi_{Hm,i} \quad ; \quad \varphi_{H,i}(l_i,0) = \varphi_{Hn,i} \end{cases} \quad (67)$$

The previous Poisson equation is the Euler-Lagrange equation of the functional:

$$U_H = 2\sum_{i=1}^{N}\int_0^{l_i}\int_{-\frac{t_i}{2}}^{\frac{t_i}{2}}\left[\frac{1}{2}\left|\nabla\varphi_{H,i}(s,n)\right|^2 - \frac{k_\nu}{k_H}\eta_i(s)\varphi_{H,i}(s,n)\right]dsdn \quad (68)$$

The warping function can be seen as the sum of two functions: the first one $\varphi^*_{H,i}(s)$ defined on the branch centre line and variable with the curvilinear abscissa *s*, the second one $\delta_{H,i}(s,n)$ variable along the thickness and the branch and null in correspondence of the centre line:

$$\varphi_{H,i}(s,n) = \varphi^*_{H,i}(s) + \delta_{H,i}(s,n) \quad \text{with } \delta_{H,i}(s,0) = 0 \tag{69}$$

The two functions solution of the Neumann problem are:

$$\varphi^*_{H,i}(s) = \varphi^*_{Hm,i} + \left(\frac{\varphi^*_{Hn,i} - \varphi^*_{Hm,i}}{l_i} + \frac{k_V}{k_H}\frac{l_i(\eta_{n,i} + 2\eta_{m,i})}{6}\right)s - \frac{k_V}{k_H}\left(\eta_{m,i} + \frac{\eta_{n,i} - \eta_{m,i}}{3l_i}s\right)\frac{s^2}{2} \tag{70.1}$$

$$\delta_{H,i}(s,n) = \beta_V\left[\eta_i\varsigma_i\alpha_{nz,i} + \frac{\alpha_{ny,i}}{2}\left(\eta_i^2 - \varsigma_i^2\right)\right]n \tag{70.2}$$

To determine the warping function's nodal values, it is necessary to search for the extremals of the functional U_H. Denoting by *N* the number of branches on the cross-section, the stationarity condition permits to write *W* linear equations, if W is the nodes number on the cross-section.

Denoting – on each branch concurrent in the *k-th* node – by *r* the node different from the *k-th* one, the following system is obtained:

$$\sum_{i=1}^{n(k)} \frac{t_i}{l_i}\left(\varphi^*_{\mathrm{H,k}} - \varphi^*_{\mathrm{Hr,i}}\right) = \frac{k_V}{k_H}\frac{1}{6}\sum_{i=1}^{n(k)} t_i l_i\left(2\eta_k + \eta_{r,i}\right) \tag{71}$$

for k=1,…W

The restriction to the *i-th* branch of the stress components becomes:

$$\begin{cases} \sigma_{\mathrm{xH,i}}(x,s) = \sigma_{\mathrm{xB\text{-}H,i}}(x,s) \\ \tau_{xsH,i}(s,n) = \tau_{M-H,i}(s) + \tau_{G-H,i}(s) + \tau_{T-H,i}(s,n) \end{cases} \tag{72}$$

The normal stress can be so expressed:

$$\sigma_{\mathrm{xB\text{-}H,i}}(x,s) = -\frac{\mathrm{M}_\varsigma(\mathrm{x})}{\mathrm{I}\varsigma}\left(\eta_{m,i} + \frac{\eta_{n,i} - \eta_{m,i}}{l_i}s\right) \tag{73}$$

while the tangential ones are the sum of three terms:

$$\begin{cases} \tau_{M-H,i}(s) = \dfrac{Q_H}{I_\varsigma}\dfrac{d\varphi^*_{H,i}}{ds} \\ \tau_{G-H,i}(s) = -\beta_V\dfrac{Q_H}{I_\varsigma}\left[\eta_i(s)\varsigma_i(s)\alpha_{sz,i} + \dfrac{\alpha_{sy,i}}{2}\left(\eta_i(s)^2 - \varsigma_i(s)^2\right)\right] \\ \tau_{T-H,i}(s,n) = \dfrac{Q_H}{I_\varsigma}\dfrac{\partial}{\partial s}\delta_{H,i}(s,n) \end{cases} \tag{74}$$

with:

$$\frac{d\varphi^*_{H,i}}{ds} = \frac{\varphi^*_{H_{n,i}} - \varphi^*_{H_{m,i}}}{l_i} + \frac{k_V}{k_H}\frac{l_{\mathrm{i}}(\eta_{\mathrm{n,i}} + 2\eta_{\mathrm{m,i}})}{6} - \frac{k_V}{k_H}\left(\eta_{\mathrm{m,i}} + \frac{\eta_{\mathrm{n,i}} - \eta_{\mathrm{m,i}}}{2l_{\mathrm{i}}}\mathrm{s}\right)s \tag{75.1}$$

$$\frac{\partial}{\partial s}\delta_{H,i}(s,n) = -\beta_V\left(\varsigma_{m,i} + \frac{\varsigma_{n,i} - \varsigma_{m,i}}{l_i}s\right)n \tag{75.2}$$

The constant k_H can be evaluated as follows:

$$k_H = \frac{k_V}{1 + \dfrac{\beta_V}{I_\varsigma}\left(H_1 + H_2 - H_3\right)} \tag{76}$$

with:

$$\begin{aligned} H_1 &= \frac{1}{6}\sum_{i=1}^{N}\frac{t_i}{l_i}\left(\eta_{n,i} - \eta_{m,i}\right)\left(\varsigma_{n,i} - \varsigma_{m,i}\right)\left(2\eta_{m,i}\varsigma_{m,i} + 2\eta_{n,i}\varsigma_{n,i} + \eta_{m,i}\varsigma_{n,i} + \eta_{n,i}\varsigma_{m,i}\right) \\ H_2 &= \frac{1}{6}\sum_{i=1}^{N}\frac{t_i}{l_i}\left(\eta_{n,i} - \eta_{m,i}\right)^2\left(\eta_{m,i}^2 + \eta_{n,i}^2 + \eta_{m,i}\eta_{n,i}\right) \\ H_3 &= \frac{1}{6}\sum_{i=1}^{N}\frac{t_i}{l_i}\left(\eta_{n,i} - \eta_{m,i}\right)^2\left(\varsigma_{m,i}^2 + \varsigma_{n,i}^2 + \varsigma_{m,i}\varsigma_{n,i}\right) \end{aligned} \tag{77}$$

As regards the shear center vertical position, it can be immediately obtained, taking into account that the horizontal shear, applied in correspondence of the section barycentre, can determine a twist moment, and so considering the equivalence of the following systems:

$$\left\{G(x), Q_H\hat{j}; M_H\hat{i}\right\} \Leftrightarrow \left\{P(0,\varsigma_Q), Q_H\hat{j}\right\} \tag{78}$$

having denoted by M_H the twist moment, generated by the horizontal shear, and by ς_Q the shear center vertical position as regards the Cartesian frames sketched in *Fig. 1*. Now, as the two systems must have the same resultant, the following equivalence is valid

$$\left(P(0,\varsigma_Q) - G(x)\right)x\hat{j} = \frac{M_H}{Q_H}\hat{i} \tag{79.1}$$

and then:

$$\varsigma_Q\hat{k}x\hat{j} = \frac{M_H}{Q_H}\hat{i} \tag{79.2}$$

finally obtaining:

$$\varsigma_Q = -\frac{M_H}{Q_H} \tag{79.3}$$

The twist moment generated by the horizontal shear can be so expressed:

$$M_H = \int_A \left(\vec{r} \; x \, \tau_{xs} \hat{s} \circ \hat{i} \right) dA \tag{80.1}$$

with $\vec{r} = P - G(x) = \eta \, \hat{j} + \varsigma \, \hat{k}$. The equation (80.1) becomes:

$$M_H = \sum_{i=1}^{N} t_i \int_0^{l_i} \left(\vec{r}_i \; x \, \tau_{xs,i} \hat{s} \circ \hat{i} \right) ds \tag{80.2}$$

Now, as all branches are straight, it is possible to verify that the mixed product can be so rewritten:

$$\vec{r}_i \; x \, \tau_{xs,i} \hat{s} \circ \hat{i} = h_i \tau_{xs,i} \tag{81.1}$$

with:

$$h_i = \frac{\eta_{m,i} \varsigma_{n,i} - \eta_{n,i} \varsigma_{m,i}}{l_i} \tag{81.2}$$

Substituting the expressions (80.2) and (81.1) in the eq. (79.3), the shear center vertical position is immediately obtained:

$$\varsigma_Q = - \frac{\sum_{i=1}^{N} t_i h_i \int_0^{l_i} \frac{d\varphi^*_{H,i}}{ds} ds - \beta_\nu \sum_{i=1}^{N} t_i h_i \int_0^{l_i} \left[\eta_i \varsigma_i \alpha_{sz,i} + \frac{\alpha_{sy,i}}{2} \left(\eta_i^2 - \varsigma_i^2 \right) \right] ds}{I_\varsigma} \tag{82.1}$$

and then:

$$\varsigma_Q = - \frac{Z_1 - \beta_\nu Z_2}{I_\varsigma} \tag{82.2}$$

with:

$$Z_1 = \sum_{i=1}^{N} t_i h_i \left(\varphi^*_{Hn,i} - \varphi^*_{Hm,i} \right) \tag{83.1}$$

$$Z_2 = \sum_{i=1}^{N} t_i h_i \left(Z^I_{2,i} + Z^{II}_{2,i} \right) \tag{83.2}$$

where:

$$Z^{II}_{2,i} = \frac{\varsigma_{n,i} - \varsigma_{m,i}}{6} \left(2\eta_{m,i} \varsigma_{m,i} + 2\eta_{n,i} \varsigma_{n,i} + \eta_{m,i} \varsigma_{n,i} + \eta_{n,i} \varsigma_{m,i} \right) \tag{84.1}$$

$$Z^{I}_{2,i} = \frac{\eta_{n,i} - \eta_{m,i}}{6} \left(\eta^2_{m,i} + \eta^2_{n,i} + \eta_{m,i} \eta_{n,i} - \varsigma^2_{m,i} - \varsigma^2_{n,i} - \varsigma_{m,i} \varsigma_{n,i} \right) \tag{84.2}$$

8. THE LINK BETWEEN THE SAINT-VENANT AND VLASOV THEORIES FOR BENDING AND SHEAR IN THIN-WALLED BEAMS

The results achievable applying the Vlasov theory, and so regarding as totally restrained the lateral contraction of the beam cross-section, can be immediately obtained by the following limit operations:

$$\beta_{\nu-VLASOV} = \lim_{\nu \to 0} \beta_\nu = 0 \tag{85.1}$$

$$k_{\nu-VLASOV} = \lim_{\nu \to 0} k_\nu = 1 \tag{85.2}$$

$$k_{VLASOV} = \lim_{\nu \to 0} k = 1 \tag{85.3}$$

$$k_{H-VLASOV} = \lim_{\nu \to 0} k_H = 1 \tag{85.4}$$

Thanks to these positions, starting from (46), it is possible to obtain immediately the *x*-projection of the indefinite equilibrium equation achievable applying the Vlasov theory:

$$\sum_{i=1}^{n(k)} \frac{t_i}{l_i} \left(\varphi_{\mathrm{k}} - \varphi_{\mathrm{r,i}} \right) = \frac{1}{6} \sum_{i=1}^{n(k)} t_i l_i \left(2\varsigma_k + \varsigma_{r,i} \right) \tag{86}$$

where the unknown nodal values have lost the asterisk, in order to remember that they are evaluated in the context of Vlasov theory and not of Saint-Venant one.
The tangential stress field becomes:

$$\begin{cases} \tau_{\mathrm{M,i-VLASOV}}(\mathrm{s}) = \frac{\mathrm{Q}}{\mathrm{I}} \frac{\mathrm{d}\varphi_{\mathrm{i}}}{\mathrm{ds}} \\ \tau_{\mathrm{G,i-VLASOV}}(\mathrm{s}) = 0 \\ \tau_{\mathrm{T,i-VLASOV}}(\mathrm{s,n}) = 0 \end{cases} \tag{87}$$

with:

$$\frac{d\varphi_i}{ds} = \frac{\varphi_{n,i} - \varphi_{m,i}}{l_i} + \frac{l_{\mathrm{i}} \left(\varsigma_{\mathrm{n,i}} + 2\, \varsigma_{\mathrm{m,i}} \right)}{6} - \left(\varsigma_{\mathrm{m,i}} + \frac{\varsigma_{\mathrm{n,i}} - \varsigma_{\mathrm{m,i}}}{2\, l_{\mathrm{i}}} \mathrm{s} \right) s \tag{88}$$

It notices that also this last position can be immediately obtained starting from (50.1), deleting formally the asterisk and imposing $k = k_\nu = 1$. The same positions can be done for the horizontal shear, too.
Concerning the vertical shear position, it is clear that:

$$\varsigma_{Q-VLASOV} = \lim_{\nu \to 0} \varsigma_Q \tag{89}$$

Substantially, it is shown that, by the limit condition $\nu \to 0$, all the results achievable applying the Vlasov theory can be obtained starting form this new generalized one, developed according to the Saint-Venant bending-shear displacement field.

9. A NUMERICAL APPLICATION TO THE SECTION CONSIDERED BY HUGHES

In order to estimate the differences between the Vlasov and Saint-Venant theories for the shear stress determination, an application has been carried out, based on the simplified structure considered by Hughes [2].

Particularly, a numerical comparison with the vertical shear tangential stresses obtained by a FEM analysis is carried out, in order to verify the goodness of the two theories. In *Tab. 1*, the section geometry data are presented. Particularly, for each branch, numbered from 1 to 6, the extremity' nodes, the thickness and length are shown (see also *Fig. 3*). Then in *Tab. 2* for each branch the vertical shear normalized tangential stresses $\tau^n_{xs,i}$, in m^2, are presented, having done the following position: $\tau^n_{xs,i} = \tau_{xs,i}\frac{I}{Q}$. Finally, in *Fig. 4*, the tangential stress distribution is shown for each branch. The red curves are relative to the Vlasov values, the black ones to the Saint-Venant values, the blue ones to the values obtained by the FEM analysis carried out by ANSYS.

Tab. 1 – Section geometry data

SECTION GEOMETRY DATA				
Branch	**I node**	**II node**	**t (m)**	**l (m)**
1	1	2	0.0032	10
2	2	5	0.0032	20
3	2	3	0.0032	10
4	3	4	0.0032	20
5	4	5	0.0068	10
6	5	6	0.0060	10

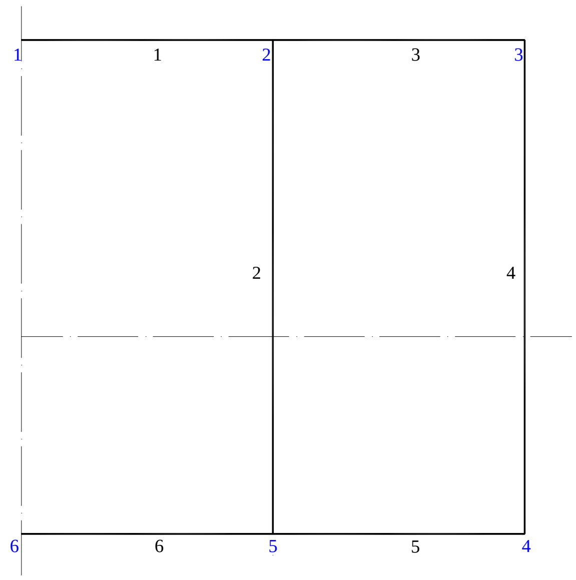

Fig. 3 Section scheme

Tab. 2 Vertical shear- normalized tangential stresses

Branch 1	**FEM**	**Vlasov**	**Saint-Venant**
First node	0.00	0.00	0.00
Half branch	-66.64	-60.00	-62.67
Second node	-133.94	-120.00	-125.33
Branch 2	**FEM**	**Vlasov**	**Saint-Venant**
First node	-132.77	-137.42	-125.20
Half branch	-191.27	-207.42	-198.30
Second node	-143.94	-177.42	-166.97
Branch 3	**FEM**	**Vlasov**	**Saint-Venant**
First node	-1.13	17.42	2.39
Half branch	-68.47	-42.58	-60.28
Second node	-131.31	-102.58	-122.95
Branch 4	**FEM**	**Vlasov**	**Saint-Venant**
First node	-131.32	-102.58	-110.06
Half branch	-189.25	-172.58	-183.17
Second node	-154.44	-142.58	-151.84
Branch 5	**FEM**	**Vlasov**	**Saint-Venant**
First node	-82.19	-67.10	-80.76
Half branch	-51.88	-27.10	-38.99
Second node	-14.63	12.90	2.79
Branch 6	**FEM**	**Vlasov**	**Saint-Venant**
First node	-80.54	-80.00	-83.56
Half branch	-40.94	-40.00	-41.78
Second node	0.00	0.00	0.00

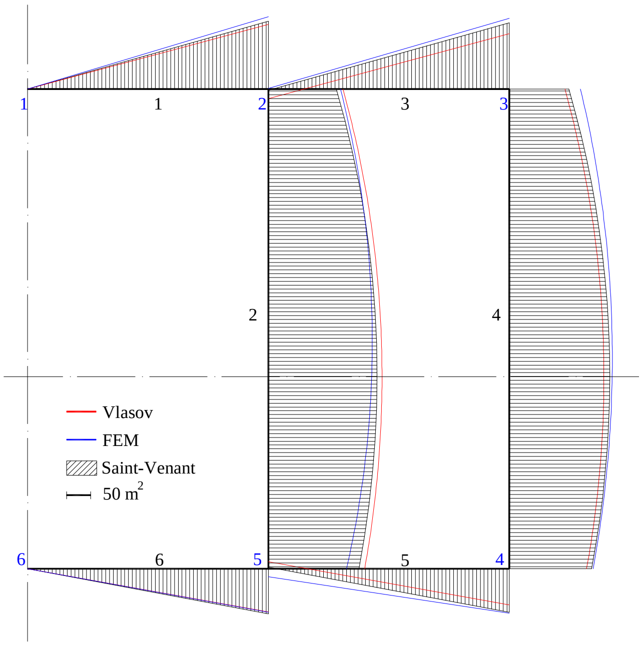

Fig. 4 Vertical shear – normalized tangential stresses

In *Tab. 3* and *Fig. 5* the normalized horizontal shear stresses $\tau^n_{xsH,i}$, in m^2, for each branch are shown, having done the position $\tau^n_{xsH,i} = \tau_{xsH,i}\frac{I_\varsigma}{Q_H}$.

Tab. 3 Horizontal shear- normalized tangential stresses

Branch 1	**Vlasov**	**Saint-Venant**
First node	443.36	455.57
Half branch	430.86	441.52
Second node	393.36	399.37
Branch 2	**Vlasov**	**Saint-Venant**
First node	83.42	97.96
Half branch	-16.57	-14.42
Second node	-116.57	-126.81
Branch 3	**Vlasov**	**Saint-Venant**
First node	309.94	315.21
Half branch	247.44	244.97
Second node	159.94	146.63
Branch 4	**Vlasov**	**Saint-Venant**
First node	159.94	188.95
Half branch	-40.06	-35.82
Second node	-240.06	-260.59
Branch 5	**Vlasov**	**Saint-Venant**
First node	-112.97	-94.65
Half branch	-200.47	-192.99
Second node	-262.97	-263.23
Branch 6	**Vlasov**	**Saint-Venant**
First node	-360.21	-361.33
Half branch	-397.71	-403.47
Second node	-410.21	-417.52

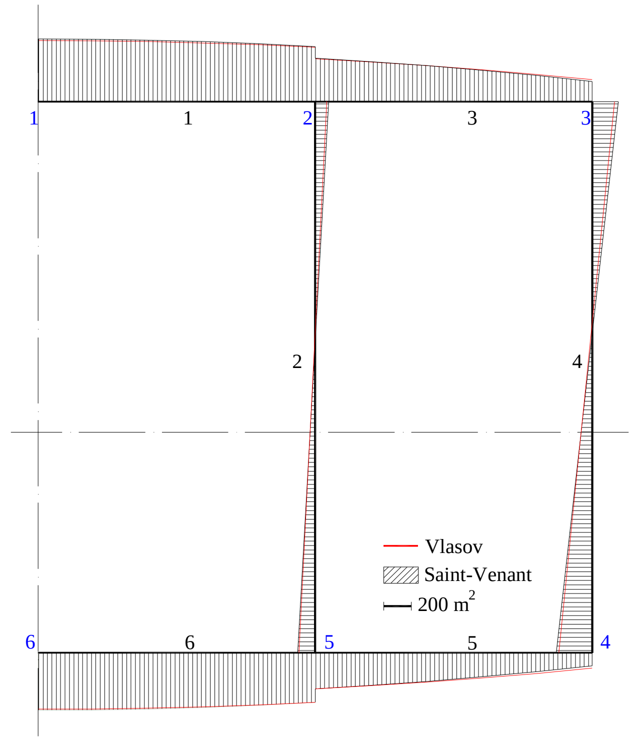

Fig. 5 Horizontal shear- normalized tangential stresses

Concerning the vertical position of the shear center, the following results are obtained, applying the two theories:

$\varsigma_{Q\ from\ B.L.} = 6.15\, m$ (Saint-Venant)

$\varsigma_{Q\ from\ B.L.} = 6.28\, m$ (Vlasov)

It seems that this new theory, developed starting from the Saint-Venant bending-shear displacement field, furnishes, respect to the classical Vlasov one, results closer to the ones obtained by the FEM analysis, especially for the branches at deck and bottom. Some differences can be seen in the normalized tangential shear stress determination, as well as in the evaluation of the shear center vertical position.

10. A NUMERICAL APPLICATION TO A BULK-CARRIER

In order to estimate the feasibility of the proposed method, an application has been carried out for a bulk carrier, with the following main dimensions:

$L_{O.A.}$= 221.00 m; B = 32.24 m; D = 19.70 m; T= 14.33 m;

Δ= 86850 t; I =221.03 m^4; I_ζ =516.62 m^4; ζ_G =7.89 m.

In *Fig. 6* and *Tab. 4* the section geometry data and the section scheme are presented. In *Tab. 5-6* and *Fig. 7-8* the vertical and horizontal shear normalized tangential stresses, evaluated applying the two theories, are shown. No particular differences are obtained in the evaluation of the shear center vertical position.

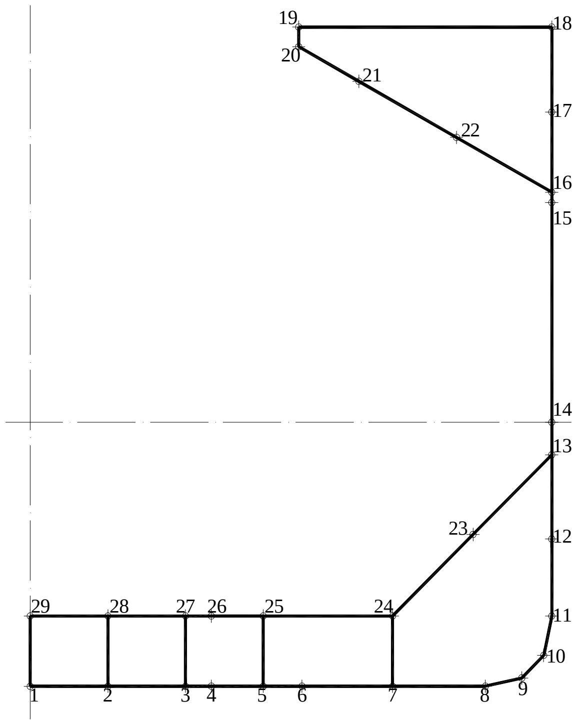

Fig. 6 – Bulk carrier section scheme

Tab. 4 – Bulk carrier section geometry data

SECTION GEOMETRY DATA				
Branches	**I node**	**II node**	**t (m)**	**l (m)**
1	1	2	0.0226	2.40
2	2	3	0.0243	2.40
3	3	4	0.0205	0.80
4	4	5	0.0242	1.60
5	5	6	0.0223	1.20
6	6	7	0.0224	2.80
7	7	8	0.0246	2.87
8	8	9	0.0170	1.15
9	9	10	0.0170	0.96
10	10	11	0.0170	1.20
11	11	12	0.0225	2.30
12	12	13	0.0235	2.52
13	13	14	0.0210	0.97
14	14	15	0.0210	6.57
15	15	16	0.0215	0.30
16	16	17	0.0243	2.40
17	17	18	0.0236	2.54
18	18	19	0.0317	7.82
19	19	20	0.0250	0.59
20	20	21	0.0249	2.13
21	21	22	0.0220	3.45
22	16	22	0.0243	3.37
23	13	23	0.0220	3.41
24	23	24	0.0242	3.48
25	24	25	0.0262	4.00
26	25	26	0.0235	1.60
27	26	27	0.0290	0.80
28	27	28	0.0260	2.40
29	28	29	0.0225	2.40
30	1	29	0.0073	2.10
31	2	28	0.0175	2.10
32	3	27	0.0160	2.10
33	5	25	0.0160	2.10
34	7	24	0.0160	2.10

Tab. 5 Vertical shear- normalized tangential stresses

	Normalized tangential stresses (m^2)			
	Vlasov		**Saint-Venant**	
Branches	I node	II node	I node	II node
1	0.77	19.72	0.71	20.57
2	19.60	38.55	20.46	40.31
3	45.51	51.83	46.77	53.38
4	43.90	56.53	46.04	59.27
5	55.90	65.37	58.68	68.60
6	65.08	87.18	68.33	91.49
7	57.86	80.52	64.30	88.04
8	116.51	125.50	122.87	132.29
9	125.50	132.43	133.62	140.88
10	132.43	140.13	137.53	145.60
11	105.88	116.56	111.80	123.00
12	111.60	117.23	118.40	124.30
13	313.79	314.26	306.55	307.05
14	314.26	292.71	307.05	284.47
15	285.90	283.89	278.16	276.05
16	135.67	116.32	138.62	118.33
17	119.77	93.01	121.53	93.50
18	69.24	-23.08	87.13	-9.59
19	-29.26	-36.05	-22.89	-30.00
20	-36.20	-58.95	-41.71	-65.55
21	-66.72	-98.93	-72.73	-106.49
22	115.51	89.57	124.98	97.81
23	-174.30	-166.91	-173.88	-166.14
24	-151.74	-135.82	-152.07	-135.39
25	-96.46	-73.28	-97.26	-72.97
26	-66.73	-57.46	-66.90	-57.19
27	-46.56	-41.93	-47.09	-42.23
28	-37.77	-23.87	-38.38	-23.81
29	-17.76	-3.86	-18.15	-3.58
30	-2.40	11.97	-5.98	9.08
31	-1.76	12.62	-5.04	10.02
32	0.24	14.61	-2.15	12.91
33	7.60	21.98	6.42	21.48
34	33.10	47.47	34.49	49.55

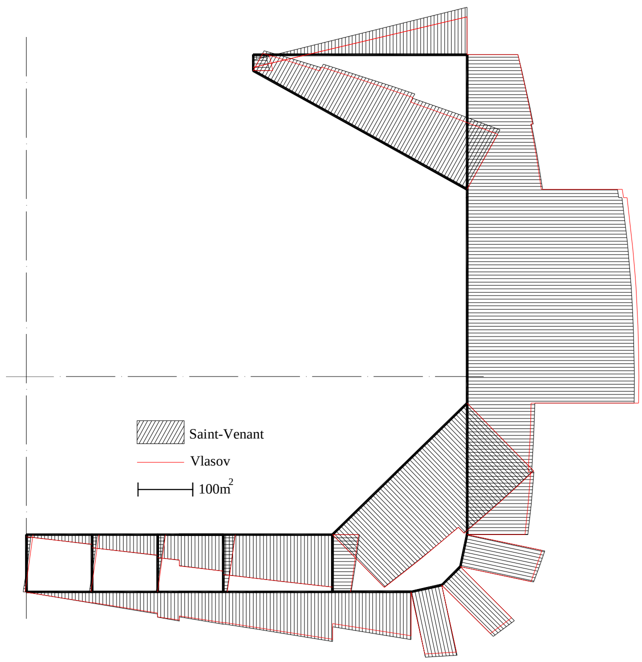

Fig. 7 Vertical shear – normalized tangential stresses

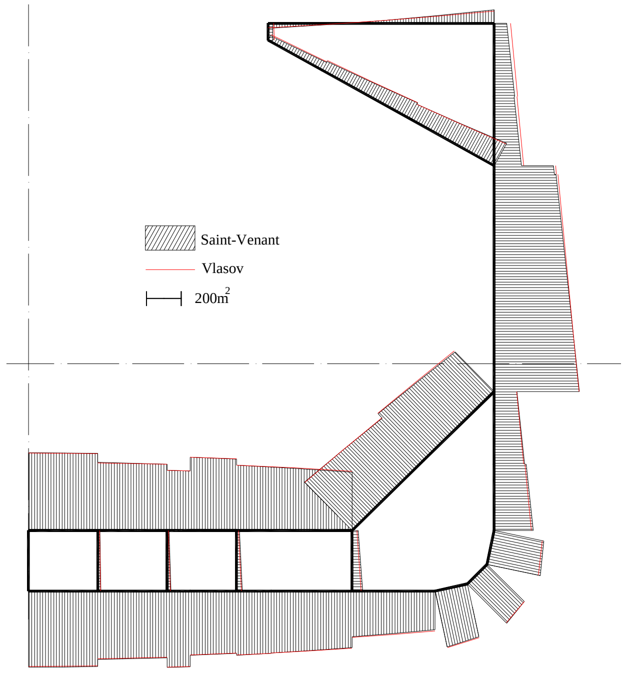

Fig. 8 Horizontal shear – normalized tangential stresses

Tab. 6 Horizontal shear- normalized tangential stresses

	Normalized tangential stresses (m^2)			
	Vlasov		**Saint-Venant**	
Branches	I node	II node	I node	II node
1	435.85	432.97	440.20	436.99
2	391.50	382.86	395.45	385.80
3	439.69	435.53	442.72	438.08
4	368.94	358.70	371.37	359.94
5	369.47	360.11	370.72	360.27
6	358.50	331.06	358.66	328.02
7	267.88	231.62	264.72	224.23
8	335.16	318.23	330.90	311.99
9	318.23	303.51	321.22	304.78
10	303.51	284.21	314.07	292.53
11	214.74	177.66	225.86	184.46
12	170.10	129.48	176.88	131.52
13	489.83	474.20	492.50	475.04
14	474.20	368.29	475.04	356.77
15	359.72	354.89	348.19	342.79
16	170.89	132.20	158.46	115.26
17	136.12	95.17	119.18	73.46
18	70.86	-24.63	77.91	-28.72
19	-31.23	-36.12	-20.01	-25.48
20	-36.27	-55.89	-28.29	-50.20
21	-63.26	-103.47	-57.55	-102.45
22	143.11	93.68	147.87	92.67
23	-329.26	-380.07	-320.47	-377.22
24	-345.52	-388.79	-342.61	-390.93
25	-341.95	-378.75	-337.27	-378.37
26	-413.78	-424.02	-413.46	-424.90
27	-343.60	-347.76	-344.34	-348.98
28	-382.94	-391.58	-384.22	-393.87
29	-444.34	-447.22	-446.73	-449.94
30	0.00	0.00	0.00	0.00
31	15.52	10.48	17.72	12.10
32	18.12	8.04	22.51	11.26
33	27.59	12.47	34.17	17.29
34	51.62	28.10	61.88	35.61

Concerning the vertical position of the shear center, the following results are obtained applying the two theories:

$$\varsigma_{Q\ from\ B.L.} = -9.67\,m \qquad \text{(Saint-Venant)}$$

$$\varsigma_{Q\ from\ B.L.} = -9.63\,m \qquad \text{(Vlasov)}$$

11. CONCLUSIONS

It seems that the following results may be obtained:

- it is possible to adopt the Saint-Venant theory for the bending-shear stress in thin-walled beams;
- in the Saint-Venant theory it is possible to evaluate the tangential stress term variable along the thickness that, thanks to its smallness, is totally negligible;
- the Vlasov theory is the limit of the Saint-Venant one when $\nu \to 0$;
- it is possible to verify that the Saint-Venant theory, in more general hypotheses (free section contraction), produces the same shear stresses achievable applying the Vlasov theory for thin-walled beams with monoconnected section;
- as it has been verified for the Hughes' section and the bulk-carrier, the cross-section contraction produces a quite appreciable tangential shear stress re-distribution, in thin-walled beams with multiconnected sections, especially at deck and bottom.

12. REFERENCES

1. CAMPANILE, A., MANDARINO, M., PISCOPO, V., TURTORO, M., 'A numerical method for the shear stress determination', ICMRT 2007 - Ischia (NA).
2. HUGHES, O., 'Ship Structural design', John Wiley & Sons.
3. FRANCIOSI, V., 'Scienza delle Costruzioni', Liguori Editore Napoli.
4. BALDACCI, R., 'Scienza delle costruzioni', UTET.
5. SPARACIO, R., RUSSO SPENA, F., 'Scienza delle costruzioni', UTET.
6. FIORENZA, R., 'Appunti delle lezioni di Analisi Funzionale', Gli Strumenti di Coinor, 2005.
7. TANG. K. T., 'Mathematical Methods for Engineers and Scientists 3', Springer-Verlag.
8. POLYANIN, A.D., 'Linear partial differential equations for Engineers and Scientists', CHAPMAN & HALL/CRC.

A NONLINEAR MATHEMATICAL MODEL OF MOTIONS OF A PLANING MONOHULL IN HEAD SEAS

Alex van Deyzen, Delft University of Technology, The Netherlands

SUMMARY

A nonlinear mathematical model for the simulation of motions and accelerations of planing monohulls, having a constant deadrise angle, in head waves has been formulated. The model is based on 2-dimensional strip theory. The original model, developed by Keuning [9], who based his model on Zarnick [25], is extended to three degrees of freedom: surge, heave and pitch motion can be simulated. The simulations can be carried out for a planing boat sailing in (ir)regular head seas, using either a constant forward speed or constant thrust. The hydromechanic coefficients in the equations of motion are determined by a combination of theoretical and empirical relationships. The sectional hydromechanic forces are determined by the theory of a wedge penetrating a water surface. The wave excitation in vertical direction is directly integrated in the expressions for the hydromechanic forces and is caused by the vertical orbital velocity in the wave and the geometrical properties of the wave, altering the total wetted length and the sectional wetted breadth and immersion. An overall frictional resistance has been estimated. A constant thrust force can be set as input. When simulating with a constant thrust, the surge motion is induced by the frictional resistance and the horizontal component of the hydrodynamic force (hull pressure resistance).

The total calm water resistance has been validated. Existing experimental data of two models, a conventional double chined planing monohull (DCH) and a modern axebow (Axehull), planing in calm water showed a fair agreement with the calculated drag. A large sensitivity of the hydromechanic coefficients on the computated results for the total resistance, vertical motions and accelerations was found as well.

NOMENCLATURE

β	Deadrise angle of cross section
ν	Dynamic viscosity of water
τ	Propulsor shaft's angle
$\theta,\dot{\theta},\ddot{\theta}$	Pitch angle, velocity and acceleration
ξ,χ,ζ	Body fixed coordinate system
A	Cross sectional area
a	Reduction length for transom correction function
a_{bf}	Buoyancy force correction factor
a_{bm}	Buoyancy moment correction factor
a_{nondim}	Dimensionless reduction length for transom correction function
A_w	Total wetted area
b	Half breadth of cross section
$C_{D,c}$	Cross flow drag coefficient
C_f	Friction coefficient
C_m	Added mass coefficient
C_{pu}	Pile-up factor
C_{tr}	Transom correction function
C_v	Froude number over breadth $\left(\frac{V_s}{\sqrt{g \cdot B_m}}\right)$
D	Total frictional resistance force along the hull
F_θ	Total hydromechanic pitch moment
$F_\theta^{'}$	Total hydromechanic pitch moment minus terms associated with motion acceleration
f_b	Sectional buoyancy force
f_{cfd}	Sectional viscous lift associated with the cross flow drag of a calm water penetrating wedge
F_{dyn}	Total hydrodynamic force
f_{fm}	Sectional hydrodynamic lift associated with the change of fluid momentum
F_{N_∇}	Froude number over displacement $\left(\frac{V_s}{\sqrt{g \cdot \nabla^{1/3}}}\right)$
F_{sta}	Total hydrostatic force
F_x	Total hydromechanic force in x-direction
$F_x^{'}$	Total hydromechanic force in x-direction minus terms associated with motion acceleration
F_z	Total hydromechanic force in z-direction
$F_z^{'}$	Total hydromechanic force in z-direction minus terms associated with motion acceleration
h	Immersion of cross section
I_a	Pitch moment of inertia of the total added mass
I_{yy}	Pitch moment of inertia
L_c	Wetted chine length
L_k	Wetted keel length
L_m	Mean wetted length
M	Mass of ship
M_a	Total added mass
m_a	Sectional added mass
Q_a	Total added mass moment
R_F	Frictional resistance of bare hull
R_n	Reynolds number $\left(\frac{V_s L}{\nu}\right)$
R_P	Hull pressure resistance
R_{SR}	Total spray rails resistance
R_S	Total spray resistance
R_{VP}	Viscous pressure resistance
R_V	Total viscous resistance
R_W	Total wavemaking resistance
T	Thrust force

V	Water entry velocity of penetrating wedge
V_s	Forward speed
W	Weight of ship
w	Vertical orbital velocity at the undisturbed water level
x,y,z	Earth fixed coordinate system
x_1	x-coordinate measured from stern
x_a	Moment arm of hydrodynamic lift force
x_b	Moment arm of hydrostatic lift force
$x_{CG},\dot{x}_{CG},\ddot{x}_{CG}$	Displacement, velocity and acceleration of CG in x direction relative to earth fixed axes system
x_d	Moment arm of frictional resistance force
x_s,y_s,z_s	Steady translating coordinate system
x_t	Moment arm of thrust force
$z_{CG},\dot{z}_{CG},\ddot{z}_{CG}$	Displacement, velocity and acceleration of CG in z direction relative to earth fixed axes system

1 INTRODUCTION

The behaviour of planing monohulls in waves has been a widely researched topic since more and more semi-planing and planing monohulls appeared after the Second World War. Typical planing monohulls are: patrol vessels, pilot-boats, rescue vessels, coast guard vessels and small navy vessels.

The pressure acting on planing vessels running in calm water is characterized by a hydrostatic and hydrodynamic part. Due to the high forward speed and trim of the vessel there is a relative velocity between the hull and water and a hydrodynamic pressure proportional to the square of this relative velocity is generated. At high forward speed a large part of the weight of the vessel is carried by the dynamic pressure. In waves the relative velocity and thus the dynamic pressure gets additional contributions from the vessel's motions and the motions of the waves. The resulting nonlinear impact loads have a significant influence on the motions and accelerations in more or less every wave encounter and are crucial for the extreme responses.

For example, when such vessels are sailing in rough head seas, violent motions and large vertical acceleration peaks occur. The hull is subjected to high impact loads and the crew experiences high transient vertical accelerations and in most cases the crew needs to lower speed in order to avoid damage to the hull.

A good understanding of the behaviour of fast vessels in waves is necessary in order to be able to develop planing vessels with large operability. Moreover, most of the afore mentioned type of planing monohulls must be able to operate in (extremely) rough weather.

In [18] Savitsky presented an analysis is made of available data on the seakeeping behaviour of planing hulls in order to define and categorize those hydrodynamic problems associated with various speeds of operation in a seaway. He distinguished different behaviour in the low speed range ($F_{N_\nabla} < 2$) (semi-displacement), where the seakeeping characteristics are very similar to the displacement hull and the high speed range ($F_{N_\nabla} > 2$), where the hydrodynamic lift forces are predominate and where high impact forces can occur.

Fridsma [2, 3] executed systematic model tests with a serie of constant-deadrise models, varying in length. His results, presented in the form of response characteristics, cover a wide range of operating conditions and show, quantitatively, the importance of design parameters on the rough water performance of planing hulls. At this time it already became apparent that planing monohulls show a significant nonlinear behaviour in head waves.

The study of planing monohulls is closely related to the study of flat and V-bottom prismatic planing surfaces and to the study of a 2-dimensional wedge penetrating a calm water surface. These studies were initially carried out in order to get a better understanding of the hydrodynamics involved with the landing of seaplanes (for over nearly hundred years these topics have been studied, but the works of Von Karman [22] and Wagner [23, 24] can still be seen as the most important contributions in this field), but later were also used to get more insight of planing of monohulls, see for example Savitsky's work [17].

Zarnick [25], [26] [1]) developed a nonlinear mathematical model of motions of a planing monohulls in head seas, where the solution is solved in the time domain. His model is based on 2-dimensional strip theory and the forces acting on a cross section are determined by the theory of a wedge penetrating a fluid surface. The instantaneous values of wetted length, trim and sinkage are taken into account using strip theory in the time domain. The coefficients in the equations of motion are determined by a combination of theoretical and empirical relationships. His model showed remarkably good agreement with experimental data.

His work forms the theoretical basis for the simulations models developed by Akers (Powersea) [1] and Keuning (Fastship) [9].

Garme [6, 4] developed a similar time domain simulation model for the motions of a planing monohulls in head seas, but his model distinguishes from Zarnick's model, because he implemented pre-calculated cross section data, so that the hull geometry is better accounted for.

Later, Garme [5] improved his time domain simulation model by adding a near-transom pressure correction function, which reduces the pressure near the stern gradually to zero at the stern.

In the present research the original mathematical model of motions of a planing monohull in head seas, developed by Zarnick and later extended by Keuning, is extended to three degrees of freedom: the surge, heave and pitch motion in (ir)regular head seas can be simulated. The simulations can be carried with either a constant forward speed or constant thrust.

[1]This publication was not found, but is mentioned for the completeness

Fridsma [3] discovered in his extended research on the behaviour of hard-chine planing monohulls in head seas that little or no surge motion was measured for models sailing at high speeds. This would mean that if towed at constant forward speed, a model planing hull would behave exactly as if it would be tested at constant thrust. He proved that this hypothesis is also true for the lower speed range ($F_{N_\nabla} \approx 1.5$). However, he only used one model and two seastates to proof his hypothesis. With the present computational model Fridsma's hypothesis can be verified or rejected, using the calculated results of more than two scenarios.

In the industry there is an increasing need to predict the motions and accelerations of a planing vessel in the design state. The nonlinear mathematical model developed in this research paper provides a computational design tool, with a rather simple input of the hull and little computer calculation time, for designers of fast planing monohulls to predict the operability in various sea states.

Moreover, in the near future, the effect of active control of the thrust (variation of the forward speed) when sailing in head seas on the vertical peak accelerations needs to be investigated. This mathematical model will be a valuable simulation tool for this research.

2 THEORETICAL BACKGROUND

The nonlinear mathematical model presented in this section is an extension of the work of Zarnick [25] and Keuning [9]. The simulation model is termed Fastship.

2.1 APPLIED THEORY, ASSUMPTIONS AND LIMITATIONS

Strip theory is used for the determination of the motions and accelerations of the system of a fast monohull in waves. When strip theory is used the assumptions are made that interaction effects within the 2-dimensional flows of the cross sections are negligible and thus that the hydromechanic forces, acting on the hull, can be approximated by integrating forces on cross sections over the ship's length.

Zarnick used the theory of a calm water penetrating wedge for determining the forces acting on a cross section. When looking at one slice of water (no waves), a planing monohull passing through it is like a wedge penetrating the water surface with a constant velocity, see figure 1.

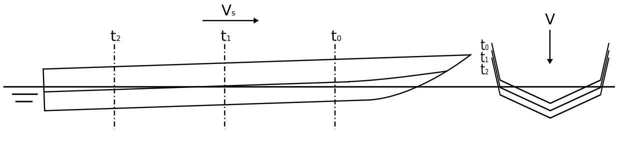

Figure 1: A planing monohull can be seen as a wedge penetrating the water surface

Since the theory of a penetrating wedge is used, hard chined hulls can be analysed with a better accuracy than rounded bilges, since the model simplifies cross sections to a knuckled wedge.

Zarnick used the time domain approach for the determination of the behaviour of fast monohulls in head waves, because with the time domain approach the nonlinearities are seized better than with a frequency domain approach [12].

Furthermore, he assumed that the flow around the hull must be treated as quasi steady (every time instant the equilibrium of the forces and moments are analysed and from there the accelerations are determined) and that surface wave generation (wave resistance) and forces associated with unsteady circulatory flow can be neglected.

The wavelengths are assumed to be large in comparison with the ship's dimensions and the wave slope is small. Because of the large wavelengths diffraction forces can be neglected (only the Froude-Krylov forces are of importance).

The wave excitation in vertical direction is directly integrated in the expressions for hydromechanic forces and is caused by:

1. the geometrical properties of the wave, altering the total wetted length, the sectional wetted breadth and immersion and

2. the vertical orbital velocity.

Because the ships under consideration are generally shallow with respect to the height of the waves, the orbital velocity is taken at the undisturbed water surface in the plane $z = 0$.

The influence of the horizontal orbital velocities on both the horizontal and vertical motions is neglected, because these velocities are considered to be relatively small in comparison with the forward speed of the ship.

The wave excitation in horizontal direction is very difficult to model when applying strip theory. Together with the assumption that the wavelengths are large (small wave slopes), the present model is limited to moderate surge motions. Severe surge motions when diving into a wave when sailing in head seas cannot be simulated. The most important force in longitudinal direction at that specific moment is the wave excitation in horizontal direction (Froude-Krylov and diffraction).

2.2 EQUATIONS OF MOTION

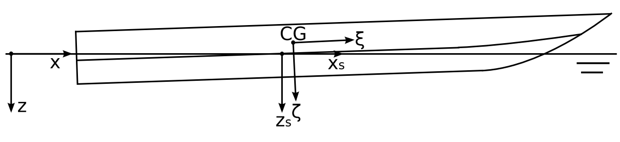

Figure 2: Coordinate system

The coordinate system used in the computational model is presented in figure 2. It consists of:

- an earth fixed coordinate system with $x,\ y,\ z-$axes, with the $x-$axis lying in the undisturbed water surface pointing in the direction of the forward velocity,
- a steady translating coordinate system with $x_s,\ y_s,\ z_s$ axes, with the $x-$axis lying in the undisturbed water surface pointing in the direction of the forward velocity and travelling with a given constant velocity and
- a body fixed coordinate system with $\xi-,\ \chi-$ and $\zeta-$axes, with the origin in the centre of gravity of the ship and of which the $\xi-$axis is the longitudinal axis pointing forward.

The forces acting on a fast monohull are visualized in figure 3.

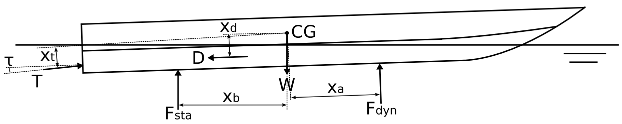

Figure 3: Definition of the forces acting on the ship

The equations of motion can be written as:

$$\begin{aligned} M\cdot\ddot{x}_{CG} &= T\cos(\theta+\tau)-F_{dyn}\sin\theta-D\cos\theta \\ M\cdot\ddot{z}_{CG} &= -T\sin(\theta+\tau)-F_{dyn}\cos\theta-F_{sta}+D\sin\theta+W \\ I_{yy}\cdot\ddot{\theta} &= Tx_t+F_{dyn}x_a+F_{sta}x_b-Dx_d \end{aligned} \tag{1}$$

The thrust force T is assumed to be constant. However, the efficiency loss of a (nearly) airborne propulsor has to be taken into account. In the computational model the total thrust efficiency decreases linear to zero with the submergence of the aft section.

In order to be able to investigate the effect of the surge motion on the vertical peak accelerations when performing simulations in head seas, a resistance dependent on the forward speed, wetted surface and pitch angle must be modelled. The estimate of the resistance will only be used to model a surge motion, not for resistance calculations. Therefore, constant and/or negligible small resistance components are left out of the equation of motion for surge. The inputted thrust might not be the actual thrust of the vessel, but may be somewhat smaller, due to the underestimation of the resistance.

Air friction is not taken into account. The superstructure is not defined in the computational model and the dependence of this resistance force on variation of the forward speed is assumed to be minimal.

According to Müller-Graf [13] the total bare hull resistance in calm water of a (semi-)planing monohull consist of the following components:

$$R_H = R_W + R_P + R_S + R_{SR} + R_V \tag{2}$$

where:

- R_W: wave resistance
- R_P: hull pressure resistance (horizontal component of the dynamic lift force, here: $F_{dyn}\sin\theta$)
- R_S: spray resistance
- R_{SR}: spray rails resistance
- R_V: viscous resistance

Zarnick assumed that wave resistance can be neglected. However the wave resistance can be significant, especially when semi-planing. For now, this resistance component has been left out of the equation, especially because no direct formulation is available. The spray and spray resistance are difficult to model, although recently a paper has been published about this topic [19]. The results of that study have not yet been incorporated in the simulation model.

The viscous resistance of the bare hull consists of a frictional and a viscous pressure resistance component:

$$R_V = R_F + R_{VP} \tag{3}$$

The viscous pressure resistance, caused by viscous effects of the hull shape and by flow separation and eddy making, can be neglected for $F_{N_\nabla} > 1.5$.

This leaves only two time dependent resistance components (see also [17]):

$$\begin{aligned} R_P &= F_{dyn}\sin\theta \\ R_F &= D \end{aligned}$$

The determination of these resistance components will be explained in section 2.4 and 2.7.

2.3 SECTIONAL HYDROMECHANIC FORCES

The force acting on a cross section is visualized in figure 4 and consists of three components (force per unit length):

- a hydrodynamic lift associated with the change of fluid momentum (f_{fm})
- a viscous lift force associated with the cross flow drag of a water penetrating wedge (f_{cfd})
- a buoyancy force related to the momentaneous displaced volume (f_b)

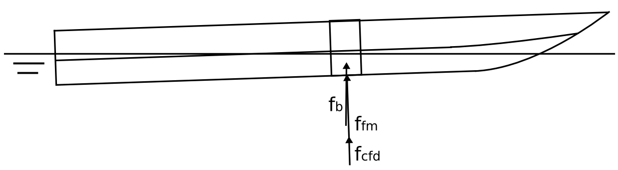

Figure 4: Orientation of forces acting on a cross section

The first force component prevails more in the fore part of the ship, where the chines are still dry, the last more in the aft part, where the chines are immersed. The lift component associated with the cross flow drag of a penetrating wedge is small, but not negligible.

The sectional hydromechanic forces are determined according to the theory of a calm water penetrating wedge. The 2-dimensional penetrating wedge is replaced by a flat lamina by the assumption that the fluid accelerations are much larger than the gravitational acceleration [22, 23, 24]. The flat lamina is expanding at the same constant rate at which the intersection width of an immersing wedge is increasing in the undisturbed water surface, see figure 5. This expanding rate is dependent on deadrise angle:

$$\frac{db}{dt} = \frac{V}{\tan\beta} \tag{4}$$

Wagner included a term for water pile-up, which he gave the value of $\pi/2$.

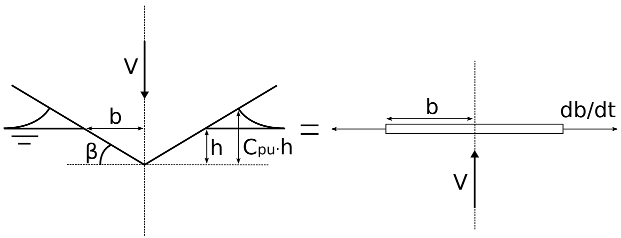

Figure 5: A wedge penetrating a calm water surface and expanding lamina theory

Payne [15] presented an approximation of the added mass variation with chines immersed and a conventional cross flow drag hypothesis as an additional lift component. He found, that the lift increment due to the chines immersed added mass variation is the same as the one due to the cross flow drag, so that adding the two together results in a chines immersed dynamic force which is twice the correct value.

In both Zarnick's as Keuning's computational model the additional lift component due to the cross flow drag has been applied.

Payne [14] also suggested that using a pile-up factor of $\pi/2$ too high impact loads were found when compared with experiments. Later, Payne [16] found that the results originally found by Pierson, in which he formulated that the pile-up is dependent on the deadrise, agreed very well with results found by Zhao and Faltinsen [27]. The expression for a deadrise dependent pile-up factor is:

$$C_{pu} = \frac{\pi}{2} - \beta\left(1 - \frac{2}{\pi}\right) \tag{5}$$

where a value for the pile-up factor of $\pi/2$ can be seen as the upper limit.

Hydrodynamic lift associated with the change of fluid momentum

The hydrodynamic lift associated with the change of fluid momentum is given by the rate of change of momentum of the oncoming fluid in terms of the added mass of the particular cross section under consideration:

$$f_{fm} = \frac{D}{Dt}(m_a \cdot V) = m_a \cdot \dot{V} + \dot{m}_a \cdot V - \frac{\partial}{\partial\xi}(m_a \cdot V) \cdot \frac{d\xi}{dt} \tag{6}$$

The difference with the ordinary strip theory methods is found in the time dependent added mass. Strip theory is 2-dimensional, therefore a lengthwise variation of the added mass has to be included, which is represented in the last term.

Change of the sectional added mass over the length plays an important role. Since the added mass of the sections is related to the beam of that section at the momentaneous waterline and since the beam of planing craft hulls generally decreases in the aft body to minimize wetted area, a negative lift could occur using these formulations. The formulation of the negative slope of the added mass is neglected if it occurs and the hydrodynamic lift force arising from the fluid momentum is set to zero for these sections [8].

The added mass for a penetrating wedge can be approximated by the high frequency solution:

$$m_a = C_m \cdot \frac{\pi}{2} \cdot \rho \cdot b^2 \tag{7}$$

and its time derivative as:

$$\frac{\partial m_a}{\partial t} = \dot{m}_a = C_m \cdot \pi \cdot \rho \cdot b \cdot \frac{db}{dt} \tag{8}$$

where C_m is the added mass coeffficient and $b = h \cdot \cot\beta$, in which h is the time dependent immersion of the wedge. When the term for pile-up is included, the breadth is expressed as: $b = C_{pu} \cdot h \cdot \cot\beta$. The determination of the added mass coefficient C_m will be explained in section 2.6.

Additional lift term due to cross flow drag

The additional lift term due the cross flow drag on the surface of a water penetrating wedge is expressed as:

$$f_{cfd} = C_{D,c} \cdot \cos\beta \cdot \rho \cdot b \cdot V^2 \tag{9}$$

where $C_{D,c}$ is the cross flow drag coefficient. The determination of the cross flow drag coefficient $C_{D,c}$ will be explained in section 2.6

Buoyancy force

The buoyancy force on a segment is assumed to act vertically and to be equal to the equivalent static buoyancy of the section multiplied with a correction factor a_{bf}:

$$f_b = a_{bf} \cdot \rho \cdot g \cdot A \tag{10}$$

where A is the immersed cross sectional area of the wedge.

The full amount of static buoyancy is never realized, because at the high speeds under consideration the flow separates from the chines and the stern, reducing the pressures at these locations to the atmospheric pressure. Therefore the total pressure distribution deviates considerably from the hydrostatic pressure distribution when applying Archimedes Law. Therefore, the coefficient a_{bf} always has a value between 0 and 1. When the moment of this force is determined another correction factor, namely a_{bm}, is used.

The determination of the values of the buoyancy force and moment correction factors will be explained in section 2.6

2.4 TOTAL HYDROMECHANIC FORCES AND MOMENTS

The total hydromechanic force on the ship in the vertical plane is obtained by the summation of the three (f_{fm}, f_{cfd} and f_b) force components for each segment and by integration of these sectional forces over the length of the ship , see figure 4.

The total hydromechanic force in each direction can be expressed as:

$$
\begin{aligned}
F_x &= -F_{dyn}\sin\theta = \\
&= -\int_L f_{fm}\sin\theta d\xi - \int_L f_{cfd}\sin\theta d\xi = \\
&= -\int_L \left\{ m_a\dot{V} + \dot{m}_a V - U\frac{\partial}{\partial\xi}(m_a V)\right\}\sin\theta d\xi \\
&\quad -\int_L C_{D,c}\cos\beta\cdot\rho b V^2\cdot\sin\theta d\xi
\end{aligned} \tag{11}
$$

$$
\begin{aligned}
F_z &= -F_{dyn}\cos\theta - F_{sta} = \\
&= -\int_L f_{fm}\cos\theta d\xi - \int_L f_{cfd}\cos\theta d\xi - \int_L f_b d\xi = \\
&= -\int_L \left\{ m_a\dot{V} + \dot{m}_a V - U\frac{\partial}{\partial\xi}(m_a V)\right\}\cos\theta d\xi \\
&\quad -\int_L C_{D,c}\cos\beta\cdot\rho b V^2\cdot\cos\theta d\xi \\
&\quad -\int_L a_{bf}\cdot\rho g A d\xi
\end{aligned} \tag{12}
$$

and the total hydromechanic pitch moment around the centre of gravity is expressed as:

$$
\begin{aligned}
F_\theta &= F_{dyn}x_a + F_{sta}x_b = \\
&= \int_L f_{fm}\cdot\xi d\xi + \int_L f_{cfd}\cdot\xi d\xi + \int_L f_b\cos\theta\cdot\xi d\xi = \\
&= \int_L \left\{ m_a\dot{V} + \dot{m}_a V - U\frac{\partial}{\partial\xi}(m_a V)\right\}\cdot\xi d\xi \\
&\quad +\int_L C_{D,c}\cos\beta\cdot\rho b V^2\cdot\xi d\xi \\
&\quad +\int_L a_{bm}\cdot\rho g A\cdot\{\xi\cos\theta + \zeta\sin\theta\} d\xi
\end{aligned} \tag{13}
$$

The velocities along U and normal V to the baseline of the ship can be expressed as:

$$
\begin{aligned}
U &= \dot{x}_{CG}\cdot\cos\theta - (\dot{z}_{CG} - w)\sin\theta \\
V &= \dot{x}_{CG}\cdot\sin\theta + (\dot{z}_{CG} - w)\cos\theta - \dot{\theta}\cdot\xi
\end{aligned} \tag{14}
$$

And the acceleration normal to the baseline is expressed as:

$$
\begin{aligned}
\dot{V} &= \ddot{x}_{CG}\cdot\sin\theta + \ddot{z}_{CG}\cdot\cos\theta - \ddot{\theta}\cdot\xi \\
&\quad + \dot{\theta}\{\dot{x}_{CG}\cdot\cos\theta - \dot{z}_{CG}\cdot\sin\theta\} \\
&\quad - \dot{w}\cdot\cos\theta + \dot{\theta}\cdot w\cdot\sin\theta
\end{aligned} \tag{15}
$$

The hydromechanic forces can now further be elaborated into:

$$
\begin{aligned}
F_x = \Big\{ &-M_a\cdot\ddot{x}_{CG}\sin\theta - M_a\cdot\ddot{z}_{CG}\cos\theta + Q_a\cdot\ddot{\theta} \\
&-M_a\cdot\dot{\theta}(\dot{x}_{CG}\cos\theta - \dot{z}_{CG}\sin\theta) + \int_L m_a\dot{w}\cos\theta d\xi \\
&-\int_L m_a\dot{\theta}w\sin\theta d\xi - \int_L \dot{m}_a V d\xi + \int_L UV\cdot\frac{\partial m_a}{\partial\xi}d\xi \\
&-\int_L U m_a\frac{\partial w}{\partial\xi}\cos\theta d\xi - \int_L U m_a\dot{\theta} d\xi \\
&-\int_L C_{D,c}\cdot\cos\beta\cdot\rho b V^2 d\xi \Big\}\sin\theta
\end{aligned} \tag{16}
$$

$$
\begin{aligned}
F_z = \Big\{ &-M_a\cdot\ddot{x}_{CG}\sin\theta - M_a\cdot\ddot{z}_{CG}\cos\theta + Q_a\cdot\ddot{\theta} \\
&-M_a\cdot\dot{\theta}(\dot{x}_{CG}\cos\theta - \dot{z}_{CG}\sin\theta) + \int_L m_a\dot{w}\cos\theta d\xi \\
&-\int_L m_a\dot{\theta}w\sin\theta d\xi - \int_L \dot{m}_a V d\xi + \int_L UV\cdot\frac{\partial m_a}{\partial\xi}d\xi \\
&-\int_L U m_a\frac{\partial w}{\partial\xi}\cos\theta d\xi - \int_L U m_a\dot{\theta} d\xi \\
&-\int_L C_{D,c}\cdot\cos\beta\cdot\rho b V^2 d\xi \Big\}\cos\theta \\
&-\int_L a_{bf}\cdot\rho g A d\xi
\end{aligned} \tag{17}
$$

$$
\begin{aligned}
F_\theta = \; &Q_a\cdot\ddot{x}_{CG}\sin\theta + Q_a\cdot\ddot{z}_{CG}\cos\theta - I_a\cdot\ddot{\theta} \\
&+ Q_a\cdot\dot{\theta}(\dot{x}_{CG}\cos\theta - \dot{z}_{CG}\sin\theta) - \int_L m_a\dot{w}\cos\theta\cdot\xi d\xi \\
&+\int_L m_a\dot{\theta}w\sin\theta\cdot\xi d\xi + \int_L \dot{m}_a V\cdot\xi d\xi \\
&-\int_L UV\cdot\frac{\partial m_a}{\partial\xi}\cdot\xi d\xi + \int_L U m_a\frac{\partial w}{\partial\xi}\cos\theta\cdot\xi d\xi \\
&+\int_L U m_a\dot{\theta}\cdot\xi d\xi + \int_L C_{D,c}\cdot\cos\beta\cdot\rho b V^2\cdot\xi d\xi \\
&+\int_L a_{bm}\cdot\rho g A\cdot\{\xi\cos\theta + \zeta\sin\theta\} d\xi
\end{aligned} \tag{18}
$$

where

$$M_a = \int_L m_a\cdot d\xi \tag{19}$$

$$Q_a = \int_L m_a\cdot\xi d\xi \tag{20}$$

$$I_a = \int_L m_a \cdot \xi^2 d\xi \tag{21}$$

2.5 NEAR-TRANSOM PRESSURE CORRECTION FUNCTION

Garme and Rosén [6, 7] studied the pressure distribution on the hull of planing craft in calm water, head and oblique regular and irregular waves. Later, Garme [5] formulated a correction operating on both the hydrostatic and the hydrodynamic terms of the load distribution. He based his correction on the assumption that the pressure is atmospheric at the dry transom stern. A strictly 2-dimensional analysis of the lift distribution on the planing hull over estimates the lift in near transom region [6], see figure 6.

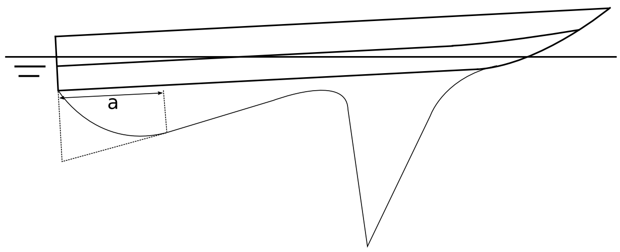

Figure 6: The principal lift distribution on a hull with a dry transom stern (the dotted line indicates the strictly 2-dimensional lift distribution)

Further, it is assumed that the difference between the 2-dimensional lift distribution and the actual pressure is largest at aft and decreasing afore. The correction approach is to multiply the 2-dimensional load distribution by a reduction function that is 0 at transom, that approaches 1 at a distance afore, and has a large gradient at aft which decreases towards zero with with increasing distance from the stern.

The near-transom pressure correction function is expressed as:

$$C_{tr}(x_1) = \tanh\left(\frac{2.5}{a} \cdot x_1\right) \tag{22}$$

in which a is a reduction length, see figure 6.

Garme rewrote the reduction length into nondimensional form:

$$a_{nondim} = \frac{a}{B_m \cdot C_v} \tag{23}$$

in which B_m is the full breadth of the mainsection and C_v is the Froudenumber over breadth: $C_v = \frac{V_s}{\sqrt{g \cdot B_m}}$.

After a systematic research on several model experiments Garme chose a value of 0.34 for a_{nondim}, which is applicable for medium and high speed configurations, $C_v \geq 2$.

The near-transom pressure correction function can now be rewritten into:

$$C_{tr} = \tanh\left(\frac{2.5}{0.34 \cdot B_m \cdot C_v} \cdot (\xi - \xi_{tr})\right) \tag{24}$$

in which ξ_{tr} is the body fixed coordinate of the stern.

Garme validated the reduction function on basis of the model test measurements of the near-transom pressure, and on published model data on running attitude. This correction improves the simulation in both calm water and in waves for a wider speed range.

Although, a constant correction length is questionable if the ship motions are large and the wetted hull length is small as for sequences when the hull leaves or is close to leaving the water.

The transom reduction function reduces the sectional forces in the aft ship and has to be inserted within the integrals for the sectional hydrodynamic forces as follows:

$$F_x = -\int_L C_{tr} \cdot f_{fm} \sin\theta d\xi - \int_L C_{tr} \cdot f_{cfd} \sin\theta d\xi \tag{25}$$

$$\begin{aligned} F_z = & -\int_L C_{tr} \cdot f_{fm} \cos\theta d\xi - \int_L C_{tr} \cdot f_{cfd} \cos\theta d\xi \\ & -\int_L C_{tr} \cdot f_b d\xi \end{aligned} \tag{26}$$

$$\begin{aligned} F_\theta = & \int_L C_{tr} \cdot f_{fm} \cdot \xi d\xi + \int_L C_{tr} \cdot f_{cfd} \cdot \xi d\xi \\ & + \int_L C_{tr} \cdot f_b \cos\theta \cdot \xi d\xi \end{aligned} \tag{27}$$

2.6 DETERMINATION OF HYDROMECHANIC COEFFICIENTS

The integrals for the total hydromechanic forces and moments can be evaluated when the four hydromechanic coefficients ($C_{D,c}$, C_m, a_{bf} and a_{bm}) are known.

The lift force due to the cross flow drag is of minor importance, when compared with mass flux and buoyancy, so fixing the value of the cross flow drag coefficient has only a marginal effect on the total lift. Both Zarnick as Keuning fixed the value of $C_{D,c}$, according to the approach of Shuford [20]. Zarnick assumed that $C_{D,c} = 1.0$ and and Keuning assumed that $C_{D,c} = 1.33$. The latter one is used in the present computational model.

Originally, Zarnick used constant values for C_m, a_{bf} and a_{bm}. He assumed that the added mass coefficient C_m was equal to 1 and that the buoyancy correction a_{bf} was equal to $1/2$ and that a_{bm}, the correction for the longitudinal distribution of the hydrostatic lift, was equal to $1/2 \cdot a_{bf}$. He used a pile-up factor independent of deadrise: $C_{pu} = \pi/2$.

Keuning showed that Zarnick's method is only applicable to very high speeds, because of the constant values he used for the hydrodmechanic coefficients. Keuning, together with Kant [8], approximated the trim angle and sinkage of the craft under consideration using polynomial expressions derived from the results of systematic model tests, the Delft Systematic Deadrise Series (DSDS) [10, 11].

The solution of the equations of motion, describing the steady state planing in calm water, is known, because of these polynomial expressions. Substituting these values for sinkage and trim in the equations of motion results in a system of two equations and three unknowns. Keuning and Kant assumed that there is no additional factor for the correction of the longitudinal distribution of the hydrostatic lift: $a_{bm} = 1$. The values of C_m and a_{bf} can now be determined.

By determining the hydromechanic coefficients in this way, the hydrodynamic lift is brought into the computational model with a higher level of accuracy than in the original Zarnick model and the model can be used for a broader speed range. The present model is applicable for speeds ($F_{N_\nabla} > 1.5$), but it also restricted to hull forms similar to the models used in the DSDS.

Determination of hydromechanic coefficients C_m and a_{bf}

A planing vessel, sailing in calm water with a constant speed, is sailing in stationary condition. Sinkage and trim are constant in time. The sinkage and trim are determined by three components of the hydromechanic force in the vertical force and moment equilibrium. If only steady state planing is considered the following simplifications may be introduced in the equations:

$$\begin{aligned} \ddot{\theta} &= \ddot{x}_{CG} = \ddot{z}_{CG} = 0 \\ U &= \dot{x}_{CG} \cdot \cos\theta \\ V &= \dot{x}_{CG} \cdot \sin\theta \end{aligned} \tag{28}$$

The equations of motion in the stationary condition in calm water are reduced to ($\dot{x}_{CG}$ = constant):

$$\begin{aligned} &\text{Heave:} \quad F_z^{'} + W = 0 \\ &\text{Pitch:} \quad F_\theta^{'} = 0 \end{aligned} \tag{29}$$

where:

$$\begin{aligned} F_z^{'} = &\int_L C_{tr}(\xi) \cdot UV \cdot \frac{\partial m_a}{\partial \xi} \cos\theta d\xi \\ &- \int_L C_{tr}(\xi) \cdot C_{D,c} \cos\beta \cdot \rho b V^2 \cos\theta d\xi \\ &- \int_L C_{tr}(\xi) \cdot a_{bf} \cdot \rho g A d\xi \end{aligned} \tag{30}$$

$$\begin{aligned} F_\theta^{'} = &- \int_L C_{tr}(\xi) \cdot UV \cdot \frac{\partial m_a}{\partial \xi} \cdot \xi d\xi \\ &+ \int_L C_{tr}(\xi) \cdot C_{D,c} \cos\beta \cdot \rho b V^2 \cdot \xi d\xi \\ &+ \int_L C_{tr}(\xi) \cdot a_{bf} \cdot \rho g A \cdot \{\xi \cos\theta + \zeta \sin\theta\} d\xi \end{aligned} \tag{31}$$

in which $F_z^{'}$ and $F_\theta^{'}$ are the total hydromechanic forces minus terms associated with motion accelerations.

2.7 FRICTIONAL RESISTANCE FORCE

The total frictional resistance can be determined by:

$$D = C_F \cdot \frac{1}{2} \cdot \rho \cdot U^2 \cdot A_w \tag{32}$$

The velocity along the baseline U can be expressed as: $U = \dot{x}_{CG} \cdot \cos\theta - \dot{z}_{CG} \cdot \sin\theta$. The influence of the orbital velocities is negligible and can therefore be omitted.

At each timestep the mean wetted length, the Reynolds number and the friction coefficient are calculated.

The mean wetted length is the average between the wetted keel length and wetted chine length and is formulated as:

$$L_m = \frac{L_k + L_c}{2} \tag{33}$$

and the Reynolds number as:

$$R_n = \frac{U \cdot L_m}{\nu} \tag{34}$$

The friction coefficient is determined using the ITTC formula.

$$C_f = \frac{0.075}{(\log R_n - 2)^2} \tag{35}$$

The total wetted surface minus the dry stern is estimated by adding the surfaces of the wetted sections. The moment arm of this force is estimated by assuming that the centre of effort lies halfway the average immersion of the cross sections.

2.8 SOLUTION OF THE EQUATIONS OF MOTION

The equations of motion form a set of three coupled second order nonlinear differential equations, which are solved in the time domain using standard numerical techniques. The equations of motions can be written in matrix form:

$$M \cdot \bar{\ddot{x}} = \bar{F} \Rightarrow$$

$$\begin{pmatrix} M + M_a \sin^2\theta & M_a \sin\theta\cos\theta & -Q_a \sin\theta \\ M_a \sin\theta\cos\theta & M + M_a \cos^2\theta & -Q_a \cos\theta \\ -Q_a \sin\theta & -Q_a \cos\theta & (I + I_a) \end{pmatrix} \cdot \begin{pmatrix} \ddot{x}_{CG} \\ \ddot{z}_{CG} \\ \ddot{\theta} \end{pmatrix}$$

$$= \begin{pmatrix} T\cos(\theta + \tau) + F_x^{'} - D\cos\theta \\ -T\sin(\theta + \tau) + F_z^{'} + D\sin\theta + W \\ Tx_t + F_\theta^{'} - Dx_d \end{pmatrix} \tag{36}$$

in which $F_x^{'}$, $F_z^{'}$ and $F_\theta^{'}$ are the total hydromechanic forces minus terms associated with motion accelerations.

The solution of these sets may be found by:

$$\bar{\ddot{x}} = M^{-1} \cdot \bar{F} \tag{37}$$

The procedure used to solve these equations is the Runge-Merson method. Knowing the vessel's orientation in the earth fixed coordinate system and the velocities at $t = t_0$ the equations are simultaneously solved for the small time increment dt to yield the solution on $t_0 + dt$.

3 VALIDATION OF CALM WATER RESISTANCE

Data of existing model tests were used to validate the total calm water resistance [21]. Two different hull shapes were used for these tests: a double chined planing monohull (DCH, 17° deadrise angle in aft ship) and a modern axebow (Axehull). The main dimensions are given in table 1 and a sketch of the hull geometries are given in figures 7 and 8.

Table 1: Main dimensions DCH and Axehull

Designation	Unit	DCH	Axehull
Length over all	m	19.34	20.00
Beam over all	m	6.3	5.65
Draft amidships	m	0.96	0.90
LCG rel to app	m	6.8	8.2
VCG	m	1.67	1.67
Displacement	m^3	33.66	35.22
k_{yy}	m	5.45	5.5

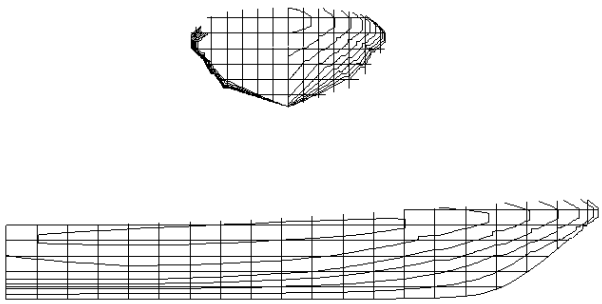

Figure 7: Sketch DCH

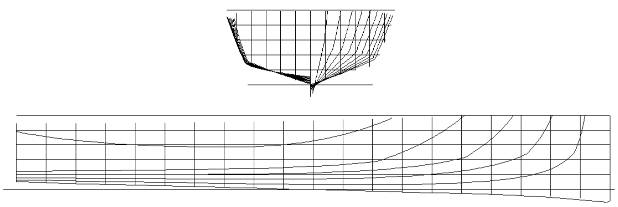

Figure 8: Sketch Axehull

The values of the hydromechanic coefficients a_{bf} and C_m were difficult to determine, because of the fact that the geometry of two models deviate significantly from the DSDS. Therefore the coefficients were estimated by using a parent hull from the DSDS with a comparable deadrise in the aftship (model 363, 19° deadrise angle) as a reference. This resulted in the following values:

Table 2: Used values of hydromechanic coefficients

$F_{N\nabla}$ $[-]$	a_{bf} $[-]$	C_m $[-]$
<2.5	0.7	2
$2.5-3$	0.65	1.75
$3-3.5$	0.6	1.25
>3.5	0.5	1

For the validation the total resistance has been calculated at a constant forward speed. The working line of the thrust force T and the frictional resistance force D act through CG (no additional moments) and the vertical components of T and D are negligible small with respect to the other hydromechanic forces involved (no additional vertical force components) [25, 9].

Figures 9 to 13 show respectively the results of measured and calculated sinkage, trim, wetted surface, friction coefficient and resistance of the DCH.

The general trend of the sinkage has been captured, although a small deviation can be seen in the lower to middle speed range. At higher speeds the trim is underpredicted. Perhaps water spray on the two spray rails of the hull cause a larger trim angle than calculated. In the mathematical model no spray rails have been modelled. The wetted surface is underpredicted over the whole speed range. This results in a small underprediction of the total frictional resistance force, although a small overprediction of the friction coefficient compensates this effect slightly.

The residuary resistance is clearly underpredicted. The underprediction of the trim at higher speeds might yield a underestimation of the hull pressure resistance. At lower speeds the magnitude of the wave resistance might be significant. This resistance component should decrease towards higher speeds. At lower speeds, the calculated residuary resistance is about 25 percent of the measured residuary resistance, while at higher speeds it is 50 percent. The magnitude of the spray and spray rails resistance is still unknown.

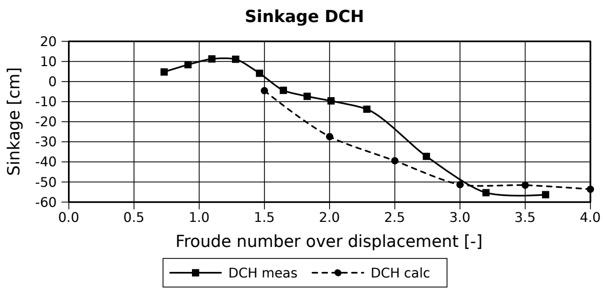

Figure 9: Measured and calculated sinkage DCH

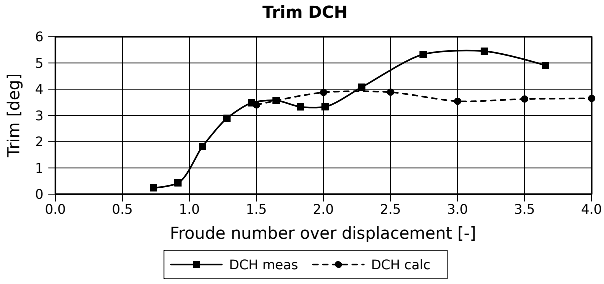

Figure 10: Measured and calculated trim DCH

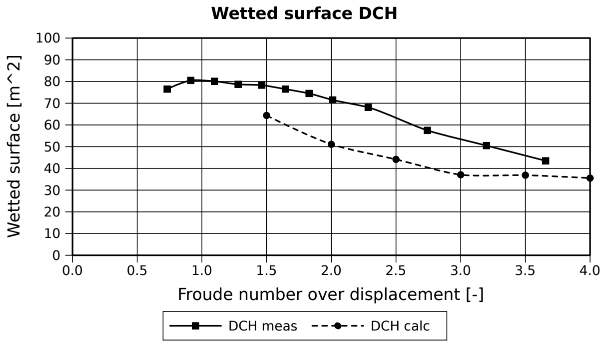

Figure 11: Measured and calculated wetted surface DCH

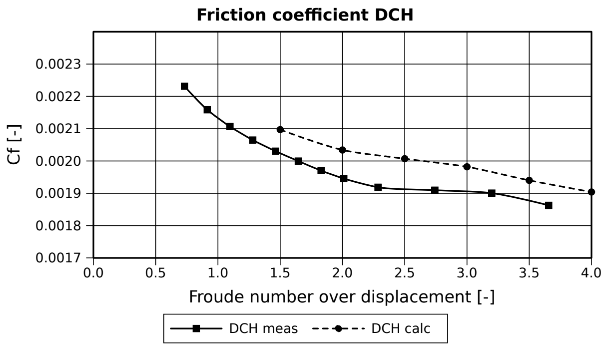

Figure 12: Measured and calculated friction coefficient DCH

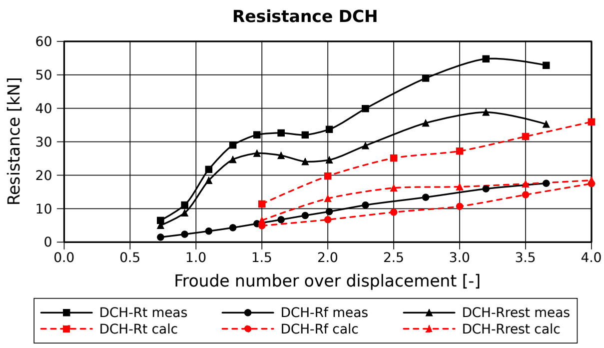

Figure 13: Measured and calculated resistance DCH

Figures 14 to 18 show respectively the results of measured and calculated sinkage, trim, wetted surface, friction coefficient and resistance of the Axehull.

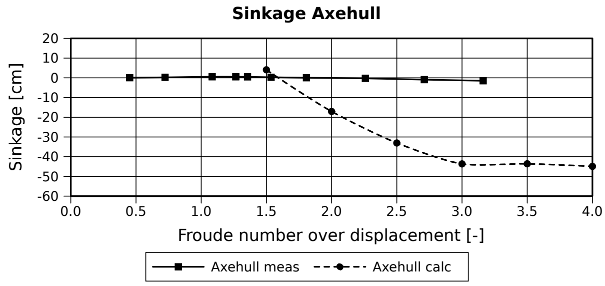

Figure 14: Measured and calculated sinkage Axehull

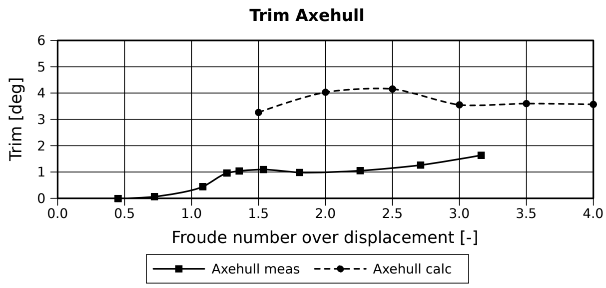

Figure 15: Measured and calculated trim Axehull

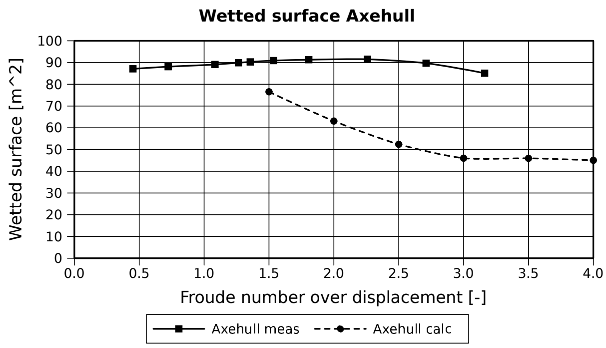

Figure 16: Measured and calculated wetted surface Axehull

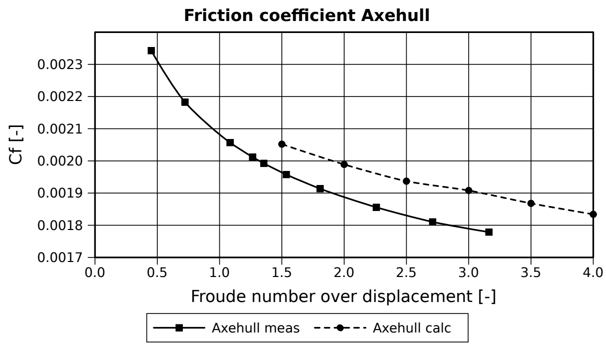

Figure 17: Measured and calculated friction coefficient Axehull

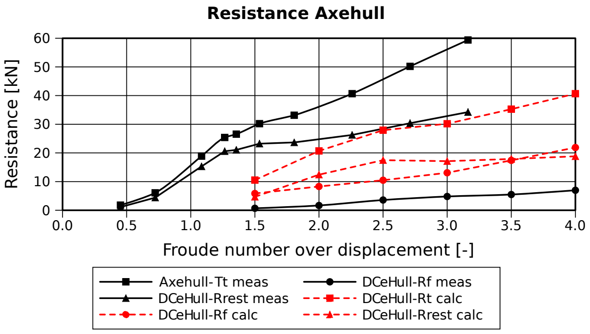

Figure 18: Measured and calculated resistance Axehull

The measured sinkage of the Axehull is nearly zero over the whole speed range. The mathematical model does not predict this constant value. The trim is overpredicted. The wetted surface is underpredicted over the whole speed range, probably because of the overprediction of the rise of the vessel. This results in an underprediction of the total frictional resistance force.

The erroneous calculated results for the sinkage and trim of the Axehull might also be caused by the estimated values for the hydromechanic coefficients. Perhaps the used values are not applicable for axebow hull shapes. At this moment it is not known what more appropriate values should be for these kind of hull shapes.

Generally, it can be concluded that the frictional resistance force is predicted accurate enough. But the residuary resistance and therefore the total resistance is clearly underpredicted using only the hull pressure resistance. The remaining resistance components should be incorporated into the model.

However, the mathematical is not developed for accurate calculations of the resistance; we are only interested in the time varying resultant force in longitudinal direction. For now, it is assumed that an accurate surge motion can be simulated, using only the hull pressure and frictional resistance.

4 SIMULATIONS ADDRESSING THE DIFFERENCE BETWEEN CONSTANT SPEED AND CONSTANT THRUST

Fridsma [3] observed little to no surge motion during his measurements at high speeds. Simulations with constant speed and thrust at high speeds show this trend as well. In the lower speed range he observed some surge motion. He tested a 10° deadrise model ($L/B = 5$, $B = 22.9$ cm) at $F_{N_\nabla} = 1.5$ in two sea states (a Pierson-Moskowitz spectrum with $H_s/B = 0.444$ and ($H_s/B = 0.667$), both with a constant thrust and constant speed. The average total resistance agreed very well. The distribution of the crest and throughs of the heave and pitch motions were nearly equal, as well as the distributions of the vertical accelerations at the bow and the centre of gravity.

Simulations carried out for the DCH and the Axehull in moderate sea states in order to address a possible difference between while simulating with a constant forward speed and a constant thrust, neither showed a remarkable difference. A wave realisation has been made according to the Jonswap spectrum. Three forward speeds ($V_s = 20, 30, 40$ kn), three significant wave heights ($H_s = 1.0, 1.5, 2.0$ m) and three peak periods ($T_p = 7, 10, 13$ s) have been chosen. The total run length was 1100 seconds. While simulating with constant thrust, the average forward speed over the total runlength has been used as a measure for the thrust.

The computational model has been validated for the motions in head seas by both Zarnick as Keuning using the results of model tests. They carried out model tests with constant forwards speed. Because of the fact that the results of simulations carried out with constant thrust show no remarkable difference with the results of simulations carried out with constant forward speed, it can be assumed that the motions and accelerations are predicted with the same level of accuracy as the original computational model.

However, the accuracy of the calculated results for the motions and accelerations for the Axehull is still questionable. The results are very sensitive to the used values of the hydromechanic coefficients.

5 CONCLUSIONS AND FUTURE WORK

A nonlinear mathematical model of a monohull having a constant deadrise angle, planing in head waves, has been formulated using strip theory. Keuning's [9] nonlinear mathematical model, based on Zarnick's model [25], has been extended to the possibilty to simulate with either constant forward speed or constant thrust.

The time domain approach is used for the determination of the motions. Each time step the sectional forces are elaborated and the total vertical and horizontal hydromechanic force and the total hydromechanic pitch moment are found by integrating the sectional forces and moments over the length of the vessel.

The surge motion is induced by a speed dependent frictional force and the horizontal component of the hydrodynamic force (hull pressure resistance), which varies with speed, trim angle and wetted surface. The thrust force is assumed to be constant. In order to find a more accurate surge motion, the wave, spray and spray rails resistance [19] still need to be incorporated.

Diffraction forces are neglected, only Froude-Krylov forces are of importance. Therefore the assumption is made that the wave lengths are long in comparison to the vessel's length and that wave slopes are small.

The coefficients in the equations of motion are determined by a combination of theoretical and empirical relationships. The two most relevant coefficients, the buoyancy correction factor and the added mass coefficient, are determined by the results of systematic model tests, the Delft Systematic Deadrise Series (DSDS). Polynomial expressions derived from the results of the DSDS approximate the trim angle and sinkage for the situation of steady state planing in calm water. The values of the two most relevant coefficients are determined by substituting these values for sinkage and trim in the equations of motion.

However, this approach is very sensitive to errors. If the hull geometry deviates significantly from the DSDS, a value for the hydromechanic coefficients cannot be found and has to be estimated using a model of the serie with similar deadrise in the aftship.

In order to increase the level of accuracy of the computational model for modern hull shapes a thorough investigation into the hydromechanic coefficients should be carried out. Instead of applying a constant buoyancy correction factor and the added mass coefficient over the whole hull, a solution can be found in sectional hydromechanic coefficients, dependent on forward speed, deadrise, trim and sectional width. Research of the pressure distribution of planing V-bottom prismatic surfaces might give some insight in a finding a more accurate approximation of the (sectional) buoyancy correction factor and the added mass coefficient.

The computational model has been validated for the motions in head seas by both Zarnick as Keuning using the results of model tests. They carried out model tests with constant forwards speed.

Simulations with constant forward speed and constant thrust, carried out for a double chined hull (DCH) and an axebow hull shape (Axehull) showed no remarkable differences in motions and vertical accelerations. It can therefore be assumed that the motions and accelerations, calculated with constant thrust, are predicted with the same level of accuracy as the original computational model (constant forward speed). Fridma's hypothesis that model tests and thus simulations with constant forward speed generate the same results for the motions and vertical accelerations as model tests or simulations with constant thrust has been verified for moderate sea states.

However, it is still recommended to carry out model tests with free sailing self propelled models in head seas. The relation between thrust, resistance, motions, accelerations and wave profile needs to be studied more thoroughly. It is also expected that the number of (very) large vertical peak accelerations in higher sea states decreases when executing model tests with a constant thrust. Next, the influence of active control of the thrust can be studied using this simulation model.

The present nonlinear mathematical model of motions of a planing monohull in head seas provides designers of planing vessels a computational tool, with little calculation time, that is able to predict the surge, heave and pitch motion and the vertical accelerations in various seas states. The model is applicable for speeds larger than $F_{N_\nabla} \geq 1.5$. The geometry of cross sections of the hull are approximated by the shape of a hard chined wedge. The designer is able to analyse magnitude and probability of exceedence of large vertical peak accelerations when sailing in head seas.

References

[1] R.H. Akers. Dynamic analysis of planing hulls in the vertical plane. Technical report, 1999.

[2] G. Fridsma. A systematic study of the rough-water performance of planing boats. Technical Report R1275, Stevens Institute of Technology, Davidson Laboratory, November 1969.

[3] G. Fridsma. A systematic study of the rough-water performance of planing boats (irregular waves-part ii). Technical Report 1495, Stevens Institute of Technology, Davidson Laboratory, March 1971.

[4] K. Garme. *Modelling of planing craft in waves*. PhD thesis, Royal Institute of Technology KTH, Department of Aeronautical and Vehicle Engineering, Stockholm, Sweden, September 2004.

[5] K. Garme. Improved time domain simulation of planing hulls in waves by correction of the near-transom lift. *International Shiipbuilding Progress*, 52(3):201–230, 2005.

[6] K. Garme and A. Rosén. Time domain simulations and full scale trials on planing craft in waves. *International Shipbuilding Progress*, 50(3):177–208, 2003.

[7] K. Garme and A. Rosén. Model experiment addressing the impact pressure distribution on planing craft in waves. *International Journal of Small Craft Technology*, 146, 2004.

[8] R. Kant. Tijdsdomein simulatie programma voor de bewegingen van planerende schepen in golven. Master's thesis, Delft University of Technology, Ship Hydromechanics Laboratory, May 1989.

[9] J.A. Keuning. *The nonlinear behaviour of fast monohulls in head waves*. PhD thesis, Delft University of Technology, Ship Hydromechanics Laboratory, 1994.

[10] J.A. Keuning and J. Gerritsma. Resistance tests of a series of planing hull forms with a 25 degrees deadrise angle. *International Shipbuilding Progress*, 29(337):222–249, September 1982.

[11] J.A. Keuning, J. Gerritsma, and P.F. van Terwisga. Resistance tests of a series of planing hull forms with a 30 degrees deadrise angle, and calculation model based on this similar systematic series. Technical Report MEMT 25, Delft University of Technology, Ship Hydromechanics Laboratory, June 1993.

[12] M. Martin. Theoretical predictions of motions of high-speed planing boats in waves. *Journal of Ship Research*, 22(3):140–169, 1978.

[13] B. Müller-Graf. Part i: Resistance components of high speed small craft. In *25th WEGEMT School*

NTUA Small Craft Technology, Athens, Greece, October 1997. Department of Naval Architecture and Marine Engineering, National Technical University of Athens.

[14] P.R. Payne. The vertical impact of a wedge on a fluid. *Ocean Engineering*, 8(4):421–436, 1981.

[15] P.R. Payne. A unification in the added mass theory of planing. *Ocean Engineering*, 19(1):39–55, 1992.

[16] P.R. Payne. Recent developments in added mass planing theory. *Ocean Engineering*, 21(3):257–309, 1994.

[17] D. Savitsky. Hydrodynamic design of planing hulls. *Marine Technology*, 1(1):71–95, 1964.

[18] D. Savitsky. On the seakeeping of planing monohulls. *Marine Technology*, 5(2):164–174, April 1968.

[19] D. Savitsky, M.F. DeLorme, and R. Datla. Inclusion of whisker spray drag in performance prediction method for high-speed planing hulls. *Marine Technology*, 44(1):35–56, January 2007.

[20] C.L. Shuford Jr. A theoretical and experimental study of planing surfaces including effects of cross section and plan form. Technical Report 1355, National Advisory Committee for Aeronautics, Washington DC., 1957.

[21] G.L. Visch. Damen axehull and double chine hull test series in calm water and head waves. Technical Report 1552-O, Delft University of Technology, Ship Hydromechanics Laboratory, November 2007.

[22] T. Von Karman. The impact of seaplane floats during landing. Technical Report 321, National Advisory Committee for Aeronautics, Washington DC., 1929.

[23] H. Wagner. Landing of seaplanes. Technical Report 622, National Advisory Committee for Aeronautics, 1931.

[24] H. Wagner. The phenomena of impact and planing on water. Technical Report 1366, National Advisory Committee for Aeronautics, August 1932.

[25] E.E. Zarnick. A nonlinear mathematical model of motions of a planing boat in regular head waves. Technical report, David W. Taylor Ship R&D Center, USA, March 1978.

[26] E.E. Zarnick. A nonlinear mathematical model of motions of a planing boat in irregular head waves. Technical report, David W. Taylor Ship R&D Center, USA, 1979.

[27] R. Zhao and O.M. Faltinsen. Water entry of two-dimensional bodies. *Journal of Fluid Mechanics*, 246:593–612, 1993.

A DESIGN METHOD FOR CONTRA ROTATING PROPELLERS BASED ON EXACT LIFTING SURFACE CORRECTION

Emilio Tincani, Davide Grassi, Stefano Brizzolara
Marine CFD Group, Department of Naval Architecture and Marine Technology, University of Genoa, Italy

SUMMARY

The paper presents some theoretical extensions of the lifting line design method for optimum contra-rotating propellers developed by the Marine CFD Group of DINAV. The original method and computational design program, in fact, has been enhanced in some fundamental aspects to be directly applied into practical design activities of commercial CRP sets for stern or podded drives, without further empirical corrections or adaptations. Now the case of propellers with non-optimum circulation along the radius can be solved and the main hydrodynamic parameters of blade sections can be corrected with an exact lifting surface theory. The main theoretical/numerical developments of the improved design method are given in the paper as well as the results obtained in an exemplary application to the design case of a real case of CRP set for a high speed motor boat with modern podded propulsion. The different propeller geometries found by using a non-optimum loading distribution and with the exact lifting surface corrections, are critically discussed also with respect to the different number of blades. From the discussion, some guidelines about the application of the method for the design of fast CR propellers and the relevance of using exact lifting surface corrections are finally drawn in the conclusions.

1. INTRODUCTION

The demand for high performance propellers, related to lower fuel consumption at cruise condition and higher top speeds at given power, is recently stressing the problem of the propeller design not only in the field of commercial vessels but also in the field of pleasure and charter mega-yachts. A well known mean of overcoming the limitation in the efficiency of a single conventional propeller is the adoption of a contra-rotating propellers set. This concept can be more readily applied to podded drives or azimuth thrusters, but also on conventional shaft lines. The interest of accurate and flexible design tools among propulsion system manufacturers is hence evident. In this context, also the CFD Marine Group of DINAV has been recently interested developed of a design tool of CRP for new podded drives of different sizes ranging from small units in planing motor yachts (35-50 feet) or larger units in high speed semi-planing yachts (65-100 feet).

The original method developed by the same authors (Brizzolara et al., 2007), was based on the original work of Lerbs and Morgan (1960) as conveniently revisited in order to ameliorate the prediction of the interaction effects between the two propellers by a fully numerical lifting line method. The method, though, was not able to deal with generic circulation distribution, being conceived for optimum loadings, while unloaded propeller at tip and root are essential in the design a fast CRP set, usually very close to the limit of cavitation at tip and near the root of blades. This kind of cavitation can be dangerous for durability of propellers and it can be avoided only by adopting such modified span-wise load curves.

Beside the definition of the optimum loading along the radius for a prescribed design condition obtained by the classical lifting surface theory, many efforts have been made in the past to take into account the effect of three-dimensional shape of the blade in order to determine the proper amount of camber and angle of attack and hence section pitch which gives the correct thrust.

A wide variety of correction procedures have been adopted for the lifting line model: e.g. those by Gutsche, Ludwieg and Ginzel, Lerbs etc. In 1961, Pien published a work which is more general than the former one in terms of blade outline and loading distribution over the blade area. Furthermore, in his method, the induced mean line is calculated along the entire chord length instead than just at mid chord as done instead by Ludwieg and Ginzel. In 1965, Cheng focused his attention to enlarging the scope of the previous works in order to solve also the problem of non uniform chordwise distribution. Finally, Morgan-Silovich-Denny published in 1968 a milestone work, presenting a parametrical application of the lifting surface theory to calculate the correction factors for a large number of practical design case of that age.

More recently, Greeley and Kerwin (1982) proposed a vortex/source lattice design method which is very general in terms of loading distribution along the radius and the chord and treats in a efficient and effective way the problem of the wake in terms of contraction and alignment with the local flow. The modifications to the design method presented in this work is closely based on the theory developed in this last work, with the appropriate adaptations to integrate it in the case of two CR propellers.

This part of the method is detailed in the paper. On the contrary, other parts of the design method, such as the numerical evaluation of the entire velocity field in the wake of the a propeller by a full numerical lifting line model with slipstream contraction effect, or the method to determine the chord pitch and camber distribution to respect the given margins of cavitation and strength, are not repeated in this paper, as they were already described in previously mentioned publication (Brizzolara et al., 2007). The last section of the paper illustrates an example of practical application of the method to the case of a fast planing boat with podded drives. The unloaded (non-optimum) propellers obtained and the two different lifting surface correction methods are compared and the main geometrical differences highlighted.

2. OUTLINE OF THE THEORETICAL AND NUMERICAL PROCEDURE

As already anticipated, the computer aided design method has been developed revisiting the methodology by Morgan (1960), theoretically based on Lerbs' lifting line theory (1952, 1955) for the determination of hydrodynamic characteristics of single and contra-rotating propellers (CRP), in the light of state of the more recent propeller design codes, actually employed for high performance commercial and navy propellers in Italy, as a practical automatic blade geometry optimization routines with strength and cavitation constraints have been added as detailed in Brizzolara et al. (2007). The theoretical method relays on the following simplifying assumptions:

each propeller operates at the same rotational speed (same rpm) and about the same torque. This assumption is true for most applications and it is actually almost verified in the case of stern podded drives for fast planing crafts. The hydrodynamic action of each blade is modeled by a lifting line approach, lifting-surface effects are added a posteriori as a correction. The continuously variable bound circulation on the lifting line is represented by a Fourier sine series. Finally, propeller blades are designed with respect to the axial-symmetric time averaged flow, i.e. at each radius the mean value of the induced velocities on the circumferential direction is considered.

Operatively the following input data need to be known or to be supposed and verified with a trial and error procedure:

- propellers thrust (T)
- fraction of thrust produced by camber on all blade sections (the rest is produced by angle of attack) (p)
- number of propeller blades, (Z)
- maximum propeller diameter (D)
- propeller revolutions (equal on both props) (n)
- expanded area ratio (A_E/A_O)
- local and effective wake fraction (w_x,w_o)
- ship speed (V_s)
- maximum blade thickness at root (t_{min})
- rake angle (θ_{rk})
- radial distribution of skew angle (θ_{sk})
- hub diameter (D_h)
- axial distance between fore-and-aft propellers, (d)
- radial distribution of unloading curve (λ_G) to be applied to the optimum circulation (G*) to obtain the non optimum circulation (F*)

In the following the complete computational design method is resumed following the flow diagram of the program.

The main topic of this paper regards the new "Block A modified", and the new optional "Block D new" with respect to the procedure already described in detail in Brizzolara et al. (2007). For sake of clarity a main description of the fuctions of each block is given in the followings, while the next two sections will described in more detail the two new blocks.

Block A: the procedure define the so-called "Equivalent propeller" (EqP): a virtual optimum propeller whose hydrodynamic pitch angle is the mean hydrodynamic angle of the two CR propellers, modeled by two systems of lifting lines collapsed at the same axial position. Under the hypothesis of an optimum propeller the ideal hydrodynamic pitch angle distribution is calculated for the EqP, as for a single propeller for instance with the Kramer method. Then the optimum circulation distribution G* on the EqP is found through an iterative scheme to achieve the imposed thrust and the consistency on the hydrodynamic pitch angles, calculated through the induced velocities. At this time the hydrodynamic characteristic of the EqP are known.

Block A modified: this block has been developed to impose a non optimum loading distribution along radius. With a dedicated iterative procedure starting from the hydrodynamic values calculated before for the Equivalent Optimum Propeller, the new hydrodynamic working condition consistent with the modified load distribution, can be found, still ensuring the same target thrust.

The Lerbs' theory for the design of a single non optimum propeller, adequately adapted with respect to the EqP representative of the CR set, has been developed to solve the problem. As a result of this block, a modified circulation distribution is generated.

Block B: this block is dedicated to the definition of both fore and aft single propellers, on the base of the previously defined EqP. From input data of the CR set as axial distance between props (d) the diameter contraction (δ) of fore propeller slipstream, the wake fraction w_{x1} and w_{x2}, and the mutual interference factors f_a, f_t, g_a, g_t can be evaluated. This data contains information about the axial and tangential interference between single propellers in self and mutual induced velocity. f_a and f_t are factors for obtaining circumferential average interference velocities, as g_a and g_t are factors to correct the circumferentially mean axial and tangential induced velocities for the axial distance between propellers. Once these values are calculated, it is possible to find the distribution along the radius of induced velocities u_a, u_t for both fore and aft propeller (where index 1 means fore prop and 2 means aft prop) and therefore also the two distribution of circulation.

Block C: this block is dedicated to the definition the actual geometry of the CR propellers, to respect the loading distribution and strength and cavitation constraints. The approach of Grossi (1980) was selected to verify the margin on the maximum admissible stress and that on local cavitation index for each blade section. In minimal terms, this is an iterative procedure, which considers cavitation inception criteria and local stress evaluation, to define consistent chord-length (*c*) and thickness (*t*) distribution along radius. On this basis, the actual pitch angle and camber distribution are then calculated, according the relative weight on the thrust production, given as input data.

Block D: finally, lifting surface corrections are applied to pitch and chamber distribution of each propeller previously determined, according the method devised by VanOssanen (1968) and valid rigorously for single propeller with moderate skew.

Block D new: alternatively to the approximate correction of Block D, based on parametric regression formulae, the exact lifting surface theory is used in this block to evaluate the effective pitch and camber distribution of each blade section

To describe the newly devised block ('A modified') it is necessary to resume the main theory behind the EqP model ('A'), which is given in the next paragraph. Next, a comprehensive description of the theoretical/numerical method devised to define the hydrodynamic design of non optimum CR propellers is presented.

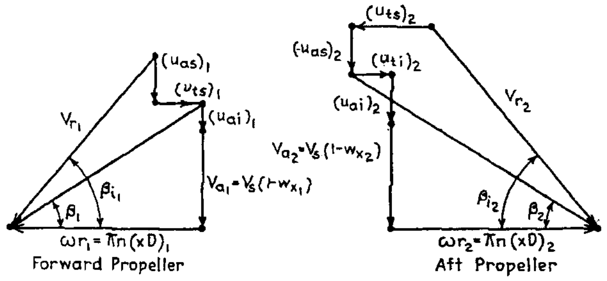

Figure 1 – velocity triangle of CR propellers

THE EQUIVALENT PROPELLER (BLOCK A)

This block calculates the characteristics of the optimum Equivalent Propeller, i.e. as previously mentioned, a propeller representative of the average of the two in the set, hence producing half of the total thrust and absorbing half of the total torque which. The general diagram of figure 1 is valid for the mutual and self induced velocities generated by the two CR propellers.

The induced velocity components on the single EqP are divided in two components, according the work of Morgan (1960): the interference velocities, indicated in the diagram of figure 1 with the subscript *i* due to the mutual induced velocity of one propeller on the other of the CR set; the self induced velocity components, indicated in the diagram with subscript *s*, can be evaluated with the traditional lifting line method, valid for each single propeller. The following expressions between the interference velocities and the self-induced velocities can be made on the basis of momentum theory:

$$\begin{aligned}(u_{ai})_1 &= (u_{ai})_2 (f_a)_2 [1-(g_a)_2]\\ (u_{ti})_1 &= 0\\ (u_{ai})_2 &= (u_{as})_1 (f_a)_1 [1+(g_a)_1]\\ (u_{ti})_2 &= 2(u_{ts})_1 (f_t)_1 [1+(g_t)_1]\end{aligned} \tag{1}$$

in which f_a and f_t come from the circumferential average of the interference velocities, while g_a and g_t are correction for the wake contraction and are in general dependent from the distance between the two CR propellers. In all the rest of the paper, subscript 1 and 2 refers to the forward and aft propeller, respectively.

According Morgan (1960) the following law can be defined:

$$f_t = \frac{G^*}{2x\left(\dfrac{u_t}{V_s}\right)} \cong f_a \tag{2}$$

where G* is the non-dimensional circulation along the blade radius. The other assumption of Morgan is that $g_{a1} \cong g_{a2}$ and the value of g_a is calculated on the basis of results obtained by Tachmindji (1959) in his work with an infinitely bladed propeller model without hub. Both relations on *g* and *f* can be better substituted by a more exact lifting line model as already verified and presented (Brizzolara S. et al., 2007).

With reference to the two velocity triangles of figure 1 and bringing the distance between the two propellers to zero, it follows that the inviscid velocity components and consequently the hydrodynamic pitch angle β_i for fore propeller are:

Axial component = $V_a + u_a(1+f_a)$ (3)

Tangential component = $\omega r - u_t$ (4)

$$\tan(\beta_i)_1 = \frac{V_a + u_a(1+f_a)}{\omega r - u_t} \tag{5}$$

and for the aft propeller:

Axial component = $V_a + u_a(1+f_a)$ (6)

Tangential component = $\omega r - u_t(1-2f_t)$ (7)

$$\tan(\beta_i)_1 = \frac{V_a + u_a(1+f_a)}{\omega r - u_t(1-2f_t)} \tag{8}$$

Thus for the equivalent propeller, $tan(\beta_i)_{eq}$ is calculated as the average of the values found at the same section on forward and aft propellers and, neglecting second order terms, results:

$$\tan(\beta_i)_{eq} = \frac{V_a + u_a(1+f_a) - \dfrac{V_a}{\omega r} u_t(1-f_t)}{\omega r - 2u_t(1-2f_t)} \tag{9}$$

the initial value of the hydrodynamic pitch angle is calculated with the classic formula proposed by Morgan (1960), in which ideal efficiency η_i that is determined from the and the usual procedure, for instance Kramer relation:

$$\tan(\beta_i)_{eq} \cong \frac{\tan(\beta_i)_{eq}}{\eta_i}\left[\frac{(1-w_0)}{(1-w_x)}\right]^{1/2} \tag{10}$$

As in the case of a single propeller, the non dimensional circulation distribution over the lifting lines of the EqP, which is an unknown function in our design problem, is discretized as a sum of a finite number of n odd sinusoidal functions. So the problems reduces to the calculation of the n coefficients of the sinusoidal finite series G^*_m. Thus from the above the following relation for G* has been used:

$$G^* = \sum_{m=1}^{n} G^*_m \sin m\varphi \tag{11}$$

in which ϕ is the free variable, which is related to the non dimensional radial position x of each blade section through the following formula:

$$x = \frac{1}{2}(1+x_h) - \frac{1}{2}(1-x_h)\cos\varphi \tag{12}$$

According Lerbs' (1952) induction factors theory, the induced velocity components are related to the non-dimensional circulation G* on the blades, through the following discretized expressions which approximate the integral definitions:

$$\frac{u_a}{V_s} \cong \frac{1}{Z(1-x_h)}\sum_{m=1}^{n} mG^*_m h^a_m \tag{13}$$

$$\frac{u_t}{V_s} \cong \frac{1}{Z(1-x_h)}\sum_{m=1}^{n} mG^*_m h^t_m \tag{14}$$

In which h^t_m and h^a_m are the Lerbs' improper integrals (1952) which represent the induction factors and depend in general from the coordinate of the collocation points on the lifting line and from the hydrodynamic pitch angle β_i which is given to the free vortex lines in the wake.

Expressing the induced velocities in terms of the circulation distribution with relations (13) and (14), and the circumferential averaging factors (f) in terms of circulation distribution using (2) and the sine series expansion for the circulation distribution (11) the kinematic condition (9) becomes:

$$(1-x_h)(1-w_x)\left[1-\left(\frac{\tan\beta_i}{\tan\beta}\right)_{eq}\right] =$$

$$\sum_{m=1}^{n} G^*_m \left\{ \begin{array}{l} \frac{m}{Z}\left[(\tan\beta - \tan\beta_i)_{eq} h^t_m - h^a_m\right] - \\ -(1-x_h)\frac{\sin m\varphi}{2x}\left[(\tan\beta - 2\tan\beta_i)_{eq} + \frac{u_a}{u_t}\right] \end{array} \right\} \tag{15}$$

This equation is written n times, one for each selected point on the lifting line, forming non linear system of equation which is solved for the unknowns G_m* terms, because of the contribution of last term u_a/u_t which is dependent on the circulation distribution.

Once the circulation of the EqP is found, it is possible to calculate the ideal inviscid thrust of the equivalent propeller:

$$C^*_{Tsi} = 8\int_{x_h}^{1} G^*\left[\frac{1}{(\tan\beta)_{eq}} - \frac{u_t}{V_s}(1-f_t)\right]dx \tag{16}$$

Since this thrust in general is not equal to the ideal thrust initially imposed, the calculation procedure up to this point is iterated, multiplying $\tan(\beta_i)_{eq}$ at all sections by a scalar factor proportional to the difference between the requested and the actual thrust, until the convergence is found. The equivalence, though, must consider a correction, as suggested by Morgan (1960), to allow for the rather crude simplifying assumption of the dynamic equivalence between the EqP and the actual two CR propellers.

3. NON OPTIMUM RADIAL DISTRIBUTION OF CIRCULATION G* (BLOCK A MOD)

As already mentioned, through the concept of EqP can it possible to avoid the simultaneous problem of design of two coupled CR propellers into a more conventional problem of design of a single optimum propeller. The well known Lerbs' (1952) lifting line design method for single propeller, valid also in the case of non-optimum propellers, has been applied by the authors also to the equivalent propeller. The application is not straightforward and requires some modifications, in relation to the peculiar hydrodynamic operation of a CR propellers set.

The optimum circulation distribution calculated by block A with the method outlined in the previous paragraph, is modified by an unloading factor λ_G, variable across the radius. An example of this unloading curve is given in figure 2. Special care must be taken to ensure a very smooth behaviour of this unloading curve to ensure a regular distribution of modified final circulation, avoiding unrealistic peaks predicted by the induction factor theory. Applying this variable unloading factor λ_G to the optimum circulation G* the modified circulation distribution F* can be found. Also this new curve can be expressed in terms of a sine series, in which the n terms F^*_m are to be found by the calculation procedure:

$$F^* = \lambda_G G^* = \sum_{m=1}^{n} F^*_m \sin m\varphi \tag{17}$$

The value of the design ideal thrust should be maintained and met by scaling this new generated load distribution by a constant factor k iteratively changed until the .

The final unloaded circulation distribution respecting the thrust constrain will be referred to L* and defined as:

$$\begin{cases} L^* = kF^* \\ \frac{u_t}{V_s} = \frac{k}{(1-x_h)Z}\sum mF^*_m h^t_m \end{cases} \tag{18}$$

through (17) (18), it is possible to express the formula for the final ideal thrust coefficient from (16), valid for the unloaded counter rotating propellers, keeping the usual assumption of Morgan of the equivalence of the induction factors f_a e f_t :

$$C^*_{Tsi} = 8\int_{x_h}^{1} L^*\left[\frac{x}{\lambda} - \frac{u_t}{V_s} + \frac{L^*}{2x}\right]dx \tag{19}$$

introducing the k scale factor and differentiating the thrust coefficient with respect to radial coordinate the following expression in obtained:

$$dC^*_{Tsi} = 8kF^*\left[\frac{x}{\lambda} - \frac{k}{(1-x_h)Z}\sum mF^*_m h^t_m + \frac{kF^*}{2x}\right] \quad (20)$$

which integrated becomes:

$$C^*_{Tsi} = \frac{8k}{\lambda}\int_{x_h}^{1} F^* x\,dx - \frac{8k^2}{(1-x_h)Z}\int_{x_h}^{1} F^* \sum mF^*_m h^t_m\,dx + 8k^2\int_{x_h}^{1}\frac{F^{*2}}{2x}dx \quad (21)$$

This system must be solved with respect to the unknown scale factor k, hence can be rearranged as:

$$k^2\left[\frac{8}{(1-x_h)Z}\int_{x_h}^{1} F^* \sum mF^*_m h^t_m\,dx + 8\int_{x_h}^{1}\frac{F^{*2}}{2x}dx\right] - k\frac{8}{\lambda}\int_{x_h}^{1} F^* x\,dx + C^*_{Tsi} = 0 \quad (22)$$

While the circulation F^* (and its sinusoidal component amplitudes F^*_m) are known and kept constant during the searching of the solution, the unknowns to be found by an iterative converging algorithm are the scale factor k and the functions h^t_m , h^a_m, which in turn depend on the hydrodynamic pitch angle of the trailed vortical wake β_i, at each radial position x considered in the calculation.

With reference to the velocity diagrams of figure 1, yet following the EqP model of Morgan, the relations between the self and mutually induced velocities of (9) can be rewritten as a function of L^*, as follows:

$$tg\beta_i = \left(\frac{\sin\beta_i}{\cos\beta_i}\right) \text{ in which}$$

$$\sin\beta_i = V_A + u_{a\,\mathrm{mod}}\left(1 + \frac{kF^*}{2x\frac{u_t}{V_s}}\right) - \frac{V_A}{2\pi nr}u_{t\,\mathrm{mod}}\left(1 - \frac{kF^*}{2x\frac{u_t}{V_s}}\right) \quad (23)$$

$$\cos\beta_i = 2\pi nr - 2u_{t\,\mathrm{mod}}\left(1 - \frac{kF^*}{2x\frac{u_t}{V_s}}\right) \quad (24)$$

The solution method developed by the authors and implemented in the design code is detailed in the following.

The value of k factor is calculated using an iterative procedure in which at the first step the system (22) is solved assuming the induction factors h^a, h^t, i^a i^t the axial and tangential velocity components V_a V_t and the pitch distribution β_i, previously found in Block A and valid for the optimum propeller. Contemporary, as proposed by Lerbs (1952) the induced velocities are neglected.

After solution of equation (22), having found the scaling factor k, *t*he corresponding hydrodynamic characteristics and the velocity field generated by the unloaded circulation L* (18) can be found with the following expressions:

$$u_{a\,\mathrm{mod}} = \frac{V_s k}{(1-x_h)Z}\sum_{m=1}^{n} mF^*_m h^a_m \quad (25)$$

$$u_{t\,\mathrm{mod}} = \frac{V_s k}{(1-x_h)Z}\sum_{m=1}^{n} mF^*_m h^t_m \quad (26)$$

The knowledge of the new induced velocities (25) and (26) will permit the calculation of the hydrodynamic angle β_i, and hence the new induction functions as defined by Lerbs (1952). This procedure is repeated until the current value of the ideal thrust coefficient C^*_{Tsi} (21) meets the design value given as input. Usually three or four iterations are needed to converge within a sufficient tolerance. The difference in terms of propeller geometries which the adoption of a curve

4. EXACT LIFTING SURFACE CORRECTION (*BLOCK D NEW)*

Here is presented a brief review of the basic mathematical features of the theory involved in computation.

A Cartesian coordinate system is fixed on the propeller; the x axis is the axis of the propeller shaft with its positive pointing upstream, the y axis is an axis on the first blade arbitrarily selected so as to pass through the mid chord at r = 0.7 R with its positive outward, and the z axis is the third axis and has its positive in accordance with the right-hand rule. It also possible to define a cylindrical coordinate system (showed in Figure 2) in which a point in space can be defined by (r, θ, x) where r is the radial coordinate, θ is the angular coordinate and x is the same as defined above.

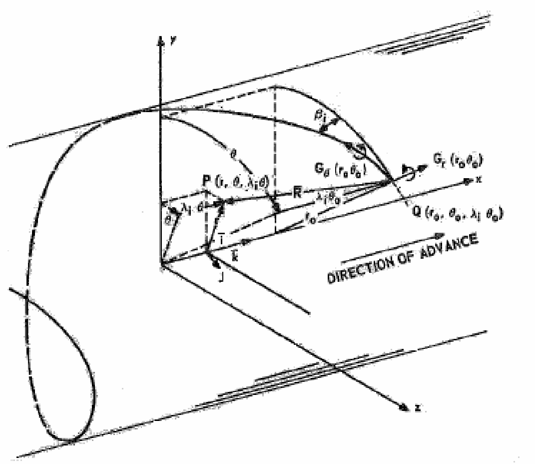

Figure 2 – reference system for bound and free circulation
(same of Greeley-Kerwin, 1982)

Fundamental assumption for the development of the theory can be summarized as follows:

- Propeller blade are modelled by a lattice of bound vortices for loading effect and sources/sinks for thickness effect;
- The lattice is located on the mean surface of the propeller;
- The effect of slipstream contraction and wake alignment in terms of pitch and radial distribution of the free vortices is considered following Greeley-Kerwin work
- The fluid is inviscid and incompressible
- The flow is steady and axisymmetric

The strength of the bound circulation (defined by the lifting line calculation) is given by

$$G(r)=\int_{\theta_t(r)}^{\vartheta_l(r)} G_r(r,\vartheta)d\vartheta \tag{27}$$

$\theta_r(r)$ and $\theta_l(r)$ defines the angular position of the blade section leading edge and trailing edge while G is the non dimensional circulation defined as:

$$G=\frac{\Gamma}{\pi D v} \tag{28}$$

The strength of the helical free vortices can be easily calculated as stated in the following:

$$G_f=-\frac{dG(r)}{dr}dr \tag{29}$$

By combining equation (27) and (29) one obtain the relation between the strength of the free vortices and the strength of the spanwise vortices:

$$G_f(r)=-\frac{d}{dr}\int_{\vartheta_t(r)}^{\vartheta_l(r)} G_r(r,\vartheta)d\vartheta dr=-\int_{\vartheta_t(r)}^{\vartheta_l(r)}\frac{\partial G_r(r,\vartheta)}{\partial r}d\vartheta dr \tag{30}$$
$$-G_r(r,\vartheta_l)\times\frac{d\vartheta_l}{dr}dr+G_r(r,\vartheta_t)\frac{d\vartheta_t}{dr}dr$$

It is now possible to calculate the strength of the chordwise vortices on the blade surface:

$$G_f(r,\vartheta)=-G_r(r,\vartheta_l)\frac{d\vartheta_l}{dr}dr-\int_{\vartheta}^{\vartheta_l(r)}\frac{\partial G_r}{\partial r}(r,\vartheta_0)d\vartheta_0 dr, \tag{31}$$
$$\vartheta_l\geq\vartheta\geq\vartheta_t$$

In order to align the mean surface of the blade with the local velocity the calculation of the induced velocities by this vortex/sources structure $\mathbf{V_i}$ is needed: by the application of Biot-Savart law one obtains:

$$\frac{V_i(P)}{V}=-\frac{1}{2}\iint_{A_1} G_r(r,\vartheta)\left(\frac{S\times dr}{S^3}\right)d\vartheta+$$
$$-\frac{1}{2}\iint_{A_1+A_2} G_f(r,\vartheta)\left(\frac{S\times dl}{S^3}\right) \tag{32}$$

where **S** and **dl** are respectively a vector from the vortex segment to the point P and the elementary vector tangent to the vortex line. A_1 and A_2 are the area of the lifting surface and the area of the helical surface behind the trailing edge of the blade.

By further defining as A_3 the area between the trailing edge and a generating line along which a lifting line would be placed, it is possible to rewrite equation (32) as follows:

$$\frac{\mathbf{V_i}(P)}{V}=-\frac{1}{2}\iint_{A_1} G_r(r,\vartheta)\left(\frac{\mathbf{S}\times\mathbf{dr}}{S^3}\right)d\vartheta+\frac{V_i}{V_{liftingline}}+$$
$$+\frac{1}{2}\iint_{A_1}[G_r(r,\vartheta_l)\frac{d\vartheta_l}{dr}+\int_{\vartheta}^{\vartheta_l(r)}\frac{\partial G_r}{\partial r}(r,\vartheta_0)d\vartheta_0]\left(\frac{\mathbf{S}\times\mathbf{dl}}{S^3}\right)dr+ \tag{33}$$
$$-\frac{1}{2}\iint_{A_3}\frac{dG}{dr}(r)\left(\frac{\mathbf{S}\times\mathbf{dl}}{S^3}\right)dr$$

Since this equation gives the induced velocity by a single blade it is necessary to sum all the contribution due to the whole propeller.

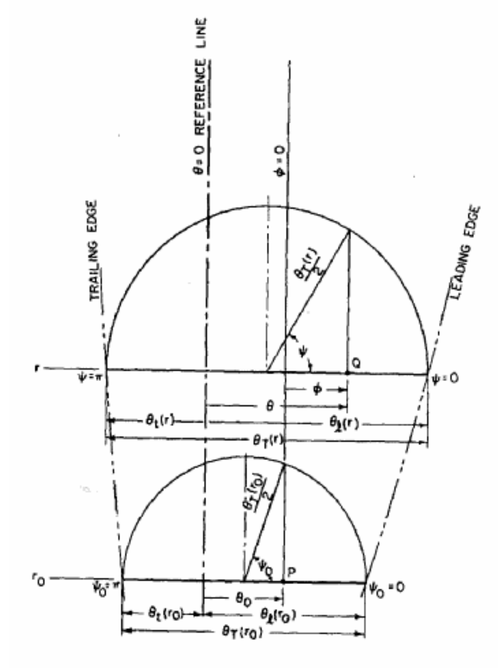

Figure 3 – Chordwise coordinate transformation ψ
(as from Greeley-Kerwin, 1982)

The bound circulation distribution Γ_r in the previous equations can be expressed by the following equation:

$$\Gamma_r(r,\vartheta)=\gamma(r)\left[C_0(r)+A_0(r)\cot\frac{\psi}{2}+\sum_{n=1}^{m}A_n(r)\sin(n\psi)\right] \tag{34}$$

where $\gamma(r)=\Gamma(r)/(\theta_t-\theta_l)$; C_0, A_0, and A_n are constant coefficients and, in general, are functions of r; and ψ is the new chordwise coordinate and is defined as per Figure 3:

$$\psi=\cos^{-1}\left[1-\frac{2}{\vartheta_t(r)}\left(\vartheta_l(r)-\vartheta\right)\right] \tag{35}$$

The first term of equation (34) represent a constant load distribution due to angle of attack; the third, some arbitrary distribution in the form of a sine series with amplitude functions A_n. The first three coefficients must have a relationship of

$$C_0(r)+\frac{\pi}{2}\left[A_0(r)+\frac{1}{2}A_1(r)\right]=1 \tag{36}$$

so that equation (27) is satisfied.

The effect of the thickness is then addressed by introducing a source-sink system distributed over the blade as a lattice whose strength σ(r,θ) is calculated by the use of the classical linear approximations from airfoil theory.

$$\left(\frac{\mathbf{V}_i(P)}{V}\right)_{thickness} = \int_{rh}^{1}\int_{\vartheta_l(r)}^{\vartheta_t(r)} \sigma(r_0,\vartheta_0)\times\mathbf{H}_S(P,r_0,\vartheta_0)\left|\frac{\partial x_c}{\partial \vartheta_0}\right| d\vartheta_0 dr_0 \qquad (37)$$

Where H_S is the velocity induced at the point P by a unit source located at point r, θ.

Once the total induced velocity $V_{i_{tot}} = V_i + V_{i_{thickness}}$ is computed it is possible to state the boundary condition to be satisfied on the blade surface:

$$\alpha\ (r) + \frac{\partial f_p(r,x_c)}{\partial x_c} = \frac{(V_{itot})_n}{V_r}(r,x_c) - \frac{U}{V_r}(r) \qquad (38)$$

where α(r) is the angle of attack, f_p is the camber along the chord x_c, V_r is the resultant inflow velocity to the blade section, U is the resultant induced velocity from lifting line theory, and $(V_{i\ tot})_n$ is the induced velocity normal to blade chord. To determine α the following integral is computed starting from the leading edge to the trailing edge, being f_p equal to zero:

$$f_p(r,x_c) + x_c\alpha(r) = \int_0^{x_c}\left[\frac{U_n(r,\vartheta)}{V_r} - \frac{U(r)}{V_r}\right]d\vartheta \qquad (39)$$

Then a new nose-tail line can be drawn based on the new pitch and a new camber distribution along the chord can be computed.

5. APPLICATION TO THE CASE OF A HIGH SPEED CRP SET

In the following, the results obtained from the application of the design tool to the case of propellers having 3 or 4 blades is presented. In addition to the presentation of the main characteristics of the designed propellers with different number of blades, this application test case is also used to present the main differences implied by the application of the newly developed fully numerical lifting surface corrections method and the previous one based on the parametric regression formulae of Van Oossanen (1968), interpolating the results obtained by Morgan-Silovic-Denny (1968), in the case of modern high speed propeller sets.

Four sets of propellers, with moderate skew, have been designed for the same operational point, but with alternative methods. In all design cases, a ratio of 100% / 0% of thrust produced by camber and by angle of attack has been imposed (for both propellers). The following design variants have been considered:

- **HIPER 08_Z3_Par** - Propellers with 3 blades, designed with parametric solution for lifting surface corrections
- **HIPER 08_Z3_Num** - Propellers with 3 blades, designed with numerical solution for lifting surface corrections
- **HIPER 08_Z4_Par** - Propellers with 4 blades, designed with parametric solution for lifting surface corrections
- **HIPER 08_Z4_Num** - Propellers with 4 blades, designed with numerical solution for lifting surface corrections

The design condition is summarize in Table 1.

Table 1 – Design input values

Diameter Max	0,39	[m]
Thrust required	7600	[N]
Rotational speed	2085	[RPM]
Ship Speed	36	[knots]
Blades	3 or 4	
Wake fraction w_x	0,04	
EAR	0,65	
J	1,366	

The numerical results obtained are presented in table 2 and 3 for the CRP sets with 3 blades, while in table 4 and 5 for the sets, having 4 blades. The table also contains the relevant geometric parameters of some indicative blade sections, in order to better directly evaluate the influence of the design variants on the designed propellers geometries.

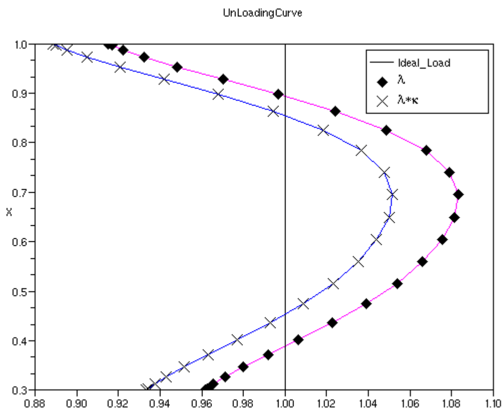

Figure 4 – Unloading Curve initially imposed (λ_G) and calculated at convergence (λ_G*k) on the given thrust

In all cases, the designed propellers have been obtained by adopting the radial unloading curve represented in figure 4, and hence with a non optimum radial circulation distribution. This according the usual design practice in modern propeller design. In fact, the load on the blades has been increased in the central sections, while reduced at the tip and root, in order to delay the cavitation inception that first occurs in these zones. The sections presented in the tables 2,3,4 and 5 are at about x=0.37, x=0.65 and x=0.92. The presented results are the main geometric characteristics of the blade sections, i.e. the pitch (P/D), the max camber (f/c) and the thickness (t/c). The results are distinguished in three columns: the first lists the values obtained with the parametric L.S. corrections, the second the exact (numeric) L.S. corrections and the third the relative differences between the two methods. In the followings, results obtained for each propeller is reported and commented.

- HIPER08_Z3:

Tables 2 and 3 present respectively, the results obtained for the fore and aft propeller of the CRP set with three blades. In both cases the design conditions for the propellers are the same; the difference is only in the method used to calculate the L.S. corrections. The complete picture of geometric and hydrodynamic characteristics of the all the blade sections is given in the graphs of figures 5 to 16 in the relative section in the appendix. Among all the graphs reported it is worth posing the attention to the behaviour of the calculated radial distribution of induced axial and tangential velocities, resultant from the interactions of the two propellers, figures 9 to 11. Figure 9 present the U_{ai} and U_{ti} as calculated with the theory of equivalent propeller, while the subsequent figures 10 and 11 present the same variables as transported on the fore and aft propellers, according the theory of Tachmindji (1959). In particular, the tangential component of induced velocity on the fore propeller is null, since the effect of the aft propeller on the fore results only in a moderate increase of the mean axial flow. The results presented for the 3-bladed set evidence a marked difference in adopting the approximate (parametric) method to calculate L.S. correction and the numeric one, though the results appear congruent between themselves.

Table 1 – HIPER 08 Z3 – Fore propeller

FW Prop	Z = 3	Par	Num	Δ %
x = 0,370	P/D	1,6024	1,623	1,3
	f/c	0,0161	0,0234	31,2
	t/D	0,0233	0,0231	-1,0
x = 0,650	P/D	1,5728	1,5884	1,0
	f/c	0,021	0,018	-19,8
	t/D	0,0107	0,0107	-0,2
x = 0,920	P/D	1,5014	1,4821	-1,3
	f/c	0,018	0,019	6,1
	t/D	0,002	0,0021	4,7

Taking for instance the graph of figure 12 and 13, presenting the pitch distribution calculated with the lifting line theory and with the two different Lifting Surface corrections methods, show qualitative the same trend. It is the amount of correction that mainly differ between the two methods. Main differences are at the root for the fore propeller and at the tip for the aft propeller.

Table 2 – HIPER 08 Z3 – Aft propeller

AF Prop	Z = 3	Par	Num	Δ %
x = 0,370	P/D	1,555	1,5628	3,7
	f/c	0,019	0,023	18,1
	t/D	0,0281	0,0278	-1,1
x = 0,650	P/D	1,6748	1,677	3,4
	f/c	0,024	0,019	-26,8
	t/D	0,0133	0,0133	-0,3
x = 0,920	P/D	1,594	1,5687	1,7
	f/c	0,022	0,020	-10,6
	t/D	0,0027	0,0029	7,1

Major differences are noted in the camber distribution. Comparing the results obtained in figure 14 and 15, as expected, the numeric method has a radical correction of the values of camber at root., still maintaining the trend found with the lifting line method. The difference between the two methods here . At tip, instead, the parametric correction appear exaggerated also due to the fact that the original data of Morgan et al, (1968) are not defined above x=0.9, while the parametric interpolation devised by Van Oossanen (1968) extrapolates a ('a-posteriori' non-reliable) result there. Anyhow also the numerical method shows some inversion of trend for the correction at the tip, though it is believed more reliable for $0.9<x<1.0$.

- HIPER08_Z4:

This 4-bladed CRO set has the same design data of the three-bladed one, so in general the results obtained, are in line with the previous ones.

Table 3 – HIPER 08 Z4 – Fore propeller

FW Prop	Z = 4	Par	Num	Δ %
x = 0,370	P/D	1,5855	1,5994	0,9
	f/c	0,0146	0,0195	25,4
	t/D	0,0218	0,0216	-1,0
x = 0,650	P/D	1,5336	1,5444	0,7
	f/c	0,017	0,014	-23,2
	t/D	0,0103	0,0103	0,2
x = 0,920	P/D	1,4741	1,4561	-1,2
	f/c	0,016	0,014	-12,4
	t/D	0,0019	0,0021	7,9

A better agreement between the L.S. corrections between the two methods is noted This is better evidenced by the analysis of the global distribution of geometric parameters in the relative graphs of the appendix, than from the punctual data reported in Tables 4 and 5.

With reference to figure 24 and 25 it can be noted that there is a very good agreement between the pitch distribution calculated with the two methods for the fore and aft propellers, at least up to x=0.8. For what regards the camber distribution, figures 26 and 27, the same qualitative difference between the two methods exists, although the relative values are less pronounced.

Table 4 – HIPER 08 Z4 – Aft propeller

AF Prop	Z = 4	Par	Num	Δ %
x = 0,370	P/D	1,537	1,5426	3,6
	f/c	0,017	0,019	13,5
	t/D	0,0261	0,0258	-1,0
x = 0,650	P/D	1,636	1,636	3,3
	f/c	0,020	0,015	-28,1
	t/D	0,0127	0,0127	0,0
x = 0,920	P/D	1,574	1,543	1,3
	f/c	0,021	0,016	-32,3
	t/D	0,0026	0,0027	4,1

In synthesis, there is a non negligible difference between the correction of the camber distribution predicted by the parametric and exact lifting surface method especially at the root and tip of the blades. The difference at root might be due to the assumption made by the simplified method that the load at the root is null, while the difference at tip (x>0.9) might most probably due to the extrapolation of the parametric regression formulae proposed by Van Oossanen (1968) in that region. This is evidenced by the graph of figure 16, that shows the behaviour of the camber and pitch corrections coefficients kα and kc vs. the radial position, as evaluated by the parametric method for the 3-bladed propeller. The last point avaluated at x=1 is evidently out of trend. In the whole, the numeric lifting surface method should be preferred to the approximate one for more exact propeller designs which can really guarantee the margin to cavitation inception defined as input data to the design procedure.

6. CONCLUSION AND FUTURE OUTLOOK

The design method for contra rotating propellers presented in this paper is able to find the best CRP geometry for a given operating point, with non optimum load distribution along radius, overcoming the parametric lifting surface corrections. The new possibility to impose an unloading curve to optimum circulation along the radius and to use exact lifting surface corrections, right in the hydrodynamic design procedure, opens great opportunities in order to create consistent CR propellers sets, avoiding a usual deprecate practice of imposing 'a posteriori' alterations of the geometry, not theoretically justified and most often based on experience. With the alternative 'Block D new' , in fact, by running an exact lifting surface numerical method, bypassing the approximated regression formulae used up to now, it is possible to considerably improve the corrections to the angle of attack and to the camber distribution, avoiding final lack or excess of thrust or earlier cavitation inception than predicted.

The new devised computer program is hence a valid design tool with which it is possible to investigate and compare, in short time, a number of alternative designs parametrically generated, for a wider spectrum of design constraints. The final best candidates, then, can be further verified with a more refined method based, for example, on the time averaged lifting surface theory (Grassi, Brizzolara, 2008) or non stationary panel method (Gaggero, Brizzolara, 2008), developed by the same research group. These methods, in fact, result more accurate in the prediction of the ideal potential flow around CR sets and can give valid indications on the final geometry modification in order to obtain the CR propellers sets with the requested performance.

A systematic full scale experimental program of tests is currently programmed to validate the global performance of the CR propeller designs obtained by present method. Hopefully the correlations obtained by this experimental campaign will be very useful for the assessment and finally calibration of the presented design method.

7. LIST OF SYMBOLS

A_E	blade expanded area
A_O	propeller disk area
Q	propeller torque
C_L	lift coefficient of blade section
r	radius of any propeller-blade section
T	propeller thrust
t	maximum blade section thickness
u_a	axial-induced velocity
u_{ai}	interference-induced axial velocity
u_{as}	self-induced axial velocity
u_t	tangential-induced velocity
u_{ti}	interference-induced tangential velocity
u_{ts}	self-induced tangential velocity
CR	CounterRotating
C^*_{Tsi}	total non viscous thrust coefficient based on ship speed
V_a	speed of advance
c	chord length
V_s	ship speed
D	maximum propeller diameter
d	axial between fore-and-aft propeller
EqP	Equivalent Propeller
f_a , f_t	factors for obtaining circumferential averages of axial and tangential velocities interference velocities
f_{max} =	maximum section camber
F^*	total non-dimensional unloaded circulation
G	non-dimensional circulation per blade
G^*	total non-dimensional circulation at each radius of one propeller
G^*_m	Fourier coefficient of non dimensional circulation, G
g_a , g_t	factors for obtaining effect of axial distance between propellers on axial and tangential interference velocities
$h_m{}^t$, $h_m{}^a$	functions of induction factors and radius
L^*	total non-dimensional unloaded circulation that ensure the desired total thrust.
k	multiplying coefficient calculated for scaling the unloaded circulation F^*
n	speed of rotation (rpm)
p	value of lifting fraction generated by camber.
P	blade section pitch
w_0 , w_x	effective and local wake fraction
x_h =	non dimensional hub radius
x =	non dimensional radius (r/R)
Z =	number of propeller blades
α =	angle of attack
β =	advance angle
β_i =	hydrodynamic pitch angle

δ = slipstream contraction factor

$\overline{\delta}$ = average contraction ratio of slipstream at aft propeller

ζ = circulation factor

$\overline{\zeta}$ = average circulation factor

φ = parameter at radius x

η_i = ideal propeller efficiency

λ_G = unloading factor, variable across the radius.

ω = tangential angular velocity

8. AKNOWLEDGMENTS

The present work has been developed in the framework of a long term research project with ZF-Marine Italy, devoted to the development of a new generation line of podded drives with CR propellers. The authors wish to thank the research department of ZF-Marine Italy to the continued and fruitful collaboration established with the Marine CFD Group of the University of Genova.

REFERENCES

Brizzolara, S., Tincani, E. P. A. (2008): "A Design Method for Contra Rotating Propellers with Non-Optimum Radial Loading Distribution", III International Symposium on Motor and Sailing Yacht Design and Production, Madrid, 26-27 June 2008

Brizzolara, S., Tincani, E. P. A. and Grassi, D. (2007): "Design of contra-rotating propellers for high-speed stern thrusters", Ships and Offshore Structures, Publication n. 2:2, 169 – 182

Castagneto, E. Maioli, P.G. (1968): "Theoretical and experimental study on the Dynamics of hydrofoils as applied to naval propellers", 7th Symposium of Naval Hydrodynamic, Roma

Conolly, J.E. (1961): "Strength of Propellers", Trans. Royal Institution of Naval Architects, Vol. 103, pp 139-154, Discussion: 155-160

Gaggero S., Brizzolara S. (2008): "A Potential Panel Method for the Analysis of Propellers ihn Unsteady Flow", Int. Conference on High Speed Marine Vehicles HSMV 2008, June 2008, Naples, Italy

Grassi D., Brizzolara S. (2008): "Numerical Analysis Of Counter-Rotating Propeller Performance By Lifting Surface Theory". Int. Conference on High Speed Marine Vehicles HSMV 2008, June 2008, Naples, Italy

Grassi D., Brizzolara S. (2007): "Numerical Analysis Of Propeller Performance By Lifting Surface Theory" 2nd ICMRT, 28-30 June 2007, Ischia, Naples, Italy

Grossi L. (1980), "PESP: un programma integrato per la progettazione di eliche navali con la teoria della superficie portante", CETENA Report n.1022 (in Italian).

Lerbs, H.W. (1952): "Moderately loaded Propellers with a Finite Number of Blades and an Arbitrary Distribution of Circulation", Trans. Society of Naval Architects and Marine Engineers, Vol. 60, pp 73-117, Discussion: 118-123

Lerbs, H.W. (1955): "Contra-Rotating Optimum Propellers Operating in a Radially non-uniform Wake", David Taylor Model Basin, Report 941

Morgan, W.B., Silovic, V. , Denny, S.B. (1968): "Propeller Lifting-Surface Corrections", SNAME Transaction 76: 307-347

Morgan, W.B., (1960): "The Design of Counter-rotating Propellers Using Lerbs' Theory", Trans. Society of Naval Architects and Marine Engineers, Vol. 68, pp 6-31, Discussion: 32-38

Van Oossanen, P.(1968): "Calculation of Performance and Cavitation Characteristics of Propellers Including effects of non uniform flow and viscosity", Netherland Ship Model Basin, Publication n.457.

Tachmindji, A.J. (1959): "The Axial Velocity Field Induced of an Optimum Infinitely Bladed Propeller", David Taylor model Basin report 1294, Jan. 1959.

HIPER 08_Z3

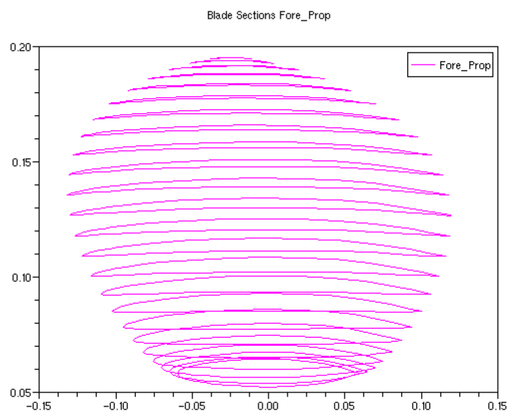

Figure 5– Z3_ Mod - Sections of FW Blade

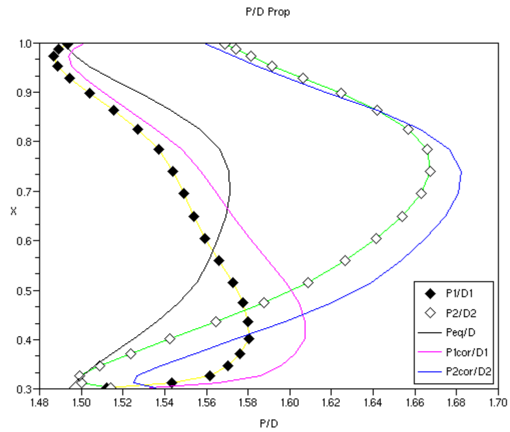

Figure 8 – Z3 - Radial distribution of non dimensional pitch – P/D

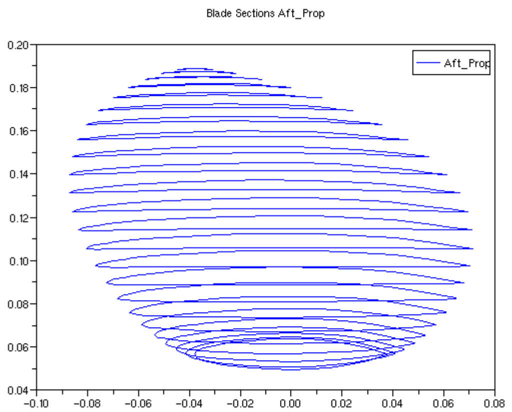

Figure 6 - Z3_ Mod - Sections of AF Blade

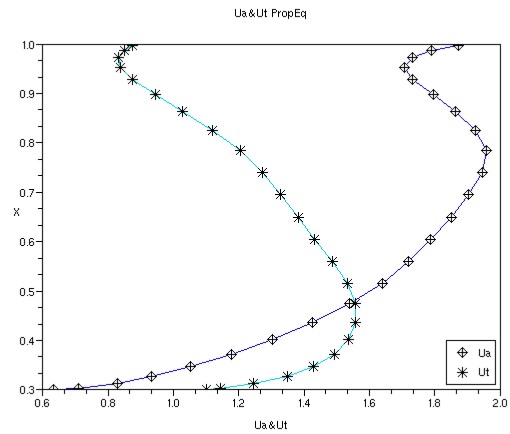

Figure 9 – Z3_ Mod - Radial distribution of induced velocities U_a and U_t on EqP

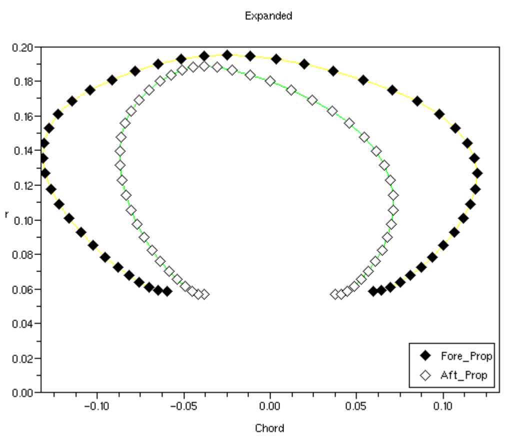

Figure 7 - Z3_ Mod - Expanded of CR set

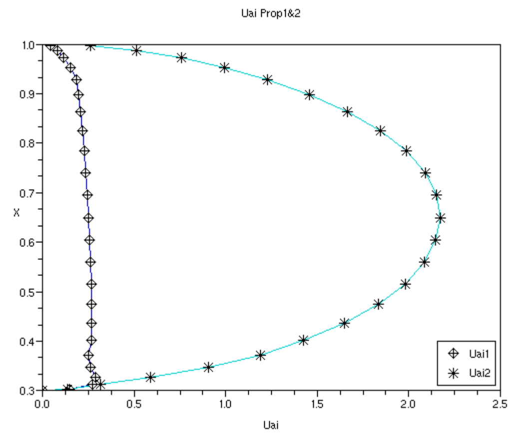

Figure 10 – Z3_ Mod - Radial distribution of induced axial velocities U_a on Fore and Aft propellers

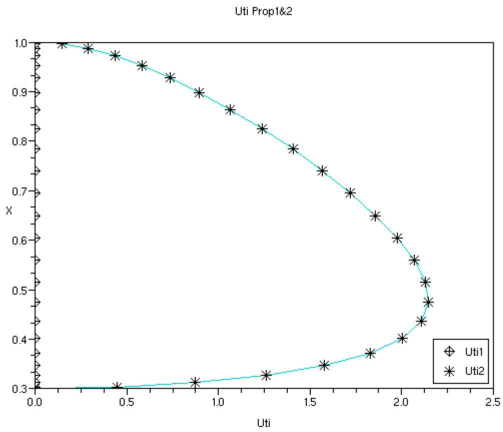

Figure 11 – Z3_ Mod - Radial distribution of
induced tangential velocities U_t on Fore and Aft propellers

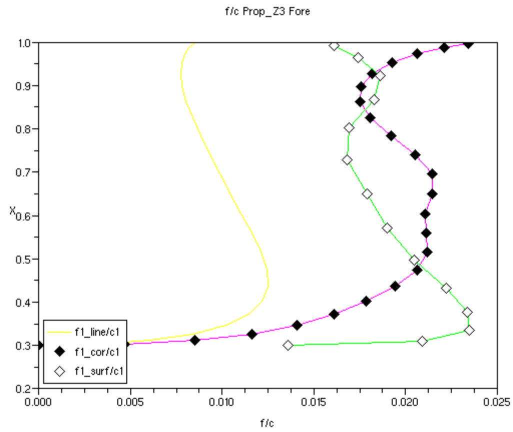

Figure 14 – Z3 - Radial distribution of
non dimensional Camber on Fore Propeller – F/c

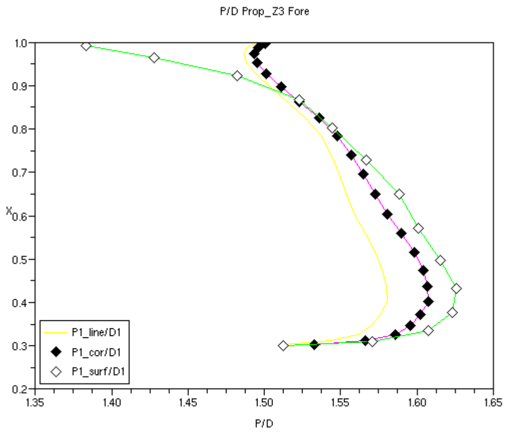

Figure 12 – Z3 - Radial distribution of
non dimensional Pitch on Fore Propeller – P/D

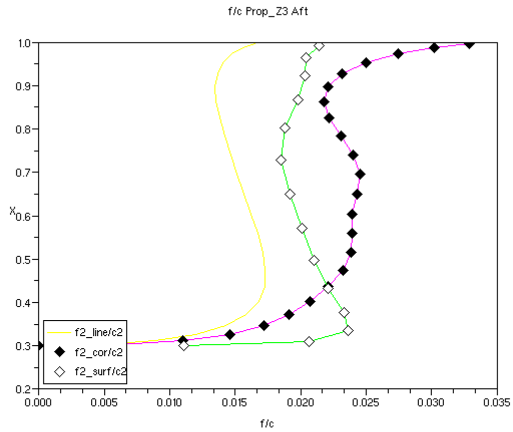

Figure 15 – Z3 - Radial distribution of
non dimensional Camber on Aft Propeller – F/c

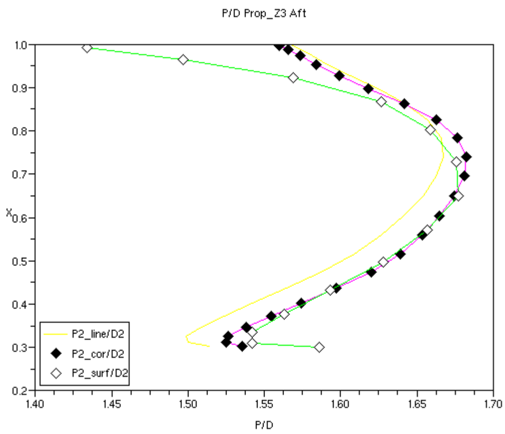

Figure 13 – Z3 - Radial distribution of
non dimensional Pitch on Aft Propeller – P/D

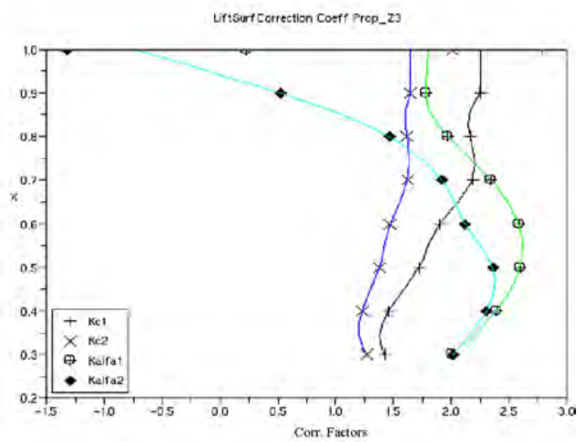

Figure 16 – Z3 - Radial distribution of
Lifting surface correction Coefficients

- **HIPER 08_Z4**

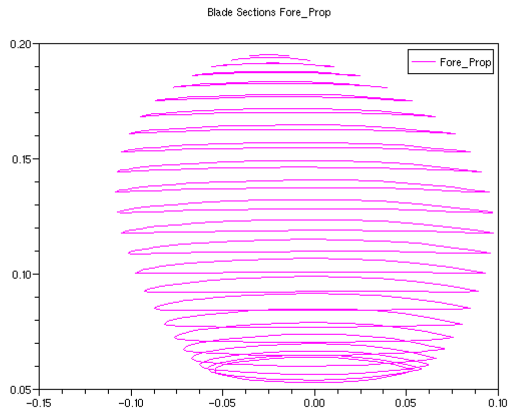

Figure 17– Z4 - Sections of Fore Blade

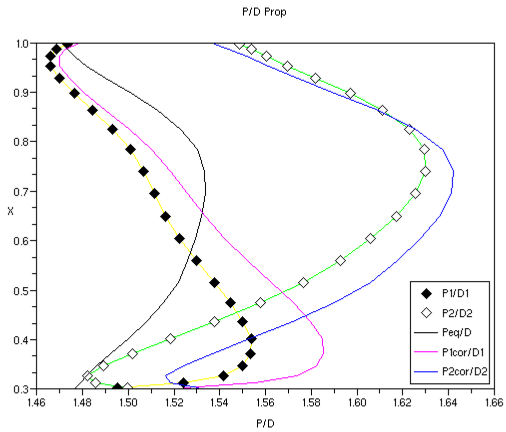

Figure 20 – Z4 - Radial distribution of non dimensional pitch – P/D

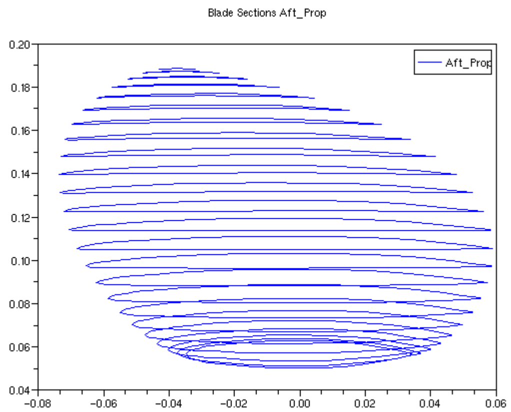

Figure 18– Z4- Sections of Aft Blade

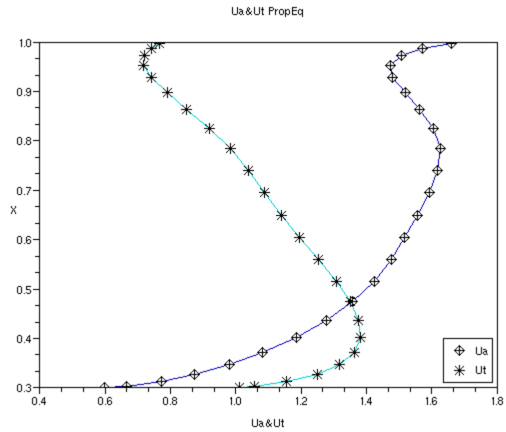

Figure 21 – Z4 - Radial distribution of induced velocities U_a and U_t on EqP

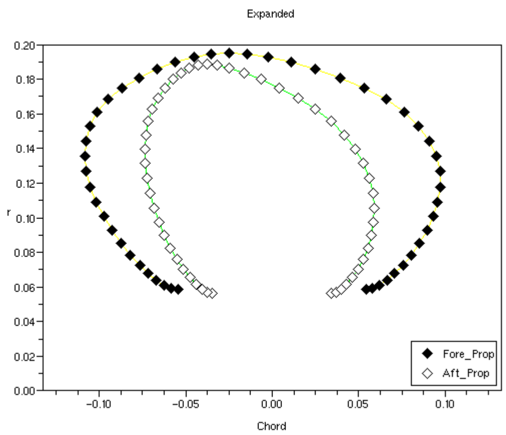

Figure 19 – Z4 - Expanded of CR set

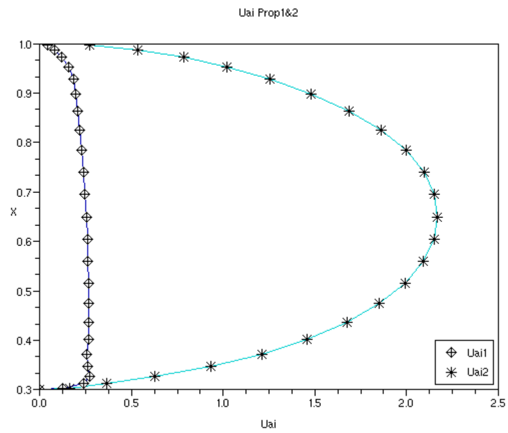

Figure 22 – Z4 - Radial distribution of induced axial velocities U_a on Fore and Aft propellers

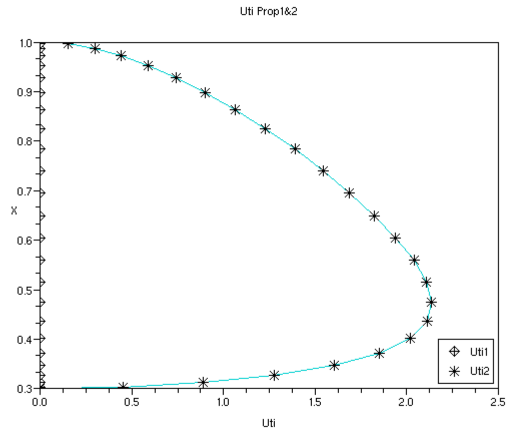

Figure 23 – Z4 - Radial distribution of
induced tangential velocities U_t on Fore and Aft propellers

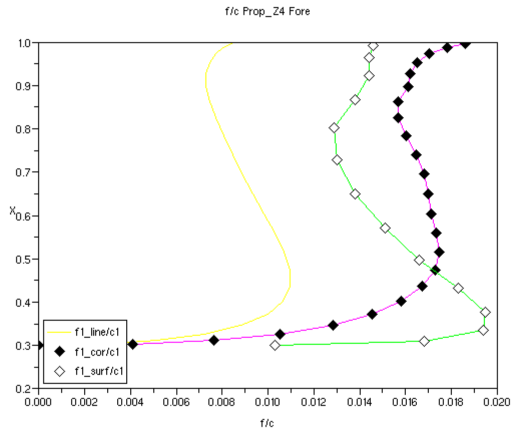

Figure 26 – Z4 - Radial distribution of
non dimensional Camber on Fore Propeller – F/c

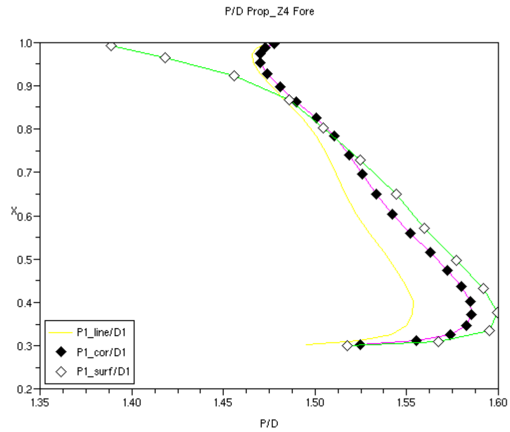

Figure 24 – Z4 - Radial distribution of
non dimensional Pitch on Fore Propeller – P/D

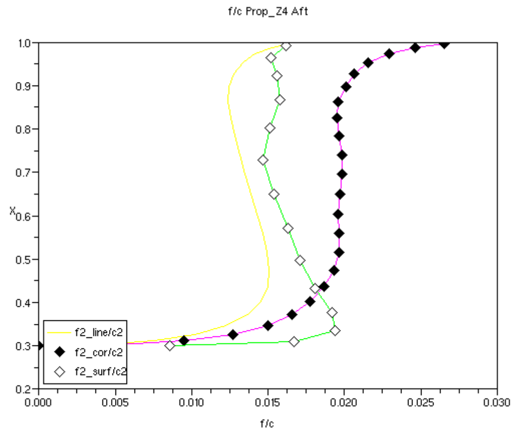

Figure 27 – Z4 - Radial distribution of
non dimensional Camber on Aft Propeller – F/c

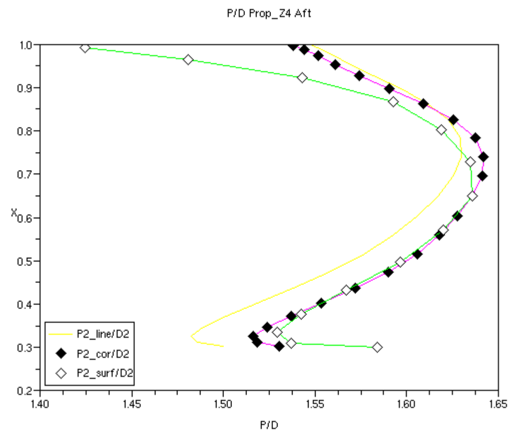

Figure 25 – Z4 - Radial distribution of
non dimensional Pitch on Aft Propeller – P/D

RELIABILITY OF WEIGHT PREDICTION IN THE SMALL CRAFT CONCEPT DESIGN

IZVOR GRUBISIC, University of Zagreb, Croatia

SUMMARY

Weight prediction is an important part of naval architect's work. Reliability of weight prediction in the concept phase of small craft design is scrutinized in order to aid designers in selecting appropriate margins. Two databases are formed, one consisting of 34 vessels for which a detailed weight breakdown is available and the other consisting of 143 vessels where only lightship weight is known. Included are small craft of variable service type, hull structural material and propulsion devices. Different approaches to weight estimating ere attempted and compared to the database. Structural and nonstructural weight is analyzed separately according to the first level weight breakdown. A practical weight prediction method is developed which is specialized for small fast craft. Parametric equations for predicting weight of each group will be useful not only in concept design but also in cost estimate. Statistical analysis of the unexplained weight difference gives standard deviation of about 13%.

1. INTRODUCTION

1.1. BACKGROUND

Ship weight estimating methods are the principal tools of the profession since the introduction of Archimedes' law in practical ship design. Archimedes lived from 298 BC to 212 BC, but his law was used for ship design purposes almost 2000 years later by Pierre Bouguer in "Traité de navire", (1746) and by Fredrik Henrik af Chapman in his "Architectura Navalis Mercatoria" (1775).

In principle everything is simple with weight estimating. A sum is made of the individual weights of all elements that go into the ship. The problem is that the iterative nature of ship design makes detailed calculations at the concept design stage impractical, since design is not yet defined in enough detail to find individual weights.

For the concept design phase of ship design a "numeral" approach is usually the most utilized. It is supposed that weight of the ship is proportional to the numeral. The numeral itself is composed of readily available principal dimensions and coefficients.

At this level usually a simple weight breakdown is necessary. Many systems of weight breakdown were developed and almost every designer has his/her own favorite system. This makes it difficult to compile and compare weight data based on different and not always published systems.

1.2. SCOPE OF VESSELS

In a well known classical works on design in naval architecture: Watson (1998), Schneekluth (1998), Parsons (200), presented is a number of methods developed for the weight prediction of the large steel ships, both commercial and naval.

In present work special attention will be given to small craft which are different from large vessels in many aspects, relative speed, hull form, structural material, propulsion, to mention the most important. Here "small craft" is defined as: vessels of up to approximately 60 m length overall, made of different structural materials, for different services at sea and relatively fast as defined by a IMO HSC code.

A database of small vessels was compiled through several years. Unfortunately weight data are not often published, therefore, a personal contacts with designers and shipyards are necessary in order to collect enough data. Some of the data are given in confidence and it would be appropriate here to acknowledge this contribution.

Reliability of the data is tested by comparison with other vessels. Obviously, it is not possible to guarantee 100% correct data, but every effort is made to eliminate error and to homogenize the sample. Sometimes data had to be sacrificed and eliminated from the sample because they are evidently erroneous and far away from trends.

1.3. DEFINITION OF FAST VESSEL

According to the HSC (art.1.4.24) the maximum sustained speed of the fast vessel should be over the speed defined by (1).

$$v > 3,7 \cdot \nabla^{0,1667} \text{ m/s} \tag{1}$$

where, ∇ is maximal operating displacement volume in m^3. On the other hand a minimal speed of the planning hull, that is completely dynamically supported, is defined via volumetric Froude number of 3,5, i.e.

$$F_{N\nabla} = \frac{v}{\sqrt{g \cdot \nabla^{0,3333}}} = 3,5 \tag{2}$$

By evaluating the expression and inserting g=9,80665 m/s^2, the minimal speed of completely dynamically supported craft is:

$$V_{DYN} = 21,3 \cdot \nabla^{0,1667} \text{ kn} \tag{3}$$

as compared to the HSC defined speed of fast vessels:

$$V_{HSC} = 7,19 \cdot \nabla^{0,1667} \text{ kn} \tag{4}$$

Therefore, both, semi displacement and full planning hulls are included in the sample.

2. DATABASE

2.1. DATABASE STRUCTURE

Initial data were collected when study of the Maritime administration vessels was made by Grubisic et al. (1996). After completion of that work, new data were systematically gathered and added to the original database. Database is collected from different sources and sometimes the reliability is not as satisfactory as expected.

The database is structured in EXCEL work sheet containing all basic ship design data. Actually there are two groups of vessels:

- the first group (DB1) consists of vessels for which weight data subdivided into groups is available
- the second group (DB2) consists of the vessels for which only lightship weight is known.

The idea behind this division is to be able to develop procedure using the first database and after that to test the procedure using the second database.

2.2. DATABASE CONTENTS

Describing database in detail would use to much space, therefore only principal information are given here.

All data necessary for the weight analysis are not available from the original sources. Therefore, some of the data were synthesized by the application of the following approach:

- Scaling from the published general arrangement plans to find missing L_{WL} or D_X or T_X.
- If GT was available depth could be estimated as:
$$D_X \approx 10{,}29 \cdot \frac{GT}{(L_{OA} + L_{WL}) \cdot B_M} \qquad (5)$$
- Often the maximal beam at waterline was missing. Regression provided the relation:
$$B_X \approx 0{,}897 \cdot B_M \qquad (6)$$
- Synthesizing lightship weight by subtracting all variable weights (as published) from the full load displacement.
$$W_{LS} = W_{FL} - (W_{PL} + W_{FO} + W_{FW} + W_{CR}) \qquad (7)$$
where,
$$W_{CR} = 0{,}125 \cdot N_{CR} \qquad (8)$$
The payload W_{FL} includes passengers and luggage with assumed weight of:
$$W_{PAX} = 0{,}105 \cdot N_{PAX}$$
Fuel density was assumed to be 860 kg/m^3

2.3. DATABASE DB1

The first database (DB1) consists of 34 vessels that are grouped by the service type as shown in Table 1:

Table 1. Vessels in the DB1 by type

N	service	service description
2	WORK	work boat
1	FIRE	fire vessel
12	MIL	military / naval
5	MY	motor yacht
8	PATROL	patrol / paramilitary
3	PAX	passenger & ferry
3	SAR	search & rescue

Grouping by hull structural material is shown in Table 2:

Table 2. Vessels in the DB1 by structural material

N	material	hull structural material
7	MS	mild steel
12	HTS	high tensile steel
7	FRP	fiber reinforced
8	AL	aluminum

Mean hull length of the sample, as defined by (24), is shown in Figure 1:

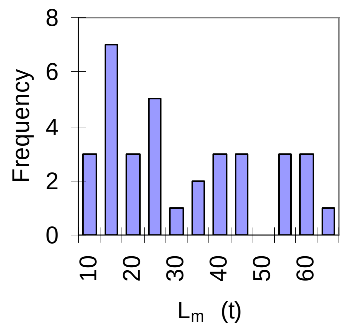

Figure 1. Database DB1 -vessel length distribution

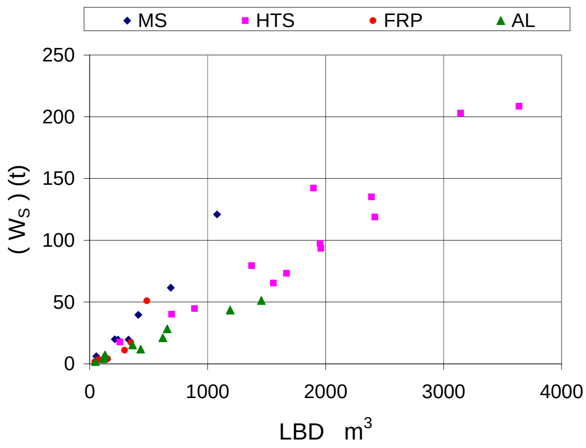

Figure 2. Structural weight of the DB1 vessels

In Figure 2 the structural weight of the vessels is shown grouped per hull material in relation to the cubic number.

2.4. DATABASE DB2

The second database (DB2) is much larger, since lightship weight data is easier to obtain, and it consists of 143 vessels. More service types are included than in the first database comprising the types in Table 3:

Table 3. Vessels in the DB2 by type

N	service	serv. description
2	CARGO	cargo transport
6	PAX	passenger & ferry
5	CREW	crew boat
3	FISH	fishing vessels
9	FIRE	fire vessel
1	MEDIC	medical service
4	MIL	military / naval
14	MY	motor yacht
56	PATROL	patrol/paramilitary
19	PILOT	pilot vessel
1	POLICE	police craft
3	RESEARCH	research vessel
12	SAR	search & rescue
8	WORK	work boat

Hull structural material is distributed as in Table 4:

Table 4. Vessels in the DB2 by type

N	material	hull structural mat.
21	MS	mild steel
3	HTS	high tensile steel
41	FRP	fiber reinforced
75	AL	aluminum
3	WLAM	laminated wood

Mean hull length of the sample is distributed as shown in Figure 3.

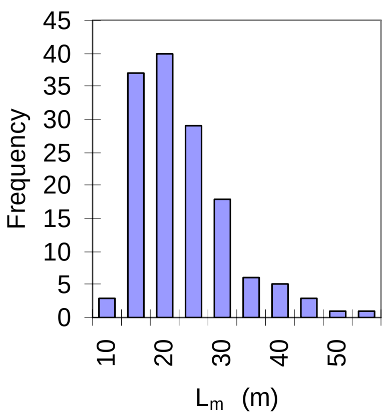

Figure 3. Histogram of length of the DB2 vessels

Spread of lightship weight of the vessels from DB2 is shown in Figure 4 related to the cubic number.

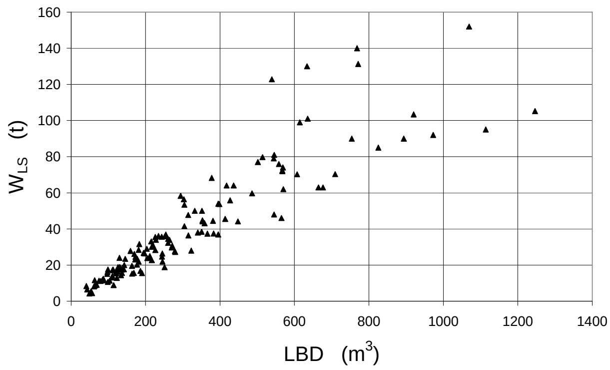

Figure 4. Lightship weight of the DB2 vessels

3. WEIGHT BREAKDOWN

3.1. FIRST LEVEL WEIGHT BREAKDOWN

Data collected and saved in the DB1 are quite variable regarding the applied system of weight breakdown, different origin, different practices, different countries, different rules, etc. Basically the system of grouping is shown in Figure 5.

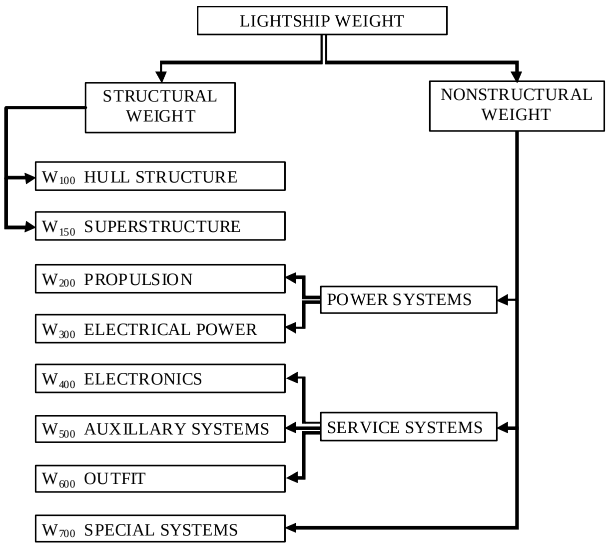

Figure 5. First level weight breakdown

Before proceeding with further analysis, a common weight breakdown had to be introduced.

Basically grouping is treated as if a USN SWBS system was applied to all vessels. If data did not provide enough information, redistribution of weight was necessary in order to group weight consistently.

Here is obviously a potential for introducing error but every precaution was taken to minimize it.

3.2. GROUPING OF WEIGHTS

Full load weight of the vessel is divided into lightship and deadweight (9).

$$W_{FL} = W_{LS} + W_{DWT} \quad (9)$$

Deadweight is composed of payload, fuel, water, crew and provisions (10)

$$W_{DWT} = W_{PL} + W_{FO} + W_{FW} + W_{CR} \quad (10)$$

Lightweight may be subdivided in many different ways but two major approaches are in general usage:

- A breakdown system according to the naval ship practice is given by (11).

$$W_{LS} = W_{100} + W_{200} + W_{300} + W_{400} + W_{500} + W_{600} + W_{700} \quad (11)$$

- A breakdown system common to the merchant ship practice is given by (12).

$$W_{LS} = W_S + W_M + W_O \quad (12)$$

4. WEIGHT PREDICTION BY NUMERALS

4.1. SELECTION OF NUMERALS

In the history of ship design a great number of weight prediction methods and appropriate numerals were developed. All of them rely on the small number of ship parameters that are available at the concept design level.

Selection of suitable numeral depends on correlation of the numeral and the weight concerned. Therefore, it is highly recommended that there should be some physical relation between the numeral and the weight (e.g. power and weight of engine). Selection of the most frequently used numerals is shown in sequel.

Hull weight:

$$W_S = k \cdot L \cdot B \cdot D \quad (13)$$

$$W_S = k \cdot L \cdot B \cdot D \cdot C_{BD} \quad (14)$$

$$W_S = k \cdot \left[L \cdot (B + D) \right]^n \quad (15)$$

$$W_S = \left(K_1 \cdot L \cdot \frac{L}{D} + K_2 \cdot D \right) \cdot L \cdot B \cdot C_B^{1/2} \quad (16)$$

Machinery weight:

$$W_M = k \cdot P^n \quad (17)$$

$$W_M = k \cdot (L \cdot P)^n \quad (18)$$

Outfit weight:

$$W_O = k \cdot L \cdot (B + D) \quad (19)$$

$$W_O = k \cdot (L \cdot B \cdot D)^n \quad (20)$$

$$W_O = k \cdot L \cdot B \quad (21)$$

Coefficients in the equations (13) – (21) are found from prototype vessel or by the regression analysis of number of similar vessels.

The similarity is here the most problematic element since the data for a homogenous group of vessels is not easily found. Therefore, the analysis must deal with vessels which are only partly similar (maybe here word "similar" should be replaced by "affine").

Additional difficulty comes from the vessels being built at different times when requirements, materials, practices and rules, were different from what is used today. All this influences the reliability of the weight prediction.

4.2. SELECTION OF PARAMETERS

At the concept design level only small number of parameters is known. They comprise: length, beam, depth, draft, block coefficient, displacement, installed power, etc. Due to the variability of hull forms it is necessary to somehow neutralize influence of unusual shapes on the weight prediction. Typically the length is suspect due to the variability of stem and stern shapes. The length to be used in the numerals may be taken as:

$$L = L_{PP} \quad (22)$$

$$L = 0,96 \cdot L_{WL} \quad (23)$$

$$L = (L_{OA} + L_{WL})/2 \quad (24)$$

$$L = (L_{OA} + 2 \cdot L_{WL})/3 \quad (25)$$

4.3. STRUCTURAL WEIGHT –WATSON

Structural weight estimating that produces reliable prediction in the merchant and in the naval ship design was introduced by Watson and Gilfillan (1976). Since the method was developed for the usage in "big" steel ship design, it should be tested when applied to the small craft.

The method is based on the early version of Lloyd's Register equipment numeral defined by (26).

$$E = L \cdot (B + T) + 0,85 \cdot L \cdot (D - T) + 0,85 \cdot \sum l_1 \cdot h_1 + 0,75 \cdot \sum l_2 \cdot h_2 \quad (26)$$

Watson and Gilfillan found that the structural weight data of steel ships in their database were best approximated by the exponential curve (27).

$$W_S = K \cdot E^{1,36} \quad (27)$$

Span of the coefficients and numerals for the small steel ships is given in the book by Watson (1998) of which an excerpt is given in Table 5:

Table 5. Coefficients and numerals - Watson's method

Type	*K*	*E*
Fishing vessels	0.041 – 0.042	250 – 1300
Coasters	0,028 – 0,032	1000 – 2000
Offshore supply	0,040 – 0,050	800 – 1300
Tugs	0,042 – 0,046	350 – 450
Fregates&Corvettes	0,023	

4.4. STRUCTURAL WEIGHT –KARAYANIS

By an approach based on Watson's method, Karayanis et al. (1999) proposed a weight prediction method suitable for fast ferries in the range of 40 - 120 m length. It is based on the numeral (28), that takes into account different specific weights of the underwater part of hull and above water part, but not superstructures and erections:

$$E_m = L\cdot(B+T)+0{,}85\cdot L\cdot(D-T) \tag{28}$$

Comparing database vessels it was established that an even older equipment numeral (29)

$$E_o = L\cdot(B+D) \tag{29}$$

is so highly correlated to the E_m numeral that it may replace it completely without loss of accuracy, Figure 6.

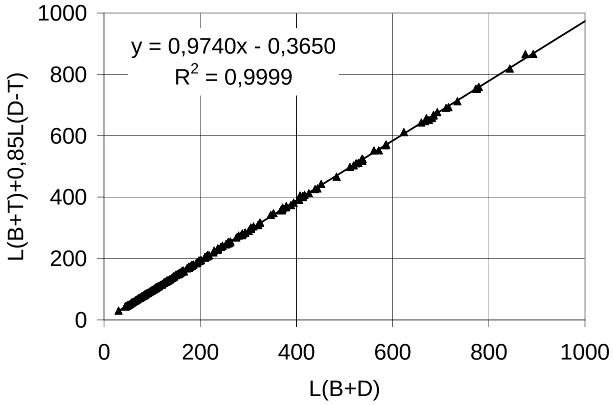

Figure 6. Correlation of numerals

Table 6. shows the results of the application of the Karayanis's procedure to the small fast craft from the database DB1.

Table 6. Coefficients and numerals - KARAYANIS'S method applied to the DB1 vessels

Hull material	K	E_m
Aluminum	0.0082 – 0.0169	47 – 523
FRP	0,0084 – 0,0169	44 – 176
Mild steel	0,0197 – 0,0283	57 – 407
HTS	0,0135 – 0,0213	140 – 988

The variability of the coefficients in Table 6. is somewhat high, therefore, for the high speed craft that are considered here, we need a new type of numeral that closer approximates structural surface areas and their respective relative specific weight.

5. SMALL CRAFT WEIGHT PREDICTION

5.1. PROPOSAL

Following the original idea of Watson and Gilfillan, i.e. that the prediction of structural weight is based on numeral representing structural surface area, new proposal is to use even closer approximation of the area that is possible by the statistical analysis of hull forms. The hull forms in databases of small vessels comprise only vessels with transom stern, therefore, surface approximation takes that as a starting point.

All other weights except the structural weight have to be predicted also. The idea is to find the most suitable numerals and to predict each of these weights by separate method. The sum of predicted weights should in theory equal the lightship weight. Since the variability of data, there will appear either positive or negative difference. The quality of weight prediction will be judged by the standard deviation of the residual weight (i.e. unexplained weight).

In sequel a systematic development of the prediction method is presented.

5.2. STRUCTURAL WEIGHT MODEL

Weight of the hull structure is based on estimating plating area of the four major components, i.e. bottom, sides, deck and bulkheads. Relative surface weights are estimated due to the differences in pressure loading of specific area. This approach was developed by Grubisic and Begovic (2003) and applied to small fast craft. Four principal surface areas were estimated by expressions (30) – (33).

Bottom: $$S_1 = 2{,}825\cdot\sqrt{\Delta_{FL}\cdot L_P} \tag{30}$$

Sides: $$S_2 = 1.09\cdot(2\cdot L_{OA}+B_M)\cdot(D_X-T_X) \tag{31}$$

Deck: $$S_3 = 0{,}823\cdot\left(\frac{L_{OA}+L_{WL}}{2}\right)\cdot B_M \tag{32}$$

Bulk.: $$S_4 = 0.6\cdot N_{WTB}\cdot B_M\cdot D_X \tag{33}$$

Since weight of each area is different a reduced surface area is predicted by taking into account the different loading of the respective parts of complete area:

$$S_R = S_1 + 0{,}73\cdot S_2 + 0{,}69\cdot S_3 + 0{,}65\cdot S_4 \tag{34}$$

In order to make allowance for the influence of full load displacement a correction factor is applied. It is developed from the Lloyds' Register rules for fast craft where the standard displacement was defined as:

$$\Delta_{LR} = 0{,}125\cdot\left(L_{LR}^2-15{,}8\right)\ \text{t} \tag{35}$$

Neglecting the 4% difference of the respective lengths, the displacement correction factor is determined by (36).

$$f_{DIS} = 0{,}7+2{,}4\cdot\frac{\nabla}{L_{WL}^2-15.8} \tag{36}$$

Correction for the influence of the T/D ratio is best described by:

$$C_{T/D} = 1.144\cdot(T_X/D_X)^{0.244} \tag{37}$$

When applied to the database vessels (DB1) both correction factors are estimated to be in the range from minimal to maximal values as shown in Table 7.

Table 7. Correction factors

Correction factor	f_{DIS}	$C_{T/D}$
minimal value	0,906	0,828
maximal value	1,274	1,042

Effective surface area is estimated from the reduced surface area S_R by correction for displacement and T/D, respectively. Finally the new structural numeral is given by (38).

$$E_S = f_{DIS} \cdot C_{T/H} \cdot S_R \quad \mathrm{m}^2 \qquad (38)$$

By the analogy with the Watson's and Gilfillan's method the value of the exponent is found to be 1,33 as shown in Figure 7. This is surprisingly close to the original exponent of 1,36. The structural weight is now determined by the equation (39).

$$W_K = K_0 \cdot E_S^{1,33} \quad \mathrm{t} \qquad (39)$$

where:

K_0=0,0112

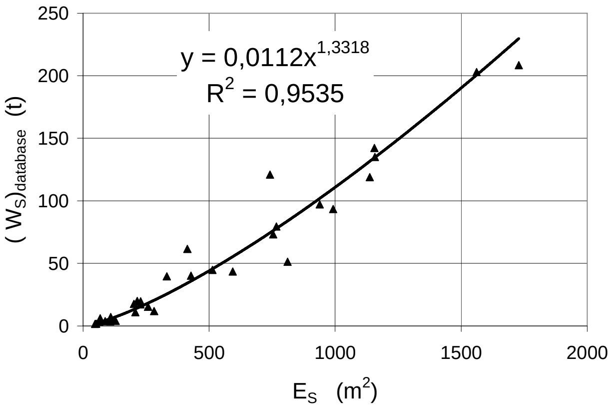

Figure 7. structural weight - relation to the numeral

The coefficient K_0 is subsequently replaced by the three factors taking care of the service area, service type and structural material influence as given by (40).

$$W_S = K_S \cdot f_{SAR} \cdot f_{SRV} \cdot f_{MAT} \cdot E_S^{1,33} \qquad (40)$$

The remaining factor K_S describes each individual vessel and for general case is assumed to be unity. When prototype vessel is at hand the value of K_0 may be determined from that data.

Other factors in (40) are determined as follows:

Service area notation is related to the bottom pressure via design pressure factor. The bottom pressure is related to the weight of bottom structure. Table 8. is composed from the data given by the LR SSC rules (1996):

Table 8. LR SSC service areas definition

Service area notation	N_{LR}	Range to refuge NM	Min. wave height $H_{1/3}$ m	Design pressure factor
G1	1	sheltered waters	0,6	0,60
G2	2	20	1,0	0,75
G3	3	150	2,0	0,85
G4	4	250	4,0	1,00
G5	5	>250	>4,0	1,20
G6	6	unrestricted service	>4,0	1,25

The vessels in the database were of variable origin and not built at the same time neither according to the consistent set of rules. Therefore, a best estimate of the corresponding service area notation is made. The influence of service area is estimated by comparing complete hull weights of the database vessels to the LR service area notation. The best correlation is found as in equation (41).

$$f_{SAR} = 0,7202 + 0,0628 \cdot N_{LR} \qquad (41)$$

Service type factors f_{SRV} determined from the database vessels are shown in Table 9.

Table 9. Service type correction factor

Service type	f_{SRV}
MIL	1,007
MY	1,013
PATROL	1,089
WORK	1,384
SAR	1,439

Hull material factors are determined by fitting data for the respective database craft grouped by hull material. The analysis of database produced tentatively the hull material factors in Table 10.

Table 10. structural material correction factor

Hull structural material	f_{MAT}
MILD STEEL	17,28
HTS	11,03
AL	7,86
FRP	11,36
FRPS	7,00
WLAM	9,00

Here it must be said that the separation of hull and superstructure material is not possible due to small number of data in each category. Therefore HTS hull, that is in all cases combined with the aluminum or FRP superstructure, reflects the combined effect of the two materials.

The procedure is applied to the database vessels and it reproduced original data with relatively high level of confidence as shown in Figure 8.

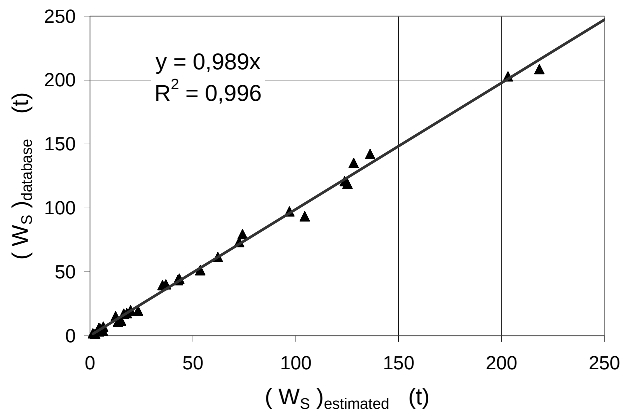

Figure 8. Reproduction of the DB1 structural weight

5.3. PROPULSION WEIGHT MODEL

Propulsion weight is closely related to the propulsion power but general size of the vessel also has some influence. Watson (1998) proposed that engine weight should be separated and the rest of engine room weight estimated separately. In the small craft the propulsion systems are much more variable than is the case with big ships. Rating of the same engine (having practically the same weight) depends on the service type and a number of operating hours per year. Table 11. gives the guide on diesel engine selection suitable for small craft as used by CATERPILLAR.

Table 11. Propulsion engine ratings

Rating	% time at rated power	Service	Rated power time	min h/yr	max h/yr
A	100%	tugs trawlers	12 / 12 hours	5000	8000
B	85%	crew boats supply boats	10 / 12 hours	3000	5000
C	50%	ferries offshore service displ.yachts	6 / 12 hours	2000	4000
D	16%	fast ferry patrol craft naval vessels planing hulls	2 / 12 hours	1000	3000
E	8%	pleasure craft harbor craft pilot boats	1/2 h / 6 hours	250	1000

Weight of dry diesel engine should be increased to compensate for the liquids that are permanently present within the engine in service. The analysis of high performance diesel engines indicated an average ratio of wet to dry engine weight of 1,066.

$$\frac{W_{WET}}{W_{DRY}} \cong 1,066 \qquad (42)$$

Propulsor weight estimates were published in Grubisic and Begovic (2003). Weight of the average propeller, strut and shaft arrangement is estimated by (42).

$$W_{FPP} \cong 1,1 \cdot D_P^3 \cdot \frac{A_E}{A_0} \quad \text{t} \qquad (43)$$

Weight of the SPP installation depends on different setups, equation (44) applies to LDU (Levi Drive Unit) as a representative.

$$W_{SPP} \cong \frac{P_S^{1,271}}{8375} \quad \text{t} \qquad (44)$$

Total weight of the water jet includes entrained water since it is the added weight to be transported by the vessel.

$$W_{WJW} \cong \frac{P_S^{1,286}}{8771} \quad \text{t} \qquad (45)$$

If the engines are not selected at this stage of design, it is possible to estimate weight of the propulsion group W_{200} from the analysis of database (Figure 9.).

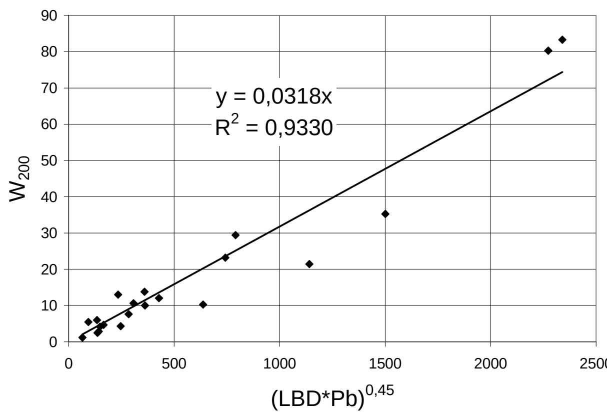

Figure 9. Propulsion machinery weight

$$W_{200} = \frac{\left(L \cdot B \cdot D \cdot \sum P_B\right)^{0,45}}{31,45} \quad \text{t} \qquad (46)$$

$$R^2 = 0,933$$

5.4. ELECTRICAL POWER WEIGHT MODEL

Sometimes the weight of the electrical power group is hidden within engine room weight where it is taken together with propulsion power.

Weight of the electrical power group is highly correlated to the cubic module irrespective of the ship type (Figure 10.).

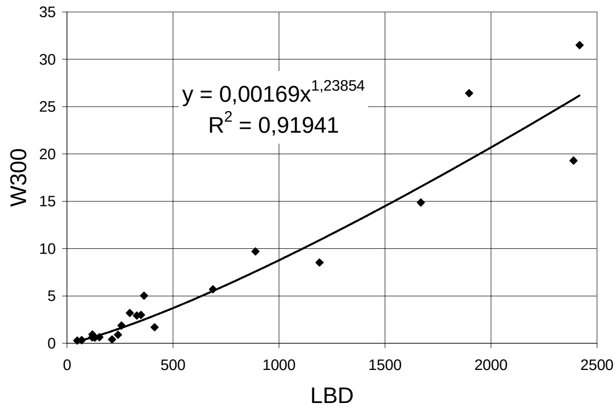

Figure 10. Electrical machinery weight -LBD

$$W_{300} = \frac{(L \cdot B \cdot D)^{1,24}}{592} \quad \text{t} \tag{47}$$
$$R^2 = 0,919$$

If the generator power is known, weight may be found by the relation (48) as shown in Figure 11.

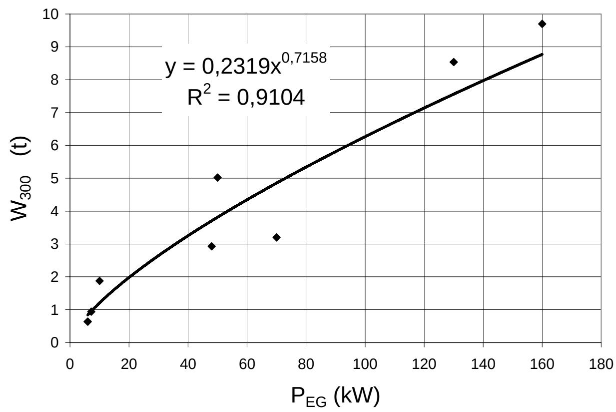

Figure 11. Electrical machinery weight -P_{EG}

$$W_{300} = 0,232 \cdot P_{EG}^{0,716} \quad \text{t} \tag{48}$$
$$R^2 = 0,910$$

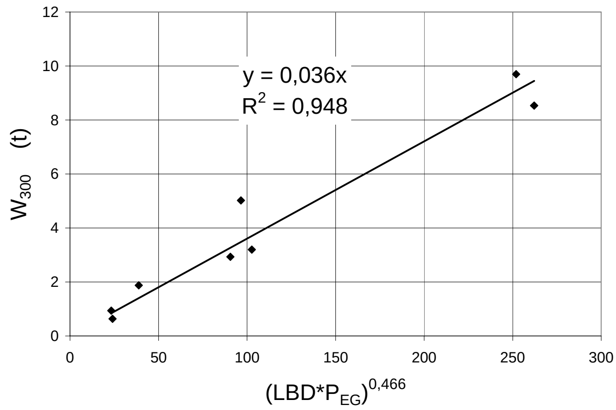

Figure 12. Electrical machinery weight –LBDxP_{EG}

Alternatively, (based on small number of data) electrical machinery weight that takes into account electrical power and size of the ship may be estimated by (49) as shown in Figure 12.

$$W_{300} = 0,036 \cdot \left(L \cdot B \cdot D \cdot \sum P_{EG}\right)^{0,466} \quad \text{t} \tag{49}$$
$$R^2 = 0,948$$

5.5. ELECTRONIC EQUIPMENT WEIGHT MODEL

Electronic equipment is very variable and the rate of development is probably the highest in engineering practice. Besides it reflects the policy of the owner towards accepting new solutions. Database provided limited information (Figure 13. and 14.) that can be useful only at the very beginning:

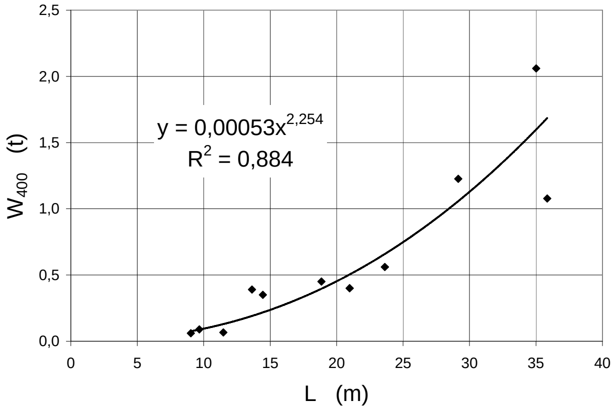

Figure 13. Electronic equipment weight

$$W_{400} = 0,00053 \cdot L^{2,254} \quad \text{t} \tag{50}$$
$$R^2 = 0,884$$

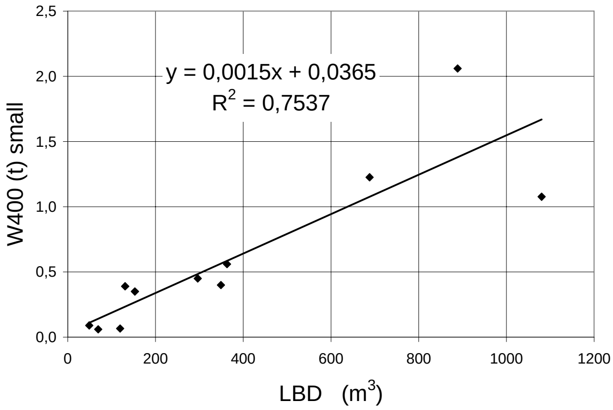

Figure 14. Electronic equipment weight –small vessels

$$W_{400} = 0,0365 + 0,0015 \cdot L \cdot B \cdot D \quad \text{t} \tag{51}$$
$$R^2 = 0,75$$

5.6. AUXILIARY MACHINERY WEIGHT MODEL

Auxiliary machinery systems are correlated with ship size and type but it is very difficult to take into account variability of owners requirements. The best correlation was found as shown in (52) and Figure 15.

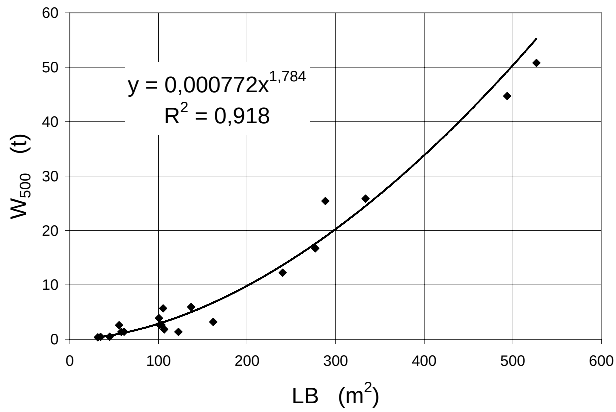

Figure 15. Auxiliary machinery weight

$$W_{500} = 0,000772 \cdot (L \cdot B)^{1,784} \ \text{t} \quad (52)$$
$$R^2 = 0,918$$

5.7. OUTFIT WEIGHT MODEL

Weight of outfit is highly dependent on the equipment standard of the vessel. The best correlation was found relative to the length of the vessel (53) and Figure 16.

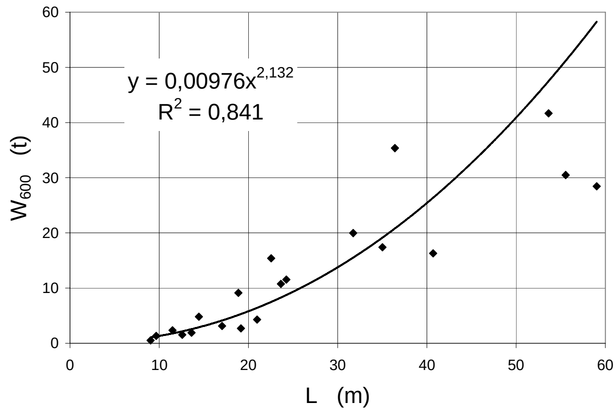

Figure 16. Outfit weight

$$W_{600} = 0,0097 \cdot L^{2,132} \ \text{t} \quad (53)$$
$$R^2 = 0,841$$

5.8. SPECIAL SYSTEMS WEIGHT MODEL

Weight of special systems was originally meant to relate to the armament only, but here we consider that W_{700} means all weight that is specific to the ship main purpose, i.e. passenger equipment for ferries, research equipment for research ships, etc. In principle this group is not meant to cover the equipment that is found on every type of vessel, only the specific weight for the purpose of vessel function. The best correlation was found with ship length as shown in Figure 17.

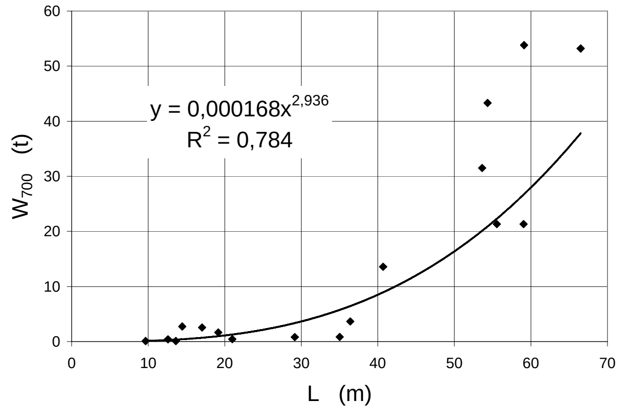

Figure 17. Special systems weight

$$W_{700} = 0,000168 \cdot L^{2,936} \ \text{t} \quad (54)$$
$$R^2 = 0,784$$

Alternatively, the relation from Figure 18. may be used.

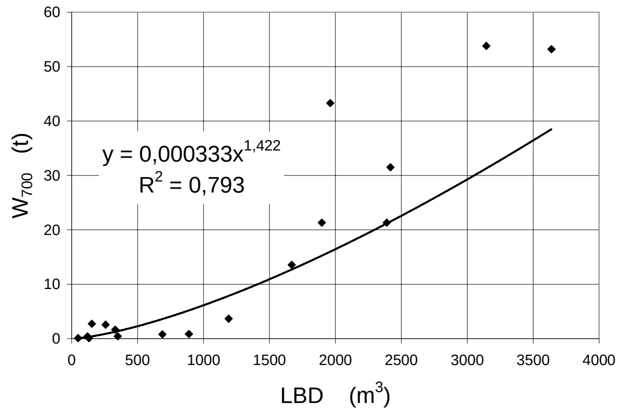

Figure 18. Alternative special systems weight

$$W_{700} = 0,000333 \cdot (L \cdot B \cdot D)^{1,422} \ \text{t} \quad (55)$$
$$R^2 = 0,793$$

5.9. VARIABLE WEIGHTS MODEL

W_{800} comprises all variable weights including payload and all consumables.

Interestingly it was found that the lightship weight is highly correlated to the full load displacement (Figure 19.).

$$W_{FL} = 1,256 \cdot W_{LS} \ \text{t} \quad (56)$$
$$R^2 = 0,995$$

Since the difference consists of the variable weight only, it means that the size of variable weight a fast small vessel can carry (i.e. payload, fuel, consumables etc.) may be pretty accurately estimated (57) or by (58) as soon as the full load displacement is decided upon.

$$W_{800} = 0,204 \cdot W_{FL} \quad \text{t} \tag{57}$$

$$W_{800} = 0,256 \cdot W_{LS} \quad \text{t} \tag{58}$$

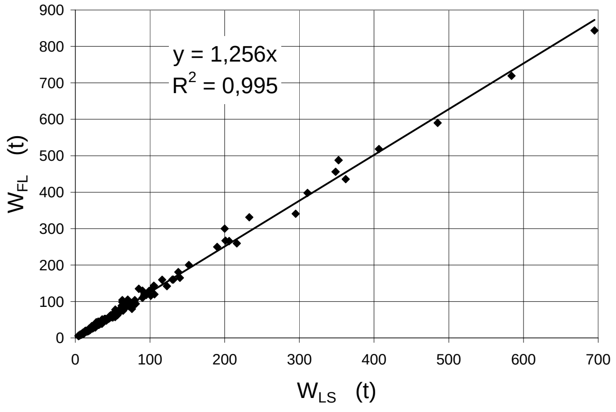

Figure 19. Variable weight

Alternatively the variable weight is related to the LB and LBD respectively, as shown in Figures 20. and 21.

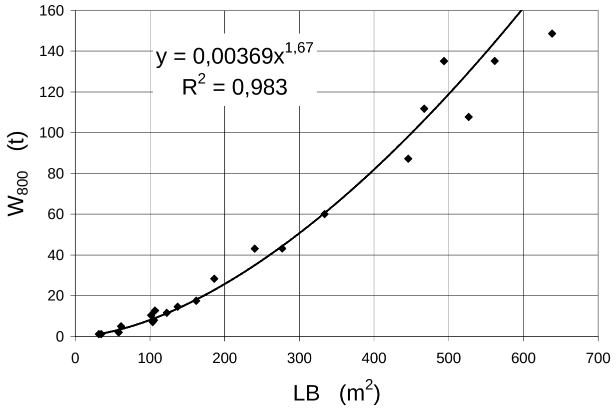

Figure 20. Alternative variable weight

$$W_{800} = 0,00369 \cdot (L \cdot B)^{1,67} \quad \text{t} \tag{59}$$

$$R^2 = 0,983$$

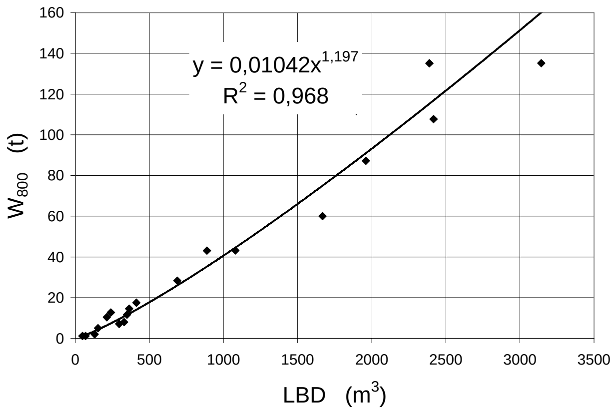

Figure 21. Alternative variable weight

$$W_{800} = 0,01042 \cdot (L \cdot B \cdot D)^{1,197} \quad \text{t} \tag{60}$$

$$R^2 = 0,968$$

5.10. TESTING THE METHOD

For the purpose of testing the method only vessels from the database DB2 are used. After summing up all weights as explained by the regression equations for individual groups there still remains the difference that could not be explained by the relations.

This remaining weight is examined and compared to several ship parameters. The best correlation was found with the full load displacement. Therefore this weight was treated as unknown weight. It can be added to some of the standard weight groups but it can also be treated separately:

$$W_U = 0,036 \cdot W_{FL} \quad \text{t} \tag{61}$$

Therefore, equation for prediction of lightship weight may be rewritten as:

$$W_{LS} = W_{100} + W_{200} + W_{300} + W_{400} + W_{500} + W_{600} + W_{700} + W_U \tag{62}$$

When this predicted lightship weight is subtracted from the recorded lightship weight of the database vessels, the percentage of the remaining unexplained weights (positive and negative) are distributed as shown in Figure 22. while Table 12 contains the statistics of the prediction.

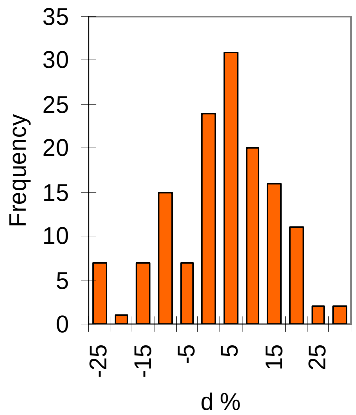

Figure 22. Unexplained weights (%) distribution

Table 12. statistics of the lightship weight prediction

Mean	0,285 %
Standard Error	1,105 %
Standard Deviation	13,22 %
Sample Variance	174,77 %
Confidence Level(95,0%)	2,185
Count	143

The weight prediction of the lightship weight by the proposed method gives predictions with the standard deviation of 13,22 %.

To be on the safe side designer will usually add reserve weight that amounts to one standard deviation. Margin policy will be treated in sequel.

6. WEIGHT MARGINS AND RELIABILITY

6.1. MARGINS

Weight estimating is not an exact procedure. Therefore a wise addition of a margin is necessary. There are several kinds of margins that apply and for different reasons:

- Margin to cover unreliable initial data
- Margin to compensate error of the weight prediction method
- Margin that covers expected but unintentional growth of weight in the future (applies to all ships)
- Margin that will be used in the future when upgrading some systems and when new generation of technology will become available (usually for naval craft)

The first two margins will change while the design is developed from the concept phase to the final design and actually building the vessel. More data and more reliable data will become available as the design develops. There will be less space for errors to creep in the weight prediction. More detailed methods for weight prediction will be used and it will lead to the additional reduction of margins.

The second two margins are usually decided in advance when design requirements are made and will not be treated here.

Margins for the structural weight are also dependent on the structural material.

- Steel structures are subject to variability of thickness due to the mill tolerance and due to the corrosion treatment applied.
- Composite structures weight is variable depending on the technology applied, i.e. hand layup, vacuum bagging, infusion, ..etc. Fiber content in the laminate will vary depending on the work force training and on the quality control of the process. Variable overlapping of composite layers and variability of materials are also present.

At the concept design level margins are necessarily high, since the level of insecurity is high and reducing them will often result in repeating the design from the scratch when insufficient buoyancy would lead to cutting off some of essential deadweight and, therefore, make the design infeasible.

Tentatively, margins at the concept design level may be estimated from Table 13.

Table 13. Tentative margins by weight groups

	WEIGHT ELEMENT	MARGIN
M_{100}	Steel structure	12%
M_{100}	Aluminum structure	10%
M_{100}	Composite structure	15%
M_{200}	Propulsion system	10%
M_{300}	Electrical power system	10%
M_{400}	Electronic systems	50%
M_{500}	Auxiliary systems	10%
M_{600}	Outfit	12%
M_{700}	Special systems	5%
M_{800}	Deadweight	6%

Assuming that margin is related to the uncertainty that is quantified by a standard deviation, it is reasonable to add a margin of one standard deviation to the mean value. Finding standard deviation requires a database of previous cases. If there is not sufficient previous knowledge it is possible to use subjective method as borrowed from the operations research.

If two estimates of the respective weight are made:

W_{MAX} -Pessimistic weight prediction
W_{MIN} -Optimistic weight prediction

Standard deviation is predicted by the expression:

$$\sigma = \frac{W_{MAX} - W_{MIN}}{5} \quad (63)$$

6.2. RELIABILITY

Dividing weight into several groups reduces the uncertainty of the light ship prediction as a whole.

An example calculation in Table 14. shows the advantage of using several groups instead of only one.

Table 14. Margins by weight groups

	W_{MEAN}	σ	W_{MARGIN}	W_{TOTAL}
Lightship	83,0	10%	8,3	91,3
Hull	40,0	10%	4,0	44,0
Power	25,0	10%	2,5	27,5
Outfit	18,0	10%	1,8	19,8
Lightship	83,0	6,083%	5,049	88,049

Standard deviation of a whole is related to the standard deviations of components as defined by (64)

$$\sigma = \sqrt{\sigma_1^2 + \sigma_2^2 + \sigma_3^2} \quad (64)$$

For the example case it means:

$$W_M = \sqrt{4,0^2 + 2,5^2 + 1,8^2} = \sqrt{25,49} = 5,049 \text{ t}$$

Therefore:

$$\sigma_M = 6,083$$

It means that by dividing the lightship weight into three groups and estimating each of them with the same standard deviation, the reliability of lightship weight prediction is improved from 10% to 6,083%

Obviously, every further division, i.e. increasing *n*, brings less improvement as defined by the equation:

$$\sigma_M = \frac{\sigma_0}{\sqrt{n}} \tag{65}$$

7. CONCLUSIONS AND PROPOSALS

7.1. CONCLUSIONS

- The proposed method of lightship weight prediction gives acceptable results for the concept design stage.
- Standard deviation of the prediction is about 13% and it is expected that further reduction will be possible by different treatment of some component weights.
- The method is sensitive to hull structural material variation, takes care of the service area and service type. It makes the method suitable for inclusion in the concept design model that will be used in the optimization procedure.

7.2. PROPOSALS FOR FUTURE WORK

- Obviously, weight data are scarce and the quest for increasing database is a permanent occupation of designer. In that respect all information is welcome.
- The weight of superstructures is at present not treated adequately since it is hidden within structural weight. Implicitly it is assumed that all vessels have an average proportions of the superstructures. This is obviously not the case. Future work will include collecting data on the superstructure and some rearrangement of equations for structural weight prediction.
- Weight of individual propulsion engines together with gearboxes, transmission and propulsors should be collected with more precision in order to split the machinery weight into propulsion engines and the rest of engine room weight. It is expected that accuracy will be improved.

NOMENCLATURE:

B_X	Waterplane beam at max. section (m)
B_M	Maximal molded beam (m)
C_B	Block coefficient
D_P	Propeller diameter (m)
D_X	Hull depth amidships (m)
GT	Gross tonnage
$H_{1/3}$	Significant wave height (m)
L_{OA}	Length over all (excluding extensions) (m)
L_{WL}	Length on water line (m)
M	Margin (%)
P	Engine power (kW)
S	Surface area (m^2)
Δ	Full load displacement (t)
∇	Displacement volume (m^3)
W	Weight in general (t)

REFERENCES

1. WATSON, D. G. M., and GILFILLAN, A. W., “Some Ship Design Methods”, *Transactions RINA*, Vol. 119, 1977.
2. WATSON, D. G. M., "Practical Ship Design", Elsevier Science & Technology Books, 1998
3. SCHNEEKLUTH and BERTRAM, "Ship Design for Efficiency and Economy", Butterworth-Hainemann, 1998
4. PARSONS, M., G., “Parametric Design, in Ship Design and Construction”, Edited by Lamb, T., *The Society of Naval Architects and Marine Engineers*, New Jersey, pp 11-1 to 11-48, 2003.
5. BAS engineering, "The Ship Weight concept", www.**shipweight**.com/download/swbackground.doc
6. KARAYANIS, T., MOLLAND, A. and SARAC-WILLIAMS, "Design Data for High-Speed Vessels", FAST 1999, Seattle, p.p. 605-615
7. GRUBISIC, I. et al., "Study of the Development of the Maritime Administration Fleet", Ministry of Maritime Affairs (in Croatian), Zagreb, 1999.
8. LLOYD'S REGISTER, "Rules and Regulations for the Classification of Special Service Craft", London, 1996.
9. GRUBISIC, I. and BEGOVIC, E., "Multi-Attribute Concept Design Model of Patrol, Rescue and Antiterrorist Craft", FAST 2003
10. CATERPILLAR Application Guidelines for Marine Propulsion Engines, http://www.cat.com/cda/layout?m=37601&x=7

AN OPTIMIZATION PROCEDURE FOR THE PRELIMINARY DESIGN OF HIGH-SPEED RORO-PASSENGER SHIPS

Sotirios Skoupas, National Technical University of Athens, Greece
George Zaraphonitis, National Technical University of Athens, Greece

SUMMARY

An integrated methodology for the preliminary design and optimization of high-speed monohull ROPAX vessels is presented. The core of the developed procedure encompasses the parametric design of ROPAX vessels, based on a selected set of design parameters. Suitable macros have been developed for the design of the vessel's hull form, internal layout and hull structure. Additional modules are developed to perform relevant calculations for the evaluation of the design, namely the preliminary evaluation of weights, stability in intact and damaged condition, powering and finally for the economic assessment of the resulting designs. The parametric ship design application has been linked with an optimization software, facilitating the design space exploration in a rational and efficient way. Results from the application of the above procedure to the preliminary design and optimization of two high-speed ROPAX vessels are presented and discussed.

1. INTRODUCTION

During the preliminary Ship Design phase, important decisions with significant impact on the vessel's performance have to be made by the designer, usually based on very limited information. In such cases, the designer has to rely on his experience and engineering judgement, occasionally supported by the exploration of relevant data from past designs. An integrated design and optimization methodology, facilitating the fast exploration of a series of design alternatives would be of great assistance to the designer, in search of the 'optimum' solution subject to specific owner's requirements.

The application of optimization methods in ship design is not new. The work of Leopold (1) and Mandel et al. (2) and (3) goes back to mid sixties and early seventies. In recent years, optimization methods are increasingly used in various ship design tasks, such as in the hull form optimization, in association with advanced CFD software tools. Harries et al. in (4) apply parametric hull modelling techniques along with CFD tools and formal optimization methods for the design of minimal wave resistance hullforms. Most design problems involve multiple objectives, which quite often are mutually conflicting. This type of problems is in principle not tractable with the 'conventional', single-objective optimization methods, unless a reformulation is introduced, some times based on crude assumptions and simplifications. Alternatively, this type of design problems could be formulated and treated as a typical multiple criteria optimization problems, as discussed by Sen in (5) and (6). A multicriteria optimization model for the design of Containerships is discussed by Ray et al. in (7). Hutchinson et al. (8) apply the Genetic Algorithm method for the optimization of RO-RO Passenger Ferries, based on the probabilistic stability standards. Brown et al. (9) apply the Multiattribute Value Theory (MAVT) and the Analytical Hierarchy Process (AHP) to synthesize an 'effectiveness function' for the evaluation of naval ships. The Genetic Algorithm method is subsequently used to search the design parameter space.

An integrated methodology for the preliminary design, evaluation and optimization of conventional ROPAX vessels, has been presented in (10). The extension of this work for the preliminary design and optimization of high-speed monohull ROPAX vessels is presented in the following. The developed methodology has been applied for the design and optimization of a series of vessels of various sizes on selected routes, connecting Greek islands with the mainland. Typical results from these studies are presented and discussed.

2. NOMENCLATURE

AC	Vessel's acquisition cost
B_{OA}	Beam over all
B_{WL}	Beam at water line
C_B	Block coefficient
C_R	Residual resistance coefficient
D	Depth
DWT	Dead Weight
FB	Free Board
GM	Metacentric Height
GM_{cr}	GM critical
GM_m	GM margin, above regulatory requirements
g	Gravitational acceleration
LCB	Longitudinal Centre of Buoyancy
L_{OA}	Length over all
L_{BP}	Length between perpendiculars
L_{WL}	Length at waterline
NPV	Net Present Value index
RFR	Required Freight Rate
R_T	Total resistance
T_D	Design draught
T_R	Roll eigenperiod
V_S	Service speed in kn
Δ	Displacement
η	Water jet propulsion efficiency
τ	Running trim

3. PARAMETRIC DESIGN OF ROPAX VESSELS

An integrated methodology for the parametric design of high-speed monohull ROPAX vessels has been developed within the well known commercial ship design software NAPA (11), taking advantage of the programming capabilities of the NAPA macro language. The vessel's hull form and internal layout are generated automatically by a series of NAPA macros, followed by a preliminary structural design. Subsequently, suitable macros or external software codes are called to perform the assessment of the technical, operational and economic performance of each design. The basic tasks of the developed parametric design methodology are:

1. Hull form development
2. Resistance and propulsion estimations
3. Development of internal layout
4. Preliminary structural design
5. Weights estimation
6. Intact and damaged stability calculations
7. Assessment of economic performance

A brief description of the above tasks is presented in the following.

3.1 Hull form development

A set of Napa macros has been developed to facilitate the automatic development of the vessel's external surface, based on two parent hulls forms: The first one is derived from the parent hull of the NTUA high-speed, Deep-V, double chine systematic series, presented in (12). The second alternative is a round-bilge hullform, derived from the well known NPL series (13). Each hullform is derived from the corresponding prototype, according to the user's selection (either double-chine or round bilge), applying a linear transformation based on the specified principal dimensions. The cross-sections of a typical Deep-V, double chine hull with L_{WL}/B_{WL}=5.917 and B_{WL}/T_D=5.13 derived by the developed Napa macros is presented in Figure 1. The cross-sections of a round bilge hull with L_{WL}/B_{WL}=6.142 and B_{WL}/T_D=2.954 derived from the NPL series is presented in Figure 2.

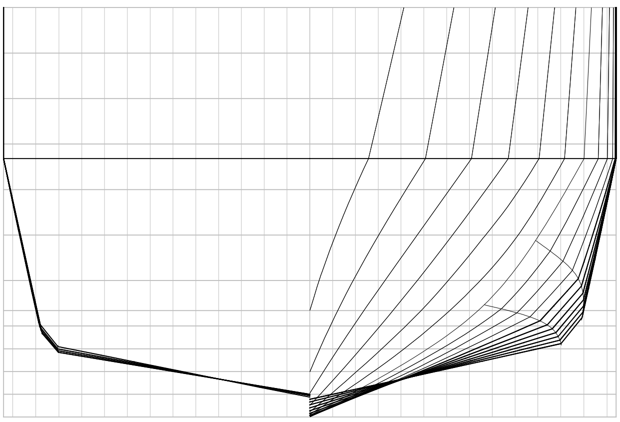

Figure 1. Body plan of a Deep-V, double chine vessel

Since a linear transformation has no effect on the form coefficients, all hard-chine vessels created by the present application have a block coefficient equal to 0.395, with their centre of buoyancy located at 0.382L_{WL} from the transom. The corresponding values for the round bilge hulls are C_B=0.397 and LCB=0.436L_{WL}.

3.2 Resistance and propulsion estimations

For the Deep-V, double chine vessels, estimations are based on the decomposition of total resistance in a frictional and a residual component. The corresponding frictional resistance coefficient is calculated applying the ITTC empirical formula. The residual resistance coefficient is calculated by a polynomial expression presented in (14), derived from the regression analysis of experimental measurements:

$$10^3 C_R = \sum_{i=1}^{31} \alpha_i x_i \qquad (1)$$

The variables x_i, appearing in equation (1) are functions of the vessel's main particulars. Expressions for their calculation, along with the values of the α_i, coefficients are given in (14). Similar expressions are also given for the calculation of the vessel's running trim:

$$\tau = \sum_{i=1}^{31} b_i x_i \qquad (2)$$

For the round bilge hulls, the total resistance is calculated directly, by a polynomial expression of the form:

$$\frac{R_T}{g\Delta} = \alpha_0 + \sum_{i=1}^{27} \alpha_i x_i \qquad (3)$$

The expressions for the calculation of the variables x_i and for the coefficients a_i appearing in equation (3) are given by Radojcic et al. in (15). The vessel's running trim is calculated using expressions in the form of equation (2), also given in (15).

For water-jet propelled vessels, the required propulsion power estimation is based on empirical expressions for the calculation of the overall propulsion efficiency (e.g. equation (4) from (16)):

$$\eta = aV^3 + bV^2 + cV + d \qquad (4)$$

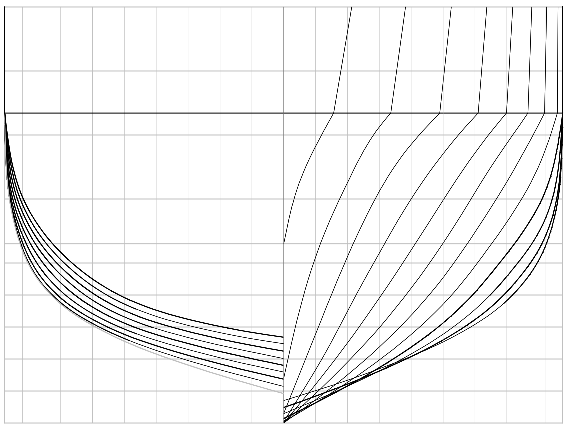

Figure 2. Body plan of a round bilge NPL vessel

where V is the vessel's speed in [kn] and

a = 2.963e-19
b = -0.0003
c = 0.0295
d = -0.0250

The resulting propulsion power is increased by a suitable power margin to derive the required propulsion engines maximum continuous rating.

3.3 Development of the internal layout

The development of the vessel's internal layout starts with the definition the watertight subdivision bellow the main vehicles deck. The first step consists of the definition of the bulkhead deck, the strength deck, the double bottom and the remaining vehicles decks, according to the particular design characteristics. The double bottom height is accordingly defined to ensure effective protection in the event of racking damage, as defined in Chapter 2, Regulation 2.6 of the HSC Code. In the second step, the size and position of the main engines rooms and the pump room is determined from the installed propulsion power, using suitable empirical expressions, derived from existing vessels. Subsequently, the transverse watertight bulkheads, forward of the engine room are automatically positioned.

The user has limited control on the resulting compartmentation, mainly by overriding the default values of the relevant design parameters. The number of car decks is either defined by the user, or is internally calculated according to the required private cars transport capacity. In the former case, the private cars transport capacity is calculated by the design software, while in the later case it is treated as a design parameter. Alternative layouts with central or side casings may be specified by the user. A number of upper decks are then created to provide the required accommodation and public space areas. Once again, the number of accommodation decks may be either defined by the user, in which case the design software calculates the resulting passengers transport capacity, or may be calculated according to the required number of passengers. A typical General Arrangement of a relatively large vessel (L_{OA}=135.6m, L_{WL}=119.5m, B_{OA}=20.7m, T_D=2.8m), developed by the parametric design software is presented in Figure 3. This vessel, with a transport capacity of 1600 passengers, 385 private cars, or 4 trucks and 290 private cars, has a main car deck of ample height and strength for the carriage of 30t trucks, an upper car deck of reduced height for the carriage of private cars and two superstructure decks for the passenger spaces and the crew accommodation.

3.4 Preliminary structural design

The preliminary structural design is performed by a set of Napa macros, developed for the calculation of the required plate thickness, along with the section modulus and other cross-sectional characteristics of the attached primary and secondary stiffeners. Calculations are performed applying the Det Norske Veritas rules for the Classification of High-Speed Craft (17). The ship is longitudinally subdivided in a number of sections, between successive transverse bulkheads. The sections are vertically subdivided in sub-sections between successive decks up to the strength deck, above which the superstructures sub-sections are defined. The construction material is selected by the user. The available options include construction of the entire vessel from high tensile steel or aluminum alloys, or the partial use of HTS grades for the hull, up to a deck defined by the user (either the subdivision deck, or the top of the upper vehicles deck, herein considered as the strength deck), combined with aluminum superstructure.

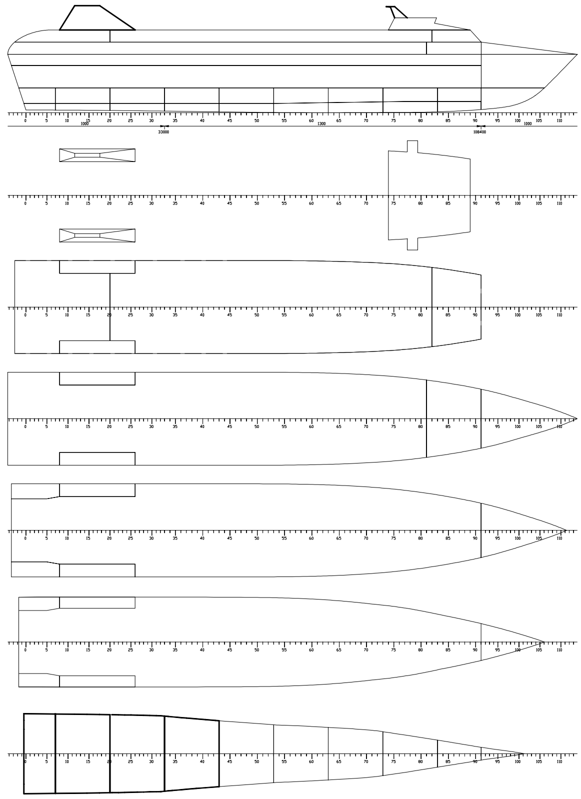

Figure 3. General Arrangement of a ROPAX vessel

Following the definition of the geometry of the various parts of the ship structure, the local loading calculations are performed and the maximum allowable stresses for the local strength analysis are determined according to the Class rules. The required thickness for the plates along with the section modulus and other cross-sectional characteristics of the attached stiffeners are subsequently calculated. Based on the above requirements, the selection of structural members is finalized, with an appropriate corrosion thickness allowance. Secondary stiffeners, minimising the combined plate-stiffener weight, are selected from a data base. For the primary stiffeners, built-up cross sections, minimising steel weight, while satisfying all the structural requirements and geometric constraints are evaluated.

Based on the results of the preliminary structural analysis module, a detailed structural arrangement is created within the NAPA environment. Following a bottom-up procedure, the plate elements with the attached stiffeners are combined to form planar or curved panels. The elementary panels are grouped together to form sub-arrangements corresponding to larger parts of the outer shell, entire decks and bulkheads. The sub-arrangements are then combined to create the structural arrangement of the entire steel structure (Figure 4). Based on the definition of the structural arrangement, the attained section modulus amidships is calculated, using standard tools available within the Napa Steel module. Compliance with the Class requirements with respect to vertical bending in calm waters and in waves is verified. If the attained section modulus is less than the required, the bottom and strength deck scantlings are accordingly increased and the procedure is repeated.

3.5 Weights estimation

The vessel's light weight is divided in the following basic weight categories: structural, propulsion, auxiliary, deck machinery and outfitting, electrical, piping, heating and air-conditioning, accommodation and miscellaneous. With the vessel's detailed structural arrangement readily available, the structural weight is obtained by direct calculation. Machinery weight is further divided in sub-items (main engines, gear-boxes, shafting, water-jets). The remaining basic weight categories are also further divided in sub-items and relevant expressions have been developed for the estimation of the corresponding weights and weight centres. The results of the above procedure have been compared with available data from a number of existing vessels and appropriate correction coefficients have been derived. Payload is determined, subtracting the light weight and the various DWT items (consumables, provisions, stores etc.) from the vessel's displacement.

3.6 Intact and damaged stability calculations

Stability calculations are performed for the vessel in intact and damaged condition (both for side damage and bottom racking) to verify compliance with the requirements of the 2000 High-Speed Craft Code (18). A series of macros has been prepared to control the process flow, while the actual stability analysis is performed using the calculation capabilities provided by the NAPA software. Calculations are performed for a predetermined range of initial draughts at zero trim and also for specific loading cases, with 100% passengers and variable vehicles loadings, both in the departure and arrival condition. The selected vehicles loadings correspond to:

a. private cars loading at 100%, 30% and 0% of the vessel's total capacity without trucks and
b. for the ships with truck carrying capacity, the specified number of trucks, combined with 100%, 30% and 0% of the remaining private cars capacity.

3.7 Assessment of economic performance

Building and operating costs are decomposed in major items and sub-items and suitable expressions have been derived for their calculation. Crew synthesis and the corresponding crew costs are determined according to the Greek statutory regulations. The annual income is calculated for the particular service conditions specified by the user. Based on these calculations, the vessel's economic performance is assessed using appropriate economic indices, such as the Required Freight Rate, or the Net Present Value. These are complex criteria, encompassing in a rational way the building and operating costs as well as the annual revenues. Transport capacity and propulsion power are therefore accounted, via the annual income, the fuel costs and the acquisition cost of the propulsion plant.

4. OPTIMIZATION ENVIRONMENT

The developed parametric design software has been linked to a commercial multi-objective optimisation code, namely modeFRONTIER (19), to form an integrated design and optimization environment. The method of Genetic Algorithms was selected as the most suitable choice for the specific problem, for its inherent capability to deal with multi-objective optimisation problems with mixed continuous-discrete variables and discontinuous and non-convex design spaces.

4.1 Objective functions

The objective functions, available to the user are of economic or technical type. Building and operational costs and annual revenue may be used. Other economic criteria, such as the Required Freight Rate (*RFR*) or the Net Present Value (*NPV*) however are considered more suitable, revealing the vessel's economic performance on a selected route in a more rational way. Propulsion power can be used as an objective function, although its effect is indirectly accounted in the *RFR* and the *NPV*.

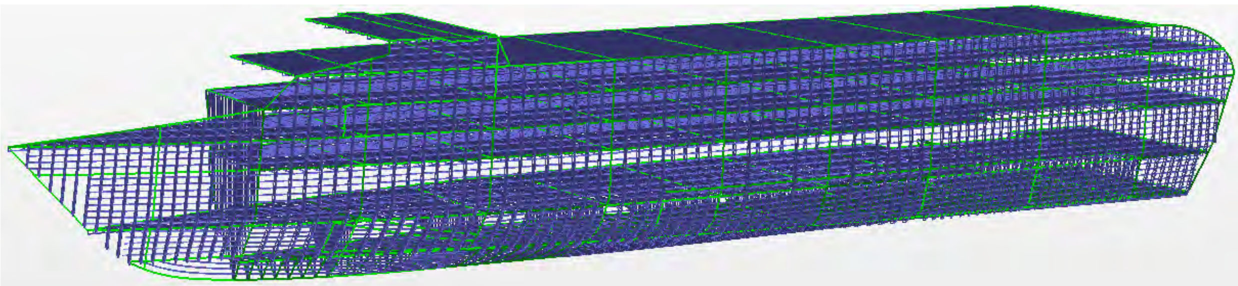

Figure 4. Structural Arrangement of a typical high speed ROPAX vessel

The maximization of stability reserve, in excess of the regulatory requirements may be also used as objective function. An alternative and more conventional approach would be to treat stability as a constraint, instead of an objective function, by requiring the fulfilment of the regulatory requirements, preferably with a small safety margin, to account for the possibility of an underestimation of the light ship's centre of gravity height.

Seakeeping performance is also an important issue, especially for high-speed passenger vessels; therefore appropriate links have been established between the design environment and a seakeeping software, enabling its use for the assessment of the vessel's response in a seaway. Once again, the user has the choice of treating seakeeping performance as a constraint instead of an objective function, specifying acceptable limits regarding the vessel's performance (motions, accelerations or sea-sickness index) in specific sea-states. Other objective functions can also be used if required, since the design software architecture is quite flexible.

4.2 Demonstration studies

The developed methodology has been applied to the design and optimization of a series of high-speed ROPAX vessels of various sizes and on selected routes, between a number of Aegean islands and the Greek mainland. In the following, two examples of the obtained results are presented and briefly discussed.

The first example corresponds to an optimization exercise for a relatively large vessel, operating between the port of Piraeus and the island of Naxos in the central Aegean Archipelagos (Figure 5). The length of the route is 125sea miles. With a required service speed of 40kn the time at sea for a one-way trip is around 190min. The upper and lower bounds for the vessel's main particulars are presented in Table 1.

Figure 5. Studied routes

Instead of requiring a specific transport capacity in terms of passengers and private cars, the number of decks has been given (i.e. two vehicles decks and two passenger decks). The actual transport capacity of each design alternative is calculated by the design software, based on the available deck area and the vessel's load carrying capacity, with an additional requirement of four trucks capacity with an average weight of 30t (an average number of two trucks per one-way trip was used for the calculation of the vessel's revenue). A minimum metacentric height margin $GM_m \geq 0.30$m, above the requirements of the intact and damaged stability regulations has been specified. The calculation of the Net Present Value index has been performed for an average fare of 50€ per passenger, and a freight rate of 75€ for the private cars and 165€ for the trucks. The Required Freight Rate calculations were performed for a standard ratio of the private cars freight rate to the passenger's fare equal to 1.5. The trucks to private cars freight rate ratio was equal to 2.2.

Table 1. Vessel's main particulars and operating requirements for the Piraeus-Naxos route

Main Particulars		From	To
L_{BP}	[m]	100.0	120.0
B_{OA}	[m]	18.0	20.0
T_D	[m]	2.5	3.5
FB	[m]	2.5	3.5

The optimization exercise has been performed for the following objective functions:

a. minimization of the Required Freight Rate and

b. maximization of the attained stability margin in excess of the requirements of the intact and damaged stability regulations.

The second example corresponds to a smaller vessel, operating between the port of Rafina, 27km east of Athens and the island of Andros (Figure 5). The length of the route is 45 sea miles. With a required service speed of 35kn the time at sea for a one-way trip is around 90min. The upper and lower bounds for the vessel's main particulars are presented in Table 2. A transport capacity of 750 passengers has been defined. Instead of specifying the private cars transport capacity, the number of car decks has been given (i.e. two vehicles decks) and the actual transport capacity of each design is calculated by the design software. In this case also, a minimum metacentric height margin $GM_m \geq 0.30$m has been specified. The *NPV* calculations have been based on an average fare of 30€ per passenger and a freight rate of 48€ for the private cars. The *RFR* calculations were carried out assuming a standard ratio of the private cars freight rate to the passenger's fare equal to 1.6.

Table 2. Vessel's main particulars and operating requirements for the Rafina-Andros route

Main Particulars		From	To
L_{BP}	[m]	75.0	95.0
B_{OA}	[m]	16.0	18.00
T_D	[m]	2.0	3.0
FB	[m]	2.5	3.5

In this case a different formulation of the optimization problem has been selected: In order to improve performance in beam and quartering seas, vessels with relatively large roll eigenperiod were searched for. An approximation of the roll eigenperiod was obtained according to the IMO Resolution A-749(18) by the following expression:

$$T_R = \frac{2C \cdot B_{OA}}{\sqrt{GM}} \quad (5)$$

where:

$$C = 0.373 + 0.023\frac{B_{OA}}{T} - 0.043\frac{L_{WL}}{100} \quad (6)$$

Therefore the second optimization exercise has been performed for the following objective functions:

a. the minimization of the Required Freight Rate and
b. the maximization of the roll eigenperiod.

In both studies the vessels have been considered operating for 12 years. The price of each vessel at the end of the 12 years period was set at 33% of the corresponding acquisition cost. A 50% loan with a 7% interest and a ten years payback period has been considered for both studies. The discount rate was set at 8%, while a 40% tax rate was assumed. The Fuel and Diesel oil prices were set at 600€/t and1250€/t respectively.Some additional assumptions regarding the seasonal conditions for the two routes are summarized in Table 3 and Table 4.

Table 3. Seasonal conditions (Piraeus – Naxos route)

Season	High	Medium	Low
Months per year	3	3	5
Round trips per day	2	1	1
Passengers loading	70%	40%	20%
Private cars loading	70%	20%	10%
Trucks number	2	2	2

Table 4. Seasonal conditions (Rafina – Andros route)

Season	High	Medium	Low
Months per year	3	3	5
Round trips per day	3	2	1
Passengers loading	70%	30%	15%
Private cars loading	70%	20%	10%

In both studies the vessel's hullform was derived from the Deep-V, double chine, NTUA systematic series. The 5083 aluminum alloy was selected as the construction material both for the main hull and the superstructures.

The Multiple Objectives Genetic Algorithm optimisation scheduler of *modeFRONTIER* has been applied for the optimisation studies. Using the Steady-state GA algorithm MOGA, 120 generations were derived with a population of 20 designs per generation. The genetic operations were executed with a 5% probability of selection, 50% probability of directional crossover, 10% probability of mutation, 10% DNA string mutation ratio and penalize objectives for treating constraints.

Results from the first optimization example are presented in the following.

Table 5 summarises the main characteristics of the designs that meet the Pareto optimality: A design is Pareto optimal if it satisfies the constraints and is such that no criterion can be further improved without causing at least one of the other criteria to decline. The main characteristics of the 15 feasible designs with the smaller *RFR* value are presented in Table 6. The attained *RFR* of the feasible designs varies from 39.20€ to 66.75€, while their *GM* margin varies from 0.322m to 2.121m. The design minimising *RFR* is found in the 47th generation. Alternative designs of almost equally low *RFR* where identified however quite earlier (e.g. the design 222 in the 12th generation, with an *RFR* of 40.33€, or the design 371 in the 19th generation with an *RFR* of 39.46€). Figure 6 presents the history diagram of the attained *RFR* for the first 40 generations. The circles correspond to the feasible designs, while the triangles to the unfeasible ones (i.e. those failing to satisfy at least one of the specified constraints). Figure 7 presents the history chart of the attained *GM* margin of the first 40 generations. In the first generations a number of unfeasible designs may be observed, some of them with negative *GM* margin (i.e. designs not meeting the stability requirements) and others with GM_m<0.3m (the minimum acceptable *GM* margin was set at 0.3m). After some generations however, the unfeasible designs practically disappear and high values of the *GM* margin are obtained. Figure 8 presents the scatter diagram of the *GM* margin versus *RFR*. The Pareto designs are highlighted. The scatter diagram of the *RFR* vs. the Installed Propulsion Power is presented in Figure 9. The corresponding diagram of the *RFR* vs. the vessel's Acquisition Cost is presented in Figure 10. Finally, the scatter diagrams of *RFR* vs. L_{BP} and B_{OA} are presented in Figure 11 and Figure 12 respectively and that of GM_m vs. B_{OA} in Figure 13.

Table 7summarises the main characteristics of the obtained Pareto designs from the second design exercise (the Rafina-Andros route). The main characteristics of the 120 feasible designs with the smaller *RFR* value are presented in Table 8. The attained *RFR* of the feasible designs varies from 24.40€ to 44.78€, while their *GM* margin varies from 0.303m to 1.614m. The design minimising *RFR* is found in the 43th generation. Alternative designs of almost equally low *RFR* where identified in the 5th generation (design number 83 with *RFR*=24.87€), or in the 15th generation (design number 297 with *RFR*=24.58€). Figure 14 presents the history diagram of the attained *RFR* for the first 60 generations. The circles correspond to the feasible designs, while the triangles to the unfeasible ones (i.e. those failing to satisfy at least one of the specified constraints). Figure 15 presents the history chart of the attained roll eigenperiod. Figure 16 presents the scatter diagram of the roll eigenperiod versus *RFR*. The Pareto designs are highlighted. The scatter diagram of the *RFR* vs. the Installed Propulsion Power is presented in Figure 17. The corresponding diagram of the *RFR* vs. the vessel's Acquisition Cost is presented in Figure 18. Finally, the scatter diagrams of *RFR* vs. L_{BP} and B_{OA} are presented in Figure 19 and Figure 20 respectively and that of the attained roll eigenperiod vs. B_{OA} in Figure 21.

After the Pareto Front is obtained, a multiple criteria ranking is applied to capture the preferences of the decision maker. The decision maker is asked to compare pairwise a collection of design attributes. Using these preferences a set of step-wise marginal utility functions is derived analytically for all the attributes of a design. The marginal utility functions are then combined to form a composite fitness function used by multi-objective GA. Following the above multi objective decision making procedure, the design number 1129 with *RFR*=25.18€ and T_R=7.07sec has been identified as the preferable solution.

5. CONCLUSIONS

An integrated methodology for the preliminary design, evaluation and optimization of high-speed ROPAX vessels has been presented. The core of the developed procedure encompasses the parametric design of ROPAX vessels within the commercial ship design software NAPA, based on a selected set of design parameters. Suitable macros have been developed for the design of the vessel's hull form, the development of the internal layout and the preliminary structural design evaluation. Additional modules perform relevant calculations for the evaluation of each design alternative, including stability analysis in intact and damaged condition, powering, weights and transport capacity estimation and finally for the assessment of the economic potential of the vessel in a selected route. All these modules are integrated in a design environment facilitating the investigation of various design alternatives in very short time. The parametric design and evaluation of a relatively large vessel (L_{WL}≈120m) takes approximately 100sec in a personal computer with an Intel® Core™ 2 CPU 6600 processor at 2.4GHz. The most time consuming tasks are the preliminary structural design, requiring approximately 75sec and the damaged stability analysis, with approximately 15sec.

To further increase the effectiveness of the developed procedure, the parametric ship design application has been linked to a commercial multi-objective optimization software (i.e. mode FRONTIER), facilitating the design space exploration in a rational and efficient way. To demonstrate its potential, the developed design methodology has been applied for a series of design and optimization studies. Results from the optimization of two high-speed ROPAX vessels were presented and discussed.

6. ACKNOWLEDGMENTS

Mr Skoupas contribution to the present work has been partially supported by the Greek State Scholarships Foundation (IKY).

7. REFERENCES

1. Leopold, R., 'Mathematical Optimization Methods Applied to Ship Design', MIT, Department of Naval Architecture and Marine Engineering, Report 65-8.
2. Mandel, P. and Leopold, R., 'Optimization Methods Applied to Ship Design', SNAME Transactions, vol. 74, 1966.
3. Mandel, P. and Chryssostomidis, C., 'A Design Methodology for Ships and Other Complex Systems', Philosophical Transactions, Royal Society of London, A273, 1972.
4. Harries, S. and Abt, C., 'Formal Hydrodynamic Optimization of a Fast Monohull on the Basis of Parametric Hull Design', Proceedings of the 5th International Conference on Fast Sea Transportation – FAST '99, Seattle, USA, 31 Aug.-2 Sept. 1999.
5. Sen, P., 'Marine Design: the Multiple Criteria Approach', Transactions of the Royal Institution of Naval Architects, vol. 134, Part B, pp 261-276, 1992.
6. Sen, P. and Yang, J.B., 'Multiple Criteria decision Support in Engineering Design', Springer-Verlag London, ISBN: 3540199322, 1998.
7. Ray, T. and Sha, O.P., 'Multicriteria Optimization Model for a Containership Design', Marine Technology, vol. 31, no. 4, 1994.
8. Hutchinson, K.W., Sen, P., Buxton, I.L. and Hills, W., 'Multiple Criteria Design Optimisation of RO-RO Passenger Ferries with Consideration of recently proposed Probabilistic Stability Standards', The 7th International Symposium on Practical Design of Ships and Mobile Units, PRADS '98, The Hague, The Netherlands, 20-25 Sept. 1998.
9. Brown, A.J. and Thomas, M., 'Reengineering the Naval Ship Concept Design Process', Research to Reality in Ship Systems Engineering Symposium, ASNE, Sep. 1998.
10. Zaraphonitis, G., Papanikolaou, A., Loukakis, T., Tsouvalis, N., Skoupas, S., Mitsotakis, K. and Antoniou, A., 'Development and demonstration of an integrated methodology for the design of RoRo-Passenger ships for the needs of short sea shipping in Greece', Proceedings of the 12th International Congress of the International Maritime Association of the Mediterranean (IMAM 2007), Varna, Bulgaria, 2-7 Sep. 2007.
11. Napa Oy, the Naval Architectural Package (NAPA), http://www.napa.fi
12. Grigoropoulos, G.J. and Loukakis T. A., 'Resistance and Seakeeping Characteristics of a Systematic Series in the Pre-planing Condition (Part I)', SNAME Transactions, vol. 110, pp. 77-113, 2002
13. Bailey, D., 'The NPL high speed round bilge displacement hull series', Marine Technology Monograph No. 4, Royal Institution of Naval Architects, 1976.
14. Radojcic, D., Grigoropoulos, G., Rodic, T., Kuvelic, T., Damala, D., 'The Resistance and Trim of Semi-Displacement, Double-Chine, Transom-Stern Hull Series', Proceedings of the 6th International Conference on Fast Sea Transportation – FAST2001, Southampton, UK, Sept. 2001.
15. Radojcic, D., Rodic, T. and Kostic, N., 'Resistance and Trim Predictions for the NPL High Speed Round Bilge Displacement Hull Series', International Conference On Power, Performance and Operability of Small Craft, Southampton, UK, Sept. 1997.
16. Knox, J., 'Ferries' in Ship Design and Construction, vol. 2, edited by T. Lamb, ISBN: 0-939773-41-4,

published by the Society of Naval Architects and Marine Engineers, SNAME, 2004.

17. DNV, 'Rules for the Classification of High-Speed, Light Craft and Naval Surface Craft, Part 3 & 5', Det Norske Veritas, 2002.

18. IMO, 'International Code of Safety of High-Speed Craft', International Maritime Organization, MSC 73/21/Add.1, Annex 5, 2000.

19. E.STE.CO, modeFRONTIER, http://www.esteco.it

Table 5. Pareto designs, Large Vessel

Des Id	L_{BP} (m)	B_{OA} (m)	T_D (m)	FB (m)	Pass. Numb.	Cars Numb.	DWT (t)	Δ (t)	Inst. Power (kW)	AC (m€)	GM_{cr} (m)	GM_m (m)	RFR (€)
119	116.00	20.00	2.70	2.60	1606	287	591	2251	35621	55.09	8.108	1.651	45.96
191	120.00	20.00	2.65	2.50	1692	235	545	2286	39569	56.44	8.100	1.821	49.18
318	113.20	20.00	2.55	2.50	1570	158	434	2075	36812	54.46	8.418	1.961	51.94
391	120.00	20.00	2.60	2.50	1677	195	494	2244	39016	57.95	8.186	1.925	50.63
486	120.00	19.85	2.65	2.50	1668	298	605	2269	33105	52.86	8.308	1.516	41.20
588	100.00	20.00	2.70	2.50	1333	198	462	1940	38856	51.00	7.734	2.121	60.65
760	108.60	19.90	2.65	2.60	1494	253	532	2057	32776	49.34	8.304	1.533	45.63
771	100.80	20.00	2.70	2.50	1357	201	469	1956	38943	51.33	7.734	2.112	59.75
822	101.20	20.00	2.70	2.50	1358	205	473	1963	38796	51.36	7.749	2.110	59.37
849	105.00	20.00	2.70	2.50	1423	238	516	2037	37162	51.73	7.904	2.022	53.80
929	118.80	19.95	2.65	2.50	1646	327	635	2258	31422	51.72	8.604	1.447	39.20
932	112.80	19.95	2.70	2.50	1538	265	558	2183	36048	53.86	7.921	1.812	48.57
960	116.00	19.95	2.70	2.50	1601	271	572	2245	36036	55.06	7.916	1.798	46.88
1024	117.20	20.00	2.70	2.70	1625	285	591	2275	35703	55.73	8.108	1.549	45.75
1050	114.40	19.95	2.65	2.50	1575	313	610	2174	31534	50.33	8.596	1.464	40.89
1116	113.80	20.00	2.70	2.50	1588	284	585	2208	35632	54.20	8.127	1.708	46.26
1254	118.80	19.95	2.55	2.50	1661	174	465	2174	38102	55.10	8.416	1.853	50.15
1262	117.20	19.95	2.55	2.50	1624	181	469	2144	37719	54.22	8.491	1.908	50.42
1454	102.60	20.00	2.70	2.50	1384	221	493	1990	37924	51.33	7.830	2.058	56.60

Table 6. Minimum *RFR* designs, Large Vessel

Des. Id	L_{BP} (m)	B_{OA} (m)	T_D (m)	FB (m)	Pass. Numb.	Cars Numb.	DWT (t)	Δ (t)	Inst. Power (kW)	AC (m€)	GM_{cr} (m)	GM_m (m)	RFR (€)
929	118.80	19.95	2.65	2.50	1646	327	635	2258	31422	51.72	8.604	1.447	39.20
644	119.00	19.95	2.65	2.85	1662	317	624	2262	31453	52.32	8.644	1.224	39.26
640	118.80	19.95	2.65	2.75	1660	311	617	2258	31422	52.24	8.577	1.255	39.39
924	119.00	19.95	2.65	2.75	1660	312	618	2261	31453	52.30	8.580	1.257	39.41
659	120.00	19.95	2.65	2.80	1675	321	631	2280	31941	52.76	8.608	1.257	39.42
371	119.00	19.95	2.65	2.80	1661	310	616	2262	31453	52.38	8.575	1.219	39.46
838	120.00	19.95	2.65	2.70	1673	320	630	2281	31941	52.70	8.581	1.310	39.47
811	118.60	19.95	2.65	2.80	1660	306	611	2254	31397	52.27	8.567	1.217	39.49
656	118.40	19.95	2.65	2.60	1635	321	626	2250	31371	51.72	8.595	1.378	39.54
931	118.60	19.95	2.65	2.85	1661	302	606	2254	31397	52.39	8.549	1.177	39.58
558	118.40	19.95	2.65	2.80	1649	308	612	2250	31371	52.14	8.569	1.210	39.61
744	117.60	19.95	2.65	2.65	1633	312	615	2235	31286	51.58	8.583	1.330	39.67
690	118.20	19.95	2.65	2.70	1636	314	618	2246	31351	51.84	8.578	1.294	39.68
698	118.40	19.95	2.65	2.70	1636	315	619	2250	31371	51.91	8.581	1.300	39.69
677	120.00	19.95	2.65	2.90	1676	308	616	2281	31941	53.08	8.551	1.157	39.76

Table 7. Pareto designs, Small Vessel

Des. Id	L_{BP} (m)	B_{OA} (m)	T_D (m)	FB (m)	Cars Numb.	DWT (t)	Δ (t)	Inst. Power (kW)	AC (m€)	GM_{cr} (m)	GM_m (m)	T_R (sec)	RFR (€)
147	79.60	17.65	2.75	2.95	262	448	1352	22377	30.63	6.385	0.303	7.24	26.86
223	84.60	18.00	3.00	3.50	293	491	1483	25339	34.02	6.167	0.307	7.32	29.08
239	83.00	17.60	2.80	2.90	272	462	1402	23344	31.91	6.146	0.303	7.31	27.71
297	94.00	16.55	2.20	2.50	162	317	1232	16402	28.61	6.982	0.550	6.54	24.58
331	75.00	17.85	2.80	2.70	245	426	1276	21876	29.05	6.541	0.420	7.18	26.40
365	82.00	17.70	2.75	3.50	286	478	1431	22926	32.31	6.279	0.370	7.26	27.08
476	75.00	18.00	2.75	3.05	259	442	1324	21722	29.74	6.614	0.714	7.08	26.06
496	75.00	18.00	2.75	3.30	257	440	1333	21722	30.08	6.573	0.596	7.16	26.25
571	75.00	18.00	2.75	3.50	252	434	1334	21722	30.36	6.543	0.491	7.23	26.59
585	84.40	18.00	3.00	3.50	293	491	1478	25294	33.92	6.176	0.309	7.31	29.01
855	94.00	17.95	2.35	2.50	269	452	1426	19524	30.38	8.406	0.996	6.28	24.40
925	94.00	16.50	2.20	2.50	154	308	1228	16650	28.74	6.878	0.516	6.56	25.13
1129	75.60	17.30	2.65	2.50	234	410	1243	20644	27.38	6.353	0.341	7.07	25.18
1228	75.60	17.80	2.70	2.70	248	429	1288	21378	29.09	6.635	0.552	7.08	25.92

Table 8. Minimum *RFR* designs, Large Vessel

Des. Id	L_{BP} (m)	B_{OA} (m)	T_D (m)	FB (m)	Cars Numb.	DWT (t)	Δ (t)	Inst. Power (kW)	AC (m€)	GM_{cr} (m)	GM_m (m)	T_R (sec)	RFR (€)
855	94.00	17.95	2.35	2.50	269	452	1426	19524	30.38	8.406	1.368	6.28	24.40
297	94.00	16.55	2.20	2.50	162	317	1232	16402	28.61	6.982	0.550	6.54	24.58
560	93.80	16.55	2.20	2.50	158	313	1228	16417	28.62	6.969	0.547	6.39	24.73
762	94.00	16.55	2.20	2.60	159	314	1231	16402	28.72	6.978	0.476	6.43	24.73
958	93.60	16.55	2.20	2.50	157	311	1226	16435	28.60	6.963	0.549	6.39	24.78
500	93.40	16.55	2.20	2.50	156	310	1224	16451	28.58	6.958	0.546	6.39	24.81
83	93.40	16.55	2.20	2.55	155	309	1223	16451	28.62	6.961	0.508	6.40	24.87
1050	94.00	17.95	2.35	2.70	262	444	1426	19524	31.59	8.359	1.242	6.32	25.02
542	92.20	16.60	2.20	2.50	149	302	1211	16500	28.51	6.962	0.588	6.40	25.07
353	94.00	16.55	2.20	2.70	151	304	1231	16402	28.90	6.964	0.391	6.45	25.08
85	93.40	16.55	2.20	2.75	150	303	1223	16451	28.82	6.961	0.356	6.47	25.13
570	95.00	16.50	2.20	2.50	159	314	1241	16765	28.93	6.917	0.528	6.38	25.13
925	94.00	16.50	2.20	2.50	154	308	1228	16650	28.74	6.878	0.516	6.56	25.13
784	94.00	16.55	2.20	2.80	150	303	1231	16402	28.98	6.973	0.308	6.48	25.16
1129	75.60	17.30	2.65	2.50	234	410	1243	20644	27.38	6.353	0.341	7.07	25.18
1010	92.20	18.00	2.35	2.55	253	433	1403	19902	30.42	8.375	1.363	6.30	25.19
326	81.20	17.60	2.20	2.60	119	264	1132	15951	27.47	7.969	1.198	6.33	25.23
748	92.60	16.55	2.20	2.50	149	302	1213	16695	28.57	6.920	0.572	6.39	25.28
101	94.00	16.95	2.25	2.90	181	342	1289	17456	29.88	7.291	0.514	6.49	25.35
252	84.20	17.85	2.25	2.95	155	310	1217	17007	28.99	8.167	0.864	6.47	25.51

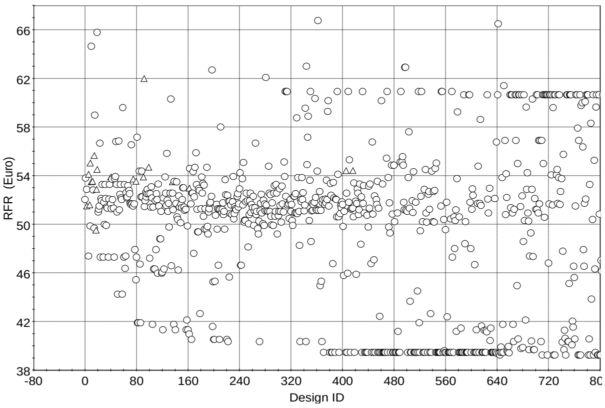

Figure 6: *RFR* history diagram (first 40 generations)

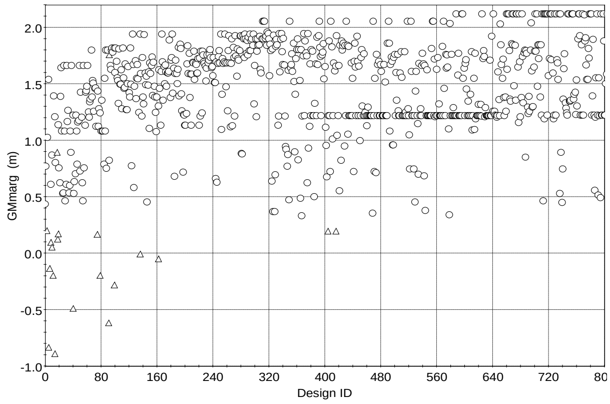

Figure 7. GM_m history diagram (first 40 generations)

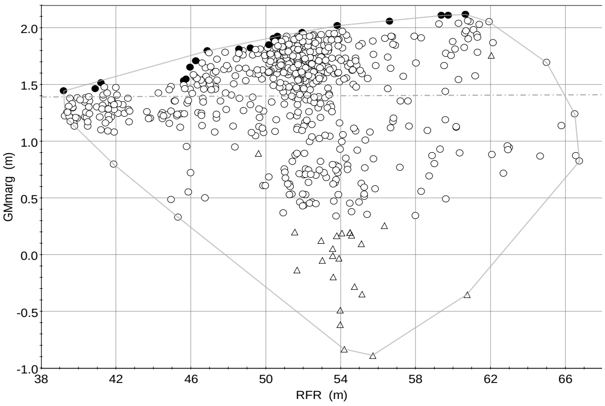

Figure 8. Scatter diagram, GM_m vs. *RFR*

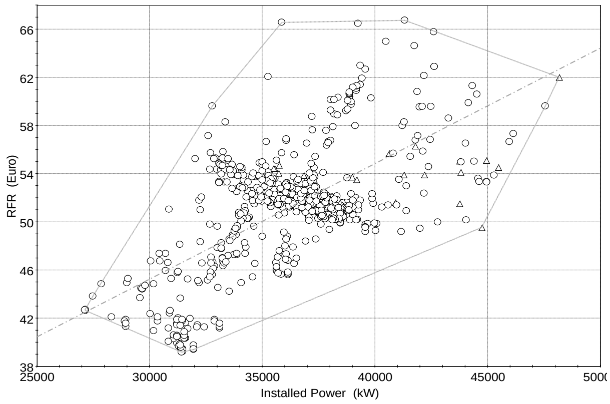

Figure 9. Scatter diagram, *RFR* vs. Installed Power

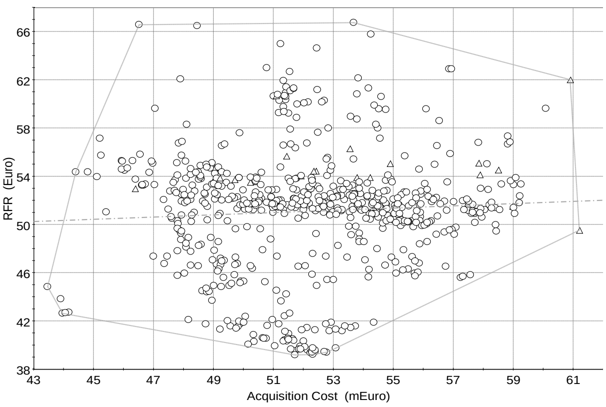

Figure 10. Scatter diagram, *RFR* vs. Acquisition Cost

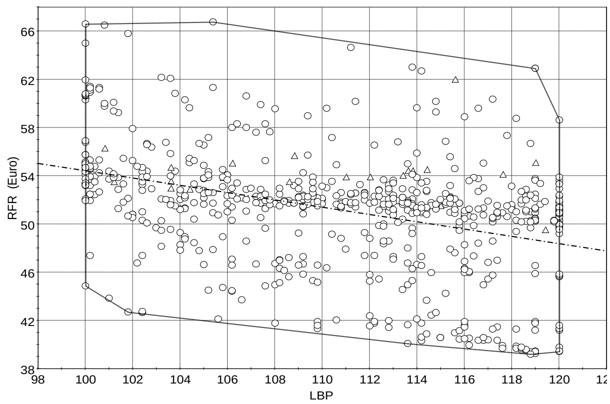

Figure 11. Scatter diagram, *RFR* vs. L_{BP}

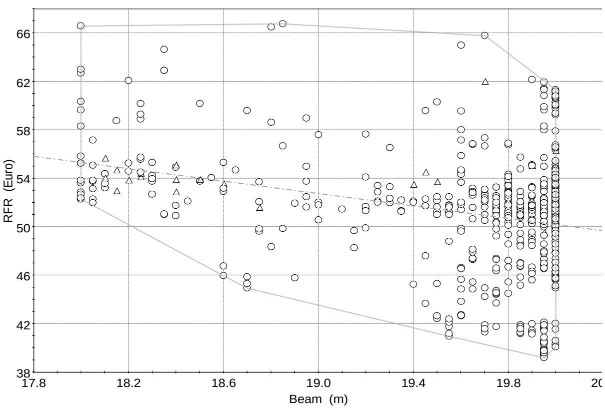

Figure 12. Scatter diagram, *RFR* vs. B_{OA}

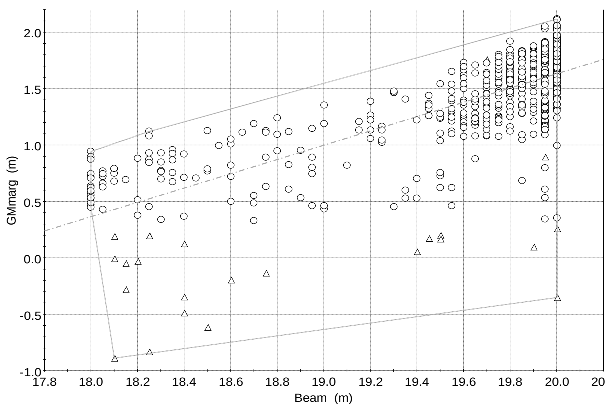

Figure 13. Scatter diagram, GM_m vs. B_{OA}

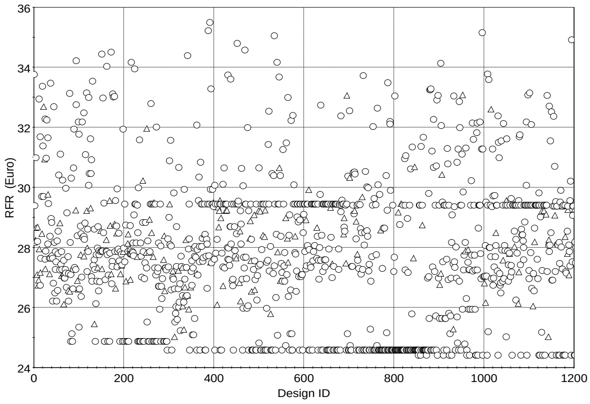

Figure 14: *RFR* history diagram (first 60 generations)

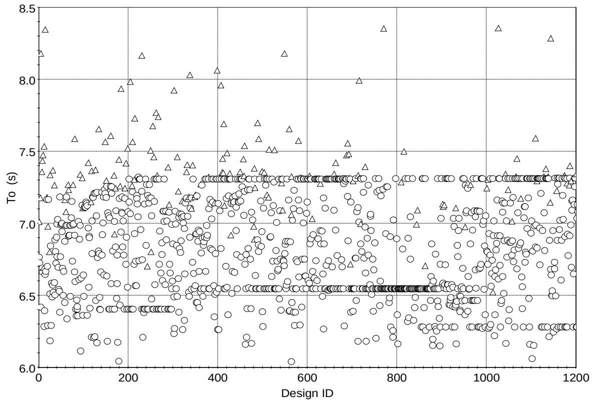

Figure 15. T_R history diagram (first 60 generations)

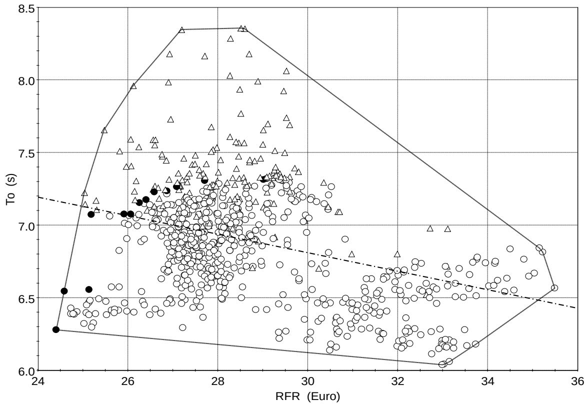

Figure 16. Scatter diagram, T_R ratio vs. *RFR*

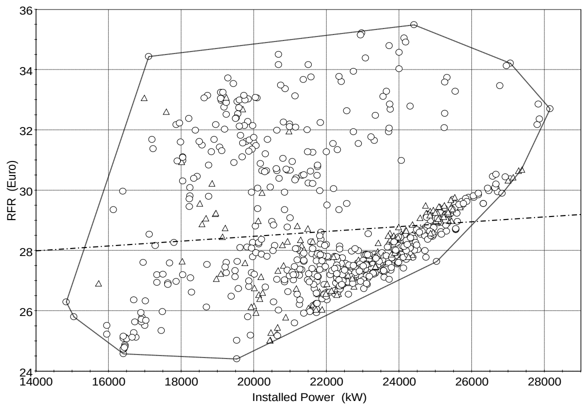

Figure 17. Scatter diagram, *RFR* vs. Installed Power

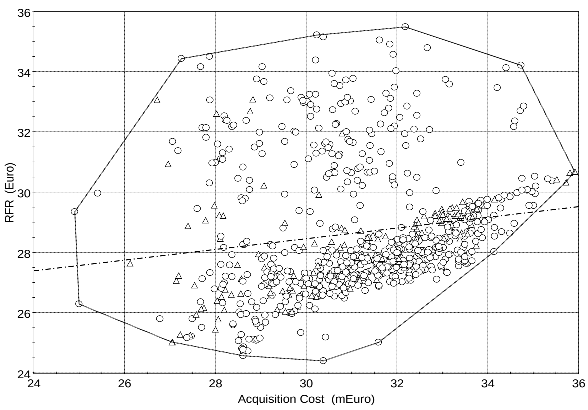

Figure 18. Scatter diagram, *RFR* vs. Acquisition Cost

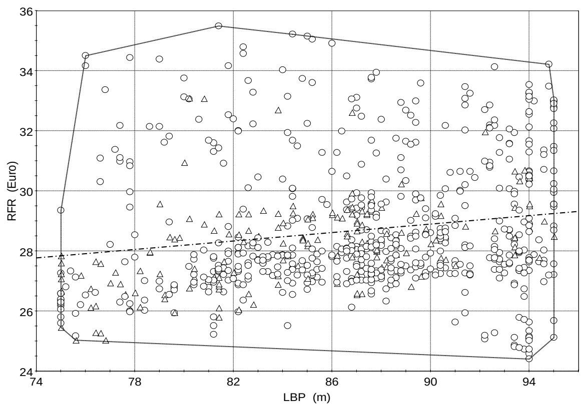

Figure 19. Scatter diagram, *RFR* vs. L_{BP}

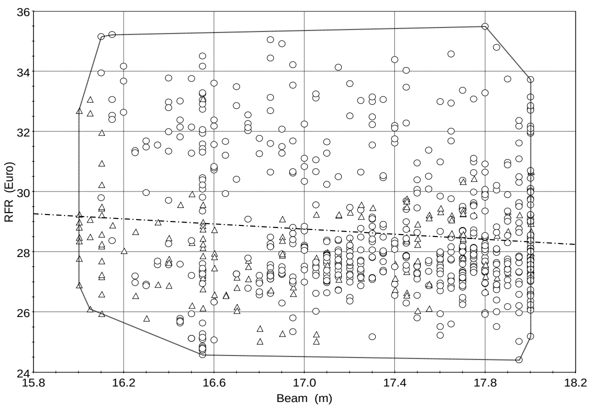

Figure 20. Scatter diagram, *RFR* vs. B_{OA}

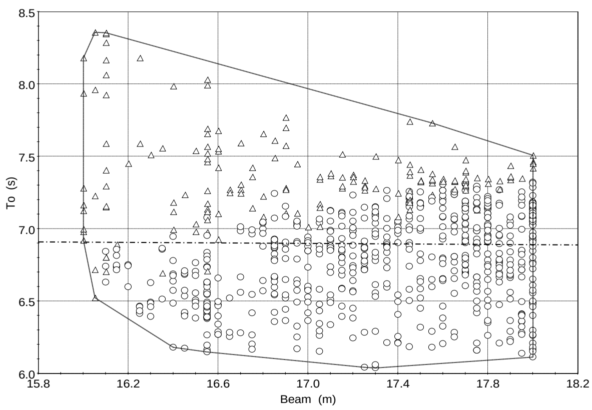

Figure 21. Scatter diagram, T_R vs. B_{OA}

A STUDY ON THE PREDICTION METHOD OF WAVE LOADS OF A MULTI-HULL SHIP TAKING ACCOUNT OF THE SIDE HULL ARRANGEMENT

Yoshitaka Ogawa, National Maritime Research Institute, Japan

SUMMARY

A practical prediction method for wave loads acting on the multi-hull ship is developed. The present method is extension of the methodology of the application to catamaran using Newman's Unified Theory to a multi-hull ship.

First, outline of the present method is indicated in terms of the trimaran. Second, the present method is validated having compared with the existing experimental data and computation for catamaran and trimaran. It is verified that present method gives good agreement with experiments and computation by means of 3D panel method in the case of zero speed. Finally, the effect of the arrangement of side hulls on wave loads is examined using the present method. It is clarified that arrangement of side hull has effects on the wave loads acting on the trimaran.

1. INTRODUCTION

It is considered that a seakeeping performance is an important factor for assessing the total performance of multi-hull ships. In particular, assessment of wave loads acting on multi-hull ships is important. In those assessments, not only the wave-induced bending moment but also splitting loads between a main hull and side hulls, torsional loads and impact loads due to cross-deck slamming should be examined. Therefore, it is important to develop a practical prediction method of wave loads acting on multi-hull ships in arbitrary direction of wave.

Based on this background, author develops a practical prediction method for utilizing in a design stage without waste of huge computation time. Present method is developed in accordance with the Enhanced Unified Theory approach, which is extended theory of Newman's Unified Theory[1)2)] by Kashiwagi[3)4)]. Author extends that theory for taking account of the effect of side hulls on the prediction of wave loads acting on a trimaran.

Validation of the present method is carried out having compared with a series of experiments. It is confirmed that hydrodynamic force and ship motions taking account of the interaction force between a main hull and side hulls gives favorable agreement with experiments.

In addition, the effect of the arrangement of side hulls on wave loads is examined using the present method. In the present examination, it is found that with shifting side hulls rearward, response amplitude of ship motion and wave loads change. It is clarified that arrangement of side hull has effects on the wave loads acting on the trimaran.

2. THEORY OF MOTIONS OF TRIMARAN

2.1 MATHMATICAL FORMULATION

The application of unified theory to the catamaran had been carried out by Kashiwagi[5)6)] and Ronaess[7)]. In accordance with the present methodology, theory of motions of a multi-hull can be derived without difficulty. In the present study, these methodologies are extended to the multi-hull ship. For the convenience, the formulation for trimaran is indicated in the present paper.

We consider a trimaran advancing with constant speed U and undergoing oscillatory motions with circular frequency ω in deep water. The analysis will be performed using a Cartesian coordinate system, which moves steadily with the same constant speed as a ship. The x-axis is directed to the ship's bow and z-axis is directed downward. The coordinate systems defined in the present study shows in Figure 1. Coordinate of the main hull $(\bar{x}, \bar{y}, \bar{z})$ can be described by means of the coordinate of side hulls as:

$$(\bar{x},\bar{y},\bar{z})=(x_R+a,y_R+D,z_R)=(x_L+a,y_L-D,z_R). \qquad (1)$$

Subscript R denotes a side hull in the right side of the main hull and L denotes a side hull in the left side of the main hull.

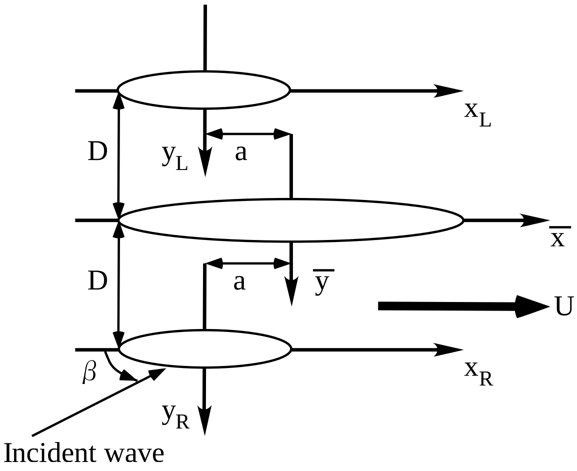

Figure 1 Definition of coordinate system of the trimaran. The z-axis is pointing downwards, and $\bar{z}, Z_R$ and $Z_L=0$ corresponds to mean free surface.

Assuming, the inviscid fluid with irrotational motion, the flow can be described with the velocity potential, with is expressed as

$$\Phi=U\left[-x+\phi_s(x,y,z)\right]+\mathrm{Re}\left[\phi(x,y,z)e^{i\omega t}\right]. \qquad (2)$$

$$\phi=\frac{gA}{i\omega_0}(\phi_0+\phi_d)+i\omega\sum_{j=1}^{18}X_j\phi_j\ . \qquad (3)$$

$$\phi_0=e^{-k_0z-ik_0y\sin\beta}e^{ilx} \qquad (4)$$

$$\omega=\omega_0-k_0U\cos\beta, k_0=\frac{\omega_0^2}{g}, l=-k_0\cos\beta \qquad (5)$$

Where ϕ_0 denotes the incident wave potential; A, ω_0, k_0, β are the amplitude, the circular frequency, the wave number and the incident angle of incoming wave, respectively. g is the gravitational acceleration. ϕ_s in Eq.(2) denotes the steady disturbance potential due to the forward motion of a ship. ϕ_d in Eq.(3) denotes the diffraction potential. ϕ_j for j=1, 2, 3,…..,17, 18 denotes the radiation potential of the 3×6 mode and X_j denotes the complex amplitude of the 3×6 mode of each hull.

The body boundary condition for the unsteady potentials is

$\frac{\partial\phi_j}{\partial n}=n_j+\frac{U}{i\omega}m_j$ on S_M for j=1,2…,6, on S_L for j=7,8,…,12 and on S_R for j=13,14,…,18

$\frac{\partial\phi_j}{\partial n}=0$ on S_M for j=13,14…,18, on S_L for j=1,2,…,6,13,14,…,18 and on S_R for j=1,2,…,12 (6)

$\frac{\partial\phi_j}{\partial n}=-\frac{\partial\phi_0}{\partial n}$ on S_M, S_L and S_R for j=d (7).

S_M, S_L and S_R are the mean wetted surface of the main hull and side hulls, respectively. *j*=1,2,….,18 are referred to as the radiation problem, while j=d corresponds to the diffraction problem.

n_j and m_j denote the j-th component of the unit normal directing into the fluid and of so-called m-term representing interactions with the steady flow.

2.2 RADIATION PROBLEM

In the inner region close to the ship hull, variation of the flow along the x-axis is small compared to that in the transverse section and the wave radiation at infinity is out of concern. As a result, the velocity potential in the inner region satisfies

$$\left(\frac{\partial^2}{\partial y^2}+\frac{\partial^2}{\partial z^2}\right)\phi_j=0 \ for \quad z\ge 0 \qquad (8)$$

$$\frac{\partial\phi_j}{\partial z}+K\phi_j=0 \, on \quad z=0 \qquad (9)$$

where $K=\omega^2/g$.

The general inner solution satisfying Eq.(6), (8) and (9) takes the following form:

$$\phi(x,y,z)=\varphi_j(y,z)+\frac{U}{i\omega}\hat{\varphi}_j(y,z)+C_{Sj}(x)\varphi_j^{HS}(y,z)$$

for j=1, 3, 5, 7, 9, 11, 13, 15, 17 (10)

$$\phi(x,y,z) = \varphi_j(y,z) + \frac{U}{i\omega}\hat{\varphi}_j(y,z) + C_{Aj}(x)\varphi_j^{HA}(y,z)$$

for j=2, 4, 6, 8, 10, 12, 14, 16, 18 (11)

Where φ_j and $\hat{\varphi}_j$ denote the particular solutions, corresponding to the first and second terms of the right hand side of Eq.(6), respectively. C_{Sj} and C_{Aj} are the interaction coefficient which is to be determined by the matching with the outer solution. φ_j^{HS} denotes a homogeneous solution, which can be explicitly given by $\varphi_j^{HS} = \varphi_3 - \overline{\varphi}_3$ (j=1,3,5), $\varphi_j^{HS} = \varphi_9 - \overline{\varphi}_9$ (j=7,9,11) and $\varphi_j^{HS} = \varphi_{15} - \overline{\varphi}_{15}$ (j=13,15,17) for the symmetric modes, where $\overline{\varphi}_j$ means the complex conjugate of φ_j. φ_j^{HA} denotes a homogeneous solution, which can be explicitly given by $\varphi_j^{HA} = \varphi_2 - \overline{\varphi}_2$ (j=2,4,6), $\varphi_j^{HA} = \varphi_8 - \overline{\varphi}_8$ (j=8,10,12) and $\varphi_j^{HA} = \varphi_{14} - \overline{\varphi}_{14}$ (j=14,16,18) for the antisymmetric modes.

In the present study, contribution of ϕ_s are neglected in computing the m-term and thus m_j=0 for j=1, 2, 3, 4, 7, 8, 9, 10, 13, 14, 15, 16, m_5= n_3, m_6= -n_2, m_{11}= n_9, m_{12}= -n_8, m_{117}= n_{15} and m_{18}= -n_{14}. Moreover, with slenderness assumption, n_5= -xn_3, n_6= xn_2, n_{11}= -xn_9, n_{12}= xn_8, n_{17}= -xn_{15} and n_{18}= xn_{14}.

In accordance with these approximations, particular solutions can be approximated as follows:

$\hat{\varphi}_j = 0$ (for j=1, 2, 3, 4, 7, 8, 9, 10, 13, 14, 15, 16)

$\hat{\varphi}_5 = \varphi_3$, $\hat{\varphi}_6 = -\varphi_2$, $\hat{\varphi}_{11} = \varphi_9$, $\hat{\varphi}_{12} = -\varphi_8$, $\hat{\varphi}_{17} = \varphi_{15}$, $\hat{\varphi}_{18} = -\varphi_{14}$

$\varphi_5 = -x\varphi_3$, $\varphi_6 = x\varphi_2$, $\varphi_{11} = -x\varphi_9$, $\varphi_{12} = x\varphi_8$, $\varphi_{17} = -x\varphi_{15}$, $\varphi_{18} = x\varphi_{14}$ (12).

An inner solution is expanded to large distances from the hull to be able to match this inner solution with the outer solution. The outer expansion of radiation potential is described as follows:

$$\begin{aligned}\phi_j &\approx \left(\sigma_j + \frac{U}{i\omega}\hat{\sigma}_j\right)G_{2D}(y,z) + \left(\mu_j + \frac{U}{i\omega}\hat{\mu}_j\right)H_{2D}(y,z) \\ &+ C_{Sj}(x)(\sigma_3 - \overline{\sigma}_3)G_{2D}(y,z) - iC_{Sj}(x)\overline{\sigma}_3 \cdot e^{-Kz}\cos Ky \\ &+ C_{Aj}(x)(\mu_2 - \overline{\mu}_2)H_{2D}(y,z) + iC_{Aj}(x)\overline{\mu}_2 \cdot e^{-Kz}\sin Ky\end{aligned} \tag{13}$$

where σ_j, $\hat{\sigma}_j$, μ_j and $\hat{\mu}_j$ are the 2D Kochin functions to be computed from φ_j and $\hat{\varphi}_j$, respectively. $\sigma_j = 0$ for j=2, 4, 6, 8, 10, 12, 14, 16, 18 and $\mu_j = 0$ for j=1, 3, 5, 7, 9, 11, 13, 15, 17. G_{2D} and H_{2D} satisfy the 2D Laplace equation and the free surface condition.

In the outer region far away from a ship, the potential is represented by distributions of three dimensional singularities along the center line of each hull. The singularities satisfy three dimensional Laplace's equation and the free surface condition. For each hull, contributions are divided into a symmetric and antisymmetric part, the former represented by sources and the latter by dipoles. The outer solution is described as follows:

$$\begin{aligned}&\phi_j^O(x,y,z) \\ &= \int_{L_M}\left[q_j^M(\xi) - d_j^M(\xi)\frac{\partial}{\partial\eta}\right]G_{3D}(x-\xi, y-\eta, z-\varsigma)\Big|_{\varsigma=0}d\xi \\ &+ \int_{L_L}\left[q_j^L(\xi) - d_j^L(\xi)\frac{\partial}{\partial\eta}\right]G_{3D}(x-\xi, y-\eta, z-\varsigma)\Big|_{\varsigma=0}d\xi \\ &+ \int_{L_R}\left[q_j^R(\xi) - d_j^R(\xi)\frac{\partial}{\partial\eta}\right]G_{3D}(x-\xi, y-\eta, z-\varsigma)\Big|_{\varsigma=0}d\xi\end{aligned} \tag{14}$$

M denotes the main hull. L and R denote side hull of the left side and the right side. The outer solution is expanded near the main hull, side hull of the left side and side hull of the right side, respectively. The inner expansion near the main hull is

$$\begin{aligned}
&\phi_j^O(x,y,z)\\
&\cong q_j^M(\xi)G_{2D}(y,z)-\frac{1+Kz}{2\pi}\int_{L_M} q_j^M(\xi)g_{MM}(x-\xi)d\xi\\
&+d_j^M(\xi)H_{2D}(y,z)-\frac{Ky}{2\pi}\int_{L_M} d_j^M(\xi)h_{MM}(x-\xi)d\xi\\
&-\frac{1+Kz}{2}\int_{L_L} q_j^L(\xi)g_{LM}(x-\xi)d\xi\\
&+\frac{Ky}{2}\int_{L_L} q_j^L(\xi)f_{LM}(x-\xi)d\xi\\
&+\frac{1+Kz}{2}\int_{L_L} d_j^L(\xi)f_{LM}(x-\xi)d\xi\\
&-\frac{Ky}{2}\int_{L_L} d_j^L(\xi)h_{LM}(x-\xi)d\xi\\
&-\frac{1+Kz}{2}\int_{L_R} q_j^R(\xi)g_{RM}(x-\xi)d\xi\\
&-\frac{Ky}{2}\int_{L_R} q_j^R(\xi)f_{RM}(x-\xi)d\xi\\
&-\frac{1+Kz}{2}\int_{L_R} d_j^R(\xi)f_{RM}(x-\xi)d\xi\\
&-\frac{Ky}{2}\int_{L_R} d_j^R(\xi)h_{RM}(x-\xi)d\xi
\end{aligned} \tag{15}$$

Here (x, y) is $(\bar{x}, \bar{y})$. q_j and d_j denote the strength of source and dipole, respectively, which are unknown due to lack of the body boundary condition. The inner expansion near the side hull of the left side and the side hull of the right side can be similarly derived. Kernel functions $f(x-\xi)$, $h(x-\xi)$ and $g(x-\xi)$ represent 3D and forward speed effects. The fourier transformations of these kernel function was clearly indicated by Newman[1)], Kashiwagi[5)] and Ronaess[7)].

Matching with inner solutions, following relation can be obtained

$$\begin{aligned}
&q_j^M(\xi)+i\frac{\left(\sigma_3^M-\bar{\sigma}_3^M\right)}{2\sigma_3^M}\left\{\frac{1}{\pi}\int_{L_M} q_j^M(\xi)g_{MM}(x-\xi)d\xi\right.\\
&+\int_{L_L} q_j^L(\xi)g_{LM}(x-\xi)d\xi-\int_{L_L} d_j^L(\xi)f_{LM}(x-\xi)d\xi\\
&\left.+\int_{L_R} q_j^R(\xi)g_{RM}(x-\xi)d\xi-\int_{L_R} d_j^R(\xi)f_{RM}(x-\xi)d\xi\right\}\\
&=\sigma_j^M+\frac{U}{i\omega}\hat{\sigma}_j^M
\end{aligned} \tag{16}$$

$$\begin{aligned}
&d_j^M(\xi)-i\frac{\left(\mu_2^M-\bar{\mu}_2^M\right)}{2\mu_2^M}\left\{\frac{1}{\pi}\int_{L_M} d_j^M(\xi)h_{MM}(x-\xi)d\xi\right.\\
&-\int_{L_L} q_j^L(\xi)f_{LM}(x-\xi)d\xi+\int_{L_L} d_j^L(\xi)h_{LM}(x-\xi)d\xi\\
&\left.+\int_{L_R} q_j^R(\xi)f_{RM}(x-\xi)d\xi+\int_{L_R} d_j^R(\xi)h_{RM}(x-\xi)d\xi\right\}\\
&=\mu_j^M+\frac{U}{i\omega}\hat{\mu}_j^M
\end{aligned} \tag{17}$$

$$\begin{aligned}
&q_j^L(\xi)+i\frac{\left(\sigma_3^L-\bar{\sigma}_3^L\right)}{2\sigma_3^L}\left\{\frac{1}{\pi}\int_{L_L} q_j^L(\xi)g_{LL}(x-\xi)d\xi\right.\\
&+\int_{L_M} q_j^M(\xi)g_{LM}(x-\xi)d\xi+\int_{L_M} d_j^M(\xi)f_{LM}(x-\xi)d\xi\\
&\left.+\int_{L_R} q_j^R(\xi)g_{LR}(x-\xi)d\xi+\int_{L_R} d_j^R(\xi)f_{LR}(x-\xi)d\xi\right\}\\
&=\sigma_j^L+\frac{U}{i\omega}\hat{\sigma}_j^L
\end{aligned} \tag{18}$$

$$\begin{aligned}
&d_j^L(\xi)-i\frac{\left(\mu_2^L-\bar{\mu}_2^L\right)}{2\mu_2^L}\left\{\frac{1}{\pi}\int_{L_L} d_j^L(\xi)h_{LL}(x-\xi)d\xi\right.\\
&+\int_{L_M} q_j^M(\xi)f_{LM}(x-\xi)d\xi+\int_{L_M} d_j^M(\xi)h_{LM}(x-\xi)d\xi\\
&\left.+\int_{L_R} q_j^R(\xi)f_{LR}(x-\xi)d\xi+\int_{L_R} d_j^R(\xi)h_{LR}(x-\xi)d\xi\right\}\\
&=\mu_j^L+\frac{U}{i\omega}\hat{\mu}_j^L
\end{aligned} \tag{19}$$

$$\begin{aligned}
&q_j^R(\xi)+i\frac{\left(\sigma_3^R-\bar{\sigma}_3^R\right)}{2\sigma_3^R}\left\{\frac{1}{\pi}\int_{L_R} q_j^R(\xi)g_{RR}(x-\xi)d\xi\right.\\
&+\int_{L_M} q_j^M(\xi)g_{RM}(x-\xi)d\xi+\int_{L_M} d_j^M(\xi)f_{RM}(x-\xi)d\xi\\
&\left.+\int_{L_L} q_j^L(\xi)g_{LR}(x-\xi)d\xi-\int_{L_L} d_j^L(\xi)f_{LR}(x-\xi)d\xi\right\}\\
&=\sigma_j^R+\frac{U}{i\omega}\hat{\sigma}_j^R
\end{aligned} \tag{20}$$

$$\begin{aligned}
&d_j^R(\xi)-i\frac{\left(\mu_2^R-\bar{\mu}_2^R\right)}{2\mu_2^R}\left\{\frac{1}{\pi}\int_{L_R} d_j^R(\xi)h_{RR}(x-\xi)d\xi\right.\\
&+\int_{L_M} q_j^M(\xi)f_{RM}(x-\xi)d\xi+\int_{L_M} d_j^M(\xi)h_{RM}(x-\xi)d\xi\\
&\left.-\int_{L_L} q_j^L(\xi)f_{LR}(x-\xi)d\xi+\int_{L_L} d_j^L(\xi)h_{LR}(x-\xi)d\xi\right\}\\
&=\mu_d^R+\frac{U}{i\omega}\hat{\mu}_j^R
\end{aligned} \tag{21}$$

$$q_j^M=\left(\sigma_j^M+\frac{U}{i\omega}\hat{\sigma}_j^M\right)+C_{Sj}^M(x)\left(\sigma_3^M-\bar{\sigma}_3^M\right) \tag{22}$$

$$d_j^M=\left(\mu_j^M+\frac{U}{i\omega}\hat{\mu}_j^M\right)+C_{Aj}^M(x)\left(\mu_2^M-\bar{\mu}_2^M\right) \tag{23}$$

$$q_j^L = \left(\sigma_j^L + \frac{U}{i\omega} \hat{\sigma}_j^L \right) + C_{Sj}^L(x)\left(\sigma_3^L - \overline{\sigma}_3^L\right) \quad (24)$$

$$d_j^L = \left(\mu_j^L + \frac{U}{i\omega} \hat{\mu}_j^L \right) + C_{Aj}^L(x)\left(\mu_2^L - \overline{\mu}_2^L\right) \quad (25)$$

$$q_j^R = \left(\sigma_j^R + \frac{U}{i\omega} \hat{\sigma}_j^R \right) + C_{Sj}^R(x)\left(\sigma_3^R - \overline{\sigma}_3^R\right) \quad (26)$$

$$d_j^R = \left(\mu_j^R + \frac{U}{i\omega} \hat{\mu}_j^R \right) + C_{Aj}^R(x)\left(\mu_2^R - \overline{\mu}_2^R\right) \quad (27)$$

Once integral equations (Eq.(16)-(21)) for q_j and d_j are solved, it is straightforward to compute C_j from Eq.(22)-(27), thereby the complete inner solutions. Then hydrodynamic forces and motions can be computed from the inner solutions.

2.3 DIFFRACTION PROBLEM

In the case of the diffraction problem, the diffraction potential is described in the form of

$$\phi_d = \varphi_d(x; y, z)e^{ilx} \quad (28).$$

The governing equation and boundary conditions for φ_d are given as

$$\left(\frac{\partial^2}{\partial y^2} + \frac{\partial^2}{\partial z^2} - l^2 \right)\varphi_d = 0 \ for \quad z \geq 0 \quad (29)$$

$$\frac{\partial \varphi_d}{\partial z} + k_0 \varphi_d = 0 \ on \quad z = 0 \quad (30)$$

$$\frac{\partial \varphi_d}{\partial n} = \left(n_3 + in_1 \cos\beta + in_2 \sin\beta\right) \times k_0 e^{-k_0 z - k_0 y \sin\beta} \quad (31).$$
$$on \quad S_M, S_L and S_R$$

The governing equation is the 2D modified Helmholtz equation and the wave number in Eq.(30) is not K but k_0. In accordance with the similar manner for radiation problem, the outer expansion of diffraction potential is described as follows:

$$\begin{aligned} \varphi_d &\approx \sigma_d G_{2D}(y,z) + \mu_d H_{2D}(y,z) \\ &+ C_{Sd}(x)\left(\sigma_d - \overline{\sigma}_d\right)G_{2D}(y,z) + iC_{Sd}(x)\overline{\sigma}_d \cdot e^{-Kz} \cos Ky \\ &+ C_{Ad}(x)\left(\mu_d + \overline{\mu}_d\right)H_{2D}(y,z) + iC_{Ad}(x)\overline{\mu}_d \cdot e^{-Kz} \sin Ky \end{aligned} \quad (32).$$

Here $C_{Sd}(x)$ and $C_{Ad}(x)$ are the unknown symmetric and antisymmetric interaction coefficient for diffraction problem. σ_d and μ_d are the 2D Kochin functions to be computed from φ_d.

The result of matching, following relation can be obtained

$$\begin{aligned} & q_d^M(\xi) - i\frac{\left(\sigma_d^M - \overline{\sigma}_d^M\right)}{2\sigma_d^M}\left\{ \frac{1}{\pi}\int_{L_M} q_d^M(\xi) g_{MM}(x-\xi)d\xi \right. \\ &+ \int_{L_L} q_d^L(\xi) g_{LM}(x-\xi)d\xi - \int_{L_L} d_d^L(\xi) f_{LM}(x-\xi)d\xi \\ &\left. + \int_{L_R} q_d^R(\xi) g_{RM}(x-\xi)d\xi + \int_{L_R} d_d^R(\xi) f_{RM}(x-\xi)d\xi \right\} \\ &= \sigma_d^M \cdot e^{-k_0 x \cos\beta} \end{aligned} \quad (33)$$

$$\begin{aligned} & d_d^M(\xi) - i\frac{\left(\mu_d^M + \overline{\mu}_d^M\right)}{2\mu_d^M}\left\{ \frac{1}{\pi}\int_{L_M} d_d^M(\xi) h_{MM}(x-\xi)d\xi \right. \\ &- \int_{L_L} q_d^L(\xi) f_{LM}(x-\xi)d\xi + \int_{L_L} d_d^L(\xi) h_{LM}(x-\xi)d\xi \\ &\left. + \int_{L_R} q_d^R(\xi) f_{RM}(x-\xi)d\xi + \int_{L_R} d_d^R(\xi) h_{RM}(x-\xi)d\xi \right\} \\ &= \mu_d^M \cdot e^{-k_0 x \cos\beta} \end{aligned} \quad (34)$$

$$\begin{aligned} & q_d^L(\xi) - i\frac{\left(\sigma_d^L - \overline{\sigma}_d^L\right)}{2\sigma_d^L}\left\{ \frac{1}{\pi}\int_{L_L} q_d^L(\xi) g_{LL}(x-\xi)d\xi \right. \\ &+ \int_{L_M} q_d^M(\xi) g_{LM}(x-\xi)d\xi + \int_{L_M} d_d^M(\xi) f_{LM}(x-\xi)d\xi \\ &\left. + \int_{L_R} q_d^R(\xi) g_{LR}(x-\xi)d\xi + \int_{L_R} d_d^R(\xi) f_{LR}(x-\xi)d\xi \right\} \\ &= \sigma_d^L \cdot e^{-k_0 x \cos\beta} \end{aligned} \quad (35)$$

$$\begin{aligned} & d_d^L(\xi) - i\frac{\left(\mu_d^L + \overline{\mu}_d^L\right)}{2\mu_d^L}\left\{ \frac{1}{\pi}\int_{L_L} d_d^L(\xi) h_{LL}(x-\xi)d\xi \right. \\ &+ \int_{L_M} q_d^M(\xi) f_{LM}(x-\xi)d\xi + \int_{L_M} d_d^M(\xi) h_{LM}(x-\xi)d\xi \\ &\left. + \int_{L_R} q_d^R(\xi) f_{LR}(x-\xi)d\xi + \int_{L_R} d_d^R(\xi) h_{LR}(x-\xi)d\xi \right\} \\ &= \mu_d^L \cdot e^{-k_0 x \cos\beta} \end{aligned} \quad (36)$$

$$\begin{aligned} & q_d^R(\xi) - i\frac{\left(\sigma_d^R - \overline{\sigma}_d^R\right)}{2\sigma_d^R}\left\{ \frac{1}{\pi}\int_{L_R} q_d^R(\xi) g_{RR}(x-\xi)d\xi \right. \\ &+ \int_{L_M} q_d^M(\xi) g_{RM}(x-\xi)d\xi + \int_{L_M} d_d^M(\xi) f_{RM}(x-\xi)d\xi \\ &\left. + \int_{L_L} q_d^L(\xi) g_{LR}(x-\xi)d\xi - \int_{L_L} d_d^L(\xi) f_{LR}(x-\xi)d\xi \right\} \\ &= \sigma_d^R \cdot e^{-k_0 x \cos\beta} \end{aligned} \quad (37)$$

$$d_d^R(\xi) - i\frac{\left(\mu_d^R + \overline{\mu}_d^R\right)}{2\mu_d^R}\left\{\frac{1}{\pi}\int_{L_R} d_d^R(\xi) h_{RR}(x-\xi)d\xi\right.$$
$$+ \int_{L_M} q_d^M(\xi) f_{RM}(x-\xi)d\xi + \int_{L_M} d_d^M(\xi) h_{RM}(x-\xi)d\xi \quad (38)$$
$$\left. - \int_{L_L} q_d^L(\xi) f_{LR}(x-\xi)d\xi + \int_{L_L} d_d^L(\xi) h_{LR}(x-\xi)d\xi \right\}$$
$$= \mu_d^R \cdot e^{-k_0 x\cos\beta}$$

$$q_d^M = \sigma_d^M + C_{sd}^M(x)\left(\sigma_d^M - \overline{\sigma}_d^M\right) \quad (39)$$
$$d_d^M = \mu_d^M + C_{Ad}^M(x)\left(\mu_d^M - \overline{\mu}_d^M\right) \quad (40)$$
$$q_d^L = \sigma_d^L + C_{sd}^L(x)\left(\sigma_d^L - \overline{\sigma}_d^L\right) \quad (41)$$
$$d_d^L = \mu_d^L + C_{Ad}^L(x)\left(\mu_d^L - \overline{\mu}_d^L\right) \quad (42)$$
$$q_d^R = \sigma_d^R + C_{sd}^R(x)\left(\sigma_d^R - \overline{\sigma}_d^R\right) \quad (43)$$
$$d_d^R = \mu_d^R + C_{Ad}^R(x)\left(\mu_d^R - \overline{\mu}_d^R\right) \quad (44)$$

Once integral equations (Eq.(33)-(38)) for q_d and d_d are solved, it is straightforward to compute C_d from Eq.(39)-(44), thereby the complete inner solutions.

2.4 SHIP MOTIONS

In the radiation problem, the force acting in the i-th direction is computed in terms of radiation pressure p_R and the results are described as follows:

$$F_i = -\iint_{S_M+S_L+S_R} p_R n_j dS$$
$$= -(i\omega)^2 \sum_{j=1}^{6}\left[A_{ij} + B_{ij}/i\omega + A_{i+6\,j+6} + B_{ii+6\,j+6}/i\omega + \right. \quad (45)$$
$$\left. A_{i+12\,j+12} + B_{i+12\,j+12}/i\omega\right]X_j$$

$$A_{ij} + B_{ij}/i\omega$$
$$= -\rho\int_L dx \int_{C_S}\left(n_i + \frac{U}{i\omega}m_i\right)\left\{\varphi_j + \frac{U}{i\omega}\hat{\varphi}_j\right\}ds$$
$$-\rho\int_L C_{Sj}(x)dx\int_{C_S}\left(n_i + \frac{U}{i\omega}m_i\right)\varphi_j^{HS}ds \quad (46)$$
$$-\rho\int_L C_{Aj}(x)dx\int_{C_S}\left(n_i + \frac{U}{i\omega}m_i\right)\varphi_j^{HA}ds$$

where A_{ij} and B_{ij} are the added-mass and damping coefficients in i-th direction due to the j-th mode of motion. The contour C_s in Eq.(46) means the contour along the transverse section at each station.

The wave-exciting force E_i in i-th direction also can be computed in accordance with the same manner in the case of radiation problem.

Using these hydrodynamic forces, ship motions can be computed from the coupled motion equations:

$$\sum_{j=1}^{6}\left[-\omega^2\left(M_{ij} + A_{ij} + M_{i+6\,j+6} + A_{i+6\,j+6} + \right.\right.$$
$$\left. M_{i+12\,j+12} + A_{i+12\,j+12}\right) + i\omega\left(B_{ij} + B_{i+6\,j+6} + B_{i+12\,j+12}\right)$$
$$\left.\left(C_{ij} + C_{i+6\,j+6} + C_{i+12\,j+12}\right)\right]X_j = E_i$$

for i=1,2,3,4,5,6 (47).

3. COMPUTAION AND VALIDATION

3.1 APPLICATION TO CATAMARAN

Firstly, the present method, which can be applied to the catamaran without difficulty, is applied to the evaluation of the hydrodynamic forces of catamaran for the validation of the present method because many numerical and experimental studies had been carried out in terms of the hydrodynamic force.

The present method is validated through the comparison with experiments and computation by 3D panel method by Kashiwagi[5)]. Figure 2 and 3 show the heave added-mass and damping coefficient of twin half-immersed spheroids as a function of non-dimensional wave number $k_0B/2$ (B: ship Breadth), respectively. Prior to the present study, it is verified that present method also gives excellent agreement with the computation by Unified Theory applied to twin-hull by Kashiwagi[5)]. It is found that present method gives excellent agreement with the computation by 3D panel method, which becomes same as the present computations in the case of zero speed. It is clarified that interaction force is not negligible because there are certain discrepancy between computation of single hull and computation of twin hulls. It is also found that there are certain discrepancies between computation by the present method and computation by the strip method. It is verified that accurate consideration of interaction force is important to estimate hydrodynamic force of the multi-hull ship accurately.

Figure 4 and 5 show yaw-connecting added moment of inertia and damping coefficient on the left hull induced by pitching of twin half-immersed spheroids as a function of non-dimensional wave number $k_0B/2$ (B: ship Breadth), respectively. It is also found that present method gives excellent agreement with the computation of antisymmetric hydrodynamic force by 3D panel method[5)]. It is verified that the present method evaluate the hydrodynamic force of multi-hull ship in the case of zero speed accurately.

Figure 6 and 7 show the Pitch added moment of inertia coefficient and damping coefficient of twin Lewis-form ships as a function of non-dimensional wave number k_0L (L: ship length), respectively. It is found that present method agrees with experiments qualitatively. In particular, agreement with experiments is remarkably modified in comparison with the strip method. In the meanwhile, there are certain quantitative discrepancy between the present method and experiments. It is considered that present method doesn't take account of 3D and forward speed effect completely in the case of non-zero ship speed. However, it is clarified that the present method can evaluate the hydrodynamic force of a multi-hull ship rationally without waste of huge computation time.

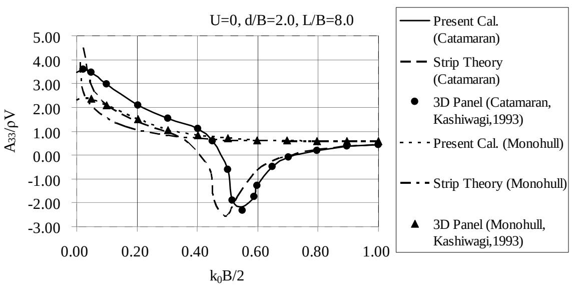

Figure 2 Heave added-mass coefficient of twin half-immersed spheroids with L/B=8 and D/B=2 at U=0 (Head seas)

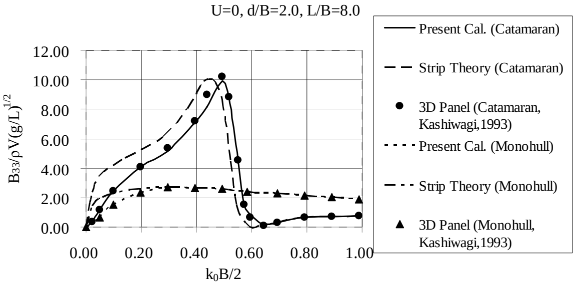

Figure 3 Heave damping coefficient of twin half-immersed spheroids with L/B=8 and D/B=2 at U=0 (Head seas)

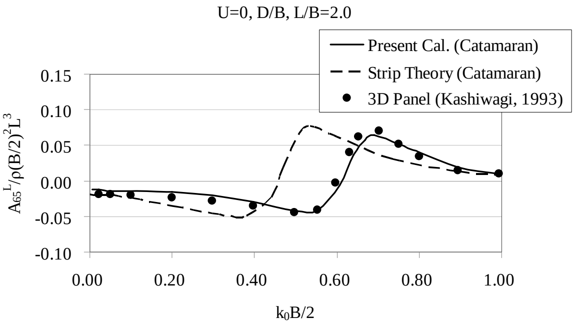

Figure 4 Yaw-connecting added moment of inertia on the left hull, induced by pitching of twin half-immersed spheroids with L/B=8 and D/B=2 at U=0 (Head seas)

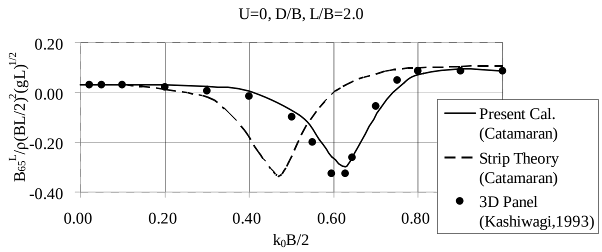

Figure 5 Damping coefficient of yaw-connecting moment on the left hull, induced by pitching of twin half-immersed spheroids with L/B=8 and D/B=2 at U=0 (Head seas)

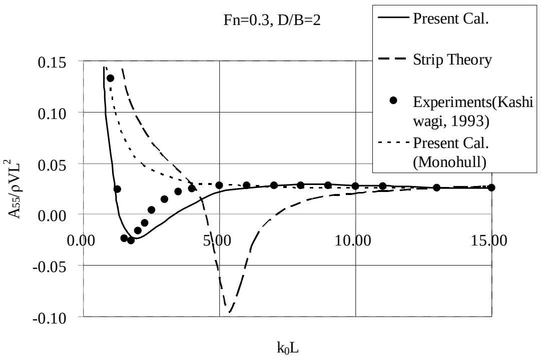

Figure 6 Pitch added moment of inertia coefficient of twin Lewis-form ships with D/B=2 at Fn=0.3 (Head seas)

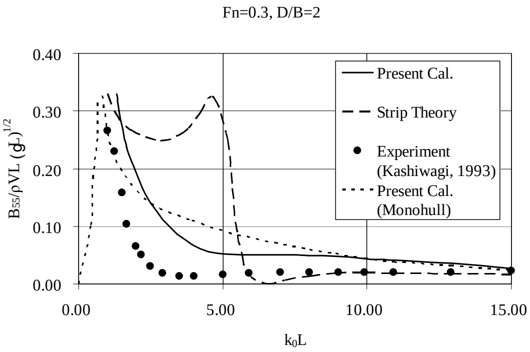

Figure 7 Pitch damping coefficient of twin Lewis-form ships with D/B=2 at Fn=0.3 (Head seas)

3.2 APPLICATION TO TRIMARAN

National Maritime Research Institute (NMRI) is planning to carry out the comprehensive study for the seakeeping performance of a trimaran. As a part of this study, computed wave loads will be verified through the comparison with experimental data.

Prior to the comprehensive study, present method is verified through the comparison with the existing experimental data. In addition, the effect of arrangement of side hull on the wave loads is examined using present method.

As examples of verification of the present method, the response amplitude operator of pitch as a function of wave length ratio are shown figure 8 and 9. Pitch amplitude is divided by the $k_0\varsigma$ (ς: wave amplitude). For the verification, experimental data by Yasukawa[8] is used. In that experiment, arrangement of side hull was varied as follows:

Tri-F: connected side hulls at S.S. 5 of the main hull

Tri-M: connected side hulls at S.S. 3.5 of the main hull

Tri-A: connected side hulls at S.S. 1.875 of the main hull.

It is found that with shifting side hulls rearward, pitch motion increase in the long wave length range and decrease in the short wave length range. It is also found that present method agrees well with experiments qualitatively although there are some discrepancies quantitatively. It is clarified that present method is useful for the evaluation of ship motion of trimaran.

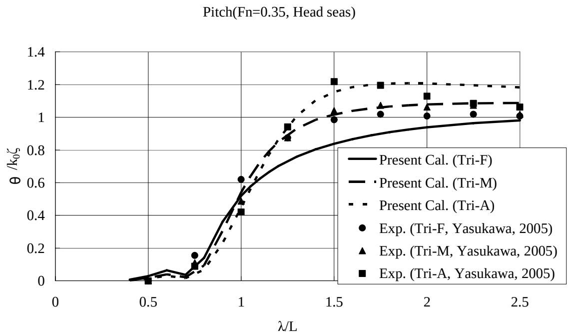

Figure 8 Response amplitude operator of Pitch of trimaran (Fn=0.35)

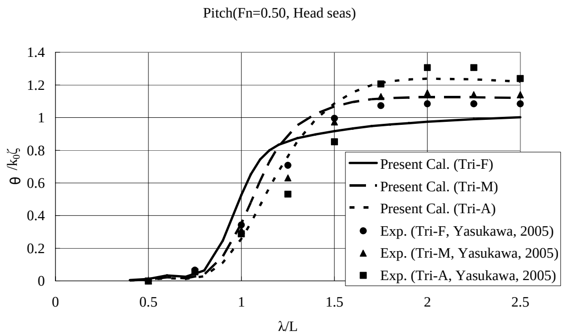

Figure 9 Response amplitude operator of Pitch of trimaran (Fn=0.5)

Using present method, the effect of arrangement of side hull on the wave loads is examined. Figure 10 shows the response amplitude operator of vertical bending moment at midship of main hull as a function of wave length ratio. Amplitude of vertical bending moment M_v is divided by the $\rho gB\varsigma L^2$ (ρ: density of fluid, g: acceleration of gravity).

It is found that with shifting side hulls rearward, vertical bending moment increase in the long wave length range and decrease in the short wave length range. It is consistent with the characteristics of ship motions. It is clarified that arrangement of side hull has effects on the wave loads acting on the trimaran.

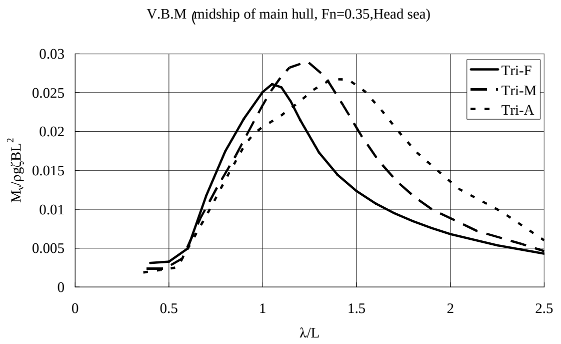

Figure 10 Response amplitude operator of vertical bending moment of main hull of trimaran (Fn=0.35)

4. CONCLUSION

In the present study, a practical prediction method of ship motion of multi-hull is developed in accordance with the Unified Theory approach. Having compared with experiments, the present method is verified. The effect of arrangement of side hull is examined. Conclusions are as follows:

1) Present method agrees well with experiments qualitatively although there are some discrepancies quantitatively in the case of high speed condition.

2) Present method can evaluate the hydrodynamic force of a multi-hull ship rationally without waste of huge computation time.

3) Arrangement of side hull has effects on the wave loads act on the trimaran.

REFERENCES

1. Newman, J.N., “The theory of Ship Motions”, Advanced Applied Mechanics, vol. 18, pp. 221-283, 1978.

2. Sclavounos, P.D., “The diffraction of Free-Surface Waves by a slender Ship”, Journal of Ship Research, vol. 28, No.1, pp. 29-47, 1984.

3. Kashiwagi, M., “Added resistance, wave-induced steady sway force and yaw moment on an advancing ship”, Ship Technology Research, vol. 39, No.1, pp. 3-16, 1992.

4. Kashiwagi, M., “Prediction of surge and its effect on added resistance by means of the enhanced unified theory”, Transaction of West-Japan Society of Naval Architects, vol. 89, pp. 77-89, 1995.

5. Kashiwagi, M., “Interaction Force between Twin Hulls of a Catamaran Advancing in Waves (Part 1: Radiation Problem)”, Journal of Society of Naval Architects of Japan, vol. 173, pp. 119-131, 1993.

6. Kashiwagi, M., “Interaction Force between Twin Hulls of a Catamaran Advancing in Waves (Part 2: Wave-Exciting Forces and Motions in Waves)”, Journal of Society of Naval Architects of Japan, vol. 174, pp. 181-190, 1993.

7. Ronaess, M., “Wave Induced Motions of Two Ships Advancing on Parallel Course”, Ph.D. thesis, NTUT, Trondheim, 2002.

8. Yasukawa, H. et al., “Influence of Outrigger Position on the Performance of a High speed Trimaran (2nd Report: Wave-induced Motions in Head Seas)”, Journal of The Japan Society on Naval Archtects and Ocean Engineers, vol. 2, pp. 189-195, 2005.

TRIMARAN MANEUVERING SIMULATION BASED ON THREE-DIMENSIONAL VISCOUS FREE SURFACE FLOW SOLVER

M.R. Javanmardi, M.S. Seif, E. Jahanbakhsh, H. Sayyaadi
Marine Lab., Dept. of Mechanics, Sharif University of Technology, Tehran, Iran , seif@sharif.edu

SUMMARY

In this paper the effect of three longitudinal positions of outriggers in a Trimaran maneuvering is studied. For hydrodynamic simulations NUMELS –Numerical Marine Eng. Lab. Sharif- code is used. This software was developed for simulating three dimensional, time dependent, two phases, viscous flow coupled with rigid body motion. Different case studies have been performance and numerical results have shown good agreement with experimental data. Based on maneuvering simulation of trimaran vessel different conclusion are made. The results show that longitudinal positions of outriggers have great effect on maneuverability of trimaran.

1. INTRODUCTION

Wave making resistance is a significant component of ship resistance. It is very effective at higher speeds and will require more attention in designing of high speed ships. Normally large slenderness ratio ($L/V^{1/3}$) is necessary to decrease the wave making resistance. Therefore the ship hull should be as slender as possible for attaining higher speeds. But the main drawback of this effect is that the transverse stability decreases. Hence to overcome this challenge, the single body must be changed to multi-hull with proper separation distance. It means that a trimaran vessel which is composed of a main slender body and two outriggers can be appropriate solution to improve vessel transverse stability, while the efficient wave interaction, created by main body and outriggers is able to compensate for wetted surface increase and guaranties slender bodies with good stability at high Froude numbers. Trimarans share most of the characteristics of catamarans, but in few aspects, trimarans are more efficient than catamarans. Lyakhovitsky compared a trimaran with a mono-hull and a catamaran of same characteristics and showed that the trimaran is better in hydrodynamic performances compared to other alternatives [1]. In addition trimarans have some other privileges such as: extended deck, lower draft and better transverse stability compared with single body vessels. In additional, for military vessels, possibility of engine exhaust conductance between bodies makes less traceable [2]. In order to study the effect of outriggers position on trimaran resistance, some experimental tests are done and results show that the outriggers location has considerable effect in hydrodynamic performance of the vessel [3], but in vessel design, some cases such as maneuverability must be consider. Optimization procedures increasingly demand the performance of a ship to be assessed in its early design stage. This leads to a prediction tool independent of experimental results, although model tests will still be indispensable. CFD modeling based on numerical solution of the governing equations is a good choice. It must be remembered that, such a problem combines the complexity of free surface flow with rigid body motions. NUMLES code which originally developed in Sharif University of technology [13] provides an effective numerical tool for hydrodynamic simulation. Trimaran maneuvering simulation is a complex hydrodynamic problem that should be considered as multi physics phenomenon. In solving such a problem, one encounters to three subproblems which are: a) velocity and pressure distribution, b) free surface deformation and c) rigid body motion. Solving the first two subproblems results in interfacial flow simulation. By computation of velocity and pressure distribution, tangential and normal stresses are calculated. Integration of such stresses over the body yeilds to forces and moments acting on it. Solving the last subproblem, in conjunction with such values, gives a time-history of body motions in one or two phases e.g. submarine maneuvering or ship seakeeping. The important point is that, although potential theory methods [4] are capable of predicting motions with lower run time but they are not suitable where viscosity breaking waves or large amplitude motions play an important role. For many practically important cases, large errors are introduced by the potential theory assumptions. The motion of a floating body is a direct consequence of the flow-induced forces acting on it while at the same time these forces are functions of the body movement itself. Therefore, the prediction of flow-induced body motion in viscous fluid is a challenging task and requires coupled solution of fluid flow and body motions. In recent two decades, with the changes in computer hardware, ship motion simulation is the subject of many numerical hydrodynamic researches. These researches were started from the restricted motions such as trim or sinkage by Miyata [5], Hochbaum [6] Alessandrini [7] and Kinoshita [8] and continiued to the evaluation of 6-DoF motions by Miyake [9], Azcueta [10], Vogt [11], Xing [12] and Jahanbakhsh et. al [17].

In this paper, numerical NUMELS software has been used. The trimaran motion and the effect of outriggers positions on trimaran manouvering are studied.

2. FORMULATIONS AND SOLUTION ALGORITHM

Here a finite volume time dependent three-dimensional viscous free surface flow solver is used [10]. Velocity and pressure fields are coupled using fractional step of Kim and Choi [11]. One must take into account the presence of high density ratio phases e.g. water and air in discretisation of pressure gradient integral which is treated here in a new way [10]. Also, a surface capturing method is used which solves a transport equation for calculation of fluids volume fraction. CICSAM interpolation has great advantages in comparison to other interpolations and used in this study for approximation of face volume fraction [15]. There are a variety of motion simulation strategies in numerical hydrodynamic applications. Here, a body-attached mesh following the time history of body motions is used [10]. In other words, linear and angular momentum equations are solved in each time step which results in 6-DoF motions. Such motions are applied on body and computational domain simultaneously to make it ready for the next time step. It must be noted that, all of the fluid governing equations are written for a moving control volume in Newtonian Reference system [16] which results in using relative face velocity for convection flux calculation while keeps the simplicity of equations.

As mentioned earlier, one encounters to three sub-problems in CFD simulation of ship motions. These parts which are marked with dashed lines are solved in a loop as shown in Fig.1.

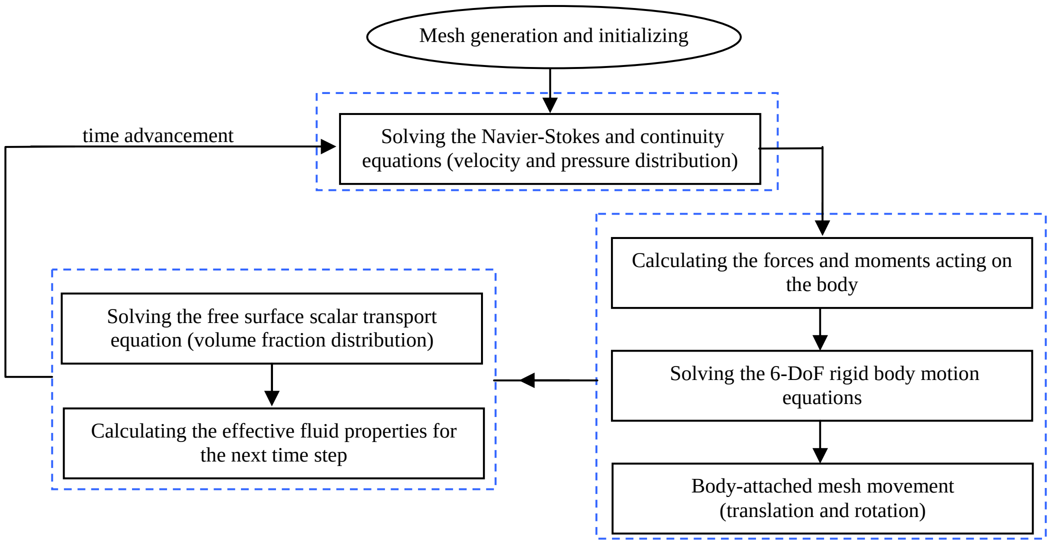

Fig.1: Solution algorithm for numerical modeling

3. NUMERICAL RESULTS

Coupling of rigid body motion with fluid dynamics has been studied by this software in former researches [17, 18, 19, and 20]. In those researches the numerical simulation of cylinder slamming, 2-DoF barge resistance and 3-DoF barge and 6-DoF catamaran turning maneuver has been performed and its results showed acceptable concordance with experiments.

In this study, behavior of Trimaran configurations as a 6-DoF rigid body is studied in calm water. Table 1 and Table 2 present the characteristics and configurations of trimaran, respectively. The parameters defined in table 1 and 2, are illustrated in Fig.2. The trimaran configuration is defined by the ratios d/L_M and s/L_M , where d is the longitudinal distance between the bows of the main hull and the outriggers, and s is the transverse distance between the centerline of outriggers. In Table 2 and Fig.2, the under notes M and O are pointed to main hull and outriggers respectively.

Domain around trimaran body has been meshed with nearly 150000 hexahedral cells. Boundary conditions of the problem were considered as an impermeable wall and no-slip condition at the body and 6 outlet far-field conditions for sides. Fig.3 shows mesh and configuration of boundary conditions on computational domain.

Table 1: Trimaran characteristics

	Main hull	Outriggers
Length L(m)	2.4	1.2
Breadth B(m)	0.24	0.12
Draft T(m)	0.15	0.075
Displacement (kg)	40.0	5.0
Wetted surface (m^2)	0.88	0.44

Table 2: Trimaran configurations

d/L_M \ d/L_M	0	0.25	0.5
0.2	A	B	C

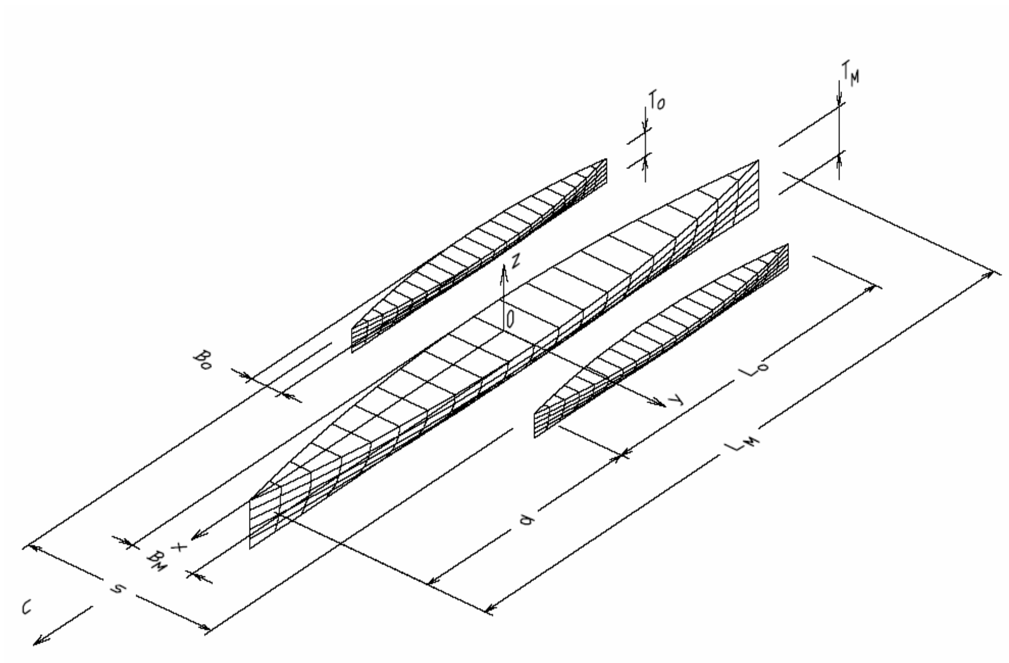

Fig. 2: Trimaran configuration with main particulars and relative position of hulls

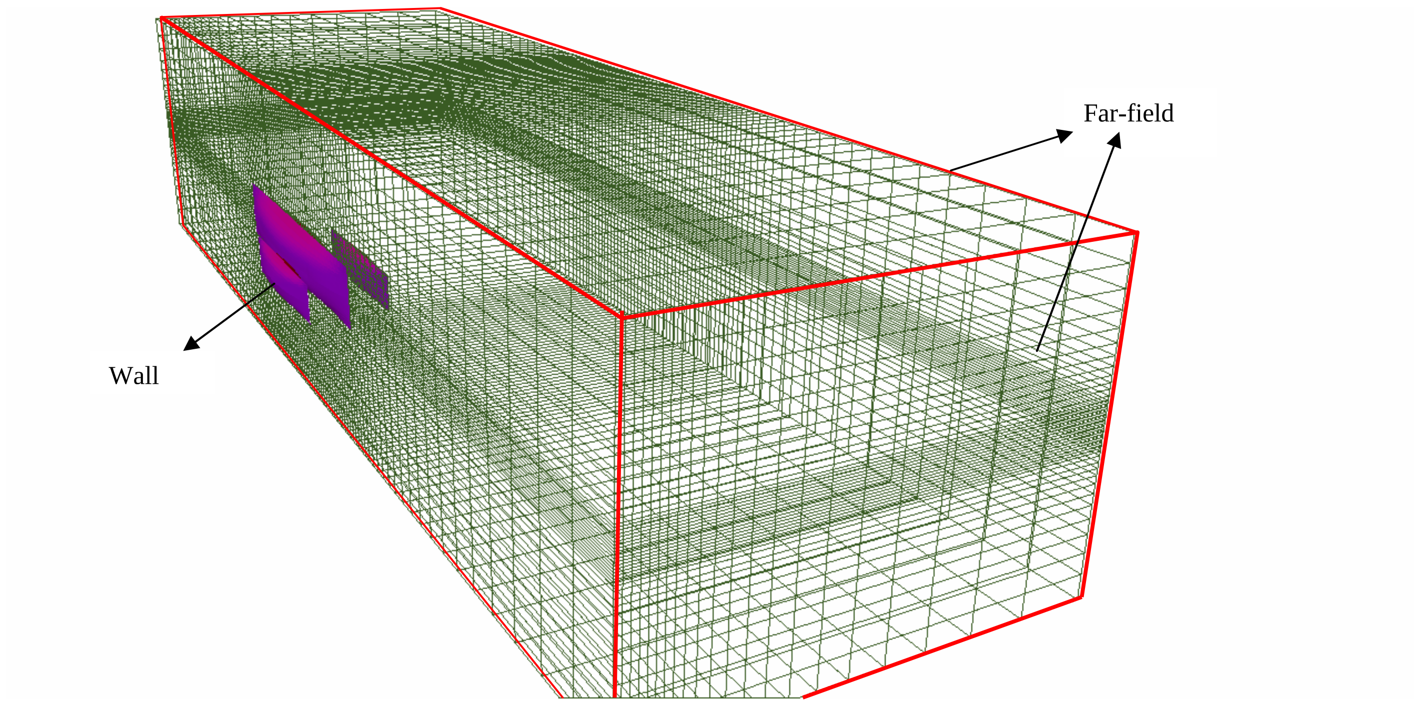

Fig.3: Computational domain

Applying forces and moments of maneuvering is performed by rotation of thrusters. So there is no rudder here and whole of propulsion system assumed to be rotated. Angle of rotation which applied on the trimaran's propulsion systems is 30 degrees. It should be noted that propulsion system assemble on the main hull and turning starts just after 10 seconds from the beginning of simulation. This permits the ship to reach a nearly steady forward motion due to thrusters' force. At first, various trimaran configurations are simulated at 4 m/s speed and required force to reach this speed is calculated which is shown in table 3. It is clear that for each configuration the thruster force is equal to its corresponding total resistance forces.

Table 3: Total drag at 4 m/s speed for different configuration

Configuration	A	B	C
Total drag (N)	43.92	55.00	48.24

Fig.4 shows the time history of ship speed for different configurations. It can be seen that for A configuration decreasing speed at turning is more than other configurations. Path of ship's center of gravity is shown in Fig.5. In the turning circle, The diameter of rotation circle for A configuration is most magnitude and for B and C configuration is close together.

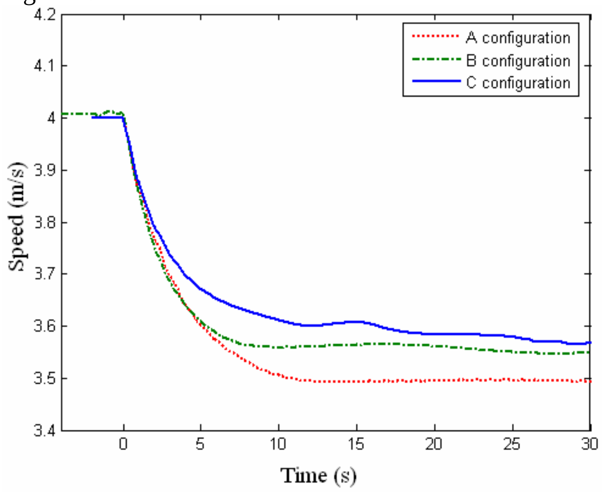

Fig.4. Speed time history for different configurations

In Fig. 6 trim angle of the vessel are shown. It is obvious that when the side bodies stem are aligned with main hull stem, the vessel trim is more than B and C configuration and when the three bodies stern of vessel are aligned (C configuration), trimaran has least trim angle. Therefore when the outriggers are in front of vessel (A configuration), it leads to a large trim angle which causes some section of side hulls come out of water and therefore stability decreases. In Fig.7, heel angle of various trimaran configurations is plotted. It can be seen that A configuration has least heel angle and its magnitude is near 1.5 degree, but oscillation magnitude is more than other configurations. Drift angle of three different configurations is also plotted in Fig.8. It is clear that trimaran with A configuration has not stable drift angle. Fig.9 shows Time history of yaw speed. It can be seen that A configuration has lowest yaw speed. Least yaw speed and unstable drift angle for A configuration can be reason of largest diameter of turning circle relate to other configurations.

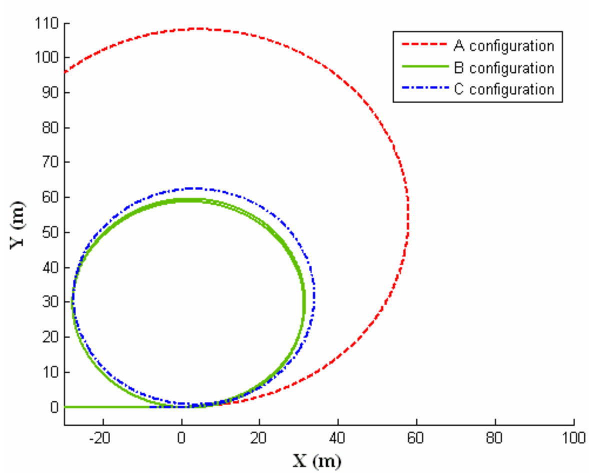

Fig.5. Ship mass center path

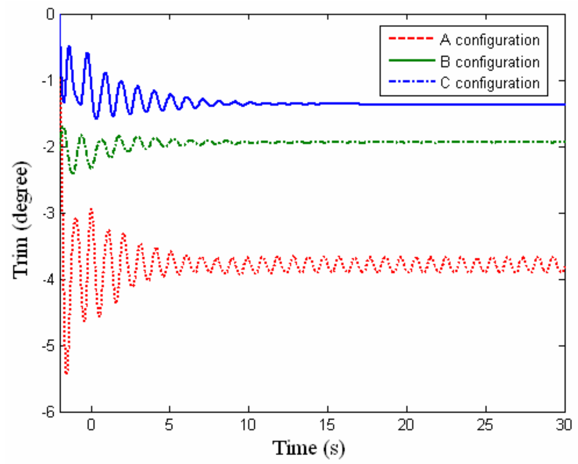

Fig. 6: Trim angle time history for different configuration

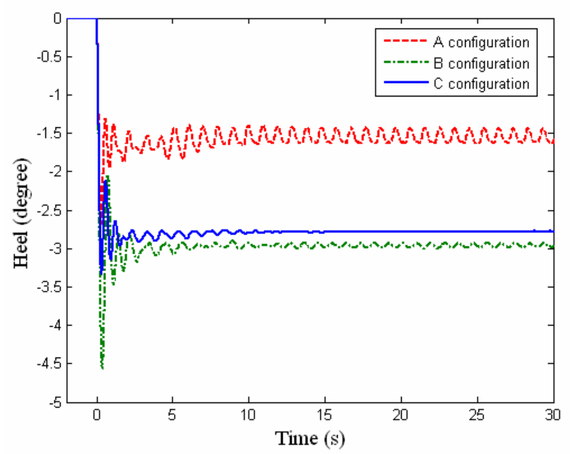

Fig 7: Heal angle time history for different configurations

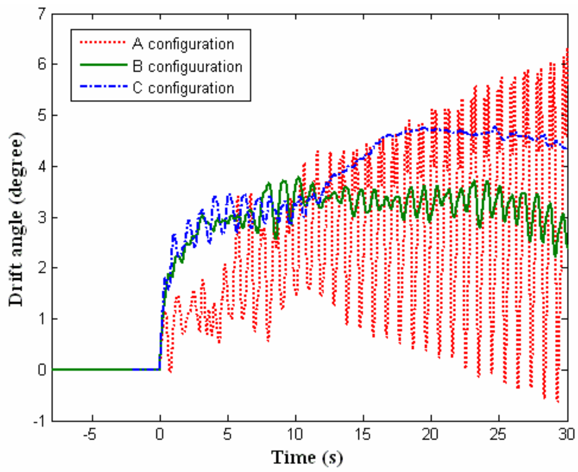

Fig.8: Drift angle time history for different configuration

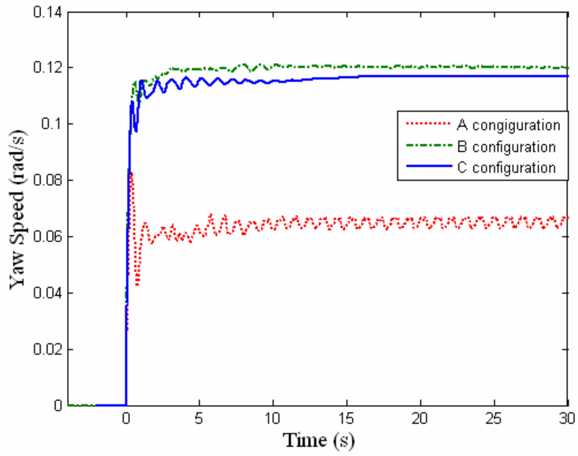

Fig. 9: Yaw speed time history for different configurations

Figs 10~12 includes few snapshots of trimaran and free surface around it during turning maneuver. The unsymmetrical waves generated during turning can be seen in this figure.
Figs 13 and 14 are better view of rout close to the starting point of maneuver.

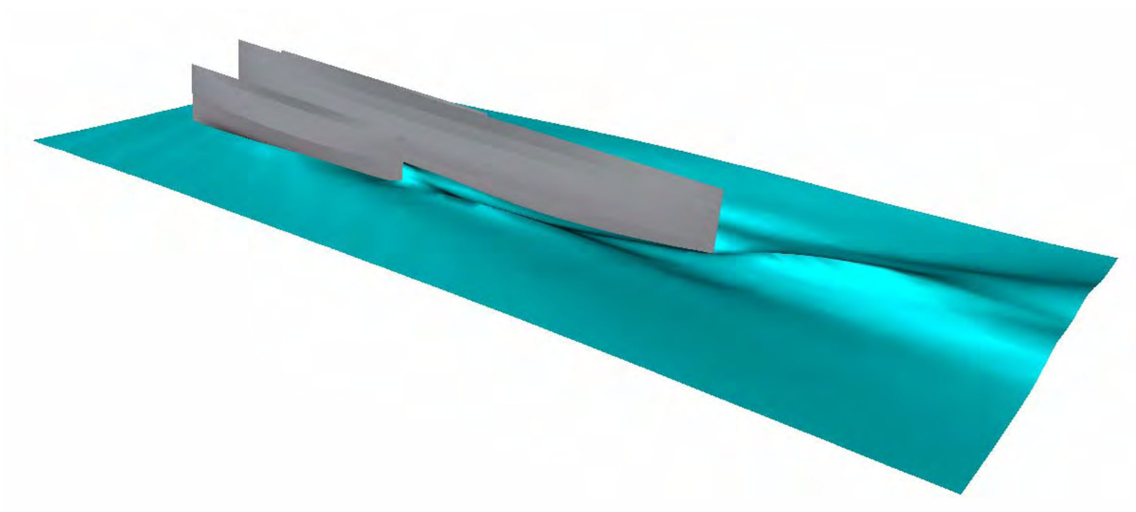

Fig.10: Free surface for A configuration

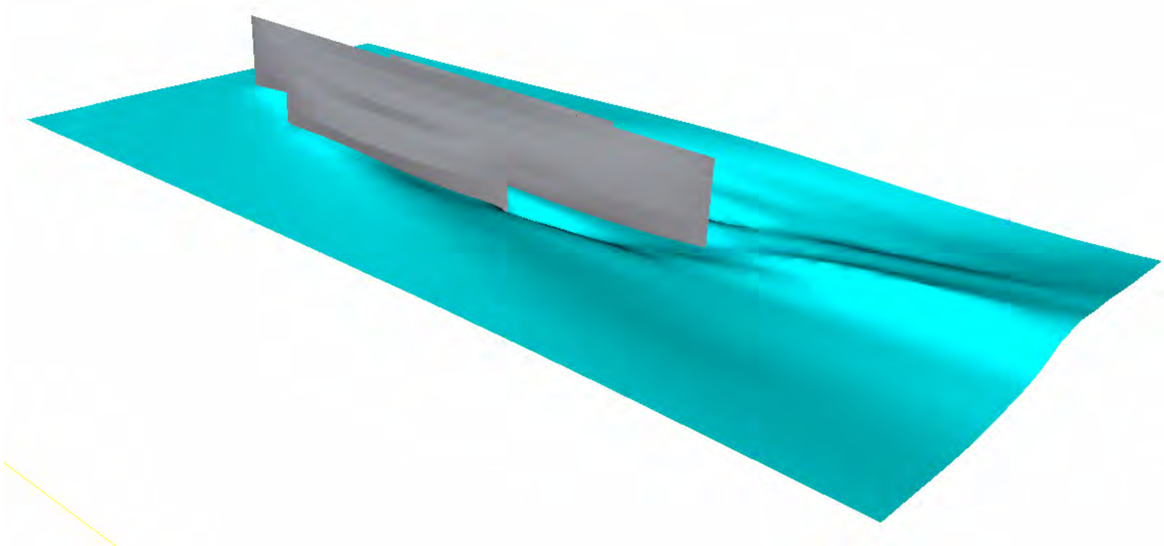

Fig.11: Free surface for B configuration

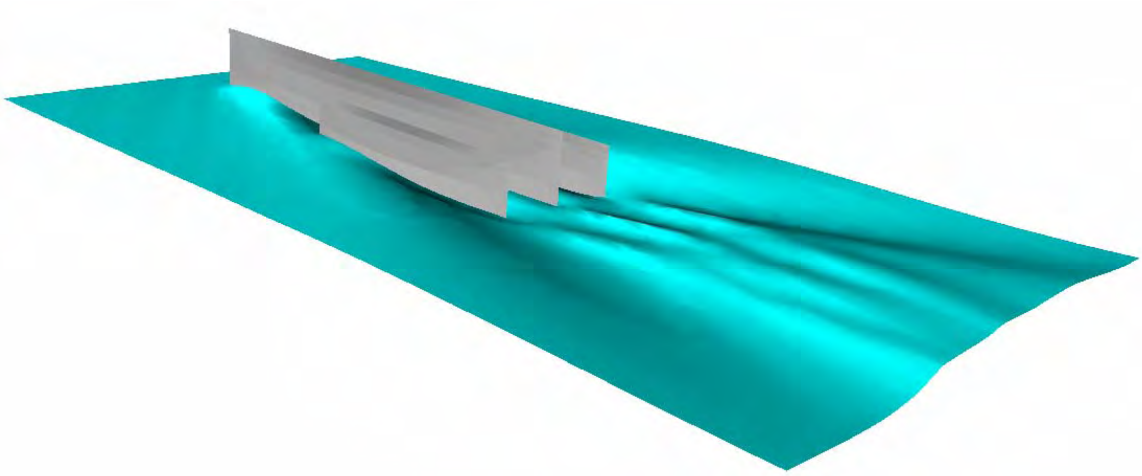

Fig.12: Free surface for C configuration

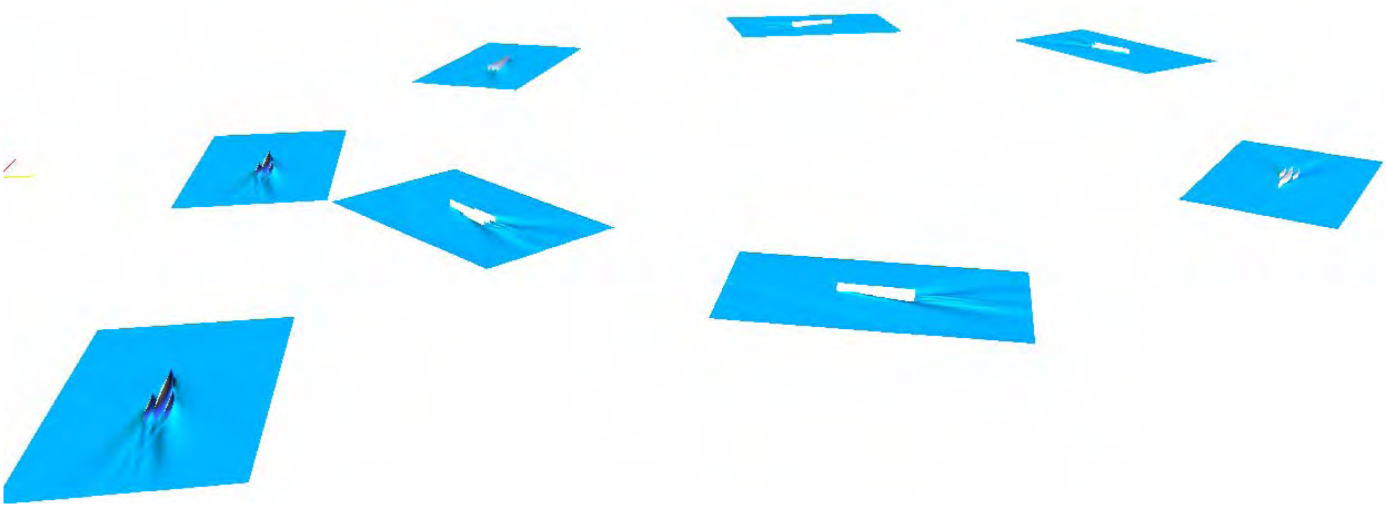

Fig.13: Trimaran turning simulation 6-DoF with C configuration

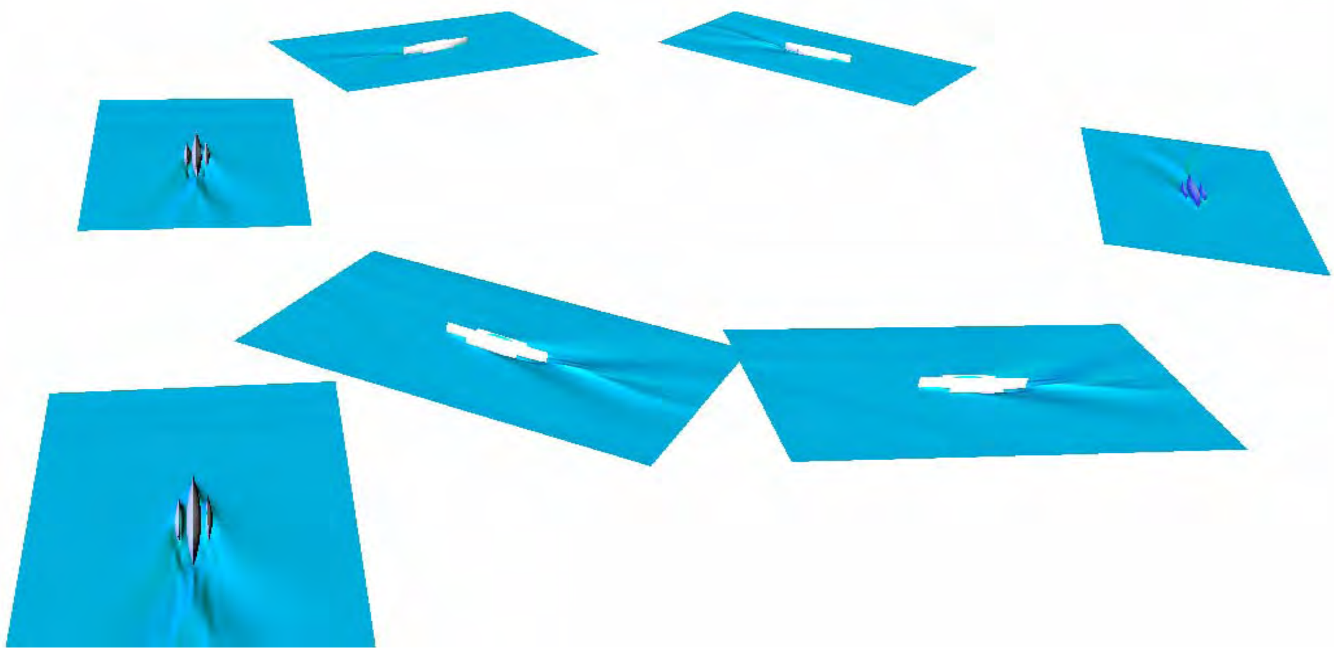

Fig.14: Trimaran turning simulation 6-DoF with B configuration

4. CONCLUSION

Maneuvering of a trimaran vessel has been investigated in present paper taking into account 6-DoF rigid body motion. Numerical results show that outriggers position has great effect on trimaran maneuverability. Based on these results, it can be seen that when the bow of three bodies are aligned, it is not an appropriate configuration for maneuvering, because in this case, vessel trim causes outriggers to come out from water, therefore stability decreases. With comparison B and C configurations, the circles of turning have almost same diameter but since C configuration needs less thrust force than other case, so it is more efficient configuration, from resistance point of view.

5. REFERENCES

1. V.Dubrovsky & A.Lyakhovitsky, *Mullty Hull Ships*, Backbone Publishing,USA, (2001).
2. N. Degiuli, A. Werner, I. Zotti, *an experimental investigation into the resistance components of Trimaran configurations*, FAST (2005).
3. K. Kang , C. Lee , D. Kim, *Hull form development and powering performance characteristics for a 2500ton class Trimaran*, Practical Design of ships and Other Floating Structures, (2001).
4. V. Bertram, *Practical ship hydrodynamics*, Butterworth-Heinemann, Oxford, (2000).
5. H. Miyata, T. Sato and N. Babo, *Difference solution of a viscous flow with free-surface wave about an advancing ship*, J. Comput. Phys., Vol.72, p.393-421, (1987).
6. C. Hochbaum, *A finite volume method for turbulent ship flows*, Ship Technology Research Schiffstechnik, Hamburg, Germany, (1994).
7. B. Alessandrini and G. Delhommeau, *Simulation of three-dimensional unsteady viscous free surface flow around a ship model*, Int. J. of Numerical Math. Fluids, Vol.19, p.321-342, (1994).
8. T. Kinoshita, H. Kagemoto and M. Fujino, *A CFD application to wave-induced floating-body dynamics*, 7th Int. Conference on Numerical Ship Hydrodynamics, Nantes, France, (1999).
9. R. Miyake, T. Kinoshita and H. Kagemoto, *Ship Motions and loads in large waves*, 23rd ONR Symp. On Naval Hydrodynamics, Val de Reuil, France, (2000).
10. R. Azcueta, *Computation of turbulent free surface flow around ships and floating bodies*, PhD Thesis, Teschnichen Universitat Hamburg-Harburg, (2001).
11. M. Vogt and C. Hochbaum, *Numerical simulation of ship motions in head waves with a RANSE method*, HSVA Report 1649, Hamburg, Germany, (2002).
12. Y. Xing-Kaeding, *Unified approach to ship seakeeping and maneuvering by a RANSE method*, PhD Thesis, Teschnichen Universitat Hamburg-Harburg, (2004).
13. E. Jahanbakhsh, R. Panahi, and M.S. Seif, *Numerical Simulation of Three-Dimensional Interfacial Flows*, International Journal of Numerical Methods for Heat & Fluid Flow, Vol. 17, Issue 4, (2007).
14. D. Kim, and H. Choi, *A second-order time-accurate finite volume method for unsteady incompressible flow on hybrid unstructured grids*, J. of Comput. Phys., Vol.162, p.411-428, (2000).
15. R. Panahi, E. Jahanbakhsh, and M.S. Seif, , *Effect of interpolation in interface capturing methods*, 8th Numerical Towing Tank Symposium (NuTTs'05), Varna, 2-4 October, (2005).
16. F.M. White, *Fluid mechanics*, Mc Graw-Hill, 4th Ed, (2001).
17. E. Jahanbakhsh, R. Panahi, and M.S. Seif, *Ship dynamic simulation, based on a three-dimensional viscous free surface flow solver*, 9th Numerical Towing Tank Symposium (NuTTs'06), (2006).
18. R. Panahi, E. Jahanbakhsh, and M.S. Seif, *Development of a VoF fractional step solver for floating body motion simulation*, Applied Ocean Research, Vol.28, No.3, p 171-181, (2006).
19. R. Panahi, E. Jahanbakhsh, and M.S. Seif, *Development of a numerical hydrodynamic tank for ship motion simulation*, European Conference on Computational Fluid Dynamics (ECCOMAS), (2006).
20. E. Jahanbakhsh, R. Panahi, M.S Seif, *High-Speed Planing Catamaran Maneuvering Simulation, Based on a Three-Dimensional Viscous Free Surface Flow Solver*, 10th Numerical Towing Tank Symposium, (2007).

AN EXPERIMENTAL AND NUMERICAL STUDY ON CAVITATION OF HULL APPENDAGES

Luca Savio, Department of Naval Architecture and Marine Engineering (DINAV), Genoa University, Italy
Chiara Pittaluga, Hydrodynamics Department, CETENA, Italy
Michele Viviani, Department of Naval Architecture and Marine Engineering (DINAV), Genoa University, Italy
Marco Ferrando, Department of Naval Architecture and Marine Engineering (DINAV), Genoa University, Italy
Francesco Conti, Fincantieri C.N.I. Spa – Naval Vessel Business Unit - Genoa, Italy

SUMMARY

In the present work a study on cavitation of hull appendages, such as stabilizer fins or rudders, is presented. The attention is focused on tip related cavitation and especially on tip vortex cavitation. Devices, such as end plates and tip fairing, commonly adopted to reduce this phenomenon are analyzed trough experiments and numerical calculations. Various solutions are compared underlining their advantages and shortcomings, considering the effect on cavitation inception and vortex intensity. With this aim, a model of control surface was fitted with different end plates and with a tip fairing and tested at various angles of attack. Experiments were carried out in the cavitation tunnel of the University of Genoa while CFD computations were performed by CETENA. Moreover a comparison between experiments and numerical results is presented showing the relation existing between the two different approaches. As a result a simplified technique to predict cavitation phenomenon by means of numerical simulations calibrated with experimental results is outlined.

1. INTRODUCTION

Cavitation is one of the most important issues in propeller and hull appendages design. Among various types, vortex cavitation, in particular its inception, is still nowadays considered far from being completely understood [1]. With the increase in ships performance, more strict requirements in terms of environmental impact of ships and inboard comfort, this particular type of cavitation is gaining more and more relevance. Vortex cavitation is a source of radiated noise, but also of pressure pulses, and being able to propagate far downstream can interact with appendages (for example propeller tip and hub vortex with rudder).
From the design point of view what is more needed is to achieve a technique to predict the inception of vortex cavitation, because procedure to scale model test to full size are well known and reliable, see for instance reference [2]. In this scenario CFD computations may be a feasible way to solve the problem.
For the above reasons Cetena has been involved in CFD calculations for long time, dealing with different problems, among which evaluation of cavitation inception. As an example in the activities of the EU funded research project Leading Edge attention was focused on tip vortex cavitation inception on propellers. The study was mainly carried out with numerical simulations, but besides achievement obtained in this project the need of comparison between numerical solutions and experimental tests was stressed. This need was mainly linked to difficulty of computations in fully predicting tip vortex cavitation inception. [3]
The present study deals with this complicated topic partly simplifying the problem, by considering tip cavitation on a typical hull appendage, such as a stabilizer fin or a rudder in open water, thus dealing with a simpler geometry with respect to the propeller case. The wing dimensions were chosen to be as close as possible to an average hull appendage in order to add value to results. The low aspect ratio of the tested wing and its tip shape led to the identification of two different tip cavitation types, as described in the following paragraphs. This paper therefore focuses also on their interaction.
This work was fully supported by Fincantieri C.N.I, who also supplied the geometry of the wing.

2. MODELS AND TEST DESCRIPTION

In the following, the experimental set-up is briefly described; in particular, in paragraph 2.1 different models geometries are reported, in paragraph 2.2 the experimental facility is described and in paragraph 2.3 the tested conditions are listed.

2.1 MODELS

As anticipated, three different appendage models have been considered in the present study; in particular, all models are derived from the same initial geometry, with modification of the tip shape, and in particular:

- Squared tip (model 1)
- Faired tip (model 2)
- Squared tip + end plate (model 3)

The choice of utilizing the same geometry (in terms of macroscopic characteristics, i.e. aspect ratio, taper ratio, thickness/chord ratio and sectional profiles) is linked to the wish to analyse specifically the influence of the tip shapes on the tip vortices inception, without taking into account other factors such as load distribution on the appendage.

It has to be noted, from this point of view, that the appendage might be indifferently a fin or a rudder, for which application of different tip shapes has been documented in literature [4][5][6].

In the following table 1, main non-dimensional characteristics of the appendage are reported (where t/c is thickness / chord ratio, a.r. is geometrical aspect ratio and λ is the taper ratio), while in following figures 1-4 photographs of the models tested are reported.

t/c	0.18
a.r.	1.10
λ	0.80

Table 1: Main non-dimensional characteristics

.Fig. 1: Overall view of the appendage

Fig. 2: Model 1 tip (squared)

As it can be seen from figure 4, the end plate utilized is somehow different from conventional ones, being applied only in the forward part of the appendage and not up to the trailing edge. This choice is due to the interest in analyzing end plates which can be easily adopted both to appendages with and without flaps, therefore its extension has been chosen in order to avoid covering the possible movable flap part.

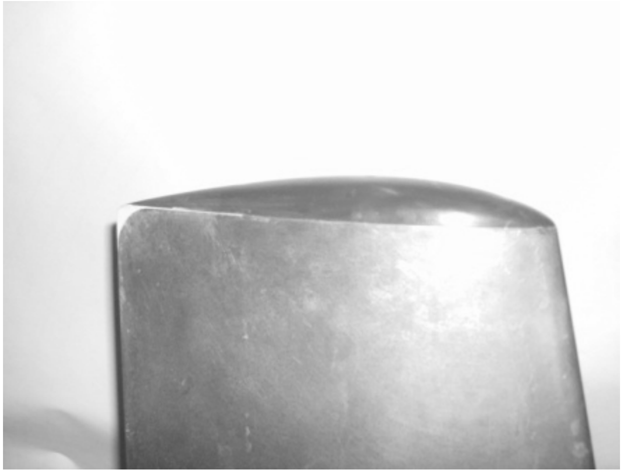

Fig. 3: Model 2 tip (faired)

Fig. 4: Model 3 tip (squared + end plate)

In order to analyse also the possible disturbance of a flap actuator, this has been schematized with two cylinders in the aft part of the root section, even if no flap has been included in the present analyses for the sake of simplicity.

2.2 EXPERIMENTAL FACILITY

The experiments are carried out at the Cavitation Tunnel facility of the Department of Naval Architecture and Marine Engineering of the University of Genoa (DINAV), represented in figure 5.

The facility is a Kempf & Remmers closed water circuit tunnel with a squared testing section of 0.57 m x 0.57 m, having a total length of 2 m. Optical access to the testing section is possible through large windows.

The nozzle contraction ratio is 4.6:1, and the maximum flow speed in the testing section is 8.5 m/s. Vertical distance between horizontal ducts is 4.54 m, while horizontal distance between vertical ducts is 8.15 m.

Flow speed in the testing section is measured by means of a differential venturi-meter with two pressure plugs immediately upstream and downstream of the converging part.

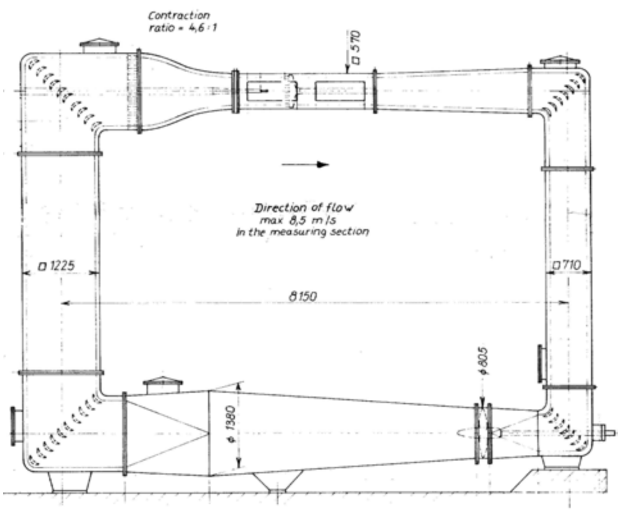

Fig. 5: DINAV Cavitation Tunnel

A depressurization system allows obtaining an atmospheric pressure in the circuit near to vacuum, in order to simulate the correct cavitation index for propellers and profiles (2D and 3D).

In the present experimental campaign, the 3D appendage has been connected to one of the tunnel windows (simulating a completely flat hull surface) with a low gap between the root section and the wall (about 4 mm), and with the possibility of setting the angle of attack to different values.

The appendage dimensions have been chosen in order to allow a good visualization of cavitation phenomena, in particular the span is 200 mm.

Cavitation phenomena visualization in the testing section has been made with two Allied Vision Tech Marlin F145B2 Firewire Cameras, with a resolution of 1392 x 1040 pixels and a frame rate up to 10 fps.

In the following Figure 6, the testing setup is presented, while in following Figures 7 and 8 two typical pictures from the two cameras are provided.

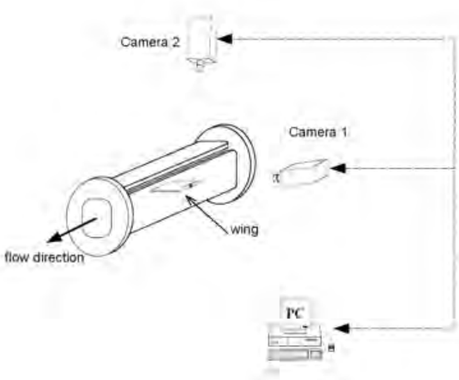

Fig. 6: Testing set-up

For what regards forces evaluation, this was not performed in the present testing campaign since the tunnel is not equipped with a measuring equipment; it has to be pointed out once more that main objective of this experimental campaign has been the evaluation of tip vortices inception.

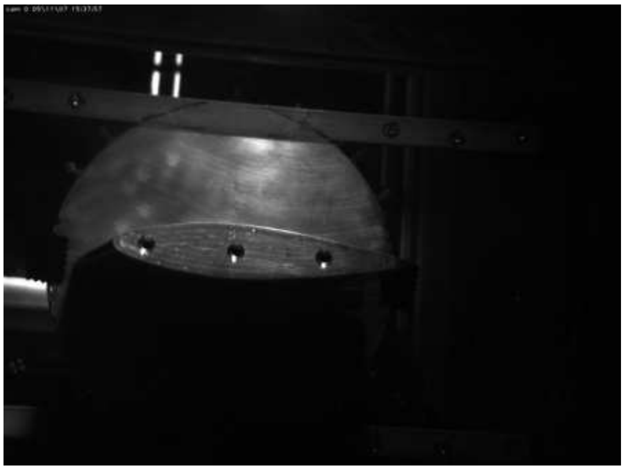

Fig. 7: Camera 1 view

Fig. 8: Camera 2 view

2.3 TESTED CONDITIONS

For all appendage configurations, a series of tests at different cavitation index values have been performed. In particular, cavitation index values tested range from 5.5 to 1. Moreover, all tip configurations have been tested in correspondence to an angle of attack of 5° and 10°.

The limitation of the angles to these two values is due to the particular interest of the industrial partner to these configurations, which correspond to the range utilised for the greatest part of operating time.

The flow speed has been kept as high as possible; in order to have a sufficiently high Reynolds number (over 1.0 10^6 for all tests); in particular, these tests have been carried out at a 8 m/s flow speed for the 5° configuration, whereas the flow speed has been reduced to 6 m/s for the 10° configuration, in order to limit lift forces considering the experimental set-up.

Regarding cavitation index, the formulation used is obviously the one related to the flow speed, as follows:

$$\sigma_0 = \frac{p_0 - p_v}{1/2\,\rho V^2} \tag{1}$$

where p_0 is the pressure in correspondence to the appendage, considering atmospheric pressure and hydrostatic pressure, p_v and ρ are water vapour pressure and density and V is flow speed.
In particular, apart making visual observations of cavitation phenomena (and their extent) in correspondence to different cavitation index values, inception values have been recorded for both vortex related phenomena experienced (see next paragraph 3.1).

3. EXPERIMENTAL RESULTS

3.1 ANALYSED PHENOMENA

As already anticipated, main aim of this study has been the analysis of vortex related phenomena. In particular, two different vortices have been evidenced during trials, one which detaches from the sheet cavitation which develops on the tip section in correspondence to the sharp angle at leading edge (see Figures 9 and 10) and one which detaches from about midchord location (model 1 and 3) or trailing edge (model 2) on the suction side of the appendage (see Figures 11, 12 and 13).

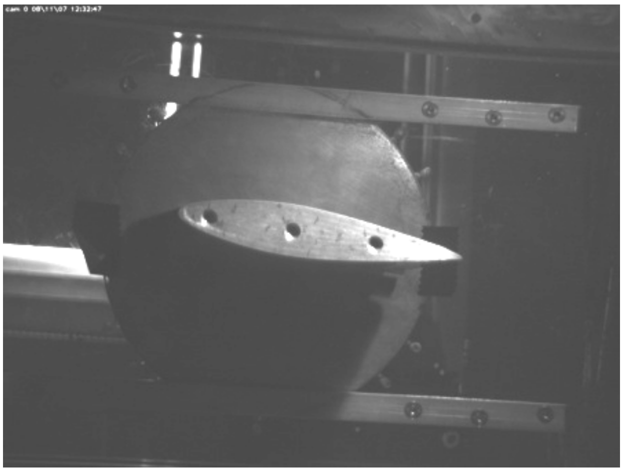

Fig. 9: Squared tip – $\alpha = 5°$ – Vortex from sheet cavitation

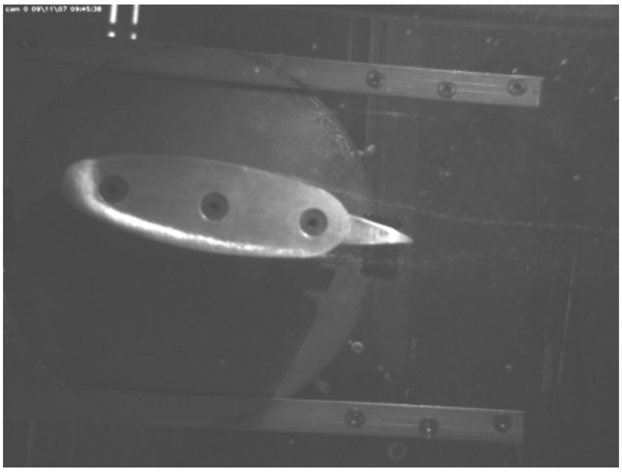

Fig. 10: Squared tip + end plate – $\alpha = 5°$ Vortex from sheet cavitation

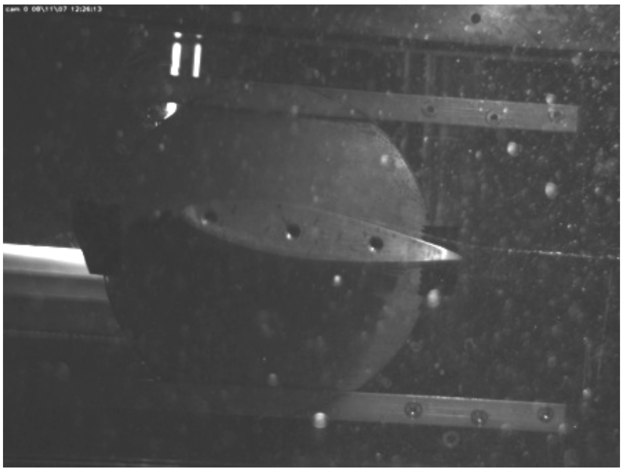

Fig. 11: Squared tip – $\alpha = 5°$ – Vortex from midchord

Fig. 12: Squared tip + end plate – $\alpha = 5°$ – Vortex from midchord

Fig. 13: Faired tip – $\alpha = 5°$ – Vortex from trailing edge

As it can be seen, the first phenomenon is present only in correspondence to squared tip configuration (as expected), both with and without endplate, and is strictly connected to the sharp angle at the leading edge, not present in the faired tip configuration.

On the contrary, the second phenomenon is present in correspondence to all configurations tested; for model 1 and 3 (squared shapes), the inception of this phenomenon is anyway in correspondence to lower values of the cavitation index. When both vortices are present, they tend to collapse into each other forming a unique vortex which continues downstream. This phenomenon is clearly visible in following Figure 14.

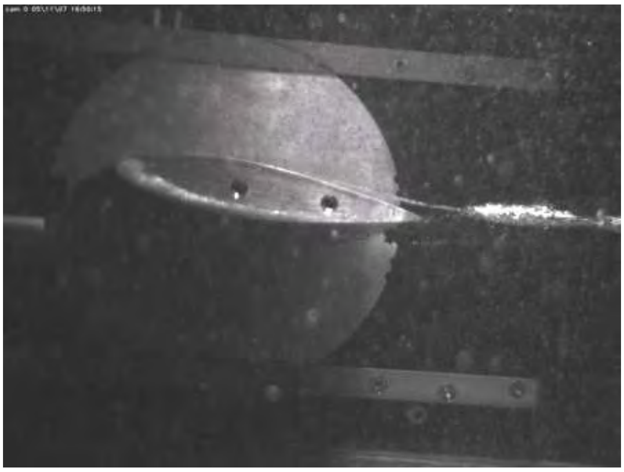

Fig. 14: Squared tip – $\alpha = 5°$ – Vortices collapse

Previous figures are all referred to an angle of attack of 5°, but the above reported considerations can be extended also to the higher value. Only inception values experience a considerable modification from 5° to 10° angle of attack, as it is reported in the next paragraph.

During various tests performed, also other cavitation phenomena have been experienced (both bubble cavitation at midchord and sheet cavitation), as represented in following figures 15 and 16

Fig. 15: Faired tip – $\alpha = 10°$ – Sheet cavitation

Fig. 16: Faired tip – $\alpha = 5°$ Bubble cavitation

Nevertheless, their detailed analysis is not reported in the present paper since main interest has been devoted to tip vortices. This choice was also due to the different nature of these phenomena, being tip vortex cavitation highly related to viscous effect, while sheet and bubble cavitation do not show this strong dependence. Vortex cavitation occurs at lower cavitation index in model scale with respect to full scale, therefore phenomena such as sheet and bubble cavitation may be present in tunnel test when studying tip vortex cavitation, but they are not present in full size at same cavitation index.

3.2 INCEPTION VALUES

In figures 17 and 18, inception values recorded during tests for both vortex-related phenomena are reported in correspondence to the angle of attack of 5° and 10° respectively.

As it can be seen, in correspondence to different values of the angle of attack, different behaviours have been experienced.

In particular, at the lower angle, the faired tip configuration appears as the best one, eliminating completely the “sheet cavitation vortex” and delaying the “midchord vortex” more than the other configurations.

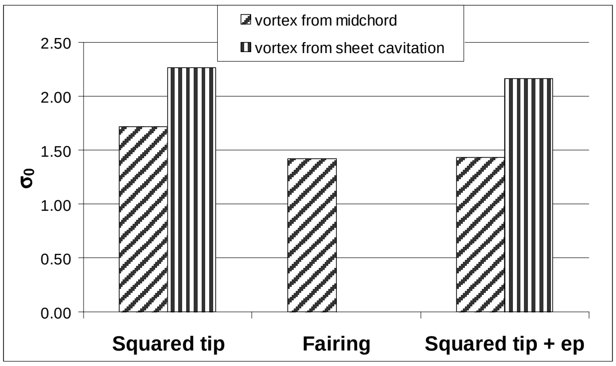

Fig.17: $\alpha = 5°$ - Vortex inception values –

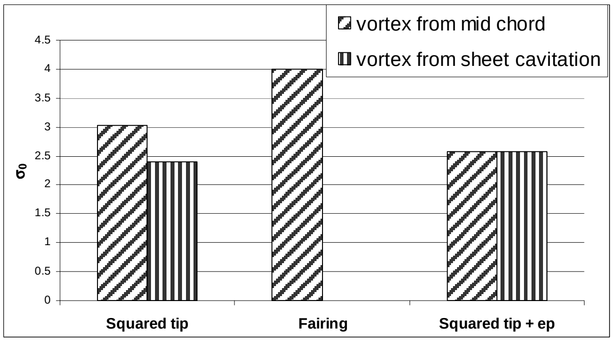

Fig. 18: $\alpha = 10°$ - Vortex inception values

This behaviour is considerably modified in correspondence to the higher angle, where the faired tip configuration still eliminates the "sheet cavitation vortex", but fails to delay the "midchord vortex" more than the other configurations.

Regarding the sheet cavitation, inception values are similar for both configurations for which the phenomenon is present, and they are not influenced strongly by the angle of attack, with a slight increase in correspondence to the higher value.

4. DESCRIPTION OF NUMERICAL METHOD

4.1 RANSE SOLVER

The complexity of numerical prediction of vortex flow structure shed by body submerged and the related possibility of cavitation is mainly connected to the physics of the viscous phenomena in turbulence dominated flows. Regarding naval appendages, they are usually positioned in a region of fully turbulent flow.

Despite the important development gained by researches in the potential flow, these methods cannot properly describe local three-dimensional structure such as the tip vortex, in which viscosity plays a fundamental role.

The Navier-Stokes equations describe theoretically the viscous flow but unfortunately, no rigorous theoretical treatment of turbulence is nowadays possible, this means that empirical turbulence models have to be used and results have to be tested against model experiments.

The approach adopted is the Reynolds Navier Stokes equations, commonly referred to as RANSE. These equations describe the transfer of mass and momentum in a viscous flow and can be coupled with additional equations reproducing specific phenomena such as water cavitation and transport of scalar quantities. Tip vortex cavitation is an extremely complex phenomena and RANSE supply a new tool for the control and the study of vortexes that originate partly at the pressure side and detach at suction side of the tip.

The numerical model used to solve the RANSE is the finite volume method. This method requires the discretisation of the region of fluid of interest, called 'fluid domain' in a set of small volumes, the 'finite volumes' or 'cells', that make up a tridimensional grid in the fluid domain. The RANSE equations are defined and solved at each cell. The dimensions of the cells depend on the scale of the phenomena to be investigated and have to be small enough to make the calculation results independent of the calculation grid.

4.2 NUMERICAL SET-UP

For the present work the commercial code ANSYS-CFX 11, has been used, together with the mesh generator code ANSYS-ICEMCFD 11.

Solution of the RANSE in a fluid domain requires that proper boundary conditions are set at the domain boundaries. The boundary conditions are known properties of the flow that the RANSE solution is required to satisfy at the boundaries. Because of the need to set boundary conditions, the definition of the fluid domain is a delicate issue: the domain has to be large enough for the boundaries to be at locations where the fluid has a known behaviour, but not too large as this way the solution of the RANSE would require an unaffordable computational effort because of the large number of cells.

The fluid domain adopted is shaped as the cavitation tunnel layout with a section 0.57 m with rounded corners, the inlet in the tunnel has been set 2m in front of the models and the outflow at a distance of 6m in order to satisfy the condition of unperturbed flow (see figure 19).

The boundary conditions applied to the domain borders are as follows:

- at the inflow section the undisturbed velocity is applied
- at the outflow section a "zero" pressure gradient is given
- tunnel walls and the fins blade are no-slip walls with a scalable wall function.

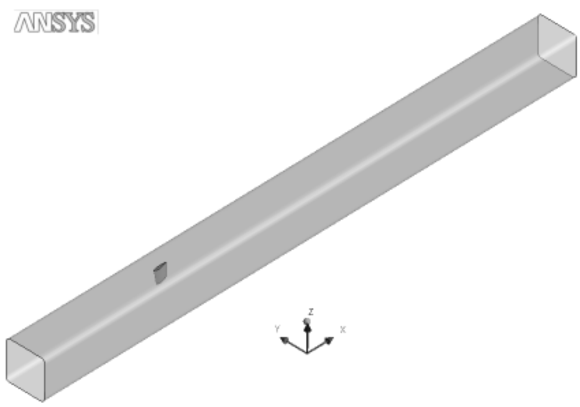

Fig. 19: Fluid Domain

The relation between the grid and the calculation results is a rather important issue. Because of this, and in order to properly define the grid dimensions, prior to any calculations a sensitivity analysis was carried out, consisting in solving the RANSE with different grids of increasing fineness, until independence of the solution is achieved.

The mesh is a structured multi-block grid; therefore the decomposition of domain has been studied in order to refine the grid around the appendage model, in the tip wake region and around the tunnel walls in order to properly describe the boundary layer of the walls and the pressure and velocity distribution in the tip vortex core.

A H-Grid topology is applied to split the volume in the 3 Cartesian directions, so the initial block is subdivided in 9 blocks; then into the inner domain and around the blade, an O-Grid topology is applied with the generation of two new blocks.

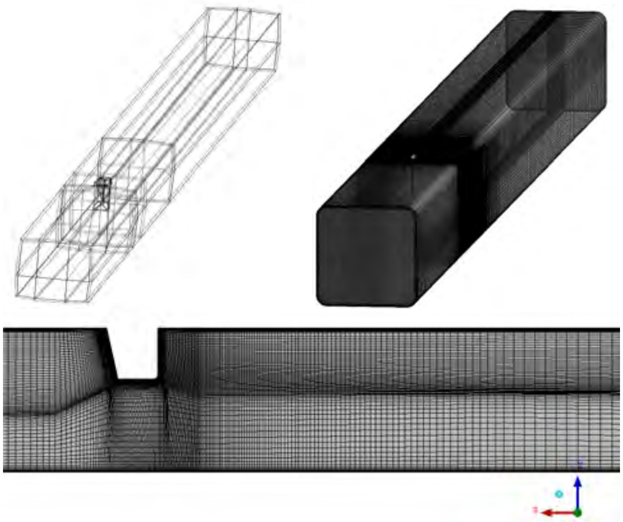

Fig. 20: Domain decomposition, surface mesh at the tunnel and in the longitudinal mid section.

A total of 4369644 nodes have been used. Figure 20 presents the block structure, together with the node distribution around the boundary of the domain; in the longitudinal mid section.

The node distribution for model 1, squared tip, is given in figure 21. Note that the node distribution are refined at the leading/trailing edge and particular attention is given to capture the flow at the fin extremity.

The node distribution for model 2, faired tip, is given in figure 22. Note that the surface mesh structure has been modified in order to capture the flow detachment at the closure of the fairing at the trailing edge.

The node distribution for model 3, squared tip with plate, is given in figure 23. The mesh from the model 1 has been modified in order to take into account for the plate where it has been largely increased.

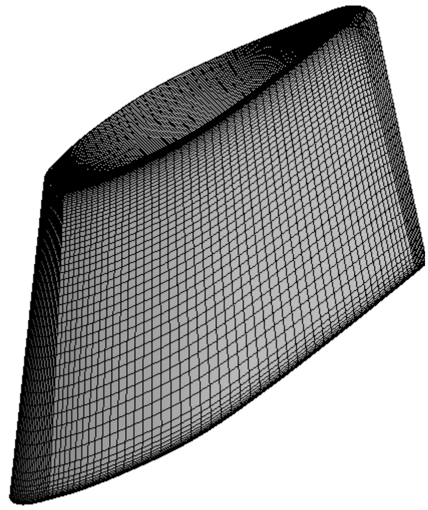

Fig. 21: Surface mesh, squared tip.

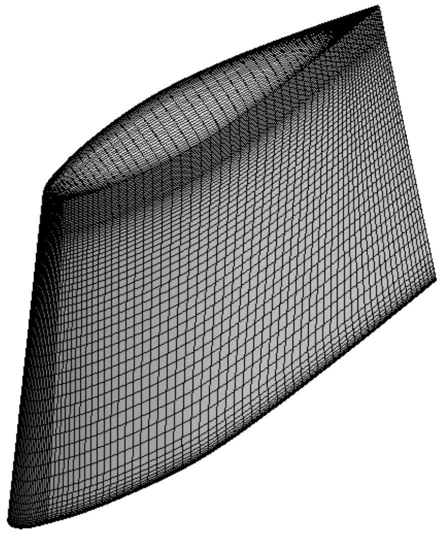

Fig. 22: Surface mesh, faired tip.

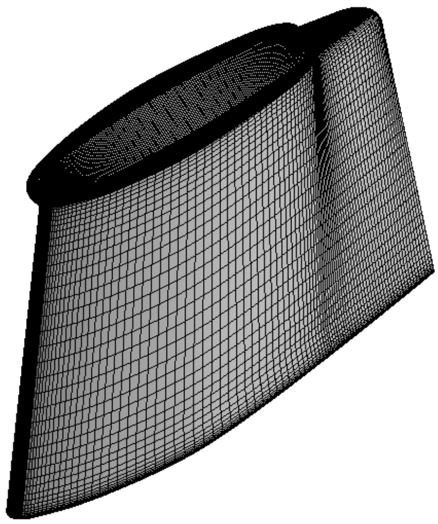

Fig. 23: Surface mesh, squared tip+ plate.

The K-ε turbulence model is used, the convergence has been achieved with about 10^3 iterations and has been carried out using different resolution scheme up to high resolution, RMS < 10^{-6}.

It was decided not to adopt any cavitation scheme in calculations in order to keep them as simple as possible. In particular, calculation for each configuration tested was completed in about 3 hours with a 4 processor cluster, which is considered a time compatible with design needs.

5. NUMERICAL RESULTS

The RANSE equations are defined and solved at each cell, their solution produces the pressure rate (total pressure, dynamic pressure, static pressure and gravity pressure) and the velocity field at each node of the grid.

In order to be able to compare the results with the experiments the numerical data are presented in terms of pressure coefficient:

$$C_p = \frac{P - P_\infty}{0.5 * \rho * V_\infty^{\ 2}} \qquad (2)$$

V_∞ is the velocity of the main flow at the inlet and P_∞ is the pressure value of the main flow at the outlet section.

The study of the vortex detachment has been analysed by 3D streamlines that represents the path of a particle that detach, as an example, from the fin surface and is driven in the fluid domain in addition to the visualisation of the vorticity and helicity in the wake.

The vorticity in the axial direction is obtained from the differences between the derivatives of the transversal velocity therefore it points out the tendency of the flow to rotate in the direction of the main motion.

$$\omega_x = \frac{\partial Vz}{\partial y} - \frac{\partial Vy}{\partial z} \qquad (3)$$

Moreover the helicity pattern has been analysed, which is a scalar variable representing the intensity of the vorticity along the main flow direction.

Helicity = (V • ∇xV) (4)

Therefore the *Helicity* is zero if a vortex move perpendicular to the main flow direction and higher in the flow direction (due to the velocity component of the flow). Due to its mathematical formulation the Helicity pattern seems to be the best compromise to point out a vortex in the ship wake that in the stern zone has the tendency to close the flow at the propeller region and as a consequence of the transversal velocity is no more aligned with the main flow direction.

In formula the *Helicity* is obtained by the scalar product between velocity and vorticity:

$$V_x * \left(\frac{\partial Vz}{\partial y} - \frac{\partial Vy}{\partial z} \right) + V_y * \left(\frac{\partial Vx}{\partial z} - \frac{\partial Vz}{\partial x} \right) + V_z * \left(\frac{\partial Vy}{\partial x} - \frac{\partial Vx}{\partial y} \right) \qquad (5)$$

5.1 VORTICES CAPTURING ABILITY

In order to better understand the concepts introduced in the above section, in figures 24, 25 and 26 a detail of the streamlines detachment from the tip region and, at a transversal plane 0.08m astern the model, the velocity vectors and the *Helicity* contour plot are presented. For all the cases the incidence of the flow is 5°.

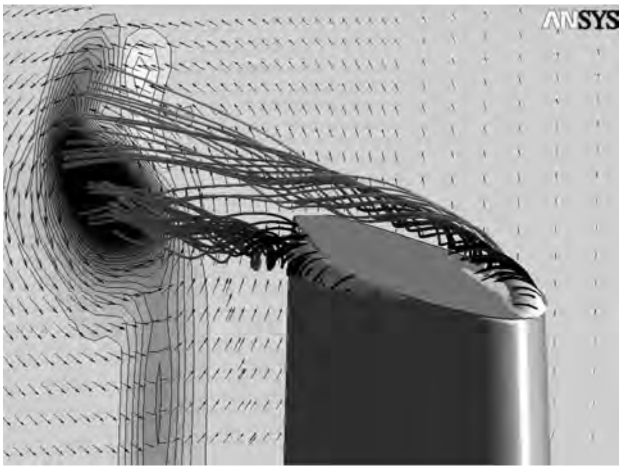

Fig. 24: Helicity along a transversal plane 1m astern the model 1 squared tip, flow incidence 5°

The flow astern the squared model is dominated by the main tip vortex but still the strength of the vortex that detach at the leading edge from sheet cavitation inception is well captured. The main tip vortex detaches at midchord; at a distance of 0.08m from the model the two vortexes are not completely merged.

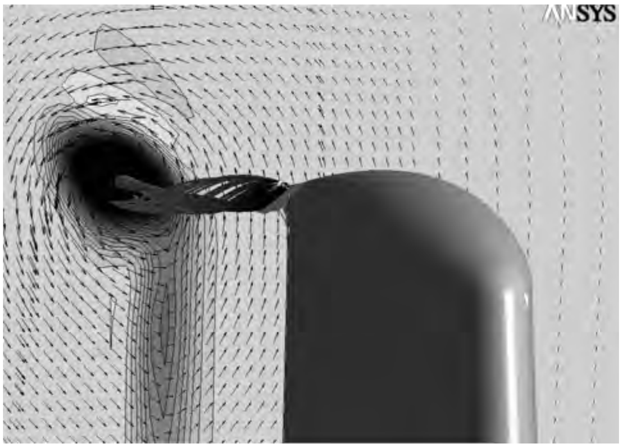

Fig. 25 Helicity along a transversal plane 1m astern the model 2 faired tip, flow incidence 5°

Regarding the flow separation from the faired tip model, only one vortex structure detaches at the tip region, close to the trailing edge, as a result only one vortex core is captured at the transversal section.

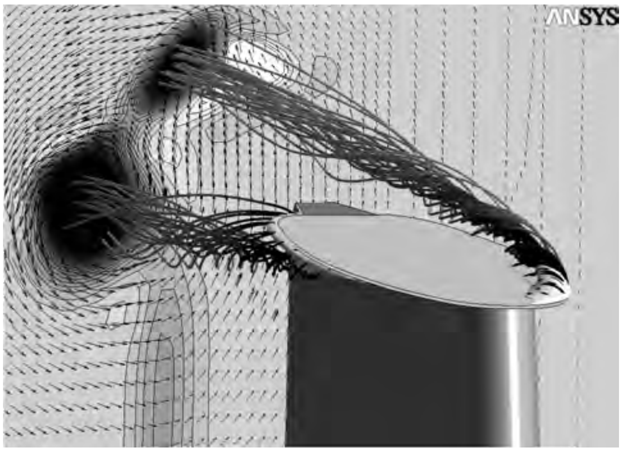

Fig. 26: Helicity along a transversal plane 1m astern the model 1 squared tip + plate, flow incidence 5°

Fig. 27: Squared tip– α = 5° - Horizontal view - Experimental

The flow astern the squared model with end plate is dominated from the main midchord tip vortex and from the vortex that detaches from sheet cavitation inception.

At a distance of 0.08m from the model the two vortexes core are completely independent. Again it can be noticed that the main tip vortex detaches from midchord, moreover the strength of the vortex from sheet cavitation inception is increased, compared to the model 1 results.

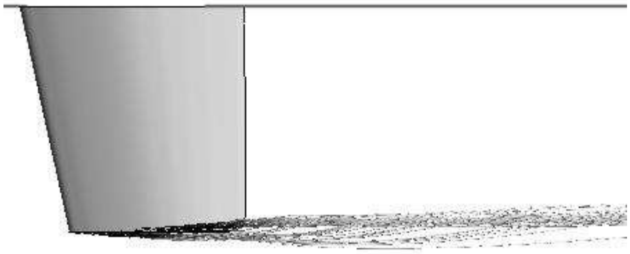

Fig. 28: Squared tip– α = 5° - Horizontal view - Numerical

In the following figures rendering camera location is chosen to be similar to the physical camera setup used during experiments. In particular vortexes trajectories are compared to streamlines showing a good agreement with experiments.

As described above when the two vortical structures are present they tend to collapse into a unique vortex. It was also noted that the effect of the end plate was not only of postponing the inception of the midchord vortex, but also to move downstream the coalescence point.

Another phenomenon analyzed is the tip fairing effect of moving the starting point of the vortex propagating downstream from the midchord to the trailing edge. All these findings are showed in the following figures, where it can be also noted the good capability of the solver to describe these phenomena. Figures 27 to 38 refer to an angle of attack of 5 degrees, for all configurations considered.

For what concern the 10 degrees configuration the effect is to move upstream the coalescence point and form more complicated trajectories. This will appear clearly considering the figures 39-42, referred to the squared tip configuration.

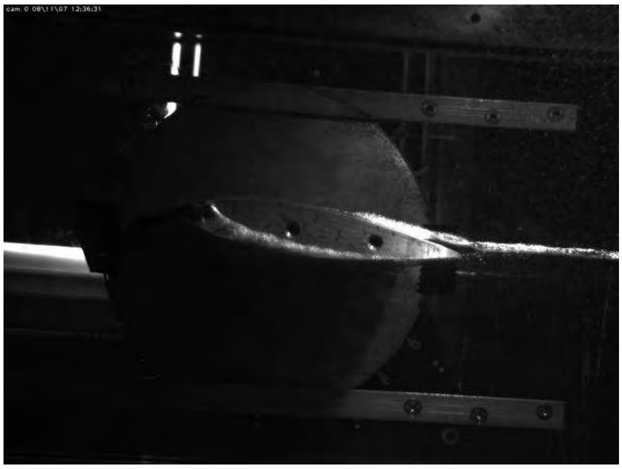

Fig. 29: Squared tip– α = 5° - Longitudinal view - Experimental

Fig. 30: Squared tip– α = 5° - Longitudinal view - Numerical

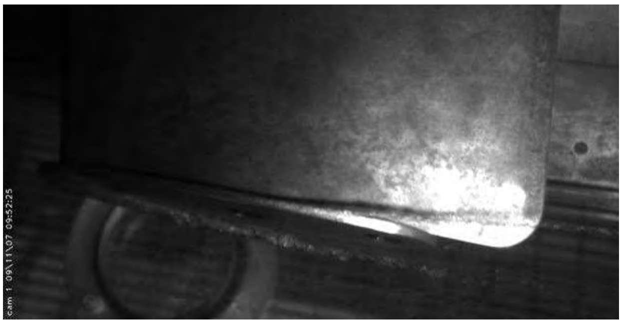

Fig. 31: Squared tip + endplate– $\alpha = 5°$ - Horizontal view - Experimental

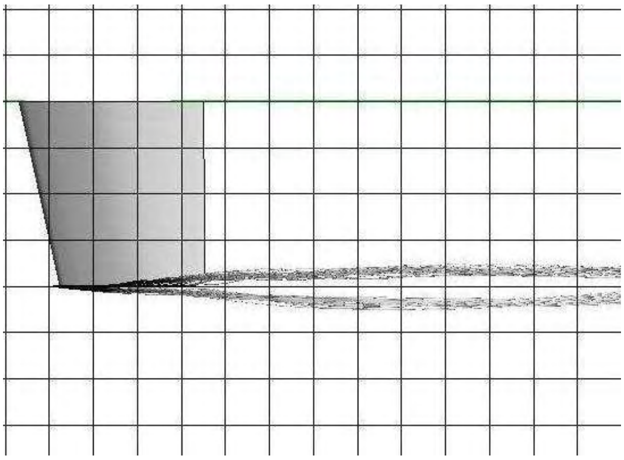

Fig. 32: Squared tip + end plate– $\alpha = 5°$ - Horizontal view – Numerical

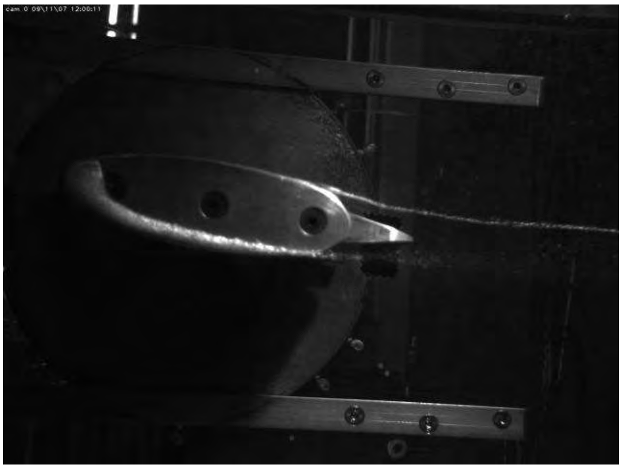

Fig. 33: Squared tip + endplate– $\alpha = 5°$ - Longitudinal view - Experimental

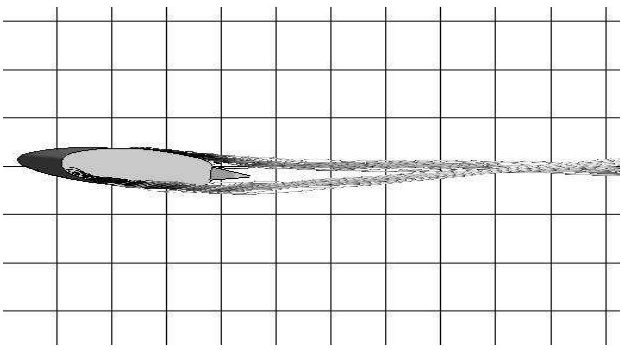

Fig. 34: Squared tip + endplate– $\alpha = 5°$ - Longitudinal view - Numerical

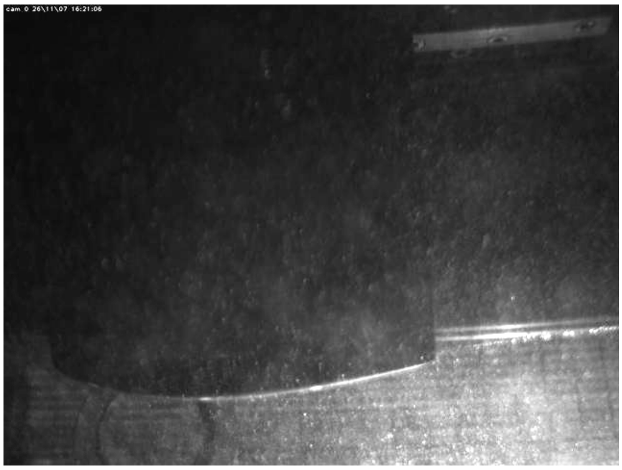

Fig. 35: Faired tip– $\alpha = 5°$ - Horizontal view - Experimental

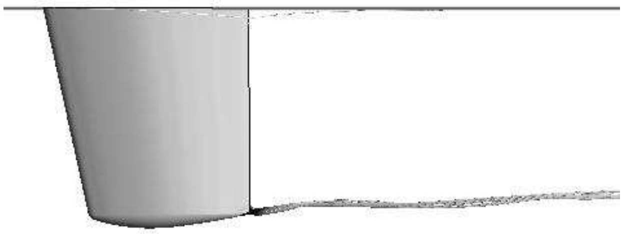

Fig. 36: Faired tip– $\alpha = 5°$ - Horizontal view - Numerical

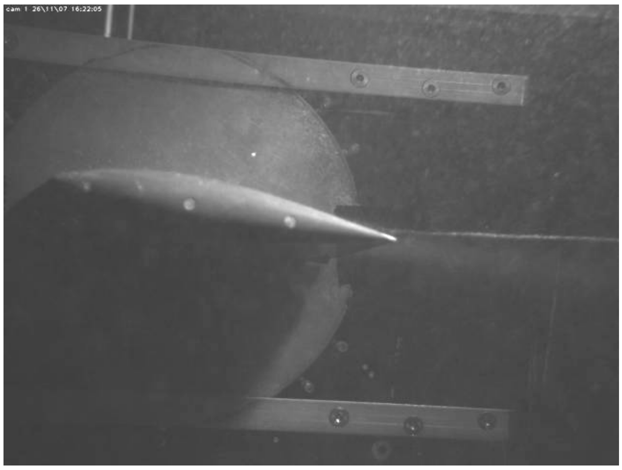

Fig. 37: Faired tip– $\alpha = 5°$ - Longitudinal view – Experimental

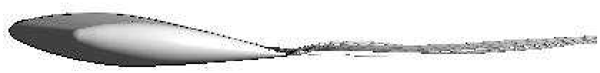

Fig. 38: Faired tip– $\alpha = 5°$ - Longitudinal view - Numerical

Fig. 39: Squared tip– α = 10° - Longitudinal view - Experimental

Fig. 40: Squared tip– α = 10° - Longitudinal view – Numerical

Fig. 41: Squared tip– α = 10° - Horizontal view – Experimental

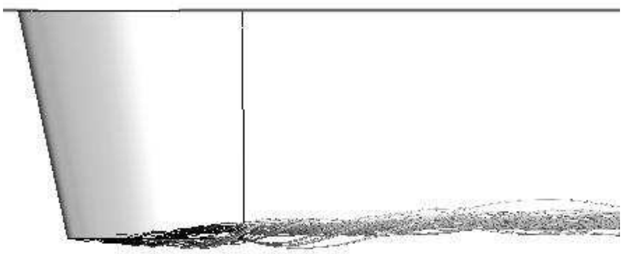

Fig. 42: Squared tip– α = 10° - Horizontal view - Numerical

5.2 VORTEX INCEPTION

In the previous paragraph a qualitative analysis of the flow capturing ability of the solver has been presented. In order to get a further insight in the phenomenon, an analysis of the possibility to predict the vortices inception has been made.

As already remarked, vortex inception prediction is still nowadays a problem in the design phase, in which a tool able to assess the merits of different solutions is strongly needed. In this paper, in particular, focus has been posed on the application of a RANSE solver; in order to simplify as much as possible the problem (with the aim of keeping computational times not too high and compatible with design procedures needs) RANS equations without cavitation model have been used. Moreover, the number of cells adopted for the computational grid has been limited to a value which, on the basis of previous experiences, is still sufficient for the vortex capturing.

Keeping this in mind, two different procedures to assess vortex inception have been adopted.

The first procedure consists in looking at different isosurfaces with pressure coefficient C_P as parameter, reducing progressively the modulus of the C_P value itself until an initial area in the vortex inception region is obtained (see figures 43 and 44 for the vortex from sheet cavitation and the midchord vortex respectively); the vortex inception region is localised clearly from the streamlines previously represented, and the values recorded for the C_P are used as an index of cavitation inception.

The second procedure is similar to the first one, but the value of interest is recorded not when an initial area is found for the isosurfaces, but when a larger region appears, with an initial vortex-like area, as represented in figures 45 and 46 for the two phenomena analysed.

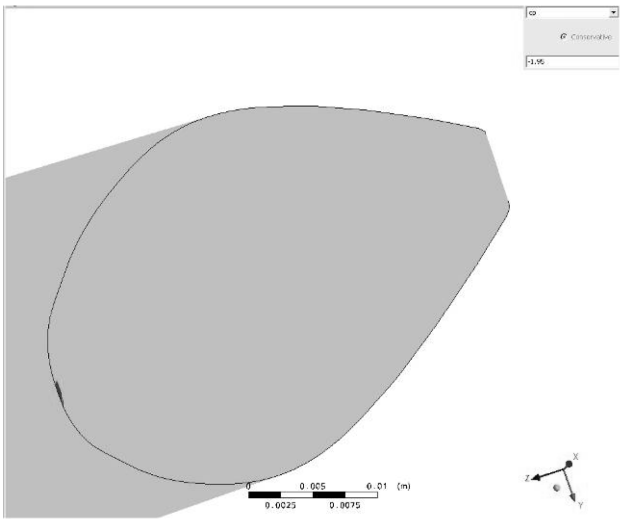

Fig. 43: Example of iso-C_P surface for vortex from sheet cavitation inception – 1st procedure

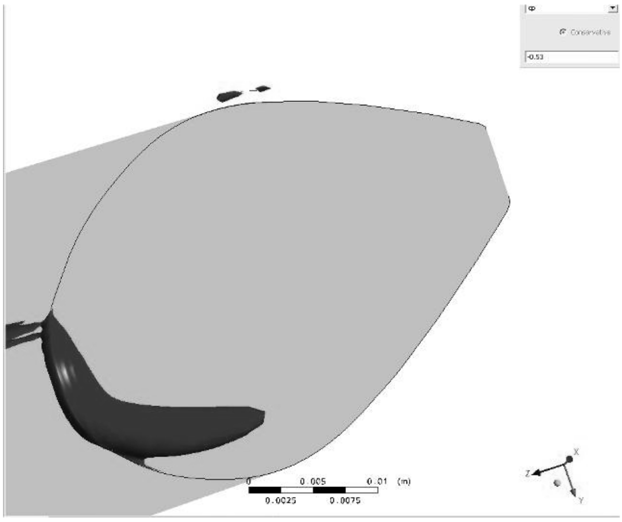

Fig. 44: Example of iso-C_P surface for midchord vortex inception – 1st procedure

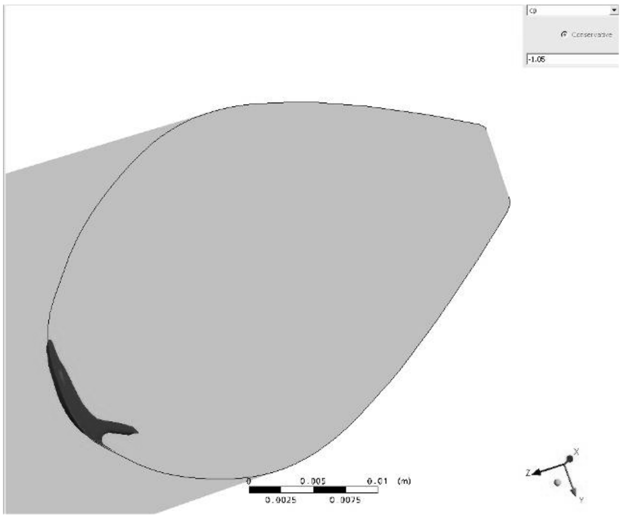

Fig. 45: Example of iso-C_P surface for vortex from sheet cavitation inception – 2nd procedure

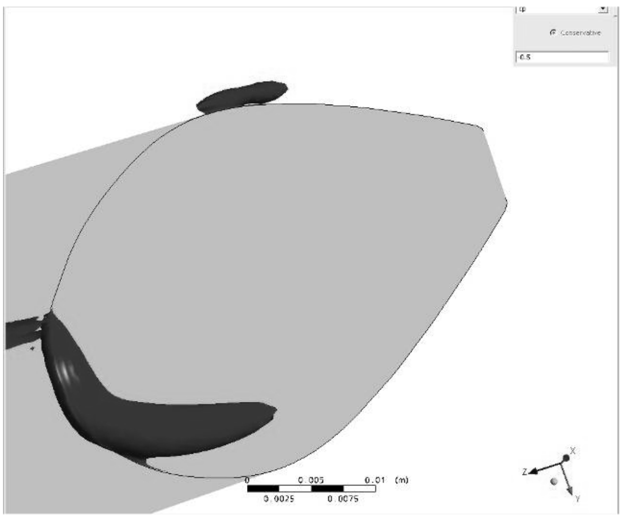

Fig. 46: Example of iso-C_P surface for midchord vortex inception – 2nd procedure

It could be argued that this second procedure presents margins of error related to the operator recognisance of the “initial vortex-like area”, but it is believed that, once the operator remains the same and the criteria adopted (e.g. extension of the vortex like area) is not varied from configuration to configuration, a rather objective procedure results. Moreover, it has to be noted that small differences in the extent of the area usually do not result in significant modifications of values recorded, thus ensuring an implicitly robust procedure.

On the other hand, moreover, it has to be underlined that the first procedure, despite seeming more objective, is more affected by possible local problems of the grid, which can result in problems for the assessment of the real merits of different configurations, as it will be reported in the following.

Finally, it has to be noticed that, in order to make a wider analysis, the two procedures have been applied not only considering iso-C_P surfaces, but also iso-helicity surfaces. This additional analysis has been made because, as already remarked, helicity is a very good parameter to highlight vortices, resulting even better than vorticity in some cases. The concept underlying in this choice is to link the vortex strength (represented by helicity) to the cavitation inception.

In the following figures 47 and 48, values of C_P recorded, obtained with the first and second procedure respectively, for all configurations considered and for the two phenomena analysed are reported on the y axis, while on the x axis the correspondent experimental value of the cavitation index is reported. Angle of attack considered is 5°.

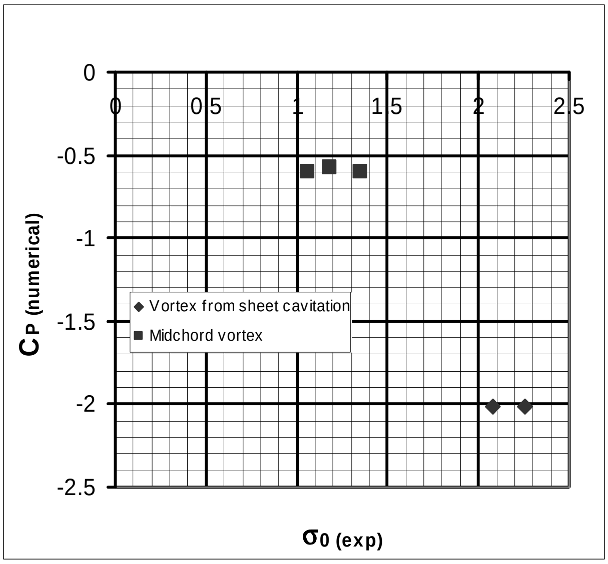

Fig. 47: Vortex inception based on C_P – 1st procedure - $\alpha = 5°$

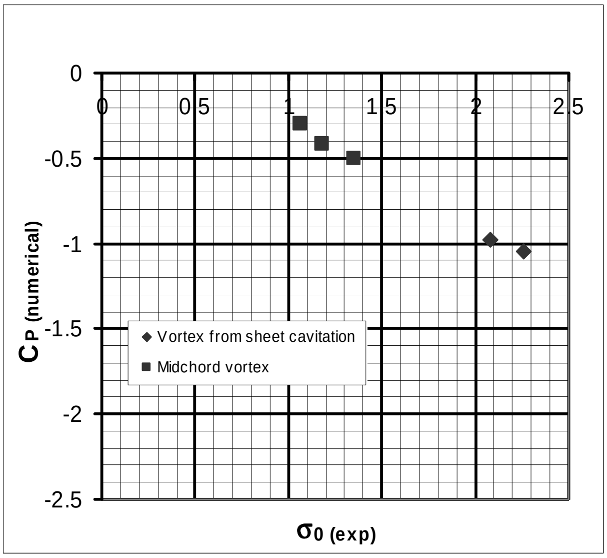

Fig. 48: Vortex inception based on C_P – 2[nd] procedure - $\alpha = 5°$

As it can be seen, the application of the first procedure does not allow obtaining a merit index among the various configurations, for which a similar value of the C_P index is found. The reason for this is probably linked to local effects of the grid, which should be further refined to capture correctly the phenomenon.

On the contrary, the second procedure allows to find a clear (and correct) tendency for both phenomena analysed, thus confirming its supposed capability of avoiding local numerical problems.

It has to be noticed, however, that none of the procedures allows to get the absolute inception value (C_P value should result equal to cavitation index), but only the relative merits of different solutions. On the basis of previous experience, it is believed that this problem could be overcome by means of a much finer local grid, but this would result in a much higher computational effort (and time), in contrast with the initial scope of this analysis.

In the following figures 49 and 50, similar results are reported, representing in this case nondimensional values of the helicity instead of pressure coefficient values.

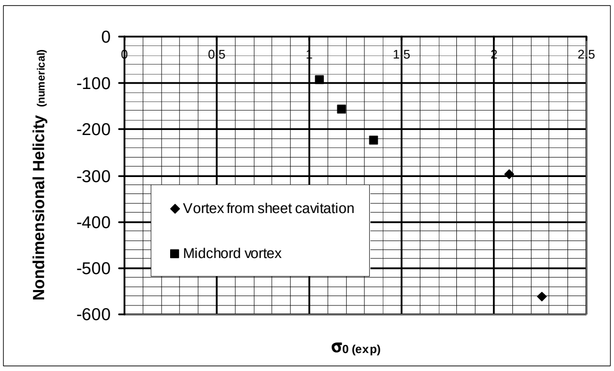

Fig. 49: Vortex inception based on helicity – 1[st] procedure - $\alpha = 5°$

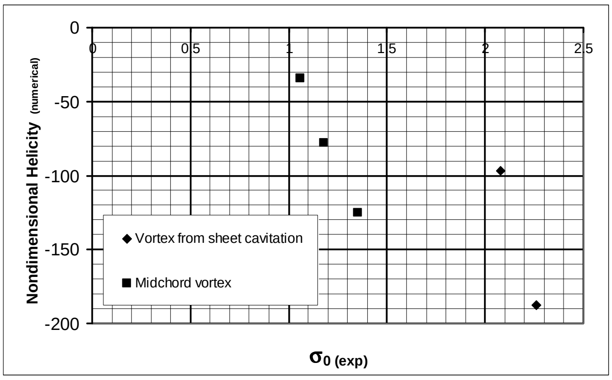

Fig. 50: Vortex inception based on helicity – 2[nd] procedure - $\alpha = 5°$

In this case, it can be noticed that both procedures are able to capture the order of merit between different configurations for both phenomena, thus confirming the vortex related phenomena capturing ability of the helicity parameter. Nevertheless, it has to be remarked that this method allows providing a merit order for the two phenomena separated from each other, while it would not be possible to define which is the first phenomenon present. It has also to be noted, however, that the stronger interest from the designer point of view is linked to the midchord vortex phenomenon which, despite having a delayed inception with respect to the other, is the one which is present downstream of the wing, thus being a more probable source of problems.

In the following figures 51-52 and 53-54, same analysis has been repeated for the higher angle of attack considered (10°). Similar conclusions can arise also from the analysis of this series of figures; in particular, the second procedure allows again finding the merit among different configurations, adopting both indices introduced. It has to be noticed that this means that the procedure has been capable of observing the modification in the merit order, with the faired tip configuration becoming worse than the others.

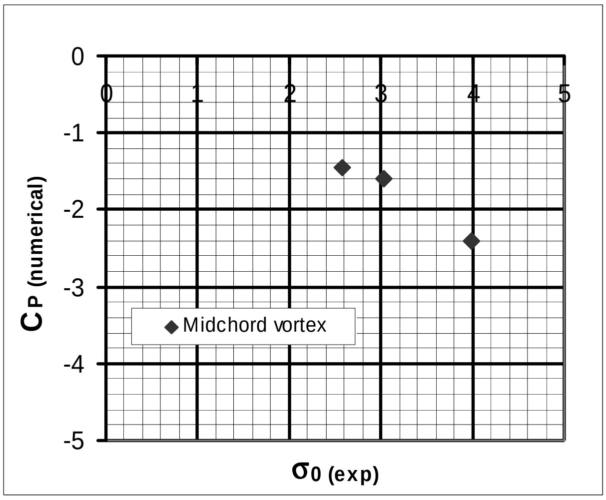

Fig. 51: Vortex inception based on C_P – 1[st] procedure - $\alpha = 10°$

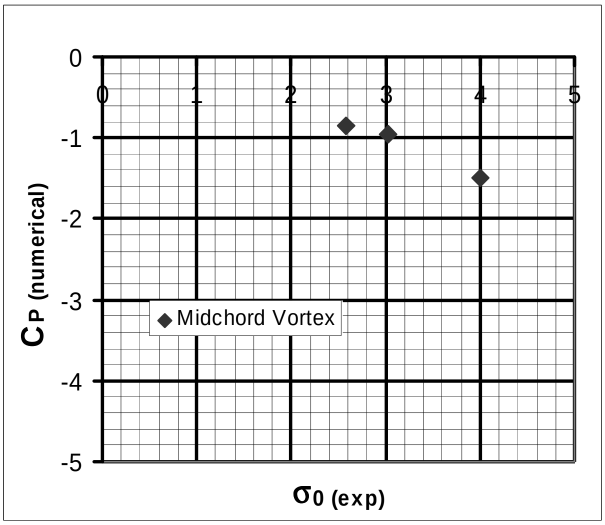

Fig. 52: Vortex inception based on C_P – 2nd procedure - $\alpha = 10°$

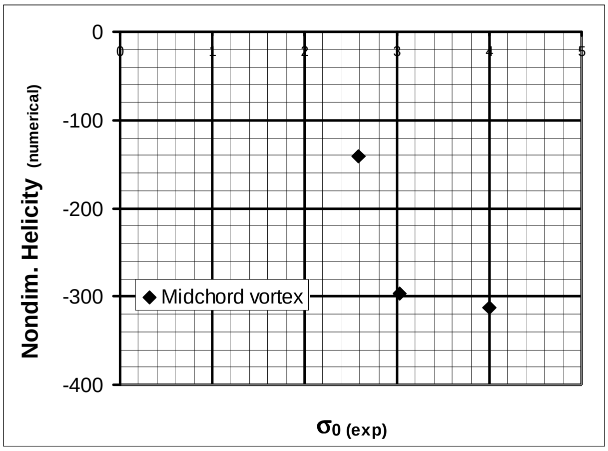

Fig. 53: Vortex inception based on helicity – 1st procedure - $\alpha = 10°$

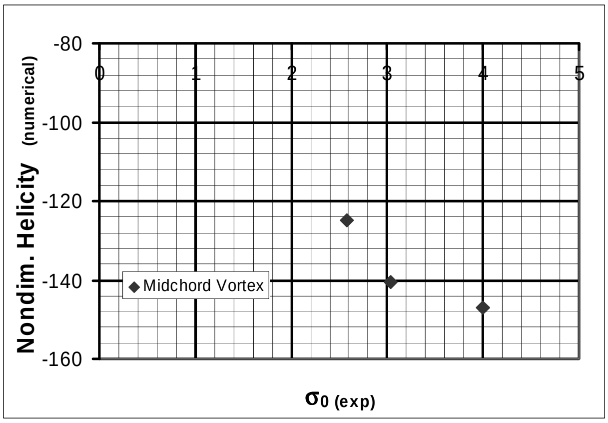

Fig. 54: Vortex inception based on helicity – 2nd procedure - $\alpha = 10°$

Regarding the first procedure, in this case the C_P index allows to capture the order, while some problems arise using helicity, with two similar values for two configurations with different cavitation inception.

6. CONCLUSIONS

In the present paper, some comparisons between numerical results obtained with a commercial RANSE solver and experimental observations about the vortex–related phenomena of a wing have been presented, considering the vortical phenomena themselves and the related cavitation inception.

The solver shows a remarkable capability in capturing the two different vortical structures present in correspondence to different configurations and angles of attack.

Regarding cavitation inception, two simplified procedures for the assessment of merit order among different configurations have been presented together with the correspondent results. In general, these two procedures (especially the second one) allow to obtain the merit order correctly in correspondence to all configurations tested without requiring a too high computational time, representing a possible useful tool in the design phase in order to compare a range of different configurations with localised geometrical variations.

It is believed, anyway, that the need for a final verification by means of model tests is still present: main reason for this is the current impossibility of assessing the absolute value of cavitation index in correspondence to the phenomenon inception with the limitations in computer burden chosen for the present study.

Further analyses will be made in order to have a clearer insight in the additional time (or computational capability) needed for a more precise assessment of the cavitation index values in correspondence to phenomenon inception and in correspondence of different geometries like those tested in the present study.

REFERENCES

[1] Keller A.P. “Cavitation scale effects. Empirically found relations and the correlation of cavitation number and hydrodynamics coefficients” Cav 2001

[2] McCormick Jr., B.W.: “On Cavitation Produced by a Vortex Trailing From a Lifting Surfaces”, Journal of Basic Engineering, September 1962

[3] C.Pittaluga, G.Cresta “Ranse calculations for the hydrodynamic analysis of a marine propeller”, NUTTS 2005

[4] Brix,J., “Manoeuvring Technical Manual”, Seehafen Verlag 1993

[5] Wicker,L.F., Felner,L.F., “Free-stream characteristics of a family of low-aspect-ratio, all-movable control surfaces for application to ship design” DTMB Report n°933, December 1958

[6] “Priciples of Naval Architecture”, SNAME publication, 1989

[7] P. Becchi C. Pittaluga: “Comparison between Rans calculations and panel method results for the hydrodynamic analysis of marine propellers”, Marine CFD 2005, Southampton, England

DISPOSAL AND RECYCLING OF HSC MATERIALS

Henning Gramann, Reinhard Krapp, Volker Bertram, Germanischer Lloyd, Hamburg/Germany,
{henning.gramann, reinhard.krapp, volker.bertram}@GL-group.com

SUMMARY

The introduction gives an overview of current IMO activities concerning the disposal of ships at the end of their life-cycle and an overview of composite materials applications in ships. After a brief discussion of relatively unproblematic aluminum alloys, the article focuses on problems for composite materials. There is little experience for end of life treatment of composites in general and in the shipbuilding industry in particular. New legislation might regulate handling and disposal of these materials even further. The article identifies existing solutions as well as open questions.

1. INTRODUCTION

1.1. Relevant IMO activities

The future IMO Convention on Ship Recycling focuses on safe and environmentally sound ship recycling, without compromising the operational safety and efficiency of ships. Therefore the whole life-cycle of ships is addressed, including dismantling and recycling or disposal of ships taking into account all materials contained. Therefore it requires for all ships above 500 GT, among other things, a compendium of detailed information related to installed materials, which must be kept up-to-date during the entire operating life of a ship. In addition to this, the proper handling (including occupational health and safety, as well as environmental protection measures during dismantling of the materials at the ship recycling facilities) is a key issue of the convention and therefore will have to undergo a comprehensive certification process as well.

The core of the above mentioned convention affecting building and operation of ships will be the Part 1 of the "inventory of hazardous materials" (IHM), which is analogous to a Hazardous Materials blueprint. With this IHM, the location of hazardous materials contained in equipment and structure of the ship shall be easily determined. The basis for the IHM is the so called "Single List", which is a summary of materials which are considered to be potentially hazardous. The Single List consists of four tables, of which Table A and Table B are relevant for the IHM in the building and operational phase of the ship, see Table I.

For preparation of the IHM, all necessary information should be requested during the design and construction phase of a ship by the building yard, and during new installation of components on board existing ships by the owner or yard, depending on contractual arrangements. Manufacturers and suppliers must check all used components, equipment and coating systems against these two tables and provide this information to the shipyard. The shipyard collects this information and summarizes it in the ship specific IHM, which after delivery has to be kept up-to-date permanently. This will become part of shipboard tasks throughout the operating life of the ship. The updated IHM will be reviewed during inspections and prior to delivery to a recycling facility. Existing ships will also have to comply, but the IHM will be prepared by experts and cover materials of Table A only.

The transition to this future ship recycling and disposal management involves several challenges. *Gramann et al. (2007)* focus on 'administrative' aspects, namely the necessary IT (information technology) support for creating and maintaining data bases with inventories of materials on board ships. We will focus here on the special challenges that high-speed craft (HSC) pose due to the different nature of the material mix usually found in these vessels.

1.2. Relevant ISO activities

ISO is developing its 30.000 series for "ship recycling management systems", which will set up international requirements for certain aspects related to ship recycling. In particular these standards will define "safe and environmentally sound ship recycling facilities", best practice for ship recycling facilities, guidelines for selection of ship recyclers including a pro forma contract; set out the requirements for bodies providing audit and certification, and the standard on information control for hazardous materials in the manufacturing chain of shipbuilding and ship operations. It has not been decided whether the ISO 30.000 will also include guidelines on surveying of ships for hazardous materials, minimum amount or content of hazardous materials to be reported, or on methods for removal of asbestos. An industry standard like the ISO 30.000 series shall positively affect the strategies for the interim period until the IMO convention enters into force, providing a common voluntary standard outside of legally binding regime.

Table I: Tables A and B of the Single List of IMO

No.	Materials		Legislation	Threshold Level	Proposed threshold level
A-1	Asbestos		SOLAS	not provided	0ppm
A-2	Polychlorinated Biphenyls (PCBs)		Stockholm Convention	50ppm	50ppm
A-3	Ozone Depleting Substances	CFCs	MARPOL, Montreal Protocol	not provided	0ppm
		Halons			
		Other fully halogenated CFCs-			
		Carbon Tetrachloride			
		1,1,1-Trichloroethane (Methyl chloroform)			
		Hydrochlorofluorocarbons			
		Hydrobromofluorocarbons			
		Methyl bromide			
		Bromochloromethane			
A-4	Organotin compounds	Tributyl Tins	AFS Convention	2,500ppm	2,500ppm
		Triphenyl Tins			
		Tributyl Tin Oxide (TBTO)			

No.	Materials	Legislation	Threshold Level	Proposed threshold level
B-1	Cadmium and Cadmium Compounds	RoHS (2002/95/EC), ELV (2000/53/EC)	100ppm	100ppm
B-2	Hexavalent Chromium Compounds		1,000ppm	1,000ppm
B-3	Lead and Lead Compounds		1,000ppm	1,000ppm
B-4	Mercury and Mercury Compounds		1,000ppm	1,000ppm
B-5	Polybrominated Biphenyl (PBBs)	RoHS (2002/95/EC)	1,000 mg/kg	1,000 mg/kg
B-6	Polybrominated Dephenyl Ethers (PBDEs)		1,000 mg/kg	1,000 mg/kg
B-7	Polychloronaphthalanes (more than 3 chlorine atoms)	Japanese Law[1)]	not provided	0ppm
B-8	Radioactive Substances	96/29/EURATOM	Becquerel	no threshold
B-9	Certain Shortchain Chlorinated Paraffins (Alkanes, C10-C13, chloro)	AFS Convention	1,00%	1%

ISO 30.000 may contribute also to successful implementation and compliance with the future IMO convention. It may provide unified standards and more guidance to all stakeholders involved than any legal instrument can provide. The main focus is on shipbuilding and the recycling preparations and processes. The standard can be applied to all ships and all facilities, without any size limits and independently from the recycling countries ratification. Therefore more facilities can fall under a unified standard than what is possible under the future IMO convention. However, the basis for the ongoing development is that nothing will contradict the IMO requirements.

1.3. HSC materials

Lightweight construction is essential for HSC, having a decisive influence on displacement, draft and thus power consumption for given speed. Lightweight construction is also frequently chosen for superstructures of other ships (like passenger ships or naval vessels) due to stability constraints. Frequently, aluminum and composite materials (like fiber-reinforced plastics (FRP)) are chosen as materials to reduce weight in critical structures, *Fach and Rothe (2000), Fach (2002).*

Aluminum alloys of the 5000 series (AlMg alloys) and the 6000 series (AlMgSi alloys) are commonly used for fast lightweight ships, Fig.1 and Fig.2. The 5000 series alloys are more corrosion resistant in the marine environment and therefore primarily employed for plates of the shell, decks and built-up girders. The 6000 series alloys are easier to extrude and therefore frequently used for extruded sections, but being less resistant to corrosion they are generally restricted to internal structures, *Bryce (2005)*. Both series alloys feature good weldability.

Fig.1: Aluminum catamaran

Fig. 2: Aluminum funnel block

FRP and other composites are used in assorted applications, Figs.3 to 6:

- For hulls in short vessels (pleasure craft, small navy craft, life boats, etc.)
- In naval vessels, for integrated masts, hangars, etc. for stealth and weight reasons, *Beauchamps and Bertram (2006).*
- In propulsion: propeller shafts, propellers, rudders, etc.
- In equipment and outfitting: boat davits, furniture, deck gratings, deckhouses, insulation

Composites have been proposed also for ship repair. Plastics are found in a variety of small structures on board ships (cables, fixings, etc.).

There is a variety of different FRP materials, due to assorted combinations of reinforcement material (fibers), laminating resins and core material:

- For reinforcement, generally glass, carbon and aramide fibers are used. More recently, natural fibers have been advocated, also within the context of recycling properties, *Umair (2006).* Carbon and aramide fibers have high tensile strength. The fibers are available in the form of rovings, mats, fabrics and non-woven fabrics and combinations of these. These materials allow tailor-made non-isotropic strength properties (depending on fiber orientation), but also quasi-isotropic behavior achieved by the respective laminate construction.
- The main laminating resins used are polyester, vinyl-ester and epoxy resins. Vinyl-ester and epoxy resins are highly resistant to hydrolysis, i.e. they absorb insignificant amounts of water and the risk of osmosis is practically excluded.

Fig. 3: FRP in superstructure of 33 m HSC yacht

Fig.4: Composite louver,
source : www.ebertcomposites.com

Fig.5: Carbon-fiber laminate propeller shafts

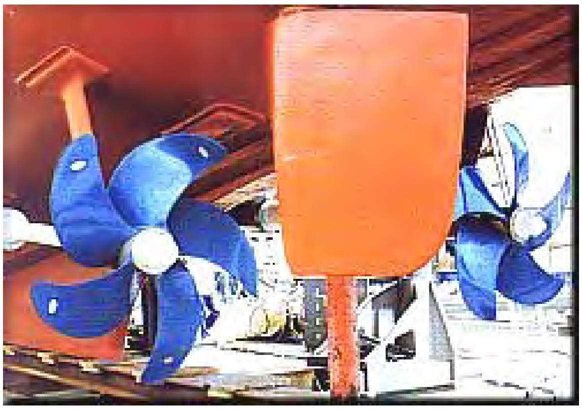

Fig.6: Contur® propeller of AIR Fertigung-Technologie GmbH

Sandwich structures are more or less complex mixtures of materials. These structures consist of a face material and a core, bonded together by a putty or adhesive bond (typically polyester). The faces mainly support the tensile and compressive stresses of the sandwich in bending, and the core material mainly supports the shear stresses. Face materials may be metal or composites like carbon fiber composites. Core materials available for sandwich laminates are generally PVC foams, polyurethane (PUR) foams, polymethacryl (PMI) foams, balsa wood and honeycombs (thin aluminum or stainless steel plate honeycombs) as well as aramide paper (Nomex honeycomb). PUR foams are rarely used, *Müller (1990).* See also *Umair (2006)* for a more detailed review of composites used in engineering particularly in shipbuilding. *Hedlund-Aström et al. (2005)* give composite mass data for the Swedish Visby class corvette. The ship contains 50 t carbon fibers, 40 t vinylester as matrix filler, 40 t of core material in sandwich structures (mixture of PVC and polymer of poly-urea/polyamid), 20 t of putty material (mainly polyester).

Sandwich structures in ships may contain assorted metallic inserts and embedded equipment. They may also contain hazardous materials. For example, the Visby class corvette sandwich structures contain 9 t of chlorine and 0.4 t of lead in the core material, in addition copper oxide in the bottom color and copper in the embedded electrical devices, *Hedlund-Aström et al. (2005)*. When chlorine is heated (e.g. during cutting operations), hydrochloric acid and dioxin is formed. Lead and copper affect health when consumed in food or drinks.

Recycling facilities specialize mainly in metal recovery. However, ships contain a multitude of materials, including composites. Composite materials are relatively young compared to the traditional metallic structural materials. Consequently, there is little experience in the industry on disposal and recycling techniques for these materials. However, increasing environmental demands from customers (navies) and authorities will force the industry to face this issue. While hazardous materials are at present the first priority problem to be solved, composite recycling and disposal will definitely be an issue for IMO regulations in the future.

In addition, recycling of FRP boats is an issue. These boats are not subject to IMO regulations and usually also outside direct class supervision. *Hayashi (1993)* estimates 30000 FRP boats built each year in Japan alone. Since disposal of these boats at the end of their life-cycle is expensive (estimated to exceed 940 Euro per boat just for the mechanical crushing, and more than 1250 Euro per boat when transport costs are included), illegal disposal of FRP boats along rivers, canals and in ports is a problem.

Traditionally, the most economical end-of-life options for composites were landfill disposal and waste incineration. However, since 2004, landfill disposal of composites has been forbidden in most European Union (EU) member states. Incineration of plastics is problematic due to the toxic byproducts. The EU End-of-Life Vehicle directive, adopted in 2003, requires 95% of each vehicle manufactured after January 2015 must be reused or recovered. These political constraints drive the dynamic evolution of a composite recycling industry. Naval architects can benefit from practice in other industries that have extensive experience with composites, namely the automotive and the aerospace industries. “Recycling and disposal of composites create issues that must be addressed. One such issue concerns end-of-life aircraft structures that contain carbon fiber composites coated with hexavalent chromium primer. These composites that are coated with hexavalent chromium can be classified as hazardous waste and thus may not be disposed on land due to possible leaching of the chrome into the ground.”, *N.N. (2003).* Indeed, the cost to dispose of a hazardous waste can be more than 20 times the disposal cost of a non-hazardous solid waste in EU. Thus, materials should be disassembled and sorted to reduce those parts containing hazardous substances to a minimum.

2. RECYCLING AND DISPOSAL

2.1. General considerations

The following waste hierarchy is suggested for waste management:

- **Reuse or product recycling:** The product is kept in its shape, dismantled and reused, sometimes after an upgrade involving energy input and additional new material. For composite structures, this could mean cutting large (flat) panels from the hull structure to be reused in other structures. Problematic paint coatings need to be removed by sand blasting or affected parts of the structure are not reused. Reuse means material continuing to circulate. It is then important to have control on hazardous materials contained. Only part of the structure can be reused. The remaining part must then be treated according to one of the following methods.

- **Material recycling:** Composite recycling efforts in the past mainly concerned grinding, shearing, chipping, or flaking the composite into suitable size to be used as filler material in new molded composite parts, e.g. as filler mixing with cement or forming plates similar to plywood.
- **Chemical recycling:** The waste is decomposed into its original raw materials or directly transformed into other petrochemical raw materials. The waste is generally first mechanically crushed to increase the material surface. This results in a higher efficiency of the chemical process. Technically viable processes for composites are pyrolysis, hydrolysis and gasification. Pyrolysis is most frequently discussed. In pyrolysis, the polymeric component is thermally decomposed into smaller hydrocarbon molecules, which can be used as fuel. Remaining material (fibers, metallic parts) are then further recycled. Pyrolysis keeps thus fibers largely unbroken. However, this pyrolysis is expensive and only practicable to a certain plate size. Hydrolysis is used e.g. for PVC cores in sandwich panels. At present, none of the chemical recycling options are economically viable for commonly used glass fiber composites in the marine industry.
- **Energy recovery:** The waste is incinerated in appropriate installation recovering energy. The option depends on the caloric value of the waste. A threshold value higher than 11 MJ/kg is required in Europe to allow incineration for energy recovery. Carbon and aramide fiber composites are well above this level, many glass fiber composites are below this level. Mixing with other material to increase the caloric value is not allowed. For carbon fiber composites, proper precautions must be taken to avoid the release of small fibers into the environment that may cause electrical interference problems, *N.N. (2003)*.
- **Disposal:** Waste may be disposed in waste incineration plants or landfills. Disposal of high-caloric waste in landfills is forbidden in the European community since 2005.

The capability to sort dissimilar materials, composites from metals, is the first step in recycling composites. Composites should be sorted by different reinforcement and filler/matrix materials. The composition of the composites determines the further processing. More valuable carbon reinforced composites, for example, will be recycled extracting the carbon fibers, while glass fiber reinforced composites may still end up in landfills (in some countries).

2.2. Aluminum

Aluminum is often called a material of perfect recyclability since the secondary metal is recovered using only 3% of the energy consumed in the production of virgin metal by electrochemical purification, www.world-aluminium.org. Practical aluminum alloys, however, include various additives such as silicon, iron, copper, manganese, magnesium, zinc, etc. Accordingly, while recycling of scrap has progressed considerably with cast products which allow a large amount of additives, rolled and shaped products which permit only a small amount of additives have been manufactured preferably from raw materials rather than recycling products. Research is active to extend also the recycling of aluminum alloys into rolled and shaped products. For the shipbuilding industry, the approach is straight-forward. The aluminum alloys in the ship structure are on record, disassembly follows standard procedures, and after sorting the different alloys, the aluminum alloy parts can be recycled in dedicated recycling facilities. The value of the scrap depends on a number of factors. Coated plates require additional processing prior to recycling and this reduces the amount paid for this scrap.

2.3. Glass-fiber composites

Glass fiber composites are the most popular composites in the boat industry. While glass can be easily recycled, the recyclate is not commercially viable due to the already low price for virgin material.

Some glass fiber composites (with lower glass fiber content) have enough caloric value to be used in energetic recycling. The main benefit is heat which may be used for district heat, steam generation, electricity generation or directly in chemical, steel or cement plants. Additional byproducts are gypsum and slag with a high content of molten glass. These are widely used in construction materials, e.g. concrete and aerated concrete. Slag without glass content may need further processing to remove hazardous substances, slag with glass content usually is unproblematic as the hazardous substances are bound in the glass. In addition to gypsum and slag, considerable amounts of ash are created. The disposal of this ash (typically in landfills) is expensive. In summary, energetic recycling of glass fiber composites is problematic due to their low caloric value and the large amount of residual ash.

At present, there are no economically viable options for chemical recycling of glass fiber composites, although it is technically feasible, as shown e.g. by *Hayashi and Yamane (1998)* for FRP boats.

In mechanical recycling, the recyclate is mainly used as filler material. Recycling glass fiber composites in Sheet Moulding Compounds (SMC) and Bulk Moulding Compounds (BMC) has been successful. These techniques allow relatively high degrees of recycled composite materials as filler, but involve high pressures and high temperature. Applications include electrical equipment, car components (headlights), and housings for electrical appliances. Recyclates have been used also for outdoor construction materials, e.g. for road cover, road markers and insulation panels. However, the amount of waste from glass fiber composites exceeds so far largely the demand in recycling products with the applications found so far.

Fig.7: Building material from recycled composites; glass foam plates (up) and gypsum blocks (center), headlight (down)

Glass fiber composites with high polyester content (60% unsaturated polyester) can be used in the cement industry. Process complications appear with the glass fibers blocking filters and dust generation requiring good filters for work place protection. Otherwise this application appears attractive as it leaves almost no residues, but it requires a large constant supply for the production plant. An estimated 10000 to 20000 t/a will be needed as supply.

2.4. Carbon-fiber composites

Carbon-fiber composites offer more attractive options for recycling. Acid digestion could be used to reclaim the carbon fibers, but appears to be impractical from an environmental point of view. Acid digestion uses hazardous chemicals and creates a mixture that will require further processing. Adherent Technologies Inc. (ATI), www.adherenttech.com, have been successful in separating carbon fibers from carbon fiber-reinforced epoxy composites and reclaiming valuable carbon fibers, Fig.8 and Fig.9, *N.N. (2003).*

Fig.8: Reclaimed carbon fibers, *N.N. (2003)*

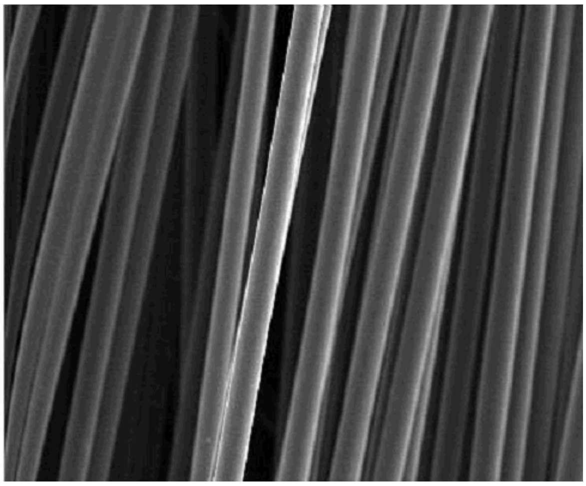

Fig.9: Microscopic view of reclaimed carbon fibers, 99.8% pure, *N.N. (2003)*

ATI employs catalytic conversion to recycle composites. Catalytic conversion produces chemicals or fuels from scrap or waste products. By-products generated include phenolic compounds used in certain adhesives. The reclaimed carbon fibers have very similar properties to virgin fibers, but are shorter. Reclaimed carbon fibers cannot be reused in applications requiring longer, continuous carbon fibers. However, the demand for chopped and milled carbon fiber is growing. Applications for such recycled carbon fibers are for example housings of cellular phones and laptop computers. "Methods exist today by which carbon fibers and prepregs can be recycled, and the resulting recyclate retains up to 90 percent of the fibers' mechanical properties. In some cases, the method enhances the electrical properties of the recyclate because the carbon recyclate can deliver performance near to or superior to virgin material. All that remains is to create demand for recycled fiber by packaging it in a form useful to end-users," *Davidson (2006).* In summary, once the carbon fiber composite has been singled out and sorted, recycling is possible by dedicated facilities.

2.5. Sandwich panels

Before cutting composite or sandwich structures, embedded electrical equipment and metallic inserts as well as the content and nature of hazardous material need to be known. The position of metallic parts is indicated in technical drawings. Hazardous content and position will have to be documented, according to the current draft convention from IMO.

The processes of dismantling and further mechanical preparation for recycling (like crushing and milling) involve potential health risks due to exposure to dust, smoke, gas, sharp fibers and other sharp material parts, and noise. For example, hydrochloric acid and isocyanates are generated when heating the PVC core in sandwich structures. These risks can be contained through proper workplace and personal protection, as regulated by national occupational health and safety regulations, but implementation throughout the ship recycling processes might remain difficult due to different circumstances (climate conditions, accessibility and additional need of space when wearing or carrying personal protection equipment, etc.).

Hedlund-Aström et al. (2005) discuss the various options for recycling and disposal of sandwich structures in ships:

- Reuse: Cutting large panels from the hull structure allows reusing sandwich material. Hazardous material bound in the core may be safe to cut and transport, but authorities like environmental agencies should be consulted. Metallic equipment or inserts not removed during disassembly are either dismantled or cut away during cutting to final size.
- Mechanical material recycling: Milling the complete sandwich has been applied to a sandwich structure consisting of a face of glass-fiber reinforced polyester and Divinycell core, *Hedlund-Aström and Olsson (1997).* The recycled sandwich mixture was blended with polyurethane. Plates similar to plywood or chipboard were manufactured through expansion in a form.
- Recycling by pyrolysis and hydrolysis were discussed. While technically feasible, they do not appear to be economically viable options.

2.6. Disassembly

There are various ways to cut composites during disassembly:

- Mechanical cutting with power saws or other cutting tools, Fig.10. The generated dust may in most cases require appropriate protection for the workers. The tools are cheap and can be portable.
- Water-jet cutting which is another form of purely mechanical cutting using a jet of water at high velocity and pressure, or a mixture of water and an abrasive substance, Fig.11. The process is essentially the same as water erosion found in nature but accelerated and concentrated by orders of magnitude, able to cut thin metals and composites. The technology is used in aerospace and other industries. The advantage is that there is no heat and no chemical process involved. Portable water-jet cutters are available on the market.

Fig.10: Mechanical cutting of boat hull
Source: *www.slashbuster.com*

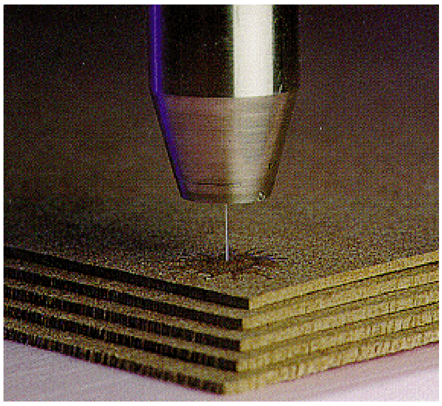

Fig.11: Water-jet cutting,
source: *wikipedia*

- Thermal cutting using oxy-acetylene; this method is frequently used for cutting steel structures in ships. The approach is problematic for most composites due to potential toxic by-products in burning plastics.
- Plasma cutting; the cutting is usually performed under water reducing dust and fumes problems, but installation are not always portable and relatively expensive, though cheaper then laser cutting. The cutting speed is relatively low compared to thermal cutting, which is an important factor for cost effective ship dismantling.
- Laser cutting; the heat is highly focused reducing health hazards, but installations are expensive and not portable.

3. PROBLEMS TO ADDRESS

3.1. Identification of material

To maximize the recovery of material and generate the best financial return, the materials must be efficiently sorted before post-processing. A significant concern in recycling and disposal is the proper identification of various materials in ships to be scrapped, and how to sort and recycle this mix.

Recycling companies must know what they shall recycle. It could be a basic epoxy matrix composite, or it could be a brominated resin matrix, with all the associated toxic complications. At present, no sophisticated and reliable knowledge/experience exists. In newbuildings, this could be documented from the start in a material database. In the large fleet of existing ships of different age, we will be commonly faced with information gaps concerning the material composition.

Just before disassembly, material samples can be taken and analyzed. However, this type of destructive testing is usually not an option while the ship is still in service. Non-destructive testing of composites is subject to research, e.g. at the Fraunhofer research centers in Germany, and is expected to drift into industry practice in due time.

An example may illustrate the scope of work needed in compiling the variety of multi-layered composites found in modern ships. The example shows extracts of the files for the cruise vessel AIDA Diva: The deck structures use sandwich panels similar in structure to those of the walls. These panels consist of stone wool as core material and zinc plates as covers, lacquered or covered by foils. The files do not give the thickness of the cover plates; the density of the core material is 130 to 150 kg/m^3. Decks, hull and bulkheads are equipped with insulation against noise, fire and heat. This insulation consists mainly of mineral wool (stone, glass). The floor of the Captain's Cabin 1001 is equipped with a fire-resistant insulating floor of type A 60. This floor insulation is labeled Tefrolith M. Furthermore, there is a layer below the carpet labeled IMO Lay.

3.2. Product alternatives

The automotive industry has investigated composites based on natural organic materials (cellulose, sisal, jute, hemp, etc.) as alternatives to classical glass or carbon fiber composites, *Marek et al. (2000).* These reinforcements are reusable, good insulator of heat and sound, degradable and cheap. They are less fire resistant and their quality varies naturally more, moisture may cause fibers to swell and price may fluctuate according to yield of crop. Despite these shortcomings, natural fiber composites are expected to see wide use in the automotive industry, due to their light weight compared to glass fibers and their recycling properties. Little is known about natural fiber composites in the shipbuilding industry. The moisture problem and uncertainties about the long-term behavior of natural fiber composites make them unlikely candidates for the marine industry.

3.3. Markets and logistics

Energy recovery is at present not a viable option for the popular glass-fiber composites. However, it is technically feasible. *Hayashi and Yamane (1998)* present for example a movable disposal system for FRP boats. The movable system, installed on two trailers, reduces transportation costs and allows decentralized service. The system is set up to incinerate most boats at original size, avoiding the pre-processing cost of crushing. The resulting stone-like solid with high silicone content are compact and can be used as stone pavement, cement, or core material for various insulation material. However, although a prototype was presented 10 years ago, the idea failed due to economic aspects. Considerable process improvement to reduce cost or subsidies would be required to change this.

The industry needs a network of specialized recycling facilities for composite structures. The decommission shipyard will typically focus on breaking the ship apart, sorting and channeling the individual items and materials for further processing by dedicated subcontractors or buyers. The task of the shipyard in this respect is identifying the composite, disassembling to the appropriate level using the appropriate technology, sorting and seeing that it gets to the appropriate dedicated specialist. While networks for more traditional materials like metals are established in shipbuilding, networks for composites still need to evolve. The relatively small amount of composite material processed in shipbuilding industry necessitates using networks and facilities developed by related industries (aeronautical, automotive, mechanical engineering).

3.4. Dissemination

Training and dissemination of knowledge concerning the problems and procedures will be a key issue for the transition of the industry towards a life-cycle management approach, particularly for the less familiar and more problematic materials in shipbuilding, like composites. Disposal and recycling add aspects for consideration already in the design stage. Besides aspects like 'Design for production', 'Design for operation' and 'Design for maintenance', we should then train engineers to consider aspects of 'Design for recycling', *Lamb (2003). Marek et al. (2000)* recommend considering two fundamental aspects for 'Design for recycling',

- Structural design (Is the item easy to disassemble?)
- Material selection (Can materials difficult to recycle be replaced by alternatives easy to recycle?)

VDI (2002) discusses Design for Recycling in more detail, drawing on experience for diverse mass production industries in Germany. Generally applicable guidelines for Design for Recycling are:

- Avoid problematic materials
  Regulated or restricted materials may require expensive disposal at the end of the life-cycle. Materials incompatible for recycling will have to be separated at considerable expense. Painting of parts generally contaminates parts. For composites, it is often preferable to use colored plastic resin.
- Use 'Design for recycling' materials
  Wherever possible, use recycled material and use recyclable material. In composite structures, use compatible adhesive bonding to allow recycling. Suitable combinations may be found in discussion with experts for adhesives. Use materials which can be recycled as a mixture.
- Reduce complexity
  Reduce the number of material types used.
- Make disassembly and sorting easy
  Use route wiring. Use modular design. Make components of different recyclable material easy to separate. Mark plastic parts according to standards, *ISO (2000)*, and in a way that allows the marking to be read even after 30 years in a maritime environment.

Many of the general guidelines coincide with advice given for Design for Production.

Landamore et al. (2007) show how assessing the disposal costs in the design stage may influence material selection, applying life cycle cost analysis to inland leisure craft.

4. CONCLUSION

Unless markets for recycled composites materials evolve, the options for certain composite materials at the end of the life-cycle are limited:

- Export of this 'problematic' waste to countries with more lenient legislation. However, there are efforts to restrict this export both on national level of developing countries and on international level. It may not be a long-term option.
- Incineration or landfill with special permit and subject to a fee or tax.

As a consequence, these composites may then reduce the value of a decommissioned ship.

5. ACKNOWLEDGEMENTS

Many colleagues have supported this paper with their special expertise, supplying text and/or figures, namely André Fuhrmann, Saskia Greiner, Shinya Hayashi, and Thomas Korbel.

6. REFERENCES

BEAUCHAMPS, B.; BERTRAM, V. (2006), *Quo vadis, navy – Trends for future high-performance naval platforms*, 5th Conf. High-Performance Marine Vehicles (HIPER), Launcerston, pp.364-373

BRYCE, R. (2005), *Recycling high speed ferries and ideas for the future*, RINA Conf. Recycling of Ships and Other Marine Structures, London, pp.107-114

DAVIDSON, J. (2006), *Carbon fiber composite recycling – An industry perspective*, Composites World, http://www.compositesworld.com/hpc/issues/2006/September/1410

FACH, K. (2002), *High Speed Craft in service*, 3rd Conf. High-Performance Marine Vehicles (HIPER), Bergen, pp.145-152

FACH, K.; ROTHE, F. (2000), *Classification experience with lightweight ship structures*, RINA Conf. Lightweight Construction Latest Developments, London

FUHRMANN, A.; GREINER, S.; KORBEL, T. (2007), *Entsorgung von Faserverbundwerkstoffen und Einsatz der Rezyklate*, Report for MaVeFa, Hochschule Bremen (in German)
http://www.faserverbund-verwertung.de/mavefa.php?site=mavefa

GRAMANN, H.; KÖPKE, M.; FLÜGGE, M.; GRAFE, W. (2007), *Data management for better ship-care and recycling*, 6th Conf. Computer and IT Applications in the Maritime Industries (COMPIT), Cortona, pp.33-41

HAYASHI, S.; YAMANE, K. (1998), *Study on the development of the recycling technology of waste FRP boats*, Papers of Ship Research Institute 35(3) (in Japanese)

HAYASHI, S. (1989), *Floating disposal system for waste FRP boats*, 16th Joint Meeting UJNR Marine Facilities Panel, Washington, pp.115-122

HAYASHI, S.; YAMANE, K. (1994), *Development of movable disposal system for waste FRP boats*, 19th Joint Meeting UJNR Marine Facilities Panel, Tokyo, pp.224-231

HEDLUND-ÅSTRÖM, A.; LUTTROP, C.; REINHOLDSSON, P. (2005), *Environmentally friendly recycling of FRP-sandwich ship hulls*, RINA Conf. Recycling of Ships and Other Marine Structures, London, pp.119-126

HEDLUND-ÅSTRÖM, A.; OLSSON, K.A. (1997), *Recycling and LCA studies of FRP-sandwich structures*, 2nd North European Engineering and Science Conf. – Composites and Sandwich Structures, EMAS Ltd, Stockholm

IMO (2007a), *Recycling of ships – Draft guidelines for the development of the Inventory of hazardous materials*, MEPC 56/3/2

IMO (2007b), *Recycling of ships – Draft guidelines for the development of the Inventory of hazardous materials*, MEPC-ISRWG 2/2

IMO (2007c), *Ship recycling*, IMO guidelines for ship recycling, IMO-I685E

ISO (1996), *Plastics – Symbols and abbreviated terms*, ISO 1043:1996

ISO (2000), *Plastics – Generic identification and marking of plastic products*, ISO/DIS 11469:2000

LAMB, T. (2003), *Design/production integration*, Ch.14 in Ship Design and Construction (Ed. T. Lamb), SNAME

LANDAMORE, M.J.; BIRMINGHAM, R.W.; DOWNIE, M.J.; WRIGHT, P.N.H. (2007), *Sustainable technologies for inland leisure craft*, J. Eng. for the Maritime Environment 221/M3, pp.97-114

MAREK, A.; BOLZE, K.; JOACHIM, T.; JUNG, O.; WIDDECKE, H. (2000), *Recycling von Verbundwerkstoffen im Automobilbau*, Workshop Kunststoffrecycling im Automobilbau, Wolfsburg (in German)

MÜLLER, L. (1990), *Faserverstärkte Kunststoffe im Boots- und Schiffbau*, Handbuch der Werften XX, Hansa-Verlag Hamburg (in German)

N.N. (2003), *Composite recycling and disposal – An environmental R&D issue*, Boeing Environmental Technotes 8/4

UMAIR, S. (2006), *Environmental impacts of fiber composite materials – Study of life cycle assessment of materials used for ship superstructure*, Master Thesis, Royal Institute of Technology, Stockholm

VDI (2002), *Recyclingorientierte Produktentwicklung (Recycling oriented product development),* VDI Guideline 2243, VDI-Verlag

SURF HYDROMECHANICS

Carlo Bertorello & Luciano Oliviero, University of Naples "FEDERICO II", Italy
luciano.oliviero@unina.it

SUMMARY

The first application of planing surface was recorded by English explorers in Hawaiian Islands at the end of eighteen century. It was a skill trial and a pleasure: the "surf".
"Surf" is the planing run on the sea wave surface of a board propelled by gravity force, and the "surfer" is the driver.
In this paper the application of planing surface model to surfboard is proposed. This work has been developed in order to highlight the geometrical and environmental parameters, and to describe the surfboard kinematic behavior.

1. INTRODUCTION

Planing crafts are one of the most common boats used all around the world for small commercial, military and pleasure craft. Despite of these, the first application of planing surface was a skill trial and pleasure ones: the "surf".
This first planing surface application was recorded by English explorers in Hawaiian Islands, at the end of eighteen century; Captain James Cook witnessed the first board surfers and recorded it in his journal: that was the Hawaiian National Pastime [1].
Surfboards will be the only planing surface application till the end of nineteen century.
A surfboard is a waterproof plank used to plan on surface sea waves.
"Surf" is the planing run on a surface sea wave of a surfboard propelled by gravity force, and a "surfer" is the driver of a surfboard.
Following notes are written only for planing surface moved by gravity force.

2. PLANING CONDITIONS

In each condition, static or dynamic, the weight of a craft is balanced by the pressure acting on the wetted surface.
This pressure is composed by two components: hydrostatic, related to the buoyancy, and hydrodynamic, related to the speed of the craft.
It is possible to classify the vessels according to the kind of pressure field acting during their steady motion:

- *displacement vessels* - if hydrostatic pressure is much higher than hydrodynamic ones,
- *semi-displacement vessels* - if hydrostatic and hydrodynamic pressure have the same order of magnitude,
- *planing vessels* - if hydrostatic pressure is much lower than hydrodynamic ones.

This classification is useful to understand physical phenomena but it is not manageable.
To avoid this , Naval Architects are use to classify vessels in these three families (displacement, semi-displacement and planing) by the value of a characteristic number, related to the craft and its steady cruising speed: the Froude number $Fn_\delta = \dfrac{V}{\sqrt{g\delta}}$, where V is the craft speed, δ is a characteristic dimension of the craft and g is acceleration of gravity.
Despite the existence of a Froude number per each characteristic dimension adopted, it is easy to show the powerful of this way of work: by the knowledge of two data (speed and characteristic dimension), via the calculation of just one number (the Froude ones), it is possible to classify the craft.
Let define the planing conditions for a surfboard riding on a wave, and advancing with the same propagation direction of the front wave.
The Froude number related to the beam b of a surfboard is

$$Fn_b = \frac{V}{\sqrt{gb}} \tag{1}$$

and the speed wave formula in shallow water[1] is

$$V_c = \sqrt{g\,h} \tag{2}$$

Starting to surf, surfer and wave have the same speed.
If the surfboard is propelled, along the front wave propagation, much slower (or much faster) than the wave, it cannot exchange energy with the wave. If the surfboard is moving slightly slower than the wave, it can be caught and pushed along and gets further accelerated by wave: the surfboard gains energy and the wave loses the same amount of energy [2].
This, and the above formulas, drive to:

$$F_{nb}^2 = \frac{h}{b} \tag{3}$$

Planing condition, of a vessel or a surfboard, cannot be defined by a unique Froude number value. Some authors suggest a range of value for each kind of Froude number; in our case, the planing condition related to the beam b is $F_{nb} \geq 1.5$ [4], and substituting in (3):

$$h \geq 2.25b \tag{4}$$

that is the first "kinematic" condition for planing, in which the beam of the surfboard b is related to the depth of water h, both in the same unit length.
Some authors [5] suggest to use the Froude number related to the total weight W:

---

1 Shallow water range: $h/\lambda < 0.04$, where h is the depth of water and λ is the length-wave[3].

$$F_{n\nabla} = \frac{V}{\sqrt{g\sqrt[3]{\frac{W}{\gamma}}}} \qquad (5)$$

and the planing condition is reached if $F_{n\nabla} \geq 3$.

Reminding the formula in (2), we have:

$$h \geq 9 \cdot \sqrt[3]{\frac{W}{\gamma}} \qquad (6)$$

This is the second "kinematic" condition for planing, in which the total weight (sum of the weight of surfer and the ones of surfboard) is related to the deep of water *h*.

These conditions are necessary but not sufficient, as a matter of fact planing is completely developed if the weight *W* is balanced only by the vertical component *F'*[2] of the hydrodynamic force *F*:

$$W = F'$$

With reference to Figure 1

$$F' = L\cos\alpha + D\sin\alpha$$

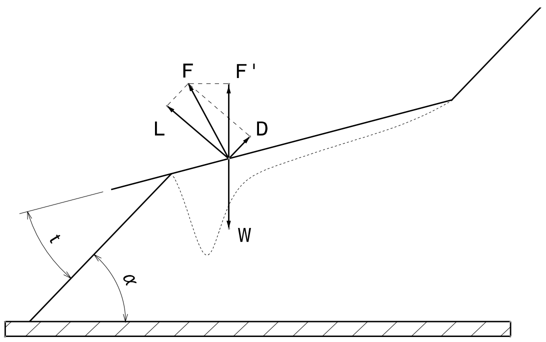

Figure 1

Reminding, for flat plate planing:

$$\frac{D}{L} = \frac{C_D}{C_L} = \tan\tau$$

we have

$$F' = L(\cos\alpha + \tan\tau\sin\alpha)$$

hence

$$W = L\frac{\cos(\alpha - \tau)}{\cos\tau}$$

or

$$W = \frac{1}{2}\rho V^2 S_w C_L(\tau, AR)\frac{\cos(\alpha-\tau)}{\cos\tau} \qquad (7)$$

For planing flat plate, a non linear lift coefficient formula is [6]:

$$C_L(\tau, AR) = \frac{0.5\pi AR}{1+AR}\tau\cos^2\tau + \frac{4}{3}\left(1 - \frac{AR}{10}\right)\sin^2\tau\cos^3\tau \qquad (8)$$

with $AR \in [0.125, 10]$.

In the range $AR \in [0.125, 10]$, $\frac{C_L}{\cos\tau}$ has a maximum value of $\left.\frac{C_L}{\cos\tau}\right|_{\max} = 0.899 < 0.9$.

Further:

$$S_w \leq S,$$
$$\cos(\alpha - \tau) \leq 1,$$

and

$$\left.\frac{C_L}{\cos\tau}\right|_{\max} S_w\cos(\alpha-\tau) < 0.9S,$$

so:

$$W = \frac{1}{2}\rho V^2 S_w C_L(\tau, AR) < 0.45\rho V^2 S$$

and reminding that:

$$V^2 = gh \text{ and } \gamma^* = \rho g$$

we have:

$$W < 0.45\gamma^* hS \qquad (9)$$

The equation (9) must be satisfied for each value of *h* from equation (4); for $h = h_{\min} = 2.25b$:

$$W < 1.01\gamma^* bS \qquad (10)$$

and for sea water ($\gamma^* = 1025\frac{kgf}{m^3} = 10055\frac{N}{m^3}$)

$$\begin{aligned} &a) \quad W < 1038\ b^2 l \quad [kgf] \\ &b) \quad W < 10181\, b^2 l \quad [N] \end{aligned} \qquad (11)$$

That is a "mechanical" condition for planing, with the dimensions of the surfboard, in meter [m], related to the total weight.

Formulas (4), (6) and (10) are the conditions to be satisfied for planing with a surfboard.

3. INCIPIENT WAVE BREAKING

Surfer has to catch the wave before its breaking.

An important geometrical parameter related to the performance of a wave, in shallow water, is the steepness of wave, H/λ which describe the incipient wave breaking[3].

As a wave approaches a beach, its shape may change increasing the steepness wave value. It has been noted, from math models and experiments, that as the depth decreases, the wave length reduces, the height of the wave increases, the speed of the wave decreases, and the period remain constant . The wave crest at the surface gradually assumes a higher speed than the wave trough in front of it and when the slope between them becomes increasingly steeper, the crest, becoming instable, spills over forming a breaker [7].

Waves break as they reach a limiting value of steepness, which is a function of the relative depth h/H and the sea bed slope $\tan\alpha_w$ [8].

The term "breaker depth index" is used to describe nondimensional breaker height:

$$\gamma_b = \frac{H_b}{h_b} \qquad (12)$$

in which the subscript "b" stands for "breaking wave".

[2] Planing is fully developed if the Archimedean force (hydrostatic force) is negligible versus the hydrodynamic one.

[3] *H* is the height of the wave and *λ* is the wave length, in the same unit of length.

Early studies on breaker indices were conducted using solitary waves (regular waves field), and the theoretically value determined was $\gamma_b = 0.78$.

For low steepness waves, we have $0.78 < \gamma_b < 1.56$, with [8]:

$$\gamma_b = 0.78 \text{ if } \alpha_w = 0 \deg$$

$$\gamma_b = 1.56 \text{ if } \alpha_w = 90 \deg .$$

Some authors suggest to use value of the break depth index in the range 1.1 to 1.3 [7].

The lowest value of the breaker depth index ($\gamma_b = 0.78$) is commonly used in engineering practice as a first estimate of the breaker index [8]. Reminding the (4), we have:

$$\begin{cases} H_{\max} = 1.75\, b \\ h_{\min} = 2.25\, b \end{cases} \tag{13}$$

with

$$H_{\max} \le 0.78\, h_{\min} \tag{14}$$

that is a "no breaking wave" condition.

4. HYDRODYNAMIC MODEL

Let consider the movement of a rigid body Γ on an inclined plane Π, which is moving at V_C speed, as shown in Figure 2:

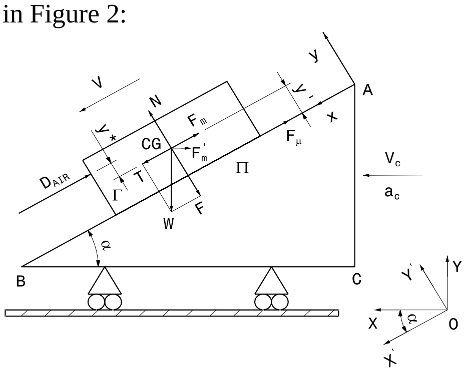

Figure 2

From the equilibrium equation of force and moments in $\{O, X', Y'\}$:

$$\begin{cases} N - F - F_m^{'} \sin\alpha = 0 \\ T - D_{AIR} - F_m - F_m^{'} \cos\alpha - F_\mu = 0 \\ F_\mu y' - D_{AIR} y^* = 0 \end{cases} \tag{15}$$

reminding that

$$F_m = \frac{W}{g} a_x$$

$$F_m^{'} = \frac{W}{g} a_c$$

$$F_\mu = \mu\left(F + F_m^{'} \sin\alpha\right)$$

$$D_{AIR} = \frac{1}{2} \rho_{AIR}\, V^2 A$$

$$F = W \cos\alpha$$

$$T = W \sin\alpha$$

we have:

$$a_x = g\left[\left(\frac{\tan\alpha - \mu}{\sqrt{1+\tan^2\alpha}}\right) - \frac{a_c}{g}\left(\frac{1+\mu\tan\alpha}{\sqrt{1+\tan^2\alpha}}\right) - \frac{1}{2}\left(\frac{\rho_{AIR}\, V^2 A}{W}\right)\right] \tag{16}$$

Let consider the inclined plane Π as a fluid body (side of a wave); at the equilibrium, the rigid body Γ will be inclined of an angle τ (angle of attack) versus the inclined plane Π.

In first approximation, let assume the hypothesis:

- all forces pass through CG, which involve that the moment equilibrium is satisfied.
- the hydrostatic force is negligible: the volume of the surfboard displaced is null $\nabla_\Gamma \cong 0$.

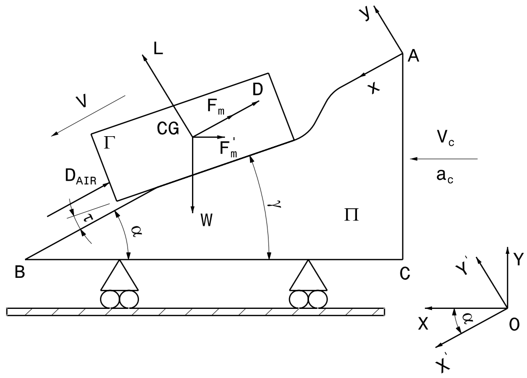

Figure 3

At the equilibrium in $\{O, X', Y'\}$

$$\begin{cases} W\cos\alpha - F_m - D - F_m^{'}\cos\alpha - D_{AIR} = 0 \\ L - F_m^{'}\sin\alpha - W\cos\alpha = 0 \end{cases} \tag{17}$$

Reminding that

$$L = \frac{1}{2}\rho V^2 S_w C_L(\tau, AR)$$

$$D = \frac{1}{2}\rho V^2 S_w C_D(\tau, AR)$$

and for flat plate planing

$$\frac{C_D}{C_L} = \frac{D}{L} = \tan\tau$$

we have:

$$a_x = g\left[\left(\frac{\tan\alpha - \tan\tau}{\sqrt{1+\tan^2\alpha}}\right) - \frac{a_c}{g}\left(\frac{1+\tan\tau\tan\alpha}{\sqrt{1+\tan^2\alpha}}\right) - \frac{1}{2}\left(\frac{\rho_{AIR} V^2 A}{W}\right)\right] \tag{18}$$

Note that equations (16) and (18) look like the same, whereas μ is known and τ is unknown.

Further, in both formulas, a_x is sum of three terms:

- the first is related to the movement of the rigid body Γ versus the wave Π;
- the second is related to the movement of the wave Π;
- the third is due to the aerodynamics.

The term related to aerodynamic drag is negligible versus the others; as a matter of fact in (17) we have

$$D = \frac{1}{2}\rho V^2 S_w C_D(\tau, AR)$$

$$D_{AIR} = \frac{1}{2}\rho_{AIR} V^2 A$$

$$o\left(\frac{\rho_{AIR}}{\rho}\right) \approx 10^{-3} \text{ and } o\left(\frac{A}{S_w C_D}\right) \approx 1,$$

$$D_{AIR} << D$$

so:

$$a_x \cong g\left[\left(\frac{\tan\alpha - \tan\tau}{\sqrt{1+\tan^2\alpha}}\right) - \frac{a_c}{g}\left(\frac{1+\tan\tau\tan\alpha}{\sqrt{1+\tan^2\alpha}}\right)\right] \quad (19)$$

It is important to remark that a surfer "fills" his weight force direction (local vertical[4]) and the trim of the surfboard, so the surfer is able to fill the pitch angle γ of the surfboard versus the horizontal plane[5]. By Figure 3, it is easy to show that $\gamma = \alpha - \tau$, with $\gamma > 0$ for surfboard nose down.

Let determine the expression of a_c.

Reminding that $V_c = \sqrt{gh}$:

$$a_c = \frac{dV_c}{dt} = g\tan\alpha_w \quad (20)$$

with α_w slope of the sea bed.

We note that for deep water constant $\alpha_w = 0$ and $a_c = 0$; while for deep water decreasing moving closer to the shoreline $\alpha_w < 0$ and $a_c < 0$.

The time length of planing is related to the difference between the speed of surfer and the speed of wave: less difference longer time.

In the "start up" phase (rising up phase before planing) surfer has to both rise up the side wave and avoid to be overtaken by the wave: $a_x \neq 0$. In the "surf" phase (planing phase), surfer tries to maximize the time of planing [or the speed (kinetic energy)], driving the surfboard with a speed close to the wave speed: $a_x \cong 0$ [or with a speed greater than the wave speed: $a_x >> 0$].

The time length of "start up" should be not greater than half period T_w of the wave: for time grater than $\frac{T_w}{2}$ the wave will overtake the surfer.

The "Start up" phase

At time $t = 0$ let $\alpha = 0$, from (19):

$$a_x\big|_{t=0} = -g\tan\tau - a_c$$

or

$$a_x\big|_{t=0} = -g\tan\tau + g\tan|\alpha_w| \quad (21)$$

If the surfboard is initially horizontal ($\gamma = 0$ and $\tau = 0$ for $t = 0$)

$$a_x = g\tan|\alpha_w| > 0 \quad (22)$$

If the speed of surfer at time $t = \frac{T_w}{2}$ is not close to the speed wave, surfboard bobs up and down as the wave goes by. To avoid this case it is possible to rise up the initial value of speed V and/or to rise up the acceleration a_x. From the (21), to get an higher initial value of a_x, surfer has to turn the surfboard to an angle $\tau < 0$: surfer waits the wave with the surfboard nose down.

At time $t = t^* > 0$, rising up the side wave, $\alpha > 0$, $\tau \geq 0$ (with $\tau < 0$ surfboard cannot plan), and for $a_x \geq 0$ it must be $\tau < (|\alpha_w| + \alpha)$, or $\gamma > -|\alpha_w|$, with $\alpha + |\alpha_w| < \frac{\pi}{2}$: surfer can get $a_x = 0$ driving the surfboard nose up with a pitch angle equal to $|\alpha_w|$, while nose up value lower than $|\alpha_w|$ drives to $a_x > 0$, further nose down angle value drives to $a_x >> 0$.

The "Surfing" phase

In the "surfing" phase, surfer will drive the surfboard trimming the pitch angle γ to get $a_x \approx 0$ (max time of planing) or $a_x >> 0$ (max kinetic energy).

For constant deep water, $\alpha_w = 0$ and $a_c = 0$:

$$a_x = 0 \quad \Leftrightarrow \quad \tau = \alpha \quad \gamma = 0$$
$$a_x >> 0 \quad \Leftrightarrow \quad \tau < \alpha \quad \gamma > 0$$

($\gamma > 0 \quad \rightarrow$ surfboard nose down).

For decreasing deep water, $\alpha_w < 0$ and $a_c < 0$:

$$\begin{aligned} a_x = 0 \quad &\Leftrightarrow \quad \tau = |\alpha_w| + \alpha \;;\; \gamma = -|\alpha_w| \\ a_z >> 0 \quad &\Leftrightarrow \quad \tau < |\alpha_w| + \alpha \;;\; \gamma > -|\alpha_w| \end{aligned} \quad (23)$$

surfer will drive the surfboard with a pitch angle related to the value of a_x.

Let determine the max speed of the surfer in the hypothesis of steady motion wave and horizontal sea bed ($\alpha_w = 0\deg$).

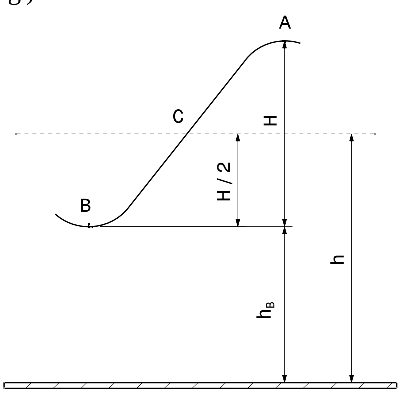

Figure 4

From the Bernoulli's equation (conservation of energy equation):

$$\frac{1}{2}mV_A^2 + mg(H + h_B) = \frac{1}{2}mV_B'^2 + mgh_B \quad (24)$$

[4] Local vertical is the local gravity force direction.

[5] Horizontal plane is a plane perpendicular to the local vertical.

we have:

$$V_B^{'} = V_B \sqrt{1 + \frac{3H}{h_B}} \qquad (25)$$

with

$$V_A = \sqrt{g(h_B + H)} \qquad V_B = \sqrt{gh_B}$$

wave speed in A and B respectively, and $V_B^{'}$ the speed of surfer in B.

From the (14) we can write $H_{max} = 0.78h$ ($\alpha_w = 0 \deg$) where h is the average depth of the wave; as shown in Figure 4, $h = h_B + \frac{H}{2}$, so:

$$H_{max} = 1.28\, h_B$$
$$V_{B.max}^{'} = 2.2\, V_B$$
$$V_A = 1.5\, V_B$$
$$V_C = 1.28\, V_B$$

and

$$V_{B,max}^{'} = 1.72\, V_C \qquad (26)$$

the speed of surfer is not greater than 1.72 times the speed of wave V_C for $\alpha_w = 0 \deg$.

If we take $H_{max} = 1.56h$ ($\alpha_w = 90 \deg$), it will be:

$$H_{max} = 7.09\, h_B$$
$$V_B^{'} = 4.7 V_B$$
$$V_A = 2.8 V_B$$
$$V_C = 2.1 V_B$$
$$V_B^{'} = 2.25 V_C \qquad (27)$$

the speed of surfer is not greater than 2.25 times the speed of wave V_C for $\alpha_w = 90 \deg$. So the maximum theoretical value of surface speed, related to the wave speed V_C, is in the range [1.72 ; 2.25].

Reminding that:

- surfer starts to coast down the advancing front of the wave, from the top A to the bottom B, before the incipient wave breaking,
- Bernoulli's equation does not take in account the loss of energy due to viscous effects,

the speed of surfer will be less than the maximum theoretical value of $V_B^{'}$.

5. "HANGING TEN" PERFORMANCE

An interesting surfing exercise is termed "hanging ten": it involves having one's 10 toes over the front end of the surfboard.

This is a trick that is not so common nowadays because for most people it requires a very heavy board, which is not readily available anymore [1].

Let analyze this performance case related to an "OLO" surfboard[6].

DATUM

$l = 18\, ft \cong 5.5\, m$ $\qquad \lambda \cong 12.5$

$W_S \cong 55\, kgf$ $\qquad W_M \cong 80\, kgf$

At the equilibrium, with a constant speed[7], we have:

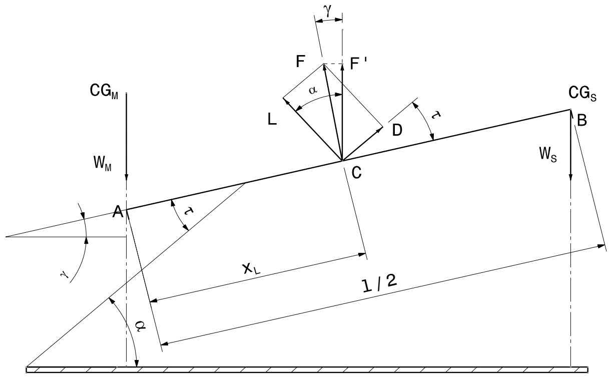

Figure 5

$$\begin{cases} F' = W_s + W_M \\ F' x_L = W_S \dfrac{l}{2} \end{cases} \qquad (28)$$

Reminding that

$$F' = L \cos\alpha + D \sin\alpha \qquad (29)$$

we have

$$\begin{cases} L \dfrac{\cos(\alpha - \tau)}{\cos\tau} = W_S + W_M \\ x_L \dfrac{L}{\cos\tau} = W_S \dfrac{l}{2} \cos(\alpha - \tau) \end{cases} \qquad (30)$$

and

$$x_L = \frac{W_S}{W_S + W_M} \frac{l}{2} \cos^2(\alpha - \tau)$$

During the *hanging ten* exercise surfer has foot closer themselves and closer to the front end of the surfboard. This drives to a set with surfer in bolt upright and surfboard in (or closer to) horizontal plane: $\gamma = \alpha - \tau \cong 0$.

Hence:

$$x_L = \frac{W_S}{W_S + W_M} \frac{l}{2} \qquad \%x_L = \frac{W_S}{2(W_S + W_M)} \qquad (31)$$

$$\%L_{CP} = 1 - \%x_L \qquad L_{CP} = \%L_{CP}\, l \qquad (32)$$

and

$$F = 135\, kg \qquad \%x_L = \frac{55\, kg}{270\, kg} = 0.2037$$

$$\%L_{CP} = 0.7963 \qquad L_{CP} \cong 4.4\, m$$

For each speed of a flat plate, the equilibrium set is known if τ and l_w (or $AR = b/l_w$) are known.

[6] The *OLO* surfboards were reserved for Hawaiian royalty; it was the biggest surfboard. Cut from native Hawaiian trees, trimmed to shape, polished with coral and finished with nut oil, an *OLO* board sometimes measured 24 feet [7.3 m] long and weighed up to 200 pounds [91 kg].

[7] In this exercise the surfer is not able to balance the inertial loads, so at the equilibrium $a_x = 0\ m/s^2$ and $\gamma = 0 \deg$.

From Wagner's model of planing flat plane [9], we know that $\forall\tau\ \exists!\frac{L_{CP}}{l_w}$, so for each fixed value of AR exists, for the equilibrium, only one value of τ obtained by Wagner's model:

$$\forall AR\ \exists!\tau:\ \left.\frac{L_{CP}}{b}AR\right|_{Surfboard} = \left.\frac{L_{CP}}{l_w}\right|_{Wagner} \tag{33}$$

The couple of value (τ, AR) that satisfy the planing condition $(F_{nb} \geq 1.5)$ will describe an "hanging ten" equilibrium set:

$$F_{nb} = \sqrt{\frac{2(W_M + W_S)AR\cos\tau}{\gamma^* b^3 C_L(\tau, AR)}} \geq 1.5 \tag{34}$$

where C_L is known by **(8)**.

The first step is to find out the range value of AR, within we define the trial values of AR.

We know that $L_{CP} < l_w \leq l$, so it follows $\frac{b}{l} \leq AR < \frac{b}{L_{CP}}$.

Let $AR_{\min} = \frac{b}{l}$ and $AR_{\max} = \frac{b}{L_{CP}}$, we have:

$$\left.\frac{L_{CP}}{l_w}\right|_{\min} = \frac{L_{CP}}{b}AR_{\min} = 1 - \left[\frac{W_S}{2(W_M + W_S)}\right]$$

$$\left.\frac{L_{CP}}{l_w}\right|_{\max} = \frac{L_{CP}}{b}AR_{\max} = 1$$

so

$$1 - \left[\frac{W_S}{2(W_M + W_S)}\right] \leq \frac{L_{CP}}{l_w} < 1$$

Values of $\frac{L_{CP}}{l_w}$ off range do not make sense, as matter of fact:

- $\frac{L_{CP}}{l_w} < 1 - \frac{W_S}{2(W_M + W_S)}$ means $l_w > l$,
- $\frac{L_{CP}}{l_w} > 1$ means that the center of pressure is out of wetted area.

In our case:

$$AR_{\min} = 0.080 \quad \text{and} \quad AR_{\max} = 0.100.$$

Let fix other two arbitrary values of AR within the range $[AR_{\min}, AR_{\max}]$, we have:

$AR = AR_{\min} = 0.080$

$\rightarrow \%L_{CP} = 0.7963 \rightarrow \tau = 15.5\deg \rightarrow$

$\rightarrow C_L = 0.1138 \rightarrow F_{nb} = 1.5 \rightarrow V = 3.0\frac{m}{s}$

$AR = 0.087$

$\rightarrow \%L_{CP} = 0.8635 \rightarrow \tau = 19.5\deg \rightarrow$

$\rightarrow C_L = 0.1613 \rightarrow F_{nb} = 1.3 \rightarrow V = 2.6\frac{m}{s}$

$AR = 0.094$

$\rightarrow \%L_{CP} = 0.9328 \rightarrow \tau = 23.0\deg$

$\rightarrow C_L = 0.2031 \rightarrow F_{nb} = 1.2 \rightarrow V = 2.4\frac{m}{s}$

$AR = AR_{\max} = 0.100$

$\rightarrow \%L_{CP} = 1.000 \rightarrow \tau = 26.0\deg$

$\rightarrow C_L = 0.2367 \rightarrow F_{nb} = 1.1 \rightarrow V = 2.3\frac{m}{s}$

there is only one "hanging ten" equilibrium set for a planing surfboard "OLO":

$$\tau \cong 15.5\deg \quad \text{and} \quad AR \cong 0.080.$$

Let repeat this procedure for a commercial surfboard:

DATUM

$l = 2.40m \qquad b = 0.61m$

$W_S = 5kgf \qquad W_M = 80kgf$

$AR_{\min} = 0.250 \qquad AR_{\max} = 0.258 \qquad L_{CP} = 2.37m$

$AR = AR_{\min} = 0.250$

$\rightarrow \%L_{CP} = 0.9706 \rightarrow \tau = 24.5\deg$

$\rightarrow C_L = 0.2797 \rightarrow F_{nb} = 0.77 \rightarrow V = 1.9\frac{m}{s}$

$AR = AR_{\max} = 0.258$

$\rightarrow \%L_{CP} = 1.000 \rightarrow \tau = 26.0\deg$

$\rightarrow C_L = 0.2992 \rightarrow F_{nb} = 0.75 \rightarrow V = 1.8\frac{m}{s}$

no "hanging ten" exercises can be performed with this commercial surfboard.

6. CROSS RUNNING

The minimum speed that a surfer can reach is the wave speed. In each point of the side wave the surfer's speed component along the wave direction (propagation) is equal to the wave speed on that point.

In fact if the surfer's speed component were less than the speed wave the surfer would bob up and down as the wave goes by, while if the surfer's speed component were higher than the speed wave the surfer should fly!

In each point on the side wave the surfer's velocity can be higher, in modulus, than the wave velocity. As matter of fact, from Bernoulli's equation, we have:

$$\frac{1}{2}mV_A^2 + mg(h_B + H) = \frac{1}{2}mV'^2 + mgh^* \tag{35}$$

with:

$$V_A^2 = g(h_B + H)$$

$$V^* = gh^*$$

so:

$V' = V^*\sqrt{\frac{3(h_B + H)}{h^*} - 2}$, with $h_B \leq h^* \leq h_B + H$.

The surfer's velocity and the wave direction, in the horizontal plane[8], define an angle θ (yaw angle), as shown in Figure 6:

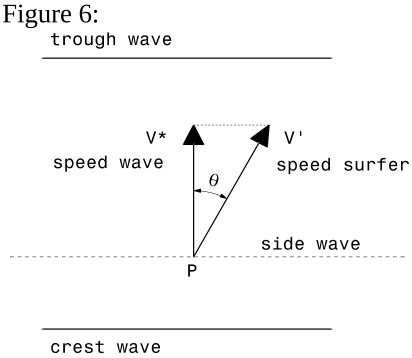

Figure 6 - Top view

and reminding that $V^* = V' \cos\theta$, we have:

$$\theta = \arccos \frac{1}{\sqrt{\dfrac{3(h_B + H)}{h^*} - 2}} \tag{36}$$

with $h^* = h_B$ in B and $h^* = h_B + H$ in A, as shown in Figure 7.

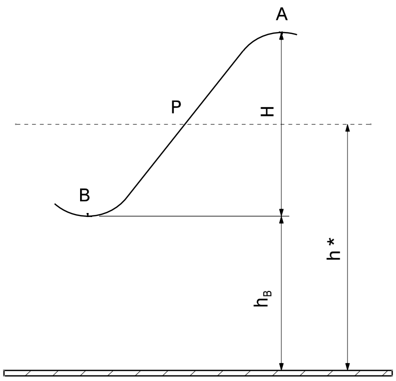

Figure 7 - Lateral view

This yaw angle θ is not constant and its value is related to the surfer's position on the side wave:

- in A (crest) $h^* = h_B + H$ $\theta_A = 0\,\text{deg}$
- in B (through) $h^* = h_B$

  $$\theta_B = \arccos \frac{1}{\sqrt{3\dfrac{H}{h_B} + 1}}$$

  and in "no braking wave" condition for $\alpha_w = 0°$ ($H \le 0.78 \cdot h$) we have $\theta_B \le 63°$ (lower limit value), while for $\alpha_w = 90°$ ($H \le 1.56 \cdot h$) we have $\theta_B \le 78°$ (upper limit value).

7. EXAMPLE

Surfboard and surfer datum:

$l = 2.40\,m$ $b = 0.61\,m$

$W_S = 5\,kgf$ $W_M = 85\,kgf$

In first approximation we have:

1° "kinematic" planing condition

$h \ge 2.25 b = 2.25 \cdot 0.61 m = 1.37\,m$ $h \ge 1.37\,m$

2° "kinematic" planing condition

$$h \ge 9 \cdot \sqrt[3]{\frac{W}{\gamma}} = 9 \cdot \sqrt[3]{\frac{90\,kg}{1025\,\dfrac{kg}{m^3}}} = 4.00\,m \qquad h \ge 4.00\,m$$

"mechanical" planing condition

$$W < 1038\,b^2 l = 1038\,\frac{kgf}{m^3} \cdot (0.61\,m)^2 \cdot 2.40\,m = 927\,kgf$$

$$W < 927\,kgf$$

(surfer <u>must</u> have a weight less than 922 kgf !)

"no breaking wave" conditions:

$$H_{\max} < 0.78 h \text{ for } \alpha_w = 0°$$
$$H_{\max} < 1.56 h \text{ for } \alpha_w = 90°$$

Let $h = 10\,m$, we have

$$H_{\max} < 7.8\,m \text{ (lower limit value)}$$
$$H_{\max} < 15.6\,m \text{ (upper limit value)}$$

1. $H_{\max} = 2.0\,m$ $h_B = h - \dfrac{H}{2} = 9.0\,m$ $\vartheta_B \cong 39°$
2. $H_{\max} = 4.0\,m$ $h_B = 8.0\,m$ $\vartheta_B \cong 51°$
3. $H_{\max} = 6.0\,m$ $h_B = 7.0\,m$ $\vartheta_B \cong 58°$
4. $H_{\max} = 7.8\,m$ $h_B = 6.1\,m$ $\vartheta_B \cong 63°$
5. $H_{\max} = 10\,m$ $h_B = 5.0\,m$ $\vartheta_B = 68°$
6. $H_{\max} = 12\,m$ $h_B = 4.0\,m$ $\vartheta_B = 72°$
7. $H_{\max} = 14\,m$ $h_B = 3.0\,m$ $\vartheta_B = 75°$
8. $H_{\max} = 15.6\,m$ $h_B = 2.2\,m$ $\vartheta_B = 78°$

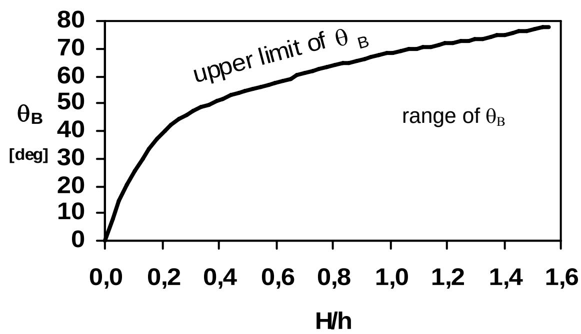

Figure 8

$$V_C = \sqrt{gh} \cong 10\,\frac{m}{s}$$

$$F_{nb} = \frac{V_C}{\sqrt{gb}} = \sqrt{\frac{h}{b}} = \sqrt{\frac{10\,m}{0.61\,m}} \cong 4 \rightarrow$$

$$\rightarrow \qquad F_{nb} \cong 4 > 1.5$$

[8] The horizontal plane is a general plane normal to the local gravity force direction.

$$F_{n\nabla} = \frac{V_C}{\sqrt{g\sqrt[3]{\frac{W}{\gamma}}}} = \sqrt{\frac{h}{\sqrt[3]{\frac{W}{\gamma}}}} = \sqrt{\frac{10\,m}{\sqrt[3]{\frac{90\,kg}{1025\frac{kg}{m^3}}}}} = 4.7 \rightarrow$$

$$\rightarrow \qquad F_{n\nabla} = 4.7 > 3$$

$$V'_{B.\max} = 1.72 V_C = 17.2\frac{m}{s} \qquad (\alpha_W = 0\deg)$$

$$V'_{B.\max} = 2.25 \cdot V_C = 22.5\frac{m}{s} \qquad (\alpha_W = 90\deg)$$

Further:

$$\frac{C_L(\tau, AR)}{AR} = \frac{W}{\frac{1}{2}\rho V^2 b^2} = \frac{90kgf\ 9.81\frac{N}{kgf}}{\frac{1}{2}1025\frac{kg}{m^3}\left(10\frac{m}{s}\right)^2 (0.61m)^2} = 0.0463$$

$$C_L(\tau, AR) = 0.0463\,AR$$

For $AR = AR_{\min} = 0.254$

$$C_L(\tau, AR) = 0.0463 \cdot 0.254 \cong 0.0118 \rightarrow \tau \cong 1.5\deg$$

$$S_{w,\max} = \frac{b^2}{AR_{\min}} = \frac{(0.61m)^2}{0.254} \cong 1.46m^2 \rightarrow l_w = 2.4m = l$$

but $l = l_w$ if and only if $\tau = 0\deg$, so this case $AR = AR_{\min}$ (with $l = l_w$ and $\tau > 0\deg$) has no physical meaning.

For $AR = AR_{\max} = 10$

$$C_L(\tau, AR) = 0.0463 \cdot 10 = 0.463 \rightarrow \tau \cong 21.5\deg$$

$$S_{w,\min} = \frac{b^2}{AR_{\max}} = \frac{(0.61m)^2}{10} = 0.037m^2 \rightarrow l_w = 0.061m$$

So for $h = 10m$:

$F_{nb} = 4 \qquad F_{n\nabla} = 4.7$

$V_C = 10\frac{m}{s} \qquad 17.2\frac{m}{s} \le V'_{B,\max} \le 22.5\frac{m}{s}$

$V'_B < 17.2\frac{m}{s} \quad (\alpha_w = 0\deg);$

$V'_B < 22.5\frac{m}{s} \quad (\alpha_w = 90\deg)$

$1.5° < \tau \le 21.5° \quad 63° \le \vartheta_{B\max} \le 78°$

and the planing will start to be over for $1.37\,m < h < 4.00\,m$ and will be off for $h < 1.37\,m$.

8. CONCLUSIONS

Planing surface models have been applied to a pleasure planing flat plate: the surfboard. This work has been developed in order to describe the kinematic behavior of a surfboard considered subjected to the gravity force only. The kinematic behavior has been related to geometrical and environmental parameters. Some formulas considering the kinematic and dynamic conditions and the "no breaking wave" condition, in order to get the surfboard in planning, are proposed. Hydrodynamic behavior has been investigated too, and some tips are proposed in order to improve the overall performances as well as to understand some fundamental performances: the fastest run, the "hanging ten" exercise and the cross running. Finally an example in order to get useful information for greater surf performance is presented.

9. SYMBOLS

BASIC

A	Crest of wave	
b	beam of surfboard	[m]
B	Trough of wave	
CG	Center of Gravity	
CP	Center of Pressure	
g	gravity acceleration:	$[m/s^2]$
h	depth of water	[m]
H	Height of wave	[m]
h*	Height of a point P on the side wave	[m]
h_B	Height of crest wave	[m]
l	length of surfboard	[m]
L_{CP}	CP location (measured from aft end of surfboard)	[m]
m	mass	[kg]
S_w	wetted surface of surfboard	[m^2]
t	time	[s]
V	speed of surfboard, along x-axis	$[m/s]$
V'	Speed of surfer in a point P of a side wave	$[m/s]$
V*	Speed of wave in a point P of the side	$[m/s]$
V_c	speed of wave	
W	total weight	[N]
x_{CP}	distance of CP versus the front end of the surfboard	[m]
α	slope of wave side (as well as of Π)	[°,deg]
α_w	slope of sea bed	[°,deg]
γ	pitch angle of the surfboard (as well as of Γ)	[°,deg]
Γ	rigid body	
θ	Yaw angle of surfer's speed vs wave direction	[°,deg]
λ	wave length	[m]
μ	friction coefficient	
Π	inclined plane	
ρ	mass density of water	$[kg/m^3]$
ρ_{AIR}	mass density of air	$[kg/m^3]$
τ	angle of attack of the surfboard vs the wave side	[°,deg]
$\{A, x, y\}$	Cartesian coordinate system, fixed on Π, with x-axis on Π and top-bottom oriented	
$\{O, X, Y\}$	Cartesian coordinate system, Earth fixed, with X-axis horizontal and oriented to the water's edge	
$\{O, X', Y'\}$	Cartesian coordinate system, Earth fixed, obtained by a counterclockwise rotation	

of magnitude α versus $\{O, X, Y\}$

DERIVED

A	projects area of Γ on a plane normal to Π	[m^2]
a_c	acceleration of the wave (or of Π)	$[m/s^2]$
a_x	acceleration component of surfer (or of Γ)	$[m/s^2]$
AR	Aspect Ratio	$AR = b^2/S_w$
$C_D = C_D(\tau, AR)$	hydrodynamic drag coefficient	
$C_L = C_L(\tau, AR)$	hydrodynamic lift coefficient	
D	hydrodynamic drag	[N]
D_{AIR}	aerodynamic drag	[N]
F	weight component normal to Π	[N]
$F_m, F_m^{'}$	inertial forces	[N]
F_{nb}	Froude number related to the beam b	$F_{nb} = \frac{V}{\sqrt{gb}}$
Fμ	friction force	[N]
h*	Height of a point P on the side wave	[m]
L	hydrodynamic lift	[N]
$l_w = S_w/b$	wetted length	[m]
$\frac{L_{CP}}{l_w}$	nondimensional location of CP related to the wetted length	
$\%L_{CP} = \frac{L_{CP}}{l}$	nondimensional location of CP related to the length	
N	reaction force of the plane Π	[N]
$S = l\,b$	projected area of the surfboard on Π	[m^2]
T	towing force: weight component on Π	[N]
T_w	Period of wave	[s]
V’	Speed of surfer in a point P of the side wave	$[m/s]$
V*	Speed of wave in a point P of the side	$[m/s]$
V_A	Speed wave in A (crest)	$[m/s]$
V_B	Speed wave in B (trough)	$[m/s]$
$V_B^{'}$	Speed of surfer in B	$[m/s]$
Vx	component of V along X-axis	$[m/s]$
x_L	Distance of CP vs the front edge of the wetted surface	[m]
$\%x_L = \frac{x_L}{l}$	nondimensional distance of CP versus the front end	
y'	moment arm of Fμ versus CG in $\{A, x, y\}$	[m]
y^*	moment arm of D_{AIR} versus CG in $\{A, x, y\}$	[m]
$\gamma^* = \rho\, g$	specific weight of water	$[N/m^3]$
γ_b	Breaker depth index	

SUBSCRIPT

b	breaking wave
M	surfer
S	surfboard

10. REFERENCES

[1] Edge, R. 2001. Surf Physics. *The Physics Teacher* Vol. 39, pp. 272-277 (ISSN: 0031-921X)

[2] Chen, F. F. 1984. *INTRODUCTION TO PLASMA PHYSICS AND CONTROLLED FUSION.*. Berlin: Springer. pp. 245-247 (ISBN 03046413329)

[3] Miranda, S. 2001 *Appunti di Architettura Navale*. Napoli: Dipartimento di Ingegneria Navale, Università degli Studi di Napoli “FEDERICO II”

[4] Savitsky, D. & Brown, P.W. 1976. Procedures for Hydrodynamic Evaluation of Planing Hulls in Smooth and Rough Water. *Marine Technology* Vol. 13, No 4, pp. 381-400

[5] Fédiaevski, C., Voïtkounski, I., Faddéev, Y. 1974. *MECANIQUE DES FLUIDES.* Moscou: Ed. MIR. pp. 542-543 (French version)

[6] Wadlin, K.L. & Christopher, K.W. 1958. A Method for Calculation of Hydrodynamic Lift for Submerged and Planing Rectangular Lifting Surfaces. *Report NACA TN 4168*. Washington, D.C. (USA).

[7] de Mestre, N. 2003. *THE MATHEMATICS AND PHYSICS OF BODY SURFING*. ICAM 2003, Sydney, Australia, 7-11 July 2003

[8] Smith, J.M. 2002. *SURF ZONE HYDRODYNAMICS.* In *Coastal Engineering Manual EM 1110-2-1100 (Part II)*. Vicksburg (Mississippi): US Army Corps of Engineers (USA). Part 2, Chapter 4, pp 1-5.

[9] Wagner, H. 1932. Über Stoss und Gleitvorgänge an der Oberfläche von Flüssigkeiten. *Z.A.M.M.* No.4 Vol.12.

NUMERICAL SIMULATION OF HIGH SPEED SHIP WASH WAVES

Kunihide Ohashi, National Maritime Research Institute, Japan
Jun Hasegawa, National Maritime Research Institute, Japan
Ryohei Fukasawa, National Maritime Research Institute, Japan

SUMMARY

An investigation of wash waves of a high speed craft is carried out. At first, the measurement of wave height using three wire resistance probes is carried out. Each probe is placed at the different position from the ship center line. These measurements are carried out in deep and shallow water conditions. The quantity of trim and wash wave height in deep and shallow conditions is discussed.

Next, the numerical simulation of wash waves is carried out. A CFD codes which has developed in NMRI is applied to the prediction of wash waves. The wave height distribution is obtained by re-generation of computational grid from reference grid. The reference computational grid covers very wide domain to resolve the wash waves. Longitudinal wave profile is compared with measured result. Through the comparison of computed and measured results, the applicability of the present method is discussed.

1. INTRODUCTION

The operation of high speed craft may be constrained in lower speed to avoid the creation of high wash waves. It would be useful to be able to predict wash waves before the craft in service. Many efforts are being made for understanding of wash waves in deep and shallow water conditions.(1)(2)(3)

In the present study, an investigation of wash waves of high speed craft is carried out. Present investigation is mainly to establish an operational guide for crew.

At first, measurement of wash waves is carried out. Wash waves in deep and shallow water conditions are measured. The measurement results of trim and sinkage are used in numerical simulation.

Next, the numerical simulation of wash waves using computational fluid dynamics is carried out. To treat a transom stern, some modeling is needed. A ship stern is extended to ship aft as if a ship hull is existed.

Through the comparison of computed and measured results, applicability of present method is examined.

2. MEASUREMENT OF WASH WAVES

2.1 SHIP MODEL

The ship model is high speed craft with single chain type. Main particulars of ship and model are listed in Table 1.

Table 1 Main particulars

	Model	Ship
Loa(m)	2.702	20.0
B(m)	0.608	4.5
D(m)	0.311	2.3

The material of model is wood, and as appendages, shaft brackets and shafts are attached.

2.2 MEASUREMENT SYSTEM

The measurements at deep water condition are carried out in the #2 towing tank of NMRI. The dimensions of the tank are, length 400m, width 24m and depth 8m.

Resistance wire probes for measurement of wash waves are positioned 2.0m(y/L=0.792), 3.0m(y/L=1.192), 6.0m (y/L=2.396) from the center line of model (Figure 1).

Forward speed of carriage is from abt. 2.0m/s (Fn=0.4) to abt. 7.0m/s (Fn=1.4). Froude number Fn is based on ship length L. The measurements are carried out in these speed, wave disturbance of tank wall is eliminated in analysis.

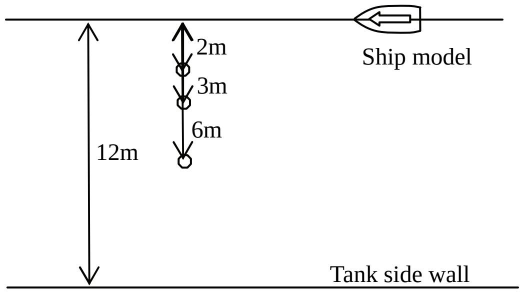

Figure 1 Layout of probes with ship model (Deep water)

The model is towed at sinkage and trim freed condition. The towing rod is set to longitudinal center buoyancy, and the rod angle is adjusted to shaft angle while the measurement.

The laser distance meter is used to determine exact moment when the model passed the wave measurement probes. Reflective plate is attached to carriage, when the carriage passed at the point of laser distance meter, pulse is marked and recorded in the measurement system.

Near stern wave measurement is also carried out in deep water condition. Wave height is measured by servo type which the probe heaves with wave surface. Measurement results are used for modeling of transom stern in computation.

The measurements in shallow water condition are carried out in the #3 towing tank of NMRI. The dimensions of the tank are, length 150m, width 12m. Depth is examined with real sea, then decided to 0.64m.

Measurements are almost as same as deep water condition, except for the number and position of probe, and carriage speeds. Only one probe is used for this measurement, and is positioned at 1.0m (y/L=0.416) from the center line of model (Figure 2). Forward speed of carriage is from abt. 2.0m/s (Fn=0.4) to abt. 4.5m/s (Fn=0.9) which are determined by the examination of the shallow water effect based on depth Froude number $Fn_h = V/\sqrt{gh}$ (Figure 3). h is a depth of water.

$Fn_h = 0.7$ means the point where the shallow water effect begins to appear. $Fn_h = 1.0$ means critical speed which the wash waves height increases dramatically.

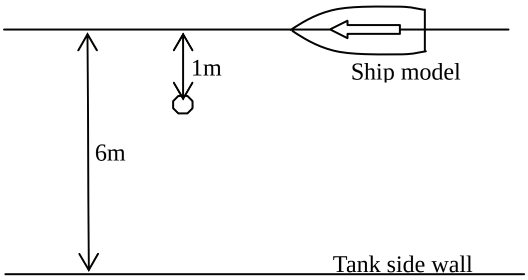

Figure 2 Layout of probes with ship model (Shallow water)

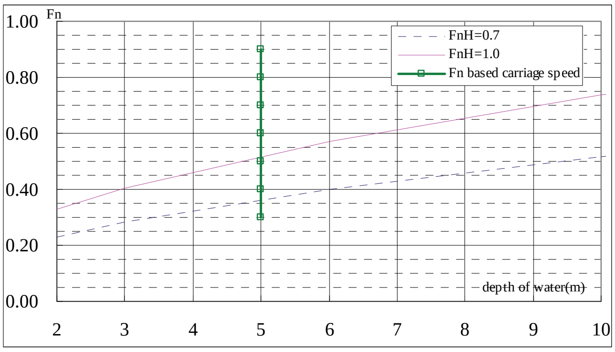

Figure 3 Shallow water effect

2.3 MEASUREMENT RESULTS

Figure 4 and Figure 5 show the measurement trim and sinkage. Aft trim and sink are positive. Fore trim of shallow water is larger than trim of deep water in lower Froude number. Also sinkage of shallow water becomes larger. Figure 6 shows measurement results of wash wave height in deep water condition. x/L=0 means fore perpendicular of the ship. It is clearly seen wash waves are consisted from bow and stern waves etc.

Figure 7 shows measurement results of wash wave height in shallow water condition. Wash waves are available in two velocities due to the tank wall reflection.

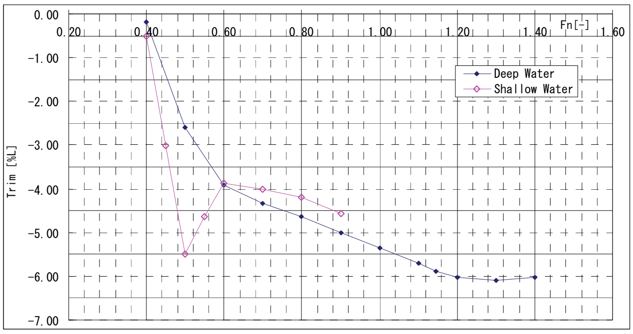

Figure 4 Measured result of trim(%L)

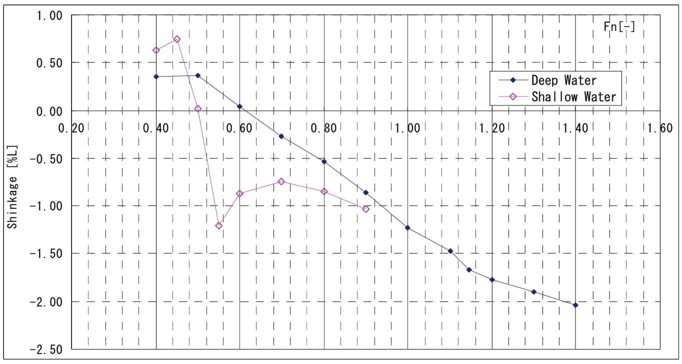

Figure 5 Measured result of sinkage(%L)

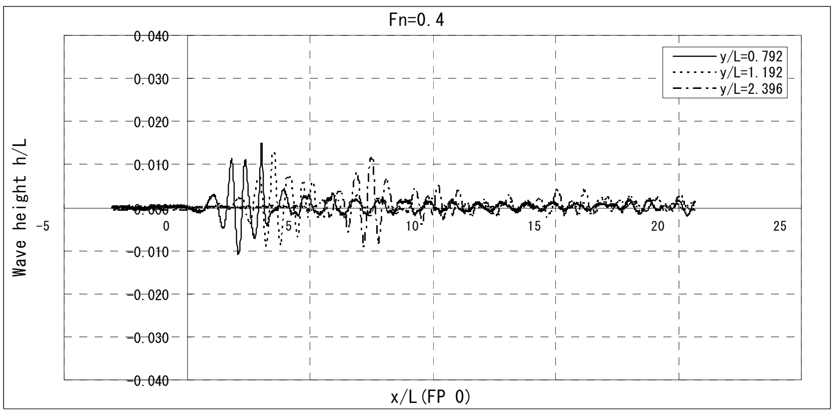

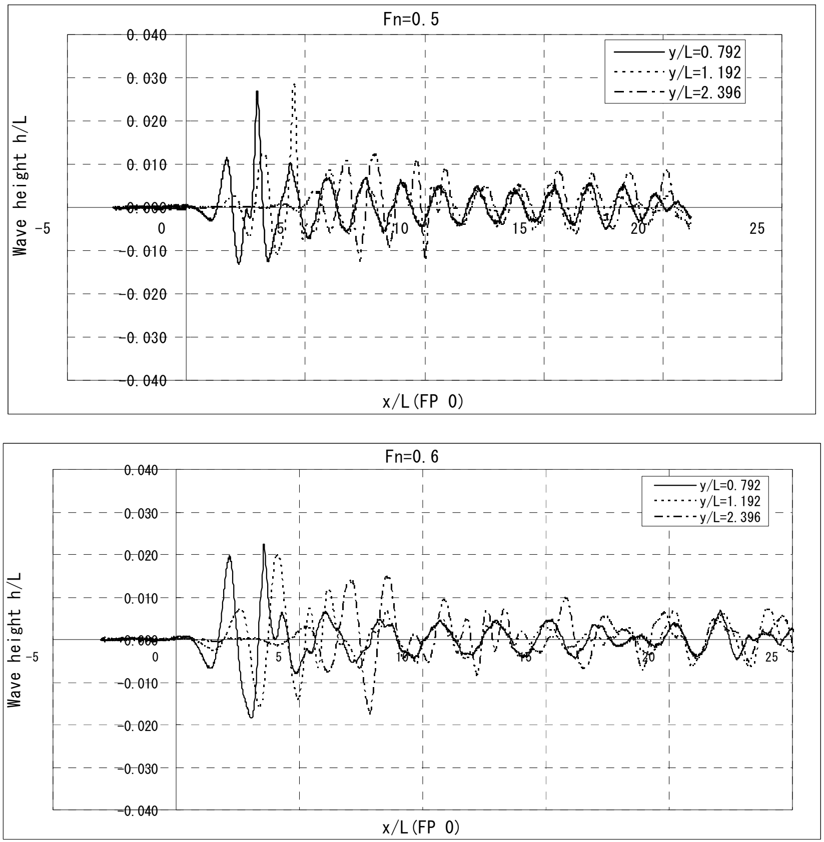

Figure 6 Wash wave measurement result (Deep water)

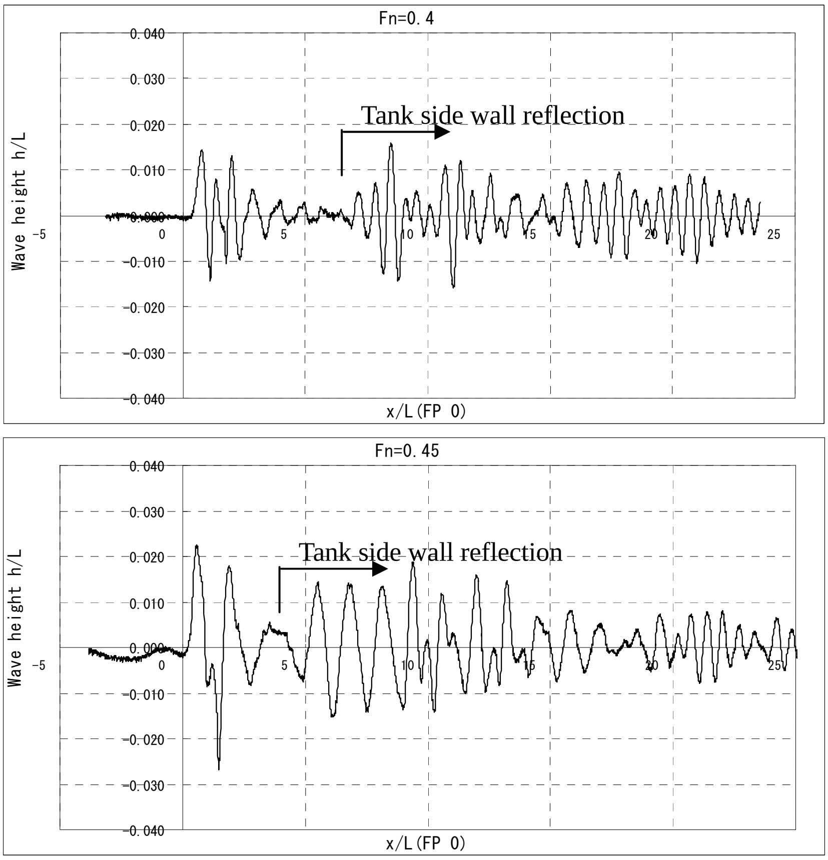

Figure 7 Wash wave measurement result (Shallow water)

3. NUMERICAL SIMULATION

3.1 CFD CODE

The flow solver used in this study is called NEPTUNE[4] which is under development at National Maritime Research Institute.

The governing equations are 3D Reynolds averaged Navier-Stokes equations for incompressible flows. Coupling between pressure and velocity is made by artificial compressibility approach. The final form can be written as follows.

$$\frac{\partial \mathbf{q}}{\partial t}+\frac{\partial(\mathbf{e}-\mathbf{e}^{v})}{\partial \mathbf{x}}+\frac{\partial(\mathbf{f}-\mathbf{f}^{v})}{\partial \mathbf{y}}+\frac{\partial(\mathbf{g}-\mathbf{g}^{v})}{\partial \mathbf{z}}=0 \qquad (1)$$

and

$$\mathbf{q}=[p\ u\ v\ w]^{T}$$

In the above, all variables are non-dimensionalized using the reference density ρ_0, velocity U_0 and length L_0. The velocity components (x,y,z) direction are expressed as (u,v,w). The inviscid fluxes **e**, **f** and **g**, viscous fluxes $\mathbf{e}^v$, $\mathbf{f}^v$ and $\mathbf{g}^v$ are defined as,

$$\mathbf{e}=\begin{pmatrix}\beta u\\ u^2+p\\ uv\\ uw\end{pmatrix},\quad \mathbf{f}=\begin{pmatrix}\beta v\\ uv\\ v^2+p\\ vw\end{pmatrix},\quad \mathbf{g}=\begin{pmatrix}\beta w\\ uw\\ vw\\ w^2+p\end{pmatrix} \qquad (2)$$

$$\mathbf{e}^{v}=\begin{pmatrix}0\\ \tau_{xx}\\ \tau_{xy}\\ \tau_{zx}\end{pmatrix},\quad \mathbf{f}^{v}=\begin{pmatrix}0\\ \tau_{xy}\\ \tau_{yy}\\ \tau_{yz}\end{pmatrix},\quad \mathbf{g}^{v}=\begin{pmatrix}0\\ \tau_{zx}\\ \tau_{yz}\\ \tau_{zz}\end{pmatrix}$$

where β is a parameter for artificial compressibility and $\tau_{ij}=(1/R+\nu_t)(\partial u_i/\partial x_j+\partial u_j/\partial x_i)$. R is Reynolds number defined as $U_0 L_0/\nu$ where ν is the kinematic viscosity. ν_t is the non-dimensional kinematic eddy viscosity which is determined by the Spalart-Allmaras one equation model.

Spatial discretization is based a structured cell-centered finite volume method. Inviscid fluxes are evaluated by the Roe scheme and MUSCL extrapolation is adopted to attain the third order accuracy, while viscous fluxes are centrally differenced. The equation is solved by an approximate Newton relaxation method with a symmetric Gauss Seidel iterative approach. The code employs multigrid approach and local time stepping method to accelerate convergence to a steady state solution

The nonlinear free-surface conditions are implemented and re-gridding technique is used to treat the free-surface deformation.

3.2 COMPUTATIONAL GRID AND CONDITIONS

Figure 8 and Figure 9 show the computational grids. Computational domain and grid detail are listed in Table 2.

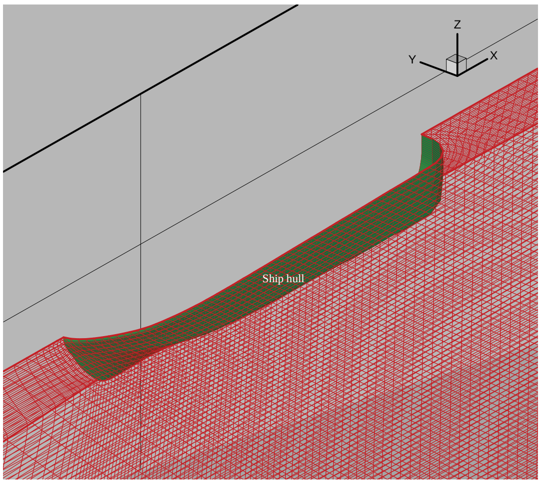

Figure 8 Computational grid near hull(deep water)

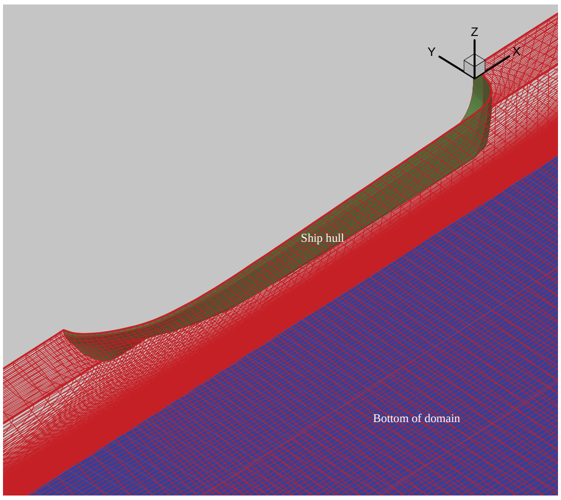

Figure 9 Computational grid near hull(shallow water)

Table 2 Computational domain and grid detail

Computational Domain	$-1.5\le x\le 11.0$ $-5.0\le y\le 0.0$(Deep water) $-7.0\le y\le 0.0$(Shallow water) $-1.9\le z\le 0.12$(Deep water) $-0.27\le z\le 0.12$(Shallow water)
Grid points	415×33×281(Deep water) 415×33×281(Shallow water)

The computational domain covers the wash waves. Minimum spacing is 5×10^{-3} at FP, 1×10^{-2} at AP and 1×10^{-2} in normal directions.

Froude number is set to Fn=0.4, 0.5, 0.6. Trim and sinkage of measurement results are used in each case. Thus ship trim and sinkage are fitted to measurement result.

A transom stern of the ship is treated by the extension of ship hull to backward of ship. The amount of this extension is examined by the comparison of wave height where the right after the ship. In the case of Fn=0.4, the amount of extension is 5%L, 10%L in Fn=0.5 and 20%L in Fn=0.6 respectively.

In the case of shallow water, boundary condition at bottom of computational domain is $\partial p/\partial n=0$ and (u,v,w)=(1,0,0).

3.3 RESULTS

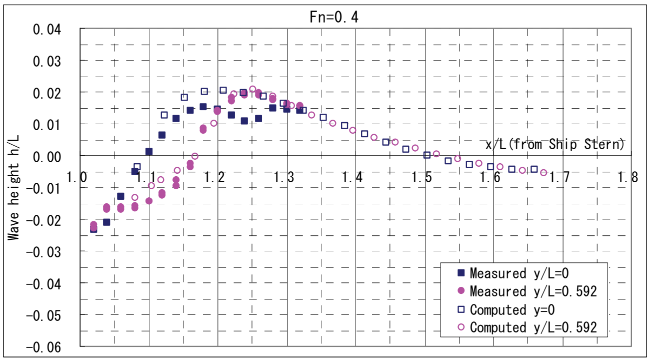

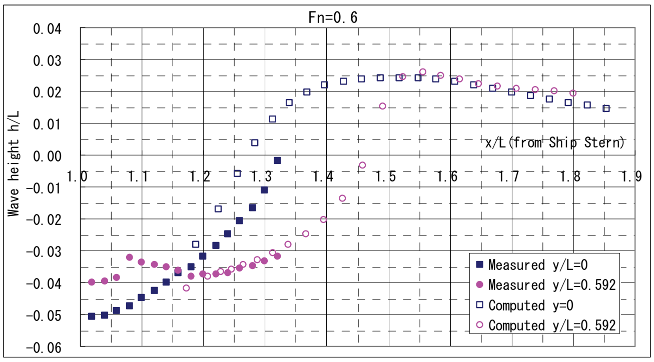

Figure 10 Comparison of near stern wave profile

Figure 10 shows comparison of near stern wave profile. Computed results show good agreement with measurement results, thus present amount of extension of ship hull can be used for prediction of wash waves.
Figure 11 and Figure 12 show comparison of wash wave profile in deep water condition. Computed results show agreement with measured result except y/L=2.396 in Fn=0.4. The deviation may be caused by the divergence of wave height.
Figure 13 shows comparison of wave profile in shallow water condition. Computed results show agreement with measured results and simulate the crests decay well.
From Figure 14 to Figure 19 show the computed wave contour in deep and shallow water conditions. Waves are diverged with Kelvin wave angle in deep water condition. On the other hand, waves in shallow water conditions show quite unique characteristics. Large transverse waves are generated in Fn=0.5 which is a critical speed. As in the case of Fn=0.6 which is supercritical speed, wave length become longer.
Finally, Figure 20 shows the comparison of maximum wave height. The maximum wave height is defined as the largest wave height in measured and computed results. Computed results show agreement with the measured results. Also, Computed results of wave height become large at the critical speed in shallow water condition.

4. CONCLUSION

Measurement and prediction of wash waves have been carried out. Computed results show agreement with measured results. Present prediction method is practical one but give useful information about wash waves. Although Sinkage and trim data are needed for present method, these data can be estimated by an empirical method or simulated directly in computation in near future.

5. ACKNOLEDGEMENT

Japan Coast Guard and Sumidagawa Shipyard Co, .Ltd. have sponsored this research, and are thanked to their permission for this publication.

REFERENCES

1. Whittaker, J.T., Doyle, R., Elasser, B., 'A Study of the Leading Long Period Waves in Fast Ferry Wash', Hydrodynamics of High Speed Craft Wake Wash & Motion Control, RINA International Conference, 2000
2. Raven, H.C., 'Numerical Wash Prediction using a Free-Surface panel Code', Hydrodynamics of High Speed Craft Wake Wash & Motion Control, RINA International Conference, 2000
3. Keuning, J.A., Visser, D.B., 'An Approximation Method For th Wake Wash of Planing of Monohulls', Hydrodynamics of High Speed Craft Wake Wash & Motion Control, RINA International Conference, 2000
4. Hirata, N., Hino, T., 'An Efficient Algorithm for Simulating Free-Surface Turbulent Flows around an Advancing Ship', Journal of the Society of Naval Architects of Japan, Vol.185, 1999

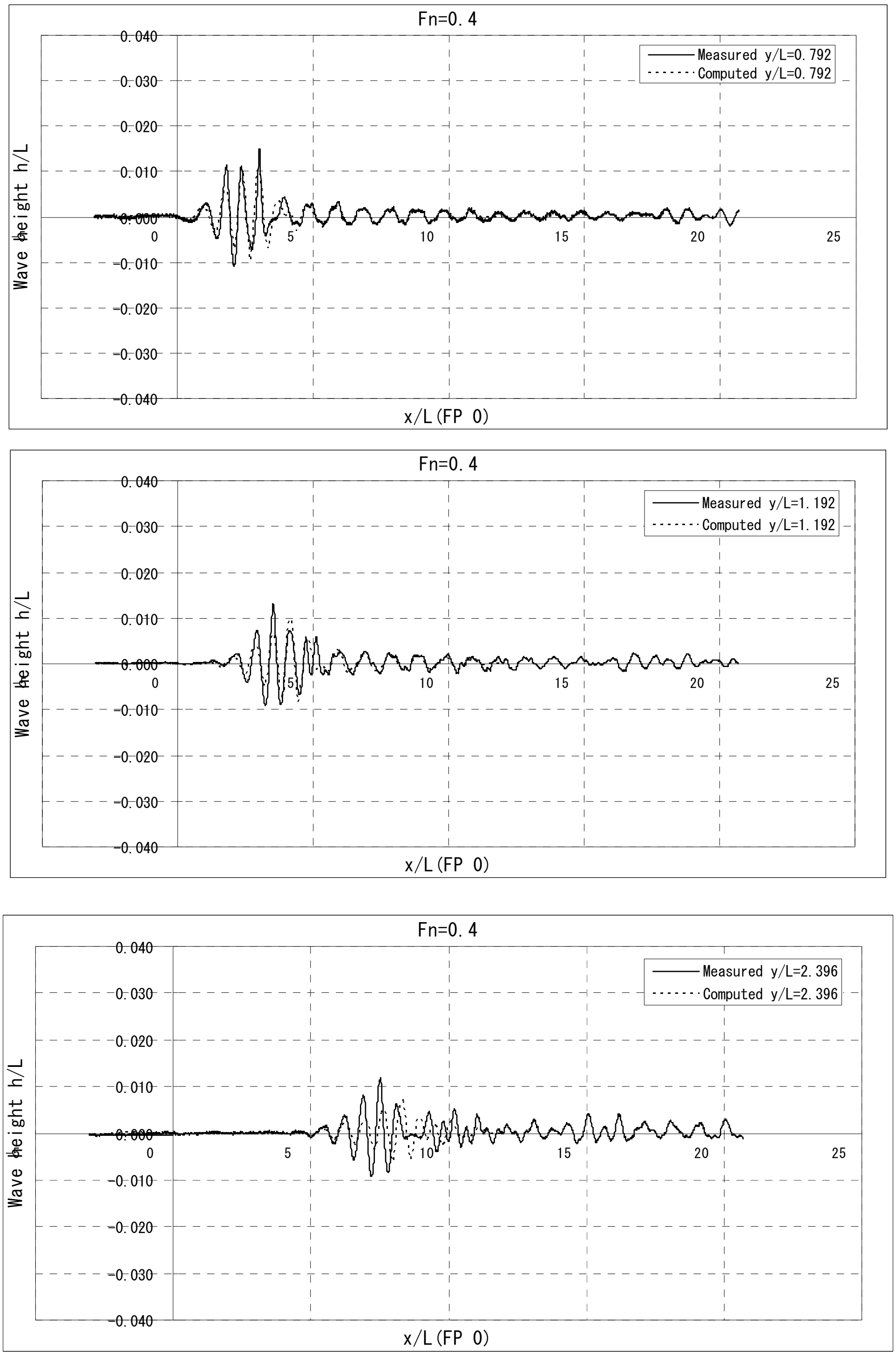

Figure 11 Comparison of wave profile(Deep water, Fn=0.4)

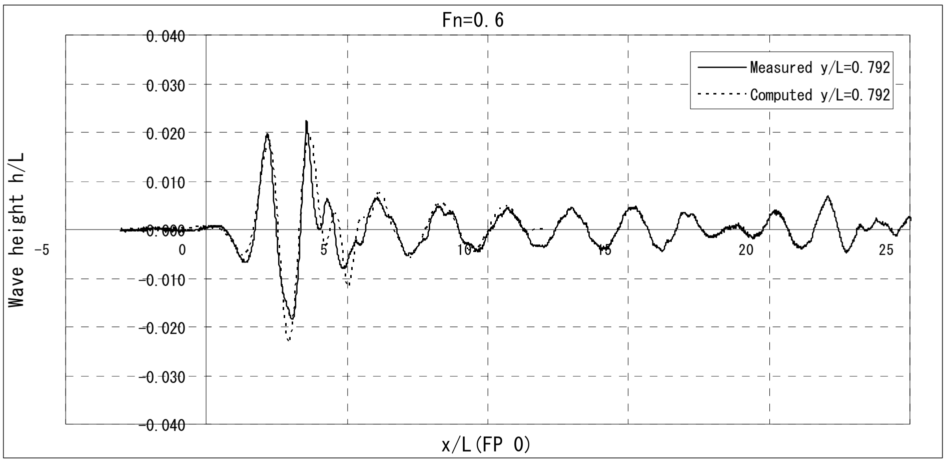

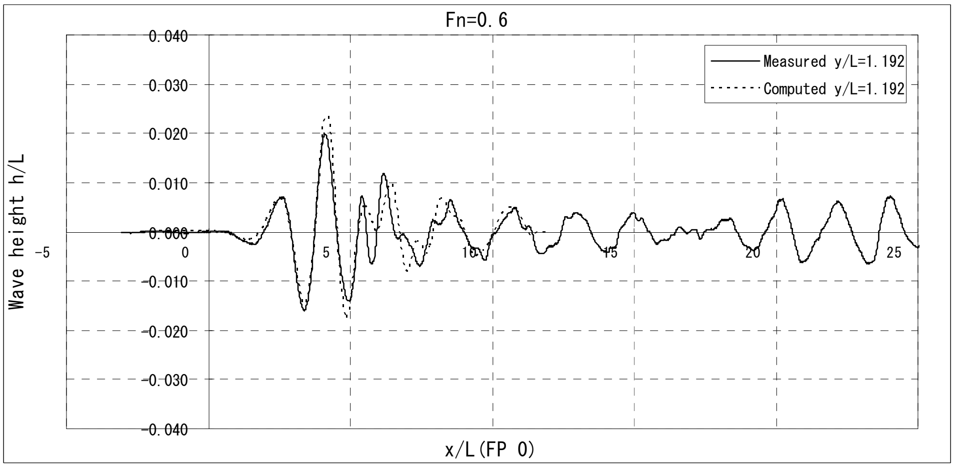

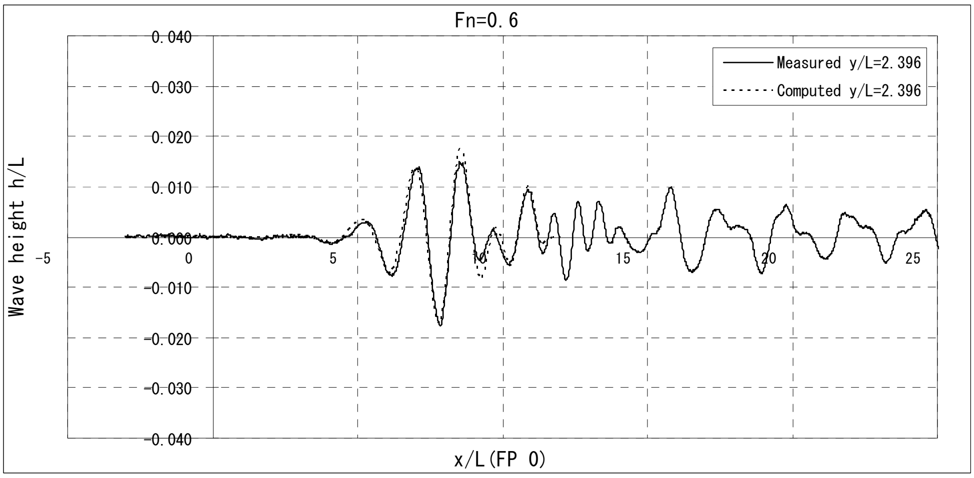

Figure 12 Comparison of wave profile(Deep water, Fn=0.6)

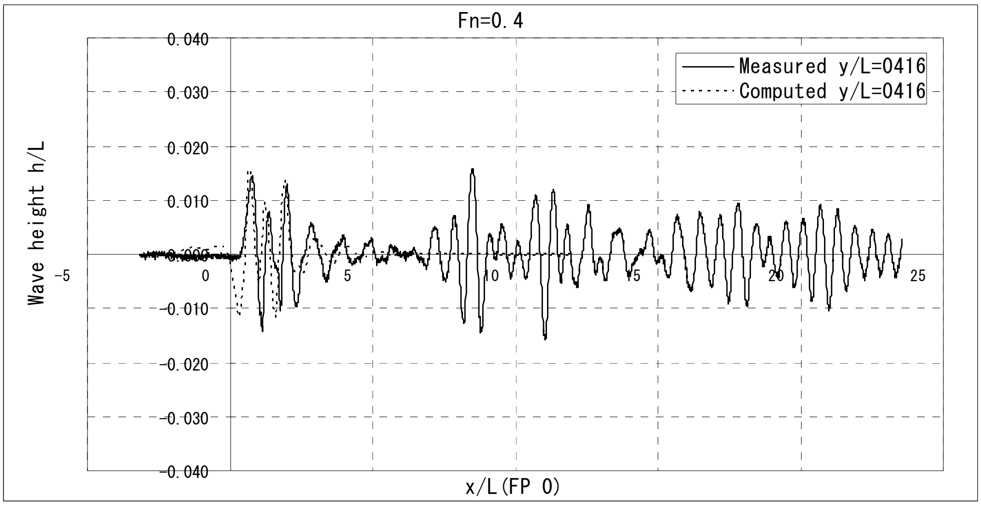

Figure 13 Comparison of wave profile(Shallow water, Fn=0.4)

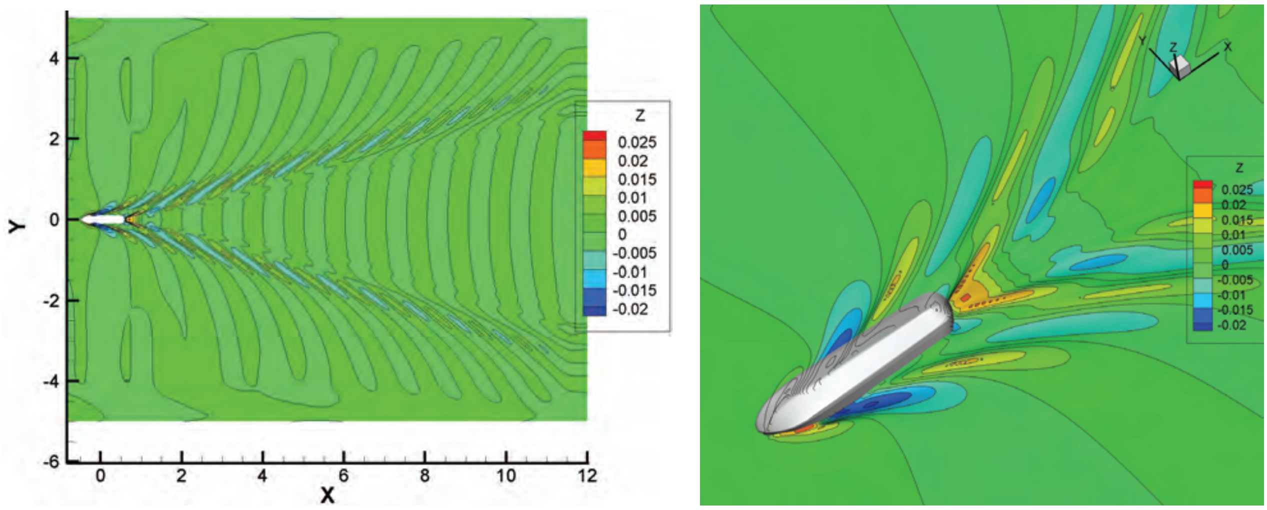

Figure 14 Computed wave contour (Deep water, Fn=0.4)

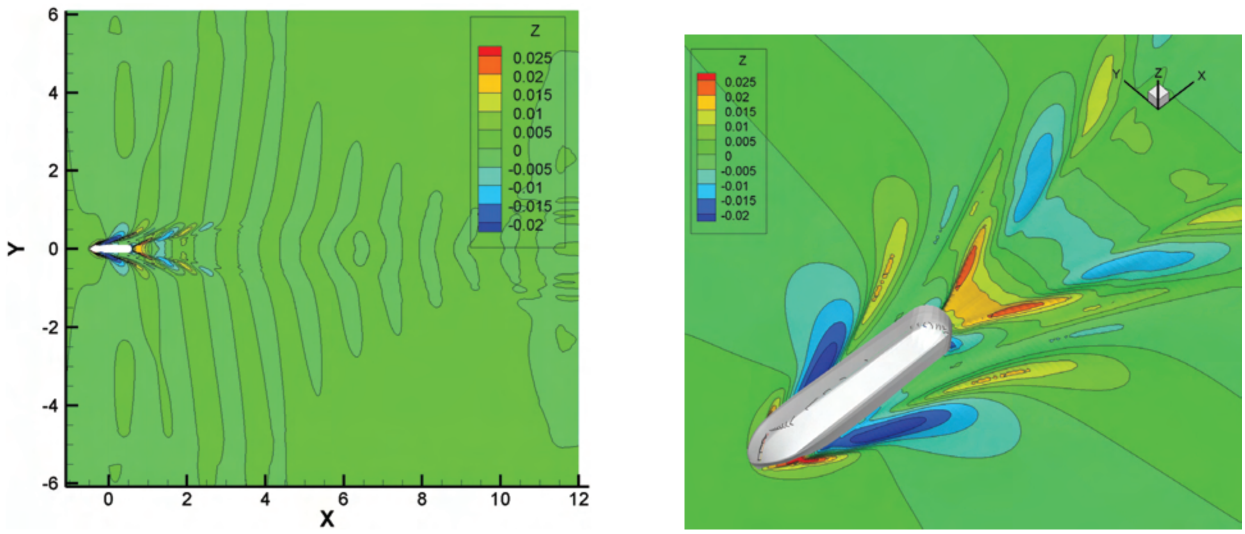

Figure 15 Computed wave contour (Shallow water, Fn=0.4)

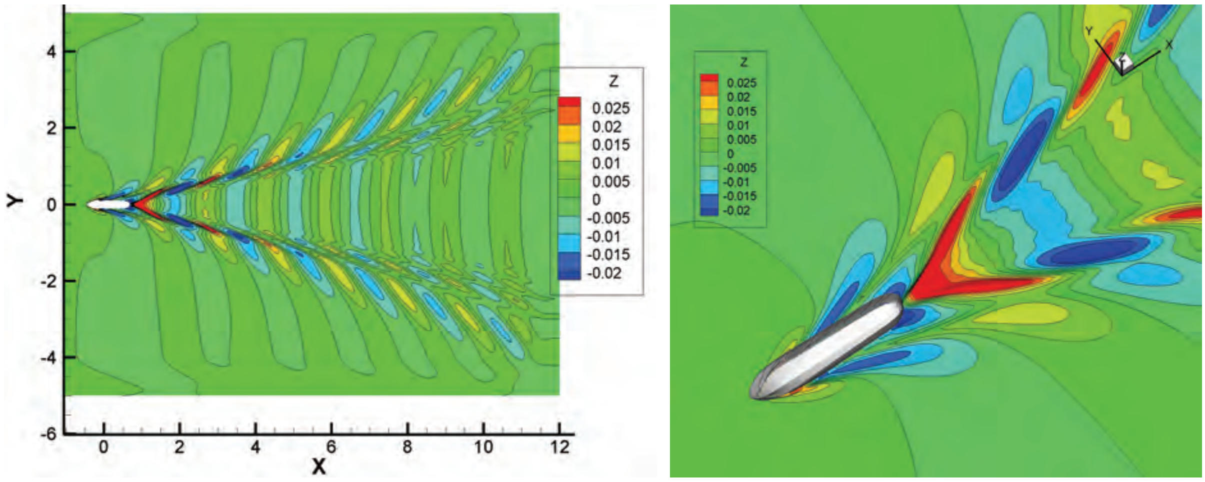

Figure 16 Computed wave contour (Deep water, Fn=0.5)

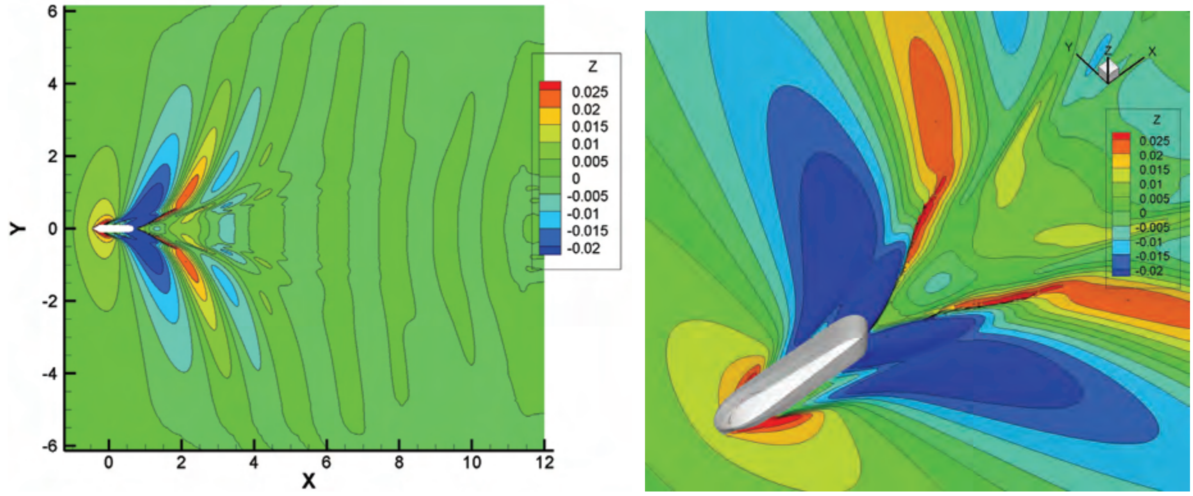

Figure 17 Computed wave contour (Shallow water, Fn=0.5)

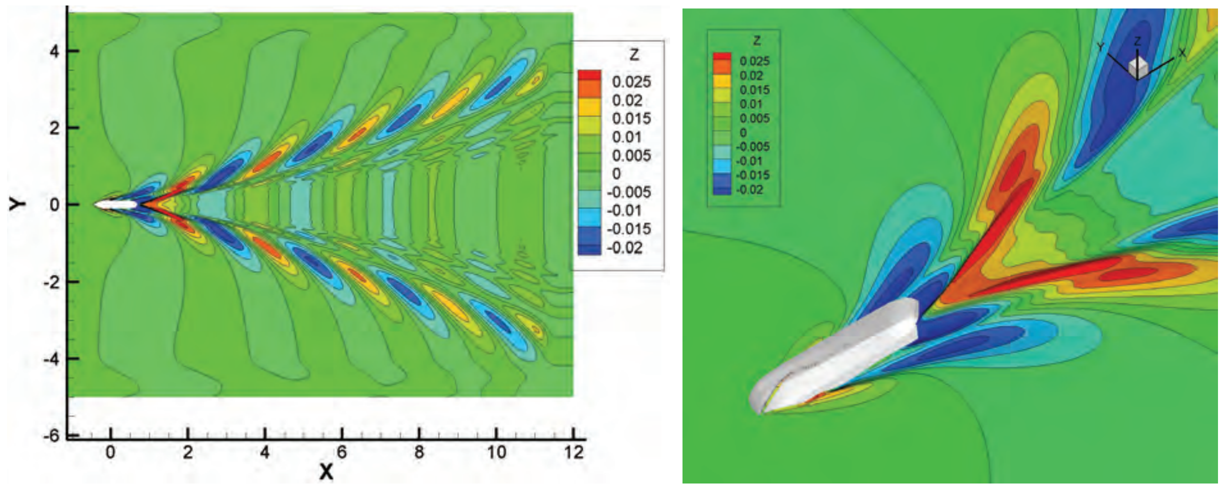

Figure 18 Computed wave contour (Deep water, Fn=0.6)

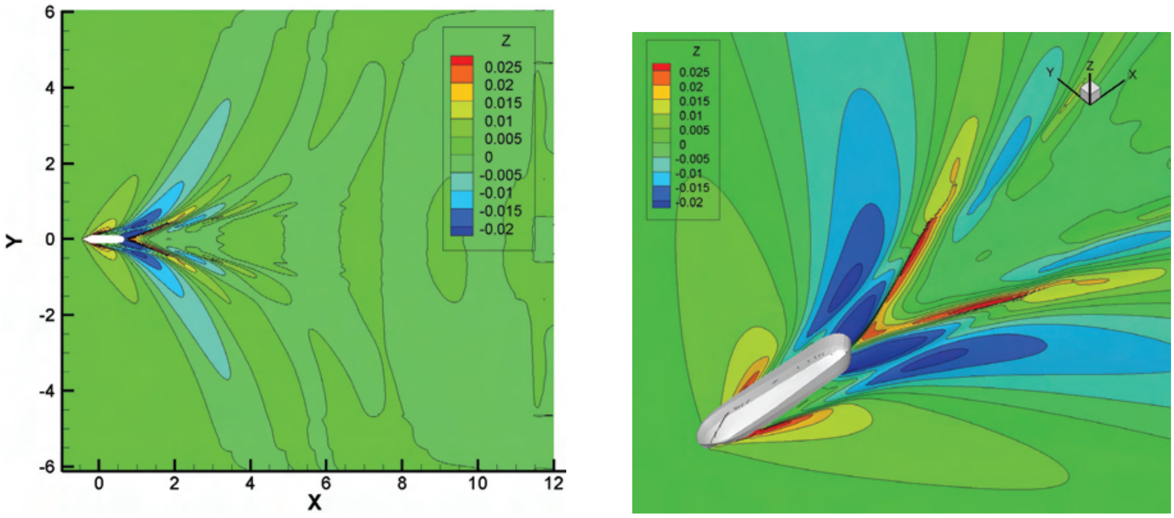

Figure 19 Computed wave contour (Shallow water, Fn=0.6)

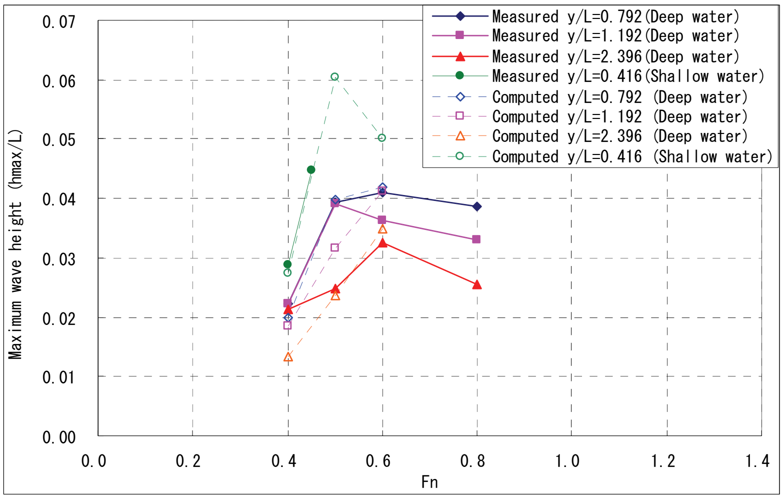

Figure 20 Comparison of maximum wave height

DYNAMICS AND STABILITY OF RACING BOATS WITH AIR WINGS

Nikolai Kornev, University of Rostock
Lutz Kleinsorge, University of Rostock
Gunther Migeotte, Icarus South Africa

SUMMARY

The aim of this paper is to derive a mathematical model for predicting the longitudinal stability of racing boats with aerodynamic support. The theory is based on a combination of stability theories developed for planing boats and wing in ground effect craft. Influence of different geometric and mass boat parameters on the stability is investigated.

1 INTRODUCTION

Since the inception of planing hulls, speeds of racing boats have been increased from speed of about 50 knots half a century ago to speed of 150 knots that are common place today with modern planing boats, see Figure 1. With continuously increasing speed, stability of these craft has become a more important consideration. The International Towing Tank Conference (ITTC) [1] has identified the following different forms of instability that affect planing craft:

- Take-off
- Loss of GM due to wave system
- Course keeping and lateral stability
- Bow diving and plough-in
- Porpoising
- Chine tripping
- Spray rail engulfing resulting in plough-in
- Effect of critical speed in shallow water

Most of these different forms of instability are quite well understood and/or mathematical models exist for predicting the onset of such instabilities and [1] gives a good list of reference works on each of these instabilities. Notably however, the problem of take-off, which is normally associated with very high speed catamarans, has according to the ITTC not been well addressed to date. Fig. 2 shows a series of video stills [2] of an Offshore Class-1 catamaran pitching-up and then taking off.
There is a very fine balance between the aerodynamic, hydrodynamic and propulsive forces at the high-speeds the boats travel at (up to 200 knots for some hydroplanes). The stability can be easily upset by waves, wind gusts, turning (asymmetrical flow). Instability is usually onset due to a pitch up motion that results in the hull taking-off and pitching about the propeller. Once airborne the vessel quickly flies out of control often with catastrophic consequences as indicated in Figure 2. Englar et al. [3] have studied this form of instability for racing hydroplanes.
The primary design consideration of such catamarans is usually high-speed. Analysis of the resistance characteristics of the vessels shows that the lowest resistance, and in turn the highest speed, is obtained by maximizing the aerodynamic lift while keeping the hydrodynamic forces to a minimum. When considering the balance of forces and moments (see Section 2) it is clear that the aerodynamic forces are the source of the instability of such boats as the center of aerodynamic lift is located ahead of the longitudinal center of gravity (LCG) of the boat. Thus increasing the aerodynamic lift component is inherently coupled with decreasing stability of the boat.
The design of such vessels is therefore a compromise between aero- and hydrodynamic considerations and retaining a fine balance between the various parameters that influence the stability. At present the stability of these vessels is usually evaluated using simple balance of moments and some simple design rules [4]. Such simple methods have however been shown to inadequate to ensure stability as pitch-up and take-off stability remains an important problem and is the cause of many accidents.
Take off and pitch tendencies are strongly associated with the aerodynamics of such hulls and are therefore only a consideration when the aerodynamic lift produced becomes a significant portion of the total lift. Typically this occurs at speeds in excess of 60 knots for most of the craft in operation today. The stability of such craft is similar to the take-off stability of Wing-In-Ground(WIG) craft and in essence the same methods can be applied to determine the stability of catamarans. Morch [5] discussed some details of the aero- and hydrodynamics of very high speed catamarans (80 knots) but discussion of stability is given. The results of his experiments and Computational Fluid Dynamics(CFD) computations however indicate that, for the 7.5m catamaran traveling at 80 knots, the aerodynamic lift forces were over 50 per cent during normal operation of the craft and that the center of aerodynamic lift is very sensitive to the running trim angle of the vessel.
The most common way to increase speed on such high speed catamarans is to run at a higher trim angle but this brings the vessel closer to its stability limits and often such crafts run in a marginally unstable condition with the pilot providing continuous correction to the running attitude. Constant vigilance is therefore

Fig. 1: Racing boat Qatar

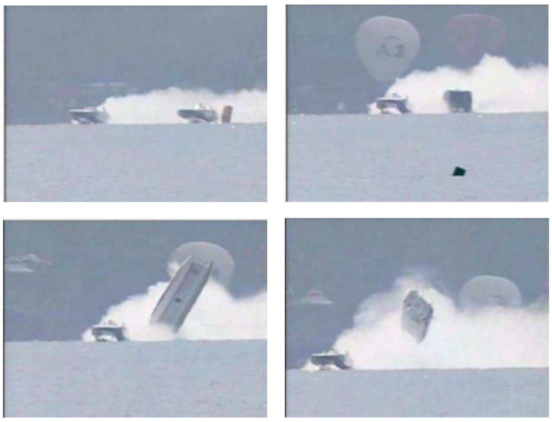

Fig. 2: Crash due to loss of the longitudinal stability [2]

required by the pilot to prevent the boat from taking off. Such boats often include some emergency measures such as water ballast tanks in the bows that can be filled with water in a very short time if the boat cannot be controlled and wants to take off.

The critical nature of the stability of these crafts is clearly evident. Proper design tools in order analyze stability of such crafts would be valuable to be able to develop designs that can possibly extend the operable limits of these crafts further. A longitudinal theory is proposed below which meets this requirement. The theory is based on two theoretical developments. The first development is the stability theory of planing boats proposed in a series of theoretical and experimental works performed during more than two decades in 60s and 70s at the Central Aerohydrodynamic Institute (TSAGI). The most valuable achievement is the simple and very robust mathematical model for the calculation of hydrodynamic forces acting on a planing surface at both steady and unsteady flow conditions. This model has been thoroughly tested in various measurements [6]. Implementation of this model within the linear stability theory results in the characteristic equation of the fourth order having a couple of conjugate roots. As Kovrizhnykh [6] and Lotov[7] shown the oscillatory instability is the most serious problem for the planing boats whereas the aperiodic instability has never been observed. Kovrizhnykh obtained the areas of the planing boat instability. At a given speed the stability gets worse as the angle of attack increases. The planing boat becomes unstable when the angle of attack attains a definite critical value. Surprisingly there is a narrow area of stability at large angles of attack which quickly disappears when the angle gets even larger. The presence of this stability region is confirmed in measurements with freely towed planing boat models [8].

The second development used in the present paper concerns WIG craft. With the development of WIG craft and Ekranoplans in the USSR, much work was done on the stability of high-speed craft making use of aerodynamic support [9]. Both the lateral and longitudinal stability of WIG craft had been thoroughly tested and well understood. In this paper we restrict ourselves on the longitudinal stability theory for WIG craft as developed by Irodov in 1970 in USSR [10] and independently by Staufenbiel in 1971 in Germany [11]. They derived the criterion of the static stability in two different forms but with the same physical meaning. Both criteria can be reduced to the same form after simple algebraic transformations. According to Irodov the WIG craft is statically stable when the aerodynamic center in height $x_h = m_z^h/C_y^h$ lies in front of the aerodynamic center in pitch $x_\vartheta = m_z^\vartheta/C_y^\vartheta$ where h is the height of flight, ϑ the pitch angle, C_y and m_z are respectively the lift coefficient and the pitching moment coefficient, $C_y^{\vartheta,h}$ and $m_z^{\vartheta,h}$ are their derivatives. According to experience, if the criterion of the static stability referred to the mean aerodynamic chord is between 0.05 and 0.12 the statically stable WIG craft is stable dynamically as well. An excessive static stability can result in the dynamic instability. A weak positive static stability is not admissible because of too weak damping of perturbations. Another important requirement widely used in the design of Russian WIG craft is the reciprocal position of aerodynamic centers and center of mass of the vehicle. The LCG shold be located between both aerodynamic centers x_h and x_ϑ closer to the aerodynamic center in height x_h [9]. In this case the dynamical properties of the WIG craft are favourable and the response of the craft to perturbations is mild. The longitudinal dynamic stability is investigated using three equations describing the translatory motions in x and y directions and pitching motions, see Figure 3. The procedure which is quite usual in the linear stability analysis leads to the characteristic equation of the fifth order which has one real root and a couple of two conjugate roots. A typical mutual position

of roots for the stable WIG craft is presented in [12]. Most important is the couple with the minimal real part which is responsible for the appearance of the dynamic oscillatory instability.
These two stability theories are used in this paper for developing the complex stability theory of planing craft with aerodynamic support.

2 THEORY OF LONGITUDINAL STABILITY

2.1 STEADY EQUILIBRIUM CONDITION

A necessary requirement for stability is that the planing boat is in a equilibrium condition. This means that the sum of vertical forces has to be zero:

$$mg - (Y_0 + C_y \frac{\rho}{2} U_a^2 S) = 0 \tag{1}$$

where Y_0 is the steady hydrodynamic lift evaluated in Section 2.4. The moment around the Z-Axis can be neglected, because an equilibrium of moments can be easily derived for every operation point by an interceptor, or an elevator unit. Equation (1) is used to determine the floating position (draught) of a racing boat at a given speed and trim angle.

2.2 MOTION EQUATIONS

When the steady equilibrium condition is fulfilled, the stability is determined through analysis of roots of characteristic equation derived from a linearized equations system describing longitudinal perturbed motion.
Equations of three-dimensional dynamics of racing boats can be obtained directly from the second law of Newton and can be stated in fixed, speed, connected or semi-connected coordinate system [13] (Figure 3). For formulation of dynamics equations the choice of coordinate system is defined by requirements of simplicity of form and convenience in presentation of forces. Most appropriate in this sense is the semi-connected system of coordinates.
A complete system of equations of three-dimensional motion is (designations see in Tab. 1):

$$\begin{aligned}
\dot{U}_d &= f_1 T - f_2 {U_a}^2 (C_x - C_z \beta_a) \\
&\quad - f_1 R_{x,hydr}(t) \\
\dot{U}_{ycg} &= f_2 {U_a}^2 C_y + f_1 T \vartheta_T \\
&\quad - 9.81 + f_1 R_{y,hydr}(t) \\
\dot{\beta}_d &= f_2 U_a (C_z + C_y \gamma + C_x \beta_a) + \omega_y \\
&\quad - T \beta_a \\
\dot{\omega}_x &= f_3 {U_a}^2 (m_x + f_4 m_y) \\
\dot{\omega}_y &= f_5 {U_a}^2 (m_y - f_6 m_x) \\
\dot{\omega}_z &= \left(f_7 {U_a}^2 m_z - f_8 T\right) + \frac{m_{z,hydr}(t)}{J_z}
\end{aligned}$$

For formulation of the equations additional parameters are used:

$$\dot{h}_{cg} = U_{y_{cg}},\ \dot{\gamma} = \omega_x - \omega_y (\vartheta - \vartheta_0),\ \dot{\psi} = \omega_y, \dot{\vartheta} = \omega_z$$

$$\beta_a = \beta_d - \frac{w_z(t)}{U_a},\ U_y = U_{y_{cg}} - w_y(t), U_a = U_d + w_x(t)$$

$$\psi_d = \psi - \beta_d,\ h = \frac{h_{cg}}{b} - (1 - \overline{x}_{cg}) \vartheta - \overline{y}_{cg}$$

$$\vartheta_T = \vartheta + \Theta_T - \vartheta_0,$$

$$f_1 = \frac{1}{m}, f_2 = \frac{\rho S}{2m}, f_3 = \frac{\rho S b}{2 J_{xc}}, f_5 = \frac{\rho S b}{2 J_{yc}}, f_7 = \frac{\rho S b}{2 J_z}$$

$$f_8 = \frac{y_T}{J_z}$$

$$f_4 = \left[1 - \frac{J_{xc}}{J_{yc}}\right] \tan(\vartheta + \varphi_c - \vartheta_0)$$

$$f_6 = \left[1 - \frac{J_{yc}}{J_{xc}}\right] \tan(\vartheta + \varphi_c - \vartheta_0)$$

$$\varphi_c = \frac{1}{2} \arctan\left[\frac{2 J_{xy}}{J_y - J_x}\right]$$

$$J_{xc} = J_x \cos^2 \varphi_c + J_y \sin^2 \varphi_c - 2 J_{xy} \cos\varphi_c \sin\varphi_c$$

$$J_{yc} = J_y \cos^2 \varphi_c + J_x \sin^2 \varphi_c - 2 J_{xy} \cos\varphi_c \sin\varphi_c$$

Since this paper is dealing only with the longitudinal stability the full motion system can be reduced to the following three equations:

$$\dot{U}_d = f_1 T - f_2 {U_a}^2 C_x - f_1 R_{x,hydr}(t) \tag{2}$$

$$\begin{aligned}
\dot{U}_{ycg} &= f_2 {U_a}^2 C_y + f_1 T \vartheta - 9.81 \\
&\quad + f_1 R_{y,hydr}(t)
\end{aligned} \tag{3}$$

$$\dot{\omega}_z = \left(f_7 {U_a}^2 m_z - \frac{y_T}{J_z} T\right) + \frac{m_{z,hydr}(t)}{J_z} \tag{4}$$

Here *hydr* stands for hydrodynamics.

2.3 AERODYNAMICS

The coefficients of aerodynamic forces can be represented as (see [9]):

$$\begin{aligned}
C_x &= C_x(\vartheta, h) + C_x^{\dot{\vartheta}}(\vartheta, h) \omega_z \frac{b}{U_a} \\
&\quad + C_x^{\dot{h}}(\vartheta, h) \frac{U_y}{U_a} \\
C_y &= C_y(\vartheta, h) + C_y^{\dot{\vartheta}}(\vartheta, h) \omega_z \frac{b}{U_a} \\
&\quad + C_y^{\dot{h}}(\vartheta, h) \frac{U_y}{U_a}
\end{aligned} \tag{5}$$

$$\begin{aligned}
m_z &= m_z(\vartheta, h) + m_z^{\dot{\vartheta}}(\vartheta, h) \omega_z \frac{b}{U_a} \\
&\quad + m_z^{\dot{h}}(\vartheta, h) \frac{U_y}{U_a}
\end{aligned} \tag{6}$$

Tab. 1: Nomenclature

b	$[m]$	Chord of the wing
C_x		Aerodynamic drag coefficient
C_y		Aerodynamic lift coefficient
C_z		Aerodynamic side force coefficient
C_T^U		Derivative of thrust coefficient on speed
C_W		Coefficient of hydrodynamic resistance
g	$[m/s^2]$	Acceleration of gravity
H	$[m]$	Submergence of the boat under center of gravity
H_0	$[m]$	Submergence at the transom of the racing boat
h	$[m]$	Height of flight
h_{cg}	$[m]$	Height of center of mass
h_t	$[m]$	Height of the boat at the transom
$J_x;\ J_y;\ J_z$	$[kgm^2]$	Mass moment of inertia
$k(\beta)$		Coefficient of added mass
L	$[m]$	Span of the wing
l_0	$[m]$	Wetted length of the hull
LCG	$[m]$	Longitudinal position of center of gravity, measured from the transom of the boat
m_0	$[kg]$	mass
$m_{hull};\ m_{wing}$	$[kg]$	Masses for estimation of J_z
m_{hydr}	$[kg]$	Added mass of planing boat cross section
$m_x;\ m_y;\ m_z$		Coefficients of aerodynamic moments around x,y,z axes
$m_{z,hydr}(t)$	$[Nm]$	Trim hydrodynamic moment
M_W	$[Nm]$	Trim moment of hydrodynamic resistance
$R_{x,hydr}(t)$	$[N]$	Hydrodynamic drag force
$R_{y,hydr}(t)$	$[N]$	Hydrodynamic lift force
S	$[m^2]$	Area of the wing
S_0	$[m^2]$	Wetted surface of the hull
$S_{wing};\ S_{hull}$	$[m^2]$	Areas for estimation of J_z
T	$[N]$	Thrust of the boat
U_a	$[m/s]$	Boat speed with wind perturbations
U_d	$[m/s]$	Boat speed
U_{ycg}	$[m/s]$	Velocity of center of gravity in vertical direction
$x_{cg};\ y_{cg}$	$[m]$	Position of center of gravity
Y_0	$[N]$	Steady hydrodynamic lift
y_T	[m]	Thrust arm of the engine
W	$[N]$	Hydrodynamic resistance
$w_x; w_y; w_z$	$[ms^{-1}]$	Wind perturbations
α		$\vartheta_0 + \vartheta$
β		Deadrise angle
β_a	$[rad]$	Drift angle with wind perturbations
β_d	$[rad]$	Drift angle
ψ	$[rad]$	Angle of course
γ	$[rad]$	Angle of roll
λ		Aspect ratio of the air wing
$\mu;\ i_z$		Dimensionless mass and mass moment of inertia
η_0	$[m]$	Distance between keel and center of gravity
ρ	$[kg/m^3]$	Density of air
ρ_W	$[kg/m^3]$	Density of water
θ_T	[rad]	Setup angle of the engine
ϑ	[rad]	Pitch or trim angle
ϑ_0	[rad]	Mean trim angle
ξ_0	$[m]$	Distance between stern and center of gravity
$\omega_x;\ \omega_y;\ \omega_z$	$[1/s]$	Angular velocities

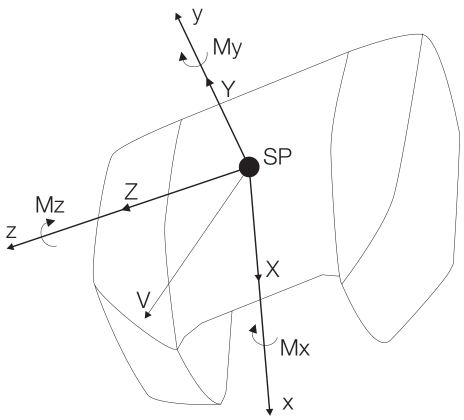

Fig. 3: Coordinate system

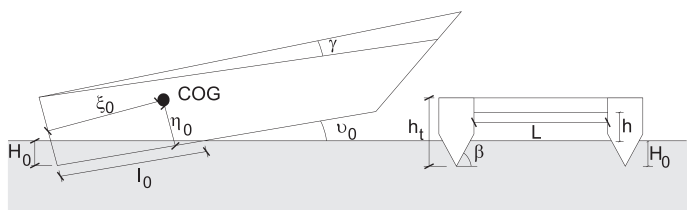

Fig. 4: Main dimensions of planing boat

The determination of aerodynamic characteristics of air wings in semi-connected coordinate system is performed using the program Autowing.

2.4 HYDRODYNAMICS

For calculation of hydrodynamic forces on a planing part of the boat a simple strip model proposed by Kovrizhnykh [6] and described in details by Lotov [7] is applied. The derivation of Kovrizhnykh starts from the Newtons second law for the local force f acting on a cross section of the planing surface:

$$f = (m_{hydr} U_n) \frac{d\alpha}{dt}$$

where U_n is the vertical velocity of the cross section. Integrating the last formulae over the whole wetted length one obtains the total lifting force acting on the hull. Taking into account that the hydrodynamic added mass for a prismatic shaped hull is

$$m_{hydr} = k(\beta)\, \rho_W h_1^2$$

the local force can be written in the form:

$$\begin{aligned} f &= \rho_W k(\beta) \left(h_1^2 U_n\right) \frac{d\alpha}{dt} \\ &= \rho_W k(\beta) \left(2 h_1 \dot{h_1} U_0 + h_1^2 \dot{U_n}\right) \end{aligned} \qquad (7)$$

Here h_1 is a local submergence of the cross section as a function of the longitudinal coordinate ξ and the unsteady angle of trim $\alpha = \vartheta_0 + \vartheta$, where ϑ_0 is the mean trim angle and ϑ is increment with respect to ϑ_0,

$$h_1 = (l - \xi_0 - \xi)\, \alpha,$$

Tab. 2: Lift and trim moment on the planing hull.

parameter	Lift derivatives F	Moment derivatives M
0	$\rho_W k(\beta) U_0^2 l_0^2 \vartheta_0^3$	$\rho_W k(\beta)\left(\frac{l_0}{3}-\xi_0\right) U_a^2 l_0^2 \vartheta_0^3$
h	$-2\rho_W k(\beta) U_a^2 l_0 \vartheta_0^2$	$-2\rho_W k(\beta)\left(\frac{l_0}{2}-\xi_0\right) U_a^2 l_0 \vartheta_0^2$
$\dot{h}$	$-2\rho_W k(\beta) U_a l_0^2 \vartheta_0^2$	$-2\rho_W k(\beta)\left(\frac{l_0}{3}-\xi_0\right) U_a l_0^2 \vartheta_0^2$
$\ddot{h}$	$-\frac{1}{3}(2-cos(\beta)) \rho_W k(\beta) l_0^3 \vartheta_0^2$	$-\frac{1}{3}(2-cos(\beta)) \rho_W k(\beta)\left(\frac{l_0}{4}-\xi_0\right) l_0^3 \vartheta_0^2$
ϑ	$2\rho_W k(\beta)\left(\frac{l_0}{2}+\xi_0\right) U_a^2 l_0 \vartheta_0^2$	$-2\rho_W k(\beta) \xi_0^2 U_a^2 l_0 \vartheta_0^2$
$\dot{\vartheta}$	$2\rho_W k(\beta) \xi_0 U_a l_0^2 \vartheta_0^2$	$-2\rho_W k(\beta)\left(\frac{l_0^2}{12}-\frac{l_0\xi_0}{3}+\xi_0^2\right) U_a l_0^2 \vartheta_0^2$
$\ddot{\vartheta}$	$-(2-cos(\beta)) \rho_W k(\beta) \frac{l_0}{3}\left(\frac{l_0}{4}-\xi_0\right) l_0^2 \vartheta_0^2$	$-(2-cos(\beta)) \rho_W k(\beta) \frac{l_0}{3}\left(\frac{l_0^2}{10}-\frac{l_0\xi_0}{2}+\xi_0^2\right) l_0^2 \vartheta_0^2$

Tab. 3: Resistance and its trim moment.

parameter	Resistance derivatives	Moment derivatives
0	$c_W S_0 \frac{\rho_W U_a^2}{2}$	$-c_W \frac{\rho_W U_a^2}{2} S_0 (\eta_0 - H_0)$
h	$-c_W \frac{\rho_W U_0^2 S_0}{H_0}$	$c_W \rho_W U_a^2 \frac{S_0}{H_0}\left(\eta_0 - \frac{3}{2}H_0\right)$
ϑ	$-c_W \frac{\rho_W U_0^2}{2} S_0 \frac{H_0 - 2\xi_0\vartheta_0}{H_0\vartheta_0}$	$c_W \frac{\rho_W U_a^2}{2} \frac{S_0}{\vartheta_0}(2H_0 - \eta_0)$

ξ_0 is the length between the stern and the longitudinal center of gravity. Expressing U_n through $\dot{h}$

$$
\begin{aligned}
U_n &= \dot{h_1} = U_0\alpha - \dot{y} - \xi\dot{\vartheta} \\
\dot{U}_n &= 2U_0\dot{\vartheta} - \ddot{y} - \xi\ddot{\vartheta}
\end{aligned} \tag{8}
$$

and substituting (8) into (7) gives

$$
\begin{aligned}
f(\xi) =& \rho_W k(\beta) [2(l-\xi_0-\xi)\alpha\left(U_0\alpha - \dot{y} - \xi\ddot{\vartheta}\right)^2 \\
&+ (2-cos(\beta))\alpha^2 (l-\xi_0-\xi)^2\left(2U_0\dot{\vartheta} - \ddot{y} - \xi\ddot{\vartheta}\right)]
\end{aligned} \tag{9}
$$

The factor $(2-cos(\beta))$ is a correction factor proposed by Logvinovich [7].
To get the resulting moment and the resulting force, the $f(\xi)$ function has to be integrated over the ship wetted length

$$
\begin{aligned}
Y_{hydr} &= \int_{-\xi_0}^{l-\xi_0} f(\xi)\, d\xi \\
m_{z,hydr} &= \int_{-\xi_0}^{l-\xi_0} f(\xi)\, \xi d\xi
\end{aligned} \tag{10}
$$

The wetted length l can also be written as

$$
l = l_0 - \frac{y}{\vartheta_0} - \frac{(l_0-\xi_0)}{\vartheta_0}\vartheta. \tag{11}
$$

Therein the index 0 stands for the steady state value. The wetted length l_0 is calculated as

$$
l_0 = H_0\vartheta
$$

where the submergence of the stern H_0 is calculated iteratively from the equilibrium condition at given speed and trim angle (see 2.1). Substituting (9) and (11) into (10) allows one to represent the hydrodynamic forces and moments in form of a truncated Taylor series with respect to y, $\dot{y}$, $\ddot{y}$, ϑ, $\dot{\vartheta}$ and $\ddot{\vartheta}$

$$
\begin{aligned}
Y_{hydr}\left(y,\dot{y},\ddot{y},\vartheta,\dot{\vartheta},\ddot{\vartheta}\right) &= Y_0 + F^y y + F^{\dot{y}}\dot{y} + F^{\ddot{y}}\ddot{y} \\
&+ F^{\vartheta}\vartheta + F^{\dot{\vartheta}}\dot{\vartheta} + F^{\ddot{\vartheta}}\ddot{\vartheta} \\
m_{z,hydr}\left(y,\dot{y},\ddot{y},\vartheta,\dot{\vartheta},\ddot{\vartheta}\right) &= M_0 + M^y y + M^{\dot{y}}\dot{y} + M^{\ddot{y}}\ddot{y} \\
&+ M^{\vartheta}\vartheta + M^{\dot{\vartheta}}\dot{\vartheta} + M^{\ddot{\vartheta}}\ddot{\vartheta}
\end{aligned} \tag{12}
$$

Coefficients of the series are presented in Table 2. The hydrodynamic resistance can also be represented in the form of the Taylor series:

$$
W = W_0 + W^y y + W^{\vartheta}\vartheta \tag{13}
$$

The hydrodynamic moment M_W caused by W is calculated as:

$$
M_W = -W(\eta_0 - H) \tag{14}
$$

where H is the submergence at the position of the center of gravity: $H = H_0 - y + \xi_0\vartheta$ and η_0 is the height of the center of gravity above keel.
The moment can also be represented in a form of the Taylor series:

$$
M_W = M_{W0} + M_W^y y + M_W^{\vartheta}\vartheta \tag{15}
$$

The coefficients are given in Table 3. The wetted surface of the hull S_0 can be calculated from

$$
S_0 = \frac{\pi}{2}\frac{H_0^2}{\vartheta_0 \sin\beta}
$$

2.5 STABILITY ANALYSIS

Substituting representations (5),(6),(12), (13) and (15) into the system (2),(3) and (4) and using the

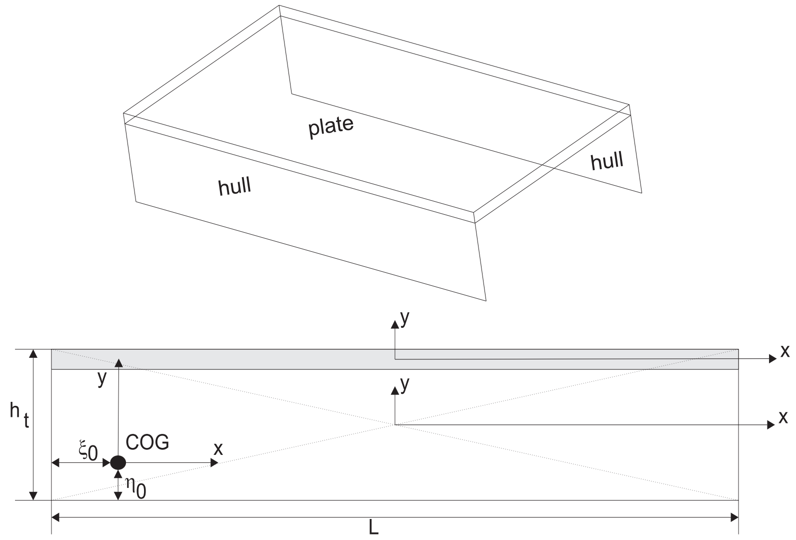

Fig. 5: Model for determination of mass moment of inertia I_z

Tab. 4: Coefficients of linearized system.

parameter	a	b	c
11	$2C_W\frac{\rho_W}{\rho} - C_T^{\overline{U}}\frac{\rho_W}{\rho} + 2c_x^0$	0	0
12	$C_x^h - 2C_W\frac{\rho_W}{\rho}\frac{S_0}{S}\frac{1}{\widetilde{H}_0}$	$C_x^{\dot{h}}\frac{1}{\mu}$	0
13	$C_x^\vartheta - C_W\frac{\rho_W}{\rho}\frac{S_0}{S}\frac{\widetilde{H}_0 - 2\widetilde{\xi}_0\vartheta_0}{\widetilde{H}_0\vartheta_0}$	0	0
21	$\left(2C_y^0 + C_T^{\overline{U}}\frac{\rho_W}{\rho}\vartheta_T\right)\mu$	0	0
22	0	$C_y^{\dot{h}} - 2\kappa$	$1 + \frac{1}{3}(2-\cos\beta)\,\widetilde{l}_0\kappa\frac{1}{\mu}$
23	$\left(C_y^\vartheta + 2\kappa\left(\frac{\widetilde{l}_0}{2} + \widetilde{\xi}_0\right)\frac{1}{\widetilde{l}_0}\right)\mu$	$C_y^{\dot{\vartheta}} + 2\kappa\widetilde{\xi}_0$	$-(2-\cos\beta)\,\kappa\frac{\widetilde{l}_0}{3}\left(\frac{\widetilde{l}_0}{4} - \widetilde{\xi}_0\right)\frac{1}{\mu}$
31	$\left[-\widetilde{y}_T\frac{\rho_W}{\rho}C_T^{\overline{U}} + 2\left(C_T^0\frac{\rho_W}{\rho} - C_W\frac{\rho_W}{\rho}\frac{S_0}{S}\left(\widetilde{\eta}_0 - \widetilde{H}_0\right)\right)\right]\frac{\mu}{i_z}$	0	0
32	$\left(m_z^h - 2\kappa\left(\frac{\widetilde{l}_0}{2} - \widetilde{\xi}_0\right)\frac{1}{\widetilde{l}_0} + 2C_W\frac{\rho_W}{\rho}\frac{S_0}{S}\frac{\widetilde{\eta}_0 - \frac{3}{2}\widetilde{H}_0}{\widetilde{H}_0}\right)\frac{\mu}{i_z}$	$\left(m_z^{\dot{h}} - 2\kappa\left(\frac{\widetilde{l}_0}{3} - \widetilde{\xi}_0\right)\right)\frac{1}{i_z}$	$\left(m_z^{\ddot{h}} - \frac{1}{3}\kappa(2-\cos\beta)\left(\frac{\widetilde{l}_0}{4} - \widetilde{\xi}_0\right)\widetilde{l}_0\right)\frac{1}{\mu i_z}$
33	$\left(m_z^\vartheta - \kappa\frac{\widetilde{\xi}_0^2}{\widetilde{l}_0} + C_W\frac{\rho_W}{\rho}\frac{S_o}{S}\frac{2\widetilde{H}_0 - \widetilde{\eta}_0}{\vartheta_0}\right)\frac{\mu}{i_z}$	$\left(m_z^{\dot{\vartheta}} - 2\kappa\left(\frac{\widetilde{l}_0^2}{12} - \frac{\widetilde{l}_0\widetilde{\xi}_0}{3} + \widetilde{\xi}_0^2\right)\right)\frac{1}{i_z}$	$1 + \kappa(2-\cos\beta)\frac{\widetilde{l}_0}{3}\left(\frac{\widetilde{l}_0^2}{10} - \frac{\widetilde{l}_0\widetilde{\xi}_0}{2} + \widetilde{\xi}_0^2\right)\frac{1}{\mu i_z}$

dimensionless time τ

$$t = \tau\frac{2m}{\rho S U_0}$$

we obtain the following linearized motion equations (see also [9]):

$$\begin{aligned}
&\Delta\dot{\overline{U}} + a_{11}\Delta\overline{U} + b_{12}\Delta\dot{\widetilde{h}} \\
&\qquad + a_{12}\Delta\widetilde{h} + a_{13}\Delta\vartheta = 0 \\
&a_{21}\Delta\overline{U} - c_{22}\Delta\ddot{\widetilde{h}} + b_{22}\Delta\dot{\widetilde{h}} + a_{22}\Delta\widetilde{h} + c_{23}\Delta\ddot{\widetilde{\vartheta}} \\
&\qquad + b_{23}\Delta\dot{\widetilde{\vartheta}} + a_{23}\Delta\vartheta = 0 \\
&a_{31}\Delta\overline{U} + c_{32}\Delta\ddot{\widetilde{h}} + b_{32}\Delta\dot{\widetilde{h}} + a_{32}\Delta\widetilde{h} - c_{33}\Delta\ddot{\widetilde{\vartheta}} \\
&\qquad + b_{33}\Delta\dot{\widetilde{\vartheta}} + a_{33}\Delta\vartheta = 0
\end{aligned} \tag{16}$$

The dimensionless parameters are introduced according to the following relations:

$$\Delta\overline{U} = \frac{\Delta U}{U_0};\ \dot{\vartheta} = \frac{\rho S U_0}{2m}\dot{\widetilde{\vartheta}};\ \ddot{\vartheta} = \left(\frac{\rho S U_0}{2m}\right)^2\ddot{\widetilde{\vartheta}}$$

$$\widetilde{h} = hb;\ \dot{h} = \frac{\rho S U_0 b}{2m}\dot{\widetilde{h}};\ \ddot{h} = \left(\frac{\rho S U_0}{2m}\right)^2 b\ddot{\widetilde{h}}$$

The coefficients a_{ij}, b_{ij} and c_{ij} are given in Table 4 where the following dimensionless parameters are used

$$\mu = \frac{2m_0}{\rho S b}\ ;\ i_z = \frac{J_z}{mb^2}\ ;\ C_T^{\overline{U}} = \frac{2T^U}{\rho U S}$$

$$\kappa = 2\frac{\rho_W}{\rho}k(\beta)\,\widetilde{l}_0^2\frac{b^2}{S}\vartheta_0^2$$

$$\widetilde{l}_0 = \frac{l_0}{b}\ ;\ \widetilde{H}_0 = \frac{H_0}{b}\ ;\ \widetilde{\xi}_0 = \frac{\xi_0}{b}\ ;\ \widetilde{\eta}_0 = \frac{\eta_0}{b}$$

According to the procedure of the linear stability analysis a differentiation operator is introduced

$$p = \frac{d}{dt}, p^2 = \frac{d^2}{dt^2}$$

into the system (16). Replacing derivatives of kinematic parameters by p and p^2 and grouping terms proportional to these parameters, one obtains the system of algebraic equations with respect to U, h and ϑ with the determinant:

$$\begin{vmatrix} p + a_{11} & b_{12}p + a_{12} & a_{13} \\ a_{21} & -c_{22}p^2 + b_{22}p + a_{22} & c_{23}p^2 + b_{23}p + a_{23} \\ a_{31} & c_{32}p^2 + b_{32}p + a_{32} & -c_{33}p^2 + b_{33}p + a_{33} \end{vmatrix}$$

Calculation of the determinant results in the characteristic equation of the system (16):

$$D_5p^5 + D_4p^4 + D_3p^3 + D_2p^2 + D_1p + D_0 = 0$$

This equation is quintic and has five roots. All of the real parts of these roots have to be negative for a stable planing.
Necessary and sufficient conditions of stability are [9]:

$$D_i > 0, (i = 1, 2, 3, 4, 5)\, ; D_1D_2 - D_3 > 0;$$

$$\begin{aligned} R_5 = &(D_1D_2 - D_3)(D_3D_4 - D_2D_5) \\ &- (D_1D_4 - D_5)^2 > 0 \end{aligned}$$

The boundary of dynamic (oscillatory) stability is determined by equation $R_5 = 0$, and the boundary of static (aperiodic) stability $D_5 = 0$ with other conditions of stability being fulfilled.

3 RESULTS OF THE STABILITY ANALYSIS

The analysis presented above was implemented into the Fortran program called STABBI and intended for the longitudinal stability analysis of racing boats with aerodynamic support. Because of luck of information on the mass moment of inertia, it was calculated under assumption that the planing boat consist of three parts, two hulls and the wing between them. They are modeled as flat rectangular plates with uniform mass distribution on areas $S_{wing} = Lb$ and $S_{hull} = L \cdot h_t$. Figure 2.4 shows this geometric model and three different coordinate systems. For a plate the mass moment of inertia around the lateral axis is defined as

$$J_z = \int (x^2 + y^2)dm$$

The mass moment of inertia J_z can be transferred to the coordinate system of the craft with the origin in the center of gravity by Steiners theorem. This results in:

$$\begin{aligned} J_z = &\frac{2}{12}m_{hull}\left(L^2 + h_t^2\right) + \frac{1}{12}m_{plate}L^2 \\ &+ 2m_{hull}\left(\left(\frac{L}{2} - \xi_0\right)^2 + \left(\frac{h_t}{2} - \eta_0\right)^2\right) \\ &+ m_{plate}\left(\left(\frac{L}{2} - \xi_0\right)^2 + (h_t - \eta_0)^2\right) \end{aligned}$$

The mass of the hull part and the wing is then calculated by:

$$m_{hull} = \frac{S_{hull}}{S_{hull} + S_{wing}}m$$

$$m_{wing} = \frac{S_{wing}}{S_{hull} + S_{wing}}m$$

. The influence of the following kinematic and geometric parameters of the racing boats on stability was studied:

- γ [deg] - setup angle of the air wing with respect to the planing surface;
- β [deg] - deadrise angle of the planing surface;
- b [m] - chord of the air wing;
- L [m] - span of the air wing between end plates;
- ξ_0 and η_0 [m] - coordinates of the center of gravity measured from the transom and the planing surface;
- h_t [m] - height of the racing boat at the transom
- m [kg] - mass;
- J_z [kgm^2] - mass moment of inertia;
- U [m/sec] - speed of motion;

Based on these parameters the following dimensionless parameters can be proposed for further investigations of the stability:

$$\gamma\ ;\ \beta\ ;\ \widetilde{\xi_0} = \frac{\xi_0}{b}\ ;\ \widetilde{\eta_0} = \frac{\eta_0}{b}\ ;\ \mu = \frac{2m_0}{\rho Sb}$$

$$i_z = \frac{J_z}{m_0b^2}\ ;\ \lambda = \frac{L}{b}\ ;\ \widetilde{h_t} = \frac{h_t}{b}\ ;\ \widetilde{U} = \frac{U}{\sqrt{\frac{m_0g}{\rho Lb}}}$$

The dimensionless parameters were varied in the range typical for modern racing boats (see Table 5).

3.1 INFLUENCE OF SPEED AND TRIM ANGLE

The diagrams of stability were obtained by variation of the speed and the trim angle. The curves of the diagrams show the border between stable and unstable planing. Beneath each curve the planing is stable at a given speed U and trim angles ϑ whereas above the line it is unstable. The stability decreases with increasing speed, because aerodynamic and hydrodynamic lifts are getting larger and the submerged part of the hull contributing to the stability becomes smaller. The same effect takes place when the trim angle is growing.

3.2 INFLUENCE OF AIR WING

Here a boat with the parameters from Table 5 was investigated. Concerning the contribution of the air wing to the stability it was found that this contribution is usually negative. Figure 6 illustrates this fact. It happens because the submerged part of the boat becomes smaller. A part of the boat weight is carried by the air wing which is unstable. In fact, the stability of wing in ground effect craft is secured mostly by the large tail unit. The WIG wing alone is unstable. The area of the stability of the boat with air wing is clearly smaller than that of the boat consisting only planing part. Only at small speed U when the influence of the aerodynamics is negligible the stability is the same for both boats.

3.3 INFLUENCE OF DIMENSIONLESS MASS

Figure 7 shows the diagram in which the value of μ was varied. For a small μ the area of stable planing is also small. When μ rising, the stability is getting better. Increase of μ is conducted by increase of the submerged part of the boat which contributes to the stability. Therefore, increase of the mass helps to avoid porpoising instability.

3.4 INFLUENCE OF DEADRISE ANGLE

Increase of the deadrise angle β influences stability in the same way as the dimensionless mass increase. Figure 8 shows a diagram for different deadrise angles β. When β is getting larger, the area of stable planing also increases.

3.5 INFLUENCE OF LONGITUDINAL POSITION OF THE CENTER OF GRAVITY

Figure 9 shows the diagram illustrating the influence of the longitudinal position of the center of gravity. The largest area of stability is observed at the smallest value of $\widetilde{\xi}$. When the longitudinal center of gravity is moved aft and $\widetilde{\xi}$ is decreased, the stability becomes better.

3.6 INFLUENCE OF VERTICAL POSITION OF THE CENTER OF GRAVITY

The diagram in Figure 10 shows that a change of $\widetilde{\eta}$ does not influence the stability very much. For different $\widetilde{\eta}$ the border curves between stable and unstable planing are nearly the same.

3.7 INFLUENCE OF THE HEIGHT OF THE BOAT AT TRANSOM

The height of the boat at the transom determines the largest flight height for the racing boat without loosing contact with the water surface. The diagram in Figure 11, in which the parameter $\widetilde{h}_t$ is varied, shows no significant change of stability for different heights of the transom.

3.8 INFLUENCE OF THE MASS MOMENT OF INERTIA

The results of the stability estimations show (see Figure 12), that the stability area for different i_z is almost the same. It has to be noted, that there were no reliable information on this parameter available. It might be that the real mass moment lies outside of the range investigated in this paper. Therefore this parameter has to be investigated more thoroughly in future works.

3.9 INFLUENCE OF THE ASPECT RATIO

The aspect ratio λ of the air wing has a great influence on stability. With increase of λ (increase of the span at constant chord) the stability area decreases sufficiently (see Figure 13). The increase of the aspect ratio leads to the increase of aerodynamic forces which reduce the submerged hull and enhance the instability.

4 CONCLUSION

A mathematical model and corresponding computer program have been developed to estimate the longitudinal stability of racing boats with aerodynamic support. It was shown that the aerodynamic forces acting on racing boats contribute to the dynamic instability. The stability can be sufficiently improved by increase of the deadrise angle, dimensionless mass and by positioning the center of gravity as close as possible to the stern. Influence of the vertical position of the center of gravity, height of the boat at the transom and mass moment of inertia is negligible. Increase of the aspect ratio of air wings enhances the instability.

References

[1] The specialist committee of high-speed marine vehicles, Final report and Recommendations to the 22nd ITTC 2001

[2] http://www.youtube.com/watch?v=h6 uNwQe4lRU&mode=related&search=

[3] Englar, R.B., Gregory, S.D. and Ford, D.A. In Ground Effect Evaluation and Aerodynamic Development of Advanced Unlimited Racing Hydroplanes AIAA Aerospace and sciencesMeeting and exhibit, Jan 9-12, 1995. AIAA 1995-745.

[4] Russel, J. Secrets of Tunnel Boat Design 2007. www.aeromarineresearch.com

[5] Morch,H.J.B., Aerodynamic properties of an offshore racing catamaran, FAST03 Southhampton, UK.

Tab. 5: Standard parameter(dimensional and nondimensional)

parameter	value
m	$4800kg$
J_z	$74436kgm^2$
γ	$0deg$
b	$12m$
L	$2m$
ξ	$4.2m$
η	$1m$
h_t	0.65

parameter	value
μ	33
i_z	0.108
β	20
$\widetilde{\xi}$	0.35
$\widetilde{\eta}$	0.083
λ	0.166
h_t	0.0542

[6] Kovrizhnykh L.D., 1978, Stability of planing of a plate with deadrise angle on the incomplete width. *Proceedings of the Central Hydro-aerodynamical Institute (TSAGI)*, issue 1972 15 – 24.

[7] Lotov V.B, 1984, Planing and impact problems. *Textbook of the Moscow Institute of Applied Physics*, 107 pages.

[8] Tikhonov A.N., 1961, *Proceedings of the Central Hydro-aerodynamical Institute (TSAGI)*, issue 1972 15 – 24.

[9] Zhukov V.I., 1993, Peculiar features of dynamics of ekranoplan. *Proceedings of the first international conference on ekranoplans.* St. Petersburg, 23 – 36.

[10] Irodov R. D., 1970, Criteria of longitudinal stability of Ekranoplan. *Technical Note of the Central Hydro-aerodynamical Institute (TSAGI)*, vol. 1, no. 4, Russia.

[11] Staufenbiel R.W., 1987, On the design of stable ram wing vehicles. *Proceedings of the Ram wing and Ground Effect Conf.*, May 19.

[12] Benedikt, K., Kornev, N. V., Meyer, M., Ebert, J., 2001, Complex mathematical model of the WIG motion including the take-off mode, *Journal of Ocean Engineering*, **29/3**, 315 – 357.

[13] Plisov.N.B., Rozhdestvensky K.V., Treshkov V.K., 1991, Aerohydrodynamics of ships with dynamic principles of support.- *L., Sudostroenie*, 248.

[14] Kornev N.V., Matveev K., 2003, Numerical modeling of dynamics and crashes of wing-in-ground vehicles, *AIAA Paper AIAA 2003-600*, 2003,1 – 9.

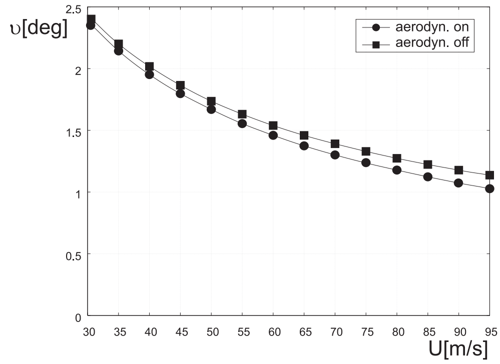

Fig. 6: Stability with and without aerodynamics

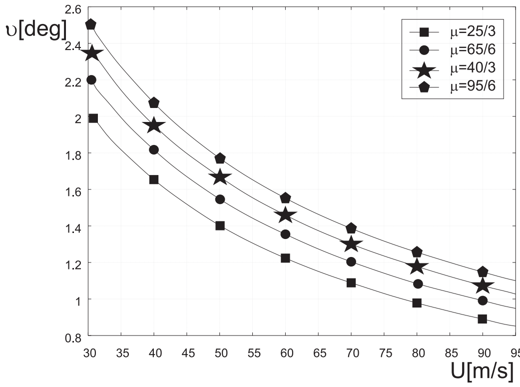

Fig. 7: Influence of μ on stability

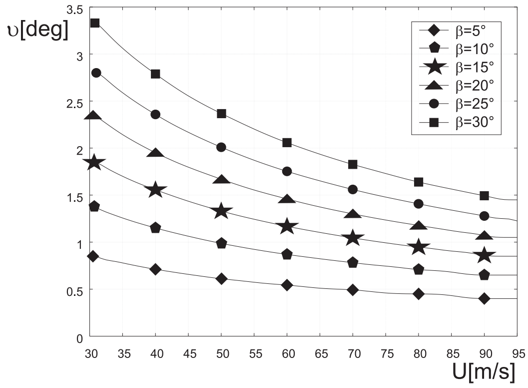

Fig. 8: Influence of β on stability

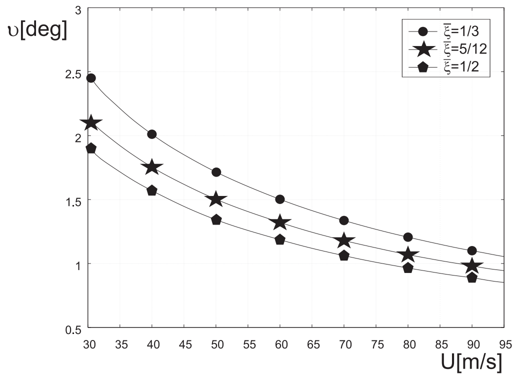

Fig. 9: Influence of $\widetilde{\xi}$ on stability

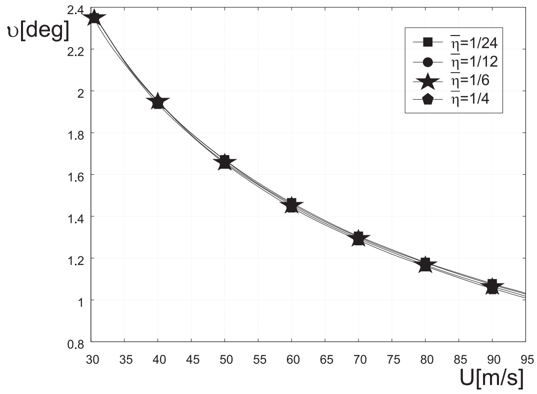

Fig. 10: Influence of $\widetilde{\eta}$ on stability

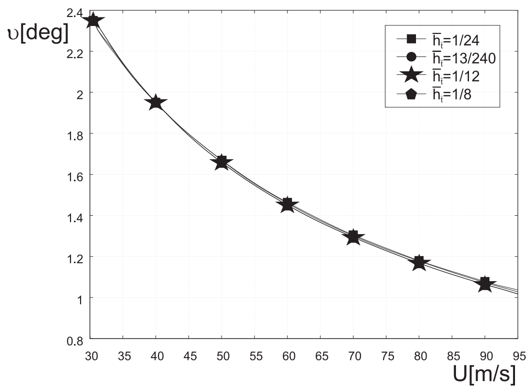

Fig. 11: Influence of $\widetilde{h}_t$ on stability

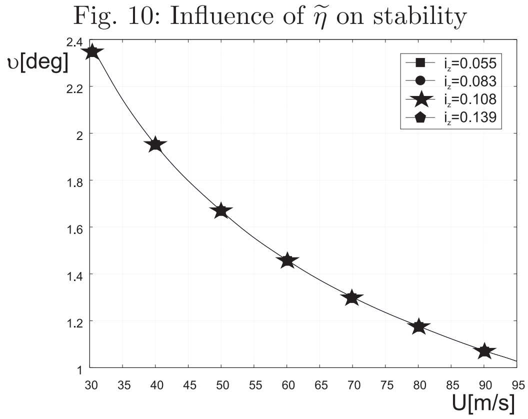

Fig. 12: Influence of i_z on stability

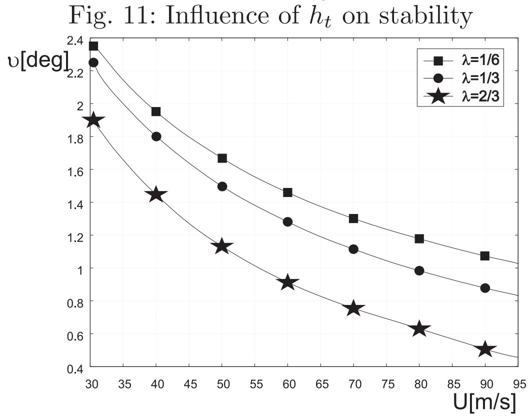

Fig. 13: Influence of λ on stability

DEVELOPMENT OF NUMERICAL TOOL FOR HYDRODYNAMICS SIMULATION OF HIGH SPEED PLANING CRAFTS

Ebrahim Jahanbakhsh
Marine Lab., Sharif Uni. of Tech., Tehran/Iran, ebrahim_jahan@yahoo.com
Roozbeh Panahi
Tarbiat Modarres Uni., Tehran/Iran, roozbeh_panahi@yahoo.com
Mohammad Saeed Seif
Dept. of Mechanics, Sharif Uni. of Tech., Tehran/Iran, seif@sharif.ir

SUMMARY
General purpose finite volume based computer software is developed to yield a time history of displacements, forces and moments, during the 6-DoF fluid-structure interaction in two phase flow. It uses a coupled VoF-fractional step method in solving the fluid flow and a boundary-fitted body attached hexahedral mesh in simulating the rigid body motions.
In this paper, the forward progress and the turning maneuver of a high speed planing catamaran is simulated. The results are analyzed and compared with the available data.

1. INTRODUCTION

Nowadays, numerical simulations are becoming a common way for assessment of ship performance in early design stages. Although model test using experimental approach is still very useful but has its own restrictions and expenses which has motivated to employ a numerical tool. Taking into account the advances in computer hardware, use of Computational Fluid Dynamics (CFD) is becoming the best choice in many cases.

In practice, a hydrodynamics problem includes turbulent viscous flow with complex free surface deformations and sometimes fluid-structure interaction. One of the practical ways to study the aforementioned coupled complicated case is to decouple it by either completely ignoring the less important phenomena or approximating them.

The motion of a floating or submerged body is a direct consequence of the flow-induced forces acting on it, while at the same time these forces are a function of the body movement itself. Therefore, the prediction of flow-induced body motions in viscous fluid is a challenging task and requires coupled solution of fluid flow and body motions. In recent two decades, with the changes in computer power, hydrodynamics motions simulation has been the subject of many numerical researches. Such studies started from restricted motions such as trim or sinkage and continued to evaluation of 6-DoF motions.

In this paper, the fundamental of a developed numerical tool which is capable of simulating the 6-DoF fluid-structure interaction is briefly presented. Then, a high speed planing catamaran is investigated in two cases of forward progress and turning maneuver. Discussion about the results is also included.

2. NUMERICAL TOOL

Here, a time dependent three-dimensional viscous free surface flow solver is implemented. The velocity and the pressure fields are coupled using fractional step of Kim and Choi. Over-relaxed and Gamma interpolations are used for the space discretization of the convection and the diffusion terms, respectively. One must take into account the presence of high density ratio phases e.g. water and air in discretization of the pressure integral which is treated in a new way. Also, a surface capturing method is used which solves a transport equation for calculation of fluids volume fraction. CICSAM interpolation has great advantages in comparison to other interpolations and used in space discretization of Volume of Fluid (VoF) transport equation. Also, the Crank-Nicholson interpolation is used in temporal discretization of all differential governing equations. More details are available in another paper of the authors to de develop a robust interfacial flow solver, Jahanbaksh et al. (1).

There are a variety of motion simulation strategies for numerical hydrodynamics applications such as deformable mesh, Chentanez et al. (2), re-mesh, Tremel et al. (3), sliding mesh Blades and Marcum (4), overlapping mesh, Carrica et al. (5), Cartesian mesh, Mittal and Iccarino (6), etc. Here, a hexahedral body-attached mesh following the time history of body motions is used. In other words, linear and angular momentum equations are solved in each time step which results in 6-DoF rigid body motions. Forces and moments of such equations are calculated by integration of normal and tangential stresses over the body surface as a result of flow solver. External loads can be also added to prepare the total forces and moments acting on the body. Such loads can be used to model the effect of rudder, thruster, mooring, etc. Resultant motions are then applied to the body as well as the mesh to make the computational domain ready for the next time step. It must be noted that, all of the fluid governing equations are written for a rigid control volume which moves with an arbitrary speed in the Newtonian Reference system. This feature which keeps the simplicity of the governing equations, results in using the relative face velocity for convection flux calculation taking into account the space conservation law. More details are presented in a recent paper by the authors, Panahi et al. (7).

The accuracy and the precision of the developed software (NUMELS-Numerical Marine Engineering Laboratory-Sharif) are strongly assessed in each stage of software development as shown in Table 1, Jahanbakhsh et al. (8), Panahi et al. (9), Jahanbakhsh et al. (10).

Table 1: Validation of the developed software

Case	Validation Problem
velocity-pressure coupling	orthogonal cavity flow
non-orthogonality	non-orthogonal cavity flow
volume fraction transport equation	scalar transport in the predefined constant oblique velocity field and Shear flow
two phase flow	Rayleigh-Taylor instability, dam breaking with and without obstacle, sloshing
wave generation and outlet boundary condition	Airy wave generation and transportation
6-DoF fluid-structure interaction	wedge and cylinder slamming, barge resistance and maneuvering, trimaran resistance

3. RESULTS

Now, the behavior of a high-speed planing catamaran shown in Fig.1 and Table 2, in forward progress and turning maneuver is evaluated.

The first step in all of the numerical simulations is to find an appropriate mesh. To simulate the catamaran, a wide variety of meshes is investigated and two of them are represented in Fig.2.

Anyway, after performing some study, an adequate mesh is found. The half domain of this mesh is shown in Fig.3 with the computational domain dimensions and the position of the craft.

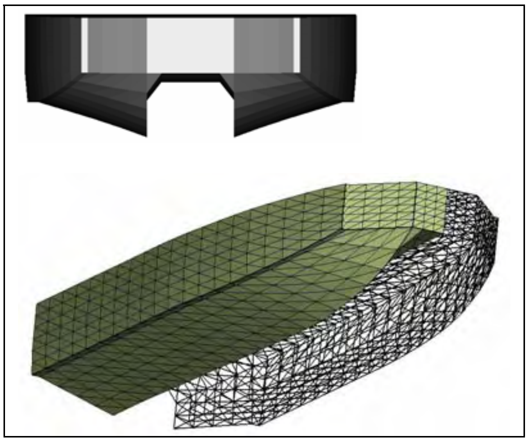

Fig.1: Catamaran geometry

Table 2: Catamaran ship characteristics

Characteristic	Value
length	12.3 m
width	4.6 m
Draft	0.45 m
Mass	17850 kg
vertical mass center position	0.25 m
longitudinal mass center position	3.81 m
Inertial moment around mass center	$\begin{bmatrix} 53274 & 0 & 0 \\ 0 & 295967 & 0 \\ 0 & 0 & 325563 \end{bmatrix}$

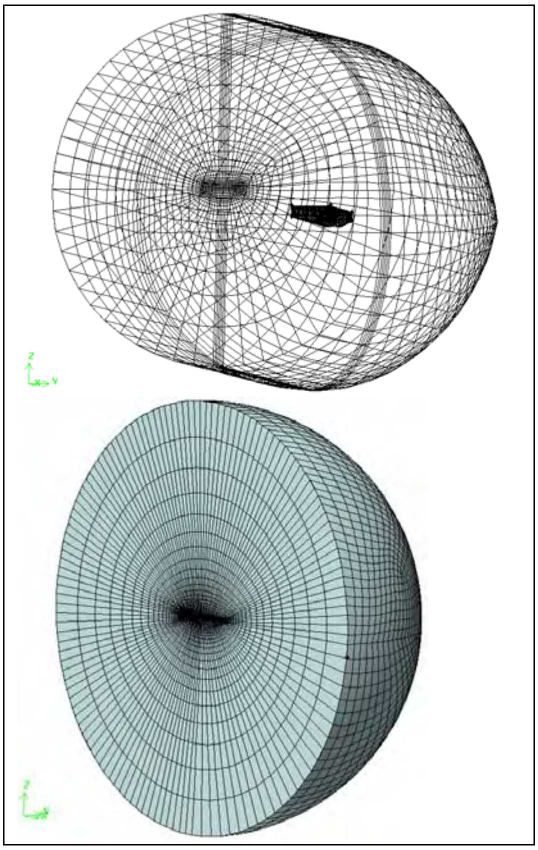

Fig.2: Two investigated catamaran mesh

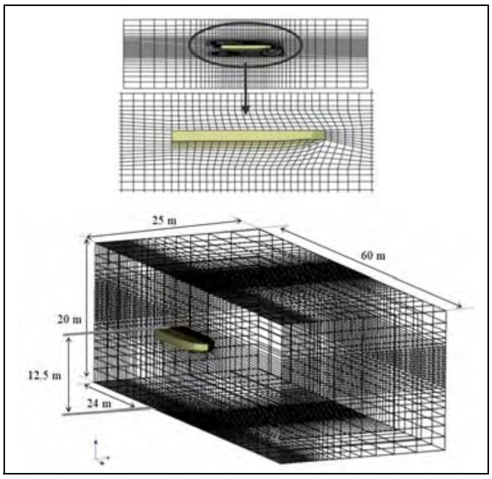

Fig.3: Catamaran appropriate mesh

3.1. Forward Progress

Forward progress in the case of the planing craft, is hardly affected by the changes in heave and pitch motions based on the hull form produced lift force. Considering the symmetry of the problem, a half domain with 95000 hexahedral cells is implemented. The thrust force is applied at 0.25 m under the mass center position, with two approaches of constant thrust and variable thrust.

In the constant thrust approach, a 40 kN force is exerted on the craft constantly from the initial time. In the variable thrust approach, an initially exerted 15 kN force is sharply changed to the next value just when an approximately steady behavior in forward progress is touched. In this approach, the examined forces are 15, 25, 30, 40, 45, and 50 kN. Such steps during 262 seconds of the simulation are presented in Table 3.

Table 3: Steps of changing thrust force

Step	Time Interval (s)	Thrust force (kN)
1	0.0-47.0	15
2	47.0-90.5	25
3	90.5-105.0	30
4	105.0-192.0	40
5	192.0-230.0	45
6	230.0-262.0	50

The time history of the results, using the second approach, is shown in Figs.4, 5, 6 and 7. As marked on the Fig.4, forward progress can be divided into three phases. In the first phase, which is from t = 0 s to t = 100 s, all diagrams behave smoothly. In this phase the craft is lifted about 0.2 m and its trim angle is increased up to 80. Velocity is about 10 kn at the end of this phase and experiences small changes except at the initial part of this phase. The second phase is between t = 100 s and t = 250 s. The distinct planing motion is occurred at the beginning of this phase during ten seconds, as it is obvious from the change in heave motion (Fig.5). In this phase, the craft is lifted about 0.55 m. The change in its trim angle is an interesting phenomenon because it is decreased from 80 to 40 in this phase, after an increase in the previous phase (Fig.6). Besides, the velocity is increased abruptly from 10 to 40 kn (Fig.7). The third phase of motion is accompanied by huge oscillations in all results. This is because of reaching an unstable dynamical position at the forward speed of 52 kn for this craft. Such a phenomenon which is accompanied with bow slamming is called propoising, and can be interpreted as a common case for such hull forms.

Fig.8 shows the plot of mean resistance versus velocity, extracted from Fig.4 and Fig.7. In this plot, the bold lines are curves fitted to result points. The left part of results belongs to 1st motion phase before planing occurrence. At this phase, the resistance experiences a 2nd order increase relative to forward speed. The right part of results belongs to 2nd and 3rd motion phases after planing occurrence. Here a 1st order increase of resistance is obvious. The dashed line which connects these two parts of results is an assumption which can be used as an estimate for the transient region. The gap is because of the fast increase in forward speed at the initial times of 2nd phase. Actually, there is no steady state position and therefore no resistance date in the mentioned interval. However, it is possible to cover this area with additional simulations.

Figs.9 and 10 show the comparison between numerical and experimental results of power and trim angle versus velocity, respectively. It is Obvious from Fig.9 that, the first approach (constant thrust) has a good performance in prediction of resistance and covers all velocities in contrast to the second approach (variable thrust). Besides, the results of the first and the second approach are near to each other. These two properties encourage using the first approach which is simpler in practice. The trim angle of the crafts is also plotted in Fig.10. It seems that using the second approach is better than the first approach in the case of trim angle, especially in evaluating its maximum value, although there is no point in that velocity.

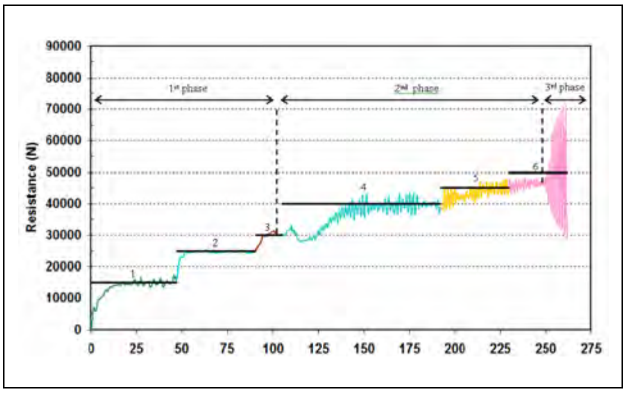

Fig.4: Resistance time history diagram using the variable thrust approach
(Bold lines represent thrust forces)

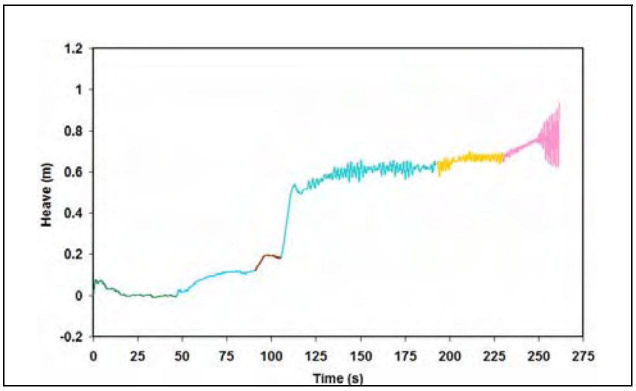

Fig.5: Heave motion time history

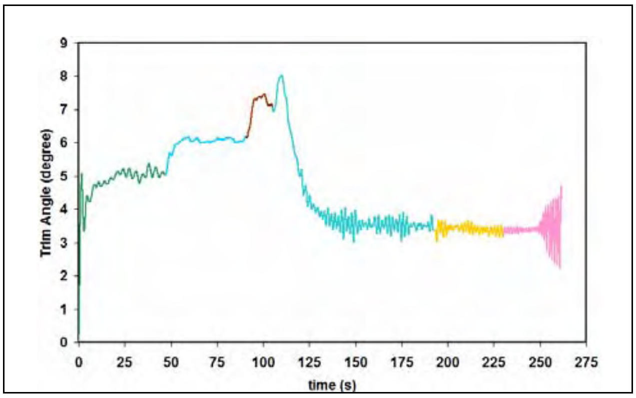

Fig.6: Pitch motion time history

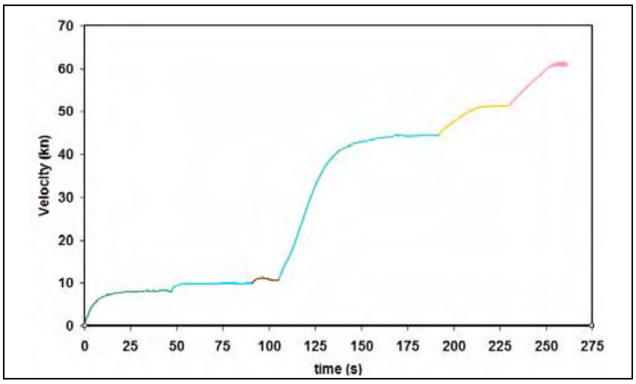

Fig.7: Velocity time history diagram

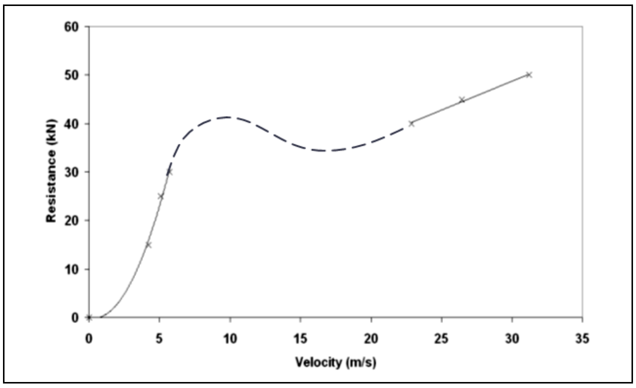

Fig.8: Resistance versus velocity

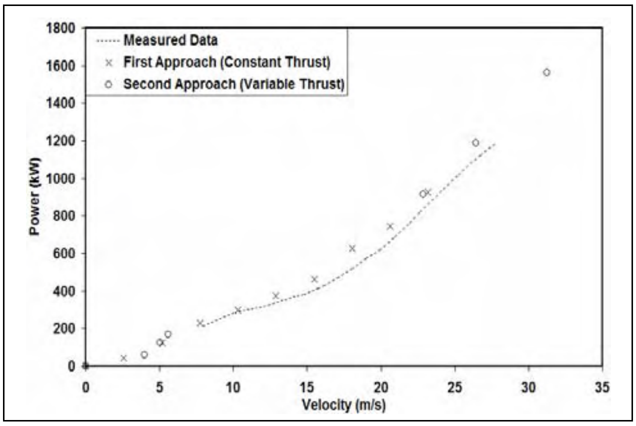

Fig.9: Numerical and experimental power

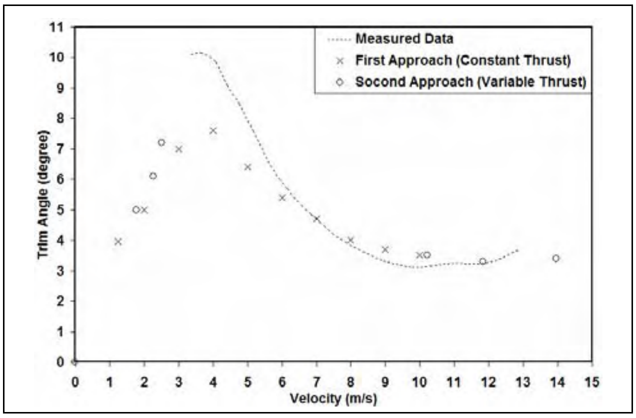

Fig.10: Numerical and experimental trim angle

Fig.11 shows some snap shots of the catamaran in different velocities. The depth of the water surface deformation at the stern of the craft is increased as the velocity is increased while its length is increased. The angle of the generated wave experiences a decrease in this manner. Wet-deck of the catamaran has different situation relative to water surface in different velocities. In low velocity and before planing the wet-deck becomes wet and in higher speeds it rises up from water as clearly represented in Fig.12.

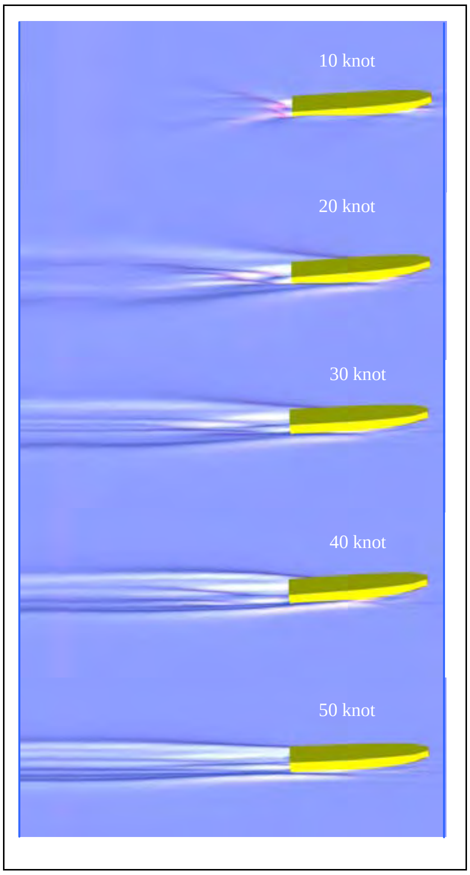

Fig.11: Snapshots and wave patterns of catamaran in different velocities

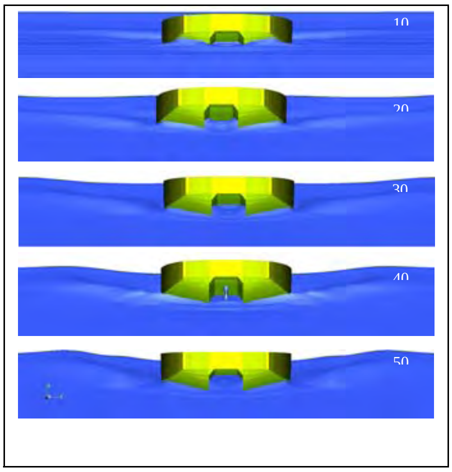

Fig.12: Front view of the catamaran

3.2. Turning Maneuver

Here the required force and moment of maneuvering are provided by apply a change in thruster angle relative to crafts longitudinal direction. Turning maneuver is simulated in two cases of 5 and 15 degrees. After 15 seconds from the beginning of the forward progress with 20 *kN* force, the thruster direction is changed to the mentioned angle. The time history of catamarans motions during the turning maneuver are presented in Fig.13.

Fig.13 (a) shows the time history of catamaran speed. It decreases until reaching a steady turning. It is obvious that, the difference between the forward (maximum) and the turning (minimum) speed and the gradient of speed change is increased as the thruster angle becomes larger.

Fig.13 (b) presents that the heel angle experiences a smooth behavior in the case of 5 degree thruster in comparison to 15 degree case which has a clear maximum value at the early stage of turning. Final trim of the catamaran is bigger in the case of 15 degree as could be predicted from the previous section. Also, yaw speed and drift angle have a same behavior during the tuning maneuver. Snapshots of catamaran are shown in Fig.13 (f).

Path of ship's center of gravity is shown in Fig.14. The turning circle and its diameter are decreased as thrusters' angle of rotation increased. Such behaviors are reasonable and qualitatively similar to experiment.

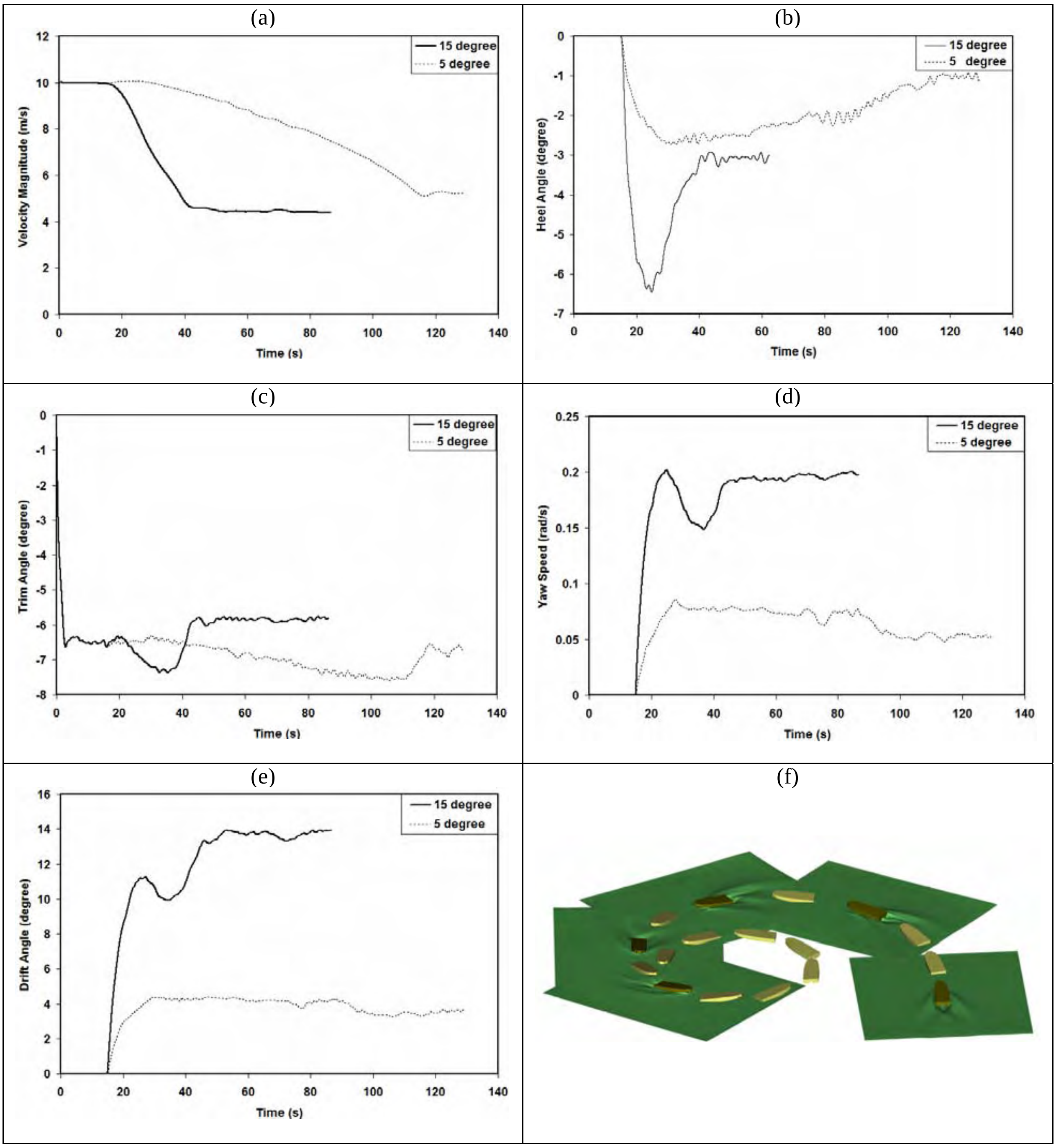

Fig.13: Catamaran turning maneuver time history

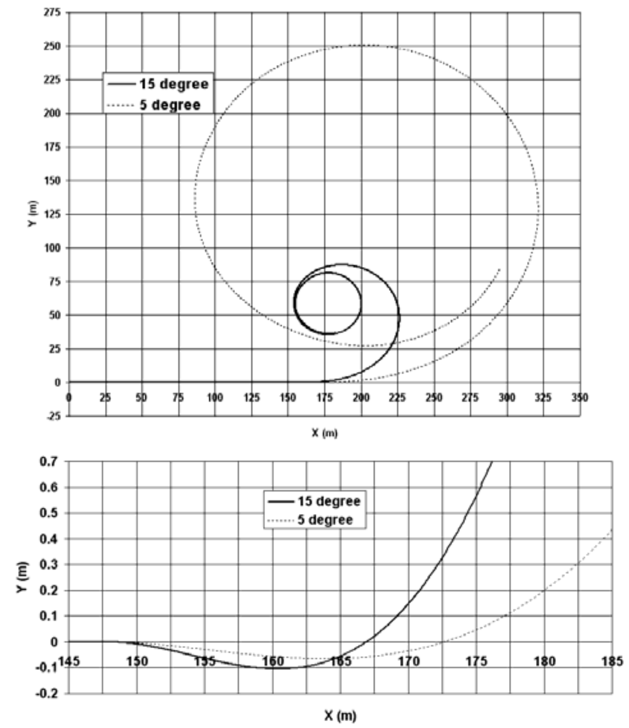

Fig.14: Ship mass center path, and overshoot

4. CONCLUSION

The proposed numerical algorithm is capable of simulating complex ship hydrodynamics problems. High speed catamaran investigated in this study is accompanied by some complicated phenomena such as planing and porpoising. However, the numerical results show a good agreement with experimental data in the case of forward progress. Besides, In the case of turning maneuver, the results are qualitatively acceptable. The presented computer software has no geometrical restriction and also an appreciable ability in a wide range of 6-DoF fluid-structure interaction including all types of crafts.

References

1. JAHANBAKHSH, E.; PANAHI, R.; SEIF, M.S. 2007, ‘Numerical Simulation of Three-Dimensional Interfacial Flows’, International Journal of Numerical Methods for Heat & Fluid Flow, 17(4):384-404

2. CHENTANEZ, N.; GOKTEKIN, T.G.; FELDMAN, B.E.; O’BRIEN, J.F. (2006), ‘Simultaneous coupling of fluids and deformable bodies’, Proceedings of the 2006 ACM SIGGRAPH/Eurographics symposium on Computer animation

3. TREMEL, U.; SORENSEN, K.A.; HITZEL, S.; RIEGER, H.; HASSAN, O.; WEATHERILL, N.P. 2007, ‘Parallel remeshing of unstructured volume grids for CFD applications’, Int. J. Num. Meth. Fluids, 53:1361-1379

4. BLADES, E.; MARCUM, D.L. 2007, ‘A sliding interface method for unsteady unstructured flow simulations’, Int. J. Num. Meth. Fluids, 53:507-529

5. CARRICA, P.M.; WILSON, R.V.; NOACK, R.W.; STERN, F., 2007, ‘Ship Motions using Single-Phase Level Set with Dynamic Overset Grids’, Computers & Fluids, doi: 10.1016/j.compfluid.2007.01.007

6. MITTAL, M.; ICCARINO, G. 2005, ‘Immersed boundary methods’, Annu. Rev. Fluid Mech, 37:239-261

7. PANAHI, R.; JAHANBAKHSH, E.; SEIF, M.S. 2006a, ‘Development of a VoF-fractional step solver forfloating body motions simuilation’, Applied Ocean Research, 28:171-181

8. JAHANBAKHSH, E.; PANAHI, R.; SEIF, M.S. 2005, ‘Multi-dimensional free surface flow simulation using two-phase Navier-Stokes solver’, 8th Numerical Towing Tank Symposium (NuTTs), Varna, 2-4 October

9. PANAHI, R.; JAHANBAKHSH, E.; SEIF, M.S., 2006b, ‘Development of a numerical hydrodynamic tank for ship motion simulation’, ECCOMAS CFD 2006, Egmond aan Zee, Netherlands, 5-8 September

10. JAHANBAKHSH, E.; PANAHI, R.; SEIF, M.S. 2006, ‘Ship Dynamic Simulation, Based on a Three-Dimensional Viscous Free Surface Solver’, 9th Numerical Towing Tank Symposium (NuTTs), Nantes, 1-3 October.

AVOIDING COMMON ERRORS IN HIGH-SPEED CRAFT POWERING PREDICTIONS

John Almeter, Naval Surface Warfare Center, Carderock Division, Norfolk, Virginia, USA

SUMMARY

Overly optimistic resistance, powering and speed predictions for high-speed craft appear to be increasing. Common errors and flaws causing excessive performance speed claims for high-speed craft, especially novel ones, are reviewed. This work will help to avoid *common performance prediction errors* and aid reviewers in identifying them.

1. INTRODUCTION

This paper is not intended to be a comprehensive text for performance prediction for the broad universe of high-speed craft. This is beyond the scope of a paper, or even an entire symposium. Equations are intentionally absent and the references sparse. However, this paper can still be useful in identifying, understanding and avoiding errors in powering predictions. For over twenty years, the author has observed numerous mistakes and errors in high-speed craft predictions. Over fifty errors or mistakes in high-speed craft powering predictions are reviewed. General categories of errors in speed prediction and claims are listed below.

Inappropriate Comparisons
Optimistic Propulsor Predictions
Inconsistent and Unclear Definitions
Low Weight Estimates
Air Lubrication and Lift
Common Powering Prediction Errors
Full Scale, Model Test and Scaling Errors
Designing to an Unrealistic Design Point

MacPherson (1) is a general reference on powering prediction errors.

2. INAPPROPRIATE COMPARISONS

It is common for performance prediction claims to be compared against alternate concepts. The author has often observed alternate concepts presented for comparison whose claimed resistances or powering are excessively high and thus making the concept promoted appear to have an advantage that may not exist. Comparisons are made unfairly with unrepresentative concepts or against bad or false data. A craft concept may also be proposed with a very efficient propulsor and compared against alternate concepts with inefficient propulsors with the performance advantage falsely attributed to the proposed hull form and not the propulsors. Traditional propeller installations can be significantly less efficient at very high speeds than surface piercing propellers or waterjets due to cavitation and appendage drag. Jacobson (2) and Almeter (3) are two of many references providing resistance and powering data as a check. Figure (1) is from Jacobson (2). It plots current transport efficiency limits against non-dimensional Froude Number (based on volume) for several different classes of hull types and provides a sanity check for performance claims.

3. OPTIMISTIC PROPULSOR PREDICTIONS

Optimistic propulsor performance prediction, high or low, can result in optimistic performance claims. As an example, low propulsor performance may be predicted for a prototype craft. This allows an unrealistically low resistance to be back calculated from the craft's measured performance. Failure to make speed is often attributed to an "inefficient" propulsor when it is really the fault of a poorly performing hull form. Unrealistically high speeds can also be predicted using unrealistically high propulsor efficiencies. In this case the high "claimed" speed is due to the propulsor and not the hull form. Blount (4) can be used as a guide to propulsor performance for high-speed craft.

4. INCONSISTENT AND UNDEFINED DEFINITIONS

Inconsistent and undefined definitions can result in unrealistic craft performance expectations even when all parties involved are reputable and competent. As an example, a proposal may claim 50 knots for their concept. Many in the US Navy would automatically assume the speed corresponds to Full Load condition at an engine rating that can be run all the time with hundred degree Fahrenheit inlet air and the like. The proposal may be making claims on entirely different conditions; such as near Lightship and intermittent power at a much lower air inlet temperature. This disconnect, often unintentional, can result in an unrealistic proposal that does not meet customer expectations.

A common area of confusion is engine ratings. Terms like Maximum Continuous Rating are not universally understood and agreed upon. Maximum Continuous may not mean maximum continuous as many believe it. Maximum Continuous Rating may only be available for a small percentage of the engine's duty cycle without premature wear. Simply, the engine cannot be run at this rating for extended periods despite the descriptive title of the rating. Machinery ratings are not consistent between manufacturers. Ambient and assumed installation conditions for engine ratings can vary greatly. These conditions include air temperature, water temperature, and inlet and outlet losses – all of which impacts engine performance.

It is critical to define terms. All parties must fully understand the definitions as used and not make assumptions. This may require what sounds like ignorant questions from all directions, but they are critical. Machinery power ratings and the impact of temperature must be clearly understood. The duty cycle or operational profile has to be understood by all parties.

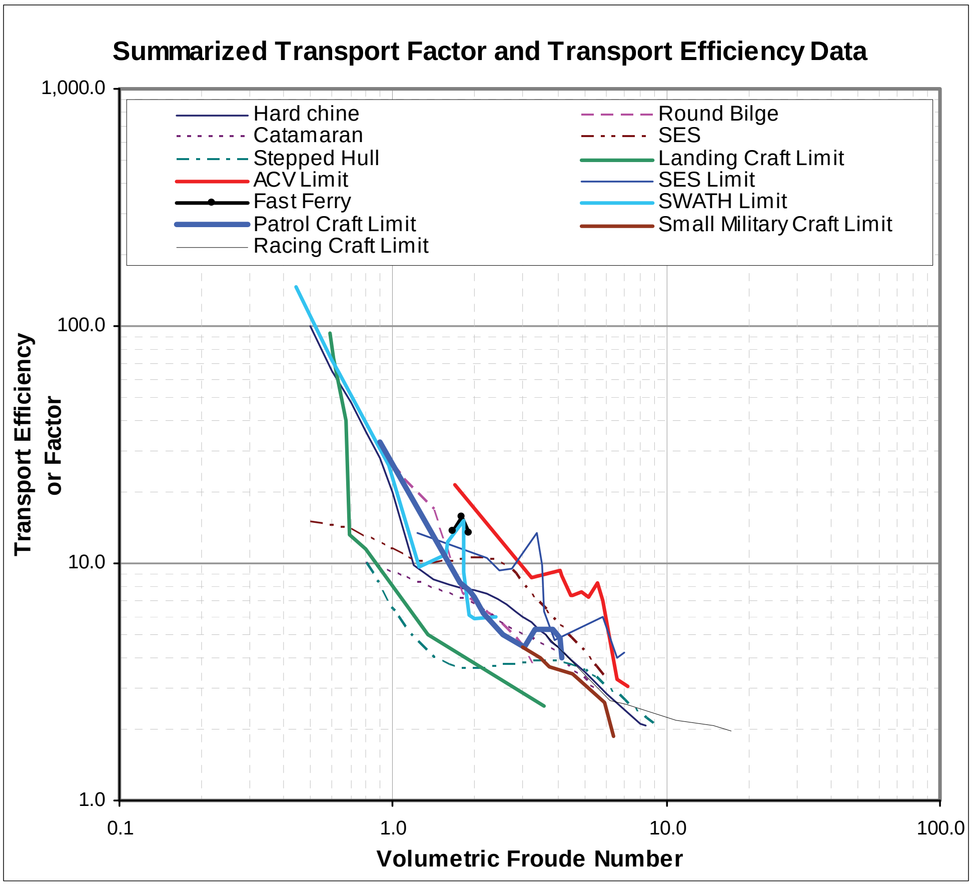

Transport Factor - defined as shown in the equation below:

$$TF = \frac{\Delta * V}{326 * P_B}$$

where:

Δ = Vessel design displacement (in pounds mass)
V = Vessel design speed (in knots)
P_B = Total installed propulsive and lift (brake) horsepower

Figure 1: Transport Factor

5. LOW WEIGHT ESTIMATES

Many high-speed hull forms are very sensitive to weight. A small increase in weight may result in a disproportionate increase in resistance. This results in greater fuel loads, increased power to obtain speed, and potentially a non-convergent design. In summary, weight is bad and a design killer for many high-speed craft concepts. Some concepts, not all, are extremely sensitive to craft weight. An error in the longitudinal center of gravity estimate can also adversely impact the performance prediction.

The author has reviewed numerous high-speed craft concepts based on unrealistically low weights resulting in unrealistic high-speed claims. The performance prediction may be correct for the assumed displacement, but if the displacement is incorrect, accordingly the prediction will be wrong. Almeter (5) and Jacobson (6) are useful references for predicting or checking weight of many high performance craft. Figure (2) is taken from Almeter (5). It plots lightship density (lightship displacement divided by total volume) against total volume for several classes of hull forms and ship types. Figure (3) is the same as figure (2) with the exception that the propulsion weights have been deducted from the lightship weight. Figures (2) and (3) are useful as a sanity check.

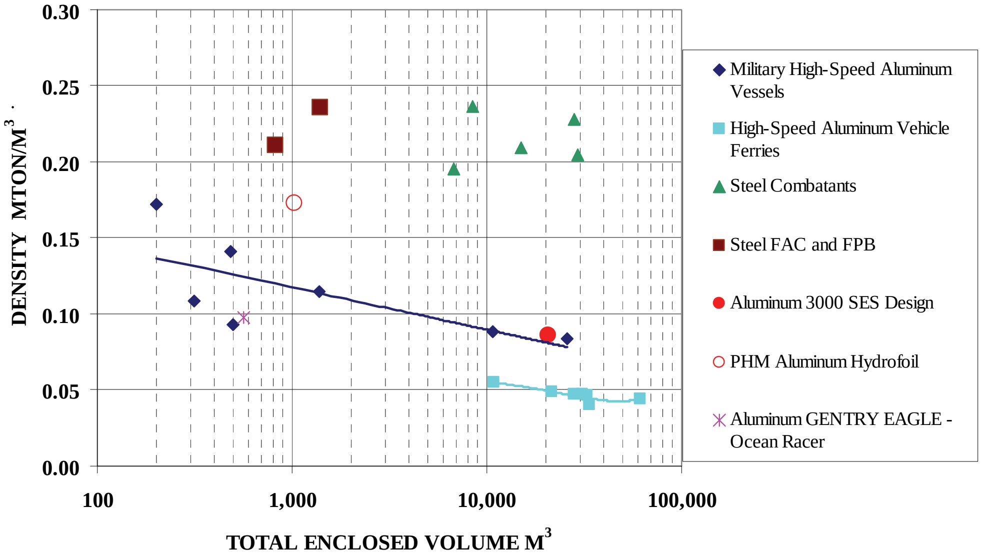

Figure 2: Lightship Density vs. Volume for Different Craft Types

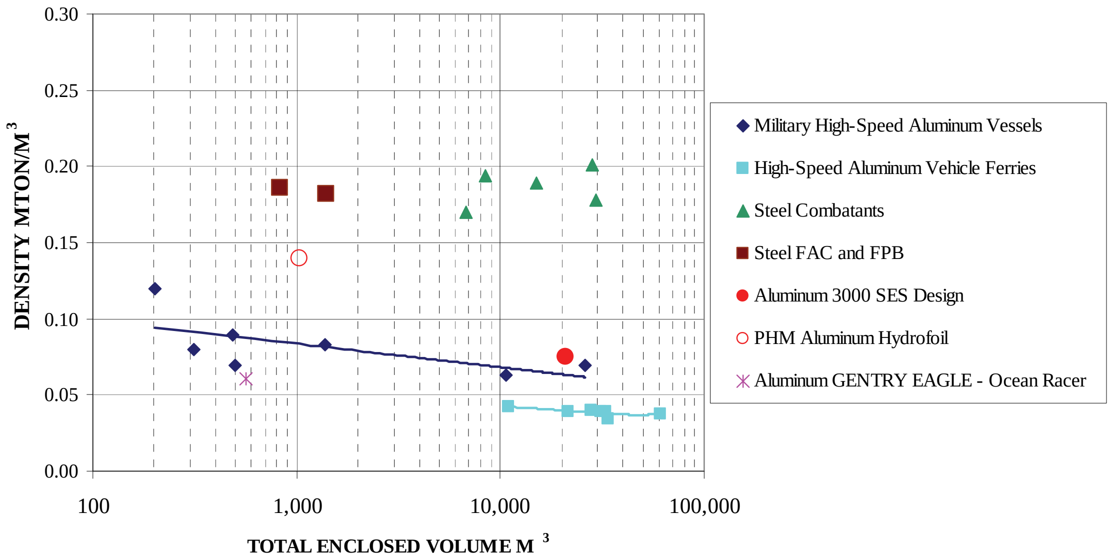

Figure 3: Lightship minus Propulsion Weight Density vs. Volume for Different Craft Types

6. AIR LUBRICATION AND LIFT

Many high performance craft claim significant benefits from aerodynamic lift and air lubrication. A proper discussion is certainly beyond the scope of this paper, but a few critical points will be made. Aerodynamic lift is real and used by hydroplanes, wing in ground (WIG) craft, and seaplanes. These three types of craft have two things in common; they are very fast and extremely lightly loaded by marine standards. Many concepts currently proposed are a fraction of the speed of the aerodynamic lift craft mentioned and dramatically heavier loaded. The Soviets extensively investigated claims that air significantly reduced the drag of inverted planing hulls and concluded it did not, Pavlenko (7). Promoters of aerodynamic lift for all but very high-speed and lightly loaded craft need to substantiate their claims.

Aerodynamic lubrication is a concept that has existed for over a hundred years as demonstrated by a cursory review of United States patents. It is critical for anyone claiming this benefit to substantiate it. Aerodynamic lubrication is not the same as air pockets or cavities found in stepped hulls, air cushion vehicles and the like.

7. COMMON POWERING PREDICTION ERRORS

Common powering prediction errors include:

Failure to include air drag for superstructure
Unrealistically low air drag coefficients
Neglecting wind speeds
Underestimate or ignore appendage drag
Neglecting momentum drag for air cushion vehicles
Ignoring drag of blisters and pods for propulsors
Underestimating or ignore spray drag
Underestimating wetted surface
Extrapolating beyond legitimate bounds of methods
Over reliance on CFD without calibration
Ignoring interference drag
Transom separation
Ignoring shallow water effects
Neglecting propeller and waterjet cavitation
Neglecting hydrofoil cavitation
Neglecting impact of foil submergence on hydrofoil performance
Underestimating skirt and seal drag
Underestimating cushion air requirements
Inconsistent friction line use
Propeller tunnels
Errors in added sea state drag
Failure to account for sea state impacts on propulsor
Neglecting propulsor lift and height of thrust line
Neglecting impact of shaft angle on propellers
Neglecting trim control devices

7.1 AIR DRAG

Air drag is significant for many high-speed craft and the author has observed air drag coefficients of 0.30 and lower for non-streamlined shapes. Air drag for superstructure is often omitted. In many resistance prediction techniques, systematic series and theoretical, there is no allowance or accounting for air drag. Air drag for hull and superstructure has to be calculated independently and added. As an example, the Soviet BK Series was run behind a shield to eliminate air drag and accordingly the series resistance does not include air drag. References addressing air drag include Walsh (8 and 9). Still air is standard in many calculations and model tests and this can cause an error if the craft has to operate into a wind. As an example, a twenty knot wind speed can almost triple the wind drag of a thirty knot craft. There can be a significant difference between wind speed on craft and free stream wind speed that needs to be addressed.

7.2 APPENDAGE DRAG

Appendage drag includes shafts, skegs, waterjet fences, struts, ride control devices, cooling water pickups and anodes. If the concept requires a large amount of raw water, the momentum drag associated with collecting the water will be significant. This is in addition to the appendage drag. Many high-speed hull forms do not readily accommodate propulsors and main machinery and require blisters, sponsons or pods. As an example, it is not unusual for the side hulls of surface effect ships to have blisters for waterjets. These blisters increase side hull drag and if neglected, the performance will be over estimated. Model tests with an appendaged model do not always properly capture the additional resistance of appendages.

7.3 SPRAY DRAG

Spray drag can be very significant for many hull forms and is often neglected or underestimated. Hydrofoil struts, shafts penetrating the water, and fine bows are a few examples of large spray generators that significantly increase the drag of a design. The spray within tunnels of many craft can be very significant. Modern planing craft designs significantly reduce spray drag through the effective use of spray rails. Spray rails may not be effective for all hull forms.

7.4 WETTED SURFACE

The author has observed several cases of significant underestimation of wetted surface. One source of error is the assumption of water separation off the sides where it does not. An example is assuming that the outboard sides of a surface effect ship are dry when they are wet. Tunnels between hulls or bodies are often claimed to be dry, often due to air lubrication, but quite often are wet.

7.5 ANALYTICAL METHOD

A common error is to use an analytical method that is not relevant to the craft under consideration. This includes resistance, propulsor, wake and thrust deduction analysis. Otherwise legitimate analytical methods are often used beyond the bounds of accuracy. Many analytical methods use equations with higher order terms that can provide false results even slightly beyond their bounds of applicability. It is critical to review applicability and bounds of analytical methods. For example, the longitudinal center of gravity and a constant design waterline are assumed fixed in many methods. This can result in significant error if the design does not match the assumed values. Far too often analytical tools are used without the users fully understanding their applicability and limitations. An unethical individual can always find an analytical method to provide the desired answer. Where possible, the author requires the references that the analytical methods are based on be delivered with calculations.

7.6 INTERFERENCE

Interference between bodies is often underestimated or even ignored. This includes interference between displacement bodies, foils, and air cushions. Interference can also adversely impact running trim that can result in an underestimation of resistance at hump speeds if neglected. Molland (10), for example, documents interference between displacement catamaran hulls.

7.7 TRANSOM SEPARATION

Separation of the water from the transom can significantly impact resistance and complicate theoretically based prediction methods and limit their applicability. It is critical to understand how the prediction methods address transom separation and establish a lower limit for its applicability.

7.8 SHALLOW WATER

The impact of shallow water on resistance cannot be ignored for those craft required to operate in shallow water. Shallow water drag may be significant where the Froude Number based on water depth approaches unity (one) and the craft is in relatively shallow water (significant draft to water depth or length to depth ratios). Paradoxically, resistance can actually reduce at Froude numbers not much greater than unity.

7.9 CAVITATION

Neglecting propulsor cavitation can result in significant over prediction of speed. Not all propeller models include the effects of cavitation. Waterjets sized for the top speed may not have significant cavitation at top speed, but may cavitate significantly at hump speeds and be unable to push the craft past it to its required speed.

Like propellers, hydrofoils can cavitate and it is critical that this be considered in predictions. The cavitation may not be captured in small models in traditional resistance and powering tests. The efficiency of hydrofoils can also significantly decrease as they approach the surface.

7.10 SKIRT DRAG

There are often errors in skirt drags of surface effect ships and air cushion vehicles. The author sympathizes with all who make these predictions who lack relevant data. There is little available in the public domain on skirt drag and it tends to be empirical and individual equations may have very limited ranges of applicability. Rigid seals, often ship like, have been proposed for surface effect ships. They are often assumed to have the same resistance characteristics of traditional flexible seals. This assumption has to be substantiated if claimed. Aerodynamic momentum drag caused by accelerating the air required for a surface effect ship or air cushion vehicle to operate cannot be ignored.

The air flow to cushions of air cushion vehicles, flexible and rigid seals, can have a significant impact on powering prediction. Not only does the air flow require fan power, but can impact resistance. The air flow should always be compared to other air cushion vehicles as a sanity check.

7.11 COMPUTATIONAL FLUID DYNAMICS

Computational fluid dynamics, CFD, is becoming more widely used and can be extremely useful. Prudent users of CFD are not reluctant to state that CFD is best used for comparative analysis, needs validation, or requires calibration with test data. The author has observed several cases where performance claims have been based solely on CFD and were found to be in significant error. The same CFD code run by different individuals under different assumptions can produce dramatically different results. Accuracy, verifications, and other CFD related discussions are addressed in numerous International Towing Tank Conference documents, including the 23rd Conference listed in the references, ITTC (11). The use of CFD alone, does not guarantee accurate predictions.

7.12 FRICTION LINES

There needs to be consistent use of friction lines and methodologies. As an example, if a prediction is made using a technique derived with a three dimensional friction line and then used with a two dimensional friction line the resistance could be significantly under predicted. The choice of friction line impacts the correlation allowance.

7.13 PROPELLER TUNNELS

Propeller tunnels can significantly impact resistance and propulsor performance. Blount (12) is a good general reference on propeller tunnels.

7.14 SEA STATES

Added drag or resistance from seas can significantly increase resistance and powering. Some hull forms, such as air cushion vehicles are more sensitive to seas than others. It is critical that added drag or resistance be addressed in many cases. Craft can have significantly different added drag in different sea spectrums of the same significant wave height. Both wave height and wave length are often significant.

Sea state can have a significant impact on propulsor performance. Cavitation, aeration, and fluctuations in load can impact the craft's ability to make speed. The amount of submergence of a surface piercing propeller can change dramatically in heavy seas resulting in wide fluctuations in loading and performance. There can also be an involuntary speed loss due to the coxswain pulling back on the throttle.

7.15 PROPULSOR LIFT, THRUST LINE AND SHAFT ANGLE

Certain propulsors, such as surface piercing propellers can generate very significant lift. This impacts resistance and the overall "balance" of the craft. As an example, the back of a hydroplane is significantly supported by its surface piercing propeller at high speed. The effect of the thrust line height often has to be considered. A waterjet, for example, generally has a significantly higher thrust line than a submerged propeller. A prediction method based on a propeller thrust can often be corrected for the different thrust line of a waterjet.

The impact of propulsor lift and thrust line can also be addressed by a thrust deduction (positive or negative). Care has to be taken to avoid "double counting" propulsor lift and thrust line with modeling and thrust deductions.

A classic text on the subject is Hadler (13). This work also discusses the impact of shaft angles on propeller performance.

7.16 TRIM CONTROL DEVICES

Trim control devices include wedges, tabs, and interceptors (guillotines). The devices can be fixed or controllable. The impact can either be minor or dramatic depending on the application. Their benefit can vary with displacement, longitudinal center of gravity and speed. Trim control devices can increase resistance in many cases, especially at very high speed. Trim control devices can also eliminate or cause dynamic instabilities.

In some cases (not all), ignoring trim control device impacts can result in significant errors in powering predictions. Most prediction techniques do not include the impact of trim control devices. However, they can often be corrected or modified by superimposing the impact of the lift control device. Savitsky (14) is one of many references on this subject.

8. FULL SCALE, MODEL TEST AND SCALING ERRORS

Bad data and scaling errors from model basin models and manned models can result in significant prediction errors. International Towing Tank Committee Conference recommended procedures for resistance tests, propulsion tests and waterjet testing are listed in the references. Hubble (15) and Wilson (16) also address model testing of a range of high-speed craft. Common data and scaling errors include:

Ship "methodologies" applied to high-speed craft
Use of outlier data
Unscientific and qualitative testing
Laminar flow – small models
Non-standard scaling methods
Friction scaling (1 + k)
Correlation allowances
Shallow water
Unrealistic wetted surface
Differences between full and model scale sea state

The ITTC procedures listed in the reference section identifies many of the basics of testing and test reporting.

8.1 HIGH-SPEED CRAFT TESTING PROCEDURES

A common problem is the use of standard displacement ship testing methods for high-speed craft where they are not applicable. This is addressed in detail in the references just cited. Standard ship testing methods often result in significant errors in the model data and the scaled predictions. Propulsor ventilation and cavitation can be much more severe on high-speed craft than on more traditional slower vessels. These phenomenons may require propulsor testing in a vacuum facility as discussed in ITTC procedure for propulsion tests or a large diameter model propeller in a cavitation tunnel. Traditional self-propelled models alone may not capture the cavitation impact.

Proper simulation of the fans in air cushion vehicle model testing, especially in added resistance tests, is extremely difficult and critical. The air flow and cushion pressure can fluctuate significantly and this impacts resistance and powering. Scaling of air cushion vehicles has unique challenges and is discussed in Yun (17) and the ITTC seakeeping procedure listed at the end of the references.

8.2 OUTLIER DATA

It is tempting to assume that every piece of data is correct. This is not always true and can result in optimistic predictions often in conflict with other data and observations. The data as the whole must be reviewed and the question asked, "How do I know it is right?" In testing, it is always prudent to know what the data should be before it is taken - partially to aid in identifing errors in the data.

8.3 UNSCIENTIFIC AND QUALITATIVE TESTING

High-speed craft testing, model or full size, needs to be accurate and quantifiable if it is used as a basis for predictions or claims. Unfortunately, often it is not much more than anecdotal observations. Basics include:

- Displacement and center of gravity of the craft
- Description of hull form with dimensions
- Propulsor descriptions with dimensions
- Propulsion plant and transmission description
- Calibrated instruments
- Recording and retention of data
- Power or resistance measurements
- Air flow and / or fan measurements
- Definition of environment (sea states, currents, winds, water depth, etc.)
- Reciprocal runs
- Repeatability of data, especially of suspect points
- RPM measurements
- Scaling methodology defined

8.4 LAMINAR FLOW

Many high-speed craft models are small and prone to laminar flow that can result in underestimating the craft's resistance. Even planing models, where the flow may appear violent, can be laminar. Various approaches exist to induce turbulence.

8.5 NON-STANDARD SCALING METHODS

The methods used to scale the data have to be reviewed. The author has observed model test data scaled using unconventional scaling methods (even by high-speed craft standards) that resulted in unrealistical high-speed claims. There is controversy and debate surrounding the viscous form factor (1+k) used in three-dimensional viscous resistance formulations. A wide range of values have been proposed for essentially the same hull. There is controversy on the methods used to measure it. A high value will result in lower predicted resistance at full size, especially where the scale ratios are large. The viscous form factor (1+k) can actually be less than one, Almeter (18). Anything beyond this mention of this subject is beyond the scope of this paper.

The author has observed several instances where a manned model is run at high-speed, say fifty knots, and is claimed to have low resistance and that the manned model running at fifty knots proves that a ship of ten times its length will also have low resistance at fifty knots. This is contrary to scaling laws. Claims like this should make reviewers suspicious.

8.6 CORRELATION ALLOWANCE

The correlation allowance is dependent on the friction line used, viscous form factor, hull form and type, test procedures and even the model basin. All must be considered when determining / selecting the correlation allowance. If one of these variables changes the correlation allowance may also have to change. Correlation allowances are also often used in empirical and analytical based predictions.

8.7 SHALLOW WATER

Shallow water effects must be addressed. This is normally done by testing in sufficient water depth to avoid significant shallow water effects. Depending on the speed, shallow water can increase or decrease resistance. If the desire is to quantify shallow water effects, then the model has to be tested in shallow water.

8.8 WETTED SURFACE MEASUREMENTS

Wetted surface measurements of high-speed craft are often in error. The wetted surface measurements can be very difficult and often require an experienced eye. The spray and the solid water, including pileup, have to be separated. A low measurement of area will result in a high scaled resistance and conversely a high measurement will result in a low scaled resistance.

8.9 DIFFERENCES BETWEEN MODEL AND FULL SCALE SEA STATES

Despite having the same scaled significant wave height, the model and full scale seas can be different. Added resistance in seas can have a strong dependency on wave length or period, craft speed, and relative heading and not just wave height. The differences, if any, between the model and full size wave spectrums have to be understood. Full scale sea states usually have a significant wind that is generally absent in model sea states.

9. DESIGNING TO AN UNREALISTIC DESIGN POINT

Designing to an unrealistic design point is not an error in itself, but can result in an unsuitable craft. As an example, if the contractual speed requirement is based on calm water in a partial load condition, the propulsors may be optimized for this condition and inadequate for many of the craft's more demanding conditions. This scenario could result in the craft failing to get past hump in a fully loaded condition. Many high-speed craft concepts have significant added drag in waves that can prevent the concept from getting past hump in anything beyond calm water. Hull fouling and degraded engine performance are additional speed killers.

10. POWERING MARGINS

A resistance or powering margin is the difference between the predicted and required performance. The predicted is after all allowances, correlations and corrections are applied. An allowance is an addition or correction to account for roughness, acceleration, sea state, poor engine performance, etc.. The terms margin and allowance are often used interchangeably and this can create the false impression more margin exists than actual. Prediction methods often require calibration or correlation. This is not the same as a margin. If a method is found to underestimate the required power by twenty percent, increasing the calculated power by twenty percent is not a margin, but a correction. The required or desired margin is dependent on the perceived potential error in the overall methodology and the willingness or tolerance of the designer to take risk. Using this logic, there should not be fixed universal margins for powering. Each analysis is unique.

The unnecessary compounding of margins must be avoided. As an example, if there was a ten percent error applied each for resistance prediction method, propulsor modeling, weight estimating, and engine performance, the accumulative error would be almost fifty percent. The use of such large margins would cause almost every successfully built high performance craft unfeasible on paper.

It is critical that the designer understands the accuracy and limitations of the total prediction methodology used. This is generally done by running test cases as illustrated by figure 4 taken from Almeter (5). Figure 4 is a plot of the difference between the SWPE (Ship Wave Patter Evaluator) thin ship computer program and measured or derived resistance for a wide range of high speed displacement hull forms, including multi-hulls, at model and full scale. The average error of this methodology was found to be only one percent (negative) with a standard deviation of eight percent, which is comparatively low for a prediction analysis for complex multi-hull forms that can be made in a few hours. Unless there was an extreme intolerance of error the margin used for this approach would be very low for craft similar to those reflected in this figure.

Errors in predictions can be huge for conventional hull forms. Figure (5) is a plot of predicted resistance using the four relevant methods in NAVCAD, a commonly used commercial software program, for a traditional mono-hull planing craft. There is a disturbingly large spread in the predictions, especially at hump. Obviously, they cannot all be right. Full size operation of the craft has shown that all of the predictions are probably wrong for this craft (not due to errors in NAVCAD). The craft's performance has been found to be much less than predicted by any of the methods shown in figure (5). The craft in question is extremely heavily loaded and probably outside the legitimate bounds of the methods, despite several of the methods documentation indicating otherwise. The craft's top end speed was seven knots less than predicted and its time to accelerate through hump was several times greater than can be expected from the predictions. These are large errors with very significant consequences. The mistake was in the use of prediction methods that were not relevant. Other methods could have been used, analytical and model testing, that would have provided better predictions. This is just one of over fifty potential mistakes discussed in this paper. However, the remedy is not conservatism and the overuse of margins, but to make responsible and knowledgeable predictions.

11. CONCLUSION

Errors of high-speed craft powering predictions are as numerous and diverse as high-speed craft concepts. Over fifty different errors are discussed in this paper and the listing is not complete. Unrealistic performance claims can result in investment of precious resources in dead ends and cause the neglect of promising concepts with legitimate performance claims. It is hoped that this paper will help in avoiding errors in predictions and to aid reviewers in their identification. If a performance claim appears too good to be true, it is deserving of close scrutiny.

There are numerous options for powering predictions of high-speed craft including simple empirical predictions, sophisticated analytical predictions, model testing, manned model and even full size testing. The most accurate prediction method is not always the most expensive.

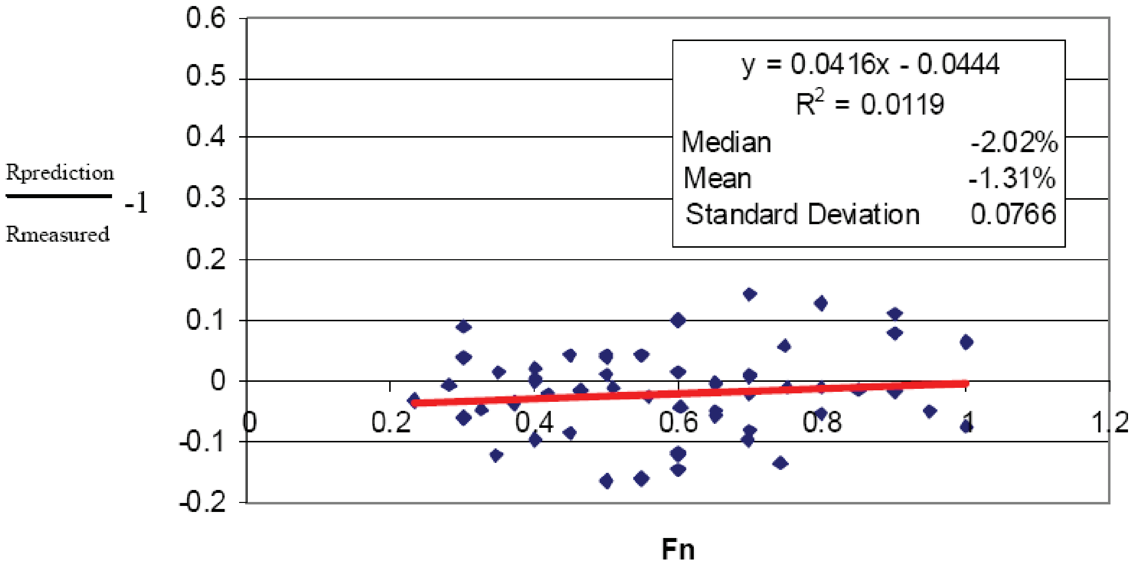

Figure 4: Error of SWPE Computer Program for Several High Speed Displacement Hull Forms

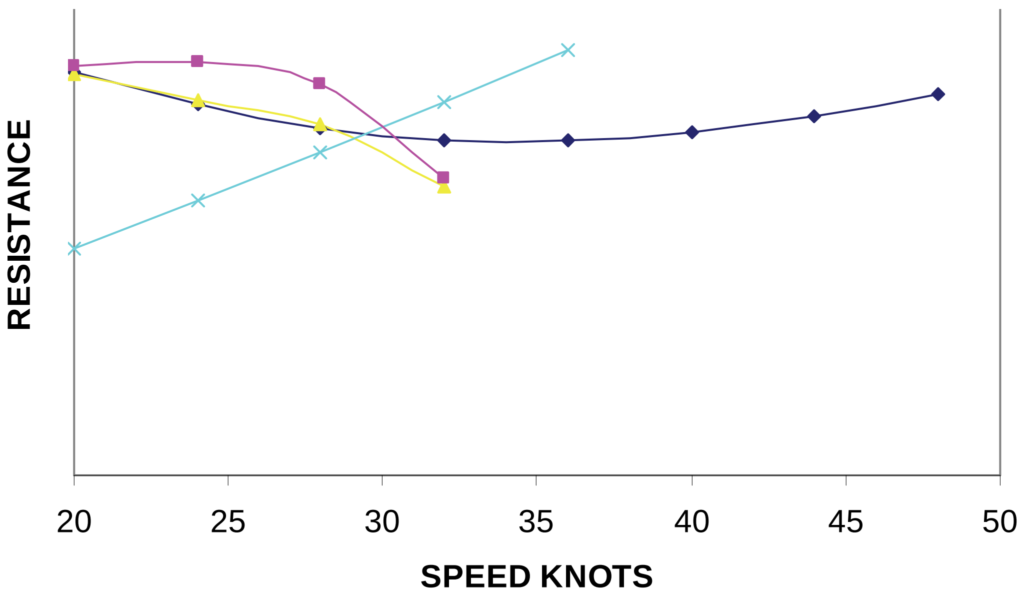

Figure 5: Comparison of Different Resistance Prediction Techniques for a Heavily Loaded Planing Hull

12. ACKNOWLEDGEMENTS

The following individuals have provided input to this paper: Donald Blount, Carl Casamassina, Donald Jacobson, Gabor Karafiath, Colen Kennell, Dan Savitsky, Willard Sokol, and Richard Wilson. Code 33 of the Office of Naval Research, supported this effort.

13. REFERENCES

1 MACPHERSON, D. M., “The Ten Commandments of Reliable Speed Prediction”, Small Craft Marine Engineering Resistance and Propulsion Symposium, University of Michigan, May 1996

2 JACOBSON, D., “Use of Comparative Performance Data in Preliminary Design and Proposal Evaluation of High Performance Craft”, MAST 2007, Genoa, Italy, 14-16 Nov 2007

3 ALMETER, J., “Resistance Prediction and Optimization of Low Deadrise, Hard Chine, Stepless Planing Hulls”, SNAME STAR Symposium, 1989

4 BLOUNT, D. L., BARTEE R. J., “Design of Propulsion Systems for High-Speed Craft”, Marine Technology, Vol. 34, No. 4, Oct 1997

5 ALMETER, J., JACOBSON, D., et al, “Review of Analytical Tools For The Us Army’s Theater Support Vessel”, ASNE High Speed / High Performance and Craft Symposium, July 2005

6 JACOBSON, D., ALMETER, J., “Concept and Early Preliminary Design Methodologies for High-speed Vessels”, HIPER 06

7 PAVLENKO, A. S., “The Hydrodynamics of Sea Sleds”, Katera I Iakhty No. 1 (23), 1970, in Russian (NAVSEA Translation Number 2150, 1987)

8 WALSH, D. E., “Measurements of Wind Forces and Moments on Models of Three Representative High-Speed Craft”, National Maritime Institute Report No. 168, August 1983

9 WALSH, D. E., “A Method for the Calculation of the Wind Resistance on High Speed Marine Craft,” National Maritime Institute Report No. 161, April 1983

10 MOLLAND, A. F., COUSER, J. F., “Resistance Experiments on a Systematic Series of High Speed Form”, RINA Transactions, 1996

11 ITTC, “Group Discussion A.2: Accuracy of CFD Predictions”, Proceedings from the 23rd ITTC, Venice, Italy, 2002

12 BLOUNT, D. L., "Design of Propeller Tunnels for High-Speed Craft", FAST '97, Sydney, Australia, July 1997.

13 HADLER, J. B., “The Prediction of Power Performance”, SNAME Transactions, 1966

14 SAVITSKY, D., BROWN, W. P., “Procedures for Hydrodynamic Evaluation of Planing Hulls in Smooth and Rough Water”, Marine Technology, Volume 13, No. 4, Oct. 1976.

15 HUBBLE, N., “Correlation of Resistance Test Results from Fixed and Free to Trim Methods for a Dynamic Lift Craft (Model 4667)”, Naval Ship Research and Development Center, Report 3544, April 1972

16 WILSON, R. A., SAVITSKY, D., et al, “Status of Hydrodynamic Technology as Related to Model Tests of High-Speed Marine Vehicles”, DTNSRDC-81/026, July 1981

17 YUN, L., BLIAULT, A., “Theory and Design of Air Cushion Craft”, John Wiley & Sons Inc., 2000

18 ALMETER, J., “Prediction of the Skin Friction Coefficient for Planing Craft Models at Low Reynolds Numbers”, Small Craft Marine Engineering Resistance and Propulsion Symposium, University of Michigan, May 1996

ITTC Recommended Procedures and Guidelines - Testing and Extrapolation Methods

High Speed Marine Vehicles Resistance Test – 7.5-0-05-01

Propulsion Test – 7.5-02-5-02

Waterjets Propulsive Performance Prediction – 7.5-02-05-03.1

Waterjet System Performance - 7.5-02-05-03.2

Waterjets, Uncertainty Analysis – Example for Propulsion Test - 7.5-02-05-03.3

Testing and Extrapolation Methods, High Speed Marine Vehicles, Sea Keeping Tests - 7.5 – 02-05 – 04

OPTIMIZATION OF THE GEOMETRICAL PARAMETERS OF A BONDED STIFFENER: FINITE ELEMENT ANALYSIS

G. Mohamad, ENSIETA, Mechanics of Naval and Offshore Structures Laboratory, Brest, France
M. Tarfaoui, ENSIETA, Mechanics of Naval and Offshore Structures Laboratory, Brest, France
V. Bertram, Germanischer Lloyd, Vorsetzen 35, D-20459 Hamburg, Germany

SUMMARY:
A numerical study analyses important fabrication parameters for adhesive bonding of stiffened plates. The focus of this study lies on two parameters: the length and the thickness of the adhesive bond. Finite element analyses for four typical load cases are applied to a chosen test case, bonding two aluminium specimens. The analyses reveal most suitable values for the length and thickness of the adhesive bond. This paper presents an numerical study which help us to understand the influence of two parameters of the adhesive joint : the adhesive thickness and the superposition length on the structural behaviour of The stiffened plates under different loads. For this reason we made several series of numerical calculation to optimize these parameters by using Abaqus software.

1. INTRODUCTION

Stiffened composite panels are extensively used in ship construction and it has immense importance in shipbuilding. These stiffeners are used to reinforce the hull of the ship and to increase its rigidity. Hashim [1] have studied the Adhesive bonding of thick steel adherents for marine structures, the main aspects include the understanding of adhesive properties and their limitations, design and behaviour of structural joints and the use of stress analysis. A range of structural adhesives were examined for bonding steel to steel, steel to GRP and GRP to GRP. also, a large number of accelerated durability test methodologies have been carried out on bonded steel joints for short periods of exposure, normally measured in weeks, to assess durability in wet/marine environment. For study the bending behaviour of bonded panels, large scale bonded panels were statically tested under four point bending. The experimental results show that the elastic central deflexion is higher than the theoretical value. They have found that the cleavage and shear strength values are very useful comparative data for selecting a structural adhesive. High strength adhesives are limited to operate at a temperature up to 100°C, which is acceptable for many marine applications. The wet environment causes a strength reduction of approximately 10% per year. Falzon [2] presented the results of an experimental programme investigating the failure of thick-sectioned stiffener runout specimens loaded in uniaxial compression. The ends of the stiffener runout have been identified as being susceptible to failure by skin-stiffener disbonding due to high interlaminar stresses. Davies [4] tested many stiffened panels using adhesively bonded pultruded sections. A number of adhesives were evaluated, including both rigid and flexible resins. They have selected tow adhesive: an epoxy and a poly-urethane, the more rigid epoxy appears quite adequate for the applied quasi-static loading , but the more ductile PU may offer advantages in blast loading. A 3D finite element model was also developed to study the mechanical behaviour.

The Virtual Crack Closure Technique (VCCT) is used with an efficient thick shell element to predict the crack growth characteristics of compressively loaded stiffener runout specimens. Three stiffener runout specimen configurations were modelled and the qualitative aspects of crack growth, in all these specimens, were successfully captured. Initial failure under compressive loading was assumed to be Mode II dominated and high compression stresses recorded at the edge of the runout [3]. The large analytical values of SERR still remains to be resolved satisfactorily, although there is evidence to support the hypothesis that high through-thickness compressive forces at the edge of the runout may effect the mode II critical fracture energy [3-5].

The aim of this work is to optimize the material parameters of the stiffened plates for naval applications and to replace the traditional method used to assemble the stiffener with the hull (the stratification), by adhesive joint. Then to study the the adhesive behaviour and the assembly under a static loading with an aim of managing to characterize the static behaviour and the associated damaging modes.

To optimize the thickness and the superposition length, two Aluminium substrate are used to carry out this series of calculation, Figure 1. Four loadings are applied to test the joint of adhesive:

- 3 pts bending
- 3 pts reverse bending
- tension
- compression

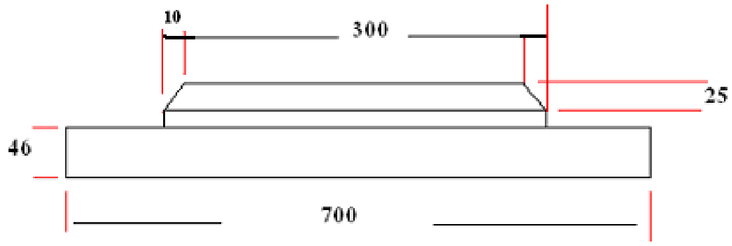

Figure 1. Stiffened plate Geometry

2. MATERIALS

The materials used for this study are presented in table 1. It consist of :

- 2 aluminium plates
- 1 joint of adhesive

The material properties are given in the table 1:

Element	Material	Mechanical characteristics	
		E (MPa)	υ
Higher substrate	Aluminium	70000	0.34
Lower substrate	Aluminium	70000	0.34
Adhesive	Araldite 2015	2000	0.277

Table 1. Material properties

3. FEA MODEL

A symmetrical 2D model with quadratic elements, standard CPS4R, is used to model the two substrates and the adhesive. On the other hand rigid elements type R2D2, figure 2, and are used to model the two supports of the load application and the boundary conditions, Figure 3.

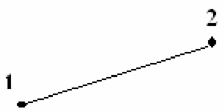

(a) Rigid element R2D2

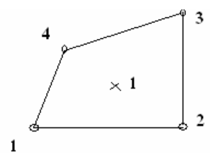

(b) Element CPS4R

Figure 2. Element type used for the finite element analysis

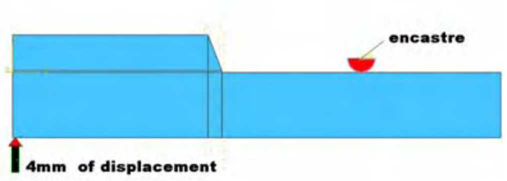

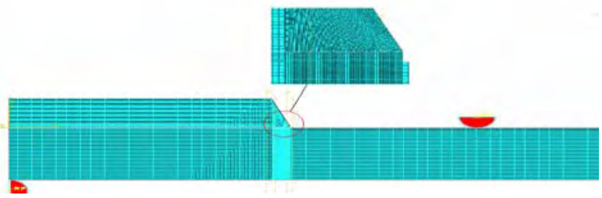

Figure 3. Mesh process and boundary condition

We utilise 20533 elements quadratic to mesh the panel, 3345 elements for the stiffener and 1000 elements in the adhesive. We use structured quad-dominated elements in the meshing controls. We have symmetrical stiffened structure and symmetric boundary condition is applied on the super surface of the panel, so we study one half of this structure for decrease the time and the data base of our simulation. A displacement of 4 mm is used for testing the stiffened structures.

4. OPTIMIZATION OF THE ADHESIVE THICKNESS

By applying the four loadings mentioned before, we have made four series of the tests by fixing all the parameters except the adhesive thickness which varies from 1 to 4.5(mm).The normal stress S11, peeling stress S22 and sheer stress S12 are recorded in the adhesive under a displacement of 4 mm. Figure 4 gives the evolution of the S12 in the adhesive along of the superposition length.

These curves show a singularity in the two tips of the adhesive. This concentration of the constraints strongly decreases when moving away from the adhesive tips .

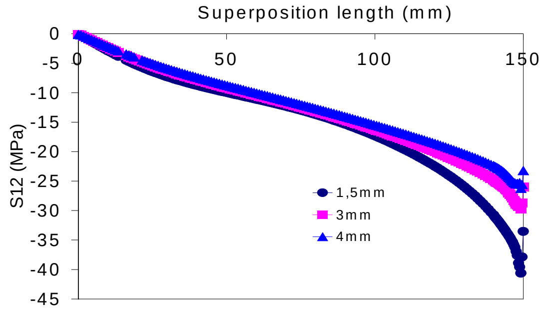

(a)

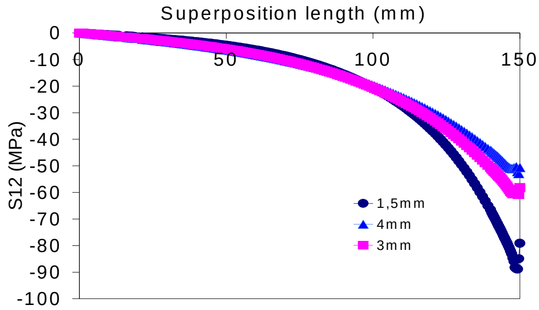

(b)

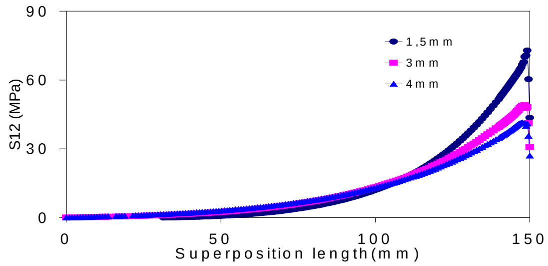

(c)

Figure 4. Evolution of the shear stress S12 for
(a) Three points bending, (b) tension and (c) compression

To study the general behaviour of the structure, we have also recorded the Von- Mises maximum stresses in the adhesive and in the whole structure.

Figure 5 shows the thickness effect on Von Mises maximum stress. The optimum thickness is localised between 3 mm and 3.5 mm. For that, the next section is done with 3mm adhesive thickness.

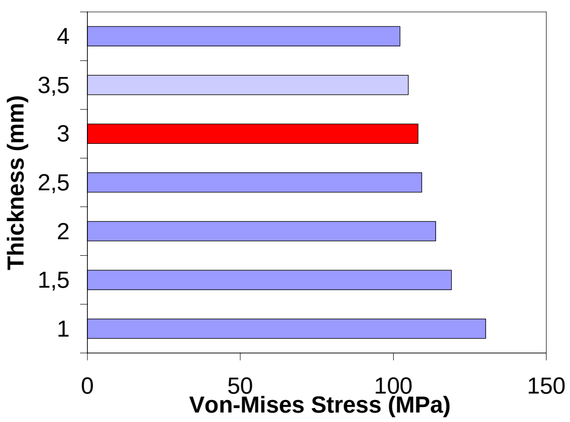

(a) Three points bending

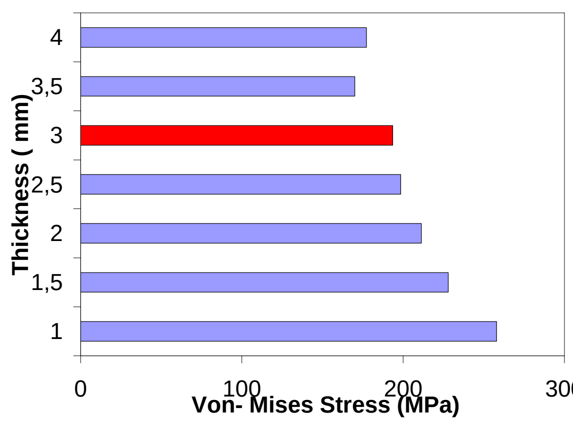

(b) Tension

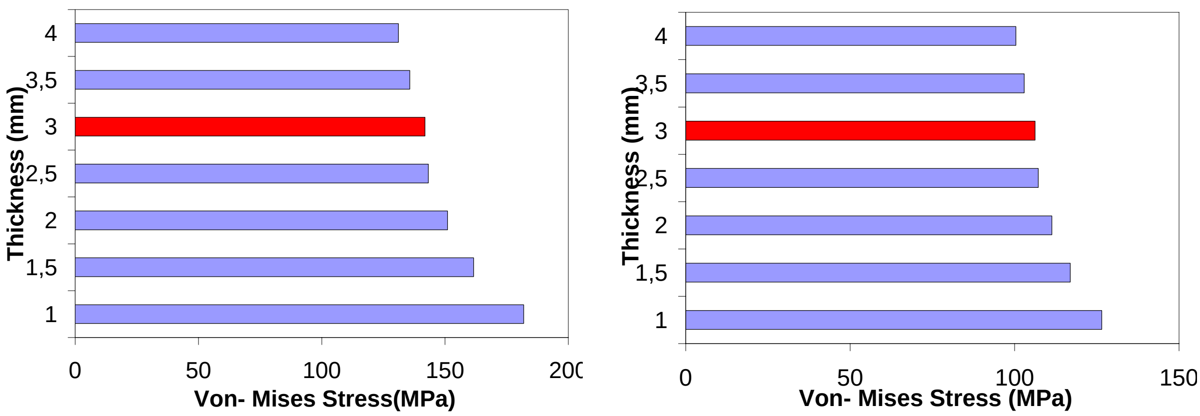

(c) Compression *(d) Three points reversed bending*

Figure 5. Von -Mises maximum stress in the adhesive for different thickness

5. SUPERPOSITION LENGTH

To find the adequate joining length, we change the adhesive length and we keep the other parameters fixed. The same symmetric model and the same properties of materials were kept.

The stresses increase with the increase of the superposition length of the joint (compression, traction), figure 6. In the case of three points deflexion tests, the stress level increase with the increase of the superposition length up to a value L = 300mm. Below this value, if we continue to increase the adhesive length, the stresses start to decrease up to a certain value corresponding to a length which we cannot exceed because of the geometry and the boundary conditions, Figure 7.

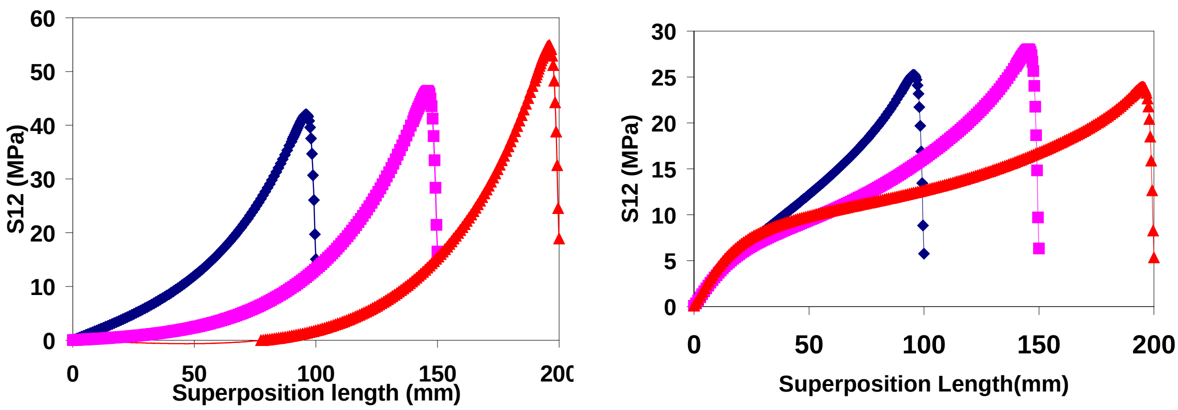

(a) Compression *(b) Three points reversed bending*

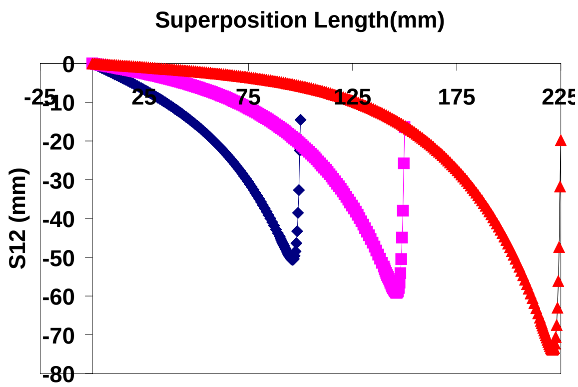

(c) Tension

Figure 6. Shear stress versus superposition length

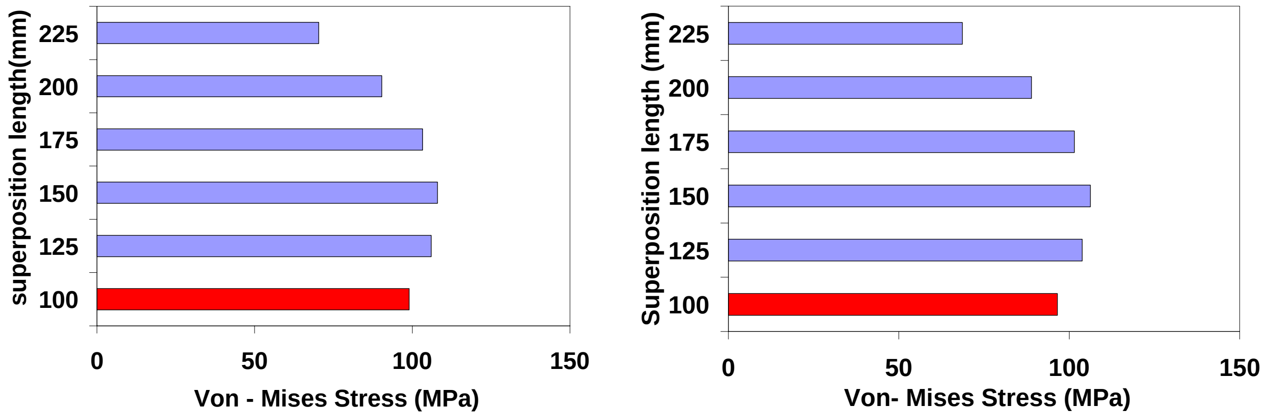

(a) three points de deflexion

(b) Three reversed points of deflexion

Figure 7. Von- Mises maximum stress versus superposition length

From these results, we have choose L=200 mm.this adhesive length give a compromise between the various results obtained under the four loading types. We could not choose a length up de 300 mm because it does not show a good behaviour under a tension and compression tests.

6. COMPARISON OF VARIOUS ASSEMBLIES

The naval structure which we study is made in composite materials; therefore it is important for us to know if the adhesive shows a good mechanical behaviour in composite structures.

The materials used in the numerical calculations are aluminium, composite and steel. Araldite 2015 is used like adhesive. Table 2 gives the mechanical properties of these materials.

The adhesive parameters of this section are:

- 3 mm thickness
- 200 mm superposition length

Mechanical proprieties	**Composite**
E_1 (MPa)	22000
E_2 (MPa)	22000
E_3 (MPa)	8900
υ_{12}	0.27
υ_{13}	0.38
υ_{23}	0.38
G_{12} (MPa)	5300
G_{13} (MPa)	3170
G_{23} (MPa)	3170

Mechanical proprieties	**Material**		
	Alu	**Steel**	**Araldite 2015**
E	70000	205000	2000
υ	0.34	0.3	0.277

Table 2. Material Proprieties used in FEA

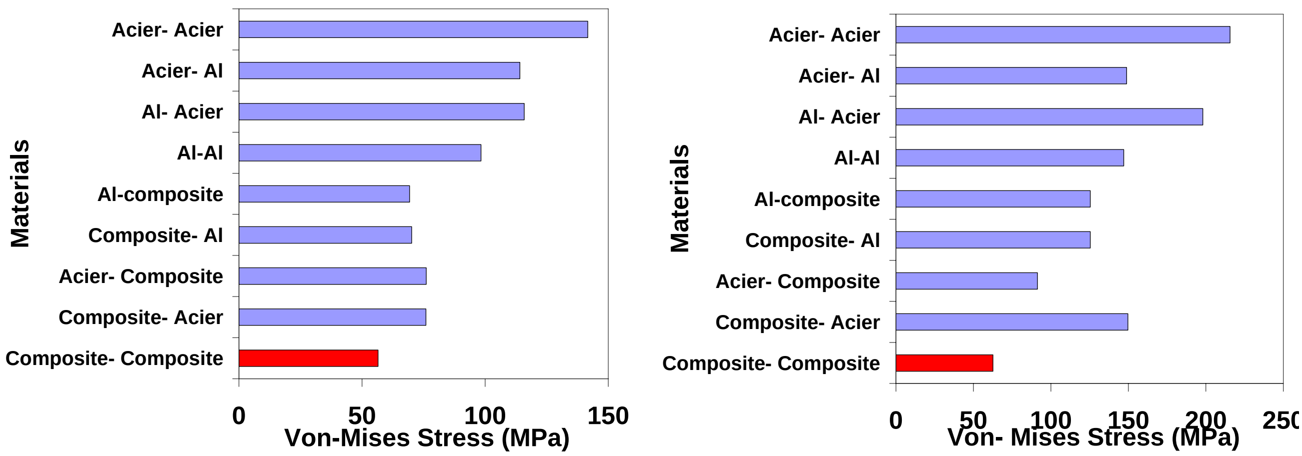

(a) Three points bending *(b) Tension*

Figure 8. Von- Mises maximum stress versus superposition length

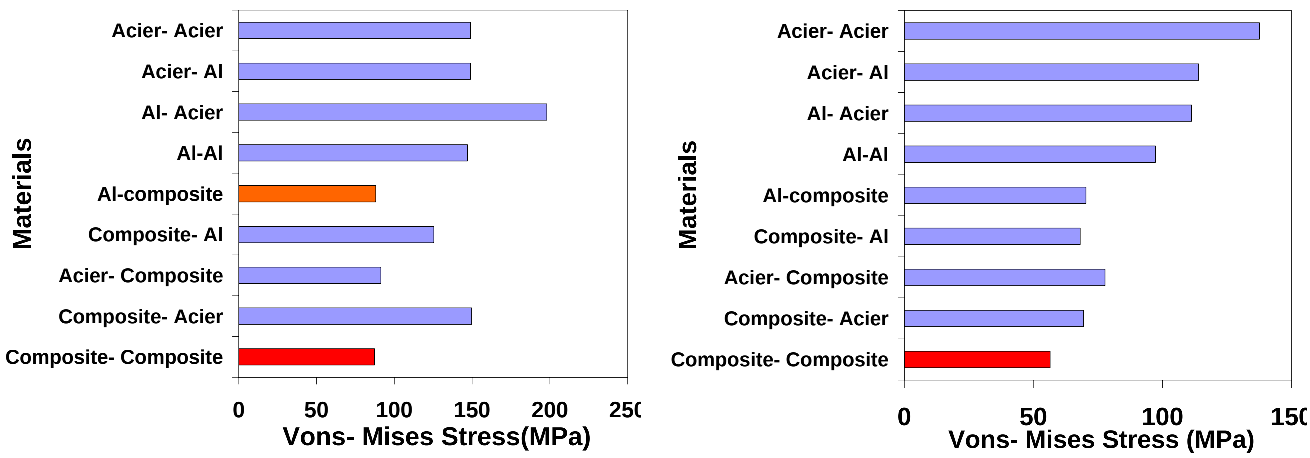

(c) Compression *(d) Three points reversed bending*

Figure 9. Von- Mises maximum stress in the adhesive

The first results show that, for the same loading, the composite assemblies of plates have a better behaviour. The composite adhesive joint shows a lower stress than that of the other assemblies, Figure 8-9.

Figure 8-9 shows that composite/composite adhesive joint gives the better behaviour for the four various loadings. There is always a singularity at the adhesive ends.

7. CONCLUSION

From the FE analyse ,that were carried out to investigate the plates stiffened for naval applications and to replace the traditional method used to assemble the stiffener with the hull (the stratification) by adhesive join, we find that the adhesive thickness(base epoxy) have not important effect on the Maximal level of Von-Mises stress. These results that we have had is similar that of Davies [3]. An adhesive superposition length of 200(mm) was selected. We can select a superposition length up de 300 mm but it does not show a good behaviour under a tension and compression loading.

From the two party 1 and 2 we can say that:

- the optimal thickness is between 3 and 3.5 mm
- the optimal length is of 200 mm
- The composite joint shows a better behaviour than the steel and the aluminium assembly.
- A stress singularity at the adhesive tips.
- We have the minimal Von-Mises stress level in the stiffener structure of Composite – Composite fig 8.

REFERENCES

1. S.A. Hashim, Adhesives bonding of thick steel adherents for marine structures, Marine Structures 12(1999) 405-423.
2. Brian G. Falzon, G.A.O. Davies, The behaviour of compressively loaded stiffener runout specimens, Parts I: experiments, London, 2002.

3. Brian G. Falzon, D. Hitchings, The behaviour of compressively loaded stiffener runout specimens, Parts II: experiments, London, 2002.
4. P.Davies, P.Parneix, D.Choqueuse, B.Bigoudan, C.Gauthier, R. Joannic and J. L'Hostis, Design, manufacturing and testing of stiffened panels for marine structures using adhesively bonded pultruded sections, Plouzané, france.
5. Cui, w., Wisnom, M.R. and Jones, M.I. (1994).Effect of Through Thickness Tensile and Compressive Stress on Delamination Propagation Fracture Energy, Journal of Composite Technology and Research, 16(4): 329-335.

SIMULATION OF PROPELLER-SHIP HULL INTERACTION USING AN INTEGRATED VLM/RANSE SOLVER MODELING.

M.N.Senthil Prakash, Department of Ocean Engineering, IIT Madras, India

V. Anantha Subramanian Department of Ocean Engineering, IIT Madras, India

SUMMARY

The objective of this work is to simulate propeller-hull interaction effects. The methodology involves coupling a Vortex Lattice Method (VLM) with a RANSE solver. The VLM code generates the propeller forces based on the inputs of required thrust and rpm. The obtained propeller forces are distributed in the domain at the cell centroids which lie close to the blade coordinates. Introducing the body forces into the fluid domain, emulates the propeller action in the field of flow with consequent influences on the flow kinematics. This approach enables to ultimately quantify the propeller performance in the realistic environment around the ship hull, fully accounting for the effective wake conditions. The coupling of the two methods therefore gives a combined numerical design and analysis tool. The approach is illustrated in the case of a high speed craft.

INTRODUCTION

The quantification of the performance of the propeller working in the vicinity of a ship hull is traditionally done through physical modeling by means of self propulsion tests. In recent years there has been steady progress in the use of numerical hydrodynamic tools (CFD) to simulate the flow past ships without and with the influence of propellers. The numerical simulation of a rotating propeller in the vicinity of the ship is a somewhat complex one. One simplification in the analysis of the above system, is to simulate the presence of the propeller by potential flow based forces in the disk area. Earlier research studies have reported findings on the basis of simplified potential flow based assessment of the kinematics [Simonsen and Stern, 2005].

The Vortex Lattice Method is basically a design tool which permits the iterative evolution of the propeller geometry with optimal pitch and camber, so as to obtain the maximum thrust for given operating conditions. The performance of the propeller is affected by the effective wake, which in itself is the result of the modified wake pattern taking into account the action of the propeller. Therefore, it is necessary to establish the kinematics in detail when the propeller works in its location at the stern of the ship. A recent research effort [Karl and Chao, 2005] has reported the introduction of propeller body forces as average in successive concentric paths traced out by multiple cells. By combining the VLM method with the numerical simulation using FLUENT, it is therefore possible to combine the design and analysis towards optimum propeller design. The present work adopts an approach whereby the cell-centered body forces are introduced into the centre coordinates of the cells in the location of the propeller at the disk and the disk is rotated at the propeller rpm. The different modules in the approach are described below.

THE VORTEX LATTICE METHOD

The Vortex Lattice Method is a lifting surface method which solves for the unsteady potential flow field around a propeller and has been used successfully since the method was first developed [Kerwin and Lee 1978], [Lee 1979] and [Breslin et al. 1982]. The force distribution over the blade can be processed either to give an averaged radial distribution of momentum sources or can be interpolated and assigned into the cells of discretized domain which lie closest to the coordinates defining the geometry of the propeller in the domain.

In the vortex lattice method a special arrangement of the line vortex and source lattice is placed on the blade mean camber surface and its trailing wake surface. The singularities that represent the propeller flow are, the vortex lattice on the blade mean camber surface and the trailing wake surface which represents the blade loading and the trailing vorticity in the wake and source lattice on the blade mean camber surface which represents the blade thickness.

The strengths of the singularities which will decide the shape of the propeller and the thrust developed by it, is determined so as to satisfy the kinematic boundary condition that the flow velocity be tangent to the mean camber surface.

PRINCIPAL CHARACTERISTICS OF THE HULL

The main dimensions as well as the characteristics of the propeller are given in Tables 1 and 2 below. The blade characteristics matching to a particular nominal wake condition are also included in Table 3 below.

Table 1 Particulars of ship

Particulars of the ship	Dimension
LENGTH OVER ALL	49.91m
LENGTH (LWL).	48.14m
BREADTH	11.00m
DEPTH AT CL	3.80m
DRAUGHT	2.90m
DISPLACEMENT	1042 t
No. of propellers	2
Resistance (kN)	79
Speed (knots)	12 (high speed displacement hull, Fn=0.28
Effective wake fraction	0.21
Thrust deduction fraction	0.2

Table 2 Propeller geometry details

Item	Value
Diameter	2m
Hub Diameter	0.4m
Number of blades	4
RPM	237
A_E/A_O	0.55
Kt	0.206
J	0.62
Thrust	52709 N

Table 3 Particulars of propeller geometry

Blade particulars matching to nominal wake						
Non dimensional radius R/RO	Pitch to dia ratio P/D	Rake X_s/D	Skew	Chord to dia ratio C/D	Max Camber to chord ratio F_O/C	Max thickness to dia ratio T_O/D
0.2	0.7612	0	0	0.2285	-0.0171	0.0403
0.25	0.9553	0	0	0.2437	0.0161	0.038
0.3	1.066	0	0	0.2588	0.0304	0.0357
0.4	1.095	0	0	0.2819	0.0306	0.031
0.5	1.069	0	0	0.2959	0.0272	0.0264
0.6	1.0588	0	0	0.3007	0.025	0.0218
0.7	1.0513	0	0	0.2948	0.025	0.0172
0.8	1.0511	0	0	0.2709	0.0249	0.0154
0.9	1.0443	0	0	0.2175	0.0278	0.0079
0.95	1.0361	0	0	0.175	0.0292	0.0056
1	1.0232	0	0	0	0.0374	0.0033

THE COMPUTATIONAL METHOD

The solver in which the propeller is applied as a body force term is the commercial software FLUENT which solves the continuity and unsteady incompressible RANS equations. For turbulence modeling, the Shear Stress Transport (SST) k-ω model was used. This model is an effective blend of the $k-\omega$ model in the near-wall region with $k-\varepsilon$ model in the far field free-stream domain. The definition of the turbulent viscosity is modified to account for the transport of the turbulent shear stress.

METHODOLOGY OF IMPLEMENTING THE USER DEFINED FUNCTION (UDF)

The user-defined function (UDF) is dynamically loaded with the FLUENT solver to enhance the standard features of the code. It helps in customizing FLUENT to fit particular modeling needs such as customization of boundary conditions, material property definitions, surface and volume reaction rates, source terms in FLUENT transport equations, source terms in user-defined scalar (UDS) transport equations, or execution upon loading of a compiled UDF library, post-processing enhancement, etc.

The domain is split to separate a cylindrical domain which is swept by the propeller blade to avoid handling large number of cell coordinates of the total domain. The UDF thread stores the coordinates of all the cell centroids in the cylindrical domain. The data file containing the coordinates of the panels on the blade shape and corresponding propeller forces are read and stored . The cell centroids in the domain, which are closest to the paneled blade coordinates, are determined by comparing the distance between the panel coordinates and the coordinates of the cell centroids around it. If one or more panels has the same cell centroids closest to it, the forces are added and assigned to these cells. The volume of all cells to which the forces need to assigned are also extracted and the forces are divided with the corresponding cell volume to obtain propeller force density. The propeller forces thus assigned at the cell centroids are treated as body force terms during the solution of the momentum equation. Once the cell centroid coordinates and the body forces are finalized the same is stored in User defined memory in FLUENT to avoid running a centroid search algorithm at each step of the iteration. The Body forces are in put into the cells by reading the UDF in the momentum source panel in FLUENT.

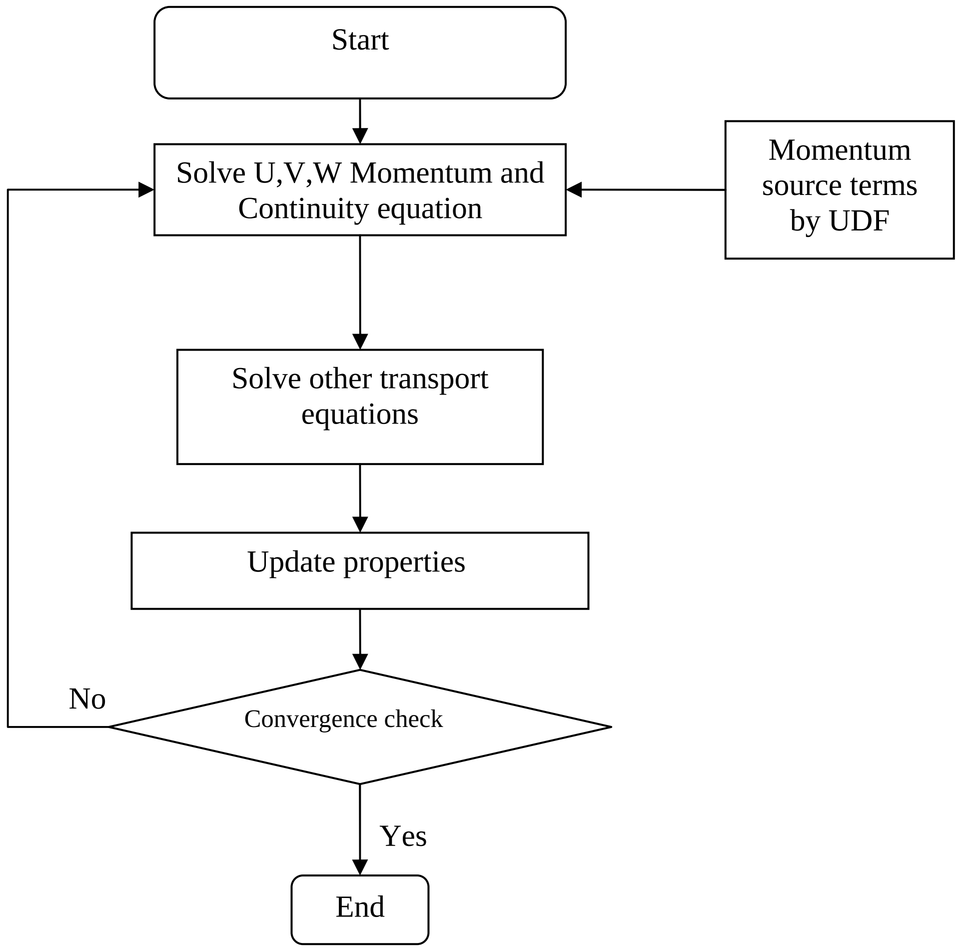

Fig 1. The schematic of RANSE solver including UDF

SETTINGS FOR FLUENT

Computational Domain And Grid System

Based on grid convergence studies, the computational domain was chosen with length of the domain upstream of the hull being 0.8 Lpp, down stream being 1.2 Lpp, width and depth being 0.8Lpp. Block structured hexahedral grid was used for the domain descretization. The final convergence was decided by the residual-source criterion. The residual parameters were set a value of 10^{-4}.

For initialization in general, all the flow variables could be set to zero values and the simulations expected to converge towards steady state. The gridded domain was marked and separated in order to demarcate water and air regions as separate entities, and the regions patched and allocated appropriate volume fraction values. In order to initialize, the Z-component (along the length) velocity at air and water inlet were set to free stream velocity of 6.1728 m/s at the start of computations and all other variables set to zero. The UDF was interpreted and the source terms added.

The boundary conditions were set with velocity inlet of 6.1728 m/s at the domain inlet, velocity inlet with negative free stream velocity(-6.1728) at domain outlet, wall with slip and zero shear (at free surface and at the bottom and side wall) and wall with no slip (over hull surface) conditions (Fig.2.).

COMPUTATIONAL GRIDS

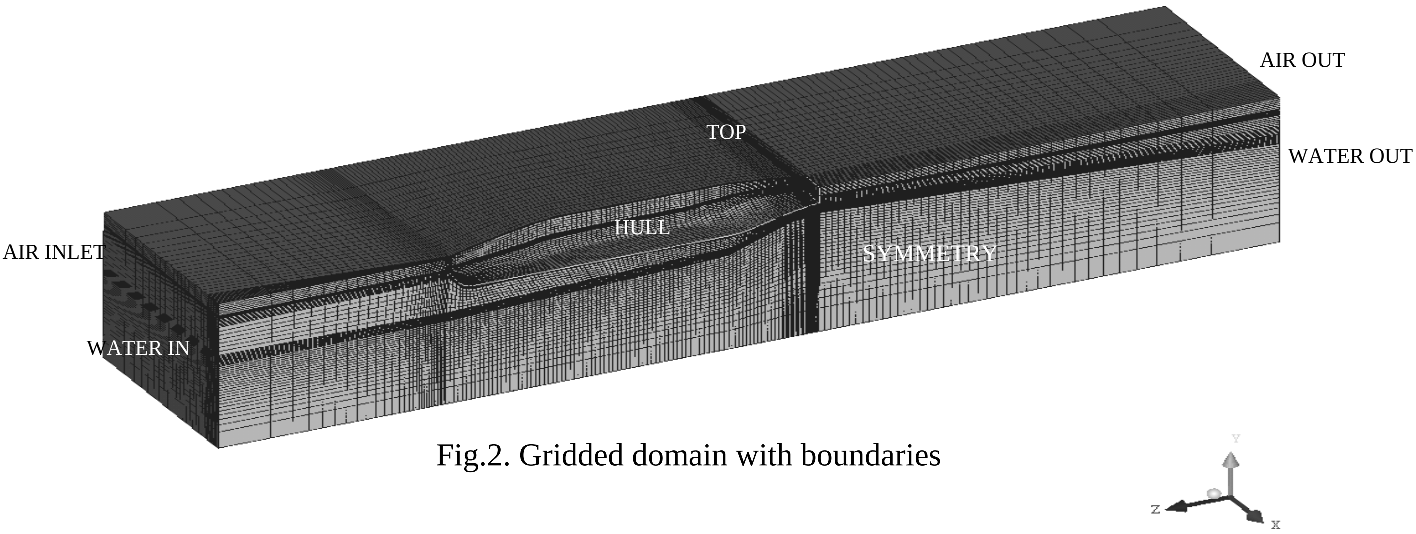

Fig.2. Gridded domain with boundaries

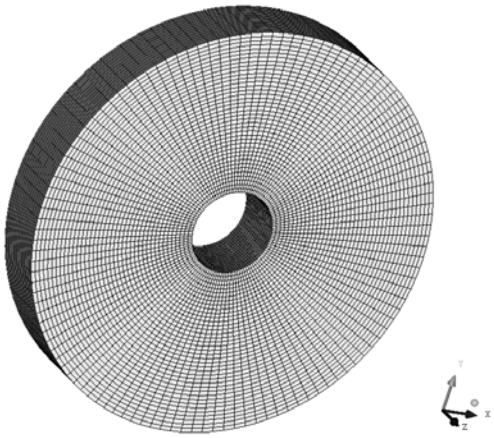

Fig.3. Domain representing the propeller swept volume

Fine meshes could be used to represent the cylinder representing the propeller swept volume by O grids thereby avoiding the task of girding the complicated geometry of the actual propeller blades, see Fig.3. The hull was meshed with O-grid to capture the frictional resistance and thus to get the hull resistance effectively. Block structured multi- block grids in ANSYS ICEM CFD was used to generate numeric grids in the domain.

Table 4. Solver parameters used for simulations

Parameter	Setting
Solver	3D Segregated, Unsteady, Implicit
Velocity formulation	Absolute
Viscous model	SST $k-\omega$
Pressure-velocity coupling	PISO (Pressure Implicit with Splitting of Operators)
Pressure discretization	Body force weighted
Momentum, turbulent kinetic energy and energy dissipation rate discretization	Second order upwind scheme
Hull and, top and bottom boundary conditions	Wall (no slip), Wall (allows slip)
Free surface model	Volume of Fluid with Geo-Reconstruct
Air and water Inlet boundary conditions	Velocity Inlet : Free stream velocity
Air and water outlet boundary conditions	Velocity Inlet : Free stream velocity(negative)

RESULTS AND DISCUSSION

The numerical scheme incorporating the VLM based propeller design and forces estimation has been successfully linked with the FLUENT analysis module by inputting the forces in cell centred co-ordinate positions using a special user defined function. It has been illustrated in the case of a 12 knots speed (Fn=0.28) displacement vessel. The resulting augumented resistance in the presence of the propeller action has been quantified and it gives a realistic thrust deduction fraction of 0.12. Similerly hull resistance without propeller action has been matched with towing tank tests.The contours of the three components of velocities, pressure contours and wake fractions have been obtained and presented here. Comparisons with published data establish that the pattern of distribution of the above parameters are well along the acceptable distributions. By incorporating a moving reference frame for the propeller disk which contains the propeller body forces, the method evolves a time efficient computational effort in obtaining the dynamics and associated kinematics of the propeller-ship interaction. In principle, the method can be extended to a combination of design and evaluation and improvement of the propeller for optimum performance.

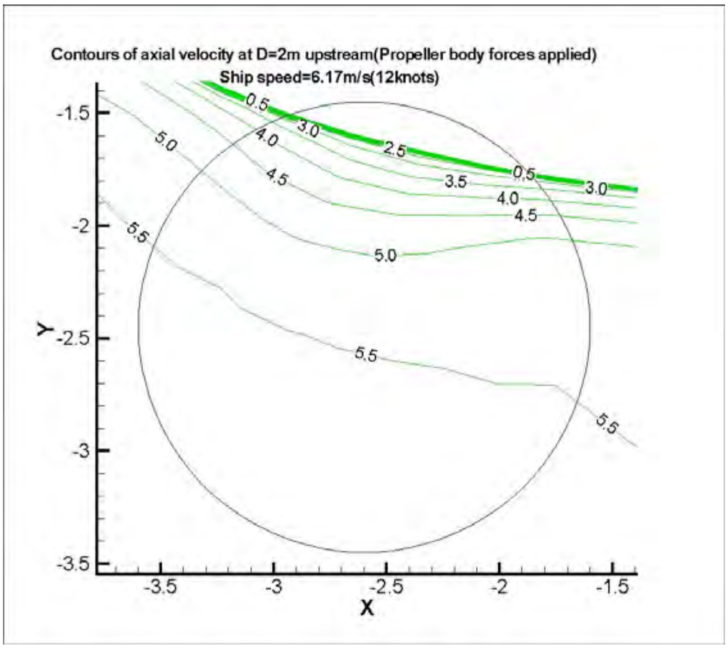

Fig.4.Contours of axial velocity component at propeller diameter D=2m upstream with the propeller body forces applied.

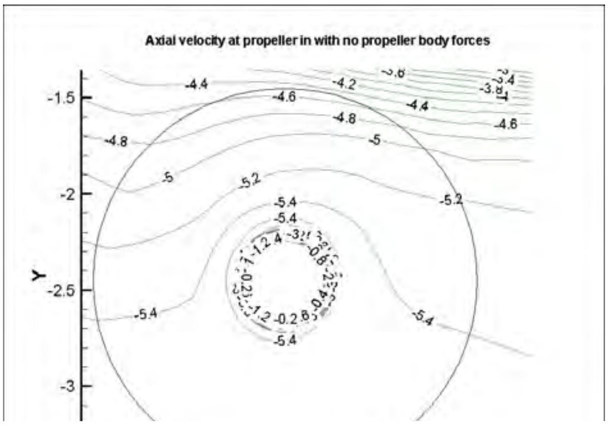

Contours of axial velocity component at propeller inlet with no propeller body forces applied.

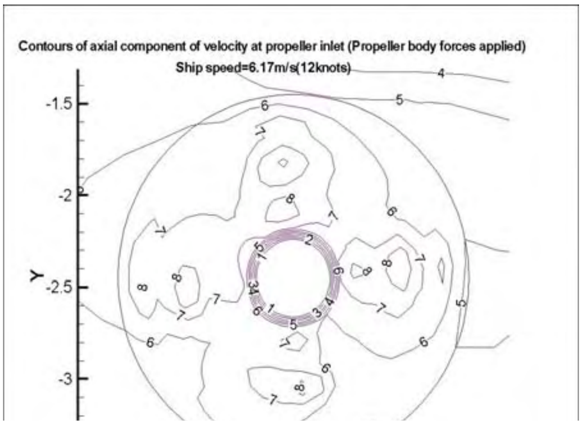

Contours of axial velocity component at propeller inlet with propeller body forces applied.

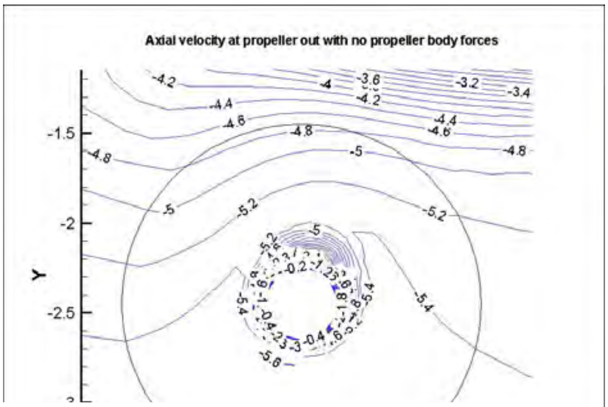

Contours of axial velocity component at propeller outlet with no propeller body forces applied.

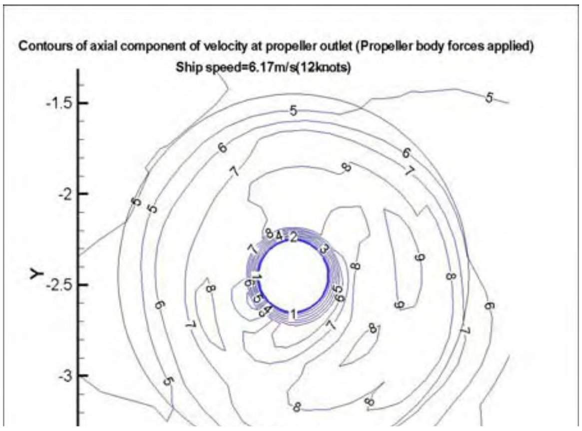

Contours of axial velocity component at propeller outlet with propeller body forces applied.

Fig.5.Comparison of Contours of axial component of velocity

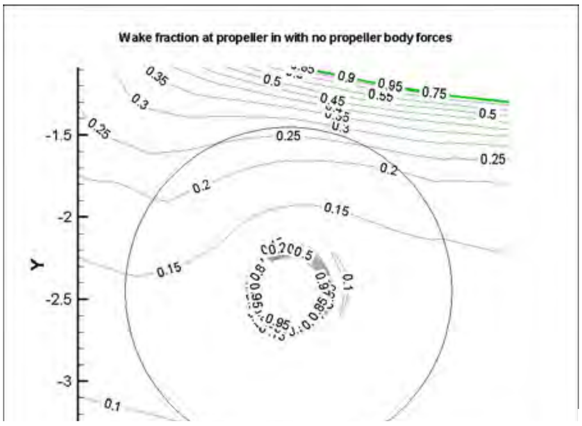

Contours of wake fraction at propeller inlet with no propeller body forces applied.

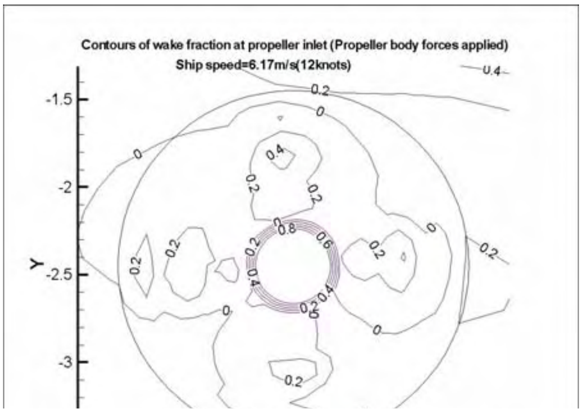

Contours of wake fraction at propeller inlet with propeller body forces applied.

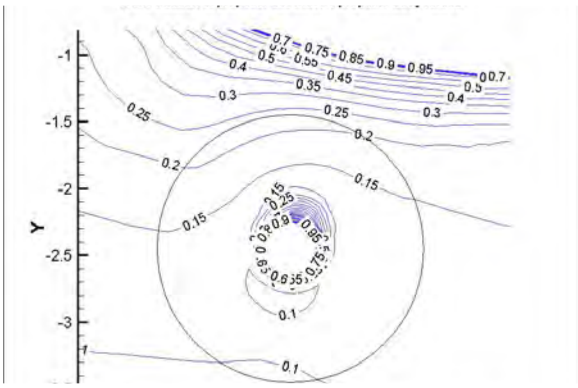

Contours of wake fraction at propeller outlet with no propeller body forces applied.

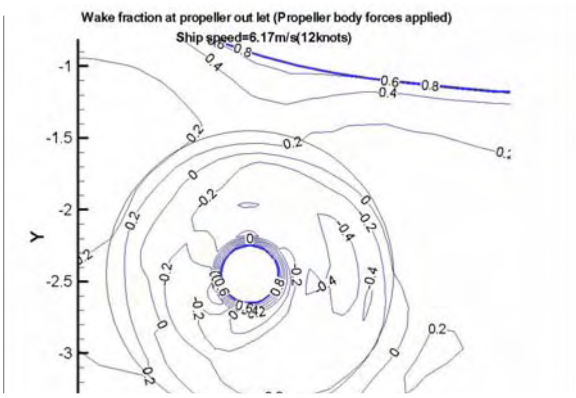

Contours of wake fraction at propeller outlet with propeller body forces applied.

Fig.6.Comparison of contours of wake fraction

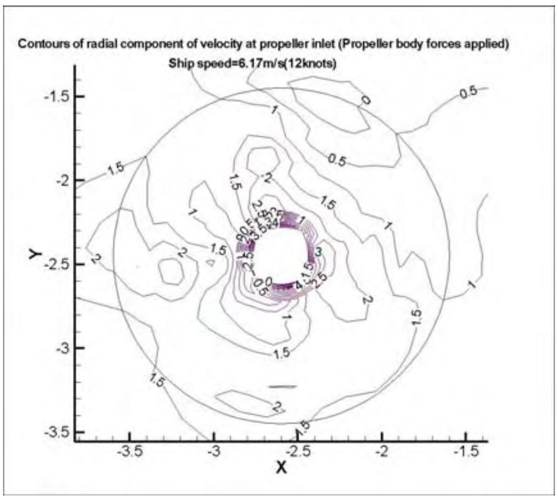

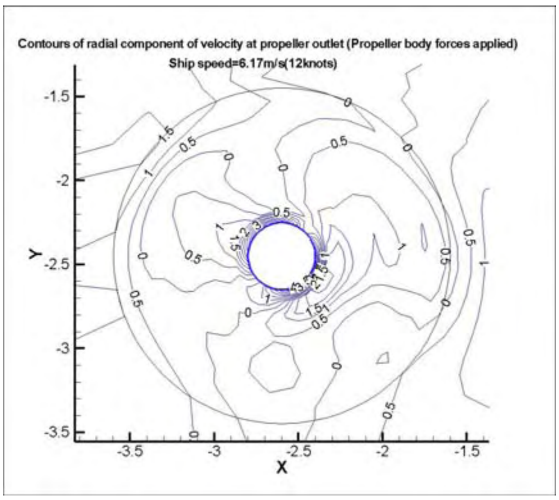

At propeller inlet At propeller outlet

Fig.7.Contours of radial velocity component with propeller body forces applied.

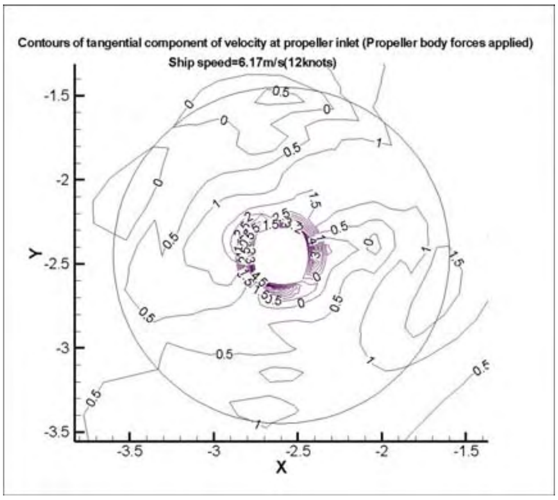

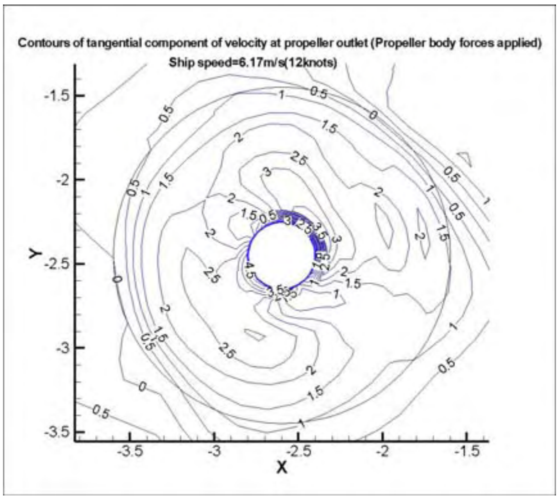

At propeller inlet At propeller outlet

Fig.8.Contours of tangential velocity component with propeller body forces applied.

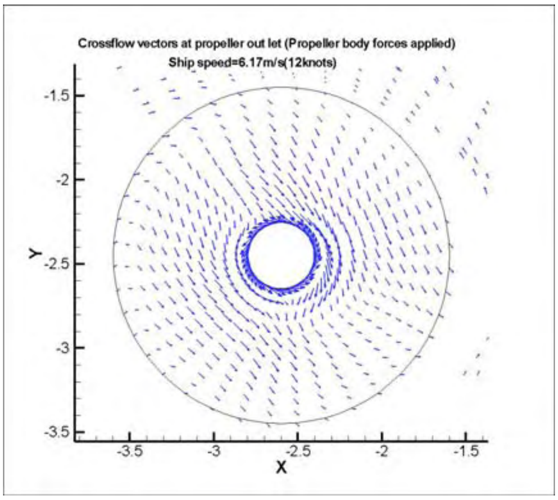

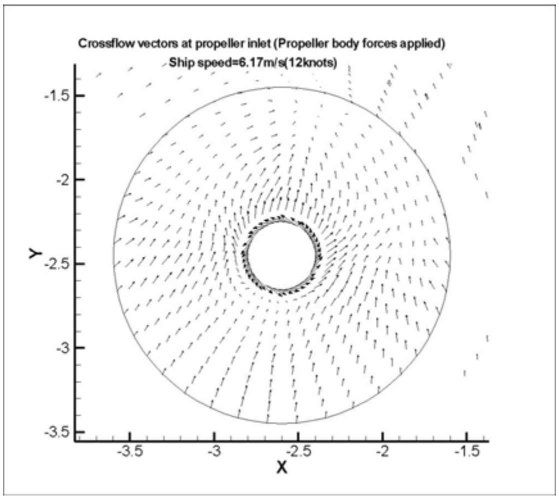

At propeller inlet At propeller outlet

Fig.9.Cross flow vectors with propeller body forces applied.

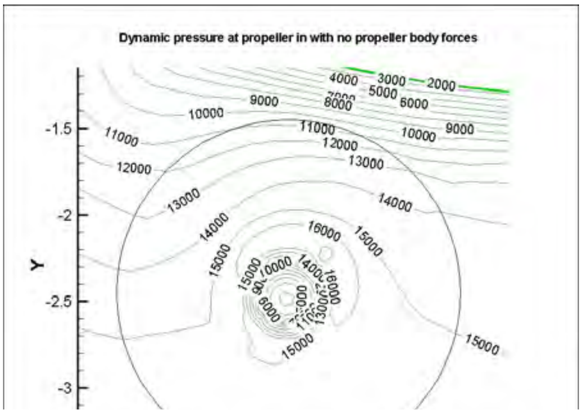

Contours of Dynamic pressure at propeller inlet with no propeller body forces applied.

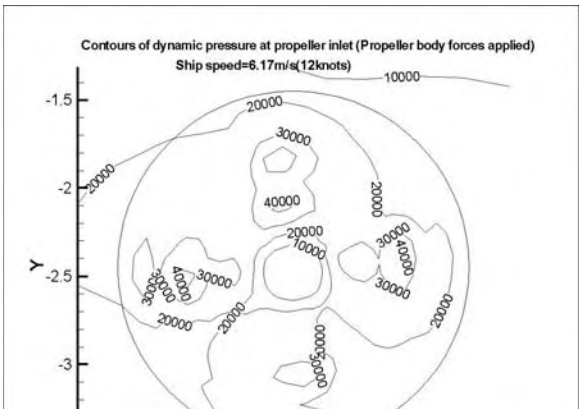

Contours of Dynamic pressure at propeller inlet with propeller body forces applied.

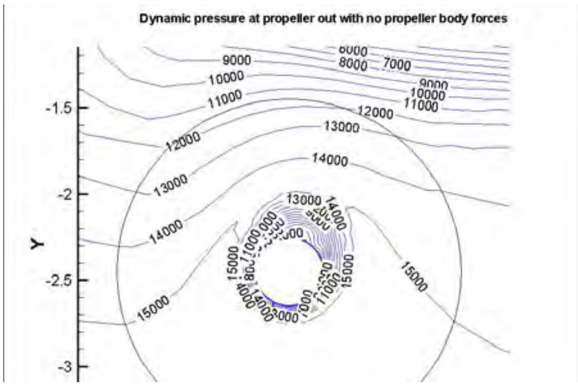

Contours of Dynamic pressure at propeller outlet with no propeller body forces applied.

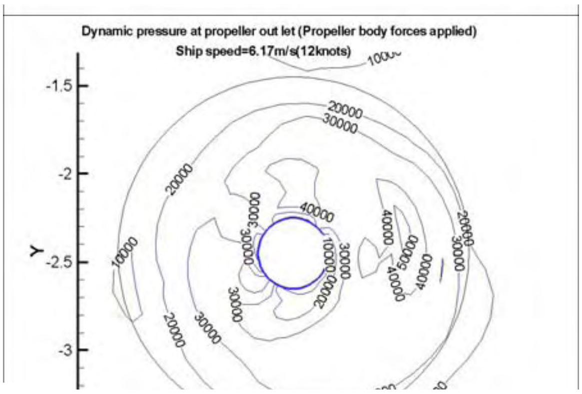

Contours of Dynamic pressure at propeller outlet with propeller body forces applied.

Fig.10.Comparison of contours of Dynamic pressure

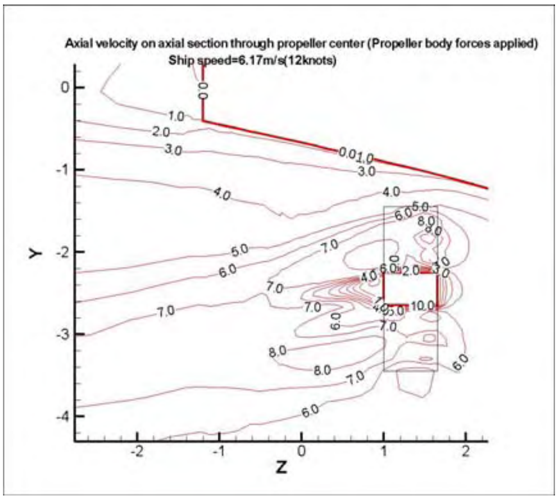

Contours of axial velocity

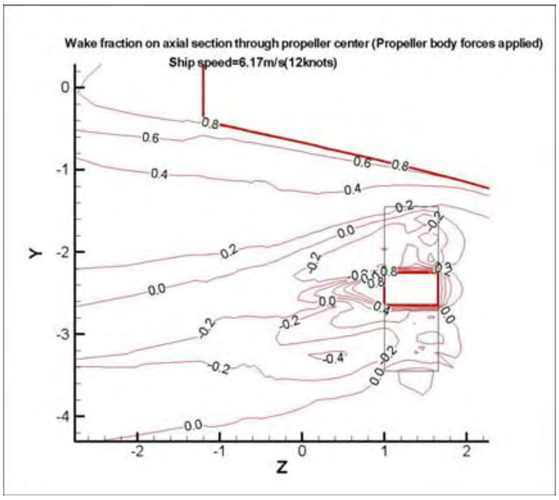

Contours of wake fraction

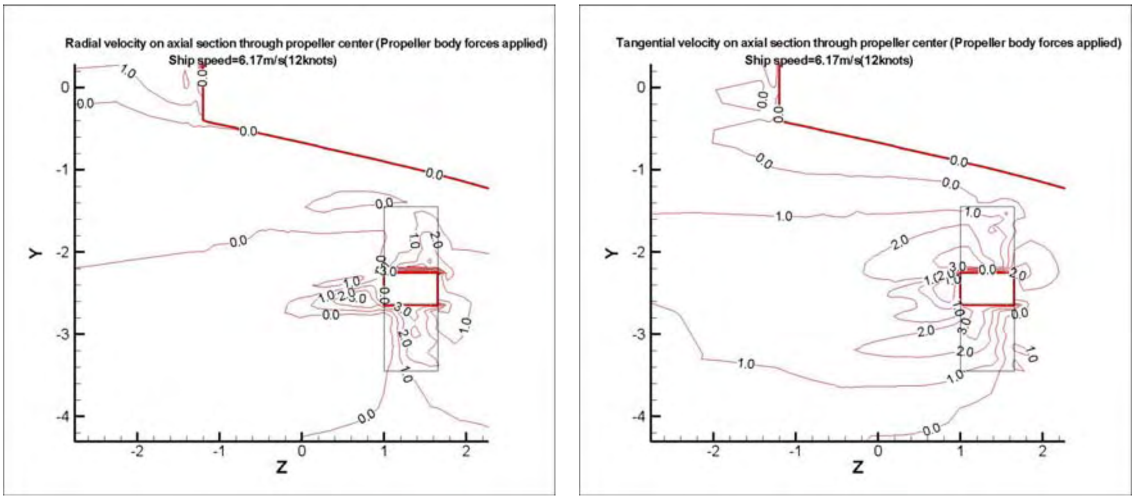

Contours of Radial velocity

Contours of tangential velocity

Fig.11.Contours of Kinematic properties on an axial section through propeller center with propeller body forces applied.

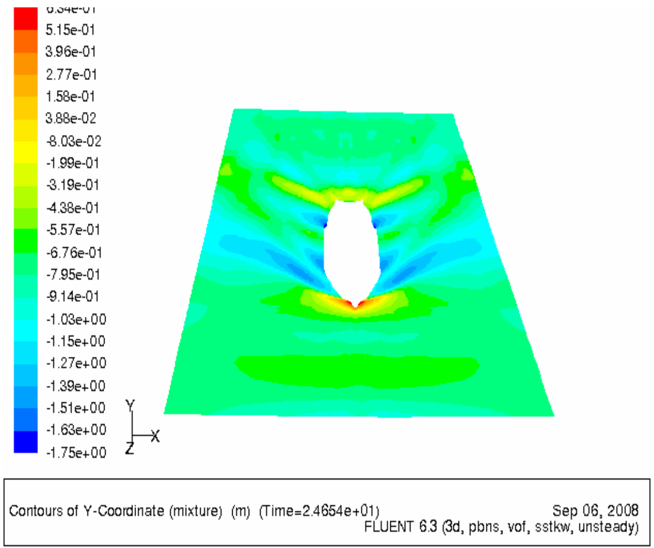

Fig.12.Contours of free surface elevation with propeller body forces applied

REFERENCES

1) **Simonsen, C. D.** and **Stern, F. (2005)** RANS Maneuvering Simulation of Esso Osaka with Rudder and a Body-Force Propeller. Journal Ship Research, Vol. 49, No. 2, pp. 98-120.

2)**.Tahara, Y., Wilson, R**., and **Carrica, P., (2005)**, “Comparison of free-surface capturing and tracking approaches to modern container ship and prognosis for extension to self-propulsion simulator”, *Proceedings, CFD workshop Tokyo 2005, 548-555*.

3).**Karl, Y., Chao**., and **Carrica, P., (2005)**, “Numeric propulsion for the KCS container ship, *Proceedings, CFD workshop Tokyo 2005, 483-489*.

4).**FLUENT 6.2** User’s Guide, Copyright Fluent Incorporate, 2006

5)**.Kerwin, J. E. (1984),** A vortex lattice method for propeller blade design, MIT PBD-10 users manual, Massachusetts institute of technology.

6)**Olsen, A. (2001)** Optimization of propellers using Vortex lattice method, PhD thesis, Denmark technical university.

7).**Kerwin, J. E.,Lee,C**.S. (1984),"Prediction of steady and unsteady marine propeller performance by numerical lifting surface theory "SNAME Transactions,Vol.86,1978,pp.218-253.